

**AD-A229 586**

**MATERIALS  
RESEARCH  
SOCIETY**  
SYMPOSIUM PROCEEDINGS

**VOLUME 151**

**Growth, Characterization  
and Properties of  
Ultrathin Magnetic Films  
and Multilayers**

**EDITORS**

**Berend T. Jonker  
Joseph P. Heremans  
Ernesto L. Marinaro**

**DTIC FILE COPY**

**DTIC**  
**ELECTE**  
**NOV 15 1990**  
**E**

**DISTRIBUTION STATEMENT A**

Approved for public release;  
Distribution Unlimited

①

# Growth, Characterization and Properties of Ultrathin Magnetic Films and Multilayers



Distribution For	
DTIC GRA&I	<input checked="checked" type="checkbox"/>
NO TAB	<input checked="checked" type="checkbox"/>
Unprocessed	<input type="checkbox"/>
Classification	
Distribution/	
Availability Codes	
First	Avail and/or Special
A-1	

DTIC  
ELECTE  
NOV 15 1990  
S E D

90 11 15 122

<b>DISTRIBUTION STATEMENT A</b>
Approved for public release; Distribution Unlimited

REPORT DOCUMENTATION PAGE			Form Approved OMB No. 0704-0188	
<small>Public reporting burden for this collection of information is estimated to average 1 hour per response, including the time for reviewing instructions, searching existing data sources, gathering and maintaining the data needed, and completing and reviewing the collection of information. Send comments regarding this burden estimate or any other aspect of this collection of information, including suggestions for reducing this burden, to Washington Headquarters Services, Directorate for Information Operations and Reports, (215) Jefferson Davis Highway, Suite 1204, Arlington, VA 22202-4302, and to the Office of Management and Budget, Paperwork Reduction Project (0704-0188), Washington, DC 20503.</small>				
1. AGENCY USE ONLY (Leave blank)	2. REPORT DATE	3. REPORT TYPE AND DATES COVERED		
		FINAL REPORT 02 May 89-01 May 90		
4. TITLE AND SUBTITLE		5. FUNDING NUMBERS		
1989 Materials Research Society Spring Meeting				
6. AUTHOR(S)		7. PERFORMING ORGANIZATION NAME(S) AND ADDRESS(ES)		
Dr Joan B. Ballance		Materials Research Society 9800 McKnight Road, Suite 327 Pittsburgh Pa 15237-6005		
		AFOSR-TR-90-1000		
8. AUTHOR(S)		9. PERFORMING ORGANIZATION REPORT NUMBER		
10. SPONSORING / MONITORING AGENCY NAME(S) AND ADDRESS(ES)		11. SPONSORING / MONITORING AGENCY REPORT NUMBER		
AFOSR/NE Bldg 410 Bolling AFB DC 20332-6448 Dr Gerald Witt		2305/C1		
12. SUPPLEMENTARY NOTES				
12a. DISTRIBUTION / AVAILABILITY STATEMENT			12b. DISTRIBUTION CODE	
UNLIMITED				
13. ABSTRACT (Maximum 200 words)				
<p>CONFERENCE WAS HELD</p> <p>(148) Chemistry and Defects in Semiconductors Heterostructures</p> <p>(151) Growth, Characterization and Properties of Ultrathin Magnetic Films and Multilayers</p>				
14. SUBJECT TERMS			15. NUMBER OF PAGES	
16. PRICE CODE			17. SECURITY CLASSIFICATION OF REPORT	
			UNCLASSIFIED	
18. SECURITY CLASSIFICATION OF THIS PAGE		19. SECURITY CLASSIFICATION OF ABSTRACT		20. LIMITATION OF ABSTRACT
UNCLASSIFIED		UNCLASSIFIED		UNLIMITED

# Growth, Characterization and Properties of Ultrathin Magnetic Films and Multilayers

Symposium held April 25-28, 1989, San Diego, California, U.S.A.

EDITORS:

**Berend T. Jonker**

Naval Research Laboratory, Washington, District of Columbia, U.S.A.

**Joseph P. Heremans**

GM Research Laboratories, Warren, Michigan, U.S.A.

**Ernesto E. Marinero**

IBM Almaden Research Center, San Jose, California, U.S.A.



**MATERIALS RESEARCH SOCIETY**  
Pittsburgh, Pennsylvania



This work was supported in part by the Office of Naval Research under Grant Number N00014-88-J-1710. The United States Government has a royalty-free license throughout the world in all copyrightable material contained herein.

This work was supported by the Air Force Office of Scientific Research, Air Force Systems Command, USAF, under Grant Number AFOSR 89-0388.

This work was supported in part by the U.S. Army Research Office under Grant Number DAAL03-89-G-0024. The views, opinions, and/or findings contained in this report are those of the authors and should not be construed as an official Department of the Army position, policy, or decision unless so designated by other documentation.

CODEN: MRSPDH

Copyright 1989 by Materials Research Society.  
All rights reserved.

This book has been registered with Copyright Clearance Center, Inc. For further information, please contact the Copyright Clearance Center, Salem, Massachusetts.

Published by:

Materials Research Society  
9800 McKnight Road  
Pittsburgh, Pennsylvania 15237  
Telephone (412) 367-3003

Library of Congress Cataloging in Publication Data

Materials Research Society, Symposium G (1989 : San Diego, Calif.)

Growth, characterization, and properties of ultra-thin magnetic films and multilayers / editors, Berend T. Jonker, Joseph P. Heremans, Ernesto E. Marinero.

p. cm. — (Materials Research Society symposium proceedings : ISSN 0272-9172 ; v. 151)

Bibliography: p.

Includes indexes.

ISBN 1-55899-024-0

1. Thin films, Multilayered—Magnetic properties—Congresses. 2. Magnetic films—Congresses. 3. Epitaxy—Congresses. 4. Superlattices as materials—Congresses. I. Jonker, Berend Thomas. II. Heremans, Joseph P. III. Marinero, Ernesto E. IV. Materials Research Society. V. Title. VI. Series: Materials Research Society.

QC176.9.M84M37 1989  
621.381'52

89-12552  
CIP

Manufactured in the United States of America

## Contents

PREFACE	ix
*TEMPERATURE DEPENDENCE OF TWO-DIMENSIONAL SPIN ANISOTROPIES Roy Richter and Jack G. Gay	3
Fe-Ag SUPERLATTICES BY MOLECULAR BEAM EPITAXY S.H. Mayer, C.J. Gutierrez, and J.C. Walker	11
VARIATIONS IN MAGNETIC HYPERFINE FIELDS FOR THIN EPITAXIAL HETEROSTRUCTURES OF (110)Fe ON (111)Ag C.J. Gutierrez, S.H. Mayer, Z.Q. Qiu, H. Tang, and J.C. Walker	17
MAGNETIC RESONANCE STUDIES OF Fe/Ag SUPERLATTICES WITH Fe LAYERS < 6 MONOLAYERS THICK J.J. Krebs, B.T. Jonker, and G.A. Prinz	23
MAGNETIC AND CRYSTALLOGRAPHIC INTERACTIONS OF ALTERNATELY DEPOSITED Fe and Al ULTRA-THIN LAYERS M. Nagakubo, T. Yamamoto, and M. Naoe	29
CALCULATION OF MAGNETIZATION PROCESSES IN MULTILAYERS WITH ANTIFERROMAGNETIC COUPLING BETWEEN ADJACENT LAYERS B. Dieny, J.P. Gavigan, and J.P. Rebouillat	35
GIANT MAGNETORESISTANCE OF (001)Fe/(001)Cr SUPERLATTICES A. Barthelemy, M.N. Baibich, J.M. Broto, R. Cabanel, G. Creuzet, P. Etienne, A. Fert, A. Friederich, S. Lequien, F. Nguyen Van Dau, and K. Ounadjela	43
*MAGNETIC MICROSTRUCTURE OF THIN FILMS AND SURFACES: EXPLOITING SPIN-POLARIZED ELECTRONS IN THE SEM AND STM D.T. Pierce, M.R. Scheinfein, J. Unguris, and R.J. Celotta	49
SPIN POLARIZED INELASTIC ELECTRON SCATTERING FROM Ni (110) H. Hopster, D.L. Abraham, and D.P. Pappas	59
SPIN POLARIZED INVERSE PHOTOEMISSION STUDY OF Fe AND Co THIN FILMS ON W(001) Qing Cai, Recep Avci, and Gerald J. Lapeyre	65
THE D-BAND EXCHANGE SPLITTING FOR THIN GADOLINIUM OVERLAYERS D. LaGrafte, P.A. Dowben, and M. Onellion	71
*MAGNETOMETRY IN ULTRATHIN FILMS USING SPIN POLARIZED CASCADE ELECTRONS Eric Kay	77

\*Invited Paper

*MAGNETIC PROPERTIES OF RARE-EARTH/Fe MULTILAYERED FILMS WITH ARTIFICIAL SUPERSTRUCTURES Teruya Shinjo, Ko Mibu, Shinichi Ogawa, and Nobuyoshi Hosoi	87
GROWTH, CHARACTERIZATION AND MAGNETIC PROPERTIES OF HCP Fe/Ru SUPERLATTICES SYNTHETIZED BY MBE M. Maurer, J.C. Ousset, M. Piecuch, M.F. Ravet, and J.P. Sanchez	99
EFFECT OF ORIENTATION AND MICROSTRUCTURE ON THE MAGNETIC ANISOTROPY OF Co/Pd MULTILAYERS Frits J.A. den Broeder, Dick Kuiper, and Willem Hoving	105
STRUCTURAL AND MAGNETIC PROPERTIES OF EPITAXIAL Co-Au SUPERLATTICES C.H. Lee, Hui He, F. Lamelas, W. Vavra, C. Uher, and Roy Clarke	111
MAGNETIZATION PROCESSES ANALYSIS IN Co-Cu SUPERLATTICES J.P. Rebouillat, G. Fillion, B. Dieny, A. Cebollada, J.M. Gallego, and J.L. Martinez	117
MAGNETIC AND STRUCTURAL STUDIES ON Au/3d-METAL MULTILAYERED FILMS WITH ARTIFICIAL SUPERSTRUCTURES Satoru Araki, Tsutomu Takahata, Hitoshi Dohnomae, Tetsuo Okuyama, and Teruya Shinjo	123
*NOVEL MAGNETIC AND OPTO-ELECTRONIC PHENOMENA IN DILUTED MAGNETIC SEMICONDUCTOR MULTILAYERS J.K. Furdyna and N. Samarth	129
*METASTABLE ZINCBLLENDE MnTe AND MnSe: MBE GROWTH AND CHARACTERIZATION R.L. Gunshor, L.A. Kolodziejski, M. Kobayashi, A.V. Nurmikko, and N. Otsuka	141
*MBE GROWTH AND CHARACTERIZATION OF Fe- AND Co-BASED DILUTED MAGNETIC SEMICONDUCTORS B.T. Jonker, J.J. Krebs, G.A. Prinz, X. Liu, A. Petrou, and L. Salamanca-Young	151
ELECTRON-SPIN POLARIZATION IN TUNNEL JUNCTIONS WITH FERROMAGNETIC EuS BARRIERS Xin Hao, J.S. Moodera, and R. Meservey	167
CARRIER-CONCENTRATION-DEPENDENT MAGNETIC PROPERTIES OF THE DILUTED MAGNETIC SEMICONDUCTOR SnMnTe H.J.M. Swagten, S.J.E.A. Eltink, and W.J.M. deJonge	171
*IN-SITU TECHNIQUES FOR STUDYING EPITAXIALLY GROWN LAYERS AND DETERMINING THEIR MAGNETIC PROPERTIES B. Heinrich, A.S. Arrott, J.F. Cochran, K.B. Urquhart, K. Myrtle, Z. Celinski, and Q.M. Zhong	177
CHARACTERIZATION OF EPITAXIAL Fe ON GaAs(110) BY SCANNING TUNNELING MICROSCOPY R.A. Dragoset, P.N. First, Joseph A. Stroscio, D.T. Pierce, and R.J. Celotta	193

\*Invited Paper

IN-SITU INVESTIGATION OF STRUCTURE AND MAGNETIC PROPERTIES OF THE EPITAXIAL SYSTEM Pd(111)/Fe(110) ON W(110) BY MEANS OF BRILLOUIN SPECTROSCOPY	199
P. Baumgart, B. Hillebrands, J.V. Harzer, and G. Güntherodt	
*STRUCTURAL AND MAGNETIC CHARACTERIZATION OF RARE EARTH AND TRANSITION METAL FILMS GROWN ON EPITAXIAL BUFFER FILMS ON SEMICONDUCTOR SUBSTRATES	203
R.F.C. Farrow, S.S.P. Parkin, V.S. Speriosu, A. Bezingé, and A.P. Segmüller	
MAGNETIC DOMAINS IN EPITAXIAL (100) Fe THIN FILMS	213
Jeffrey M. Florczak, P.J. Ryan, J.N. Kuznia, A.M. Wowchak, P.I. Cohen, R.M. White, G.A. Prinz, and E. Dan Dahlberg	
MAGNETIC ANISOTROPY CONSTANTS OF EPITAXIAL (110) Fe/GaAs FILMS FROM 77K TO 293K STUDIED BY MAGNETO-RESISTANCE	219
Daniel K. Lottis, G.A. Prinz, and E. Dan Dahlberg	
CRITICAL BEHAVIOR OF EPITAXIAL ANTIFERROMAGNETIC INSULATOR FILMS: INTERDIGITAL CAPACITANCE MEASUREMENT OF MAGNETIC SPECIFIC HEAT	225
M. Lui, A.R. King, V. Jaccarino, and G.L. Snider	
*X-RAY SCATTERING STUDIES OF THIN FILMS AND MULTILAYERS	231
G.S. Cargill III	
FERROMAGNETIC AND NUCLEAR MAGNETIC RESONANCE STUDY OF Co/Pd MULTILAYERS	243
H.A.M. de Gronckel, C.H.W. Swuste, K. Kopinga, and W.J.M. deJonge	
EXAFS STUDY OF THE STABILITY OF AMORPHOUS TbFe THIN FILMS	249
Mahesh G. Samant, Ernesto E. Marinero, Clifford Robinson, and G.S. Cargill III	
HREM STRUCTURAL STUDIES OF TbFeCo THIN FILMS	253
Z.G. Li, David J. Smith, and K. Sickafus	
LASER ABLATION DEPOSITION (LAD) OF METALLIC THIN FILMS	259
J.P. Rebouillat, B. Michelutti, Y. Souche, J.P. Gavigan, D. Givord, and A. Lienard	
TIME-DEPENDENT LANDAU-GINZBURG MODELLING OF MAGNETIC INHOMOGENEITIES AND SPIRAL DOMAIN STRUCTURES IN THIN FILMS	265
J.A. Tuszynski	
EXCHANGE ANISOTROPY IN AMORPHOUS/MICROCRYSTALLINE Co-Gd FILMS	271
A.M. Toxen, A. Hopkins, S.B. Hagstrom, and R.M. White	
X-RAY DIFFRACTION STUDY OF RARE EARTH EPITAXIAL STRUCTURES GROWN BY MBE ONTO (111) GaAs	277
W.R. Bennett, R.F.C. Farrow, S.S.P. Parkin, E.E. Marinero, and A.P. Segmüller	

\*Invited Paper

HCP-FCC TRANSITION IN EPITAXIAL Co-Cu SUPERLATTICES F.J. Lamelas, C.H. Lee, Hui He, W. Vavra, and Roy Clarke	283
THIN-FILM $Gd_4Bi_3$ GROWN ON A GLASS SUBSTRATE Kyuya Baba, H. Ishii, I. Yamaguchi, O. Nakamura, and T. Takeda	289
AUTHOR INDEX	295
SUBJECT INDEX	297

## Preface

This volume is a collection of invited and contributed papers presented at the Symposium on Growth, Characterization and Properties of Ultrathin Magnetic Films and Multilayers, held during the Spring Meeting of the Materials Research Society in San Diego, April 25-29, 1989. This symposium comprised 11 invited talks and 42 contributed papers, ran over 3 1/2 days, and provided a unique and interactive forum in which recent advances in low dimensional magnetism, diluted magnetic semiconductors, epitaxial overlayers and the utilization of in-situ and ex-situ techniques to characterize their microstructure, electronic and magnetic properties were discussed.

The study and growth of ultrathin magnetic structures is a rapidly expanding field of materials research whose growth is synergistically driven by an increasing appreciation of the degree to which the magnetic properties depend on interfacial processes, and by the utilization of growth techniques which permit the fabrication of multilayer structures with novel electronic and magnetic properties. Equally important is the fact that atomic level control of the microstructure of these layers offers new opportunities to elucidate the physics of magnetism and to rigorously test theoretical models. (TTZ)

The spirit of the meeting was to bring together a dynamic collection of leading materials scientists from Europe, Japan and the U.S.A., and it is apparent that state-of-the-art growth and characterization techniques are widening our physical understanding of magnetic phenomena at an atomic level.

The views, opinions, and/or findings contained in this report are those of the author(s) and should not be construed as an official position, policy, or decision of the U.S. Government.

It is our pleasure to acknowledge support from the Office of Naval Research, the Air Force Office of Scientific Research, the Army Research Office and the IBM Almaden Research Center.

Berend T. Jonker  
Joseph P. Heremans  
Ernesto E. Marinero

June 1989

---

MATERIALS RESEARCH SOCIETY SYMPOSIUM PROCEEDINGS

---

ISSN 0272 - 9172

- Volume 1—Laser and Electron-Beam Solid Interactions and Materials Processing, J. F. Gibbons, L. D. Hess, T. W. Sigmon, 1981, ISBN 0-444-00595-1
- Volume 2—Defects in Semiconductors, J. Narayan, T. Y. Tan, 1981, ISBN 0-444-00596-X
- Volume 3—Nuclear and Electron Resonance Spectroscopies Applied to Materials Science, E. N. Kaufmann, G. K. Shenoy, 1981, ISBN 0-444-00597-8
- Volume 4—Laser and Electron-Beam Interactions with Solids, B. R. Appleton, G. K. Celler, 1982, ISBN 0-444-00693-1
- Volume 5—Grain Boundaries in Semiconductors, H. J. Leamy, G. E. Pike, C. H. Seager, 1982, ISBN 0-444-00697-4
- Volume 6—Scientific Basis for Nuclear Waste Management IV, S. V. Topp, 1982, ISBN 0-444-00699-0
- Volume 7—Metastable Materials Formation by Ion Implantation, S. T. Picraux, W. J. Choyke, 1982, ISBN 0-444-00692-3
- Volume 8—Rapidly Solidified Amorphous and Crystalline Alloys, B. H. Kear, B. C. Giessen, M. Cohen, 1982, ISBN 0-444-00698-2
- Volume 9—Materials Processing in the Reduced Gravity Environment of Space, G. E. Rindone, 1982, ISBN 0-444-00691-5
- Volume 10—Thin Films and Interfaces, P. S. Ho, K.-N. Tu, 1982, ISBN 0-444-00774-1
- Volume 11—Scientific Basis for Nuclear Waste Management V, W. Lutze, 1982, ISBN 0-444-00725-3
- Volume 12—In Situ Composites IV, F. D. Lemkey, H. E. Cline, M. McLean, 1982, ISBN 0-444-00726-1
- Volume 13—Laser-Solid Interactions and Transient Thermal Processing of Materials, J. Narayan, W. L. Brown, R. A. Lemons, 1983, ISBN 0-444-00788-1
- Volume 14—Defects in Semiconductors II, S. Mahajan, J. W. Corbett, 1983, ISBN 0-444-00817-8
- Volume 15—Scientific Basis for Nuclear Waste Management VI, D. G. Brookins, 1983, ISBN 0-444-00780-6
- Volume 16—Nuclear Radiation Detector Materials, E. E. Haller, H. W. Kraner, W. A. Higinbotham, 1983, ISBN 0-444-00787-3
- Volume 17—Laser Diagnostics and Photochemical Processing for Semiconductor Devices, R. M. Osgood, S. R. J. Brueck, H. R. Schlossberg, 1983, ISBN 0-444-00782-2
- Volume 18—Interfaces and Contacts, R. Ludeke, K. Rose, 1983, ISBN 0-444-00820-9
- Volume 19—Alloy Phase Diagrams, L. H. Bennett, T. B. Massalski, B. C. Giessen, 1983, ISBN 0-444-00809-8
- Volume 20—Intercalated Graphite, M. S. Dresselhaus, G. Dresselhaus, J. E. Fischer, M. J. Moran, 1983, ISBN 0-444-00781-4
- Volume 21—Phase Transformations in Solids, T. Tsakalakos, 1984, ISBN 0-444-00901-9
- Volume 22—High Pressure in Science and Technology, C. Homan, R. K. MacCrone, E. Whalley, 1984, ISBN 0-444-00932-9 (3 part set)
- Volume 23—Energy Beam-Solid Interactions and Transient Thermal Processing, J. C. C. Fan, N. M. Johnson, 1984, ISBN 0-444-00903-5
- Volume 24—Defect Properties and Processing of High-Technology Nonmetallic Materials, J. H. Crawford, Jr., Y. Chen, W. A. Sibley, 1984, ISBN 0-444-00904-3
- Volume 25—Thin Films and Interfaces II, J. E. E. Baglin, D. R. Campbell, W. K. Chu, 1984, ISBN 0-444-00905-1

---

MATERIALS RESEARCH SOCIETY SYMPOSIUM PROCEEDINGS

---

- Volume 26—Scientific Basis for Nuclear Waste Management VII, G. L. McVay, 1984, ISBN 0-444-00906-X
- Volume 27—Ion Implantation and Ion Beam Processing of Materials, G. K. Hubler, O. W. Holland, C. R. Clayton, C. W. White, 1984, ISBN 0-444-00869-1
- Volume 28—Rapidly Solidified Metastable Materials, B. H. Kear, B. C. Giessen, 1984, ISBN 0-444-00935-3
- Volume 29—Laser-Controlled Chemical Processing of Surfaces, A. W. Johnson, D. J. Ehrlich, H. R. Schlossberg, 1984, ISBN 0-444-00894-2
- Volume 30—Plasma Processing and Synthesis of Materials, J. Szekely, D. Apelian, 1984, ISBN 0-444-00895-0
- Volume 31—Electron Microscopy of Materials, W. Krakow, D. A. Smith, L. W. Hobbs, 1984, ISBN 0-444-00898-7
- Volume 32—Better Ceramics Through Chemistry, C. J. Brinker, D. E. Clark, D. R. Ulrich, 1984, ISBN 0-444-00898-5
- Volume 33—Comparison of Thin Film Transistor and SOI Technologies, H. W. Lam, M. J. Thompson, 1984, ISBN 0-444-00899-3
- Volume 34—Physical Metallurgy of Cast Iron, H. Fredriksson, M. Hillerts, 1985, ISBN 0-444-00938-8
- Volume 35—Energy Beam-Solid Interactions and Transient Thermal Processing/1984, D. K. Biegelsen, G. A. Rozgonyi, C. V. Shank, 1985, ISBN 0-931837-00-6
- Volume 36—Impurity Diffusion and Gettering in Silicon, R. B. Fair, C. W. Pearce, J. Washburn, 1985, ISBN 0-931837-01-4
- Volume 37—Layered Structures, Epitaxy, and Interfaces, J. M. Gibson, L. R. Dawson, 1985, ISBN 0-931837-02-2
- Volume 38—Plasma Synthesis and Etching of Electronic Materials, R. P. H. Chang, B. Abeles, 1985, ISBN 0-931837-03-0
- Volume 39—High-Temperature Ordered Intermetallic Alloys, C. C. Koch, C. T. Liu, N. S. Stoloff, 1985, ISBN 0-931837-04-9
- Volume 40—Electronic Packaging Materials Science, E. A. Giess, K.-N. Tu, D. R. Uhlmann, 1985, ISBN 0-931837-05-7
- Volume 41—Advanced Photon and Particle Techniques for the Characterization of Defects in Solids, J. B. Roberto, R. W. Carpenter, M. C. Wittels, 1985, ISBN 0-931837-06-5
- Volume 42—Very High Strength Cement-Based Materials, J. F. Young, 1985, ISBN 0-931837-07-3
- Volume 43—Fly Ash and Coal Conversion By-Products: Characterization, Utilization, and Disposal I, G. J. McCarthy, R. J. Lauf, 1985, ISBN 0-931837-08-1
- Volume 44—Scientific Basis for Nuclear Waste Management VIII, C. M. Jantzen, J. A. Stone, R. C. Ewing, 1985, ISBN 0-931837-09-X
- Volume 45—Ion Beam Processes in Advanced Electronic Materials and Device Technology, B. R. Appleton, F. H. Eisen, T. W. Sigmon, 1985, ISBN 0-931837-10-3
- Volume 46—Microscopic Identification of Electronic Defects in Semiconductors, N. M. Johnson, S. G. Bishop, G. D. Watkins, 1985, ISBN 0-931837-11-1
- Volume 47—Thin Films: The Relationship of Structure to Properties, C. R. Aita, K. S. Sreeharsha, 1985, ISBN 0-931837-12-X
- Volume 48—Applied Materials Characterization, W. Katz, P. Williams, 1985, ISBN 0-931837-13-8
- Volume 49—Materials Issues in Applications of Amorphous Silicon Technology, D. Adler, A. Madan, M. J. Thompson, 1985, ISBN 0-931837-14-6



---

MATERIALS RESEARCH SOCIETY SYMPOSIUM PROCEEDINGS

---

- Volume 50—Scientific Basis for Nuclear Waste Management IX, L. O. Werme, 1986, ISBN 0-931837-15-4
- Volume 51—Beam-Solid Interactions and Phase Transformations, H. Kurz, G. L. Olson, J. M. Poate, 1986, ISBN 0-931837-16-2
- Volume 52—Rapid Thermal Processing, T. O. Sedgwick, T. E. Seidel, B.-Y. Tsaur, 1986, ISBN 0-931837-17-0
- Volume 53—Semiconductor-on-Insulator and Thin Film Transistor Technology, A. Chiang, M. W. Geis, L. Pfeiffer, 1986, ISBN 0-931837-18-9
- Volume 54—Thin Films—Interfaces and Phenomena, R. J. Nemanich, P. S. Ho, S. S. Lau, 1986, ISBN 0-931837-19-7
- Volume 55—Biomedical Materials, J. M. Williams, M. F. Nichols, W. Zingg, 1986, ISBN 0-931837-20-0
- Volume 56—Layered Structures and Epitaxy, J. M. Gibson, G. C. Osbourn, R. M. Tromp, 1986, ISBN 0-931837-21-9
- Volume 57—Phase Transitions in Condensed Systems—Experiments and Theory, G. S. Cargill III, F. Spaepen, K.-N. Tu, 1987, ISBN 0-931837-22-7
- Volume 58—Rapidly Solidified Alloys and Their Mechanical and Magnetic Properties, B. C. Giessen, D. E. Polk, A. I. Taub, 1986, ISBN 0-931837-23-5
- Volume 59—Oxygen, Carbon, Hydrogen, and Nitrogen in Crystalline Silicon, J. C. Mikkelsen, Jr., S. J. Pearton, J. W. Corbett, S. J. Pennycook, 1986, ISBN 0-931837-24-3
- Volume 60—Defect Properties and Processing of High-Technology Nonmetallic Materials, Y. Chen, W. D. Kingery, R. J. Stokes, 1986, ISBN 0-931837-25-1
- Volume 61—Defects in Glasses, F. L. Galeener, D. L. Griscom, M. J. Weber, 1986, ISBN 0-931837-26-X
- Volume 62—Materials Problem Solving with the Transmission Electron Microscope, L. W. Hobbs, K. H. Westmacott, D. B. Williams, 1986, ISBN 0-931837-27-8
- Volume 63—Computer-Based Microscopic Description of the Structure and Properties of Materials, J. Broughton, W. Krakow, S. T. Pantelides, 1986, ISBN 0-931837-28-6
- Volume 64—Cement-Based Composites: Strain Rate Effects on Fracture, S. Mindess, S. P. Shah, 1986, ISBN 0-931837-29-4
- Volume 65—Fly Ash and Coal Conversion By-Products: Characterization, Utilization and Disposal II, G. J. McCarthy, F. P. Glasser, D. M. Roy, 1986, ISBN 0-931837-30-8
- Volume 66—Frontiers in Materials Education, L. W. Hobbs, G. L. Liedl, 1986, ISBN 0-931837-31-6
- Volume 67—Heteroepitaxy on Silicon, J. C. C. Fan, J. M. Poate, 1986, ISBN 0-931837-33-2
- Volume 68—Plasma Processing, J. W. Coburn, R. A. Gottscho, D. W. Hess, 1986, ISBN 0-931837-34-0
- Volume 69—Materials Characterization, N. W. Cheung, M.-A. Nicolet, 1986, ISBN 0-931837-35-9
- Volume 70—Materials Issues in Amorphous-Semiconductor Technology, D. Adler, Y. Hamakawa, A. Madan, 1986, ISBN 0-931837-36-7
- Volume 71—Materials Issues in Silicon Integrated Circuit Processing, M. Wittmer, J. Stimmell, M. Strathman, 1986, ISBN 0-931837-37-5
- Volume 72—Electronic Packaging Materials Science II, K. A. Jackson, R. C. Pohanka, D. R. Uhlmann, D. R. Ulrich, 1986, ISBN 0-931837-38-3
- Volume 73—Better Ceramics Through Chemistry II, C. J. Brinker, D. E. Clark, D. R. Ulrich, 1986, ISBN 0-931837-39-1
- Volume 74—Beam-Solid Interactions and Transient Processes, M. O. Thompson, S. T. Picraux, J. S. Williams, 1987, ISBN 0-931837-40-5

---

MATERIALS RESEARCH SOCIETY SYMPOSIUM PROCEEDINGS

---

- Volume 75—Photon, Beam and Plasma Stimulated Chemical Processes at Surfaces, V. M. Donnelly, I. P. Herman, M. Hirose, 1987, ISBN 0-931837-41-3
- Volume 76—Science and Technology of Microfabrication, R. E. Howard, E. L. Hu, S. Namba, S. Pang, 1987, ISBN 0-931837-42-1
- Volume 77—Interfaces, Superlattices, and Thin Films, J. D. Dow, I. K. Schuller, 1987, ISBN 0-931837-56-1
- Volume 78—Advances in Structural Ceramics, P. F. Becher, M. V. Swain, S. Sōmiya, 1987, ISBN 0-931837-43-X
- Volume 79—Scattering, Deformation and Fracture in Polymers, G. D. Wignall, B. Crist, T. P. Russell, E. L. Thomas, 1987, ISBN 0-931837-44-8
- Volume 80—Science and Technology of Rapidly Quenched Alloys, M. Tenhover, W. L. Johnson, L. E. Tanner, 1987, ISBN 0-931837-45-6
- Volume 81—High-Temperature Ordered Intermetallic Alloys, II, N. S. Stoloff, C. C. Koch, C. T. Liu, O. Izumi, 1987, ISBN 0-931837-46-4
- Volume 82—Characterization of Defects in Materials, R. W. Siegel, J. R. Weertman, R. Sinclair, 1987, ISBN 0-931837-47-2
- Volume 83—Physical and Chemical Properties of Thin Metal Overlayers and Alloy Surfaces, D. M. Zehner, D. W. Goodman, 1987, ISBN 0-931837-48-0
- Volume 84—Scientific Basis for Nuclear Waste Management X, J. K. Bates, W. B. Seefeldt, 1987, ISBN 0-931837-49-9
- Volume 85—Microstructural Development During the Hydration of Cement, L. Struble, P. Brown, 1987, ISBN 0-931837-50-2
- Volume 86—Fly Ash and Coal Conversion By-Products Characterization, Utilization and Disposal III, G. J. McCarthy, F. P. Glasser, D. M. Roy, S. Diamond, 1987, ISBN 0-931837-51-0
- Volume 87—Materials Processing in the Reduced Gravity Environment of Space, R. H. Doremus, P. C. Nordine, 1987, ISBN 0-931837-52-9
- Volume 88—Optical Fiber Materials and Properties, S. R. Nagel, J. W. Fleming, G. Sigel, D. A. Thompson, 1987, ISBN 0-931837-53-7
- Volume 89—Diluted Magnetic (Semimagnetic) Semiconductors, R. L. Aggarwal, J. K. Furdyna, S. von Molnar, 1987, ISBN 0-931837-54-5
- Volume 90—Materials for Infrared Detectors and Sources, R. F. C. Farrow, J. F. Schetzina, J. T. Cheung, 1987, ISBN 0-931837-55-3
- Volume 91—Heteroepitaxy on Silicon II, J. C. C. Fan, J. M. Phillips, B.-Y. Tsaur, 1987, ISBN 0-931837-58-8
- Volume 92—Rapid Thermal Processing of Electronic Materials, S. R. Wilson, R. A. Powell, D. E. Davies, 1987, ISBN 0-931837-59-6
- Volume 93—Materials Modification and Growth Using Ion Beams, U. Gibson, A. E. White, P. P. Pronko, 1987, ISBN 0-931837-60-X
- Volume 94—Initial Stages of Epitaxial Growth, R. Hull, J. M. Gibson, David A. Smith, 1987, ISBN 0-931837-61-8
- Volume 95—Amorphous Silicon Semiconductors—Pure and Hydrogenated, A. Madan, M. Thompson, D. Adler, Y. Hamakawa, 1987, ISBN 0-931837-62-6
- Volume 96—Permanent Magnet Materials, S. G. Sankar, I. F. Herbst, N. C. Koon, 1987, ISBN 0-931837-63-4
- Volume 97—Novel Refractory Semiconductors, D. Emin, T. Aselage, C. Wood, 1987, ISBN 0-931837-64-2
- Volume 98—Plasma Processing and Synthesis of Materials, D. Apelian, J. Szekely, 1987, ISBN 0-931837-65-0

---

MATERIALS RESEARCH SOCIETY SYMPOSIUM PROCEEDINGS

---

- Volume 99—High-Temperature Superconductors, M. B. Brodsky, R. C. Dynes, K. Kitazawa, H. L. Tuller, 1988, ISBN 0-931837-67-7
- Volume 100—Fundamentals of Beam-Solid Interactions and Transient Thermal Processing, M. J. Aziz, L. E. Rehn, B. Stritzker, 1988, ISBN 0-931837-68-5
- Volume 101—Laser and Particle-Beam Chemical Processing for Microelectronics, D.J. Ehrlich, G.S. Higashi, M.M. Oprysko, 1988, ISBN 0-931837-69-3
- Volume 102—Epitaxy of Semiconductor Layered Structures, R. T. Tung, L. R. Dawson, R. L. Gunshor, 1988, ISBN 0-931837-70-7
- Volume 103—Multilayers: Synthesis, Properties, and Nonelectronic Applications, T. W. Barbee Jr., F. Spaepen, L. Greer, 1988, ISBN 0-931837-71-5
- Volume 104—Defects in Electronic Materials, M. Stavola, S. J. Pearton, G. Davies, 1988, ISBN 0-931837-72-3
- Volume 105—SiO<sub>2</sub> and Its Interfaces, G. Lucovsky, S. T. Pantelides, 1988, ISBN 0-931837-73-1
- Volume 106—Polysilicon Films and Interfaces, C.Y. Wong, C.V. Thompson, K-N. Tu, 1988, ISBN 0-931837-74-X
- Volume 107—Silicon-on-Insulator and Buried Metals in Semiconductors, J. C. Sturm,\* C. K. Chen, L. Pfeiffer, P. L. F. Hemment, 1988, ISBN 0-931837-75-8
- Volume 108—Electronic Packaging Materials Science II, R. C. Sundahl, R. Jaccodine, K. A. Jackson, 1988, ISBN 0-931837-76-6
- Volume 109—Nonlinear Optical Properties of Polymers, A. J. Heeger, J. Orenstein, D. R. Ulrich, 1988, ISBN 0-931837-77-4
- Volume 110—Biomedical Materials and Devices, J. S. Hanker, B. L. Giammara, 1988, ISBN 0-931837-78-2
- Volume 111—Microstructure and Properties of Catalysts, M. M. J. Treacy, J. M. Thomas, J. M. White, 1988, ISBN 0-931837-79-0
- Volume 112—Scientific Basis for Nuclear Waste Management XI, M. J. Apted, R. E. Westerman, 1988, ISBN 0-931837-80-4
- Volume 113—Fly Ash and Coal Conversion By-Products: Characterization, Utilization, and Disposal IV, G. J. McCarthy, D. M. Roy, F. P. Glasser, R. T. Hemmings, 1988, ISBN 0-931837-81-2
- Volume 114—Bonding in Cementitious Composites, S. Mindess, S. P. Shah, 1988, ISBN 0-931837-82-0
- Volume 115—Specimen Preparation for Transmission Electron Microscopy of Materials, J. C. Bravman, R. Anderson, M. L. McDonald, 1988, ISBN 0-931837-83-9
- Volume 116—Heteroepitaxy on Silicon: Fundamentals, Structures, and Devices, H.K. Choi, H. Ishiwara, R. Hull, R.J. Nemanich, 1988, ISBN: 0-931837-86-3
- Volume 117—Process Diagnostics: Materials, Combustion, Fusion, K. Hays, A.C. Eckbreth, G.A. Campbell, 1988, ISBN: 0-931837-87-1
- Volume 118—Amorphous Silicon Technology, A. Madan, M.J. Thompson, P.C. Taylor, P.G. LeComber, Y. Hamakawa, 1988, ISBN: 0-931837-88-X
- Volume 119—Adhesion in Solids, D.M. Mattox, C. Batich, J.E.E. Baglin, R.J. Gottschall, 1988, ISBN: 0-931837-89-8
- Volume 120—High-Temperature/High-Performance Composites, F.D. Lemkey, A.G. Evans, S.G. Fishman, J.R. Strife, 1988, ISBN: 0-931837-90-1
- Volume 121—Better Ceramics Through Chemistry III, C.J. Brinker, D.E. Clark, D.R. Ulrich, 1988, ISBN: 0-931837-91-X
- Volume 122—Interfacial Structure, Properties, and Design, M.H. Yoo, W.A.T. Clark, C.L. Briant, 1988, ISBN: 0-931837-92-8

---

MATERIALS RESEARCH SOCIETY SYMPOSIUM PROCEEDINGS

---

- Volume 123—Materials Issues in Art and Archaeology, E.V. Sayre, P. Vandiver, J. Druzik, C. Stevenson, 1988, ISBN: 0-931837-93-6
- Volume 124—Microwave-Processing of Materials, M.H. Brooks, I.J. Chabinsky, W.H. Sutton, 1988, ISBN: 0-931837-94-4
- Volume 125—Materials Stability and Environmental Degradation, A. Barkatt, L.R. Smith, E. Verink, 1988, ISBN: 0-931837-95-2
- Volume 126—Advanced Surface Processes for Optoelectronics, S. Bernasek, T. Venkatesan, H. Temkin, 1988, ISBN: 0-931837-96-0
- Volume 127—Scientific Basis for Nuclear Waste Management XII, W. Lutze, R.C. Ewing, 1989, ISBN: 0-931837-97-9
- Volume 128—Processing and Characterization of Materials Using Ion Beams, L.E. Rehn, J. Greene, F.A. Smidt, 1989, ISBN: 1-55899-001-1
- Volume 129—Laser and Particle-Beam Chemical Processes on Surfaces, G.L. Loper, A.W. Johnson, T.W. Sigmon, 1989, ISBN: 1-55899-002-X
- Volume 130—Thin Films: Stresses and Mechanical Properties, J.C. Bravman, W.D. Nix, D.M. Barnett, D.A. Smith, 1989, ISBN: 0-55899-003-8
- Volume 131—Chemical Perspectives of Microelectronic Materials, M.E. Gross, J. Jasinski, J.T. Yates, Jr., 1989, ISBN: 0-55899-004-6
- Volume 132—Multicomponent Ultrafine Microstructures, L.E. McCandlish, B.H. Kear, D.E. Polk, and R.W. Siegel, 1989, ISBN: 1-55899-005-4
- Volume 133—High Temperature Ordered Intermetallic Alloys III, C.T. Liu, A.I. Taub, N.S. Stoloff, C.C. Koch, 1989, ISBN: 1-55899-006-2
- Volume 134—The Materials Science and Engineering of Rigid-Rod Polymers, W.W. Adams, R.K. Eby, D.E. McLemore, 1989, ISBN: 1-55899-007-0
- Volume 135—Solid State Ionics, G. Nazri, R.A. Huggins, D.F. Shriver, 1989, ISBN: 1-55899-008-9
- Volume 136—Fly Ash and Coal Conversion By-Products: Characterization, Utilization, and Disposal V, R.T. Hemmings, E.E. Berry, G.J. McCarthy, F.P. Glasser, 1989, ISBN: 1-55899-009-7
- Volume 137—Pore Structure and Permeability of Cementitious Materials, L.R. Roberts, J.P. Skalny, 1989, ISBN: 1-55899-010-0
- Volume 138—Characterization of the Structure and Chemistry of Defects in Materials, B.C. Larson, M. Ruhle, D.N. Seidman, 1989, ISBN: 1-55899-011-9
- Volume 139—High Resolution Microscopy of Materials, W. Krakow, F.A. Ponce, D.J. Smith, 1989, ISBN: 1-55899-012-7
- Volume 140—New Materials Approaches to Tribology: Theory and Applications, L.E. Pope, L. Fehrenbacher, W.O. Winer, 1989, ISBN: 1-55899-013-5
- Volume 141—Atomic Scale Calculations in Materials Science, J. Tersoff, D. Vanderbilt, V. Vitek, 1989, ISBN: 1-55899-014-3
- Volume 142—Nondestructive Monitoring of Materials Properties, J. Holbrook, J. Bussiere, 1989, ISBN: 1-55899-015-1
- Volume 143—Synchrotron Radiation in Materials Research, R. Clarke, J.H. Weaver, J. Gland, 1989, ISBN: 1-55899-016-X
- Volume 144—Advances in Materials, Processing and Devices in III-V Compound Semiconductors, D.K. Sadana, L. Eastman, R. Dupuis, 1989, ISBN: 1-55899-017-8
- Volume 145—III-V Heterostructures for Electronic/Photonic Devices, C.W. Tu, A.C. Gossard, V.D. Mittera, 1989, ISBN: 1-55899-018-6

---

MATERIALS RESEARCH SOCIETY SYMPOSIUM PROCEEDINGS

---

- Volume 146—Rapid Thermal Annealing/Chemical Vapor Deposition and Integrated Processing, D. Hodul, T.E. Seidel, J. Gelpey, M.L. Green, 1989, ISBN: 1-55899-019-4
- Volume 147—Ion Beam Processing of Advanced Electronic Materials, N. Cheung, J. Roberto, A. Marwick, 1989, ISBN: 1-55899-020-8
- Volume 148—Chemistry and Defects in Semiconductor Heterostructures, M. Kawabe, E.R. Weber, T.D. Sands, R.S. Williams, 1989, ISBN: 1-55899-021-6
- Volume 149—Amorphous Silicon Technology-1989, A. Madan, M.J. Thompson, P.C. Taylor, Y. Hamakawa, P.G. LeComber, 1989, ISBN: 1-55899-022-4
- Volume 150—Materials for Magneto-Optic Data Storage, T. Suzuki, C. Falco, C. Robinson, 1989, ISBN: 1-55899-023-2
- Volume 151—Growth, Characterization and Properties of Ultrathin Magnetic Films and Multilayers, B.T. Jonker, J.P. Heremans, E.E. Marinero, 1989, ISBN: 1-55899-024-0
- Volume 152—Optical Materials: Processing and Science, D.B. Poker, C. Ortiz, 1989, ISBN: 1-55899-025-9
- Volume 153—Interfaces Between Polymers, Metals, and Ceramics, B.M. DeKoven, R. Rosenberg, A.J. Gellman, 1989, ISBN: 1-55899-026-7
- Volume 154—Electronic Packaging Materials Science IV, K.A. Jackson, R.C. Sundahl, R. Jaccodine, E.D. Lilley, 1989, ISBN: 1-55899-027-5
- Volume 155—Processing Science of Advanced Ceramics, I.A. Aksay, G.L. McVay, D.R. Ulrich, 1989, ISBN: 1-55899-028-3
- Volume 156—High Temperature Superconductors: Relationships Between Properties, Structure and Solid-State Chemistry, J.B. Torrance, K. Kitazawa, J.M. Tarascon, J.R. Jorgensen, M. Thompson, 1989, ISBN: 1-55899-029-1

---

MATERIALS RESEARCH SOCIETY CONFERENCE PROCEEDINGS

---

Tungsten and Other Refractory Metals for VLSI Applications, R. S. Blewer, 1986;  
ISSN 0886-7860; ISBN 0-931837-32-4

Tungsten and Other Refractory Metals for VLSI Applications II, E.K. Broadbent, 1987;  
ISSN 0886-7860; ISBN 0-931837-66-9

Ternary and Multinary Compounds, S. Deb, A. Zunger, 1987; ISBN 0-931837-57-x

Tungsten and Other Refractory Metals for VLSI Applications III, Victor A. Wells, 1988;  
ISSN 0886-7860; ISBN 0-931837-84-7

Atomic and Molecular Processing of Electronic and Ceramic Materials: Preparation,  
Characterization and Properties, Ilhan A. Aksay, Gary L. McVay, Thomas G. Stoebe,  
1988; ISBN 0-931837-85-5

Materials Futures: Strategies and Opportunities, R. Byron Pipes, U.S. Organizing Com-  
mittee, Rune Lagneborg, Swedish Organizing Committee, 1988; ISBN 0-55899-000-3

Tungsten and Other Refractory Metals for VLSI Applications IV, Robert S. Blewer,  
Carol M. McConica, 1989; ISSN: 0886-7860; ISBN: 0-931837-98-7

# Growth, Characterization and Properties of Ultrathin Magnetic Films and Multilayers

## TEMPERATURE DEPENDENCE OF TWO-DIMENSIONAL SPIN ANISOTROPIES

ROY RICHTER AND JACK G. GAY

Physics Department, General Motors Research Laboratories, Warren, MI 48090-9055

## ABSTRACT

Large anisotropy energy is an essential property of high quality permanent magnets. In previous work we have calculated the spin polarized electronic structure and anisotropy of monolayers and slabs of Fe, Ni, and V. In this work we calculate the dependence on temperature of the spin anisotropy of a ferromagnetic monolayer of Fe. We find the easy direction of magnetization is not sensitive to the temperature; the variations calculated here are likely too small to be observed. It is perpendicular to the plane of the surface for both low and high temperatures. The calculations become progressively more ill-behaved as the temperatures are lowered and require more computer time for satisfactory convergence.

For Fe/Cu {100}, we find the spins always prefer to point out of plane. Experimental results in general are consistent with this view, although the systems seem to be difficult to prepare.

## INTRODUCTION

When the electronic energy levels of a material are calculated, magnetic effects can be included to varying degrees. Initially one ignores them completely, resulting in a degeneracy of at least two for each band, since both spins have the same energy by symmetry. Allowing the two spins to vary independently results in a magnetic moment due to an imbalance in band filling for only very few materials: Fe, Ni, and Co are the traditional examples. One may then include a preferred direction of the magnetic moment into the calculations. This preference, due to a difference in energy, is referred to as the spin anisotropy[1-3]. Finally, one may calculate the dependence of the spin anisotropy with the temperature of the material. This last is the subject of this paper.

We have previously calculated[4] the spin anisotropy of monolayers of Fe, Ni, and V and thick slabs of Fe by incorporating the spin-orbit interaction into the self-consistent local-orbital(SCLO) method[5]. The result for Fe, that the easy direction of magnetization is perpendicular to the plane of the monolayer, was used to explain the fact that in the spin-polarized photoemission experiments on monolayers of Fe on Ag {100} of Jonker *et al.*[6], spin-split bands but no spin polarization was observed. Here we briefly review that work, and present calculations of the dependence of the anisotropy on the temperature used in the calculations.

## CALCULATIONAL METHOD

The SCLO method uses a slab geometry to represent a desired surface or interface. The self-consistent one-electron eigenstates of the slab are linear combinations of Bloch functions labeled by two dimensional wave vectors,  $\vec{k}_{||}$ , in the plane of the slab. The Bloch functions consist of functions constructed from the atomic orbitals of the constituent atoms plus certain polarization orbitals. Required for the anisotropy calculation are the matrix elements of the spin-orbit interaction between the eigenstates of the slab.

The spin-orbit interaction arises from the one-electron operator[7]

$$H_{so} = \frac{1}{2} \alpha^2 \vec{\sigma} \cdot (\vec{F}(\vec{r}) \times \vec{p}), \quad (1)$$



where  $\vec{F}(\vec{r})$  is the electric field at  $\vec{r}$ , and  $\vec{\sigma}$  and  $\vec{p}$  are the spin and momentum operators.  $\alpha$  is the fine structure constant. Equation (1) is in Hartree atomic units. The matrix elements of  $H_{so}$  will depend on the direction of spin quantization of the slab eigenstates relative to the spatial orientation of the slab. This is the source of the spin anisotropy.

$\vec{F}$  can be decomposed into radial spherically symmetric fields at each atomic site plus self-consistent corrections. It is a standard approximation to treat the contribution of the atomic field at a site as dominant in the vicinity of that site[2-3,8-10]. When this is done, the matrix elements of (1) between Bloch functions reduce to matrix elements between corresponding atomic functions at a single site of the operator

$$H_{so} \cong \frac{1}{2} \alpha^2 \frac{F(r)}{r} \vec{L} \cdot \vec{\sigma}, \quad (2)$$

where  $F(r)$  is the atomic radial field centered at that site and  $\vec{L}$  is the angular momentum operator[11]. Since the SCLO atomic orbitals are simple linear combinations of products of angular momentum and spin eigenfunctions times a radial function, the desired matrix elements of the spin-orbit interaction between eigenstates of the slab can be obtained from the properties of the spin and orbital angular momentum operators and the radial integrals,

$$\int d^3r R_i(r) \frac{F(r)}{r} R_j(r), \quad (3)$$

where  $R_j(r)$  is the radial function of the  $j^{\text{th}}$  orbital. We calculate only matrix elements between  $d$  orbitals: this has proven sufficient in bulk calculations[10]. The resulting spin-orbit matrix is diagonal in  $\vec{k}_{\parallel}$  but not in spin.

The spin anisotropy is obtained as the variation of the total energy of the slab with direction of spin quantization. Since the spin-orbit interaction is small, the charge density change it induces is small. We rely on this to approximate the total energy change due to the spin-orbit interaction by the difference in the sum of occupied one-electron energies with and without the interaction integrated over the first Brillouin zone of the slab. Conditions under which such an approximation is accurate have been discussed by Weinert *et al.*[12].

To obtain the spin-orbit energy for a given spin quantization, one has to diagonalize the spin-orbit matrix coupling the two spin polarizations at a number of  $\vec{k}_{\parallel}$  vectors to approximate the integral over the Brillouin zone. Because there is a preferred direction, the arms of the star of  $\vec{k}_{\parallel}$  are not in general equivalent. In addition, the spin-orbit energy is slowly convergent in the number of  $\vec{k}_{\parallel}$  vectors used to approximate the Brillouin zone integral. This slow convergence is discussed in more detail below. Spin-anisotropy calculations are thus very time consuming for slabs with many electrons per unit cell. For this reason our first calculations were done on {100} monolayers of Fe, V, and Ni at the Ag lattice constant so that our results correspond as closely as possible to overlayers on Ag or Au {100}. We argued that the spin anisotropy may not be significantly altered by interaction with inert substrates such as Ag and Au[13-15].

Symmetry considerations dictate that the anisotropy energy of a monolayer have the form

$$E_{so} = E_{so}^{(0)} + E_z^{(2)} \alpha_z^2 + E_{xz}^{(4)} (\alpha_x^2 \alpha_z^2 + \alpha_y^2 \alpha_z^2) + E_{yz}^{(4)} \alpha_x^2 \alpha_y^2 + O(\alpha^6), \quad (4)$$

where  $\alpha_x$ ,  $\alpha_y$ , and  $\alpha_z$  are direction cosines along  $\hat{x}$ ,  $\hat{y}$ , and  $\hat{z}$ .  $\hat{z}$  is perpendicular to the plane of the monolayer and  $\hat{x}$  is along a nearest-neighbor direction in the plane. Provided the 6<sup>th</sup> order corrections can be ignored, the parameters of Eq. (4) can be determined from the spin-orbit energy at four quantization directions. We will be interested primarily in  $E_z^{(2)}$ , the coefficient that determines whether the preferred direction of the magnetic moment is perpendicular ( $E_z^{(2)} < 0$ ) or parallel ( $E_z^{(2)} > 0$ ) to the plane of the slab. Thus we will refer to  $E_z^{(2)}$  as 'the spin anisotropy energy.'

## RESULTS

With this background we now turn to the effect of varying the 'temperature' parameter in the self-consistent calculations of the spin-anisotropy.

### *The Temperature parameter $T$*

In the midst of the self-consistent calculation, an integration over the two-dimensional Brillouin Zone is performed. The integration sums up the filled bands to find the total charge density. Originally, we used a step function in energy to determine which bands were filled and which were empty. The energy at which the step occurs is called the Fermi Energy  $E_f$ , determined by requiring the total charge to be equal to the number of electrons in the unit cell. The problem with this step function is that it led to poor convergence of the charge density with iteration. This is because on one iteration a certain set of levels would be filled, and on the subsequent iteration another set of levels (perhaps) would be filled. In some cases the two sets would cycle, and the calculation would never converge. We dealt with this problem by partially filling the states near the Fermi level; this was done by the introduction of a temperature parameter  $T$  that acted in much the same way as a real temperature. That is, the electronic energy levels were filled with a Fermi distribution function. The calculation then converged quickly. Setting  $T = 0$  would reduce the calculation to the previous step function behavior, if desired.

The meaning one should attach to this temperature parameter is somewhat unclear. Temperature affects a metal in many ways: One is the electronic temperature; we believe we are taking that effect into account correctly with the temperature parameter described above. A higher temperature also implies the presence of phonons, and an increased lattice constant. There are other effects, such as entropy changes and plasmon creation, that have negligible effects on the spin anisotropy. The phonons cause scattering among the electronic states, but do not change the states themselves. The change in the lattice constant changes the electronic states directly, but to a small extent. The typical lattice expansion coefficient for a transition metal is  $\approx 1.2 \times 10^{-5}/\text{deg K}$ , and is fairly uniform over the range of temperature we are considering, up to 500 K. We would expect a change in lattice constant of 0.1% to have a similar relative change in the spin anisotropy. The lattice constant change near the Fermi level induces proportional changes in quantities tied to the Fermi level, such as reflectivity, by a similar amount.

Thus we believe a significant contribution to the temperature dependence of the spin anisotropy is due to the smearing out of the states around the Fermi level by the Fermi distribution function. The effect of an expansion in the lattice constant can be calculated, we believe it to be much smaller, given the reasoning above. However, the change in electronic occupation at the Fermi level also feeds back, self-consistently, to the potential the electrons see. We look at this effect in the next section.

### *Different Converged Temperatures*

The correct way to compute the spin anisotropy at different temperatures is to calculate a self-consistent charge density using each temperature, and then calculate the spin anisotropy energies using the same temperatures used in the charge density calculations. This involves performing many calculations that differ very slightly.

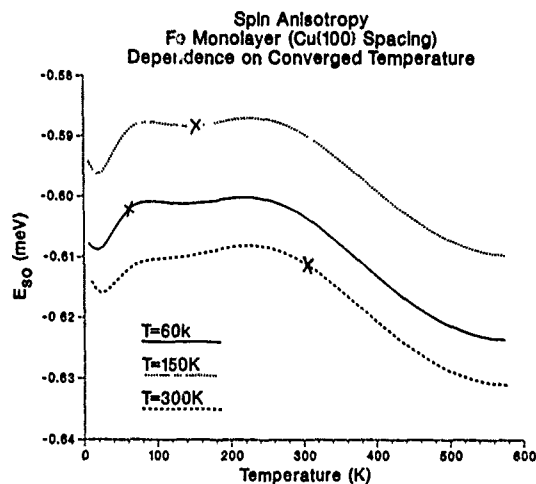


Figure 1. Fe monolayer spin anisotropy energy for different converged temperatures. The figure shows the relative sensitivity of the spin anisotropy when converged charge densities and potentials resulting from different temperatures are used.

The system is a monolayer of Fe at the Cu lattice constant of 4.8238 Bohr. The abscissa shows the variation of the temperature used in the spin anisotropy integrations. The different curves are the results for using different temperatures in the self-consistent calculations.

The only valid points are the point for the 60K curve at 60K, the 150K curve at 150K, etc., as shown by crosses. The variation of the spin anisotropy over the temperature range using the Fermi function dependence is on the same order as the dependence on the temperature used in the converged potential. What is noticeable is the weak temperature dependence of the spin anisotropy over this temperature range. We would say the spin anisotropy is -0.6 meV to the accuracy of our calculation. Any temperature variation shown here is likely too small to be observable.

#### *Same Converged Temperature, Different Brillouin Sampling*

We previously[4] noted the poor convergence in the Brillouin Zone sampling. In order to verify the temperature dependence just observed, we have calculated the temperature dependence for different mesh densities in the Brillouin Zone. The results are shown in Figure 2. These are also for the same Fe monolayer as Figure 1. We used a charge density and potential converged at 150K. One sees that at least 7744 points in the zone are needed for convergence at 150K. As the temperature drops, even more points are needed; the 7744-point and 14400-point results start differing at 150K. Thus, we cannot trust the 14400-point number much below that.

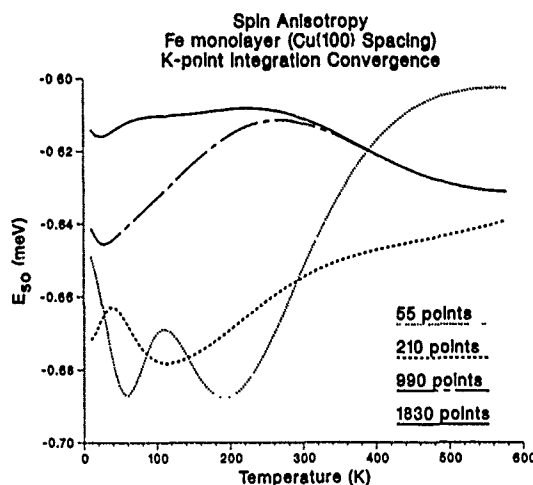


Figure 2. Fe monolayer spin anisotropy energy for different integration meshes in the Brillouin Zone. The figure shows the increasing importance of a fine mesh as the temperature is lowered. The values for 1830 points and 990 points (square meshes of 120 and 88 points on a side, respectively; or 14400 and 7744 points in the full zone) are converged down to a temperature of 350K.

An interesting point is that coarser meshes do better at high temperatures; alternatively, the lower the temperature, the finer the mesh needed. The 210-point mesh is converging to the 990-point result as the temperature increases. This is because the sharp structure of the spin anisotropy energy density is smoothed by the Fermi distribution. In Figure 3 we plot the spin anisotropy energy density for two different Fermi temperatures.

The sharp structure is smoothed out as the temperature is increased, so that it is reasonable that it is easier to capture with a smaller number of k-points. The amazing thing is that, although the structure looks large, it produces little or no effect on the spin anisotropy. Most of the anisotropy comes from broad humps that are difficult to see in the figure. The increase k-points are needed to insure that the peaks cancel.

The sensitivity of the anisotropy to details of the band structure occurs because the spin orbit operator (2) can be decomposed into a part that is independent of the direction of spin quantization and a direction dependent part that has vanishing diagonal matrix elements. This means that the anisotropy arises from second and higher orders of perturbation theory which are strongly influenced by energy denominators. There will be large contributions in second order at points in the Brillouin zone where there occur nearly degenerate occupied and unoccupied bands which are connected by spin-orbit matrix elements. It is understandable that the zone must be sampled minutely to obtain the anisotropy accurately, and that a coarse sampling may give anomalous results because of incorrect weighting of important regions of the zone. When a band passes through the Fermi level, there are large positive and negative contributions to the spin anisotropy. These contributions almost cancel, which also causes the integration to be poorly converged.

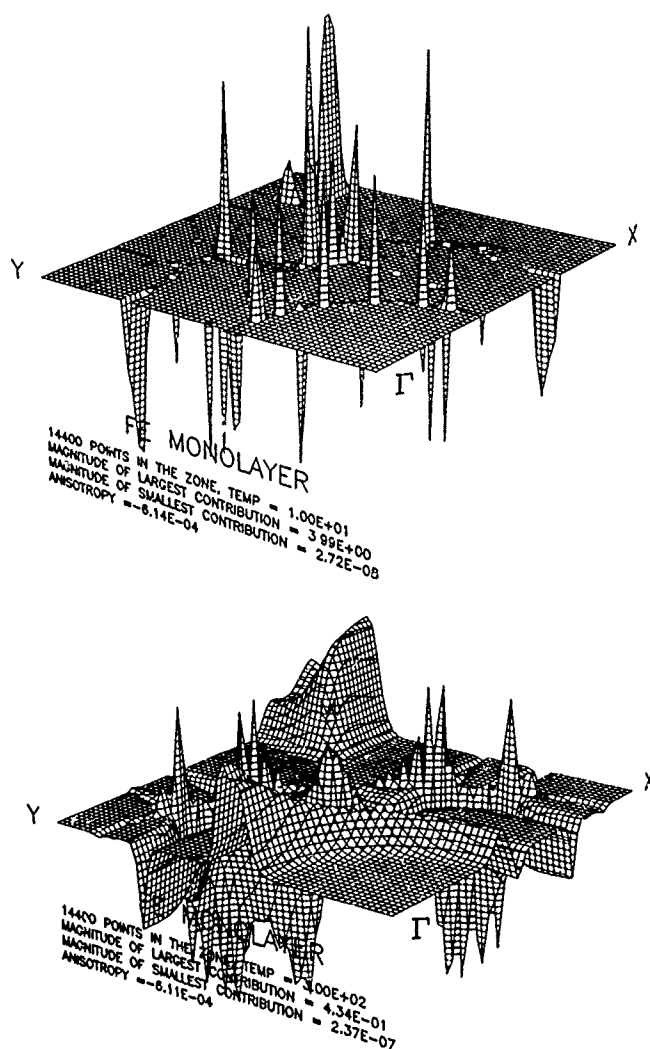


Figure 3. Fe monolayer spin anisotropy energy density over the two-dimensional Brillouin Zone. The structure of the spin anisotropy energy density is shown for two temperatures over the two-dimensional Brillouin Zone. Both plots use 14,400 point in the square Brillouin Zone. The upper plot uses a temperature of 10K and the lower 300K. The sharp structure that occurs with both positive- and negative-value branches occur when energy bands pass through the Fermi surface. This sharp structure is responsible for the convergence difficulties of the calculation.

#### *Theoretical and Experimental results for Fe/Cu{100}*

We now attempt to compare to experiment to see if the strong temperature dependence of the spin anisotropy is verified. One cannot fabricate an unsupported monolayer; the next

best thing is a monolayer of Fe on an inert substrate, say Ag or Cu. We previously calculated the spin anisotropy of Fe/Ag {100} but concluded that calculating the Ag band structure non-relativistically rendered the results unreliable[4]. Thus we attempt to calculate the spin anisotropy of Fe/Cu {100}, where the relativistic effects on the band structure should be much diminished. We modeled the system by a seven-layer slab of Cu with a layer of Fe on each side, with a Fe-Cu interlayer spacing of  $1.75\text{\AA}$ [16], the normal Cu lattice spacing of  $3.61\text{\AA}$ , and a temperature of  $317\text{K}$  (1 mH). The spin anisotropy is shown as a function of temperature in Figure 4. The anisotropy is for a monolayer of Fe on Cu {100}. It is obtained by dividing the slab anisotropy by two, since by far most of the anisotropy comes from the Fe and very little from the Cu.

The results indicate the perpendicular direction is preferred for all temperatures, with a weak variation. These values do not take into account the shape anisotropy. A continuum approximation to the shape anisotropy, with an Fe moment of  $2.6\mu_B$ , gives a demagnetization energy of  $0.4\text{ meV/layer}$ ; a calculation assuming point dipoles arranged in a lattice yields  $0.3\text{ meV/layer}$ . This implies that the shape anisotropy should pull the moment into the plane for single monolayer coverage. For thicker slabs, the anisotropy should track that of Fe on Fe, which is much higher (on the order of the Fe monolayer results shown previously). This would overcome that shape anisotropy until 3 layers are reached.

Experimental results are in general agreement with those shown here. However, there is still some confusion over sample preparation and geometry. The effects of island formation and interdiffusion are not well understood. For Fe/Cu {100} an increasing perpendicular anisotropy is seen in references 17 and 18 as the temperature is lowered; a conversion over to parallel anisotropy is seen at 6 ML and 100K in reference 19. No perpendicular anisotropy is found for a single monolayer. Similar temperature effects are seen in Fe/Ag {100}[20].

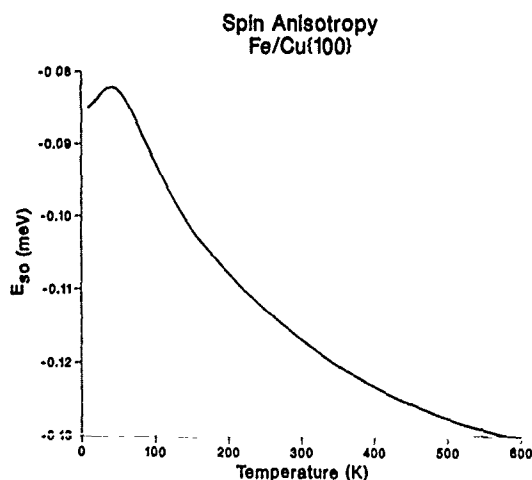


Figure 4. The spin anisotropy of a monolayer of Fe on Cu {100} as a function of temperature.

## REFERENCES

1. J. H. Van Vleck, Phys. Rev. **52**, 1178 (1937).
2. H. Brooks, Phys. Rev. **58**, 909 (1940).
3. G. C. Fletcher, Proc. Phys. Soc. (London) **A67**, 505 (1954).
4. J. G. Gay and R. Richter, Phys. Rev. Lett. **56**, 2728 (1986); J. Appl. Phys. **61**, 3362 (1987).
5. J. R. Smith, J. G. Gay, and F. J. Arlinghaus, Phys. Rev. **B21**, 2201 (1980).
6. B. T. Jonker, K. H. Walker, E. Kisker, G. A. Prinz, and C. Carbone, Phys. Rev. Lett. **57**, 142 (1986).
7. J. C. Slater, *Quantum Theory of Atomic Structure* (McGraw-Hill Book Company, New York, 1960), Vol II, p. 180.
8. A. J. Bennett and B. R. Cooper, Phys. Rev. **B3**, 1642 (1971).
9. H. Takayama, K. P. Bohnen, and P. Fulde, Phys. Rev. **B14**, 2287 (1976).
10. N. Mori, T. Ukai, and S. Ohtsuka, J. Magn. Magn. Mater. **31-34**, 43(1983).
11. We have estimated the size of the terms discarded in approximating the spin-orbit matrix by the on-site elements of Eq. (2). For an Fe monolayer the largest element left out is about 600 times smaller than a typical on-site element.
12. M. Weinert, R. E. Watson, and J. W. Davenport, Phys. Rev. **B32**, 2115 (1986).
13. R. Richter, J. G. Gay, and J. R. Smith, J. Vac. Sci. Technol. **A3**, 1498 (1985).
14. C. L. Fu, A. J. Freeman, and T. Ogouchi, Phys. Rev. Lett. **54**, 2700 (1985).
15. R. Richter, J. G. Gay, and J. R. Smith, Phys. Rev. Lett. **54**, 2704 (1985).
16. C. L. Fu and A. J. Freeman, Phys. Rev. **B35**, 920 (1987).
17. D. Pescia, M. Stampanoni, G. L. Bona, A. Vaterlaus, R. F. Willis, and F. Meier, Phys. Rev. Lett. **58**, 2126 (1987).
18. R. F. Willis, J. A. C. Bland, and W. Schwarzacher, J. Appl. Physics. **63**, 4051 (1988).
19. M. Stampanoni, A. Vaterlaus, M. Aeschlimann, and F. Meier, J. Appl. Physics. **64**, 5321 (1988).
20. N. C. Koon, B. T. Jonker, F. A. Volkening, J. J. Krebs, and G. A. Prinz, Phys. Rev. Lett. **59**, 2463 (1987); J. J. Krebs, B. T. Jonker, and G. A. Prinz, J. Appl. Phys. **63**, 3467 (1988); F. A. Volkening, B. T. Jonker, J. J. Krebs, N. C. Koon, and G. A. Prinz, J. Appl. Phys. **63**, 3869 (1988); B. Heinrich, K. B. Urquhart, J. R. Dutcher, S. T. Purcell, J. F. Cochran, A. S. Arott, D. A. Steigerwald, and W. F. Egelhoff, Jr., J. Appl. Phys. **63**, 3863 (1988).

## Fe-Ag SUPERLATTICES BY MOLECULAR BEAM EPITAXY

S.H. MAYER, C.J. GUTIERREZ AND J.C. WALKER  
 Johns Hopkins University, Baltimore, MD 21218

## ABSTRACT

We have succeeded in producing high quality (110)Fe/(111)Ag superlattices by Molecular Beam Epitaxy. Important parameters in the production of these materials were substrate temperature and effusion rates of the constituents. We have used SQUID magnetometry, Mössbauer spectroscopy and Reflection High Energy Electron Diffraction to demonstrate flatness and continuity of the films down to a thickness of approximately 2 atomic layers for the iron and 5 atomic layers for the silver. In the case of the thinnest iron layers, no large reduction of the ferromagnetic Curie temperature was observed, although this had been suggested and reported by other investigators. Furthermore, there was no indication for this particular growth system that the magnetization of the iron was out of the plane of the film. Variations of the magnetic hyperfine fields observed in the iron films were seen both as a function of iron thickness and as a function of the thickness of the intervening silver layers. For the thinnest films, the temperature dependence of the magnetization showed a linear behavior rather than the traditional  $T^{3/2}$  form.

## INTRODUCTION

In recent years technological advances have made it possible to produce high quality, crystalline metallic structures [1]. Over this same period of time there has developed considerable controversy involving ultrathin Fe films, both theoretically and experimentally, over questions such as the value of the magnetic moment at the Fe surface, the magnetic anisotropy and the reported observations of a reduced Curie temperature [2-5]. Answers to these questions can now begin to be provided by the growth of these high quality films.

In a previous paper we reported on the study of ultrathin Fe(110) films on Ag(111) grown by molecular beam epitaxy (MBE) which were analyzed by Mössbauer spectroscopy [6]. These films, which consisted of Fe components 1.3 to 8 monolayers (ML) thick, were shown to be single-crystalline, flat and continuous, with the magnetization lying in the plane of the film. Only the thinnest films showed a small superparamagnetic component. In this paper we present the first study of Fe(110)/Ag(110) superlattices.

Superlattices, as well as thin films, provide an excellent opportunity for the study of two-dimensional magnetic behavior. The additional periodicity inherent in a superlattice also allows for the study of the interactions between the magnetic layers. Of course, as the separation between individual magnetic layers becomes large the results for the superlattice should approach those for thin films.

The superlattices studied were of the form  $(\text{Ag}_x\text{Fe}_y)_{30}$  where  $x$  refers to the number of monolayers of Ag,  $y$  refers to the number of monolayers of Fe and the 30 indicates that the Fe/Ag layers were repeated 30 times. Three series of films were made, with  $y=2, 5$  and  $8\text{ML}$ . Three films were made in each series, with  $x=5, 12$  and  $20$ .

## EXPERIMENTAL

The superlattices were produced in a PHI model 430B MBE system which includes in situ analysis by reflection high energy electron diffraction



(RHEED), a residual gas analyzer, and a quartz crystal oscillator to monitor deposition rates. Ag and Fe (enriched to a concentration of 35% Fe<sup>57</sup>) were deposited from effusion cells onto a synthetic Fe-free mica substrate. The pressure during deposition was typically less than  $2 \times 10^{-9}$  torr.

We have previously shown that for a substrate temperature of 180°C Ag(111) will grow epitaxially on the mica and that Fe(110) will grow epitaxially on the Ag with only a single orientation as determined by RHEED. The high quality of the RHEED patterns obtained after deposition of both the first Ag and the first Fe layer are maintained even after the growth of 100 repetitions of each component. This indicates that the superlattice maintains its flat, single-crystalline nature from the first repetition to the last. Figure 1 shows typical RHEED patterns for the Fe/Ag superlattices taken after deposition of the Ag base layer (figure 1a), the first Fe layer (figure 1b) and the 7th Ag layer (figure 1c). Further details of film characterization and growth procedures are discussed in an earlier paper [6].

#### RESULTS AND DISCUSSION

Transmission Mössbauer spectroscopy was used to analyze both series of superlattices at temperatures from 4.2K to 300K. Transmission spectroscopy was used instead of conversion electron Mössbauer spectroscopy (CEMS) because it measures all the Fe layers in the superlattice with equal sensitivity. CEMS, on the other hand, is rather surface sensitive and thus any differences that might exist between the 30 magnetic components cannot be easily detected. Figure 2 shows the spectra at 4.2K for the six films with  $y=5$  and  $y=8$ , and figure 3 shows the same films at room temperature. There are several characteristics worthy of immediate note. First, all the films are magnetically ordered at all the temperatures measured. Second, there is no evidence of a superparamagnetic component, even at room temperature. This effectively

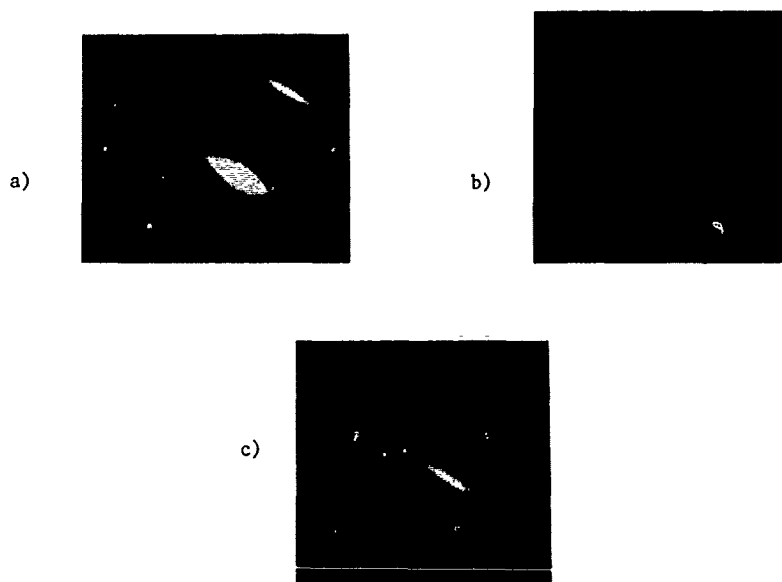


Figure 1. RHEED pattern of various film surfaces

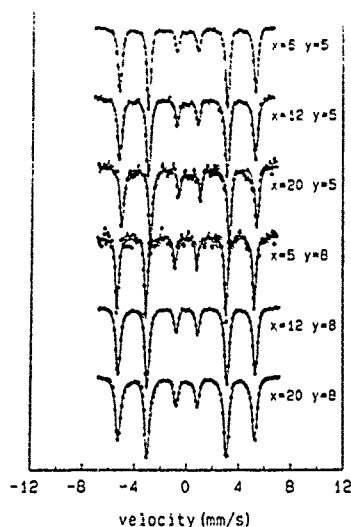


Figure 2. Mössbauer spectra for  $(\text{Ag}_x\text{Fe}_y)_{30}$  at 4.2K

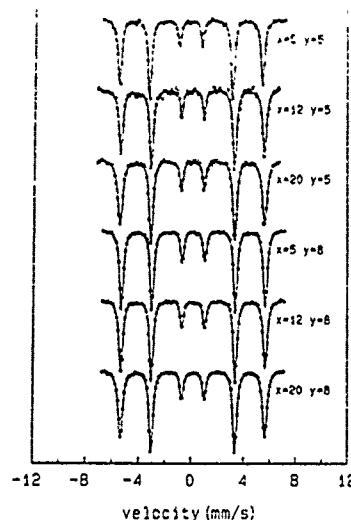


Figure 3. Mössbauer spectra for  $(\text{Ag}_x\text{Fe}_y)_{30}$  at room temperature

means that the Fe layers do not consist of small islands but rather are continuous on an atomic scale. This is in contrast to some other work, for which significant superparamagnetism was seen below 8ML of Fe [7,8].

The linewidths of all the spectra are less than 0.40 mm/sec. This value is less than that obtained from our bulk-like calibration foil. This implies that all the films are flat and continuous with all the Fe occupying sites essentially the same. This provides further evidence that each of the 30 Fe layers are similar in structure and quality. Also, the relative intensity of the lines for each spectrum is approximately 3:4:1, indicating that the magnetization of each Fe layer is in-plane. The thicker Fe superlattices all show variations of hyperfine field with  $T$ , which satisfies the usual  $T^{3/2}$  law associated with a spin-wave model of thermal magnetic excitations.

Figure 4 shows the Mössbauer transmission spectra for  $(\text{Ag}_5\text{Fe}_2)_{30}$  at different temperatures. The relative intensity of the lines forming the sextet is approximately 3:4:1, indicating that the magnetic moment of each Fe layer is nearly in-plane. Although the intensity of the additional central feature clearly increases as the temperature increases, there is no evidence that the spectrum has totally collapsed even up to 500K, indicating that the Curie temperature must be well above this value.

The central feature in all these spectra is a superparamagnetic component resulting from the thermal relaxation of the magnetic moment of a very minor Fe island component of the superlattices and is no way connected with a reduced Curie temperature. Figure 5 strikingly proves this statement. Figure 5a and 5b both show the Mössbauer spectrum of  $(\text{Ag}_{12}\text{Fe}_2)_{30}$  at room temperature, but the spectrum in figure 5b, which shows a greatly reduced central feature, was taken with a 5kG external field parallel to the film while the one in figure 5a was taken in zero field. Without the external field the central feature makes up approximately 28% of the spectrum's intensity. With the magnetic field this is reduced to less than 3%. The energy barrier supplied by the external field to each Fe atom is about  $2.2 \mu_B H = 10^{-16}$  erg, which is much less than the thermal energy at room

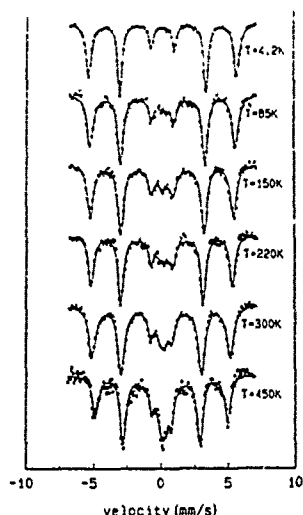


Figure 4. Mössbauer spectra for  $(\text{Ag}_5\text{Fe}_2)_{30}$  at various temperatures

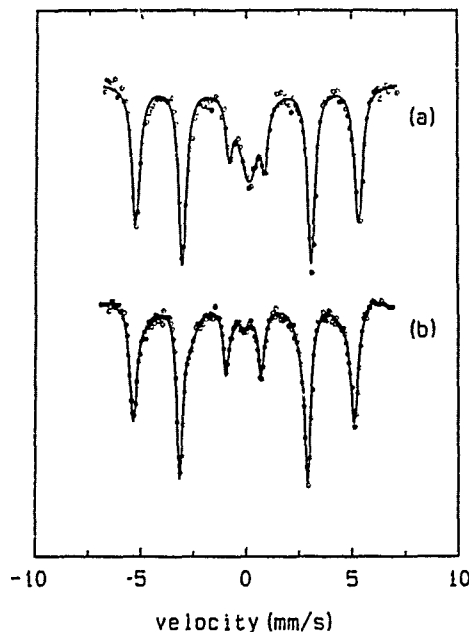


Figure 5. Mössbauer spectra for  $(\text{Ag}_{12}\text{Fe}_2)_{30}$  at room temperature  
a) with no external magnetic field  
b) with a 5kG external magnetic field

temperature,  $k_B T = 3 \times 10^{-14}$  erg. In other words, the external magnetic field is not strong enough to align the Fe moments individually. Therefore, this central feature must not be associated with the ferromagnetic coupling between Fe atoms, but must rather represent the thermal relaxation of Fe islands each of which is already ferromagnetically ordered.

The hyperfine fields of the three superlattices clearly obey a linear temperature dependence (figure 6) rather than the usual  $T^{3/2}$  dependence found for the superlattice samples with thicker Fe components. This linear behavior has frequently been observed for Fe films approaching 1ML and it has often been attributed to their quasi two-dimensional nature. However, if this were the case, we would expect that the hyperfine field would decrease more rapidly as the thickness of the Ag component increased. This trend is expected because, as the Ag becomes thicker, the interaction between neighboring Fe components becomes weaker, making it easier to excite the Fe magnetic moments [9]. In fact, as figure 6 indicates, the actual trend is just the opposite; as the Ag becomes thicker the hyperfine field decreases less rapidly. Therefore, this linear temperature dependence in all likelihood is not associated with a 2D effect. Rather, we believe, it is strictly a result of a large flat island structure in the film.

#### CONCLUSION

High quality, well-characterized Fe(110)/Ag(111) superlattices have been grown for the first time. Transmission Mössbauer spectroscopy shows

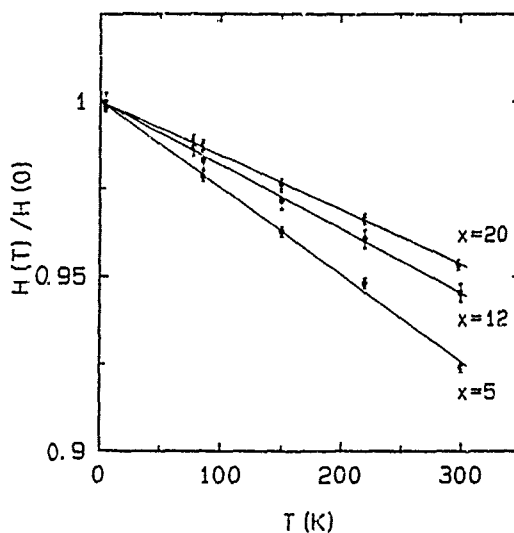


Figure 6. Hyperfine field as a function of temperature for  $(\text{Ag}_x\text{Fe}_2)_{30}$

in-plane magnetization for all superlattices and narrow sharp lines for the thicker Fe superlattices. The superlattices with 2ML Fe components show no evidence of significantly reduced ferromagnetic Curie temperature, but do give evidence of some superparamagnetism, both from a central feature in the Mössbauer spectrum and from a linear temperature dependence of the magnetic hyperfine field.

#### REFERENCES

1. I.K. Schuller and C.M. Falco, Microstructure Science and Engineering/SL, edited by N.G. Einspruch (Academic, New York, 1982).
2. C.L. Fu, A.J. Freeman and T. Oguchi, *Phys. Rev. Lett.* **54**, 2700 (1985); C.L. Fu and A.J. Freeman, *J. Magn. Magn. Mat.* **69**, L1 (1987).
3. J.G. Gay and R. Richter, *Phys. Rev. Lett.* **56**, 2728 (1986).
4. J.G. Gay and R. Richter, *J. Appl. Phys.* **61**, 3362 (1987).
5. U. Gradmann, R. Bergholz and E. Bergter, *Thin Solid Films* **126**, 107 (1985).
6. C.J. Gutierrez, S.H. Mayer and J.C. Walker, *J. Magn. Magn. Mat.* (in press).
7. G. Bayreuther and G. Lugert, *J. Magn. Magn. Mat.* **35**, 50 (1983).
8. F.A. Volkening, B.T. Jonker, J.J. Krebs, N.C. Koon and G.A. Prinz, *J. Appl. Phys.* **63**, 3869 (1988).

9. Z.Q. Qiu, H. Tang, Y.W. Du, G.P. Stern and J.C. Walker, J. Appl. Phys. 63, 3657 (1987).

# VARIATIONS IN MAGNETIC HYPERFINE FIELDS FOR THIN EPITAXIAL HETEROSTRUCTURES OF (110)Fe ON (111)Ag

C.J. GUTIERREZ, S.H. MAYER, Z.Q. QIU, H. TANG AND J.C. WALKER  
Johns Hopkins University, Baltimore, MD 21218

## ABSTRACT

We have made a study of magnetic heterostructures involving the epitaxial growth of (110)Fe on (111)Ag. The flatness and continuity of the films was verified by Reflection High Energy Electron Diffraction during the growth process. A series of structures were made with very thin intervening silver layers with thicker iron layers. The doping of appropriate layers by enriched  $\text{Fe}^{57}$  made it possible to examine the magnetic structure of the iron films as a function of depth. Preliminary results indicate that thin layers of silver sandwiched between two very thin Fe layers are able to transmit conduction electron polarization, resulting in iron behavior which resembles that of bulk iron. Implications of these results for understanding the nature of the magnetization of iron will be addressed in the following.

## INTRODUCTION

The Fe/Ag system is an attractive system for the study of magnetic interfaces and surfaces for several reasons. First, Fe and Ag are non-diffusing and nonalloying, thus forming a very sharp interface. Second, the epitaxy of Fe(110) on Ag(111) has been studied extensively [1]. Third, there is essentially no overlap of the Fe and Ag valence electron bands [2,3], resulting in a nearly two-dimensional Fe structure.

## EXPERIMENT

Our group has a long history in the production and analysis of Fe(110)/Ag(111) ultrathin films grown by evaporation [4,5]. In this paper, we report on the analysis of similar structures grown by the more sophisticated technique of molecular beam epitaxy (MBE).

This series of films was produced in a PHI Model 430B MBE system which includes in situ analysis by reflection high energy electron diffraction (RHEED) and a residual gas analyzer (RGA). The effusion rates were monitored with a quartz crystal oscillator to an accuracy of 10%. The Fe thickness was checked independently with SQUID magnetometer measurements. The effusion cells were obtained commercially from PHI and EPI systems.

As we discovered early on, the standard pyrolytic boron nitride (PBN) crucibles used in MBE semiconductor work are inappropriate for the effusion of Fe. At 1180°C the Fe and the boron in the PBN form a well-known eutectic. One consequence of this reaction is that nitrogen is liberated into the growth chamber with a dramatic pressure increase from  $1 \times 10^{-9}$  torr to  $1 \times 10^{-5}$  torr as this eutectic temperature is surpassed in the crucible. Additionally the Fe effused contains boron [6] and the effusion rates become erratic.

We replaced the PBN crucibles with commercially available alumina ( $\text{Al}_2\text{O}_3$ ) crucibles. Fe effusion from these cells gave constant rates with no indications of contamination as determined by the RGA and ex situ Auger analysis of the films. Examination of the alumina crucibles gave no evidence of breakdown.

All of the samples were grown in the following manner. A thick base layer (1500 Å) of (111)Ag was deposited on a Fe-free synthetic mica substrate

which had been outgassed in UHV at 400°C for 3 hours. The substrate temperature was maintained at 180°C throughout the growth of the film. Fe-57 (the Fe isotope which exhibits the Mössbauer effect) was then effused until the desired thickness was reached. From 5 to 20ML of Ag was then deposited followed again by deposition of the Fe. The Ag barrier was used to insure complete separation of the Fe layers. This process was repeated as many times as necessary in order to obtain the total amount of Fe needed for measurement by Mössbauer spectroscopy.

The final form of our films was  $(\text{Fe Ag})_z^x$ , where  $y$  refers to the number of monolayers of Fe,  $x$  refers to the number of monolayers of Ag, and  $z$  indicates the number of repetitions of the Fe/Ag system. A series of structures were made with  $y=2, 5.5$  and  $8$ . For this set  $x$  was either 20 or 30 while  $z$ , the number of repeats, was 3 or 4.

A second series was made with  $y=5$  and  $y=8$ . For each value of  $y$ , three structures were made with  $x=5, 12$  and  $20$ . In this second series the number of repeats was much larger with  $z=30$ . Finally, the films were covered with approximately 2000 Å of Ag to protect them from oxidation. The Ag was typically effused at rates between 0.5 and 5.0 Å/sec and the Fe was effused at approximately 1 to 3 Å/min. The base pressure was below  $7 \times 10^{-10}$  torr and during growth it was kept below  $2 \times 10^{-9}$  torr.

Typical RHEED patterns of the Ag and Fe layers at various stages of growth are shown in figure 1. The substrate temperature in this case was 180°C. The Ag pattern corresponds to the (111) surface and the sharp, uniform streaks with little diffuse background indicate a flat, single crystal. The Fe pattern corresponds to the (110) surface, and although it is not as smooth and sharp as the Ag pattern, it is still indicative of a reasonably flat, continuous crystalline structure.

#### RESULTS AND DISCUSSION

Transmission Mössbauer spectroscopy was used to analyze the films at 300K, 77K and 4.2K. Figures 2 and 3 show the spectra for the first series with  $y=30$  and 20, and  $x=8$  and 2, respectively. There are several features of these spectra that are important to note. First, all the films are magnetically ordered at all the temperatures measured.

The values of the hyperfine fields for the first series of films are shown in Table I. These values are consistent with previous work by this group and others [7,8]. At room temperature the hyperfine field of the 2ML Fe films is reduced from bulk by 4%. At 4.2K the field increases as the Fe layer thickness decreases and all of the films are enhanced over the bulk value of Fe at this temperature.

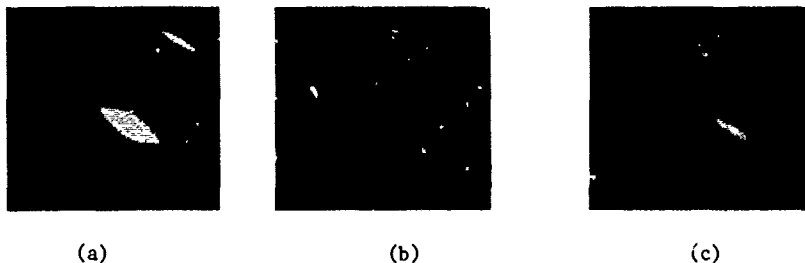


Figure 1. Typical RHEED patterns during various stages of epitaxial film growth.

- a) Typical 2000 Å (111)Ag base grown on mica. Photo overexposed to bring out weaker lines.
- b) Typical superlattice (110)Fe completed component layer.
- c) Typical superlattice (111)Ag completed component layer.

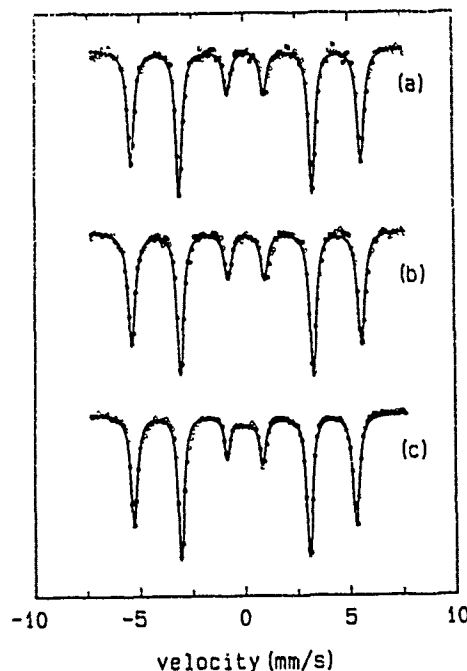
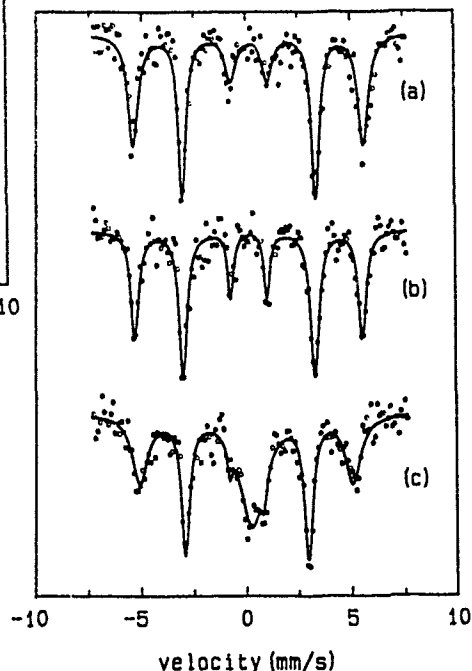


Figure 3. 2ML Fe heterostructure  
( $\text{Fe}_2\text{Ag}_{20}$ )<sub>4</sub> Mössbauer spectra  
a)  $T = 4.2^\circ\text{K}$   
b)  $T = 77^\circ\text{K}$   
c)  $T = 293^\circ\text{K}$

Figure 2. 8ML Fe heterostructure  
( $\text{Fe}_8\text{Ag}_{20}$ )<sub>3</sub> Mössbauer spectra  
a)  $T = 4.2^\circ\text{K}$   
b)  $T = 77^\circ\text{K}$   
c)  $T = 293^\circ\text{K}$



A closer analysis of the Mössbauer spectra indicates the following. The linewidths of the 8ML film are comparable to that of bulk Fe at all the temperatures measured. This implies that this film is flat and continuous with all of the Fe occupying sites that are essentially the same. Only our 2ML Fe films show significant line broadening. In all cases the relative intensity of the lines is approximately 3:4:1, indicating clearly that the orientation of the spins lie in-plane for all the films examined.

Table I. Hyperfine fields for the first series of ( $\text{Fe}_x\text{Ag}_y$ )<sub>z</sub> heterostructures. Dashed lines indicate measurements which could not be completed due to premature iron oxide contamination during measurement.

Temp	HYPERFINE FIELDS (kG)			
	Monolayers Fe			
	1.3	2	5.5	8
4.2K	347.6	344.0	343.7	342.9
77K	--	338.8	--	341.1
293K	--	316.0	322.6	329.0



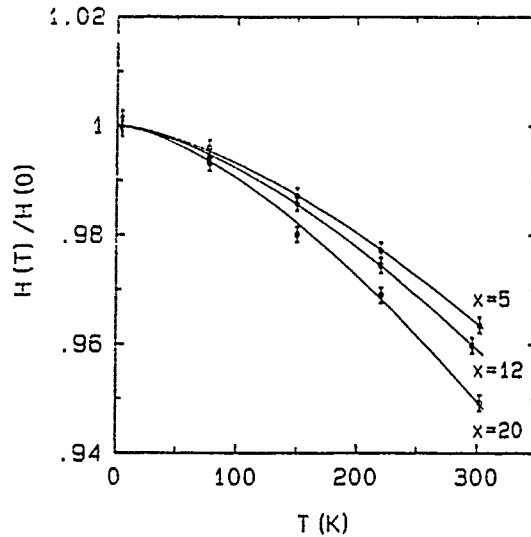


Figure 4. Magnetic hyperfine field (H) vs. temperature (T) for the 8 ML Fe superlattices. Note that  $(\text{Fe}_8\text{Ag}_x)_{30}$ , where  $x$  = Ag ML thickness.

For the second series of films we have tried to examine the effects on the Mössbauer hyperfine field of reducing the thickness of the Ag layer between Fe layers. Figure 4 shows a plot of H, the magnetic hyperfine field, versus temperature for the three 8 ML Fe structures which have Ag components of varying thickness. Figure 5 shows a similar plot for the three 5 ML Fe structures. All the curves can be fitted to the equation:

$$H(T) = H_0(1 - BT^{3/2}) \quad (1)$$

It has been well established that the hyperfine field is closely proportional to the local magnetization in the sample [9]. Therefore, the magnetization also decreases with a  $T^{3/2}$  dependence, as predicted by spin-wave theory [10,11].

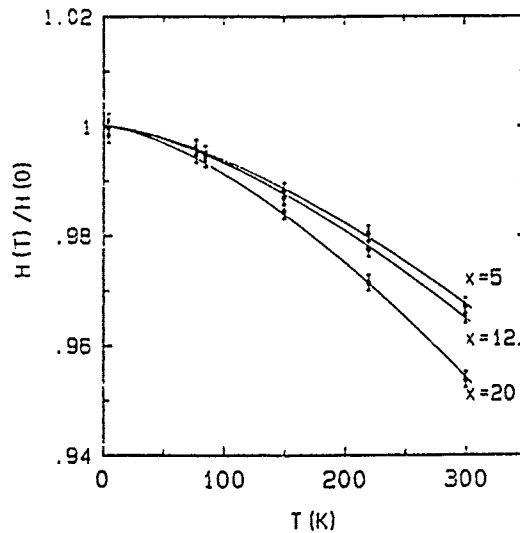


Figure 5. Magnetic hyperfine field (H) vs. temperature (T) for the 5 ML Fe superlattices. Note that  $(\text{Fe}_5\text{Ag}_x)_{30}$ , where  $x$  = Ag ML thickness.

Table II. Summary of measured values of  $H_0$  (ground state,  $T=0^\circ\text{K}$ , hyperfine field) and  $B$  for all superlattice films.

Fe(ML)	Ag(ML)	$H_0$ (kG)	$B(\text{K}^{-3/2})$
8	5	342.5	$6.25 \times 10^{-6}$
8	12	342.6	$6.75 \times 10^{-6}$
8	20	342.9	$8.81 \times 10^{-6}$
5	5	342.9	$6.96 \times 10^{-6}$
5	12	343.2	$7.88 \times 10^{-6}$
5	20	343.4	$9.75 \times 10^{-6}$

Table II lists the values of  $H_0$  and  $B$  for all the films, where  $H_0$  represents the ground state ( $T=0\text{K}$ ) hyperfine field. Both series of films have values of  $H_0$  enhanced over the bulk value of 340kG. Also, the 5ML Fe structures have values of  $H_0$  greater than those for the 8ML Fe structures. Previous investigations have determined that the surface of an Fe film in contact with Ag has a ground state hyperfine field enhanced by approximately 3% over the bulk value, to approximately 348kG [7,12]. The results for the 5ML Fe structures are consistent with this previous work. Since the Fe component of these films consists of two surface monolayers (ML) and three monolayers which are more bulk-like, the measured value of  $H_0$  is expected to be a weighted average of these two different values. Therefore, we expect  $H_0$  to be greater for the 5ML Fe structures than for the 8ML films; for these thinner films surface effects are more prominent.

The effect of the surface on the magnetic properties of the superlattices is more readily apparent from an examination of the  $B$  factor than  $H_0$ . The value of  $B$  for bulk Fe, which is a measure of how easy it is to form collective magnetic excitations (spin-waves, for example), is approximately  $5.1 \times 10^{-6} \text{K}^{-3/2}$ , as determined from a measurement of our own bulk-like calibration foil. It has been shown both theoretically and experimentally that collective magnetic excitations at the surface are created more readily than in the bulk and that as a consequence the  $B$  factor at the surface is approximately twice the bulk value [4,13,14]. Since  $B$  changes by a factor of 2 from the bulk to the surface whereas  $H_0$  changes by only 3%, any effects of the surface on the magnetic properties of the superlattice will be more easily seen by measurements of  $B$  than by measurements of  $H_0$ .

For both series of films the  $B$  factor increases as the Ag thickness increases and all of them are greater than the bulk value. For the 8ML Fe structures  $B$  is equal to  $6.2 \times 10^{-6} \text{K}^{-3/2}$  for  $x=5$  and increases to  $8.81 \times 10^{-6} \text{K}^{-3/2}$  for  $x=20$ , a value between that of the bulk and the surface. This implies that the effects of the surface on the magnetic excitations of the film are more prominent as the Ag thickness increases. This same trend is seen in the 5ML Fe films. For the film with the thinnest Ag component ( $x=5$ )  $B$  equals  $6.96 \times 10^{-6} \text{K}^{-3/2}$  and for the film with the thickest Ag component ( $x=20$ )  $B$  increases to  $9.75 \times 10^{-6} \text{K}^{-3/2}$ .

As the data indicate,  $B$  varies not only with Ag thickness, but also with Fe thickness. For any given thickness of Ag, the superlattice with the thinner Fe component has the greater  $B$  value. Since a greater fraction of the Fe component in these thinner films is at the surface, this enhancement of the  $B$  factor must be an effect associated with the Fe surface.

All of the above observations can be understood if there is a magnetic interaction between neighboring Fe components which are separated by Ag. When the Ag layer is thin the interaction between neighboring Fe surface atoms is strong and the result is more bulk-like behavior. As the Ag layer becomes thicker the neighboring surface atoms become more isolated and exhibit more nearly surface magnetic behavior. This interaction can explain not only the variations in  $B$  but also the variations in  $H_0$  seen in the 5ML Fe superlattices. For these three structures, Table II shows that as the thickness of the Ag component increases,  $H_0$  increases. For thin Ag barriers the magnetic

interaction decreases and the Fe surface layers act more like an isolated surface, yielding an enhanced value for  $H_0$ .

This conclusion concerning magnetic coupling across a nonmagnetic layer is consistent with Fe/Ag heterostructures previously studied in the laboratory for which a magnetic proximity effect was observed across an Ag barrier [15]. In another study, spin-wave modes due to exchange coupling between two Fe layers separated by several different nonmagnetic components have been detected by light scattering and microwave absorption [16]. A magnetic interaction across an Ag barrier for Ag thicknesses up to 30 Å was observed.

#### CONCLUSIONS

High quality, well-characterized epitaxial Fe(110)/Ag(111) heterostructures have been grown for the first time. In all cases the magnetization was in the plane of the film. The magnetic hyperfine field and temperature dependence of the magnetization determined by Mössbauer spectroscopy exhibit surface-like behavior as the Fe becomes thin and the Ag becomes thick. Also, a magnetic coupling was observed between neighboring Fe components separated by very thin Ag layers.

#### REFERENCES

1. H.C. Snyman and G.H. Olsen, J. Appl. Phys. 44, 888 (1973); G.H. Olsen and H.C. Snyman, Acta Metallurgica 21, 769 (1973).
2. R. Richter, J.G. Gay and J.R. Smith, Phys. Rev. Lett. 54, 2704 (1985).
3. C.L. Fu, A.J. Freeman and T. Oguchi, Phys. Rev. Lett. 54, 2700 (1985).
4. J.C. Walker, R. Droste, G. Stern and J. Tyson, J. Appl. Phys. 55, 2500 (1984).
5. J. Tyson, A. Owens and J.C. Walker, J. Magn. Magn. Mat. 35, 126 (1983).
6. J.J. Krebs, B.T. Jonker and G.A. Prinz, J. Appl. Phys. 61, 3744 (1987).
7. J. Tyson, A. Owens, J.C. Walker and G. Bayreuther, J. Appl. Phys. 52, 2487 (1981).
8. G. Bayreuther and G. Lugert, J. Magn. Magn. Mat. 35, 50 (1983).
9. I. Vincze and J. Koliar, Phys. Rev. 6, 1066 (1972).
10. D.L. Mills and A.A. Maradudin, J. Phys. Chem. Solids 28, 1855 (1967).
11. J. Mathon, Phys. Rev. B24, 6588 (1981).
12. C.J. Gutierrez, S.H. Mayer and J.C. Walker, J. Magn. Magn. Mat. (in press)
13. G.T. Rado, Bull. Am. Phys. Soc. 2, 127 (1957).
14. J. Korecki and U. Gradmann, Eur. Lett. 2, 651 (1986).
15. Z.Q. Qiu, H. Tang, Y.W. Du, G.P. Stern and J.C. Walker, J. Appl. Phys. 63, 3657 (1988).
16. P. Swiatek, F. Saurenbach, Y. Pang, P. Grunberg and W. Zinn, J. Appl. Phys. 61, 3753 (1987).

## MAGNETIC RESONANCE STUDIES OF Fe/Ag SUPERLATTICES WITH Fe LAYERS < 6 MONOLAYERS THICK

J.J. KREBS, B.T. JONKER AND G.A. PRINZ  
Naval Research Laboratory, Washington, DC 20375-5000

### ABSTRACT

X-band magnetic resonance has been used to study a set of Fe/Ag(001) superlattice (SL) samples with Fe layers only 0.9-5.5 monolayers (ML) thick. The samples (grown by MBE and previously examined by Mossbauer and magnetization techniques) were studied throughout the 5-300 K range. The SL's with  $t(\text{Fe}) < 3$  ML exhibit a marked downturn in their resonance fields below a temperature which decreases with  $t(\text{Fe})$  and, simultaneously, the linewidths increase. We suggest that this behavior is due to magnetic relaxation processes in these samples.

### INTRODUCTION

Ultrathin samples of Fe grown epitaxially on Ag(001) have proved to be a remarkably rich and fruitful system for studying how the behavior of magnetic films is modified when their thickness is reduced to only a few atomic monolayers (ML). Such films, as well as related Fe/Ag(001) superlattices containing ultrathin (<10 ML) Fe layers, have been studied extensively both experimentally [1-7] and theoretically [8-10]. These experiments include spin-polarized photoemission [1,2], ferromagnetic resonance [3], and spin-polarized SEM magnetic domain [4] studies of single Fe films, and also Mossbauer [5], magnetization [6], and preliminary magnetic resonance [7] studies of the superlattice (SL) samples reported on here.

Many of these papers were motivated by the observed lack of in-plane spin polarization for Fe/Ag(001) samples when the Fe thickness  $t(\text{Fe})$  is less than 3 ML [1]. This was in marked contrast to the theoretical predictions [8,9] of an enhanced Fe moment for such films. It was suggested in [1] that the polarization absence could be due to the Fe-film Curie temperature being below 300K or to a large surface anisotropy which forced the Fe moments to lie normal to the surface. Calculations [10] offered some support for the latter idea.

In this paper, we give a more complete account of our temperature-dependent magnetic resonance studies of Fe/Ag(001) SL samples with ultrathin Fe layers.

### EXPERIMENTAL

The Fe/Ag(001) SL's used in this work were prepared by molecular beam epitaxy and had the following structure. Starting with a

GaAs(001) substrate, a 0.2  $\mu\text{m}$  ZnSe(001) epilayer was grown to improve the surface quality. This was followed by a 500  $\text{\AA}$  thick Ag(001) base layer which was initiated with a Fe seed layer 5-10  $\text{\AA}$  thick. Then the unit consisting of a  $\text{Fe}^{57}$ (001) layer  $t(\text{Fe})$  thick and a Ag(001) layer  $t(\text{Ag})$  thick was repeated  $N$  times and finally capped with additional Ag and polycrystalline Al protective layers. The actual structure of the SL's studied is given in Table I. The details of growth procedure, the Auger characterization to check chemical purity, and the RHEED observations of single crystallinity of all the SL layers have been given earlier [5,6] and are not repeated here. We do call attention, however, to the observation [11] of well-defined superlattice satellites in the neighborhood of the Ag(002) reflection when the SL samples are examined in a  $\theta$ - $2\theta$  x-ray diffractometer. This is an indication of good periodicity and sharp ( $<0.5$  ML wide) interfaces.

The magnetization of these SL's was examined [6] over the magnetic field range 0-50 kOe and temperature range 7-300 K with the magnetic field applied either normal ( $\perp$ ) or parallel ( $\parallel$ ) to the film plane. These data were obtained with a SQUID magnetometer.

The magnetic resonance data were obtained with a Varian E-9 microwave spectrometer at 9.3 GHz and at temperatures from 5-300 K with the sample in a He gas stream. The resonance data were taken with the magnetic field  $H$   $\parallel$  or  $\perp$  to the film plane. A limited resonance data set was obtained at 35 GHz with  $H$  in the sample plane to look for in-plane anisotropy at room temperature.

Table I. Superlattice Structures

$t(\text{Fe})$ (ML)	$t(\text{Ag})$ (ML)	$N$
0.9	3.9	45
1.8	4.8	30
2.4	5.6	20
5.5	7.0	7
1 ML(Fe) = 1.43 $\text{\AA}$ , 1 ML(Ag) = 2.04 $\text{\AA}$		

#### PREVIOUSLY-DEDUCED BEHAVIOR

We briefly summarize the previous Mossbauer and magnetization results on the Fe/Ag SL samples studied here for comparison with the magnetic resonance data.

The Mossbauer studies [5] showed that for SL samples containing Fe layers  $< 3$  ML thick that the Fe moments were predominantly perpendicular to the film at low temperatures, that there was no net hyperfine field (hence, no moment) at room temperature, and that the Mossbauer linewidths were strongly dependent on both temperature and  $t(\text{Fe})$ , suggesting relaxation rates  $> 10^7 \text{ sec}^{-1}$  even when  $T < 100$  K. On

the other hand, the 5.5 Fe ML SL showed a well-resolved hyperfine spectrum at 300 K with clear evidence that the magnetization was in the plane of the film.

The  $M$  vs  $H$  data [6,7] showed that for samples with  $t(\text{Fe}) < 3\text{ML}$  that the saturation magnetization  $M_S$  has a strong  $T$  dependence between 7 and 300 K, that the low- $T$   $M_S$  value is close to that of bulk Fe, and that  $M_S$  shows an initial linear rather than quadratic dependence on  $T$  - all of which are consistent with 2-dimensional magnetic behavior. At low magnetic fields, there is a large low- $T$  susceptibility if  $H$  is perpendicular to the film so that it is easier to saturate the SL with  $H \perp$  film than for  $H \parallel$  film - in contrast to the usual case for thin Fe films. Finally, we point out that below 30 K for the 2.4 ML sample there is a remnant magnetization  $M_r$  only for  $H \perp$  film while, in contrast, for the 5.5 Fe ML sample an in-plane orientation of  $M$  is clearly favored.

The  $M_r$  values found in the 2.4 ML SL are only a small fraction of  $M_S$  and become negligibly small for  $T > 50$  K. It should be noted, however, that the zero-field Mossbauer data indicate a clear-cut local moment normal to the film for  $T < 150$  K suggesting [6] that the sample consists of many up and down magnetic domains with  $M \perp$  plane. Such a domain configuration is in fact the lowest energy state of an ultrathin ferromagnetic film when the surface anisotropy has the proper sign and magnitude to overwhelm the demagnetizing energy which favors  $M$  in the plane [12]. The temperature-dependent fluctuations of these domains [13] apparently are responsible for the decrease in  $M_r$  with increasing  $T$ .

#### MAGNETIC RESONANCE RESULTS AND DISCUSSION

The X-band magnetic resonance spectra of the 2.4 ML superlattice at room temperature are shown in Fig. 1. Note that there is a shift of 0.9 kOe between the derivative line centers for  $H \parallel$  and  $H \perp$  the film plane. All the SL's with  $t(\text{Fe}) < 3$  ML exhibit such shifts with magnitude  $\leq 0.9$  kOe at room temperature as shown in Fig. 2. On the other hand, the line shift for the 5.5 ML SL, which has a permanent magnetic moment at 300 K [5], is 5.2 kOe.

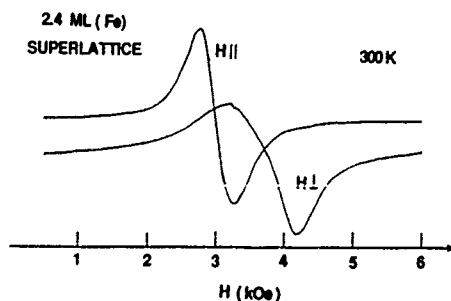


Figure 1. The 9.3 GHz magnetic resonance spectra of a Fe/Ag superlattice with Fe layers 2.4 ML thick.

These shifts can be understood qualitatively as follows. Let  $M'$  be the effective magnetization of a magnetic film and let us temporarily ignore any source of anisotropy other than the demagnetizing energy. Then one can show that the magnetic resonance fields are given by the solutions of the following equations:

$$\omega / \gamma = H - 4\pi M'_{\perp}(H) \quad H \perp \text{film} \quad (1)$$

$$(\omega / \gamma)^2 = H [ H + 4\pi M'_{\parallel}(H) ] \quad H \parallel \text{film} \quad (2)$$

where  $\omega$  is the circular microwave frequency,  $\gamma$  is the gyromagnetic ratio of the magnetic film, and we have explicitly indicated that  $M'$  is a function of  $H$  and, in general, different depending on whether  $H$  is in or normal to the SL plane.

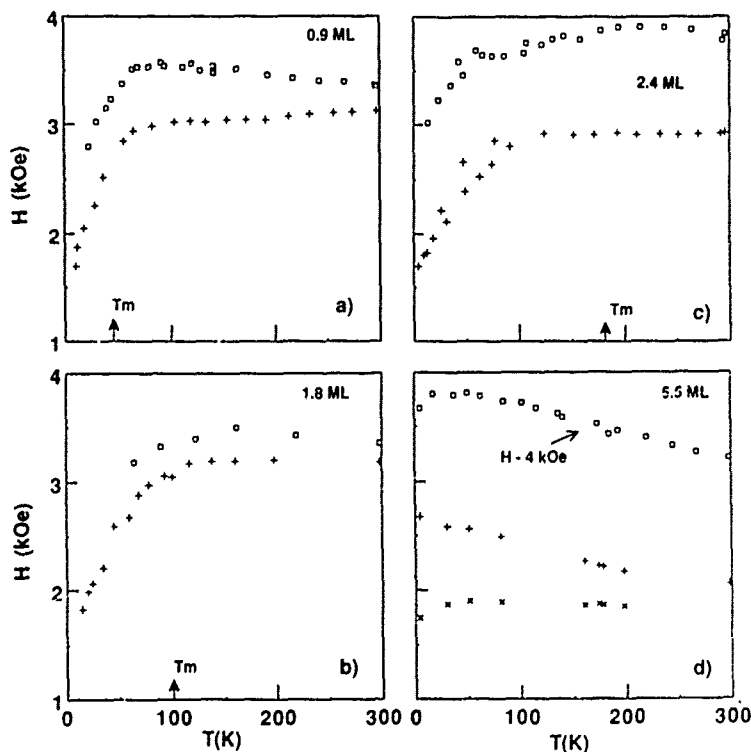


Figure 2. The temperature dependence of the magnetic resonance fields for four Fe/Ag superlattices containing ultrathin Fe layers with  $H \parallel$  (+, x) or  $H \perp$  (□) to the sample plane. The thicknesses of the Fe layers are indicated. Note that in d) the fields for  $H \perp$  film have been reduced by 4 kOe before plotting and that there are two resonance lines for  $H \parallel$  film which exchange intensity as the temperature is lowered. See text for the meaning of the arrows.

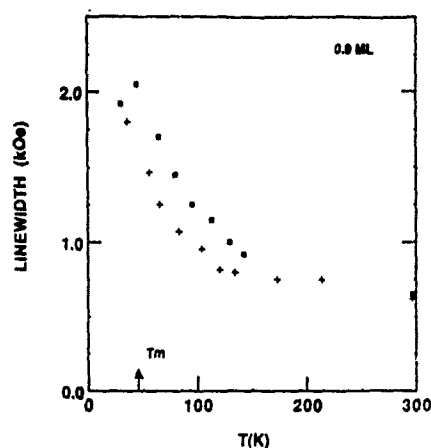


Figure 3. Temperature dependence of the resonance linewidths for the 0.9 ML superlattice. Symbol meaning same as in Fig. 2.

If there is a uniaxial anisotropy  $K_U$  normal to the plane, then  $4\pi M'(H) = 4\pi M + 2K_U/M$ . If one compares the line positions calculated from Eqs.(1) and (2) (using  $K_U = 0$ ,  $g = 2.09$ , and the measured  $M_{||,\perp}(H)$ ) for the 2.4 ML sample, one finds that the experimental shifts are much smaller than expected, consistent with a finite  $K_U$  favoring  $M \perp$  film.

Note, however, that for  $T > 100$  K the SL's with  $t(\text{Fe}) < 3$  ML always have their  $H_{\perp}$  values greater than their  $H_{||}$  ones, indicating that the magnetization induced by the applied field prefers to lie in the film plane. This is not inconsistent with zero-field Mossbauer data for which  $M(0) = 0$  at these temperatures. At very low temperatures ( $< 30$  K), for which the Mossbauer and  $M$  vs  $H$  data show that  $M$  prefers to lie normal to the film and hence one would expect  $H_{||} > H_{\perp}$ , these superlattice samples do not behave like the usual thin films in their magnetic resonance properties.

A very unusual aspect of the data in Fig. 2 for all the SL's with  $t(\text{Fe}) < 3$  ML is that when the temperature is lowered below some  $t(\text{Fe})$ -dependent value both the  $||$  and  $\perp$  resonance fields shift downward, and continue dropping down to the lowest temperature at which reliable data was obtainable. (Since the resonance linewidth increases quite rapidly with decreasing  $T$  as shown in Fig. 3, the resonance signal becomes increasingly difficult to discern clearly below 50 K especially for  $H \perp$  film because of microwave signals in the GaAs substrate.) For reference purposes, the temperatures  $T_m$  below which the Mossbauer spectrum indicates a net moment are marked by arrows in Fig. 2. Note that the sharpest drop in resonance field occurs somewhat below  $T_m$  for the film in question.



Interestingly enough, quite similar resonance behavior has been observed by Malozemoff and Jamet [13] in the spin-glass-like material  $Gd_{0.37}Al_{0.63}$ . In that case, the downward line shifts ( $\parallel$  and  $\perp$ ) and the increasing linewidth as  $T$  decreased were attributed to local demagnetizing effects in a magnetically inhomogeneous system. The shifts took place just below the paramagnetic Curie temperature of the alloy. For  $Gd-Al$ , the authors assumed (and found some evidence for) randomly-shaped ferromagnetic clusters imbedded in a weakly ferromagnetic sea. In spite of the similarity in behavior, we find it difficult to see how one could apply that model to our superlattice samples which, as far as we can tell, have well-formed ultrathin  $Fe$  layers separated by  $Ag$  in which  $Fe$  is immiscible.

At the present time, we do not have an alternative fully-developed model which can explain the temperature-dependent resonance data. We suggest, however, that the behavior probably arises from two-dimensional relaxation effects [5, 14] in these superlattice samples.

The authors wish to thank the Office of Naval Research for financial support and F. Kovanic and D. King for their technical assistance.

#### REFERENCES

1. B.T. Jonker, K.-H. Walker, E. Kisker, G.A. Prinz, and C. Carbone, Phys. Rev. Lett. **57**, 142(1986).
2. M. Stampanoni, A. Vaterlaus, M. Aeschlimann, and F. Meier, Phys. Rev. Lett. **59**, 2483(1987).
3. B. Heinrich, K.E. Urquhart, A.S. Arrott, J.F. Cochran, K. Myrtle, and S.T. Purcell, Phys. Rev. Lett., **59**, 1756(1987).
4. J.L. Robins, R.J. Celotta, J. Unguris, D.T. Pierce, B.T. Jonker, and G.A. Prinz, Appl. Phys. Lett. **52**, 1918(1988).
5. N.C. Koon, B.T. Jonker, F.A. Volkening, J.J. Krebs, and G.A. Prinz, Phys. Rev. Lett. **59**, 2463(1987); F. A. Volkening et al., J. Appl. Phys. **63**, 3869(1988).
6. J.J. Krebs, B. T. Jonker, and G.A. Prinz, J. Appl. Phys. **63**, 3467 (1988).
7. J.J. Krebs, B. T. Jonker, and G.A. Prinz, Proc. 1988 ICM, J. Phys.-Colloq. (to be published).
8. Roy Richter, J.G. Gay and John J. Smith, J. Vac. Sci. Technol. A **3**, 1498(1985), and Phys. Rev. Lett. **54**, 2704(1985).
9. C.L. Fu, A.J. Freeman, and T. Oguchi, Phys. Rev. Lett. **54**, 2700 (1985).
10. J. Gay and R. Richter, Phys. Rev. Lett. **56**, 2728(1986).
11. B. T. Jonker, private communication.
12. Y. Yafet and E.M. Gyorgy, Phys. Rev. B **38**, 9145(1988).
13. F.A. Volkening, B.T. Jonker, J.J. Krebs, G.A. Prinz, and N.C. Koon, Proc. 1988 ICM, J. Phys.-Colloq. (to be published).
14. A.P. Malozemoff and J.P. Jamet, Phys. Rev. Lett. **39**, 1293(1977).

# MAGNETIC AND CRYSTALLOGRAPHIC INTERACTIONS OF ALTERNATELY DEPOSITED Fe AND Al ULTRA-THIN LAYERS

M. Nagakubo, T. Yamamoto and M. Naoe  
Dept. of Physical Electronics, Tokyo Institute of Technology,  
1-12-1, O-okayama, Meguro-ku, Tokyo 152, Japan.

## ABSTRACT

Multilayered films consisting of ferromagnetic Fe and nonmagnetic Al layers were prepared by using ion beam sputtering, and the relationships between their crystallographic characteristics and soft magnetic properties have been investigated in detail.

The periodicity of the multilayered films was confirmed for various layer thicknesses ( $\Delta Fe$  and  $\Delta Al$ ) above  $10\text{\AA}$  from their X-ray diffraction peaks at low angle. When  $\Delta Fe$  decreased along with  $\Delta Al$  from  $100\text{\AA}$ , the coercivity  $H_c$  decreased and showed a minimum of  $1.5\text{ Oe}$  at layer thicknesses of  $20\text{\AA}$ , but at the same time, the saturation magnetization  $4\pi M_s$  which was estimated from total thickness of the Fe layers decreased from  $20\text{ kG}$  and showed drastic decrease at  $\Delta Fe$  below  $10\text{\AA}$ . For  $\Delta Fe$  above  $100\text{\AA}$ ,  $4\pi M_s$  was constant around  $20\text{ kG}$  without dependence on  $\Delta Al$ . When  $\Delta Al$  was changed for  $\Delta Fe$  of  $100\text{\AA}$ , the values of  $H_c$  had a interesting relationship with the crystallite orientation in Fe layers. Namely, the preferentially oriented planes of bcc  $\alpha$ -Fe crystallites changed from (110) to (200) in the case of Al layer thinner than  $15\text{\AA}$  and  $H_c$  showed a minimum below  $4\text{ Oe}$  for  $\Delta Al$  in this transition range of crystallite orientation, while  $4\pi M_s$  of all Fe layers themselves was kept at  $20\text{ kG}$ . Taking into consideration that the nearest atomic distance of fcc Al and the lattice constant of bcc Fe is almost the same, these results may be caused by crystallographical interaction at the interfaces between Fe and Al layers.

## INTRODUCTION

Recently, the studies on multilayered films consisting of ferromagnetic materials and nonmagnetic layers has become very interesting, since they exhibit novel magnetic properties. It has been reported that the ferromagnetic films sputtered by the ultra-thin layers of the other materials, such as  $\text{FeSi/SiO}_2$ ,  $\text{Fe/Ni}$  and  $\text{Fe-C/Fe-Ni}$  multilayered films, show a low coercivity,  $H_c$ , and high saturation magnetization,  $4\pi M_s$ , for the soft magnetic materials. They may be very useful for the magnetic layer in thin film-type head with high performance.[1][2]

However, it is very difficult utilizing conventional plasma sputtering systems to prepare the multilayered films by alternately depositing the materials with large solubility among each other because the atomic interdiffusion between adjacent layers may be induced by bombardment of high energy particles on the growing layer during deposition. In this regard, the ion beam sputtering system is very adaptable for preparing them because the glow discharge plasma in the ion source is perfectly isolated from targets and substrates, and the bombardment is almost negligible. In addition, since ion beam sputtering is performed in vacuum at very low gas pressure, the sputtered atoms can arrive at the substrate without loss of kinetic energy due to collisions with residual gas on their way and the adatoms can take enough long random walk on the film surface. Therefore, this system can form continuous films with thickness as small as a few atomic layers.

In this study, the Fe/Al system is investigated. Few studies on Fe/Al multilayered films have been reported, while the Fe-Al alloy system have been extensively investigated for soft magnetic materials.[3] The

relationships between crystal structure and magnetic properties of multilayered films as well as those of Fe and Al layers will be described.

## EXPERIMENT

Figure 1 shows the ion beam sputtering apparatus used in this study. The ion source is a Kaufman type source with two grids.<sup>-7</sup> The background pressure was  $2 \times 10^{-7}$  Torr. Argon as pure as 99.999% at the pressure of  $1.5 \times 10^{-4}$  Torr was introduced through the ion source as the working gas. Planar targets of Fe and Al with purity of 99.99% were sputtered by a uniform beam of argon ions fixed at an acceleration voltage of 500 V and extraction current of 3mA. The Fe/Al multilayered films were deposited on water-cooled glass slides by repeating clockwise and counterclockwise rotations of the target holder alternately. The deposition rates of Fe and Al were approximately 13 and 22 Å/min, respectively. The total thickness of films was kept at about 1400Å. Thicknesses of Fe and Al layers,  $\Delta Fe$  and  $\Delta Al$ , were controlled by adjusting the deposition times of Fe and Al, respectively.

Crystal structure was analyzed by means of X-ray diffractometry. Magnetic properties such as the saturation magnetization,  $4\pi M_s$ , and the coercivity,  $H_c$ , were determined from the hysteresis loops measured by using vibrating sample magnetometer.

## RESULTS AND DISCUSSION

### 1. Periodicity

Figure 2 shows the low angle X-ray diffraction diagrams which reveal apparent periodicity in the Fe/Al multilayered films. When the layer thicknesses exceeds 10Å, the diffraction peaks due to the formation of a compositionally modulated structure are observed, while the films with the layer thicknesses of 5Å did not show such diffraction peaks. The period length  $D$  calculated from  $2\theta$  angle of these peaks is slightly smaller than that obtained by adjusting the deposition parameters. The difference in  $D$  between them may be attributed to the multi-refraction effect of X-ray at the interfaces between Fe and Al layers.[4] These results could indicate that the

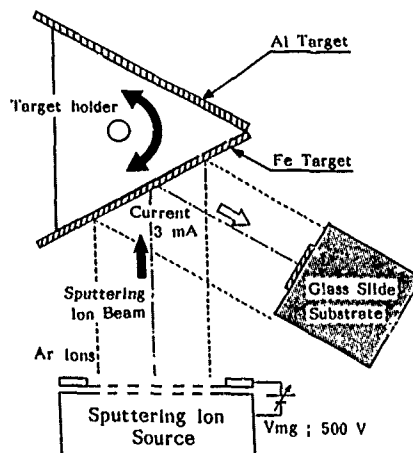


Fig.1, Schematic diagram of ion beam sputtering apparatus.

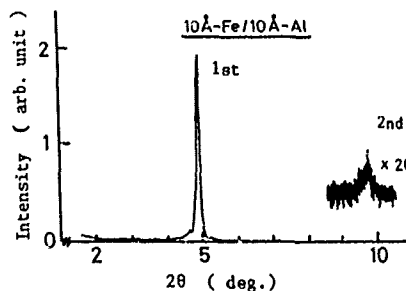


Fig. 2, The low angle X-ray diffraction diagram of Fe/Al multilayered films with layer thicknesses of 10Å.

interdiffusion between adjacent layers is negligible even for layer thickness as thin as  $10\text{\AA}$ .

## 2. Crystal structure and magnetic properties

For the first series of specimens,  $\Delta\text{Fe}$  and  $\Delta\text{Al}$  were almost the same and varied in the range of  $5 - 100\text{\AA}$ . They exhibited only one X-ray diffraction peak. The  $d$  spacing calculated from the peak position  $2\theta$  corresponded well with both  $d$  spacings of (110) planes of bcc  $\alpha\text{-Fe}$  crystallites and (200) planes of fcc Al ones. The Al single layer films with thickness of  $1400\text{\AA}$  exhibited an intense diffraction peak from (111) planes which is the closest packed plane in fcc Al crystallites. Therefore, it seems that this peak was diffracted from (110) planes of  $\alpha\text{-Fe}$  crystallites. Figure 3 shows the dependence of (110)  $d$  spacings on layer thicknesses,  $\Delta\text{Fe}$  and  $\Delta\text{Al}$ . As they decreased in the range below  $50\text{\AA}$ , the  $d$  spacing expanded from  $2.03$  to  $2.10\text{\AA}$  monotonically. However, such expansion in  $d$  spacing was substantially removed by annealing at  $300^\circ\text{C}$  for 3 hours in vacuum. This suggests that the expansion of (110)  $d$  spacing may originate from the lattice mismatch between Fe and Al layers.

Figure 4 and 5 show the dependence of  $4\pi\text{Ms}$  of all Fe layers themselves and  $H_c$  on  $\Delta\text{Fe}$  and  $\Delta\text{Al}$ , respectively. Then,  $4\pi\text{Ms}$  was about  $15\text{ kG}$  at  $\Delta\text{Fe}$  and  $\Delta\text{Al}$  in the range of  $10 - 50\text{\AA}$ . But, when they were below  $10\text{\AA}$ ,  $4\pi\text{Ms}$  decreased abruptly and took minimum value of  $10\text{ kG}$  at  $\Delta\text{Fe}$  and  $\Delta\text{Al}$  of  $5\text{\AA}$ . This may be attributed to the irregularity of layer interfaces and the inter-diffusion between adjacent layers. On the other hand,  $H_c$  depended significantly on the  $\Delta\text{Fe}$  and  $\Delta\text{Al}$  and exhibited a minimum below  $1.5\text{ Oe}$  at  $\Delta\text{Fe}$  and  $\Delta\text{Al}$  of  $20\text{\AA}$  as seen in Fig.5. Generally,  $H_c$  is closely related to the crystallites growth of  $\alpha\text{-Fe}$  because they prohibit the domain wall motion. Therefore, the decrease of  $H_c$  with decrease of  $\Delta\text{Fe}$  and  $\Delta\text{Al}$  from  $100$  to  $20\text{\AA}$  may result from the growth suppression of  $\alpha\text{-Fe}$  crystallites due to interruption by Al layers. And the increase of  $H_c$  at  $\Delta\text{Fe}$  and  $\Delta\text{Al}$  below  $20\text{\AA}$  may be the

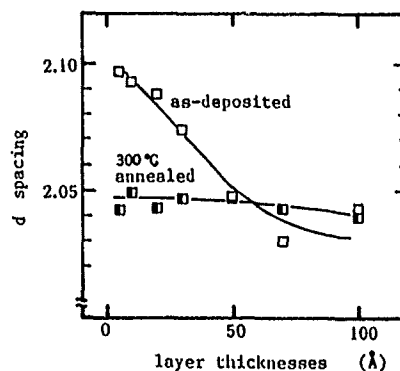


Fig.3, The dependence of (110)  $d$  spacing of  $\alpha\text{-Fe}$  crystallites on layer thicknesses. ( $\Delta\text{Fe}=\Delta\text{Al}$ )

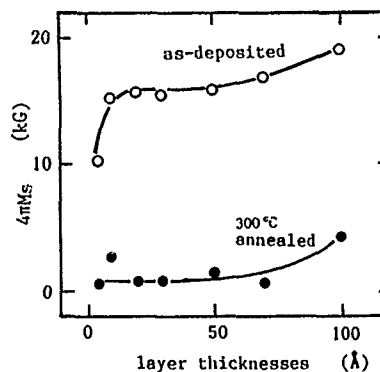


Fig.4, The dependence of  $4\pi\text{Ms}$  of Fe layers on layer thicknesses. ( $\Delta\text{Fe}=\Delta\text{Al}$ )

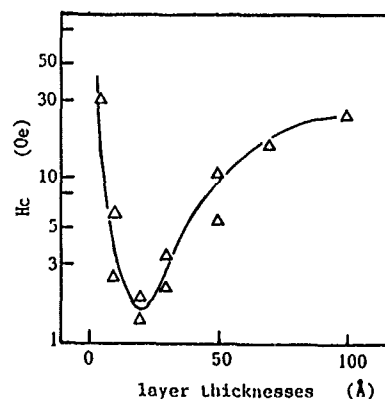


Fig.5, The dependence of  $H_c$  on layer thicknesses. ( $\Delta\text{Fe}=\Delta\text{Al}$ )

explained by the increase in the number of interfaces. When these films were annealed at 300°C for 3 hours, the  $4\pi M_s$  decreased to below 1kG and  $H_c$  increased in all range of  $\Delta Fe$  and  $\Delta Al$ . Taking it into consideration that the bcc FeAl crystallites shows paramagnetic properties, these results may be due to the FeAl crystallite growth at interface of Fe and Al layers by annealing.

Next, the characteristics of films with different layer thicknesses of Fe and Al were investigated. Figure 6 shows the dependence of the diffraction intensity and d spacing of  $\alpha$ -Fe crystallites in films with  $\Delta Al$  of 20Å on  $\Delta Fe$ . All the spectra had only one peak, that diffracted from the (110) planes of  $\alpha$ -Fe crystallites. The peak height increased abruptly as  $\Delta Fe$  increases in the range above 200Å. On the other hand, the d spacing was expanded drastically with decrease of  $\Delta Fe$  in the range below 100Å in a similar way to the films with the same layer thicknesses of Fe and Al. The expansion in d spacing was substantially removed by annealing at 300°C for 3 hours in vacuum.

Figure 7 shows the dependence of  $4\pi M_s$  of Fe layers and  $H_c$  on  $\Delta Fe$  for  $\Delta Al$  of 20Å. The value of  $4\pi M_s$  increased with increase of  $\Delta Fe$  and took constant value of about 20kG at  $\Delta Fe$  above 100Å, which is near to value of bulk Fe. However,  $H_c$  increased with  $\Delta Fe$  monotonically. As these films were annealed, films with  $\Delta Fe$  above 50Å did not show a remarkable change of  $4\pi M_s$  and showed a decrease of  $H_c$  at  $\Delta Fe$  above 200Å. This result could be caused by interdiffusion and irregularities at the layer interfaces due to annealing which is closely related to removing process of the internal stress stored to the layer interfaces.

Figure 8 shows the dependence of  $4\pi M_s$  Fe layers and  $H_c$  on  $\Delta Al$  for  $\Delta Fe$  of 100Å. The  $4\pi M_s$  of the films with  $\Delta Al$  below 100Å was constant value about 20kG approximately. From this result, it seems that the Fe layers with  $\Delta Fe$  above 100Å shows  $4\pi M_s$  above 20kG without dependence on  $\Delta Al$ . On the other hand,  $H_c$  changed significantly as  $\Delta Al$  varied. Though  $H_c$  of an Fe single layer deposited by ion beam sputtering was about 7 Oe, that of Fe/Al multilayered films with  $\Delta Al$  below 10Å and above 70Å was higher than 20 Oe. The films with  $\Delta Al$  of 15 - 25Å had the minimum of 4 Oe. Taking it into consideration that the Fe layer thicknesses are constant value of 100Å, such tendency of  $H_c$  suggests the presence of some interactions between Fe and Al layers.

In case of Fe/Si multilayered films, the compositionally modulated structure was confirmed at each layer thicknesses above 10Å in similar way to Fe/Al multilayered films. However, the decrease of  $H_c$  was not observed and showed a minimum value of about 20 Oe when  $\Delta Si$  was varied under the

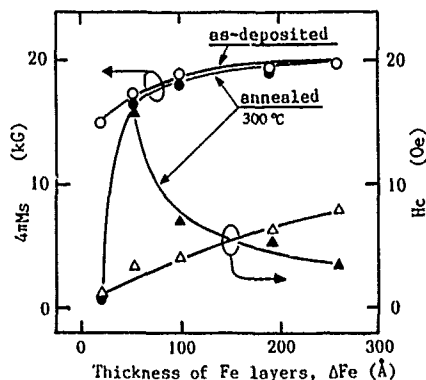


Fig.6, The dependence of diffraction intensity and d spacing of  $\alpha$ -Fe crystallites in films with  $\Delta Al$  of 20Å on  $\Delta Fe$ .

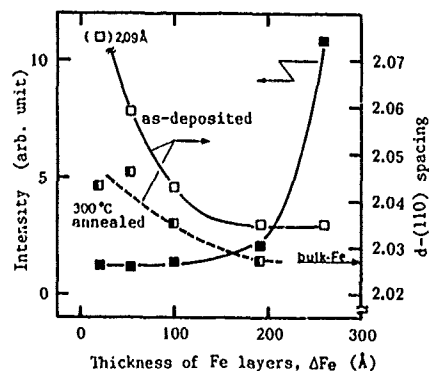


Fig.7, The dependence of  $4\pi M_s$  of Fe layers and  $H_c$  on  $\Delta Fe$  for  $\Delta Al$  of 20Å.

constant  $\Delta Fe$  of  $100\text{\AA}$ . This may show that the above-mentioned interaction between Fe and Al layers is based on each crystal structures of Fe and Al layers.

Figure 9 shows the X-ray diffraction spectra of Fe/Al multilayered films with various  $\Delta Al$  for  $\Delta Fe$  of  $100\text{\AA}$ . The films with  $\Delta Al$  above  $25\text{\AA}$  exhibited only one diffraction peak. As aforementioned, this peak might include both diffraction structure from  $\alpha$ -Fe and Al. However, it seems that the peak was diffracted mainly from (110) planes of  $\alpha$ -Fe crystallites. The diffraction intensity increased monotonically with increasing  $\Delta Al$ , while the d spacing was about  $2.04\text{\AA}$ . On the other hand, films with  $\Delta Al$  below  $15\text{\AA}$  exhibited (200) plane orientation of  $\alpha$ -Fe crystallites, where the diffraction intensity and the (200) d spacing increased with decrease of  $\Delta Al$ . With increase of  $\Delta Al$  from 15 to  $25\text{\AA}$ , the preferentially oriented plane changed from (200) to (110). The films with  $\Delta Al$  in this range exhibited very low diffraction peaks corresponding to both (110) and (200) planes and had minimum  $H_c$  among the specimen films.

As is well known, the lattice constant of  $\alpha$ -Fe ( $2.866\text{\AA}$ ) is almost the same as the distance between the nearest atoms of fcc Al ( $2.8635\text{\AA}$ ). Therefore, the (200) plane orientation of  $\alpha$ -Fe crystallites for  $\Delta Al$  below  $15\text{\AA}$  may be caused by epitaxial growth on the (200) plane of Al as seen in Fig. 10. Such crystallographical interaction at layer interfaces may lead to the growth restriction of  $\alpha$ -Fe crystallites and the enhancement of microscopic uniformity in Fe layers, as a result, the value of  $H_c$  could decrease. The dependence of plane orientation and diffraction intensity on  $\Delta Al$  revealed the significant relationship between (200) plane orientation and  $\Delta Al$ .

These results indicated that the magnetic properties of Fe/Al multilayered films may depend strongly on the crystal structure of Fe and Al layers which are sensitive to  $\Delta Fe$  and  $\Delta Al$ .

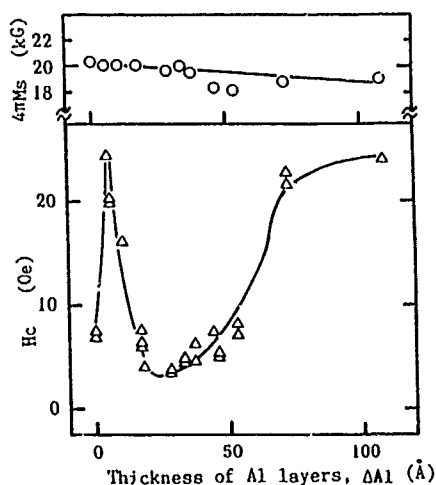


Fig.8, The dependence of  $4\pi M_s$  of Fe layers and  $H_c$  on  $\Delta Al$  for  $\Delta Fe$  of  $100\text{\AA}$ .

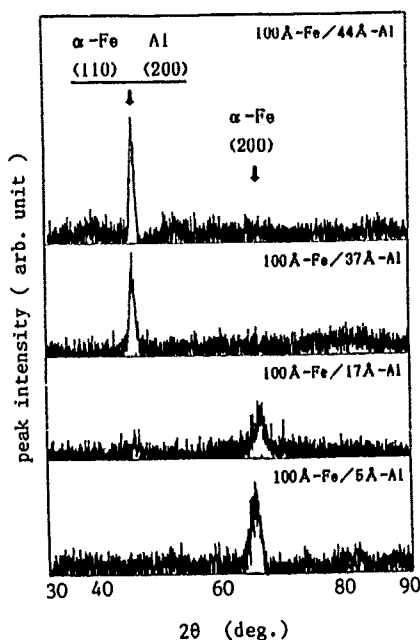


Fig.9, The X-ray diffraction diagrams of Fe/Al multilayered films with various  $\Delta Al$  for  $\Delta Fe$  of  $100\text{\AA}$ .

## CONCLUSION

Fe/Al multilayered films with various thicknesses of Fe and Al layers,  $\Delta Fe$  and  $\Delta Al$ , have been prepared by using the ion beam sputtering apparatus and the dependence of their magnetic properties and crystallographical characteristics on  $\Delta Fe$  and  $\Delta Al$  has been investigated.

(1) It was apparently confirmed that the films with  $\Delta Fe$  and  $\Delta Al$  above  $10\text{\AA}$  were composed of the compositionally modulated multilayers.

(2) For the films consisted of Fe and Al layers with the same thickness,  $H_c$  took minimum of 1.5 Oe at  $\Delta Fe$  and  $\Delta Al$  of  $20\text{\AA}$  and  $4\pi M_s$  of Fe layers was larger than 15 kG.

(3) For the films consisted of Fe and Al layers with different thickness,  $4\pi M_s$  of Fe layers was larger than 20 kG at  $\Delta Fe$  above  $100\text{\AA}$  without dependence on  $\Delta Al$ . In addition, soft magnetism of films with  $\Delta Fe$  above  $200\text{\AA}$  was rather improved after annealing at  $300^\circ\text{C}$  for 3 hours.

(4) The magnetic properties and the plane orientation of  $\alpha$ -Fe crystallites in the films with  $\Delta Fe$  of  $100\text{\AA}$  changed significantly with change of  $\Delta Al$  around  $15\text{\AA}$ . The films with  $\Delta Al$  in this range had the minimum  $H_c$  of 4 Oe and the large  $4\pi M_s$  above 17 kG. These results may be attributed to an alternate epitaxial growth between Fe and Al layers.

## REFERENCES

- [1], Y. Nagai, M. Senda and T. Toshima ; J. Appl. Phys. 63(4), 1136 (1988).
- [2], T. Kobayashi, R. Nakatani, S. Otomo and N. Kumasaka ; IEEE Trans. Magn., MAG-23, 2746 (1987).
- [3], F.J. Cadieu, M.A. Russak, and R.G. Pirich ; J. Magn. Magn. Mat. 54-57, 1598 (1986).
- [4], T. Shinjo and T. Takada ; Metallic Superlattice, Elsevier Sci. Pub., Amsterdam (1987).

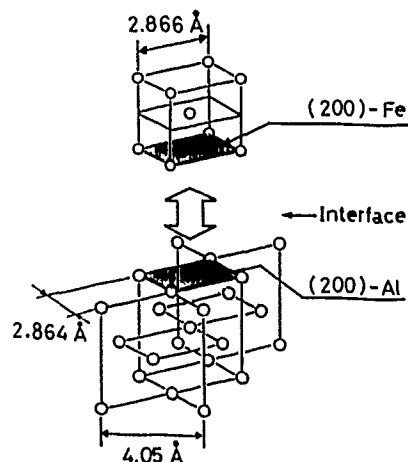


Fig.10, Geometric arrangement of atoms at the (200)-Fe/Al interface for multilayered films with  $\Delta Fe$  of  $100\text{\AA}$  and  $\Delta Al$  below  $15\text{\AA}$ .

CALCULATION OF MAGNETIZATION PROCESSES IN MULTILAYERS  
WITH ANTIFERROMAGNETIC COUPLING BETWEEN ADJACENT LAYERS

B. DIENY\*, J.P. GAVIGAN\*\*, J.P. REBOUILLAT\*

\* Laboratoire Louis Néel, C.N.R.S., 166 X, 38042 GRENOBLE cedex, France

\*\* Post doctoral research fellow of the Commission of the European Communities  
DG XII - EURAM

ABSTRACT

This paper presents calculations of hysteresis loops in ferromagnetic multilayer systems of cubic or uniaxial anisotropy with antiferromagnetic coupling between adjacent layers. The case of a bilayer has been systematically studied as a function of the strength of the anisotropy. The two limiting cases corresponding to either a coherent rotation of the magnetization or to a non-dissipative nucleation-propagation mechanism are investigated. The influence of the number of layers is also discussed.

INTRODUCTION

During the last decade, numerous artificially layered materials consisting of periodic juxtaposition of a magnetic and a non-magnetic material have been synthesised and studied [1]. In many cases (Cu/Ni, Mo/Ni, Fe/V, Co/Cu, Dy/Y...), a magnetic coupling through the non-magnetic layers has been observed or calculated, giving rise to long range order through the whole superstructure or changes in the spin-wave mode spectra. Several mechanisms have been proposed for this coupling including dipolar and RKKY interactions as well as percolation phenomena.

In this paper, we report a phenomenological study of the magnetic behaviour of model multilayer systems with uniaxial or cubic anisotropy and antiferromagnetic coupling between adjacent layers. Firstly, we compare the order of magnitude of some characteristic fields in multilayers and bulk antiferromagnets, then we present hysteresis loops calculated for a bilayer and finally we show the influence of the number of layers on the magnetization processes.



#### COMPARISON WITH BULK ANTIFERROMAGNETS

In bulk antiferromagnets with uniaxial anisotropy, it is well known that spin-flip or spin-flop transitions are observed when the field is applied along the easy axis of magnetization. Moreover, these materials are generally very difficult to saturate ( $B_{\text{saturation}} \approx 10\text{-}100$  Teslas) because of the difficulty to overcome the antiferromagnetic exchange interactions (roughly given by the Néel temperature usually of the order of 10-100 K).

In multilayers, the situation is rather different. The exchange coupling strength through the non-magnetic material is generally much weaker than the usual exchange interactions in bulk antiferromagnets. Moreover the total effective coupling between adjacent ferromagnetic films is proportionnal to the area of the interface while the total anisotropy energy and moment of the film are proportionnal to the volume of the film. As a result, the characteristic ratio of the anisotropy to exchange energy are of the order of  $10^{-2}$  to  $10^2$  instead of  $10^{-4}$  to 1 in bulk materials and the transition fields (spin-flop, saturation...) range between  $10^{-3}$  -  $10^{-1}$  T (which are easily obtained experimentally) instead of  $10$  -  $10^3$  T for bulk antiferromagnets.

#### MODELISATION

In general, magnetization processes in a magnetic material involve the nucleation of domains with domain wall propagation and/or coherent rotation of the magnetization. The tendency towards one or other mechanism depends on the domain-wall energy and on their pinning. In many multilayered systems [3], domains have already been observed in the film-plane. Due to the interlayer coupling, these domains keep their coherence over the whole superlattice thickness.

In order to take into account both mechanisms, two kinds of calculations have been carried out corresponding to the two limiting cases :

- In the first case, the magnetization of each layer is assumed to be single-domain and to rotate like a rigidly coupled block of moments (pure rotation mechanism). The total energy is minimized using a steepest descent method. For the corresponding calculation, the system remains in the same energy well, which is not necessarily the deepest one, until the barrier between the occupied well and the deepest one disappears.
- In the second case, we assume that by nucleation and propagation of domain walls the system can always reach the state of absolute minimum energy.

This fundamental state is always single-domain despite the dynamics necessary to reach it which may involve multi-domain processes. Such a calculation never gives any hysteresis contrary to the first method.

In a real sample, the magnetization process will be a more or less complicated intermediary between those calculated for the two limiting cases. For both cases the moments are assumed to move in the film plane because of the shape anisotropy or other negative perpendicular anisotropy. The multilayer is then equivalent to a one dimensional system described by the  $n$  angles  $\theta_1, \theta_2 \dots \theta_n$  between the magnetization of each of the  $n$  layers and the field. The total energy is written :

$$E = J_0 \sum_{i=1}^{n-1} \cos(\theta_i - \theta_{i+1}) - B \sum_{i=1}^n \cos \theta_i + \sum_{i=1}^n E_{Ai}$$

with  $E_{Ai} = -D \cos^2 \theta_i$  in the case of uniaxial anisotropy and

$E_{Ai} = K \cos^2 \theta_i \sin^2 \theta_i$  for cubic anisotropy.  $B$  is the applied field.

#### CASE OF BILAYER

The various hysteresis loop shapes obtained by the two calculations are shown in Fig. 1 for both anisotropy cases and with the field applied along an easy or a hard axis of magnetization.

All the transition fields in the magnetizing or demagnetizing processes have been calculated as a function of the anisotropy and plotted in the form of a phase diagram. The remanent magnetization and initial susceptibility have also been calculated. This complete study will be published elsewhere [2]. Here, we stress the main points :

- Assuming a pure rotation mechanism in the case of uniaxial anisotropy, leads to spin-flop and spin-flip transitions. Experimentally, such transitions have already been observed [4]. However, the transition field can be considerably reduced in comparison to the theoretical value through the nucleation-propagation phenomena.
- For both symmetries, the hysteresis cycle consists of two loops shifted symmetrically about the field axis as long as the anisotropy is not too strong. However, for large anisotropy (which is common in multilayers), the cycle calculated for coherent rotation becomes rectangular and resembles that of a ferromagnet. This explains how in some multilayers such as Co/Cu [5], antiferromagnetic couplings giving rise to a long-range antiferromagnetic order is observed by neutron diffraction, while the low temperature hysteresis loop rather indicates ferromagnetic behaviour.

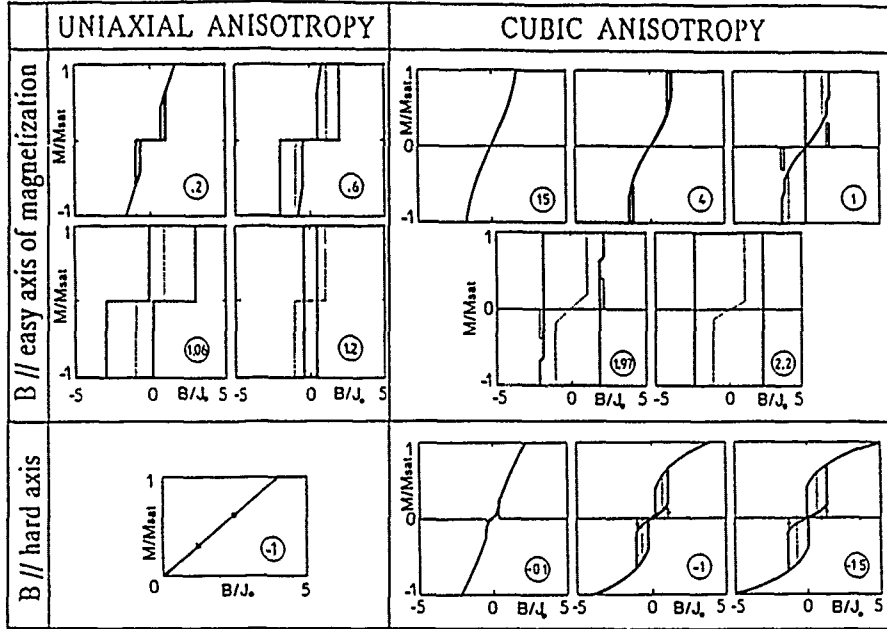


Figure 1 : Hysteresis loops of an antiferromagnetically coupled bilayer with uniaxial or cubic anisotropy. The field and anisotropy are normalized to the interlayer coupling and the value of the normalized anisotropy is written in the circle in the right low part of each figure. The full line corresponds to the pure coherent rotation mechanism and the dotted line to the solution of absolute minimum energy.

- In a real sample with cubic anisotropy, nucleation of domains plays a more important rule than for a uniaxial anisotropy. However, if strong pinning of domain walls occurs, coherent rotation of the magnetization may prevail. Calculations following the "coherent rotation" assumption in the cubic case indicate various transitions between symmetrical and non-symmetrical configuration where in the latter the two sublattices lie in two perpendicular wells of anisotropy energy. Within a domain, such configurations give rise to a transverse component of the magnetization but at a macroscopic scale the system keeps its symmetry about the field axis. Hysteresis loops measured on Fe/Cr [6] multilayers are in agreement with the calculated loop following the coherent rotation assumption in the case of a low  $K/J_0$  ratio.

However, for increasing thickness of Cr, i.e. for increasing  $K/J_0$ , ferro-magnetic like behaviour is attained without any first order transition in the magnetization process. This means that nucleation-propagation phenomena prevail when the antiferromagnetic coupling decreases. In Co/Cu [5] multilayers, the nucleation-propagation mechanism dominates at low temperature but at room temperature first order transitions are clearly observed in the magnetization-process. Thermal activation must be sufficient to induce coherent rotation of domains (in particular local spin-flip transitions) rather than progressive wall motion.

- In general, the energy dissipated per cycle is always lower when the field is applied along a hard than along an easy axis of magnetization.

#### INFLUENCE OF THE NUMBER OF LAYERS

As an example, Fig. 2 shows four hysteresis loops obtained for the same cubic anisotropy to exchange ratio ( $\frac{K}{J_0} = 0.6$ ) for four different numbers of layers, following the assumption of coherent rotation of the magnetization.

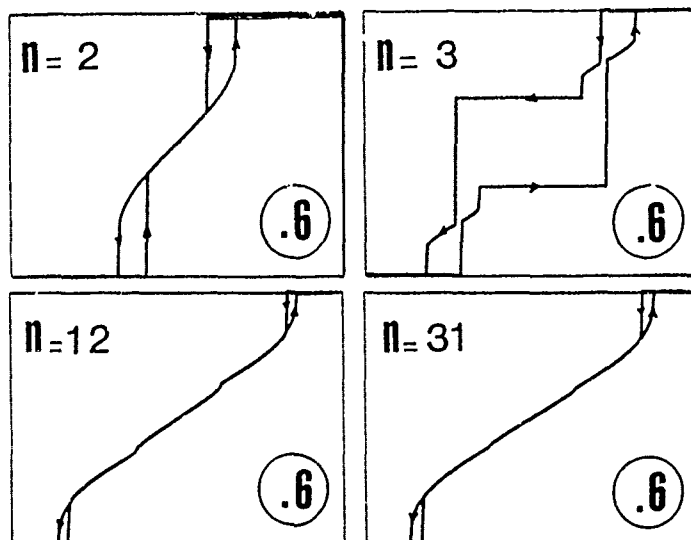


Figure 2 : Four hysteresis loops obtained for the same anisotropy and for different numbers of layers.

For a small number of layers  $n$ , a great difference exists according to whether  $n$  is even or odd (compensated magnetism or not / antiferro-ferrimagnetic behaviour). In another respects, when  $n$  increases, the hysteresis loop becomes increasingly smoother. Quantitatively, we have checked that, after a contraction of the field scale by a factor of 2, it is identical to the hysteresis loop of a bilayer with an anisotropy  $\frac{K}{J_0} = 0.3$ . This is in fact a general result in multilayers for which boundary effects vanish. In such case, all the layers labelled with an even index (similarly for an odd index) behave in a similar way so that the infinite multilayer can be considered as a bilayer with an interlayer coupling  $2J_0$  instead of  $J_0$ . As a result, the magnetization curve can be related from one case to the other by the scaling relation

$$M_{n=2} \left( \frac{K}{J_0}, \frac{B}{J_0} \right) = M_{n=\infty} \left( \frac{K}{2J_0}, \frac{B}{2J_0} \right)$$

However, this is only true if boundary effects do in fact become irrelevant when  $n$  increases. This is not always the case. As an example, starting in zero field in an antiferromagnetic configuration parallel to the easy axis of magnetization (uniaxial anisotropy) and increasing the field (also parallel to the easy axis), we have calculated the spin-flop field  $B_{SF}$  as a function of the strength of the anisotropy and the number of layers (Fig. 3).

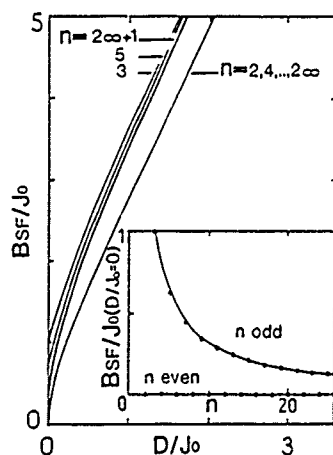


Figure 3 : Spin-flop field versus the strength of the uniaxial anisotropy for different number of layers.

The results are definitely dependent on the parity of  $n$ . For even  $n$ ,  $B_{SF}$  does not depend on  $n$ . In fact, for even  $n$ , the two extreme layers are initially antiparallel. The spin-flop process is then initialized on the surface and after propagates through the whole multilayer. As a result, the value of the spin-flop field does not depend on the number of layers. The

situation is different for odd  $n$  since all the moments oriented antiparallel to the field have two neighbours. In real samples, such effects should be observed for a small number of layers but progressively disappear with increasing  $n$ .

In conclusion, the calculations reported here display the magnetization behaviour expected for coherent rotation or non-dissipative nucleation-propagation mechanism. The real situation is never so pure. However, this study indicates some general tendencies and different kinds of transitions which may be observed experimentally.

#### REFERENCES

1. I.K. Schuller, "Physics, Fabrication and Applications of Multilayered Structures" (Springer - Berlin).
2. B. Dieny, J. Gavigan, J.P. Rebouillat, submitted to Journal of Physics : Condensed Matter (Great Britain).
3. See for instance, D.T. Pierce, proceedings of the MRS Spring Meeting, April 24-29, 1989, San-Diego (California), Symposium G, paper G2.1
4. P. Grünberg, R. Schreiber, Y. Pang, M.B. Brodsky, H. Sowers, Phys. Rev. Lett., 57, 19 (1986) 2442.
5. A. Cebollada, J.M. Gallego, R. Miranda, S. Ferrer, F. Batallan, G. Fillion, J.P. Rebouillat, Phys. Rev. B, Rapid Comm., 39 (1st May 1989) and J.P. Rebouillat, G. Fillion, B. Dieny, A. Cebollada, J.M. Gallego, J.L. Martinez, Proceedings of the M.R.S. Spring Meeting, April 24-29, 1989, San-Diego (California), Symposium G, paper G3.5.
6. M.N. Baibich, J.M. Broto, A. Fert, F. Nguyen Van Dau, F. Petroff, P. Etienne, G. Creuzet, A. Friederich, J. Chazelas, Phys. rev. Lett., 61, 21 (1988) 2472.

## GIANT MAGNETORESISTANCE OF (001) Fe / (001) Cr SUPERLATTICES

A. BARTHELEMY\*, M.N. BAIBICH\*, J.M. BROTO\*, R. CABANEL\*\*, G. CREUZET\*\*,  
P. ETIENNE\*\*, A. FERT\*, A. FRIEDERICH\*\*, S. LEQUIEN\*\*, F. NGUYEN VAN  
DAU\*\*, K. OUNADJELA\*.

\*Laboratoire de Physique des Solides, Université Paris-Sud,  
F 91405 Orsay, France

\*\*Laboratoire Central de Recherches, Thomson CSF, BP 10,  
F 91401 Orsay, France

## ABSTRACT

We present magnetoresistance measurements on (001)Fe/(001)Cr superlattices grown by MBE. The magnetoresistance is found to be very large for thin Cr layers. We ascribe this magnetoresistance to a magnetic gate effect.

We recently reported the observation of a very large magnetoresistance in (001)Fe/(001)Cr superlattices with thin Cr layers [1]. A large magnetoresistance has also been observed in Fe/Cr/Fe sandwiches [2]. In both cases, for Cr layers thinner than about 30 Å, an antiparallel coupling of the magnetization of neighbor Fe layers is indicated by magnetic, magneto-optic and light scattering measurements [1-3]. It thus turns out that the large magnetoresistance is associated with the change to parallel alignment in an applied field. In this paper, we present new data on the magnetic and transport properties of Fe/Cr superlattices and we concentrate on the discussion of the microscopic origin of the magnetoresistance.

The growth of (001)Fe/(001)Cr bcc superlattices by MBE on (001) GaAs substrates and their characterization by Reflection High Energy Electron Diffraction (RHEED), Auger Electron Spectroscopy (AES), X-ray diffraction and Scanning Transmission Electron Microscopy (STEM) have been described elsewhere [4,5]. As emphasized below, the interface roughness is an important parameter for the electron transport properties. For our samples, the main features of the STEM cross sections and of the AES profiles rule out a deep intermixing of Fe and Cr. However, with these techniques, the interface roughness cannot be really probed at the atomic scale (AES integrates the concentrations over a depth of about 12-15 Å).

In Fig 1a we show a typical hysteresis loop obtained by SQUID measurements at 5 K. Whereas, for superlattices with Cr layers thicker than 30 Å, the magnetization in the plane of the layers [6] can be saturated by a field smaller than 1 kG, it becomes harder and harder to saturate [7] when the Cr thickness  $t_{Cr}$  decreases from 30 Å to 9 Å [1,5]. For example, for the sample of Figure 1a, a field of about 5 kG is needed to saturate

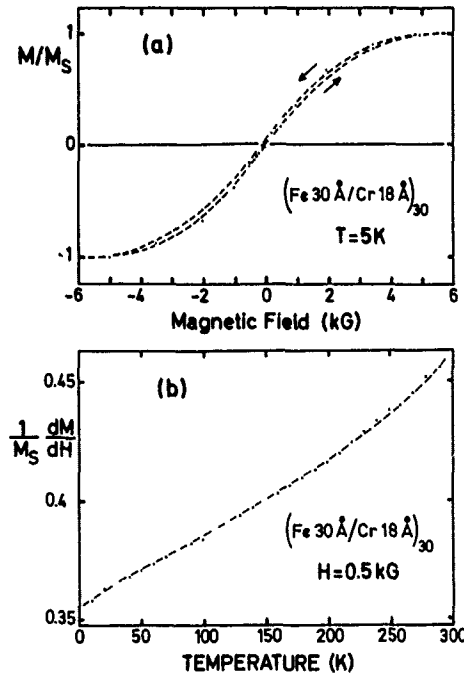


Fig 1 . SQUID data for the magnetization  $M$  of a  $(\text{Fe } 30 \text{ \AA}/\text{Cr } 18 \text{ \AA})_{30}$

superlattice. The magnetic field  $H$  is applied along  $[110]$  in the layer plane.  $M_S$  is the saturation magnetization at 5K.

a/ Magnetization loop at 5K  
b/ Temperature dependence of the initial slope of the magnetization curves,  $M_S^{-1} dM/dH$ . This slope is derived from measurements of  $M$  at 0.5 kG as a function of the temperature.

the magnetization. When the field is decreased back to zero, the magnetization comes back to a very small residual value (almost without hysteresis). This experimental behavior is what is expected for antiferromagnetic (AF) couplings between neighbor Fe layers through Cr, in agreement with the light-scattering and magneto-optical measurements of Grünberg et al [3] and the spin-polarized-low-energy-electron-diffraction (SPLEED) experiments of Carbone and Alvarado [8]. In the simple model where a fixed moment is ascribed to each Fe layer with AF couplings of the form  $J \cos \alpha$  ( $\alpha$  = angle between the moments of neighbor layers) one expects [5]

$$dM / dH = M_S^2 t_{Fe} / 4J \quad (1)$$

for the initial slope of the magnetization curves and

$$H_S = 4J / M_S t_{Fe} \quad (2)$$

for the saturation field. The progressive decrease of the initial slope and increase of  $H_S$  found in our samples can be ascribed to the increase of the AF coupling constant  $J$  when  $t_{Cr}$  is reduced from 30 Å to 9 Å. More realistic - and less simple - models taking into account the magnetic anisotropy and the finite stiffness constant of the Fe layers can be worked out to account for the experimental results more precisely [5].

As the temperature increases, whereas the saturation magnetization slightly decreases (by about 7 % from 5 K to Room Temperature), the initial slope increases. This is shown in Fig 1b and indicates that the



coupling constant slowly decreases as  $T$  increases (by about 30% between 5 K and RT). Additional measurements up to 350 K show that the slow decrease of  $J$  continues above RT and that a strong coupling still exist well above the Neel temperature of bulk Cr,  $T_N \approx 310$  K. This indicates that the interlayer coupling is not related to the antiferromagnetism of Cr, as in the models of the Hinchey-Mills type [9]. Alternative explanations - based on RKKY-type mechanisms- can be proposed. However this is not in the scope of this paper to discuss the question of the interaction mechanism and we proceed with the magnetoresistance properties.

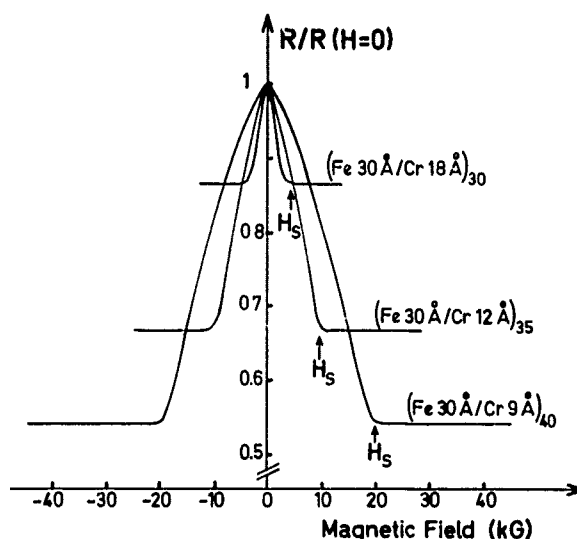


Fig 2: Magnetoresistance curves of three Fe/Cr samples at 4.2 K. The current and the magnetic field are along the same  $[110]$  axis in the plane of the layers. Arrows show the saturation field  $H_s$  for each sample. There is a small difference between the curves in increasing and decreasing fields (hysteresis) that we have not represented on the figure

Fig 2 displays magnetoresistance curves obtained at 4.2 K with magnetic field and current along the same  $[110]$  direction in the plane of the sample. When the magnetic field is applied, a large negative magnetoresistance is observed in the samples which exhibits a magnetization behavior characteristic of AF interlayer couplings (Fig 1), ie samples with  $t_{Cr} \lesssim 30$  Å. When the magnetization is saturated, for  $H > H_s$ , the resistivity is approximately constant. For the samples of Fig 2,  $H_s \approx 20.1$  kG

$R(H > H_S) / R(H = 0) \approx 0.56$  for  $(\text{Fe } 30 \text{ \AA} / \text{Cr } 9 \text{ \AA})_{40}$ ,  $H_S \approx 9.9 \text{ kG}$  and  
 $R(H > H_S) / R(H = 0) \approx 0.67$  for  $(\text{Fe } 30 \text{ \AA} / \text{Cr } 12 \text{ \AA})_{35}$ ,  $H_S \approx 5.1 \text{ kG}$  and  
 $R(H > H_S) / R(H = 0) \approx 0.88$  for  $(\text{Fe } 30 \text{ \AA} / \text{Cr } 18 \text{ \AA})_{30}$ , for  $t_{\text{Cr}} > 30 \text{ \AA}$ , the  
 magnetoresistance is much smaller. It turns out that both the  
 magnetoresistance and  $H_S$  decrease rapidly as  $t_{\text{Cr}}$  increases from  $9 \text{ \AA}$  to  
 above  $30 \text{ \AA}$ .

When the temperature increases, the magnetoresistance  
 progressively decreases and is smaller by about a factor of two at room  
 temperature. Finally, with other orientations of the field, the saturation  
 value of the magnetoresistance is practically the same (see Fig.2 of Ref  
 [1]), with, of course, a higher field needed to reach the saturation when the  
 field is perpendicular to the layers.

The experimental results - magnetization, magnetoresistance -  
 presented in fig 1 have been obtained for superlattices grown with similar  
 conditions in the same MBE run (March 1988). For the magnetic properties,  
 approximately the same results have been obtained with other series of  
 samples. In contrast the resistivity and magnetoresistance data depend  
 strongly on the growth conditions. First the resistivities turn out to be  
 randomly scattered between  $20 \mu\Omega\text{cm}$  and  $100 \mu\Omega\text{cm}$ . Also the variation of  
 the magnetoresistance as a function of  $t_{\text{Cr}}$  found for the series of Fig 2 can  
 hardly be reproduced. With samples grown in other runs we obtained some  
 very different values, for example  $R(H > H_S) / R(H = 0) \approx 0.69$  for

$t_{\text{Cr}} = 18 \text{ \AA}$  and  $R(H > H_S) / R(H = 0) \approx 0.97$  for  $t_{\text{Cr}} = 9 \text{ \AA}$ . As it will be  
 discussed below, this is probably due to the crucial role of the interface  
 roughness for the transport properties of multilayers. Our  
 characterizations by STEM and AES are not sensitive enough to probe the  
 interface roughness at the atomic scale, so that, at the moment, we are  
 unable to correlate our different resistivity and magnetoresistance results  
 with the interface quality of the corresponding samples. We have however  
 noticed that annealing our samples at  $215^\circ\text{C}$  during one hour reduces the  
 magnetoresistance without affecting the magnetic behavior significantly.  
 This again emphasizes the specific sensitivity of the transport properties  
 to the interdiffusion and interface effects.

We now discuss the origin of the magnetoresistance. In a perfect  
 metallic superlattice, as pictured in Fig.3a, the interfaces reflect  
 specularly and refract the electron waves, which cannot affect  
 significantly the longitudinal resistivity (similarly, in thin films, the  
 specular reflections do not contribute to the resistivity; in multilayers  
 the specular reflections and refractions can only change the way the  
 resistivities of the metals A and B are averaged). In contrast rough  
 interfaces act like defects of the superlattice and scatter the electrons,  
 as pictures in Fig.3b. In the case of Fe/Cr there will be scattering by "Cr  
 impurities" in Fe layers, by "Fe impurities" in Cr and by other defects of

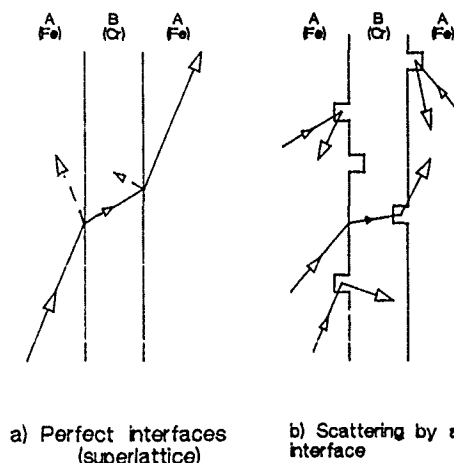


Fig 3. Schematic picture of the interface effects on the electron waves in a metallic multilayer.

a/ For a perfect superlattice, specular reflections and refractions.

b/ Scattering by a rough interface

the interface. We do not know very much on the interface roughness, which makes hard working out a model of the scattering. For our samples, which are made up of thin Cr layers between thicker Fe layer, we will assume that the main contribution arises from Cr impurities in Fe. We are then led to consider the question of impurity scattering in Fe.

In ferromagnetic transition metals, the current is mainly carried by the s band and, due to the asymmetry between the spin  $\uparrow$  (majority spin) and spin  $\downarrow$  densities of d states, the impurity scattering is generally very different for the spin  $\uparrow$  and spin  $\downarrow$  s electrons [10]. In addition, at low temperatures, the spin-flip scattering by spin waves is frozen, so that the usual scheme is that of independent spin  $\uparrow$  and spin  $\downarrow$  currents [10]. The resistivity can be written as

$$\rho_0^{-1} = \rho_{\uparrow}^{-1} + \rho_{\downarrow}^{-1} \text{ or } \rho_0 = \rho_{\uparrow} \rho_{\downarrow} / (\rho_{\uparrow} + \rho_{\downarrow}) \quad (3)$$

where  $\rho_{\uparrow}$  and  $\rho_{\downarrow}$  are the impurity resistivities for the two currents. For example, with  $\rho_{\downarrow} \gg \rho_{\uparrow}$ ,  $\rho \approx \rho_{\downarrow}$ , which expresses the short circuit effect by the less scattered electrons. In contrast, at room temperature for example, the scattering by spin waves flips frequently the s electron spins, which transfers momentum between the spin  $\uparrow$  and spin  $\downarrow$  currents and gives an average value to the resistivity [10].

$$\rho_1 = (\rho_{\uparrow} + \rho_{\downarrow}) / 4 \quad (4)$$

For Cr impurities in Fe, because the d levels of Cr lie within the spin  $\downarrow$  band of Fe and above the spin  $\uparrow$  d band,  $\rho_{\uparrow}$  is much larger than  $\rho_{\downarrow}$ . From experimental data one finds  $\rho_{\uparrow} \approx 6 \rho_{\downarrow}$  [10] and  $\rho_1 / \rho_0 \approx 2$

A mechanism similar to the "spin mixing" by spin wave scattering should

exist in Fe/Cr superlattices. At low temperatures and for  $H > H_S$  the situation is that of Cr impurities in a single domain of Fe, with a short-circuit by the less scattered electrons and  $P \approx P_0$ . At  $H = 0$ , when the electrons propagate in alternate magnetizations, the scattering rates are averaged and  $P \approx P_1 > P_0$ . A large magnetoresistance is thus expected at low temperature from the change to antiparallel alignment (as T increases spin mixing by spin waves should reduce the magnetoresistance). A theoretical model based on this mechanism has been worked out and accounts for the experimental results fairly well [11]. We however point out that this type of model is over-simplified and that additional contributions could be significant.

In conclusion the Fe/Cr system represents an interesting type of superlattice for its antiferromagnetic superstructure and its very large magnetoresistance. We have ascribed this magnetoresistance to a magnetic gate type effect in which the alignment of the magnetization opens the transmission through the Cr layers. Because spin-dependent scattering exists in many ferromagnetic alloys of transition metals a large magnetoresistance should also be observed in other multilayered systems.

#### References

- [1] M.N. Baibich, J.M. Broto, A. Fert, F. Nguyen Van Dau, F. Petroff, P. Etienne, G. Creuzet, A. Friederich, J. Chazelas, Phys. Rev. Letters 61, 2472 (1988).
- [2] G. Binasch, P. Grünberg, F. Saurenbach, W. Zinn, to be published.
- [3] P. Grünberg, R. Schreiber, Y. Pang, M.B. Brodsky, H. Sowers, Phys. Rev. Letters 57, 2442 (1986).
- [4] P. Etienne, G. Creuzet, A. Friederich, F. Nguyen Van Dau, A. Fert and J. Massies, Appl. Phys. Letters 53, 162 (1988).
- [5] F. Nguyen Van Dau, A. Fert, S. Hadjoudj, P. Etienne, G. Creuzet, A. Friederich, Proceeding of the International Conference on Magnetism, Paris, France, 1988 (to be published).
- [6] F. Nguyen Van Dau, thesis (Orsay 1989, unpublished).
- [7] Interface anisotropy effects turn out to be small, even for thin Fe 4  $\pi$ M layers. The magnetization is in the layer plane and a field of about M is needed to align it in the perpendicular direction.
- [8] The values of the saturation magnetization of our samples are scattered in the range 1300-1700 emu/cm<sup>3</sup>. The saturation magnetization of bulk Fe is 1700 emu/cm<sup>3</sup>. It may be that the lower value found in Fe/Cr is due to a small negative contribution from Cr.
- [9] C. Carbone and S.F. Alvarado, Phys. Rev. B36, 2433 (1987).
- [10] L.L. Hinckley and D.L. Mills, Phys. Rev. B33, 3329 (1986).
- [11] A. Fert and I. A. Campbell, J. Phys. F6, 849 (1976).
- [12] R.E. Camley and J. Barnas, preprint.

MAGNETIC MICROSTRUCTURE OF THIN FILMS AND SURFACES:  
EXPLOITING SPIN-POLARIZED ELECTRONS IN THE SEM AND STM

D.T. PIERCE, M.R. SCHEINFELD, J. UNGURIS AND R.J. CELOTTA  
National Institute of Standards and Technology, Gaithersburg, MD. 20899

ABSTRACT

Magnetic microstructure, that is the configuration of domains and domain walls in a magnetic material, is of both fundamental interest and of crucial importance for device applications. For example, the ultimate density of magnetic information storage is limited by the sharpness of a domain boundary. The magnetic microstructure of a thin film or surface depends sensitively on its physical structure which is strongly affected by sample preparation or growth. High resolution magnetization imaging is necessary to determine the domain configuration that occurs for a particular sample preparation and the changes that take place under external perturbations such as applied magnetic field, stress or temperature.

INTRODUCTION

Scanning Electron Microscopy with Polarization Analysis (SEMPA), in which the spin polarization of the secondary electrons is measured, is unique in domain imaging techniques using electron microscopy in that the image is directly proportional to the magnetization. In this sense it is like the magneto-optic Kerr effect without the spatial resolution of the technique being limited by optical wavelengths. Our ultimate goal of imaging spin configurations with atomic resolution may only be possible if scanning tunneling microscopy (STM) can be extended to include sensitivity to spin. Right now, the STM can be used to investigate the growth of magnetic films at the atomic level. In this article results of SEMPA studies of thin films and surfaces are possible. The further possibility of obtaining magnetic images with the STM is also discussed.

Advances in the growth of ultrathin magnetic films and multilayers suggest the possibility of atomically engineering materials to achieve special properties. Among the many magnetic properties that may differ between thin layers and those of the bulk are 1) the temperature dependence of the magnetization, both at low temperature and in the critical region (the Curie temperature itself may be different), 2) the anisotropy, to which there is a large shape dependent contribution and possibly also a significant surface contribution, 3) the size of the magnetic moments and spatial dependence of the magnetic order, 4) the magnetization processes, and 5) the magnetic microstructure. By magnetic microstructure we mean the details of the magnetization orientation in the domains and domain walls which form to lower the free energy of a ferromagnetic specimen. In this paper we focus on the magnetic microstructure, how we measure it and understand it, and show with some examples how these results are important from both a fundamental physics point of view and also for applications in magnetic technology.

MAGNETIC MICROSTRUCTURE

The main contributions to the magnetic free energy come from the magnetostatic energy, the anisotropy energy, and the exchange energy. Although the micromagnetic problem can be formulated, the actual domain configuration which is formed to minimize the energy can only be calculated

for simple geometries and ideal materials. To investigate magnetic microstructure and how it affects macroscopic properties, it is necessary in practice to observe the domain configurations. Domains have long been observed using the Bitter method, in which fine metal particles collect on the surface of a ferromagnet in the field gradients at domain walls. Higher resolution observation of domains is possible with transmission Lorentz microscopy in which the deflection of the electron beam by the magnetic field provides domain contrast. Ideally one wants to measure a quantity directly related to the magnetization rather than to the field. This is possible with the magneto-optic Kerr effect, extending the range to include at higher spatial resolution, with scanning electron microscopy with polarization analysis (SEMPA). We will describe the principle of SEMPA for obtaining high resolution magnetization images and show results pertaining to edge acuity in a thin film recording media, thickness dependence of domain structure in permalloy thin film memory elements, existence of domains in few monolayer films, and the distribution of magnetization inside a domain wall. The outlook for achieving yet higher spatial resolution using scanned tip microscopy will be discussed.

The development of electron microscopy has been key to our knowledge of microstructure from biological specimens to metallurgical ones. By exploiting the information in the degree of electron spin polarization, we obtain information on magnetic properties of a specimen. In a 3d ferromagnet such as Fe, Co, or Ni, the magnetization  $M$  is directly proportional to the net spin density,  $n_{\uparrow} - n_{\downarrow}$

$$M = -\mu_B (n_{\uparrow} - n_{\downarrow}) \quad (1)$$

where  $n_{\uparrow}$  ( $n_{\downarrow}$ ) the number of spins per unit volume parallel (antiparallel) to a particular direction. Spin polarized electron spectroscopies (photoemission, Auger, secondary electron) depend on extracting electrons from the solid without loss of information. One then measures the degree of spin polarization  $P$ , for example the  $z$  component, of the extracted beam,

$$P_z = (N_{\uparrow} - N_{\downarrow}) / (N_{\uparrow} + N_{\downarrow}) \quad (2)$$

where  $N_{\uparrow}$  ( $N_{\downarrow}$ ) are the number of electrons with spins parallel (antiparallel) to the  $z$  direction. Low energy secondary electrons are primarily the result of electron-hole pair creation and thus reflect the net spin density of the valence band. The secondary electron spin polarization can be estimated as  $P = n_B / n$ , where  $n_B$  is the magnetic moment per atom and  $n$  is the number of valence electrons per atom; one estimates  $P$  to be 28%, 19%, and 5% for Fe, Co, and Ni respectively.

The measurement of magnetic microstructure by measuring the spin polarization of secondary electrons is illustrated in Fig. 1. A finely focused electron beam is rastered across the specimen and generates secondary electrons. A measurement of the secondary electron intensity gives the familiar SEM image of the topography. If additionally the spin polarization is measured, one obtains an image of the magnetization. All three components of the magnetization can be measured to obtain a complete vector image. A new type of spin analyzer, which is exceptionally compact and efficient, has been developed for this purpose. The experimental details of the SEMPA technique are described elsewhere [1,2].

A SEMPA magnetization image of a test magnetic pattern written on a disk is shown in Fig. 2a. In this case the active material is a 70 nm thick layer of Co-Ni (approximately 80%-20%). The image displays one component of the magnetization nearly aligned along the domains. A slight offset in the writing of successive tracks resulted from an alignment error as the recording head moved radially out on the disk. These domains are about 2 micrometers wide. In practice, the information is associated with the transition from one domain to another. For example a "1" could be

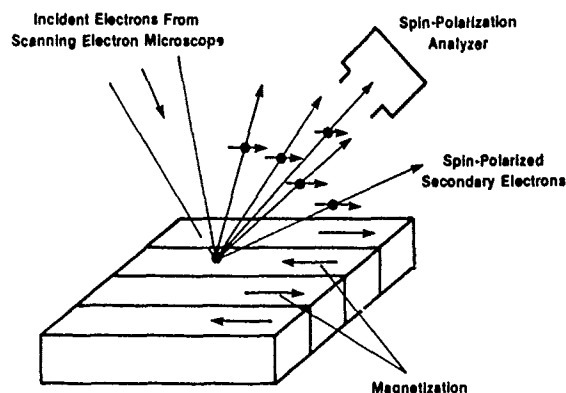


Fig. 1. A schematic illustration of the Scanning Electron Microscopy with Polarization Analysis (SEMPA) technique.

associated with a transition and a "0" with no transition. A sharp well defined boundary is desirable for the minimum noise signal. A region of Fig. 2a at ten times higher magnification is shown in Fig. 2b. At this magnification the jaggedness of the domain boundary is very evident. Clearly this puts a limitation on the recording density. The availability of SEMPA as a means to observe submicron scale magnetic microstructure can assist research efforts in recording media and the recording process to progress toward greater storage density.

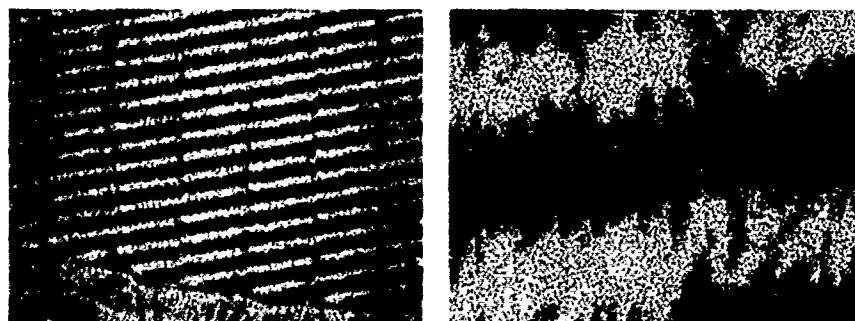


Fig. 2. Written bits in a Co-Ni recording media shown in (a) a low magnification, image 70 micrometers across, and in (b) at 10 times higher magnification.

Magnetic storage has the advantages of being nonvolatile and radiation resistant. Experimental random access memories have been tested using an array of permalloy elements which are etched into arrowhead shapes. The images of the horizontal and vertical components of the magnetization are shown in Fig. 3a and b respectively. The y-shaped domain shown in Fig. 3 is one of the two binary states. Since white represents magnetization pointing to the right and up in Fig. 3 a and b respectively, one can see that the magnetization vector rotates in a counter clockwise sense in the two elements on the left and in a clockwise sense in the two elements on the right.

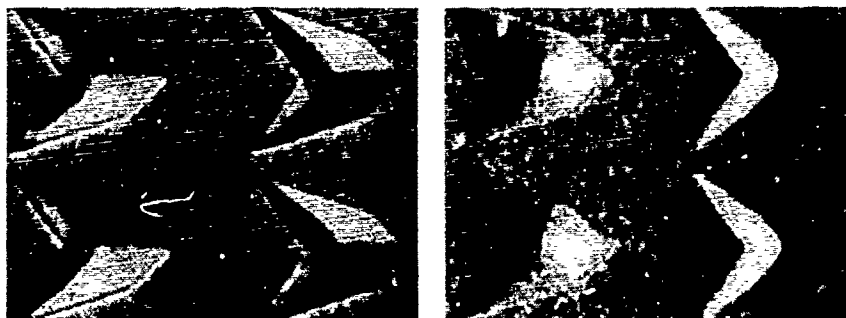


Fig. 3. SEMPA images of the (a) horizontal component and (b) vertical component of the magnetization on an array of permalloy memory elements. The images are 35 micrometers across.

the right of the figure. The magnetic state shown here represents a "1" in a memory device whereas the absence of a y-domain would represent a "0". The difference in the magnetoresistance of these two states provides the readout. One of the major advantages of magnetic imaging with SEMPA is that both in-plane magnetization components are measured simultaneously. This allows one to readily determine the rotation of the magnetization vector as just described, and in other cases to identify closure domains, edge curling, and domain walls.

The performance of magnetic memory devices depends sensitively on their shape, which influences the resultant magnetization configuration. The performance also depends on materials processing parameters such as evaporation rate, substrate temperature, and applied magnetic field during evaporation [3]. In developing such devices, the ability to observe the Y-domain configuration and its change as different geometrical and processing parameters are varied is essential. The dependence of the domains on thickness is illustrated in Fig. 4a which is a low magnification image 200 micrometers across. The elements in the left of the image are nominally 40 nm thick. Moving towards the right, the elements have been sputtered with the edge of a stationary 1keV Ar ion beam such that the permalloy thickness decreases progressively towards zero. This is seen clearly in Fig. 4b which shows a scanning Auger spectroscopy image of the Ni signal. The left most two columns of elements in Fig. 4a show the characteristic y-domain configuration. The central region of the figure shows that the domain patterns change with the decreasing thickness long before the reduced thickness is apparent in the Auger image.

An interesting question is how thin a magnetic film can be and still have magnetic domains. Some theories suggest that a monolayer film must be uniformly magnetized, that is have a single domain. However, recently Yafet and Gyorgy [4] have shown that for sufficiently large perpendicular surface anisotropy,  $K_s$ , domains form in a monolayer of ferromagnetically coupled spins. The difference in energy between the domain configuration and the uniformly magnetized configuration is small. Further theoretical work is in progress to predict below what temperature the domain configuration should be stable.

Experimentally, we have investigated [5] domains in ultrathin Fe films grown epitaxially by evaporation at room temperature on a Ag(100) surface. Figure 5 is an image of one component of the magnetization of a room temperature Fe film with an average thickness of 3.4 ML. The light region and dark region represent two oppositely magnetized domains. The difference in the degree of spin polarization of the secondary electrons



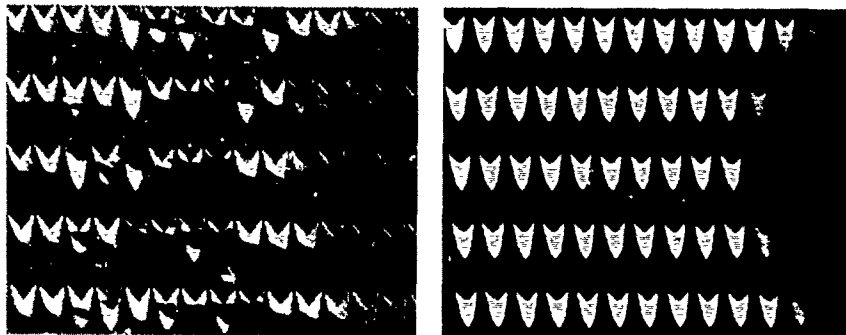


Fig. 4.(a) SEMPA and (b) Scanning Auger images of an array of experimental y-domain permalloy memory elements 200 micrometers across. The permalloy thickness varies from 40 nm at the left to zero at the right.

Fig. 5. SEMPA image of one component of the magnetization shows domains in a 3.4 monolayer average thickness Fe film evaporated on Ag(100).



from the two domains is about 40%. This image is from an area approximately 150x200 micrometers. Most of the film consisted of a single domain except for a strip approximately 1 mm wide along the edge of the film where multidomain structures such as that displayed in Fig. 5 were observed. We did not observe domains in the same region for films 2.6 ML or less in thickness.

Further experimental work is planned to determine if domains are stable in a monolayer film. Clearly it is necessary to go to low temperature. However, there is a further critical problem to be

overcome which is often overlooked in investigations which glibly speak of a single monolayer. How can a single monolayer film be prepared and how can it be verified that it has indeed been achieved? The magnetic properties of a uniform single layer may be quite different from the properties of a film consisting of epitaxial clusters such that the average thickness is one monolayer. Few substrates are smooth on an atomic scale and steps or defects could influence the magnetic properties. There is an immense amount of work to be done before we can speak confidently about and measure reproducibly the properties of a monolayer film.

Our discussion of magnetic microstructure so far has focused on the domains. Another aspect of magnetic microstructure is the internal structure of a domain wall, that is, how does the magnetization vary within the wall. In a 180 degree Bloch wall found inside a bulk ferromagnet, the magnetization rotates in the plane of the wall. Inside a thin film, with a typical thickness of a few tens of nanometers, it is energetically favorable for the magnetization to rotate in the plane of the film in order to avoid the poles which would be created if a Bloch wall intersected a surface. At intermediate thicknesses, "asymmetric" Bloch walls are known to occur [6]. For example, a view of the magnetization in the plane of a cross section through Fe films 0.1 and 0.5 micrometer thick are shown in

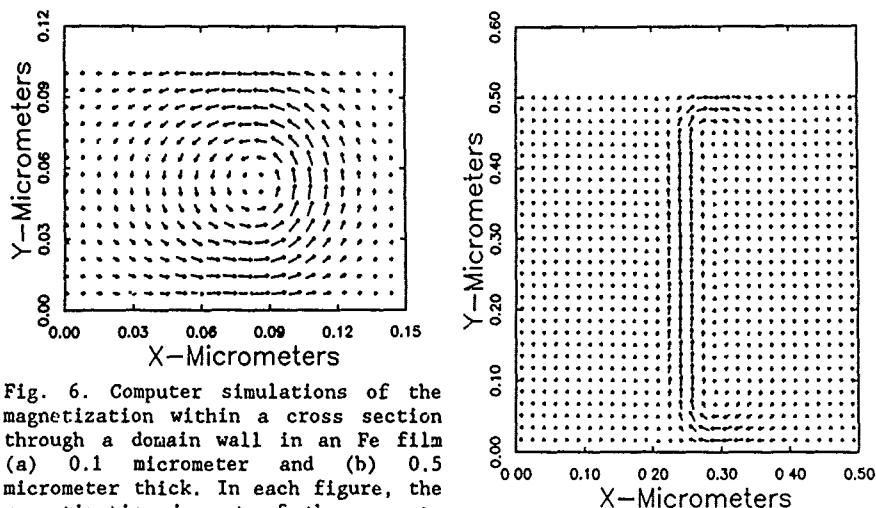


Fig. 6. Computer simulations of the magnetization within a cross section through a domain wall in an Fe film (a) 0.1 micrometer and (b) 0.5 micrometer thick. In each figure, the magnetization is out of the page to the left of the wall and into the page to the right of the wall.

Fig. 6 a and b respectively. In the thinner film, the vortex structure characteristic of an asymmetric Bloch wall in the interior is clearly apparent with Néel walls at the surface. In the thicker film, there is a well defined Bloch wall in the interior, again with Néel walls at the surface.

The magnetization distributions of Fig. 6 are the result of computer calculations in which the direction of the magnetization is varied to minimize the total magnetic energy. The calculated profiles of the surface Néel walls agree quantitatively with the profiles measured for an Fe single crystal, a Co based ferromagnetic glass, and a permalloy film [7]. A wide range of materials parameters, such as the anisotropy,  $K$ , the exchange constant,  $A$ , and the saturation magnetization,  $M_s$ , is covered by these three materials. For example, the anisotropy varies two orders of magnitude in going from Fe to permalloy. The presence of a Néel wall at the surface is a widespread phenomenon which occurs when the anisotropy energy near the surface is less than the magnetostatic energy,  $K < 2\pi M_s^2$ . A film is thick enough to have a well defined Bloch wall when the thickness is typically several times  $\sqrt{A/K}$ . The thickness of the Bloch wall in the interior is less than half the thickness of the surface Néel wall.

In the extreme case of the monolayer film, the situation is different still. For a film magnetized in plane, a uniformly magnetized single domain with no domain walls is expected. However, if the perpendicular surface anisotropy is sufficiently large to cause domain formation, the domain wall is predicted to be a Bloch wall roughly 100 lattice constants wide [4]. Experimental tests of these predictions will be possible with the next generation of SEMPA systems assuming the materials problems inherent in producing uniform monolayer films can be overcome.

The asymmetric surface Néel wall which can be most clearly seen in the calculated magnetization distribution shown in Fig. 6b has a degeneracy in that it could bend over to the left instead of to the right as shown. As can be seen in Fig. 6b, the surface Néel wall is offset to the right from the interior Bloch wall. A surface Néel wall with opposite sense would be offset to the left. This can be seen experimentally in the SEMPA image of Fig. 7 showing the horizontal component of magnetization in a ferromagnetic glass (Allied 2705M,  $\text{Co}_{89}\text{Fe}_{11}\text{Mo}_2\text{B}_{12}\text{Si}_{12}$ ). The centers of the white and black surface Néel walls are displaced from each other as expected from

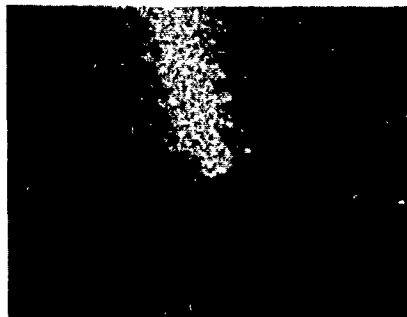


Fig. 7. SEMPA image of the horizontal component of the magnetization in a Co-based ferromagnetic glass shows the offset of two surface Néel walls. The magnetization running across the Néel walls changes sense at a point where a Bloch line intersects the surface.

Fig. 6b. The magnetization in the white wall is towards the right and that in the black wall is towards the left. Thus the magnetization in the domain on the right of the figure is downward and that on the left is upward. The point at which the Néel wall changes sense is the intersection of a Bloch line with the surface. With respect to the topology of the magnetic vector field, this point is a magnetic singularity. The magnetization circulates about this point. A component of magnetization must exist perpendicular to the surface. We have been able to detect this perpendicular component of magnetization with the present SEMPA resolution of 40 nm so the range of the singularity can be investigated.

#### TOWARD HIGHER SPATIAL RESOLUTION

We turn now to the possibility of obtaining higher spatial resolution in the lateral direction. While the present resolution of 40 nm is adequate for many applications, opportunities arise where still higher resolution would be desirable. The investigation of the magnetic singularity just discussed would benefit from higher resolution. As another example, investigation of 100 nm experimental magnetic structures requires a resolution of order 10 nm. Our present SEM with a LaB<sub>6</sub> source is optimum for SEMPA in the range above 100 nm. With a field emission source, which is optimum below 100 nm, we expect to obtain SEMPA images with a spatial resolution better than 10 nm. Note that although there is sufficient incident electron beam current to obtain SEM topography images at a resolution of a couple of nanometers, it is insufficient to obtain SEMPA images in times short enough to avoid other problems such as stage drift.

Achieving spin sensitive imaging at spatial resolutions better than that attainable with a field emission SEM remains a challenge. We have discussed [8] two general approaches: 1) scanned tip microscopy in the field emission mode to achieve a small diameter unpolarized scanned electron beam, and 2) scanning tunneling microscopy where the tip is a source of spin polarized electrons. The ultimate goal is spin sensitive imaging with atomic resolution which would allow investigation of magnetic surface reconstructions and even antiferromagnetic structures.

The most straightforward approach is scanned tip field emission microscopy which was pioneered many years ago by Young et al. [9] for imaging surface topography. Adding spin sensitivity is directly analogous to SEMPA and is illustrated by Fig. 1 with the SEM electron beam replaced by the beam from a scanning field emitter. The apparatus for this is just a scanning tunneling microscope (STM) with the tip pulled back to run in the field emission rather than the tunneling mode. The questions to be

answered are 1) what is the secondary electron yield and can these electrons be extracted to the spin analyzer, and 2) what spatial resolution can be obtained?

The voltage applied to the tip for field emission also has the undesired effect of forcing the low energy secondary electrons back to the sample. We have made calculations for a model tip consisting of a 10 nm radius spherical surface on a 10 degree shank. At a tip to sample spacing of 100 nm and with 30 V on the tip, calculation of electron trajectories show that no secondary electrons are emitted. Only electrons with more than 25 eV energy can escape the tip-to-sample field. Lower energy electrons which are returned to the sample may subsequently escape or generate other secondary electrons, but spatial resolution is then lost. Elastically scattered electrons are expected to have a polarization [10] on the order of 1% and electrons which have lost a couple of eV in scattering from an Fe-based ferromagnetic glass were shown [11] to have a polarization of 5 to 10%. Thus, even in the absence of secondary electrons, it may still be possible to obtain images of magnetic microstructure by energy and spin analysis of the scattered electrons. At the large tip to sample spacing of 1 mm, true secondary electrons can be extracted and their spin polarization measured [12]; the spatial resolution is of course very low.

The resolution of the STM is strongly determined by the details of the tunneling tip. In the field emission mode, the main contribution to the resolution originates from the transverse Fermi velocity of the emitted electrons. The electrons are therefore emitted at room temperature into an approximately 4 degree cone angle. Fink [13] has prepared well characterized single atom tips and measured such a cone angle. This translates into a potential lateral resolution of 7 nm for a 100 nm spacing as in the example above, or, for example, a resolution of 3.5 nm for a tip at a 50 nm spacing and a 20V bias. Such scanned tip microscopy is relatively inexpensive and simple compared to an SEM and can be easily integrated with STM studies. When scanned tip field emission microscopy is developed to the point of obtaining spin sensitive images, it will clearly have many applications.

It may be possible to measure spin configurations on the atomic or at least sub-nanometer scale by exploiting the tunneling of spin polarized electrons. The tunneling current from a ferromagnetic tip is expected to be spin polarized. The spin polarization of electrons field-emitted from Fe is 25% and 20% for tips oriented along the [100] and [111] axes respectively [14]. This is a substantial degree of polarization, especially since the nearly unpolarized s and p electrons are believed to tunnel with 10 to 100 times the probability of the magnetic d electrons. It is important to know the orientation of the spins at the tip and ideally to control this orientation. As the STM scans from one domain to another, the spin dependent part of the signal will change. The difficulty will be in separating a spin dependent signal which is only a few per cent of a topographic signal with large variations. Some form of modulation of the spin dependent signal is clearly necessary. Reversing the magnetization of the tip would be satisfactory if this can be done without otherwise disturbing the STM. Another possibility is spectroscopic modulation [8] in which first the bias and position is set for tunneling to nonmagnetic states and then changed to emphasize tunneling to magnetic states.

There are further complications in a spin sensitive STM employing a magnetic tip to study a magnetic sample. Bringing a tip near to the surface can change the magnetization distribution of the sample and of the tip itself. Our calculations which produced Fig. 6, have been extended to include a magnetic tip near the surface. They show conclusively that a magnetic tip cannot in general be considered to be a nonperturbative probe [15]. The tip and sample must be considered as a combination and extracting information on the magnetic microstructure will not likely be straightforward except in special circumstances. This problem has been

discussed for the case of magnetic force microscopy, where the problems are similar, and optimum conditions suggested [16].

An ideal spin-sensitive STM would consist of an emitter of spin polarized electrons, a means to easily modulate the polarization, and no perturbing interaction between tip and the sample. Conceptually, an optically pumped semiconductor provides such a source. Photoemission from negative electron affinity has been used for many years as a source of spin polarized electrons [17]. Tunneling between the GaAs tip and magnetic sample proceeds directly through the vacuum barrier without the need for any surface treatment to obtain a negative electron affinity as is required for photoemission. The spin polarized electrons are created by photoexcitation to the conduction band with circularly polarized light. The optical selection rules for circularly polarized light produce an electron spin polarization in the conduction band of 50% which can be easily reversed by reversing the helicity of the light.

We have previously discussed tunneling from an optically pumped GaAs tip and analyzed the incident light necessary to achieve a sufficient density of polarized electrons in the conduction band [8]. In brief, we took as a detection limit  $10^{18} \text{ cm}^{-3}$  electrons based on STM experiments where tunneling from dopant levels at a density of  $10^{18} \text{ cm}^{-3}$  in p-type GaAs were just detected.<sup>18</sup> With an electron-hole recombination time of order  $10^{-9} \text{ sec}$ , the steady-state excited-electron densities  $2 \times 10^{16} \text{ e}/(\text{cm}^3 \text{ mW})$ . This requires 50 mW of light focused into a  $10 \text{ }\mu\text{m}$  diameter spot to achieve the detectable density. Not only would a such photon flux heat the sample and cause drift problems, but at light fluxes near this value we observed damage in the GaAs tip. In spite of the initial attractiveness of spin polarized tunneling from GaAs tips, there are formidable engineering problems to overcome and the scheme may only be possible if a much improved STM detection sensitivity is obtained.

#### CONCLUSION

In summary, we have described how spin polarized electrons can be exploited to investigate magnetic microstructure. In SEMPA we have a powerful tool to study magnetic microstructure down to a resolution, ultimately, of order 10 nm. We showed examples of applications to problems of technological importance, where the magnetic properties of thin film recording media and memory elements depend sensitively on the materials preparation. SEMPA provides the possibility to correlate microscopic magnetic properties, such as edge acuity, with macroscopic ones, such as recording noise and allows one to further investigate the dependence of these on growth and other external parameters. Fundamental questions ranging from the ability of a monolayer film to support domains to the nature of a domain wall intersecting the surface can be addressed by SEMPA. The possibility of obtaining higher resolution by using an STM in the scanning field emission mode and measuring the polarization of the scattered electrons was described. The many challenges in measuring surface spin configurations on the atomic scale by spin dependent tunneling were discussed.

#### ACKNOWLEDGEMENTS

This work was supported in part by the Office of Naval Research.

#### REFERENCES

- [1] G.G. Hembree, J. Unguris, R.J. Celotta, and D.T. Pierce Scanning Microscopy Supplement 1, 229 (1987).

- [2] K. Koike, H. Matsuyama, H. Todokoro, K. Hayakawa, Scanning Microscopy Supplement 1,241(1987).
- [3] D.S. Lo, G.H. Cosimini, L.G. Zierhut, R.H. Dean, and M.C. Paul, IEEE Trans. Magnetics MAG-21,1776(1985).
- [4] Y. Yafet and E.M. Gyorgy, Phys. Rev. B38,9145(1988).
- [5] J.L. Robins, R.J. Celotta, J. Unguris, and D.T. Pierce, Appl. Phys. Lett. 52,1918(1988).
- [6] A. Hubert, IEEE Trans. Magnetics, MAG-11,1285(1975).
- [7] M.R. Scheinfein, J. Unguris, R.J. Celotta, and D.T. Pierce, to be published.
- [8] D.T. Pierce, Phys. Scr. 38,291(1988).
- [9] R. Young, J. Ward, and F. Scire, Rev. Sci. Instrum. 43,999(1972).
- [10] J. Unguris, D.T. Pierce, and R. J. Celotta, Phys. Rev. B29,1381(1984).
- [11] H. Hopster, R. Raue, and R. Clauber, Phys. Rev. Lett. 53,695(1984).
- [12] R. Allenspach and A. Bischof, Appl. Phys. Lett. 54,587(1989).
- [13] H.W. Fink, Phys. Scr. 38,260(1988).
- [14] M. Landolt, and Y. Yafet, Phys. Rev. Lett. 40,1401(1978).
- [15] M.R. Scheinfein, J. Unguris, D.T. Pierce and R.J. Celotta (to be published.)
- [16] U. Hartmann, J. Appl. Phys. 64,1561(1988).
- [17] D.T. Pierce, R.J. Celotta, G.-C. Wang, W.N. Unertl, A. Galejs, C.E. Kuyatt, and S.R. Mielczarek, Rev. Sci. Instrum. 51,478(1980).
- [18] R.M. Feenstra and J.A. Stroscio, J.Vac. Sci. Technol. B5,923(1987).

## SPIN POLARIZED INELASTIC ELECTRON SCATTERING FROM NI (110)

H. Hopster, D. L. Abraham,\* D. P. Pappas, Institute for Surface and Interface Science and Department of Physics, University of California, Irvine, CA 92717

## ABSTRACT

The spin dependent energy loss mechanisms in low-energy electron scattering from a ferromagnetic Ni(110) surface are studied. It is shown that exchange scattering can be the dominant loss mechanism for small energy losses. The energy-, angle and temperature dependence of spin asymmetries are studied in detail.

## EXPERIMENT

A monochromatic beam of spin polarized electrons, derived from a GaAs source, is scattered from a Ni(100) surface. The energy loss spectrum is measured and also the spin polarization after scattering can be measured by a Mott detector. By this technique the scattering rates can be deconvoluted into spin-flip ( $F^+$ ,  $F^-$ , due to exchange) and non-flip ( $N^+$ ,  $N^-$ ) processes (+, - stand for the spin of the incoming electron with respect to the majority-spin of the Ni sample) [1]. From these rates a spin asymmetry

$$A = \frac{1}{|p_0|} \frac{I_+ - I_-}{I_+ + I_-} \quad (1)$$

can be derived,  $I_+$ ,  $I_-$  are the scattering intensities for primary beam spin polarization parallel or antiparallel to the sample.  $A$  is given in terms of the rates as

$$A = \frac{N^+ + F^+ - N^- - F^-}{N^+ + F^+ + N^- + F^-} \quad (2)$$

The asymmetries can be measured without performing the spin polarization measurement.

## RESULTS

Figure 1 shows the energy loss rates (normalized to the elastic peak) for a 12 eV primary beam in  $10^\circ$  off-specular scattering geometry. The energy resolution is 80 meV. The sample is at room temperature. The elastic scattering is purely non-flip. In the loss region studied the non-flip rates show a significant spin dependence: the non-flip-down rate being larger by 50% than the non-flip-up rate. The flip-down rate rapidly emerges in the loss regime, has a maximum around 300 meV energy loss, where it is actually the largest rate, and then falls off smoothly towards higher energy losses. The flip-up rate is by far the smallest rate [2]. In Fig. 2 we show schematically the exchange scattering contributions within the relevant part of the Ni 3d bulk band-structure around the Fermi energy. The left panel shows the exchange scattering events leading to the flip-down rates: a minority-spin electron falls into the minority states above  $E_F$  and a majority-spin electron is ejected. When taking only the

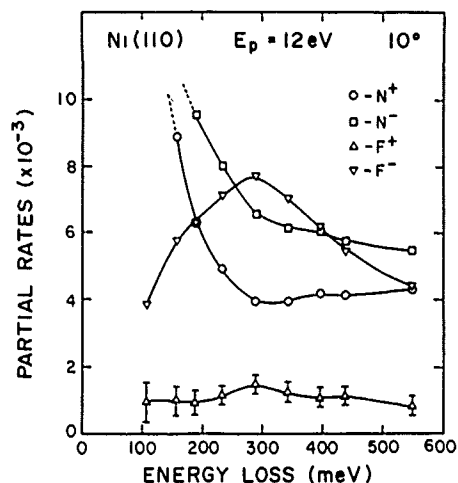


Fig. 1 Energy loss rates  
n = non-flip, F = flip, +, -  
spin-up, down, respectively

d-bands into account there is no possibility for a flip-up process. Experimentally we observe a small  $F^+$  rate, however. This might be due to some extent to the free-electron like sp-states around  $E_F$ . But the major part of  $F^+$  is probably due to transverse spin fluctuations at room temperature, which allows spin flip transitions in the "wrong" direction. In order to answer this question unambiguously low-temperature data are needed.

It is clear from Fig. 2 that there should be a threshold in the flip-down spectrum, corresponding to the Stoner gap,

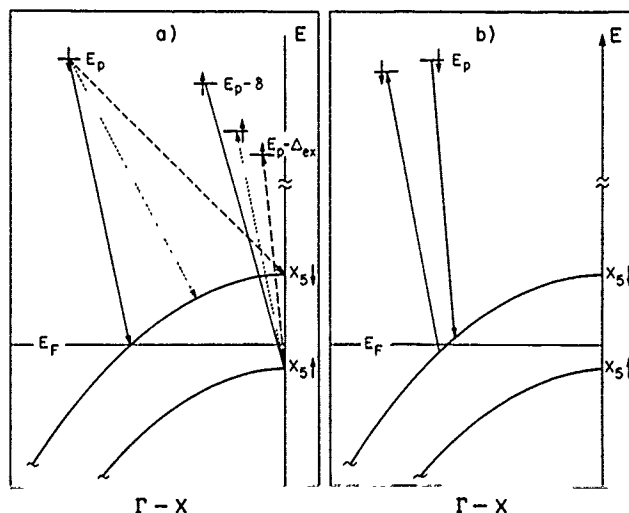


Fig. 2 Exchange scattering mechanisms  
contributing to a) flip-down, b) non-flip down



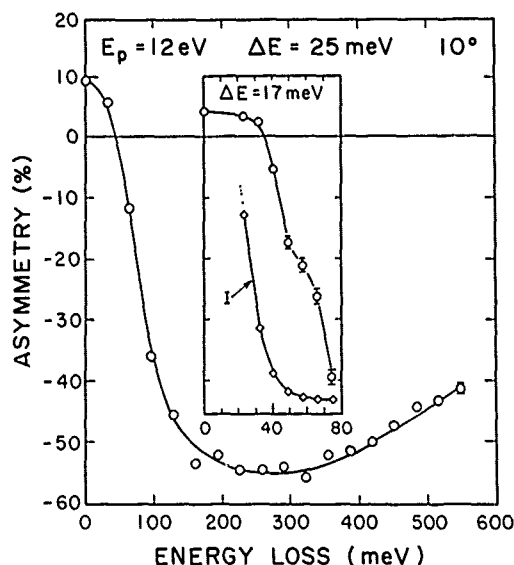


Fig. 3 High Resolution asymmetry spectra at  $E_p = 13$  eV,  $10^\circ$  off specular

i.e., the position of the  $X5\uparrow$  point below  $E_F$ . We can increase the energy resolution considerably by sacrificing the spin polarization analysis and measuring spin asymmetries only. Results of high-resolution asymmetry measurements are shown in Fig. 3., over the energy loss range of Fig. 1 with 25 meV resolution and in the inset with 17 meV resolution. First, note the very large asymmetries ( $\sim 55\%$ ) observed around 250-300 meV energy loss. Second, and more importantly, in the inset there is a shoulder visible around 60 meV energy loss. We believe this shoulder is due to the onset of the flip-down transitions, i.e., the energy corresponds to the Stoner gap. The first rapid rise of the asymmetry to  $-20\%$  when going out of the elastic peak is due to the difference in the non-flip rates.

We have studied the behavior of the asymmetry spectra as a function of primary energy and of the scattering angle off specular. Figure 4 shows asymmetry spectra as a function of primary energy over the range of 16.5 - 19 eV [3]. These spectra are taken, contrary to Fig. 1 and Fig. 3, in specular geometry. First, note that the asymmetries are smaller (maximum of 35% at 16.5 eV). Second, there is a very strong primary-energy dependence. At 19 eV the asymmetries are zero (within the statistics). This behavior over this narrow energy range is related to the elastic intensity. At 20 eV there is the strong first (quasi-3 dimensional) Bragg peak. The elastic intensity rises by a factor of 30 from 16.5 to 20 eV. In parallel, also the inelastic intensity rises proportionately over this energy range. This can be attributed to long-range (i.e., small  $q$ ) inelastic dipole scattering mechanisms, combined with elastic specular reflection. The results of Fig. 4 can be very well described by

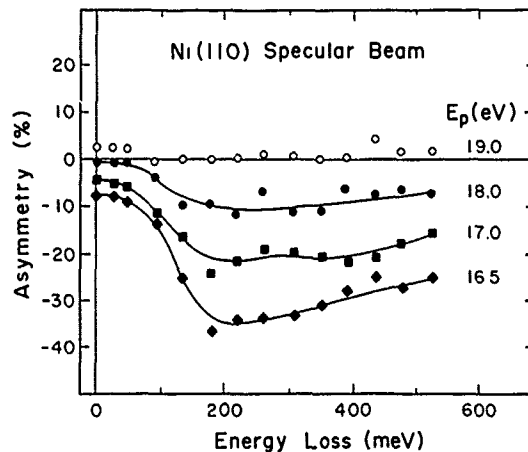


Fig. 4 Dependence on primary energy of asymmetry spectra in specular geometry

$$A = \frac{A_0 \cdot I_{im}}{I_{im} + I_{dipole}} \quad (3)$$

where  $A_0 = -0.55$ ,  $I_{im}$  is a constant impact scattering intensity, and  $I_{dipole} = \alpha \cdot I_{elastic}$  is the dipole contribution, proportional to the elastic intensity (since it involves an elastic reflection before or after energy loss).

Figure 5 shows the behavior of the asymmetry (at 19 eV primary energy) when going off-specular. The circles are the elastic and inelastic (at 300 meV energy loss) intensities

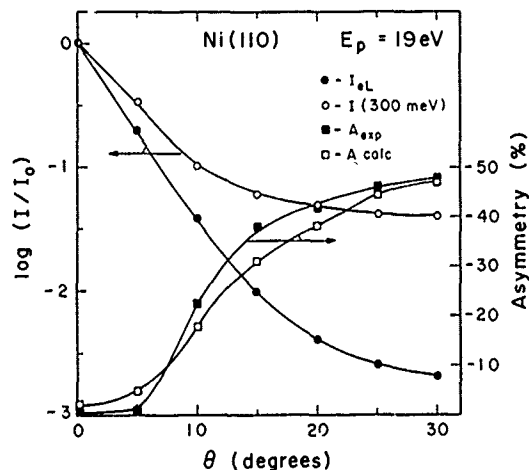


Fig. 5 Angle dependence of the asymmetry and intensity at 300 meV energy loss at  $E_p = 19$  eV

respectively and the full squares are the measured asymmetries (at 300 meV loss). It is obvious that the asymmetry emerges when going out of the strong dipole loss. The open squares are calculated asymmetries according to Eq. (3). The measurements are very well described by this relation. This, together with the results of Fig. 4, shows that the total inelastic intensity is composed of an isotropic background of large-angle inelastic events ("impact"), which are dominated by exchange processes and superimposed on this is a strongly energy and angle dependent dipole (spin independent) contribution, which is sharply peaked around the diffraction peaks.

#### TEMPERATURE DEPENDENCE

Figure 6 shows a series of temperature dependent asymmetry spectra between room temperature and  $0.97 T_c$ . As expected the asymmetries approach zero as the temperature approaches  $T_c$ , due to the loss of long-range magnetic order. The interesting question is whether there are any changes in the shape of the asymmetry spectrum with varying temperature. A possible cause for such a change would be, e.g., a reduction of the exchange splitting with increasing temperature, in a "Stoner-like" fashion. This should shift the weight of the asymmetry to lower energies, mainly due to the shift of the maximum of the  $F^-$  rate to lower energies. No significant change in the shape of the asymmetry spectra in Fig. 6 is observed. The spectra  $A(E)$  can be described very well by

$$A(E, T) = M(T) \cdot A(E, T=RT) \quad (4)$$

where  $M(T)$  is an effective magnetization (averaged over the probing depth of the measurement). This strongly suggests that only transverse fluctuations are responsible for the decrease of the magnetization. This conclusion agrees with the results of a recent similar study by Kirschner and Langenbach [4].

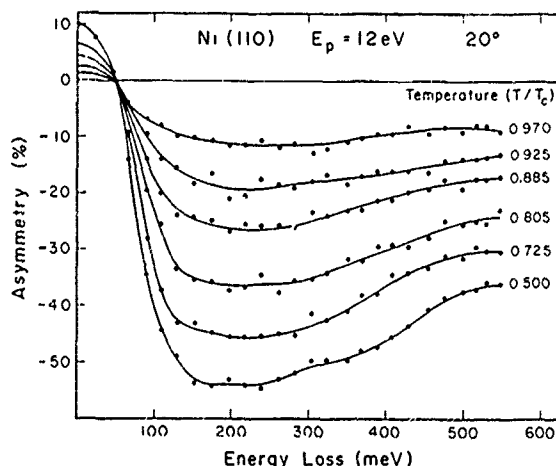


Fig. 6 Temperature dependent asymmetry spectra

This work has been supported by NSF through Grant DMR 86-00668.

## REFERENCES

- \* Present address: IBM Research Laboratory, Zurich
- 1. A. Venus and J. Kirschner, Phys. Rev. B37, 2199 (1988).
- 2. D. L. Abraham and H. Hopster, Phys. Rev. Lett. 62, 1157 (1989).
- 3. H. Hopster and D. L. Abraham, submitted to Phys Rev. B.
- 4. J. Kirschner and E. Langenbach, Solid State Commun. 66, 761 (1988).

# SPIN POLARIZED INVERSE PHOTOEMISSION STUDY OF Fe AND Co THIN FILMS ON W(001)

QING CAI, RECEP AVCI<sup>†</sup> and GERALD J. LAPEYRE  
Department of Physics, Montana State University, Bozeman, MT 59717

## ABSTRACT

Spin- (and angle-) resolved inverse photoemission spectroscopy (SPIPES) has been used for studying magnetic thin films. The spin dependence of the unoccupied electronic structure has been investigated for in-situ-grown epitaxial, ultrathin Fe and Co films on W(001). The Fe overlayers have a square lattice and exhibit in-plane magnetic remanence in the  $\Sigma$  direction of the surface Brillouin zone. Four or more atomic layers of Fe show bulklike SPIPES spectra with a majority spin peak at the Fermi energy ( $E_F$ ) and a broad minority peak 1.3 eV above  $E_F$ . The Co overlayers on W(001) show distorted hexagonal structures in the plane with an atomic density twice that of the W(001) plane. Two atomic layers of Co show strong in-plane magnetic remanence with the minority peak at 0.7 eV. The SPIPES results in general are consistent with the theoretical electronic structure for momentum-conserving radiative transition from free-electron-like bands down to the unoccupied 3d bands.

## INTRODUCTION

In ferromagnetic transition metals, the moderate overlap of the d orbitals produces a high density of band states in a narrow energy region around the neighborhood of Fermi level ( $E_F$ ). When the spin distributions are shifted by the exchange splitting, one set of spin d band is essentially occupied, and the other is essentially unoccupied. These bands are referred to as majority and minority bands, respectively, and they constitute the principal ingredients of itinerant ferromagnetism. In the 3d transition metals, the elemental ferromagnets Fe and Co are of special interest and have the largest exchange-splittings. The theoretical and experimental investigations of Fe surface magnetic properties, both bulk surfaces and their film surfaces have had some interesting achievements; on the other hand, the Co surfaces have received relatively little attention in the literature [1].

With spin-polarized inverse photoemission spectroscopy (SPIPES) containing angle-resolving capability, we have explored the spin-dependence, unoccupied electronic states of thin magnetic films of Fe and Co on non-magnetic W substrate. The SPIPES results are discussed in relation to the available theoretical band structure, in terms of momentum-conserving radiative transitions between unoccupied states. It is found that Fe forms an epitaxial overlayer with a square lattice on W(001). One monolayer of Fe is found to be ferromagnetically ordered, and the spectra for four monolayers show bulklike electronic structure. The electronic structure for films between one and four monolayers show strong thickness dependence. The Co deposited on the same W(001) surface shows a distorted hexagonal lattice. The SPIPES measurements show that two atomic layers of Co are ferromagnetic with an in-plane magnetic remanence.

## THIN FILM PREPARATION AND CHARACTERIZATION

The Fe and Co epitaxial thin films were studied under ultrahigh vacuum conditions with a base pressure  $3 \times 10^{-11}$  Torr. The Fe and Co films were deposited at room temperature on a clean W(001) crystal foil  $4 \times 6$  mm at a pressure better than  $4 \times 10^{-10}$  Torr. The thickness was monitored by a quartz crystal thickness monitor near the sample position and the deposition rate was about 0.01 Å/sec. The quality of the Fe and Co films was characterized by low energy electron diffraction (LEED) and Auger electron spectroscopy (AES). The layer-by-layer growth for several monolayers is established by the following considerations. First, while the overlayer crystalline structures are unchanged in the LEED patterns, the W Auger amplitudes decrease rapidly

to a value less than the noise level at a few monolayers coverage, behavior which is inconsistent with other growth modes (3D islands on the W substrate or islands after one monolayer). Second, detailed Auger analysis for Fe deposition shows that the Fe signal amplitude as a function of coverage can be described by a sequence of straight lines joined by kinks, which correspond to the completion of each monolayer. Further, the high surface energy of W compared with that of the transition metals favors layered growth.

LEED results show that the Fe overlayers on W(001) have a square lattice aligned with the substrate lattice. The first monolayer is pseudomorphic, since the LEED pattern is the same as for the W(001)  $p(1 \times 1)$ , Fig. 1(a), and just as sharp. With multilayer deposition of Fe the LEED patterns become fuzzy and spots blurred, Fig. 1(b).

The Co overlayers on W(001) show LEED patterns represented by Fig. 2(a). The Co hexagonal surface of either hcp(0001) or fcc(111) has the closest-packed surface and having the largest interplane distance, which is advantageous for adsorption. We suggest that Co overlayer grows in a distorted hexagonal arrangement on W(001) as shown in Fig. 2(b). For perfect registry with the substrate, the distortion from bulk Co would be from  $a_{Co}=2.51$  Å to 2.24 Å, or 10.8% compression in one bond direction, and 2.5% dilatation in the orthogonal direction. The monolayer atomic density is twice of that of the substrate. The LEED pattern shown in Fig. 2(a) is the superposition of LEED patterns from two such domains, having equal probability and rotated  $90^\circ$  to each other. The elongated streaky LEED spots corresponding to each domain indicate that a single

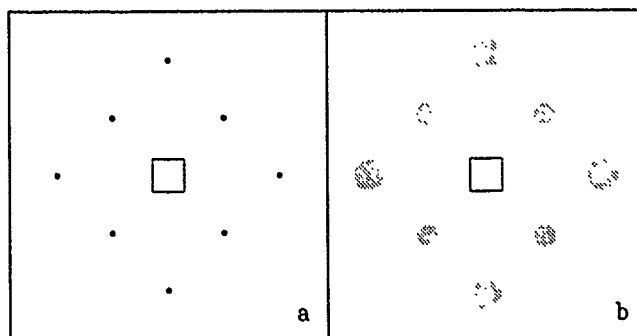


Fig. 1. LEED patterns of (a) clean W(001), and (b) Fe on W(001) with coverages  $>1$  monolayer.

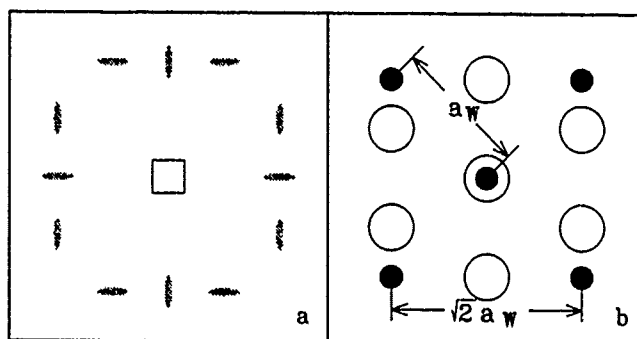


Fig. 2. (a) LEED patterns of Co overlayers on W(001), and (b) Co overlayer structure of one of the surface domain on W(001), the other domain is the  $90^\circ$  rotation of it,  $\bullet$  W atoms,  $a_W=2.87$  Å;  $\circ$  Co atoms, bulk Co  $a_{Co}=2.51$  Å.

domain shape is elongated in one direction (the direction in which the mesh is compressed).[2]

## SPIPES EXPERIMENTS AND RESULTS

The spin-polarized electrons are emitted from negative-electron-affinity GaAs at room temperature, as described by Pierce et al.[3] The spin-polarized inverse photoemission procedure, in brief, involves an incident polarized electron with low kinetic energy, which enters the solid surface and, within the penetration depth, makes a momentum-conserving radiative decay into an unoccupied state near  $E_F$ , thereby revealing information about the surface- and near-surface- unoccupied spin states.[4] In our measurements photons are detected by a bandpass UV photon detector with maximum yield at 9.8 eV and a FWHM of 1.6 eV, described elsewhere [5].

The experimental geometry for our SPIPES measurements is shown in the inset of Figure 3. The thin films are magnetized (magnetization  $M$ ) by applying a 400 Oe field in the surface plane along the  $W[110]$  axis, which coincides with the spin quantization direction of SPIPES measurement. The SPIPES data are taken with no applied field; therefore true remanence is measured. Our SPIPES spectra consist of two energy scans, first with one spin (polarization  $P$ ) then the opposite spin ( $-P$ ). The measurements are repeated for the reversed sample magnetization ( $-M$ ). Very good consistency is found between the parallel and antiparallel spectra. The SPIPES data shown here have been adjusted for the electron polarization  $P_0=27\%$  [6].

In Figure 3, we show the normal-incidence ( $\Theta=0^\circ$ ) spectra for the W substrate and for one and four monolayers of Fe. The bottom, spin-independent curve is for clean, unreconstructed  $W(001)$ , and is in good agreement with previous work [7]. For one Fe monolayer the Fe minority d band at about 1.3 eV emerged, as shown in the middle curves of Fig. 3. Also shown there is the majority intensity (lower curve) peaked at the same energy neighborhood. The spin intensity difference is unambiguous evidence for ferromagnetic ordering in the pseudomorphic Fe monolayer system, observed along the  $\Sigma$  direction of the surface Brillouin zone. With increasing Fe thickness, the intensity contrast between the spin states becomes greater and the majority peak moves down toward  $E_F$ . The thickness dependence reaches the bulklike limit at four monolayers coverage with our experimental resolution, as shown in the top curves of Figure 3.

Figure 4 shows the ferromagnetic band structure of bulk Fe along the  $\Gamma\Delta H$  line in the bcc Brillouin zone [8]. By comparing with the bulklike SPIPES spectra taken at normal incidence, with  $k_F=0$  and  $k_i$  along the  $\Delta$  line, the majority peak at  $E_F$  is identified with the unoccupied majority final states near  $H'_{25}$ , and a broad minority peak at about 1.3 eV above  $E_F$  corresponds to the d band along the  $\Delta$  direction. The initial states are provided by Fe higher-energy free-electron-like bands above the vacuum energy with the right energy difference to couple our photon detector, and possible momentum-conserving radiative transitions are indicated by the arrowed vertical lines at  $h\nu=9.8$  eV. The predominant minority intensity in the unoccupied region is reversed at  $E_F$ . This is the characteristic of Fe which is known to have unfilled majority d states. The spectral intensity for energies above d band are inelastic scattering followed by a radiative decay with photon energy in the detecting range. There is evidently some residual polarization, with minority spin dominant because there are more unfilled minority states. These features were also observed in a similar investigation of  $Fe(001)$  [9].

When the thickness decreases from four to one Fe atomic layers, the normal-incidence spin asymmetry decreases and the majority peak position shifts upward from  $E_F$  towards the minority peak position. The disappearance of the intensity reversal with decreasing film thickness may be a consequence of the majority d band at  $H'_{25}$  having fallen below  $E_F$ . This behavior is consistent with the trend towards enhanced surface magnetism with reduced dimensionality from bulk Fe (dimensionality 3 and magnetic moment of  $2.2\mu_B$ ) to the free Fe atom (dimensionality 0 and  $4\mu_B$ ). The layer-projected density of states calculations of  $Fe(001)$  also show the disappearance of the majority d bands above  $E_F$  for the surface layer. What is puzzling is the upward shift of the majority peak. A number of causes may be adduced for the shift; at this moment, we believe that a reduced Curie temperature for monolayer Fe films [10] has an effect on the changes of electronic structure.

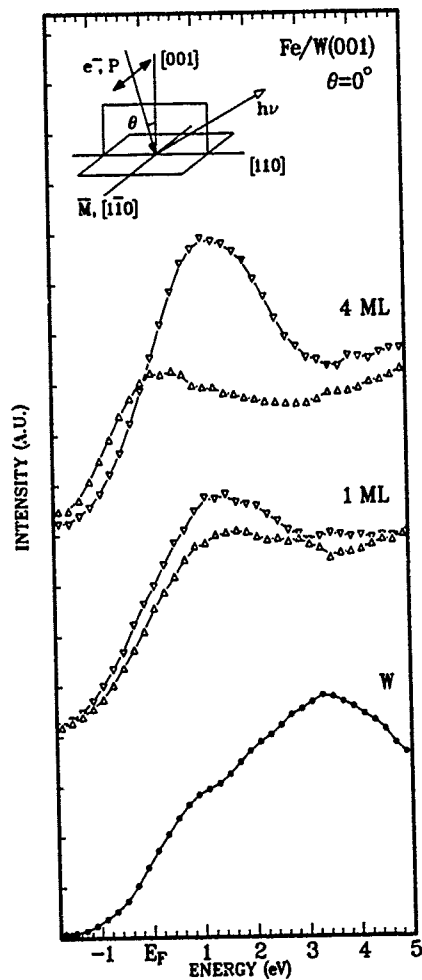


Fig. 3. Normal-incidence inverse photoemission spectra for clean W(001),  $\bullet$ , and pseudomorphic monolayer and bulklike four monolayers of Fe,  $\Delta$  majority spin and  $\nabla$  minority spin. The inset illustrates the experimental geometry, with spin quantization axis parallel to sample magnetization along  $[110]$  axis.

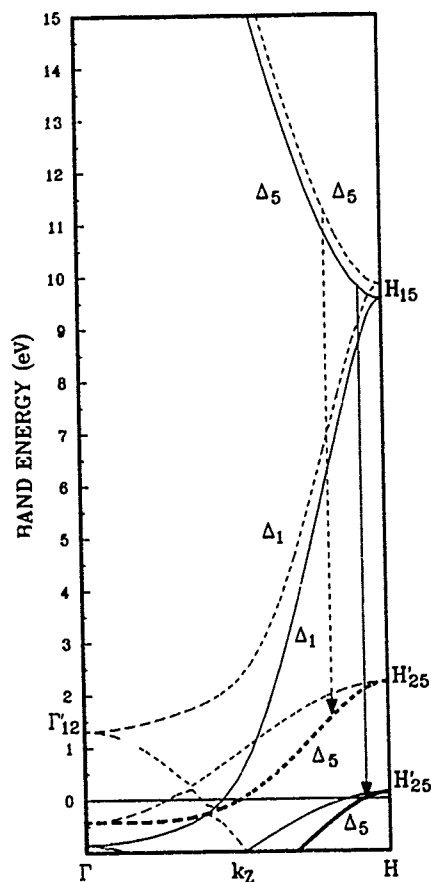


Fig. 4. Ferromagnetic bcc Fe band structure (from Ref. [8]) along the  $\Gamma\Delta H$  direction (normal electron incidence). Dashed and full arrow lines indicate possible radiative transitions at  $h\nu = 9.8$  eV.



Figure 5 shows the normal-incidence spectra for two monolayers of Co, each with twice as many atoms in the plane as the W substrate. There is a continuous minority-spin dominance in the energy region without an intensity reversal because Co, unlike Fe, has no unfilled majority d states. The minority d band peak close to 1 eV can be accounted for by a radiative interband transition along the [0001] direction of hcp Co with  $h\nu=9.8$  eV [11], however, the lower majority spin peak at that energy region or a little above 1 eV does not fit the same scheme because there are few unoccupied majority final states.

As in the case for Fe, there are a number of possible explanations for the high intensity of the Co majority spectrum. For Co, however, we have the added fact that there exist two overlayer geometric domains, rotated by  $90^\circ$  from each other, and having equal probability. Since the magnetic anisotropy is evidently lower in the surface plane, and a distorted hexagonal structure should have a unique in-plane easy axis, in our experiments, the easy axis of one domain will be parallel, and the other perpendicular to the spin quantization axis. For the latter the spectrum should be an equal mix of majority and minority spectra (equivalent to measuring an unpolarized sample) and the total measured spectrum will thus contain equal admixtures of magnetized and "unmagnetized" spectra. Following this idea, we reconstruct the presumed spectrum from a single domain by subtracting 50% of the spin-averaged spectra of Fig. 5(a). The results are shown in Fig. 5(b), which shows that the majority peak is largely removed. The strong minority spin intensity can be well assigned to a radiative transition between bulk Co bands near the middle of  $\Gamma A$  direction of the hcp Brillouin zone, (see the band structure published in Ref. [11]).

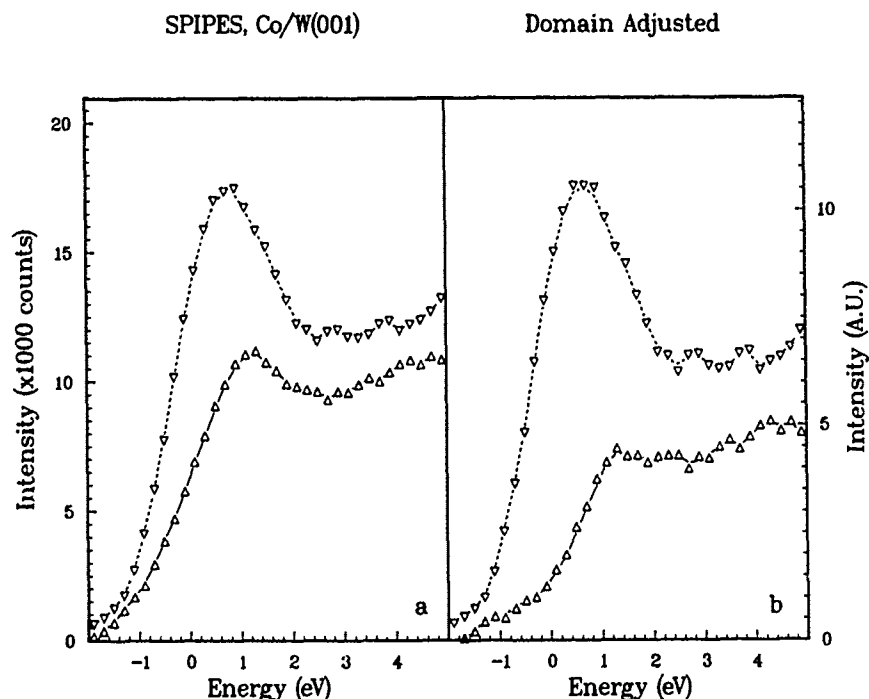


Fig. 5. Normal-incidence inverse photoemission spectra for Co bilayers on W(001), (a), and tentative decomposition of (a) for two possible  $90^\circ$  across domains, (b).  $\Delta$  majority spin and  $\nabla$  minority spin.

## CONCLUSIONS

The Fe and Co ultrathin overlayers on W(001) provide for study novel two dimensional magnetic systems with large overlayer strain or distortions. The Fe monolayer is ferromagnetic with in-plane magnetization. A strong thickness dependence is observed, and the bulklike features are in good agreement with the bcc Fe results. The Co on W(001) forms a distorted hexagonal crystalline structure. Pronounced ferromagnetism sets in only at two monolayers (each with double the W surface atomic density). The SPIES results show predominantly minority spin interband radiative transitions from free-electron-like initial-state bands into an unoccupied bulk 3d band, while  $k_{\parallel}$  is conserved.

## ACKNOWLEDGMENT

This work was supported in part by NSF under Grant Numbers DMR 8309460 and DMR 8705879. We wish to thank Dr. J. Anderson for many helpful discussions. We appreciate the technical support provided by M. Jaehnig.

## REFERENCES

- <sup>†</sup> present address: King Fahd University of Petroleum and Minerals, Department of Physics, Dhahran 31261, Saudi Arabia.
1. For surveys, see Polarized Electrons in Surface Physics, edited by R. Feder, (World Scientific, 1985); Thin Film Growth Techniques for Low-Dimensional Structures, edited by R.F.C. Farrow, S.S.P. Parkin, P.J. Dobson, J.H. Neave and A.S. Arrott, (Plenum, New York, 1987).
2. We wish to thank Dr. G.-C. Wang for helpful discussions of the LEED results.
3. D.T. Pierce, R.J. Celotta, G.-C. Wang, W.N. Unertl, A. Galeis, C.E. Kuyatt and S.R. Mileczarek, *Rev. Sci. Instrum.* **51**(4), 478 (1980).
4. J. Unguris, A. Seiler, R.J. Celotta, D.T. Pierce, P.D. Johnson and N.V. Smith, *Phys. Rev. Lett.* **49**, 1047 (1982).
5. R. Avci, Q. Cai and G.J. Lapeyre, to be published.
6. The Value of  $P_0$  is from the work by L.E. Klebanoff et al, *Phys. Rev. B* **36**, 7849 (1987).
7. I.L. Krainsky, *J. Vac. Sci. Technol.* **A5**(4), 735(1987).
8. J. Callaway and C.S. Wang, *Phys. Rev. B* **16**, 2095 (1977).
9. J. Kirschner, M. Globl, V. Dose and H. Schmidt, *Phys. Rev. Lett.* **53**, 612 (1984).
10. S.D. Bader, E.R. Moog and P. Grunberg, *J. Magn. Magn. Mtis.* **53**, L295 (1986).
11. F.J. Himpsel and D.E. Eastman, *Phys. Rev. B* **21**, 3207 (1980).

# THE D-BAND EXCHANGE SPLITTING FOR THIN GADOLINIUM OVERLAYERS

D. LAGRAFFE\*, P.A. DOWBEN\* AND M. ONELLION†

\*Department of Physics, Syracuse University, Syracuse, New York 13244-1130

†Department of Physics, University of Wisconsin, Madison, Wisconsin 53706

## ABSTRACT

Thin (0-6 monolayer) films of gadolinium on Cu(100) have been investigated using synchrotron radiation photoemission. From the definite selection of final state symmetries in photoemission, we have been able to determine a lower bound to the exchange splitting of the gadolinium 5d band. The gadolinium films on Cu(100) exhibit an exchange splitting that changes from approximately 1.1 eV to 0.6 eV as the overlayer thickness increases. The results for thicker films agree with the accepted values for the 5d exchange splitting of bulk gadolinium.

## INTRODUCTION

The investigation of the magnetic properties of ultrathin (1-10 monolayer) metallic films is an area of increasing interest [1,2], in particular since thin films exhibit qualitatively different magnetic properties compared with the bulk [3,5]. Gadolinium is of particular interest because this elemental ferromagnet has been thought to be a classic, localized ferromagnet [6].

The 4f, valence band and shallow core levels of ultra thin Gd overlayers on Cu(100) and on crystalline nickel overlayers on Cu(100) have been investigated using angle-resolved photoemission [7,8]. A definite selection of the final state symmetries for 1/2 to 4 monolayer thick Gd films indicates that the occupied Gd 5d band is predominately  $3z^2-r^2$  and  $j=3/2$  character. The  $5p_{3/2}$  was observed to be predominately  $p_z$  in character, for thin Gd overlayers on Cu(100). This occurs as a consequence of the final state electron exchange interactions between the gadolinium 5d and 5p eigenstates.

Using the known  $3z^2-r^2$  initial state symmetry of the occupied Gd 5d band, combined with studies of the resonant photoemission process, we have been able to determine a lower bound to the 5d band exchange splitting for gadolinium.

## EXPERIMENTAL

The experiments were performed in an ultra high vacuum (U.H.V.) system equipped with a hemispherical analyzer with angular acceptance window of  $\pm 1.5^\circ$  for angle resolved photoemission, as well as a retarding field analyzer for low energy electron diffraction (LEED). The vacuum system was pumped by a combination of turbomolecular, ion and titanium sublimation pumps, and was equipped with a residual gas analyzer, and the typical

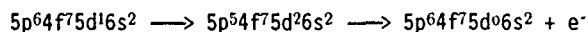
pressure gauges. The 50mm radius hemispherical analyzer was mounted in the U.H.V. system on an goniometer stage with two degrees of freedom so that a broad range of emission angles and light incidence angles could be studied. The light source for the photoemission studies was the 1 GeV ring at the Synchrotron Radiation Center, dispersed by a 3-m torodial grating monochromator.

Relative photoemission intensities (constant initial state) [7] were estimated using the maximum intensity of the photoemission feature with the resolution degraded and the intensity normalized with respect to the photon flux from the monochromator as determined by the yield of a nickel mesh diode. The electric vector potential  $\underline{A}$  of the incident light was oriented so that the component parallel to the surface was along the Cu  $\langle 110 \rangle$

direction throughout this work (The  $\Gamma$ - $\bar{X}$  direction of the clean Cu(100) surface Brillouin zone). The incidence angle of the light is defined with respect to the surface normal so that normal incidence (zero degrees) has the vector potential completely parallel with the surface (s-polarized) while glancing incidence light has a large component of the vector potential normal to the surface (p-polarized). Photoelectrons were collected normal to the surface throughout this work, except for studies of dispersion of bands and for angle-resolved Auger studies.

#### RESONANT PHOTOEMISSION

Resonant enhancement of the valence band photoemission features has been observed for a number of metals (reference [7] and the references therein) as well as for gadolinium overlayers [7,9]. The resonant enhancement of the Gd 5d band, as well as for other rare earths, has been successfully explained in terms of a 5p excitation to a low lying n1 excited electron state (mainly of 5d character) which decays via a super Coster Kronig Transition:



resulting in a final state identical to the direct 5d emission [7,9]. The two excitation pathways can resonate often resulting in an interference dip characteristic of a Fano resonance. In addition, Auger decay to final states such as:  $5p^6 4f^7 5d^1 6s^1$  and  $5p^6 4f^7 5d^2 6s^0$ , may also occur to some extent. Auger decay to the  $5p^6 4f^6 5d^1 6s^2$  and  $5p^6 4f^6 5d^2 6s^1$  contributes only to the 4f levels (at selected photon energies of course) and does not contribute to the 5d photoemission resonances.

The photoemission resonances observed (as seen in figure 1) for the Gd 5d band at the photon energies of 25 and 32 eV are a result of this 5p-5d interaction and occur just above the  $5p_{3/2}$  and  $5p_{1/2}$  thresholds at  $21.9 \pm 0.2$  eV and  $26.1 \pm 0.4$  eV respectively [7]. Since the resonance at the  $5p_{1/2}$  threshold is consistently more intense than the one at the  $5p_{3/2}$  threshold, despite the greater theoretical electron occupancy of the  $5p_{3/2}$  state, dipole selection rules dictate that the low lying n1 excited electron state is mainly of  $5d_{3/2}$  character since for a photoexcitation dipole selection require that  $\Delta l = \pm 1$ ,  $\Delta j = 0, \pm 1$ .

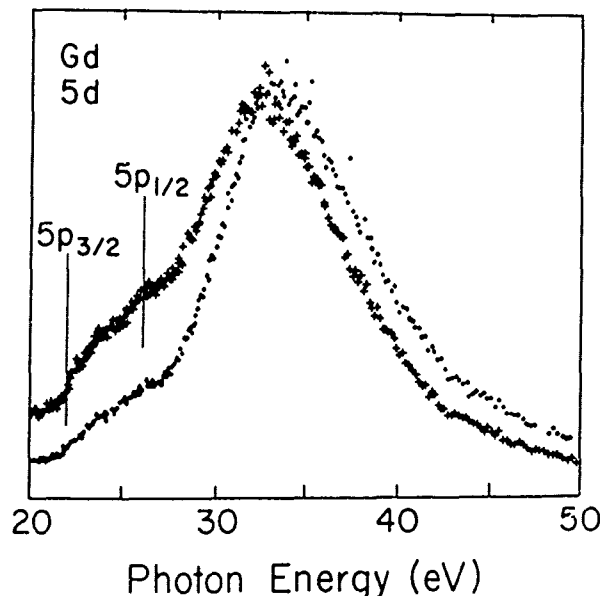


**Figure one:** Constant initial state spectra of the gadolinium 5d derived bands. The spectra are for  $34^\circ$  (+) and  $70^\circ$  (o) light incidence angles. All photoelectrons were collected normal to the surface. The nominal thickness of the gadolinium overlayer is 1 monolayer thick. The spectra are normalized for the incident photon flux. The  $5p_{1/2}$  and  $5p_{3/2}$  thresholds are indicated.

#### EXCHANGE SPLITTING

Careful analysis of the results similar to those presented in figure 1 indicate that for s-polarized light, the  $5p_{1/2}$  to 5d photoemission resonance for gadolinium on Cu(100) peaks at 31.5 eV photon energy for 1, 2 and 3 monolayer thick films. For p-polarized light, this photoemission resonance is at a maximum at 32.6 eV for one monolayer, 32.4 eV for two monolayers and 32.3 eV for three monolayers. Application of Fermi's golden rule suggests that since the  $5p_{1/2}$  initial state symmetry, selected in the photoemission process, is altered with the changing light polarization that the symmetry of the empty 5d gadolinium state involved in the resonant photoemission process is also altered. Since the overall initial and final state wavefunctions of the electron must share the same symmetry, s-polarized light (normal incidence) produces transitions between  $p_x + ip_y$  to unoccupied states of  $d_{xz}, d_{yz}$  character. p-polarized light (glancing incidence) produces transitions between  $p_z$  states and unoccupied states of  $d_{3z^2-r^2}$  character. Assuming the core levels of different symmetries are close to degenerate [10], we therefore conclude that the unoccupied  $d_{xz}, d_{yz}$  character states are closer to the Fermi level than the unoccupied  $d_{3z^2-r^2}$  character states by 1.1 eV for one monolayer thick films, 0.9 eV for two monolayer thick films and 0.7 eV for three monolayer thick films (using monolayer equivalents) of gadolinium on Cu(100).

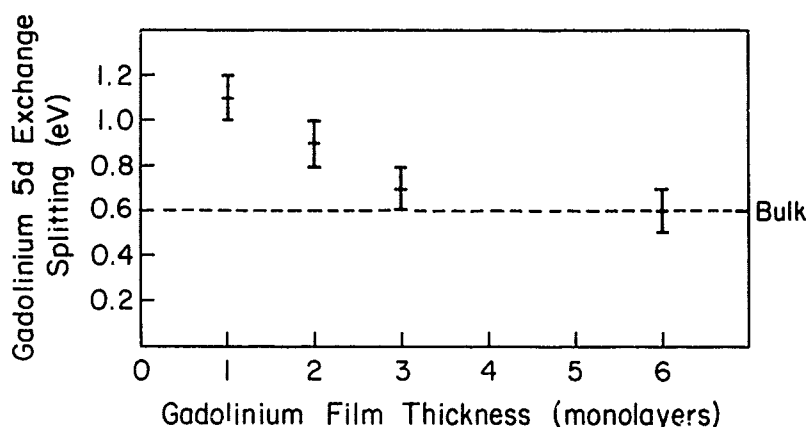


**Figure two:** The minimum exchange splitting for the Gd 5d band as a function of film thickness. The exchange splitting was determined from resonant photoemission as shown in figure one. The bulk exchange splitting is indicated [10-12].

Since the occupied 5d band is of  $d_{3z^2-r^2}$  character, the measured energy separation between the occupied and unoccupied 5d bands of  $d_{3z^2-r^2}$  character cannot be less than the energy separation between the unoccupied  $d_{3z^2-r^2}$  and  $d_{xz, yz}$  character states. By placing the unoccupied  $d_{xz, yz}$  levels just above the Fermi energy, this energy difference is the estimate of the smallest exchange splitting of the 5d band. The exchange splitting determined in this manner is thickness dependant as shown in figure 2. As the thickness of the film increases, the measured exchange splitting decreases from 1.1 eV (1 monolayer) to 0.6 eV (for a six monolayer film). This latter value is consistent with the measured value for bulk gadolinium of 0.6 – 0.7 eV [11,12].

Figure 3 illustrates the energy level diagram expected for the gadolinium 5d levels in the presence of an exchange splitting and the resonant photoemission process. While the mechanism is undoubtedly different, enhanced magnetic moments have been predicted and observed for 3d ferromagnetic and antiferromagnetic thin films [3]. Our results for gadolinium are consistent with these observations and the accepted exchange splitting for the 5d bands of bulk gadolinium.

This measurement does not distinguish between the various types of magnetic ordering (ferromagnetic, antiferromagnetic or ferrimagnetism) nor does this measurement allow us to ascertain the spatial range of the magnetic ordering. These measurements are, however, complementary with other measurements such as electron spin polarization techniques without suffering from problems associated with limited counting statistics.

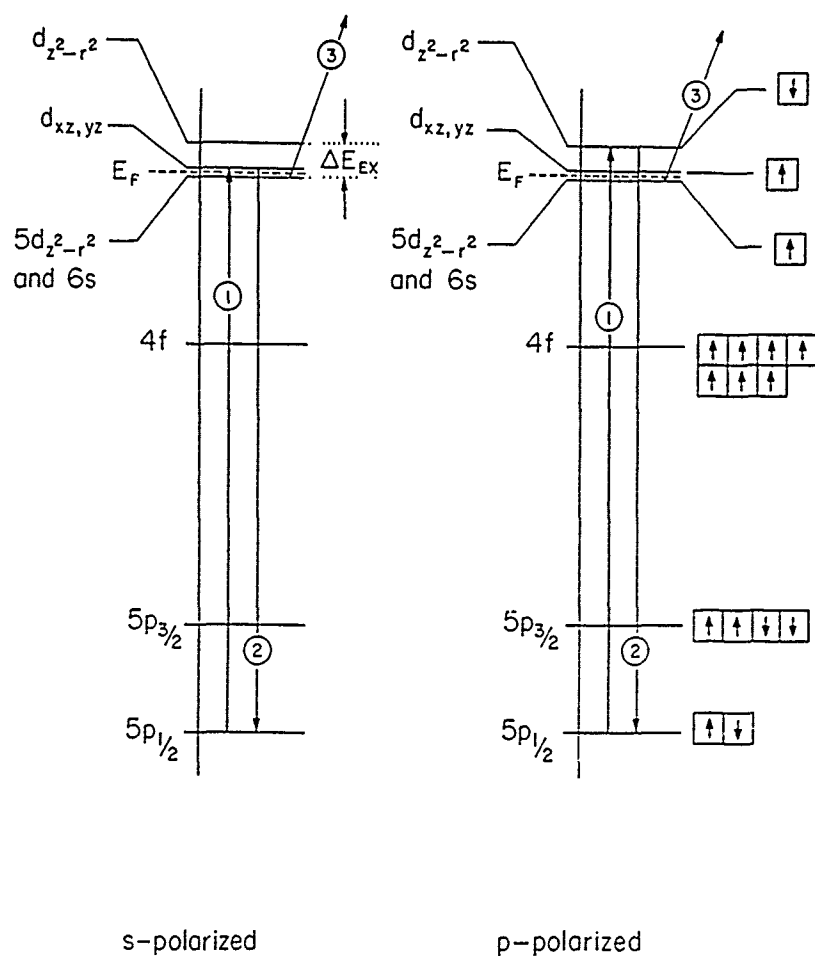


**Figure three:** The Gd energy level diagram deduced from our results, in the presence of an exchange splitting. The Gd 5d multiplet, the Gd 4f level, and the Gd 5p doublet are included. Also illustrated is the two-step process by which a Gd 5p electron can lead to enhanced emission from the Gd

## ACKNOWLEDGEMENTS

This work was funded by the U.S. DOE and was carried out at the University of Wisconsin Synchrotron Radiation Center which is funded by the NSF.

## REFERENCES

- [1] P.A. Dowben, M. Onellion, and Y.J. Kime, *Scanning Microsc.*, 2, 177 (1988).
- [2] J.L. Erskine, M.F. Onellion and M.A. Thompson, *Mat. Res. Symp.* (1987).
- [3] C.L. Fu, A.J. Freeman, and T. Oguchi, *Phys. Rev. Lett.*, 54, 2700 (1985).
- [4] Magnetic Properties of Low Dimensional Systems, Edited by L.M. Falicov and J.L. Moran-Lopez, Springer-Verlag (1986).
- [5] J. Mathon, *Rep. Prog. Phys.*, 51, 1 (1988).
- [6] J. Sticht and J. Kubler, *Solid State Commun.*, 53, 529 (1985).
- [7] P.A. Dowben, D. LaGraffe and M. Onellion, *J. Phys: Solid State* (1989).
- [8] D. LaGraffe, P.A. Dowben and M. Onellion, *Phys. Rev. B*, in press.
- [9] V. Murgai, Young-Sea Huang, M.L. den Boer and S. Horn, *Solid State Commun.*, 66, 329 (1988).
- [10] B.N. Harmon and A.J. Freeman, *Phys. Rev. B*10, 1979 (1974).
- [11] A.B. Besnosov, V.V. Eremendo, and V.P. Gnezdilov, *J. Magn. Magn. Mater.* 43, 243 (1984).
- [12] G. Schutz, M. Knull, R. Wienke, W. Wilhelm, W. Wagner, P. Kienle, and R. Frahm, *Z. Phys.* B73, 67 (1988).



## MAGNETOMETRY IN ULTRATHIN FILMS USING SPIN POLARIZED CASCADE ELECTRONS

ERIC KAY

IBM Research Division, Almaden Research Center, 650 Harry Road, San Jose, CA  
95120-6099

### ABSTRACT

In this review, we show how spin polarized cascade electron spectroscopy provides a relatively rapid and flexible approach to the study of a variety of problems of current interest in both ultrathin magnetic films and surface magnetism. Specific examples relating to the non-bulk like magnetization behavior as a function of temperature of ultrathin films are given which lead to the conclusion that stabilization of the magnetization at low temperature is a universal characteristic of ultrathin magnetic films. Comparison between ultrathin film and surface magnetic behavior is made. Evidence is given that the weakening of exchange coupling both at the surface of a bulk sample and across magnetic spacer layers between an ultrathin magnetic thin film and a bulk sample can be evaluated and dramatic effects due to minute quantities of non-magnetic nearest neighbors are demonstrated.

### INTRODUCTION

It has long since been recognized that magnetic properties at a surface of a magnetic material can be expected to be quite different from its bulk magnetic characteristics. The inherent breaking of symmetry at the surface as well as structural or compositional changes at the surface of multiconstituent materials are but a few of the reasons why large differences in surface versus bulk magnetic properties should be anticipated. In recent years a number of spectroscopies have been developed which are designed to probe magnetic phenomena uniquely in the first few monolayers of a magnetic material. The sensitivity of these spectroscopies is such that fractional monolayers of a magnetic material on nonmagnetic substrates can also be examined. This versatility allows us to examine a large variety of magnetic phenomena such as the onset of magnetic characteristics during the early stages of film growth - to the unique non-bulk-like properties in ultrathin layers due to issues relating to low dimensionality - to the onset of bulk-like characteristics as the film grows. Recently many reports have appeared in the literature on multilayered or modulated magnetic thin film structures which owe their unique overall magnetic characteristics to magnetic surface or interface phenomena or questions relating to low dimensionality.

It is the purpose of this article to describe one experimental approach which utilizes relatively well established in situ spectroscopies which lend themselves to the study of the above stated classes of problems. Several material systems have been chosen from recent work in this laboratory and are considered typical of related work throughout the literature. Emphasis in this paper will be placed on the experimental techniques and the related Material Science issues.

### SPIN POLARIZED ELECTRON MAGNETOMETRY

One of the major achievements of the past decades is that one has learned how to extract electrons from a solid and emit them into vacuum. The energy required for electron emission is mainly supplied in the form of electric fields, and the amount of energy is small compared to the energy of the rest mass of the electrons. Therefore, the non-relativistic limit applies, and the electric fields do not couple to the electron spin. This means that the spin polarization of the electrons is conserved in the process of excitation of the electrons to an escape level. However, the conservation of spin polarization as the electrons are transported out of the solid is not necessarily assured due to an as yet not well understood set of circumstances so that an independent experimental proof of a direct relationship between surface magnetization and the measured spin polarization is highly desirable for each system under study. Once the electrons have been emitted into the vacuum, one can form an electron beam and measure the spin polarization in a scattering experiment. This is the basis

instance with a spin polarized GaAs-electron gun, and the emission of light or scattered electrons is measured when the spin polarized electron beam strikes the sample under investigation. Magnetometry based on the emission or scattering of electrons requires special care relating to the sample preparation. Definition of the surface on an atomic scale is critical because of the short mean free path of the electrons in the solid. For most investigations this necessitates that the experiment be carried out in an ultrahigh vacuum system and that appropriate methods to prepare and subsequently characterize the sample surface be part of the experimental setup. When buried magnetic layers, or magnetic probing greater than several monolayers is required alternate techniques such as Kerr magneto optical rotation can be employed.

## UNIQUE FEATURES OF MAGNETOMETRY WITH SPIN POLARIZED ELECTRONS

### Spatial Resolution:

A non-polarized primary electron beam may be focused into an extremely small spot. If the electron beam strikes a magnetic solid, the spin polarization,  $P$ , of the secondary electrons is related to the magnetization of the spot from which they have been emitted. The probing depth of the secondary electrons may be a few Angstroms only, depending on their energy. By scanning the incident electron beam across the sample surface, good images of magnetic domains and domain walls have already been obtained with this technique [1,2,3].

### Element Specificity:

One can obtain element specific magnetization, in an alloy for example, if one excites electrons from specific atomic shells, as in Auger spectroscopy, and measures the spin polarization of the emitted electrons around the atom from which the electron was emitted. Striking examples include results obtained with FeGd [4].

### Time Resolution:

With lasers, one can generate a short pulse of ultraviolet light. If such a pulse of say  $10^{-12}$ s duration strikes the surface of a solid, enough electrons are emitted to perform an accurate measurement of  $P$ . Since angular momentum is conserved for the whole bunch of emitted electrons, space charge effects do not affect the spin polarization. This is clearly one of the fastest techniques for measuring magnetization [5]. Furthermore, by using laser pulses at different time delays various processes can be sorted out due to their characteristically different time dependences, when magnetization is reversed in an external field.

### Magnetization of Specific Electronic States:

In photoemission of spin polarized electrons, one can set the electron spectrometer to a specific energy and angle of emission. In this way, it is possible to measure the spin polarization of specific electronic states in the solid. Even if two otherwise equal electron states nearly coincide in energy they can still be separated if they have different spin polarization. This is ideal to detect the small exchange splitting in metals [6]. The results obtained on Fe, for example, contain a wealth of new information on metallic magnetism [7].

### Magnetism in Unoccupied Electron States:

If a spin polarized electron beam is directed onto the surface of a magnetic material, the spin dependence of light emission, or electron scattering, or electron absorption can be measured. This opens up the field of magnetism in unoccupied electron states [8]. Recently, a strong spin polarized feature was discovered at an energy as high as  $\sim 20$  eV above the Fermi-level in Fe [9].

From the above, it is obvious that magnetometry with spin polarized electrons using various excitation sources such as electron beams or lasers or tunable synchrotron radiation opens up the field of surface and interface magnetism. If, in addition, one considers the potential for time and spatial resolution, and the element specificity, and the magnetic properties of unoccupied electron states it should be clear that the understanding of surface and low dimensionality magnetic properties at a microscopic level should advance rapidly in the future.

It must be recalled that a common feature of all electron spectroscopies is that one generally obtains information that is confined to a very thin sheet due to the short interaction length of the electrons. It is therefore important to reiterate that using spin polarized electron magnetometry can only give insight to magnetic phenomena at or near the surface and only complimentary bulk magnetics studies can give a true picture if and when bulk and surface magnetism will be different. One can readily identify several general areas where non-bulk-like behavior can be anticipated.

Surface magnetic moments, surface magnetic anisotropies and surface magnetic exchange coupling are among the most obvious. There is also a lot of activity concerning the properties of new materials that do not exist in nature. New techniques for materials growth, such as molecular beam epitaxy, are capable of growing artificial material with new and unexpected magnetic properties. For example, a thin film of face centered cubic iron that does not occur naturally at room temperature and which exhibits large uniaxial surface anisotropy [10].

Not only the surface magnetization can be expected to be different from bulk but also its temperature dependence. Over the years a number of theoretical models have attempted to describe this dependence taking cognizance of the fact that the spin wave behavior at the surface or in ultra thin films will be different from bulk. Furthermore, the surface magnetization temperature dependence on a bulk magnetic material can be expected to be different than that of an isolated ultrathin magnetic film on a nonmagnetic substrate. Most recently, extension of earlier spin wave models has shown [11,12] how surface magnetization exchange can be deduced from the temperature dependence of the surface magnetization. Such temperature dependent measurements also lead to insight into critical phenomena at the surface [13].

In order to test such models it becomes necessary not only to have the ability to measure surface magnetization but to be able to do it over a large temperature range from as low as possible up to the Curie temperature.

## SPIN POLARIZED CASCADE ELECTRON SPECTROSCOPY

Perhaps the simplest approach to surface magnetometry is to irradiate the magnetic sample with an unpolarized electron beam giving rise to the emission of secondary electrons whose spin polarization can subsequently be determined by Mott scattering from a metal foil. The interpretation of the Mott scattering process which leads to the determination of the spin polarization is well established and exploits the asymmetry in the electron scattering due to the spin-orbit coupling between polarized electrons and the gold foil. For details on secondary electron emission and Mott scattering, see [14].

There are several advantages to using the spin polarization of the secondary cascade electrons to obtain surface and ultra thin film magnetics information. The large intensity of the emitted cascade (0-20 eV) electrons with a maximum at energies around 10 eV are mainly electrons ejected from the valence band. The fact that the spin polarization cross section is large in this same energy regime leads to large signals-in comparison, for example, to photo emitted spin polarized electrons, or spin polarized Auger electrons, see Fig. 1. The large intensity of the cascade electrons makes very rapid measurements possible. This reduces artifacts due to adsorption of residual gas molecules on the sample surface. It will become evident from the data to be presented that this is crucial. Furthermore, the excitation and measurement of the cascade electrons is compatible with such other spectroscopies, such as Auger spectroscopy. Hence, the surface can be spectroscopically defined before and after each magnetic measurement. The effect on surface magnetic properties due to deliberate sorption of gases or condensable species is easily monitored. The addition of electron energy analysis in the higher energy regime, where Auger electrons can be monitored, leads to atom specific, surface sensitive magnetic information. Examples given in this paper will not include results from such energy analysis prior to spin polarization detection, but it should be

### Spin Polarization of the Secondary Electron Cascade

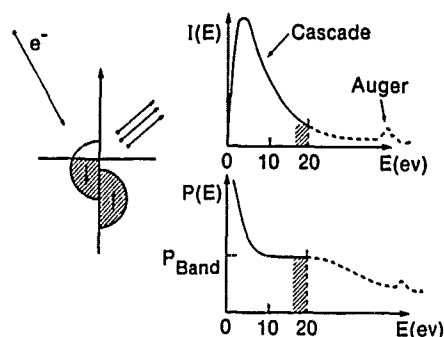


Figure 1. Schematic of spin polarization ( $P$ ) of secondary electron cascade.

pointed out that this element specific surface magnetometry promises to be most powerful, especially from a Materials Science point of view.

In order to make reliable comparisons between theory and experiment the spin polarization of the cascade electrons must be shown to be proportional to the magnetization. This is critical since the often observed enhancement of spin polarization (see Fig. 1) is not clearly understood. Furthermore, in order to make meaningful comparisons with theoretical predictions of surface magnetization and experiment it is important to be able to measure the polarization with the sample in magnetic saturation at each temperature rather than just in the remanent state. This requirement imposes the experimental problem of subjecting the sample to a large enough external magnetic field to saturate the sample while trying to extract and efficiently collect the spin polarized electrons emitted from the sample.

Our choice was to examine magnetization in the plane of the film which then necessitated a uniform, variable field to be applied in the plane of the film. This is accomplished by either placing the sample appropriately in the gap of horse shoe electromagnet or by using a metal strip arrangement as a substrate, through which a current could be passed to produce a homogenous magnetic field near the surface. The applied field is used both during deposition in order to induce uniaxial anisotropy and for the subsequent saturated hysteresis loop polarization measurements. In order to fulfill the requirement of saturating the sample and yet overcome the Lorentz deflection of the cascade electrons our experimental configuration constrained us to study materials that can be saturated at fields  $< 20$  Oe, i.e., soft materials, such as permalloy. Clearly, the remanent surface magnetization can be measured for hard materials also. The relative accuracy in the measurement of the spin polarization  $P$  can be determined by employing the fact that thick permalloy films exhibit square surface magnetization loops with magnetic saturation in external magnetic fields  $H < 5$  Oe. It follows that  $P(H)$  must be constant within experimental error at  $H \geq 5$  Oe. This provides an internal relative standard against which the precision of the apparatus can be verified. On the basis of this test, remaining systematic errors are estimated of the order of  $P \approx .1\%$ . A further more generally applicable test can be derived from the fact that hysteresis loops must be symmetrical with respect to the center ( $M = 0$ ,  $H = 0$ ) whereas stray field induced artifacts tend to be even functions of the applied field  $H$ . The  $P$  values observed in magnetic saturation as defined above are averaged and the difference between the average in positive and negative saturation yielded one datum point of the saturation spin polarization,  $P(T)$ .

Our Kerr magneto optical rotation measurements during film growth, not only provides direct comparison of hysteresis loops for ultrathin films by a second method (even at the submonolayer level (SMOKE)) but also provides the ability to monitor the integrated magnetic behavior of much thicker films, which the electron escape depth-limited spin polarized electron spectroscopy cannot. One of our most recent studies using spin polarized cascade emission serves to illustrate many of the points made so far.

## EXPERIMENTAL RESULTS AND DISCUSSION

Recent extensive studies in our laboratory on clean and modified surfaces of previously well characterized amorphous bulk FeNiB has shown that the spin polarized surface measurements are proportional to the surface magnetization as a function of temperature. In the case of such polarization measurements on crystalline materials the incoherent generation of the cascade electrons averages over effects of diffraction. In contrast to the spin dependence of the elastic scattering of electrons, as in SPLEED, the spin polarization of the cascade electrons is then expected to be proportional to the surface magnetization even with crystalline materials.

In Fig. 2, the normalized spin polarization of 4 NiFe films with less than 1% of a monolayer of surface contaminants as determined by Auger, are plotted against temperature. At each data point a surface hysteresis loop was taken and the saturation polarization measured as defined earlier. From inspection of such surface loops the importance of saturating the samples becomes evident since the observed remanent magnetization can be significantly lower than the saturation values.

Figure 2, vividly demonstrates that the temperature dependence of the surface magnetization changes dramatically as the film thickness increases from one to several monolayers of NiFe. For example, the lowest Curie temperature we were able to observe was 250 K for the thinnest film compared with a bulk value of 850 K. Furthermore Fig. 2 demonstrates how quickly the non-bulk-like behavior of ultrathin films involving transition metals is lost as the film thickness increases. At approximately the 3 to 4 monolayer level the bulk-like temperature dependence of magnetization is reached. This is consistent with the short range spin correlation length in transition metals.

The fact that the temperature dependence of the magnetization in these ultrathin films is stabilized at the lower temperatures is the subject of a separate publication in which we propose this low temperature stabilization to be quite universal for ultra thin films and due to quenching of long wave length spin modes [15]. Some recent experiments on epitaxial Fe or Co films in the monolayer range using different spectroscopies show similar temperature dependencies [16,17,18,19]. Clearly the spin wave theory which predicts a linear decrease of  $M$  at the lower temperatures [20] for ultrathin films does not hold.

As mentioned earlier besides reduced coordination and symmetry at surfaces, the presence of any magnetically dissimilar or nonmagnetic nearest neighbor atoms in the form, for example, of surface sorbates can be expected to alter the surface magnetization via electronic interactions. Likewise the presence of ultrathin non-magnetic overlayers or non-magnetic spacer layer between say, an ultrathin magnetic layer and a magnetic substrate or as part of a periodic modulated thin film structure will also influence the resultant magnetic behavior via different coupling mechanisms across the interfaces. Numerous examples of this general type have been reported in the literature in recent times. Below we present a typical example of how spin polarization magnetometry was used in our laboratory to follow some of these effects on ultrathin film structures.

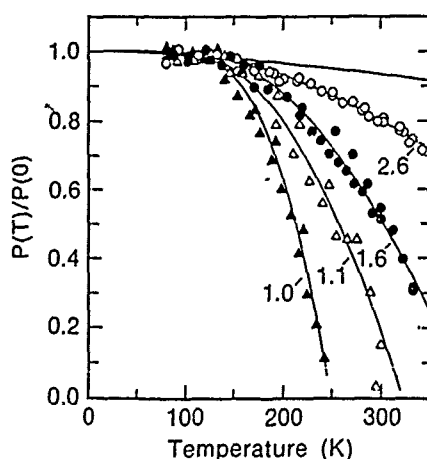


Figure 2. Normalized saturation spin polarization  $P_0(T)/P_0(0)$  versus temperature for 4 films with magnetic thicknesses  $d_m$  of 1, 1.1, 1.6 and 2.6 layers of permalloy. The temperature dependence of the bulk magnetization (upper line with no data points) is taken from Ref. 12.

Figure 3 demonstrates how sensitively the temperature dependence of the saturation spin polarization (surface magnetization) responds not only to small changes in film thickness but also the addition of submonolayer quantities of non-magnetic sorbates or non-magnetic metals during film growth up to a total film thickness of approximately 6Å.

Figure 3 shows  $P_0(T)$  for a group of thin permalloy films. Film 1 had a nominal thickness  $d_n \approx 4.5\text{\AA}$ ;  $T_c \approx 320\text{K}$  was obtained by extrapolating  $P_0(T)$ . The contamination of film 1 with C and O atoms as determined by the Auger-spectrometer was below 1% of a monolayer. No other contaminants were detected. Film 2 was obtained by depositing an additional layer of 0.75Å of permalloy, whereby  $P_0(100\text{K})$  increased from 6.6% to 9.0 and  $T_c \approx 390\text{K}$ . Film 3 was obtained after  $\sim 10\%$  of a monolayer of C and O had accumulated in 15h waiting time at a total pressure of residual gases of  $\sim 10^{-10}$  Torr;  $P_0(100\text{K})$  decreased by .8% and  $T_c$  by 20°K due to adsorption of mainly CO or CO<sub>2</sub>. Film 4 was obtained when 9% of a monolayer of Ta was deposited at the surface which caused the strong decrease of  $P_0(100\text{K})$  and  $T_c$  to 6.2% and 250K, respectively. Film 5 was then obtained by depositing .9Å of permalloy on top of this sandwich whereby  $P_0(100\text{K})$  and  $T_c$  increased again to 7.7% and 335K. The total thickness of film 5 is  $\sim 6.15\text{\AA}$  of "permalloy." However, it contains traces of Ta, C, and O as measured in the various steps of preparation. This is sufficient to induce a substantial difference to a homogeneous permalloy film of 6Å; such a film has  $P_0(100\text{K}) = 12.4\%$  and  $T_c \sim 704\text{K}$  which demonstrates the crucial role of contaminants in the magnetic properties of ultrathin films. The extreme sensitivity of  $P_0$  and  $T_c$  to contamination of permalloy can be understood by the preferential oxidation and surface segregation of Fe. Brundle, Silverman and Madix [21] showed that these phenomena occur in permalloy, but a detailed understanding of the magnetic changes concomitant the chemical changes is at present still lacking. However, the segregation of Fe occurs only if surface adsorbates are present. Therefore, we can assume that an NiFe alloy of the bulk composition exists if no surface adsorbates are detected with the Auger-spectrometer.

One of the additional features that the data in Fig. 3 demonstrates is the fact that in ultrathin film studies the nominal thin film thickness  $d_n$  of the magnetic film is not an adequate measure of the true magnetic film thickness  $d_m$ . If the substrate or an interfacial or overlayer of a different material couples at the interface such as to induce a lowered magnetization in the adjacent layers then  $d_m$  in fact will be smaller than  $d_n$ . We have shown elsewhere [22] how a true  $d_m$  can be estimated from the observed saturation spin polarization  $P_0$  at  $T \rightarrow 0$ , using the expression

$$d_m = \ell \ln(1 - P_0/P_m) \quad (1)$$

where  $\ell$  is an estimate of the probing depth of the cascade electrons [23] and  $P_m$  is the independently measured saturated spin polarization of a clean, thick film of the same magnetic material. In this latter case no substrate interfacial coupling problems need be considered and the film thickness would be much larger than the the escape depth, say 5Å,

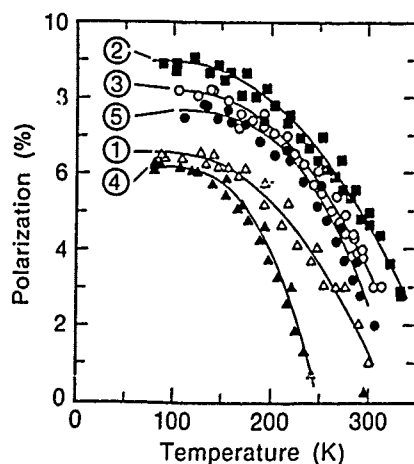


Figure 3. Saturation spin polarization  $P_0(T)$  of the low energy cascade electrons versus temperature. Film 1 was obtained by depositing 4.5Å of Ni<sub>80</sub>Fe<sub>20</sub>, film 2 by adding .76Å of Ni<sub>80</sub>Fe<sub>20</sub>, film 3 by adding 10% of a monolayer of C and O each, film 4 by adding 9% of a monolayer of Ta, and film 5 by adding .9Å of Ni<sub>80</sub>Fe<sub>20</sub>.

using the recent values of  $\ell$  reported in the literature [23]. Making the correction in this manner to obtain the true magnetic thickness and then plotting the observed Curie temperatures  $T_c$  as a function of this  $d_m$  gives very good agreement with the  $T_c$ -thickness dependence reported in the literature where direct measurements of magnetization were made using other methods [24,25]. This agreement provides further evidence that spin polarized cascade electrons can be used to make meaningful measurements of surface magnetization. The conclusion that a magnetic "dead layer" in the NiFe was induced for example by the Ta substrate in the systems reported in Fig. 3 was further corroborated by an approach in which the variation of the Auger line intensities of NiFe and Ta as a function of coverage are compared to the observed cascade spin polarization. Appropriate Auger lines for NiFe and Ta are chosen so that effects of depth dependent attenuation cancel. For details see Ref. (22).

We have already mentioned that ultrathin magnetic films on a nonmagnetic substrate do not follow the linear decrease of  $M(T)$  at low  $T$  predicted by spin wave theory for "free standing films." Figure 3 clearly demonstrates that experimental fact. On the other hand we have shown that equivalently ultrathin magnetic films adequately coupled via a nonmagnetic exchange link to a bulk magnetic substrate exhibits the  $M(T)$  behavior predicted by the spin wave theory recently described for such a coupled system [11,12]. In fact a  $T^{3/2}$  dependence is predicted similar to that for the surface magnetization of a bulk sample according to Eq. 2

$$M_0(T) = M_0(0) \cdot (1 - kCT^{3/2}) \quad (2)$$

where  $C$  is the constant describing the decrease of the bulk magnetization due to spin waves and  $k$  measures the probability of finding a reversed spin in the surface layer divided by the average magnon probability in the bulk. One of the advantages of measuring the magnetization via the spin polarization of the cascade electrons is that a magnetic film on a magnetic substrate can also be measured by virtue of the small probing depth of the cascade electrons. Examination of the data presented in Fig. 4 illustrates these points. Here Permalloy films of the nominal thickness  $d_n = 5\text{\AA}$  were coupled to a thick (bulk) Permalloy film of  $d_n = 500\text{\AA}$  via a Ta spacer. Curves a, b and c in Fig. 4 show the temperature dependence of the saturation spin polarization for such sandwich structures with the exchange link thickness of the Ta varying from .5, 1.0, and 1.5 atomic layers. The full lines are best fits through the data points using the above equation. The full line without data points is the  $T$ -dependence of bulk Permalloy taken from Ref. 12. The spin polarization data for all three coupled films are reproduced perfectly by the above equation with  $k = 2.5, 4.1$  and  $5.7$  and  $P_0(0) = 17.6\%, 16.3\%$  and  $13.4\%$  for films a, b and c, respectively. So not only is the  $T^{3/2}$  prediction met, thereby validating the applicability of the above mentioned spin wave theory, but in addition the variation of the  $k$  values following the model of Mathon and Ahmad [12] give a measure of the expected reduced exchange interaction on a path perpendicular to the spacer layer

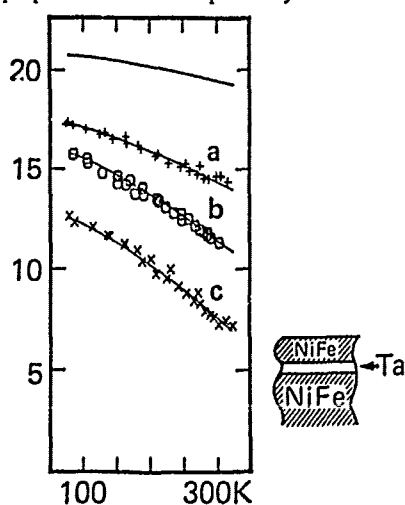
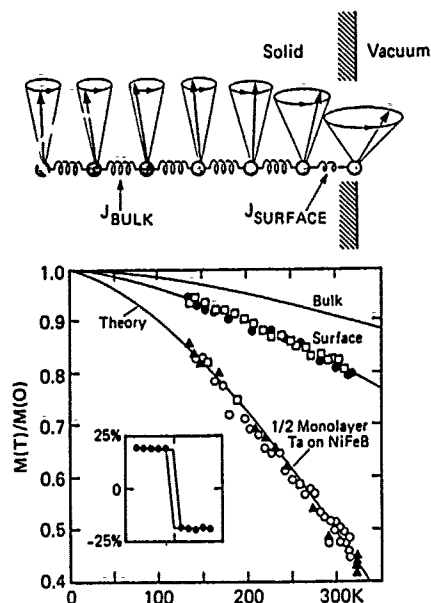


Figure 4. Temperature dependence  $P_0(T)$  of the saturation spin polarization of the cascade electrons in % for 3 coupled films a, b, c of  $d_n \approx 5\text{\AA}$ . With .5, 1.0, and 1.5 atomic layers of Ta as interface to bulk permalloy, respectively. Except for the line without data points which is the  $T$ -dependence of bulk permalloy from Ref. 12 the full lines are best fits through the data points using Eq. 2 for a, b, and c.



**Figure 5.** Temperature dependence of the low-energy cascade relative spin polarization  $P(T)/P(0)$ , for a clean surface of  $\text{FeNi}_{0.5}$  (cooling, circles; warming, asterisks) divided by  $P(0) = 21\%$ , and for same surface covered with  $\approx 1/2$  monolayer of Ta (cooling, pluses; warming, crosses) divided by  $P(0) = 12\%$ . Solid lines, temperature dependences of  $M(T)/M(0)$  calculated from Eq. 1 with  $k = 1, 2$ , and  $5.4$ . Inset: Hysteresis loop measured with the clean surface at  $T = 170\text{K}$ . The magnetic field was swept from  $+6$  to  $-6$  Oe and back. The five points in saturation were averaged, and the difference between the average in positive and negative saturation yielded one datum point of  $P(T)$ .

Clearly, since the escape depth of the spin polarized electrons is no greater than  $5\text{\AA}$  [23], one can also use this cascade electron spectroscopy to study the temperature dependence of the surface magnetization on a bulk magnetic sample. Figure 5 shows a recent example of such a measurement in our laboratory taken on a very carefully cleaned sample of the prototype material, amorphous  $\text{NiFeB}$ , whose surface was characterized by Auger as well as the absolute value of the spin polarization. Examination of Fig. 5 leads to several conclusions. The  $T^{3/2}$  dependence is rigorously followed in agreement with other authors looking at the same material. On the other hand we do not see a unique  $k$  value of 3 as observed by others who used elastic scattering of spin polarized electrons from the surface [26] or on other surfaces by Mossbauer [27,28]. In fact we have clear evidence that the  $k$  factor can be systematically altered over a large range by adsorbing submonolayer quantities of different non-magnetic species on the surface, i.e., changing the surface chemistry.

A  $k = 3$  is seen, for example, at a 20% monolayer of C, O sorbate level. Figure 6 shows a maximum  $k$  value of 5.7 for a half a monolayer of Ta deposited on  $\text{NiFeB}$ . Also shown in Fig. 6 is evidence of optimizing the spin polarization, with this material, to a value of 21%, after repeated cleaning steps. Following the recent extension of classical spin wave

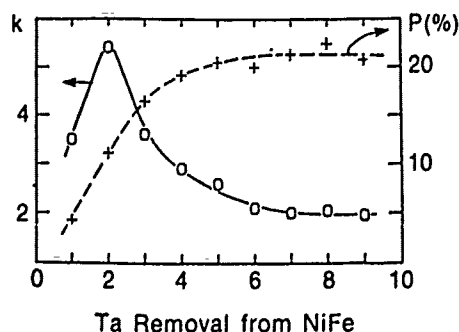


**Figure 6.**  $k$  (full line) and  $P(0)$  (dashed line) versus the number of cleaning steps. At point 1, there is  $\approx 1$  monolayer of Ta at the surface. Each step removes  $\approx 50\%$  of the Ta atoms.



theory by Mathon and Ahmad [11] in which they propose that variations in the  $k$  values up to  $T/T_c \sim 0.4$  are a direct measure of the exchange weakening in a direction perpendicular to the surface plane, Fig. 5 shows that the magnetic exchange coupling at the clean surface of the FeNiB sample is significantly less than the bulk [29]. Furthermore it is clear that surprisingly small quantities of surface deposits, e.g., Ta, weaken this surface exchange in a dramatic way. Detailed understanding of the electronic coupling mechanisms giving rise to these effects as a function of coverage await further development.

#### ACKNOWLEDGEMENT

Much of the work presented here was done in collaboration with D. Mauri, D. Scholl and H. C. Siegmann. Discussion of this manuscript with D. Mauri is especially acknowledged.

#### References

1. K. Koike, H. Matsuyama and K. Hayakama *Scanning Microscopy Supplement* 1, 241 (1987).
2. D. T. Pierce, J. Unguris and R. J. Celotta *MRS Bull.* XII 6, 19 (1988).
3. H. P. Oepen and J. Kirschner *ICM Paris SA-1* (1988).
4. M. Landolt and D. Mauri *Phys. Rev. Lett.* 49, 1783 (1982); M. Landolt, R. Allenspach and M. Taborrelli *Surface Science* 178, 311 (1986).
5. M. Aeschlimann, M. Stampanoni, A. Vaterlaus and F. Meier *ICM Paris 4D-7* (1988).
6. W. Eib and S. F. Alvarado *Phys. Rev. Lett.* 37, 444 (1976).
7. E. Kisker, K. Schroeder, W. Gudat and M. Campagna *Phys. Rev. B* 31, 329 (1985).
8. M. Donath, V. Dose, K. Ertl, U. Kolvac, H. Liebl and G. Schonhense *ICM Paris 1A-4* (1988).
9. Th. Dodt, D. Tillmann, R. Rochow and E. Kisker *Europhys Lett.* 6, 375 (1988).
10. T. G. Gay and R. Richter *Phys. Rev. Lett.* 56, 2728 (1986).
11. T. Mathon and S. B. Ahmad *Phys. Rev. B* 37, 660 (1988).
12. T. Mathon *Physica B* 149, 31 (1988).
13. W. Durr, M. Taborrelli, O. Paul, R. Germar, W. Gudat, D. Pescia and M. Landolt *Phys. Rev. Lett.* 62, 206 (1989).
14. D. Mauri, R. Allenspach and M. Landolt *J. Appl. Phys.* 58, 906 (1985).
15. D. Mauri, D. Scholl, H. C. Siegmann and E. Kay *Phys. Rev. Lett.* April 19, 1989.
16. G. Bayreuther *Magn. Mater.* 38, 273 (1983).
17. M. Stampanoni, A. Vaterlaus, M. Aeschlimann and F. Meier *Phys. Rev. Lett.* 59, 2483 (1987); R. F. Willis, T. A. C. Bland and W. Schwarzacher *J. Appl. Phys.* 63, 4051 (1988).
18. M. Przybylski and U. Gradmann *Phys. Rev. Lett.* 59, 1152 (1987).
19. D. Pescia, G. Zampieri, M. Stampanoni, G. L. Bona, R. F. Willis and F. Meier *Phys. Rev. Lett.* 58, 933 (1987).
20. W. Döring *Z. Naturforsch.* 16a, 1146 (1961).
21. C. R. Brundle, E. Silverman and R. J. Madix *J. Vac. Sci. Tech.* 16, 474 (1979).
22. D. Mauri, D. Scholl, H. C. Siegmann and E. Kay, "Applied Physics A - Solids and Surfaces in Print" (1989).
23. D. L. Abraham and H. Hopster *Phys. Rev. Lett.* 58, 132 (1987).
24. U. Gradmann, R. Bergholz and E. Bergter *Thin Solid Films* 126, 107 (1985).
25. W. Robl and G. Bayreuther "12th Intl. Colloq. on Magnetic Films and Surfaces," Le Creusot, France, Aug. 1-5, 1988.
26. D. T. Pierce, R. J. Celotta, J. Unguris and H. C. Siegmann *Phys. Rev. B* B26, 2566 (1982).
27. J. C. Walker, R. Droste, G. Stern and J. Tyson *J. Appl. Phys.* 55, 2500 (1984).
28. J. Korecki and U. Gradmann *Phys. Rev. Lett.* 55, 2491 (1985).
29. D. Mauri, D. Scholl, H. C. Siegmann and E. Kay *Phys. Rev. Lett.* 61:6, 758 (1988).

# MAGNETIC PROPERTIES OF RARE-EARTH/Fe MULTILAYERED FILMS WITH ARTIFICIAL SUPERSTRUCTURES

TERUYA SHINJO, KO MIBU, SHINICHI OGAWA AND NOBUYOSHI HOSOITO  
Institute for Chemical Research, Kyoto University, Uji, Kyoto-fu 611 Japan

## ABSTRACT

By using UHV deposition technique, multilayered films consisting of Fe and rare-earth (Dy, Nd or Y) layers were prepared. Magnetic properties of Fe layers were investigated from  $^{57}\text{Fe}$  Mössbauer spectroscopy. From SQUID magnetic measurements, the behavior of rare-earth layers was studied. In Fe/Dy and Fe/Nd multilayers, there often exists a large perpendicular anisotropy. Mössbauer spectra evidenced that, in certain samples, the magnetization changes the direction, from in-plane at high temperature to perpendicular at low temperature. The origin of the perpendicular anisotropy is attributed to interface rare-earth atoms which are magnetically coupled with ferromagnetic Fe layers even at higher than their bulk Curie temperatures.

## INTRODUCTION

Multilayered films with artificial superstructures are prepared by alternately depositing two materials with controlling each layer thickness on an atomic scale. From both fundamental and technological viewpoints a great attention has been paid to their physical properties; magnetic superconducting, electric, lattice dynamical...[1]. We have prepared various multilayers by combining magnetic elements with non-magnetic ones and studied the thickness dependences of magnetic properties and interfacial magnetic behaviors. In certain cases, the thickness of magnetic layer could be reduced to one monolayer and two-dimensional magnetic systems were synthesized [2].

Magnetic/magnetic multilayers, consisting of two magnetic constituents with different characters, also are of great importance but have not yet been enough explored. Suppose that two ferromagnetic layers, A and B, are stacked up as shown in Fig. 1, whose Curie temperatures are  $T_C(A)$  and  $T_C(B)$ , where  $T_C(A) > T_C(B)$ . In the temperature range between  $T_C(A)$  and  $T_C(B)$ , the layers of A are ferromagnetic but those of B are paramagnetic. At  $T_C(B)$ , a kind of crossover from quasi-two-dimensional to a bulk-like behavior will occur. Some signals of such a crossover may be observed in the temperature dependence of A-layer's magnetization. On the other hand, the temperature dependence of B-layer's magnetization may deviate from the usual Brillouin-like behavior because of a magnetic proximity effect with the adjacent A layers. If the magnetizations of A and B layers couples ferromagnetically, the total magnetization must be the sum of the two. Conversely, if an antiferromagnetic

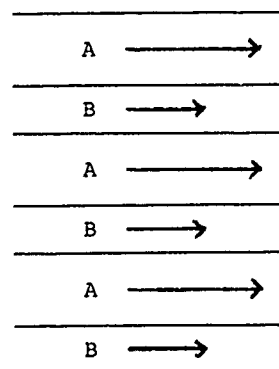


Fig.1. Schematic illustration of a multilayer structure consisting of two ferromagnetic components, A and B.

coupling is favorable, a giant ferrimagnetic system is formed. Then, a magnetic compensation might occur and the compensation temperature can be controlled by changing the thicknesses of the two components. A goal of materials research is to fabricate a material according to an appropriate design so as to realize a certain desirable property. However, this argument is over simplified. Actual situations of ultrathin magnetic films are very complicated. As will be described soon, magnetic properties of ultrathin layers depend on the thickness and in addition the behaviors of interface part in each layer are different from those of inner part.

In this article, experimental results on multilayers prepared from two elements with different magnetic characters, Fe/Dy and Fe/Nd, are presented.[3] In contrast to Fe, which is ferromagnetic with very high  $T_C$ , Dy and Nd have peculiar magnetic properties at low temperatures. Magnetic properties of the multilayers consisting of Fe and Dy or Fe and Nd layers are studied in comparison with the results on multilayers of Fe and non-magnetic element, Y. It is clear that Mössbauer spectroscopy is useful to elucidate the magnetic properties of Fe layers and from this knowledge we obtain information concerning the microscopic structure of the interface.

Many intermetallic compounds consisting of 3d and rare-earth elements are known, and some of them are very important as technological magnetic materials. By combining 3d and rare-earth metals in the form of artificially structured multilayers, we expect to find some novel magnetic materials. Recently amorphous alloy films of 3d and rare-earth metals have been extensively studied and those having perpendicular magnetization gather attention for their potential as magneto-optical recording media. The perpendicular anisotropy in the case of multilayers is one of the main subjects in the present work.

## EXPERIMENTAL

Multilayered samples were prepared by alternate deposition of Fe and a rare-earth metal (Dy, Nd or Y) in ultrahigh vacuum. The procedure is almost the same as the previous case, e.g. for Fe/Sb multilayers, which was already described elsewhere [4]. The vacuum during the deposition was in the range of  $10^{-9}$  Torr and the typical deposition rate was about  $0.3 \text{ \AA} \cdot \text{s}^{-1}$ . The number of bilayers in each sample is  $50 \sim 200$ . The substrates, kapton films and glass plates, were maintained at about  $-50^\circ\text{C}$  during the deposition in order to minimize the intermixing. Samples prepared on glass plates were used for X-ray and neutron diffraction experiments. Structural characterization was made by means of X-ray diffraction techniques using a  $\text{Cu-K}\alpha$  radiation with  $\theta - 2\theta$  scanning. Samples on kapton substrates were utilized for Mössbauer spectroscopy and SQUID magnetization measurements. In order to enhance the effective Fe thickness in Mössbauer absorbers, samples with kapton films were folded up for several time. A standard  $^{57}\text{Co}$  source (Rh matrix) and a conventional spectrometer were used for  $^{57}\text{Fe}$  transmission Mössbauer measurements.

## RESULTS

### Structural aspects

According to the X-ray diffraction measurements, the features of crystallographic structures of the multilayers, Fe/Dy, Fe/Nd and Fe/Y, are very similar. Concerning their chemical properties, the difference among these rare-earth elements is small. Their atomic radii are much larger than that of Fe and therefore an epitaxial stacking is not realized between rare-earth and Fe layers. In the crystallographic sense, therefore, the quality of Fe/rare-earth multilayers is not expected to be high. In the cases that

both Fe and rare-earth layers are rather thick (more than 30Å), both layers have their own bulk crystal structures but the coherence with each other is very poor. The Fe layers have a bcc structure and normally (110) is preferentially oriented in the film plane. The rare-earth layers have an hcp structure but the orientation is almost at random.

If the thickness of an Fe layer is less than a certain critical value, the structure may appear as amorphous from X-ray diffraction studies. If an Fe layer grows without an epitaxial relation to the substrate, very often such a structural transition from amorphous to crystalline occurs in the process of growth. The magnetic properties of amorphous Fe layers are greatly different from those of crystalline layers. Namely the Curie temperature,  $T_c$ , is much lower and the hyperfine fields are significantly distributed. As was reported already [5], in the case of Fe/Mg multilayers, an Fe layer with the thickness of 12Å is amorphous but that of 15Å is crystalline. The structural transition occurs rather abruptly in this case and the critical thickness is clearly determined. In the present cases, the Fe layers thinner than 20Å are always entirely amorphous but those between 20 and 30Å are sometimes mixtures of amorphous and crystalline phases, depending on the sample preparation conditions. Since the bonding between Fe and Mg is weak, the transition in an Fe/Mg film occurs at a small thickness value and all Fe atoms turn out to be in the crystalline phase. On the other hand, in the case of Fe and rare-earth, the bonding is stronger and therefore the critical value is thicker.

The situation of rare-earth layers is similar to the Fe layers. X-ray diffraction patterns show that the critical thickness from amorphous to crystalline is about 20Å. However, even when the thickness is more than the critical value, the size of crystallites is fairly small and almost randomly oriented. Although a bulk rare-earth metals are known to have magnetic structures with long range coherence, the magnetic properties of ultrathin layers should be different. Sample preparation was also attempted by using single crystal substrates, sapphire or NaCl, but the degree of orientation in rare-earth layers was not improved because the substrate temperature was too low.

By observing X-ray Bragg peaks in a small angle region, the establishment of artificial periodic structures was confirmed as far as each layer is not too thin. The thinnest examples having periodic structures are; Fe(4Å)/Dy(17Å), Fe(22Å)/Dy(6Å), and Fe(26Å)/Nd(3Å). As the thickness of bilayer, Fe(10Å)/Dy(10Å) and Fe(13Å)/Nd(6Å) are the minimum values in the present work. A periodic structure is not stable if both layers are extremely thin. No X-ray Bragg peak was observed for the samples prepared by alternate deposition of Fe(11Å)/Dy(3Å) or Fe(6Å)/Nd(3Å). The structure of these samples is regarded as almost homogeneously amorphous.

#### Mössbauer spectra as a function of Fe layer thickness

For all multilayer samples,  $^{57}\text{Fe}$  Mössbauer transmission spectroscopy has been applied at 300K and 4.2K. The temperature dependence between 4.2K and 300K was measured for several samples. If the Fe layer thickness is less than the critical value, the structure is amorphous and then the spectrum at 300K is usually a doublet pattern since the Curie temperature is lower than 300K. Examples of the spectra for amorphous Fe layers are shown in Fig. 2. At 4.2K, the spectrum is split by a magnetic hyperfine interaction but the line width is very large, indicating a significantly wide distribution of hyperfine fields. Such a broad spectrum is typical for ferromagnetic amorphous Fe alloys. The spectra for [Fe(15Å)/Dy(30Å)] were measured at several temperatures between 4.2K and 300K, and the average hyperfine field as a function of temperature is obtained as shown in Fig. 3. From this result, the Curie temperature is estimated to be 270K. It is to be noted that this temperature agrees with the  $T_C$  for pure amorphous Fe

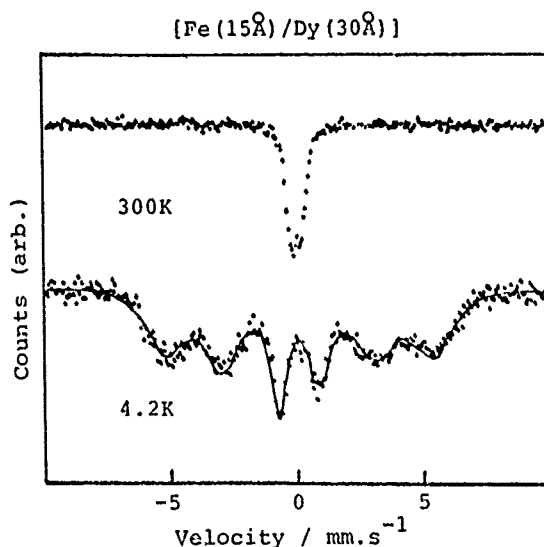


Fig. 2.  $^{57}\text{Fe}$  Mössbauer absorption spectra of  $[\text{Fe}(15\text{\AA})/\text{Dy}(30\text{\AA})]$  at 300K and 4.2K.

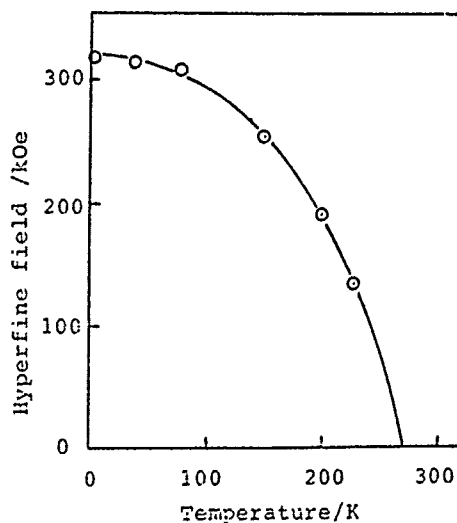


Fig. 3. The average hyperfine field at Fe in  $[\text{Fe}(15\text{\AA})/\text{Dy}(30\text{\AA})]$  as a function of temperature.

estimated by Heiman et al.[6].

If the Fe layer thickness is extremely thin, the Curie temperature becomes lower because of a thickness effect. For instance,  $\text{Fe}(2\text{\AA})/\text{Y}(20\text{\AA})$  does not show any magnetic splitting even at 4.2K. On the other hand, if the rare-earth layer is extremely thin, a small hyperfine field is sometimes observed at 300K. The reason seems to be a magnetic coupling through the rare-earth layers, which may elevate the Curie temperature. A small magnetic splitting is also observed for a sample prepared on a substrate

whose temperature was not low enough at the deposition. The reason for a higher Curie temperature in the latter case should be an intermixing of two elements. Anyway, as far as the structures of Fe layers are amorphous, the Curie temperature cannot be much higher than room temperature.

If the Fe layer thickness is beyond the critical value, the structure becomes crystalline. Then, the Fe layers are strongly ferromagnetic and the Curie temperature is very high. Accordingly, the Mössbauer spectrum is a six-line pattern with a sharp line width, which appears identical to that of standard  $\alpha$ -Fe. In Fig. 4, for example, a result at 300K of [Fe(39Å)/Nd(28Å)] is reproduced. In order to observe any deviation from the bulk magnetic behaviors, measurements at elevated temperatures are necessary. However, because of the stability of the multilayer samples, the available temperature range above 300K seems to be very limited. Measurements at higher than 300K have not yet been carried out.

In Fig. 4, together with the experimental result at 300K, a solid line is drawn, representing the spectrum for bulk  $\alpha$ -Fe. By subtracting the bulk part from the observed absorption, the resultant part with smaller hyperfine fields is estimated. The latter part corresponds to the absorption of the interface. The relative amount is 25% of the total and the average hyperfine field is 325kOe. Then, the relative amount of the bulk part is 75% of the total Fe. The inner part of each Fe layer with the thickness of 29Å (75% of 39Å) is regarded as pure  $\alpha$ -Fe. On the other hand the interface part with reduced hyperfine fields corresponds to the nominal thickness of 10Å. The reason for the reduction of hyperfine fields should be intermixing and/or intrinsic interface effect. An interface effect may exist even if the structure of Fe layer interfaces is chemically and crystallographically perfect. One atom layer at each interface, contacting with Dy atoms, may show a reduced hyperfine field. If an interface has an ideal structure, the thickness of interface Fe layer should be about 2Å. Since actual interfaces are not ideally flat, the effective value of interface thickness can be somewhat bigger. The Mössbauer spectrum indicates that the effective thickness of interface Fe layer having reduced hyperfine fields is 5Å at each interface.

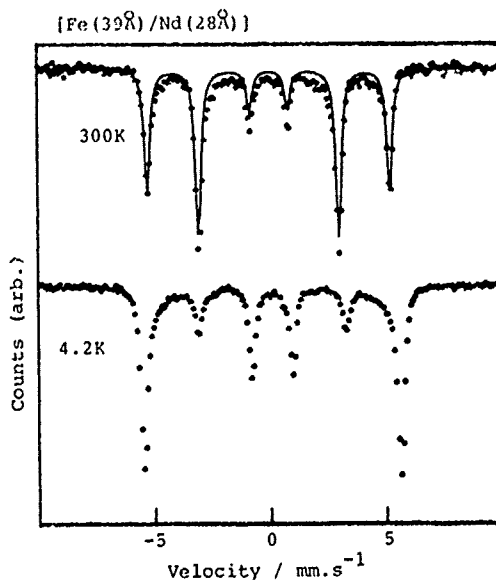


Fig.4. Mössbauer spectra of [Fe(39Å)/Nd(28Å)] at 300K and 4.2K. The solid line represents the bulk  $\alpha$ -Fe's spectrum at 300K.

From the above argument, if we assume  $3\text{\AA}$  is the thickness where an intrinsic interface effect can extend, the reason of reduced hyperfine field at the resultant part with the nominal thickness of  $2\text{\AA}$  must be attributed to an intermixing. It is therefore concluded that at each interface between Fe and rare-earth layers, an intermixing had taken place but the extent does not more than two atom layer thickness.

Regarding to the purity of amorphous Fe layers, Mössbauer patterns as shown in Fig. 2 and also in Fig. 6, do not present any direct information. As a matter of fact, the spectra for homogeneous amorphous alloys also have very similar profiles. However, comparing with the result in Fig. 4, we can claim that the Fe purity of amorphous layers in the multilayer samples is rather high. If the Fe layer thickness increases beyond the critical value, the structure changes to be crystalline. Then, the part of mixture with Fe and rare-earth was estimated to be only a few  $\text{\AA}$  in thickness. This result means that in the very thin amorphous Fe layers, the content of rare-earth is very small. Otherwise, we have to assume a sudden, negative diffusion of rare-earth metal atoms from Fe layers at the structural change, which seems impossible.

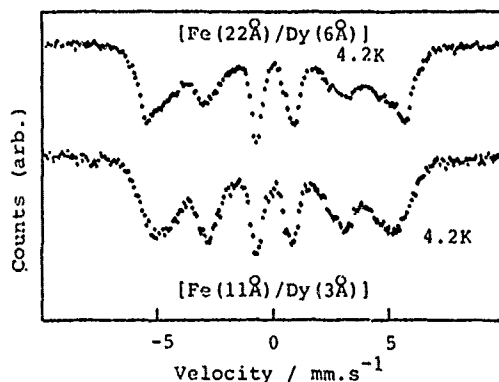


Fig. 5. Mössbauer spectra at  $4.2\text{K}$  of  $[\text{Fe}(22\text{\AA})/\text{Dy}(6\text{\AA})]$  and  $[\text{Fe}(11\text{\AA})/\text{Dy}(3\text{\AA})]$ . The former has a multi-layered structure but the latter is regarded as homogeneous amorphous.

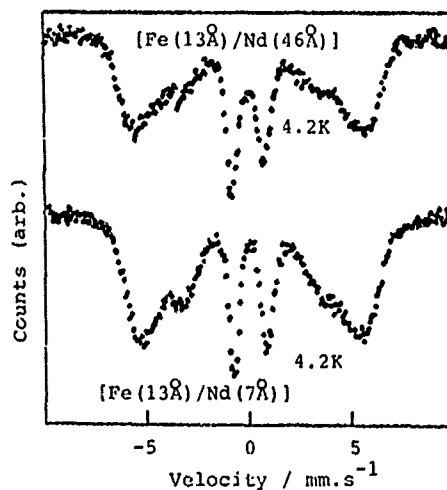


Fig. 6. Mössbauer spectra at  $4.2\text{K}$  of  $[\text{Fe}(13\text{\AA})/\text{Nd}(46\text{\AA})]$  and  $[\text{Fe}(13\text{\AA})/\text{Nd}(7\text{\AA})]$ .

### Perpendicular anisotropy

It is well known that a  $^{57}\text{Fe}$  Mössbauer spectrum of a sample with a magnetic order is a six-line pattern, whose splitting is due to a magnetic hyperfine interaction. Examples are already shown in Fig. 4. If a quadrupole interaction is negligible, the six-line spectrum has a symmetric profile and the intensities of No.1, 2 and 3 lines are respectively equal to those of No.6, 5 and 4. Their relative intensities depend on the angle,  $\theta$ , between the direction of magnetic field and the gamma-ray propagation vector. The relative intensities of No.1 (and 6), No.2 (and 5), No.3 (and 4) lines are expressed as  $3(1+\cos^2\theta) : 4\sin^2\theta : 1+\cos^2\theta$ . In usual Mössbauer measurements, the gamma-ray direction is along the film normal. Therefore  $\theta$  means the angle between the direction of magnetization and the normal axis to the film plane. If the magnetization is oriented in the plane ( $\theta=90^\circ$ ), the expected intensity ratio is 3:4:1:1:4:3. If the direction of magnetization is perpendicular to the film plane ( $\theta=0$ ), the ratio should be 3:0:1:1:0:3. The usual ratio, 3:2:1:1:2:3, observed in powder samples is the average for all  $\theta$ . Thus, by observing the relative intensity ratio of No.2 (and 5) line, we can judge the average direction of magnetization relative to the film normal.

It very often happens that the magnetization directions of thin films are in the planes because of the shape anisotropy. Then, the Mössbauer spectra exhibit nearly the intensity ratio of 3:4:1:1:4:3. In the present cases of Fe/rare-earth multilayers, perpendicular anisotropies play significant roles. It is worthwhile to estimate the magnetic easy directions from the relative intensities of No.2 (and 5) lines. Figure 5 shows the spectrum at 4.2K for  $[\text{Fe}(22\text{\AA})/\text{Dy}(6\text{\AA})]$ . Certainly the relative intensity of No.2 (and 5) line is smaller than that in a powder pattern. Since the distribution of hyperfine field is very wide and the Mössbauer lines are overlapping with each other, the estimation of individual intensity ratio cannot be very accurate. However, in a rough estimation, the intensity ratio is 3:1:1:1:1:3 and it is apparent that the magnetization is preferentially oriented towards the film normal. This tendency becomes weaker in the samples with thicker Dy layers.

Figure 5 also shows a result on a sample with a nominal structure of  $[\text{Fe}(11\text{\AA})/\text{Dy}(3\text{\AA})]$ . The compositional Fe/Dy ratio is the same with the former sample but a periodic structure does not exist in this sample. The structure is regarded as homogeneous amorphous. It has been reported that some 3d/rare-earth amorphous alloy films have perpendicular magnetizations but the origin of the perpendicular anisotropy is not yet well explained[7]. However, in the spectrum for the amorphous sample, the intensity of No.2 (and 5) line has a larger intensity. From these results, it is concluded that the perpendicular anisotropy is related to the multilayered structure and becomes dominant if the Dy layers become thinner. The mechanism of perpendicular anisotropy in amorphous alloy films may be different from that in multilayers.

In Fe/Nd multilayered samples, the perpendicular magnetization is more notable. Figure 6 shows the results at 4.2K for  $[\text{Fe}(13\text{\AA})/\text{Nd}(46\text{\AA})]$  and  $[\text{Fe}(13\text{\AA})/\text{Nd}(7\text{\AA})]$ . The intensity ratio in both cases is approximately 3:0.5:1:1:0.5:3. The degree of preferred orientation to the direction of film normal is more enhanced than the previous Fe/Dy case and the intensity ratio does not depend very much on the Nd layer thickness. This result suggests that the perpendicular anisotropy originates from the Nd atoms in the vicinity of interface.

Effects of perpendicular anisotropy are also observed in the results for the samples with thicker Fe layers with crystalline structures. At higher temperatures, the shape anisotropy is dominant. The perpendicular anisotropy relates to the magnetization of rare-earth layer and becomes significant at lower temperatures. The direction of magnetization is determined by the competition of the two anisotropies and consequently the



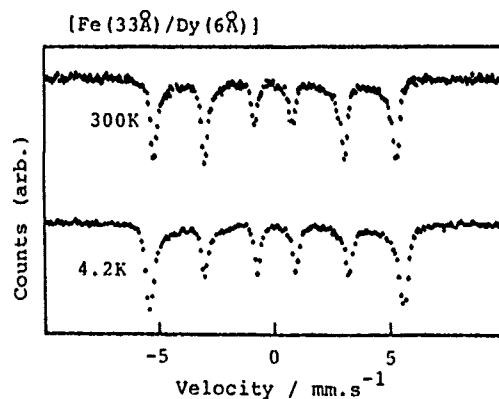


Fig.7. Mössbauer spectra of  $[Fe(33\text{\AA})/Dy(6\text{\AA})]$  at 300K and 4.2K.

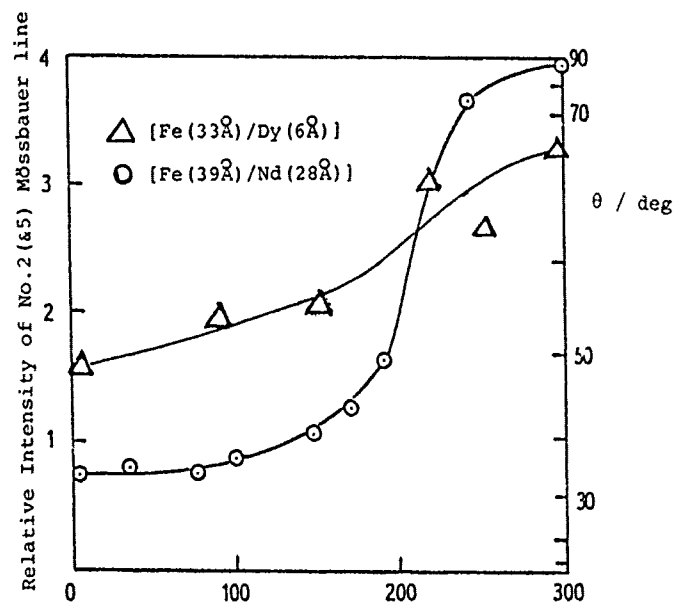


Fig.8. Temperature dependence of the average angle  $\theta$  between the film normal and the direction of magnetization in the Fe layer, estimated from the relative intensity of No.2 (and 5) lines of Mössbauer spectra. The circles correspond to an Fe/Dy sample (see Fig. 7) and the triangles, Fe/Nd (see Fig. 4).

direction may change depending on temperature. Figure 7 shows the spectra of  $[\text{Fe}(33\text{\AA})/\text{Dy}(6\text{\AA})]$  at 300K and 4.2K, which is an example whose magnetization changes the direction gradually. The average angles of magnetization from the normal axis estimated from the Mössbauer spectra are plotted in Fig. 8, as a function of temperature.

The direction of magnetization changes more clearly in Fe/Nd multilayers. Figure 4 showed the spectra of  $[\text{Fe}(39\text{\AA})/\text{Nd}(28\text{\AA})]$ , which indicate that the magnetization lies almost entirely in the plane at 300K and turns up to a direction with an angle of  $30^\circ$  from the normal, at 4.2K. The estimated average angles are also plotted in Fig. 8. A rather sharp change is observed at about 200K. In order to understand the temperature dependence of easy direction, a knowledge of the magnetic properties of rare-earth layers is required. In the next section, comparing with the results of macroscopic magnetic measurements, we will discuss further the perpendicular anisotropy.

Multilayered samples were also synthesized in the combination of Fe and non-magnetic Y layers and the Mössbauer spectroscopic measurements were applied. Examples of the spectra are shown in Fig. 9. In these samples, Fe/Y ratios are similar to Fe/Dy in the samples having perpendicular anisotropy. However, the intensity ratio of the six lines is always nearly 3:4:1:1:4:3 regardless of temperature. This result means that the perpendicular anisotropy correlates with the magnetization in Dy or Nd layers. In Fe/Y multilayers, such a perpendicular anisotropy does not exist and the magnetic easy direction is always in the film plane.

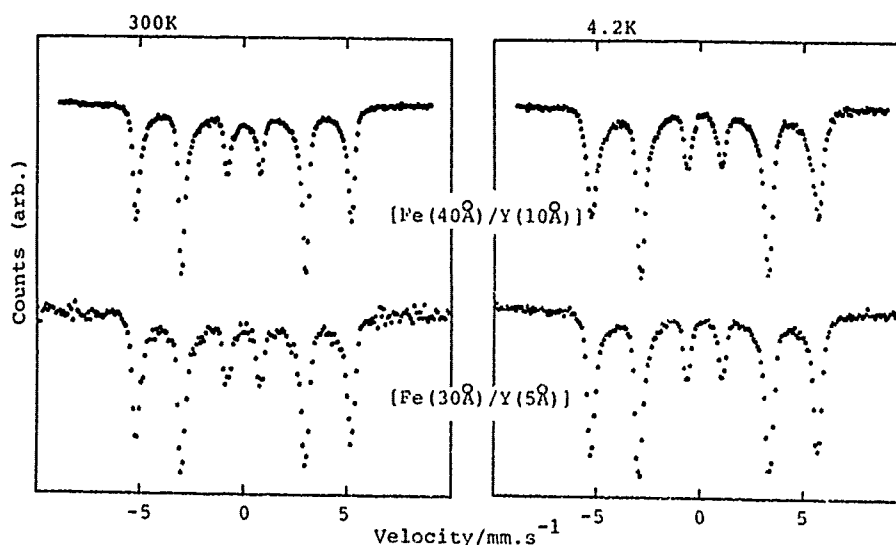


Fig. 9. Mössbauer spectra of  $[\text{Fe}(40\text{\AA})/\text{Y}(10\text{\AA})]$  and  $[\text{Fe}(30\text{\AA})/\text{Y}(5\text{\AA})]$  at 300K and 4.2K.

### Macroscopic magnetization

Magnetization measurements were carried out by using a SQUID magnetometer. From the results, the magnetic behaviors of rare-earth layers are conjectured since those of Fe layers are already known from the Mössbauer spectroscopic studies. In Fig. 10, the magnetization of [Fe(44Å)/Dy(12Å)] is shown as a function of temperature, which was measured by applying 10kOe in parallel to the film plane. Both at 5K and 270K, the magnetization is saturated by the external field, 10kOe. It is obvious that the magnetization decreases with the decrease of temperature. The thickness of Fe layers is enough large and Fe layers can be assumed to have the full magnetization even at 300K. Assuming the contribution of Fe layers is the same as the bulk magnetization, the magnetization of Dy layers is estimated as shown in the same figure. The observed magnetization at 5K is almost the same as the calculated value with the assumption that the magnetizations of both the Fe and Dy layers are saturated but aligned antiparallel. At low temperatures, therefore, the magnetic structure is regarded as a giant ferrimagnet. The magnetization of Dy layers decreases with the increase of temperature but still exist at 270K, which is much higher than the bulk Neel temperature of Dy (179K). This result means that the interface Dy layers have a strong antiferromagnetic coupling with Fe layers and contribute to the bulk magnetization up to higher than the bulk  $T_C$ . If the Dy layers are thicker, a magnetic contribution from the inner part appears at low temperature and it is not saturated even in the external field of 50kOe.

In Fe/Nd multilayers, the situation is similar but the magnetic coupling is parallel in contrast to the case of Fe/Dy. Figure 11 shows the temperature dependence of saturation magnetizations for [Fe(39Å)/Nd(10Å)] and [Fe(39Å)/Nd(46Å)]. The magnetization of the Nd layers is estimated as the difference between the observed value and the Fe layers' contribution, which is assumed to be the same as the bulk. It is thus found that the Nd layers have a magnetization even at 300K, which is considerably higher than the bulk  $T_C$ , 19K and the magnetic contribution of Nd layers becomes larger with the decrease of temperature. In the same figure, the result on a sample with thicker Nd layers, [Fe(39Å)/Nd(46Å)], also is illustrated. It is to be noted that the magnetic contribution down to about 100K of the latter sample is very similar to that of the previous one, although the Nd layers are much thicker. This fact suggests that only the interface part of Nd layer can participate in the magnetic order above 100K. An increase of

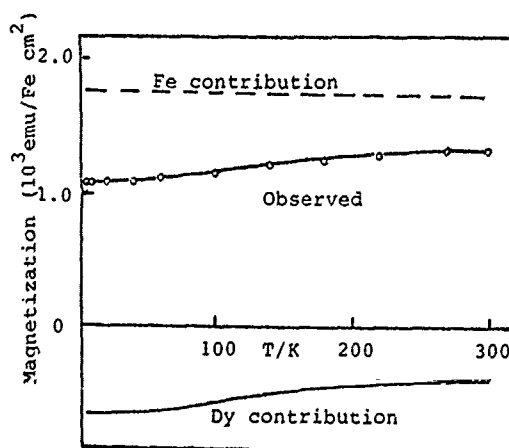


Fig.10. "Observed" means the magnetization of [Fe(44Å)/Dy(12Å)] measured after field cooling with applying 10kOe in parallel to the film plane. The broken line corresponds to bulk  $\alpha$ -Fe. The Dy contribution was obtained by subtracting "Observed" from the theoretical Fe contribution.

magnetization observed below 100K should correspond to the contribution from the inner Nd atoms. Judging from the temperature dependence of the magnetization shown in Fig. 11, the effective  $T_C$  of the interface Nd part is not much higher than 300K and that of the inner Nd part is lower than 100K. Therefore in a crude assumption, the magnetization of the sample, [Fe(39Å)/Nd(46Å)] is divided into three components, Fe layers with very high  $T_C$ , interface Nd parts with an intermediate  $T_C$  and inner parts of Nd with low  $T_C$ .

The magnetization curve obtained for the sample [Fe(39Å)/Nd(28Å)] is also very similar with those in Fig. 11. A remarkable field dependence appeared below 100K, which corresponds to the contribution of inner Nd parts. As already shown in Fig. 8, the magnetization in this sample changes the direction at about 200K. This phenomenon should be explained as the result of the competition between in-plane anisotropy due to the Fe layers and perpendicular anisotropy originated from the interface Nd atoms. At higher temperatures, the former is dominant since the Fe layers'  $T_C$  is very high but at lower temperatures, the latter becomes significant with the increase of interface Nd atoms' magnetization. The temperature where the latter overcomes must be around 200K.

By neutron diffraction technique, Bragg peaks due to the artificial periodic structures are observed and from the analysis of flopping ratio, we obtain an information on the magnetic density distribution in the multilayers. The results are consistent with the above arguments. Comparing with the present results, microscopic magnetic structures will be discussed.[8].

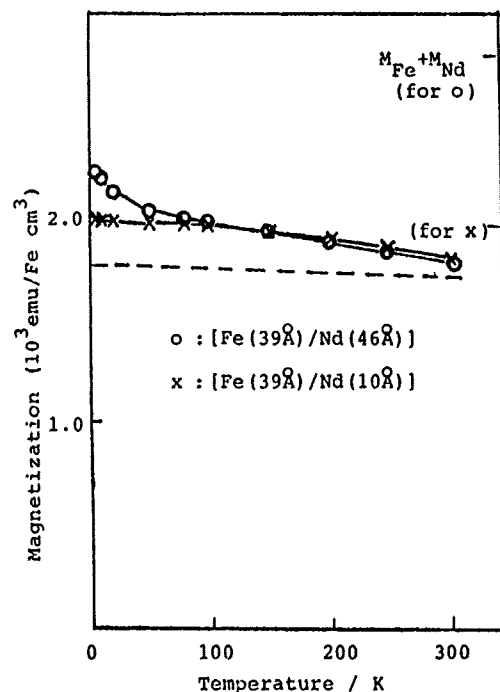


Fig. 11. Magnetization vs. temperature curves of [Fe(39Å)/Nd(46Å)] and [Fe(39Å)/Nd(10Å)]. The broken line means the theoretical Fe contribution.  $M_{Fe} + M_{Nd}$  is the expected full magnetization when Fe and Nd layers are ferromagnetically coupled.

## CONCLUSION

- (1) Multilayered films with artificial superstructures were prepared from Fe and Dy, Nd or Y. Artificial periodicities were established even when each layer is extremely thin. The structure of each layer was amorphous if the thickness is less than a certain value.
- (2) Interface parts of Nd (and Dy) layers have ferromagnetic (and antiferromagnetic) couplings with Fe layers even at higher than their bulk  $T_C$ 's.
- (3) A strong perpendicular anisotropy is originated from the orbital angular momentum of interface Nd atom, whose magnitude depends on the local magnetization at the interface Nd.
- (4) The direction of total magnetization is determined by the competition of in-plane and perpendicular anisotropies. Mössbauer spectra evidenced that in many samples, the easy directions change depending on temperature.

## ACKNOWLEDGEMENTS

The authors would like to thank K. Kawaguchi, K. Yoden and N. Nakayama for their collaborations. This work was supported by the Grant-in-Aid for Scientific Research from the Ministry of Education, Science and Culture of Japan.

References

1. Concerning metallic multilayers, review articles and references up to 1986, are presented in the following book; T. Shinjo and T. Takada eds. "Metallic Superlattices" (Elsevier, Amsterdam, 1987).
2. Ferromagnetic Fe monolayer sandwiched in between Mg layers, whose structure however is regarded as amorphous, was introduced in the following; T. Shinjo, N. Hosoiito, K. Kawaguchi, N. Nakayama, T. Takada and Y. Endoh, J. Magh. & Magh. Mater. 54-57 (1986) 737. Epitaxial ferromagnetic MnSb monolayer in between Sb layers was preliminary reported in the following and a full report is in preparation; T. Shinjo, N. Nakayama, I. Moritani and Y. Endoh, J. Phys. Soc. Jpn. 55 (1986) 2512.
3. The results on Fe/Dy multilayers was already published: K. Yoden, N. Hosoiito, K. Kawaguchi and T. Shinjo, Jpn. J. Appl. Phys. 27 (1988) 1680. A full paper on Fe/Nd system is in preparation: K. Mibu, N. Hosoiito and T. Shinjo, to be submitted to J. Phys. Soc. Jpn. A preliminary result was reported at the ICM'88 in Paris and to be published in the proceedings. Independently of us, Fe/Nd multilayers have been studied by L. T. Baczewski et al. and similar Mössbauer results with ours were presented also at the ICM conference.
4. T. Shinjo, N. Hosoiito, K. Kawaguchi, T. Takada, Y. Endoh, Y. Ajiro and J. M. Friedt, J. Phys. Soc. Jpn. 52 (1983) 3154.
5. K. Kawaguchi, R. Yamamoto, N. Hosoiito, T. Shinjo and T. Takada, J. Phys. Soc. Jpn. 55 (1986) 2375.
6. N. Heiman, K. Lee, R. I. Potter and S. Kirkpatrick, J. Appl. Phys. 47 (1976) 2634.
7. R. C. Taylor, T. R. McGuire, J. M. D. Coey and A. Gangulee, J. Appl. Phys. 49 (1978) 2885. See also, T. Miyazaki et al., J. Mag. Mag. Mater. 75 (1988) 243 and 252.
8. The results of neutron diffraction studies on Fe/Dy films are; N. Hosoiito, K. Yoden, K. Mibu, T. Shinjo and Y. Endoh, J. Phys. Soc. Jpn. in press (1989). A report on Fe/Nd films is in preparation.

# GROWTH, CHARACTERIZATION AND MAGNETIC PROPERTIES OF HCP Fe/Ru SUPERLATTICES SYNTHETIZED BY MBE

M. MAURER\*, J.C. OUSSET\*, M. PIECUCH\*, M.F. RAVET\* AND J.P. SANCHEZ\*\*

\* Laboratoire CNRS SAINT-GOBAIN, Centre de Recherches de Pont à Mousson, BP 109, 54704 Pont à Mousson, France

\*\* IPCM, Centre de Recherches Nucléaires, BP 20, 67037 Strasbourg, France

## ABSTRACT

Hexagonal-close-packed Fe/Ru superlattices with the modulation along the (0001) axis, contain fully hcp Fe layers. The interatomic Fe-Fe distances are enlarged by about 10% as compared to fcc Fe. Ferromagnetic behavior is found when Fe layers are thicker than about 4 monolayers.

## INTRODUCTION

Epitaxy offers the possibility to synthesize transition metal films possessing modified structures as compared to stable phases. Regarding the magnetism of 3d metals, it is interesting to study the effect of a controlled variation of interatomic distances and of the crystal symmetry on the magnetic properties including e.g. the saturation magnetic moment, the magnetic structure and the transition temperature. As a general rule, an increase of the saturation magnetic moment is expected upon enlarging distances, because of the reduction of the bandwidth. Simultaneously, the exchange energy will decrease, thus lowering the ordering temperature. The type of magnetic structure should also strongly depend on the crystal structure, on the thickness of the layers and on their interspacing. Moreover, the fact that 3d atoms are located in crystal sites with non-cubic symmetry, should induce anisotropic properties. In our case, the hexagonal symmetry implies an uniaxial anisotropy along the c axis.

The aim of the present work is to study the magnetism of hcp Fe layers epitaxially grown on hcp Ru. The lattice mismatch is enormous between Ru ( $a=2.706\text{\AA}$ ,  $c=4.28\text{\AA}$ ) and Fe interatomic distances in compact phases including the fcc structure ( $2.53\text{\AA}$ ) or the high-pressure hcp  $\epsilon$ -Fe phase ( $a=2.53\text{\AA}$  and  $c=3.93\text{\AA}$  if extrapolated to ambient pressure). On the other hand, the balance of heats of adsorption of Fe on Ru and of Fe on Fe is largely in favor of a wetting of Ru by Fe, as empirically evaluated by the model of Miedema [1]. Thus these simple arguments are a priori in favor of a Stranski-Krastanov mode of growth.

It is also worth noticing that the hcp Fe/Ru solid solutions are stable over an extended range of concentration:  $0 < x < 76.5$  at% [2]. These solid solutions are surprisingly non-magnetic down to low temperature, like the  $\epsilon$ -Fe phase [3].

In the present report, we describe the growth of the Fe/Ru superlattices with the Fe and Ru thicknesses ( $x$  and  $y$ ) ranging respectively from 4 to  $14\text{\AA}$  and from 4 to  $78\text{\AA}$ . The Fe growth is clearly pseudomorphous with Ru, provided that the Fe thickness  $x$  does not exceed  $14\text{\AA}$  (about 7 monolayers) while Ru layers of only  $4\text{\AA}$  are sufficient to stabilize the hcp structure. By combining

$^{57}\text{Fe}$  Mössbauer spectroscopy and bulk magnetic measurements, ferromagnetic layers are observed, provided that each Fe layer is thicker than 4 monolayers. The ordered Fe sites bear a moment of about  $2\mu_B$  at low temperature.

#### EXPERIMENTAL PROCEDURE

$\text{Fe}/\text{Ru}$  superlattices are grown by MBE (RIBER EVA 32) in residual pressures below  $10^{-10}$  Torr. The (11 $\bar{2}$ 0) sapphire substrate is firstly coated with a 200Å Ru buffer layer, thus ensuring that the surface is single-crystalline and atomically flat, as proved by RHEED streaked patterns [4]. The growth direction is along the (0001) axis of the hcp structure. It is worth underlining that we obtain the same growth when using natural mica as substrates. This is particularly interesting because these superlattices can be easily lifted-off from mica. Auger electron spectroscopy (AES) ascertains that the samples are free from contamination like e.g. oxygen. The sequential growth is achieved at 100°C in order to prevent from interdiffusion. The vapor sources are e<sup>-</sup> guns and the deposition is monitored by quartz balances, at typical rates of 0.5Å/s. The bulk magnetic properties are measured with a SQUID magnetometer with a sensitivity of  $10^{-6}$  emu [5]. We use a disc of 15 mm in diameter which is lifted-off from the mica substrate. The Mössbauer spectra are recorded conventionally in transmission geometry using a  $^{57}\text{Co}/\text{Rh}$  source. The instrumental line width amounts to 0.23 mm/s. Typically 6 discs are used, originating from the same sample as for the SQUID measurements.

#### GROWTH AND STRUCTURE OF THE SUPERLATTICES

The growth of the superlattices is investigated by RHEED and AES (in-situ) and by high resolution X-ray diffraction [4]. Starting from a flat and single-crystalline Ru (0001) surface, the RHEED patterns remain basically unaltered when growing Fe layers up to about 14Å. Indeed, no departure from a 6-fold symmetry is ever detected, but the streaks slightly broaden above about 2 Fe monolayers. This is likely due to defects introduced by strains in the Fe layer, that could give rise to dislocations. Nevertheless, it is remarkable that in all cases, Ru layers as thin as 2 monolayers are sufficient to recover the original RHEED pattern, i.e. to erase all the defects of the Fe layer. Another surprising result is that Ru layers of only 4Å i.e. the length of one unit cell along (0001), stabilize the hcp Fe structure up to at least 12Å (Fig. 1). This point is also unambiguously established by X-ray diffraction. As a general rule, all the superlattices with  $4 < x < 12\text{Å}$  and with  $4\text{Å} < y$  exhibit

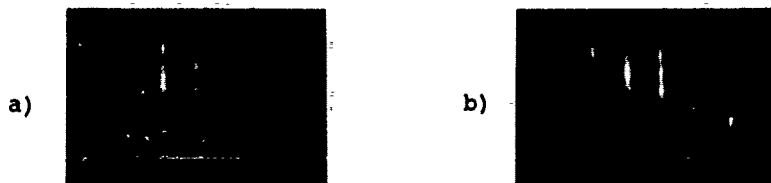


Fig. 1: RHEED pattern (30 kV) of a  $\text{Fe}_{12}\text{Ru}_4$  superlattice under the  $\langle 11\bar{2}0 \rangle$  azimuth. a) 61<sup>th</sup> Fe layer; b) 62<sup>th</sup> Ru last layer.

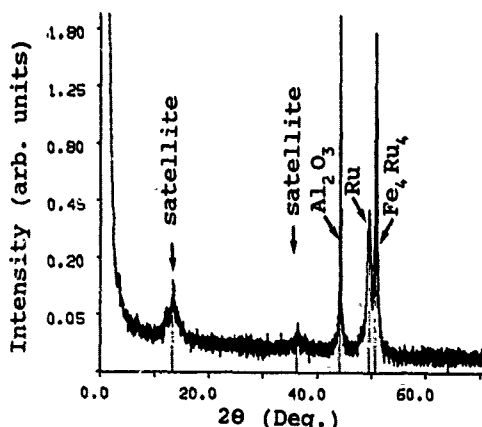


Fig. 2: High resolution X-ray diffraction of a  $\text{Fe}_x\text{Ru}_{1-x}$  superlattice ( $\text{Co } K\alpha_1$ ) in  $\theta$ - $2\theta$  geometry. Notice the low and high angle satellites peaks and pure Ru peaks (buffer).

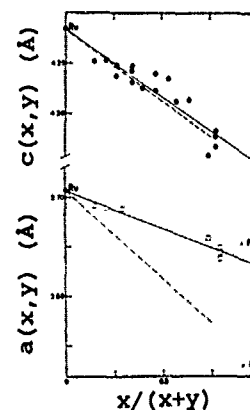


Fig. 3: Variation of the hcp unit cell parameters  $a(x,y)$  and  $c(x,y)$  vs Fe content  $x/(x+y)$ . The dashed line represents the hcp  $\text{Fe}_x\text{Ru}_{1-x}$  solid solutions.

the hcp structure. An information on the structure along the growth axis  $c^*$  is gained by  $\theta$ - $2\theta$  scans. Firstly, the magnitude of the  $c(x,y)$  parameter of the superlattice is obtained for various values of  $x$  and  $y$ . Secondly, the width of the rocking curve (less than  $1^\circ$ ) at the (0002) Bragg peaks proves the good quality of the epitaxy, practically independent of  $x$  and  $y$ . Thirdly, the occurrence of several satellite peaks, both at small angles and around the (000 2\*1) Bragg peaks, is a good test of the stacking periodicity and of the interface sharpness.

Simulations of the diffracted intensity show that the rms dispersion in the bilayer thickness is of the order of 3%, whereas the interface width is typically of 1 monolayer [4]. These points are directly illustrated by the existence of several satellites in an ultra-short period superlattice with  $x=4\text{\AA}$  and  $y=4\text{\AA}$  [Fig 2]. Since the fcc Fe structure is more stable than the hcp one, it is important to check that the superlattices follows an hcp stacking sequence (ABAB..) and that fcc stackings (ABCABC..) are ruled out. This is firstly demonstrated by diffraction on some superlattices reduced into powder, after lifting them off from mica. All the observed lines are indexed in the  $P6_3/mmc$  space group, with the modulation along  $c^*$  [4]. The other information from diffraction on powders is a rough estimate of the basal plane parameter  $a(x,y)$ . However, in order to improve the accuracy on the value of  $a(x,y)$  and to eliminate any spurious effects, it is possible to search for oblique Bragg peaks from an epitaxial superlattice on sapphire, in reflexion geometry. Knowing approximately  $a(x,y)$ , it is easy to find the diffraction condition for e.g. the (11 $\bar{2}$ 3) Bragg peak. Notice that the rocking curve of this peak, which results from both the disorientation of the  $a$  and  $c$  axes, is about  $1.5^\circ$ . Thus, we deduce that the in-plane disorientation of the crystal axes is typically  $1^\circ$ . The magnitude of  $a(x,y)$  is deduced from the (11 $\bar{2}$ 3) Bragg peaks (Fig. 3).  $a(x,y)$  and  $c(x,y)$  follow a linear behavior versus the concentration of Fe:  $x/(x+y)$ . This "Vegard law" permits us to evaluate the intrinsic parameters corresponding to an hypothetically pure Fe layer by a



simple extrapolation to  $x/(x+y)=1$ . Thus we find that  $a(\text{Fe})=2.63\text{\AA}$  and  $c(\text{Fe})=4.06\text{\AA}$ . The basal plane parameter is smaller by about  $0.07\text{\AA}$  than in pure Ru. This is an indication that there is some in-plane relaxation. However,  $a(x,y)$  remains always significantly larger than in solid solutions (Fig. 3). The value of  $c(\text{Fe})$  compares with the same parameter of hcp Cobalt ( $4.07\text{\AA}$ ) or with the value in solid solutions. Then, rather surprisingly no relaxation is observed along the  $c$  axis in spite of the basal plane expansion. This implies that the specific volume is about  $12.5\text{\AA}^3$  per Fe atom, i.e. largely expanded as compared to compact Fe phases ( $11.4\text{\AA}^3$ ).

#### MAGNETIC PROPERTIES OF THE SUPERLATTICES

Our first results concern the magnetic properties of two series of superlattices: in one series, the aim is to investigate the onset of the magnetic moment at Fe sites. The samples have a constant thickness of Ru ( $y=26\text{\AA}$ ), with the Fe thickness varying from 4 to  $14\text{\AA}$ . The other results focus on variation of magnetic properties for a constant Fe thickness of  $12\text{\AA}$  and for different Ru thicknesses, with the aim to study the magnetic coupling between the Fe layers thru Ru layers.

$\text{Fe}_x\text{Ru}_{26}$  superlattices show no sign of localized magnetism for  $x=4$  and  $6\text{\AA}$ . The onset of a stable magnetic moment is around  $8\text{\AA}$  of Fe. Above this threshold, the moment is increasing approximately linearly, with about  $2\mu_B$  per Fe layer beyond 4 layers. These results contradict the simple picture that an enhancement of Fe-Fe interatomic distances should correspond to an increase of the 3d moment. The existence of about two non-magnetic monolayers at either sides of the Fe layers, can be understood in two ways: firstly, one interface layer contains a large substitution of Fe by Ru, thus resulting in a weakening of the exchange in this plane. The second strong argument relies on a comparison with the hcp  $\text{Fe}_{1-x}\text{Ru}_x$  solid solutions. Indeed, up to Fe concentration as high as  $x=75$  at.%, no stable ferromagnetism is found. This implies that e.g. a central Fe atom remains non-magnetic with as many as 8 Fe nearest neighbors on average.  $\epsilon\text{-Fe}$ , with 12-coordinated Fe, is also non-magnetic. When they carry a magnetic moment ( $x>8\text{\AA}$ ), the  $\text{Fe}_x\text{Ru}_{26}$  superlattices behave as soft ferromagnets, with an in-plane anisotropy originating from the thin film geometry. However, the temperature dependence of the magnetization curves would rather suggest that the intrinsic magnetocrystalline anisotropy will weakly align the moments along the  $c$  axis.

The magnetization curves have also been investigated for  $\text{Fe}_{12}\text{Ru}_y$  superlattices with Ru thicknesses of  $y=6, 13, 17$  and  $26\text{\AA}$ . The most striking result is that when reducing  $y$  below  $26\text{\AA}$ , a coupling of the Fe layers induces a dramatic change in the low field magnetization behavior whereas the saturation magnetic moment does slightly change. Indeed,  $\text{Fe}_{12}\text{Ru}_y$  samples behave like hard ferromagnetic materials, with a coercive field of about 1 kOe and a large spontaneous magnetization (Fig. 4). Preliminary results on intermediate Ru thicknesses show that this effect does not change monotonously with  $y$ . More systematic investigations are now in progress [6].

<sup>57</sup>Fe Mössbauer spectroscopy brings an helpful complement to the bulk magnetic measurements. At room temperature, the spectra mainly consist in a quadrupole split doublet, with  $QS=0.28\text{mm/s}$ , whatever  $x$  and  $y$  are. Within errors, the

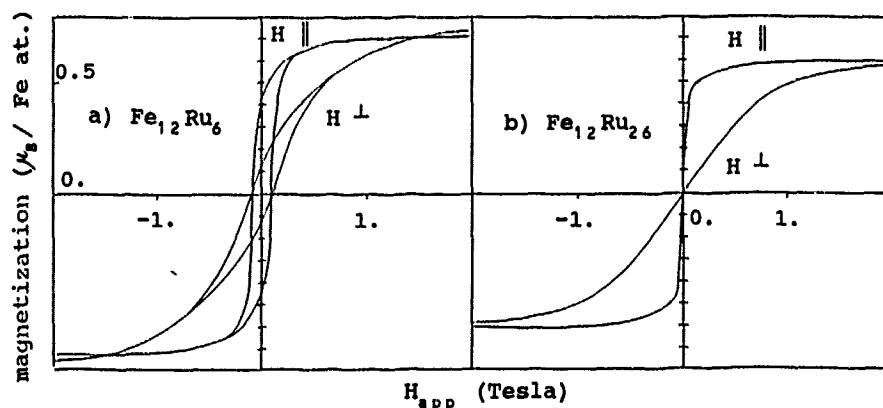


Fig. 4: Hysteresis cycles at 1.5 K for: a)  $\text{Fe}_{12}\text{Ru}_6$  and b)  $\text{Fe}_{12}\text{Ru}_{26}$  superlattices with the external applied field parallel ( $H \parallel$ ) or perpendicular ( $H \perp$ ) to the surface of the films.

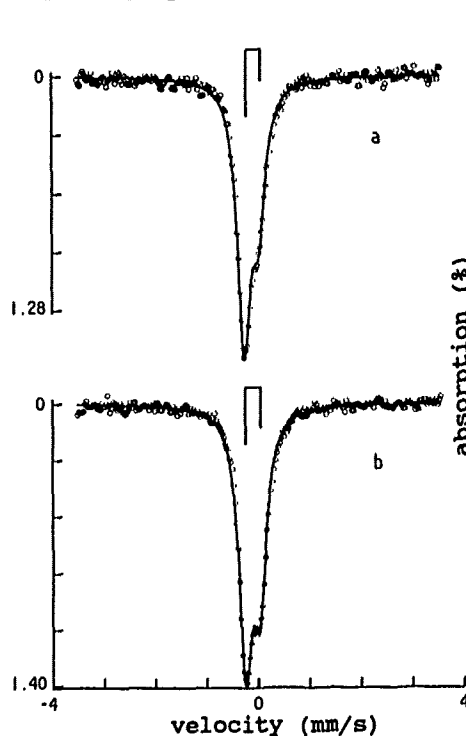


Fig. 5: Mössbauer spectra at 300 K for a  $\text{FeRu}$  superlattice ( $x=10\text{\AA}$ ,  $y=26\text{\AA}$ ) a)  $\gamma$ -ray parallel to the  $c$  axis, b) tilted by  $36^\circ$ . The bar diagram shows the positions and the relative intensities of the transitions.

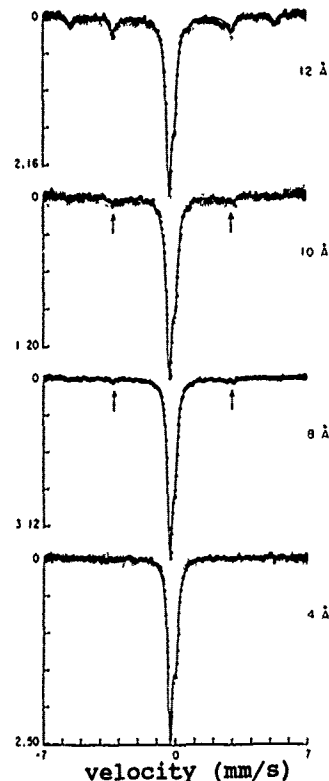


Fig. 6:  $^{57}\text{Fe}$  Mössbauer spectra at 4.2 K for different  $\text{Fe}_{12}\text{Ru}_{26}$  superlattices. The arrows indicate the most intense transitions (2 and 5) of the magnetic subspectrum. The moments are in the film plane.

isomershift is the same as in  $\alpha$ -Fe and the linewidth is about 0.30mm/s. The doublet is asymmetric because the symmetry axis i.e. the c axis, is normal to the surface of the sample (Fig.5). This explanation is definitely proved by tilting the sample with respect to the axis of propagation of the gamma-rays. This is a microscopic proof that Fe atoms are lying in an uniaxial (6-fold) symmetry. One should however mention that the theoretical ratio corresponding to a perfect texture and to an axial symmetry (1:3) is not found (0.48). This can be easily explained by the fact that the symmetry is not perfectly axial in the interface layer, due to the substitution of Fe by Ru. An average disorientation of about  $20^\circ$  with respect to the c axis is consistent with the experimental transition intensities. Notice that the principal component of the electric field gradient  $V_{zz}$  is negative, like for FeRu alloys [3] but that its magnitude is 75% larger in the superlattices. This can be explained by the fact that  $V_{zz}$  scales with the deviation of c/a from the ideal value (1.56 instead of 1.63).

The measurements at 4.2K reveal the coexistence of two well defined Fe sites (Fig.6): the first ones bears only a quadrupole interaction and the second ones carry an hyperfine field of about 336 kOe. The field distribution remains narrow. The area under the magnetic subspectrum confirms that a magnetic moment occurs only above 4 monolayers: beyond this value, the fraction of magnetic sites can be explained as if all the additional layers were fully magnetic. The ratio of the 6 spectral transitions (3:4:1:1:4:3) confirm that the moments are oriented in the plane. The hyperfine field magnitude, which is hardly smaller than in  $\alpha$ -Fe (336 versus 340 in bulk or 343 kOe in thin films), indicates that the local Fe moment is slightly reduced in the hcp superlattices, in spite of the distance enhancement.

### CONCLUSION

Hcp Fe<sub>x</sub>Ru<sub>1-x</sub> superlattices are synthesized by MBE with sharp interfaces (1 monolayer). Their hcp structure is proved by RHEED and X-ray diffraction and the hexagonal local symmetry is supported by Mössbauer spectroscopy. The lattice parameters are dramatically expanded in the hcp Fe layers. The Fe/Ru interfaces are non-magnetic over about 2 Fe monolayers. By contrast with  $\epsilon$ -Fe, a stable moment exists at the inner sites and it compares surprisingly with bcc Fe. The interlayer magnetic coupling changes with Ru thickness, inducing a hard magnetic behavior.

### REFERENCES

- [1] A.R. Miedema and J.W.F. Dorleijn, Surf. Sci. 95 447 (1979)
- [2] W.G. Moffatt, Handbook of binary phase diagrams, edited by Genium Publishing Comp., Schenectady (1988)
- [3] D.I.C. Pearson and J.M. Williams, J. Phys. F 9 1797 (1979)
- [4] M. Maurer, J.C. Ousset, M.F. Ravet and M. Piecuch, submitted
- [5] We thank R. Lemaire, D. Givord and B. Dieny for their collaboration in SQUID measurements.
- [6] J.C. Ousset et al, to appear

# EFFECT OF ORIENTATION AND MICROSTRUCTURE ON THE MAGNETIC ANISOTROPY OF Co/Pd MULTILAYERS.

Frits J.A. den Broeder, Dick Kuiper and Willem Hoving.  
Philips Research Laboratories, 5600 JA Eindhoven, The Netherlands.

## ABSTRACT

Co/Pd multilayers containing one to eight atomic layers of cobalt and ten atomic layers of palladium per modulation period were prepared in two orientations,  $[111]_{fcc}$  and  $[001]_{fcc}$ . The  $[111]$  films were polycrystalline, the  $[001]$  films were epitaxial.

In this paper we compare the magnetic anisotropy of both types of films, which can be described by an interface anisotropy contribution favouring perpendicular magnetization and a volume contribution favouring in-plane magnetization. Depending on the deposition temperature, a perpendicular anisotropy for  $[111]$  films is found for up to about six atomic layers of Co. The  $[001]$  films however, show perpendicular anisotropy only for Co monolayers or Co bilayers. The large difference between the anisotropies in the two orientations is mainly caused by a strong in-plane anisotropy volume term which exists for  $[001]$  films, and which is attributed to the structural deformation of the Co layers from cubic to tetragonal. For both orientations a higher deposition temperature is found to lead to an increase of the interface anisotropy due to smoothing of the layers.

## EXPERIMENTAL PROCEDURES.

By vapour deposition in UHV two series of Co/Pd multilayers with varying Co content from one up to eight atomic layers per modulation period have been prepared exhibiting a  $[001]_{fcc}$  and a  $[111]_{fcc}$  orientation. In both series the Co layers were separated by ten atomic layers of Pd. The total numbers of bilayers were chosen to be equivalent to a total Co thickness of about 700 Å.

Epitaxial  $[001]_{fcc}$  Co/Pd superlattices were obtained by first depositing a 1000 Å Pd base layer onto cleaved  $[001]$  NaCl at a substrate temperature  $T_s$  of 300°C, and then lowering  $T_s$  in order to reduce interdiffusion during multilayer deposition. The growth temperature of the multilayers was either 50°C or 200°C, in order to study the effect of layer smoothness on the magnetic properties [1,2].

Polycrystalline  $[111]_{fcc}$  Co/Pd multilayers with a 1000 Å Pd base layer were deposited onto glass substrates both at  $T_s = 50^\circ\text{C}$  and  $T_s = 200^\circ\text{C}$ .

X-ray diffraction (XRD) in reflection geometry was used to verify the crystalline orientation of both series. The periodic structure and the modulation period were deduced from the superlattice reflections in the X-ray diffractograms.

## RESULTS AND DISCUSSION

For all [001] oriented films with less than seven atomic layers of Co plan-view transmission electron diffraction (TED) showed a single crystalline fcc structure with fourfold symmetry. From the fact that the diffraction spots are single and without any radial asymmetry, we conclude that the Co and Pd layers are structurally coherent and consequently tetragonally deformed [1]. The TED pattern of 7Co/10Pd showed a twelve-fold symmetry, originating from a mixture of two structural variants which are oriented orthogonal to each other in the (001) plane of the Pd base layer, each having a 6-fold symmetry. In this film the Co layers are hcp with a [0001] orientation and the Pd layers are fcc with a [111] orientation. They are no longer pseudomorphic, probably because the Co is too thick to sustain the coherency stress. All [111]-oriented multilayers showed clear XRD multilayer reflections, which were appreciably more intense for the films deposited at  $T_s = 200^\circ\text{C}$  than those deposited at  $T_s = 50^\circ\text{C}$  [3,4]. This indicates that a more perfect periodic structure is obtained at higher  $T_s$ . It should be noted that magnetic measurements after several annealing treatments indicate that no interdiffusion occurs below  $300^\circ\text{C}$  [5].

The magnetic moment of the multilayers was measured at room temperature with a vibrating sample magnetometer applying magnetic fields up to 1300 kA/m both parallel and perpendicular to the film plane. From the area between the magnetization curves the anisotropy energy per unit Co volume,  $K_u$ , was determined, which is taken positive when the direction of the preferred magnetization is directed perpendicular to the film. The dependence of the product  $K_u \cdot t$  as a function of Co layer thickness  $t$  is shown in figure 1.

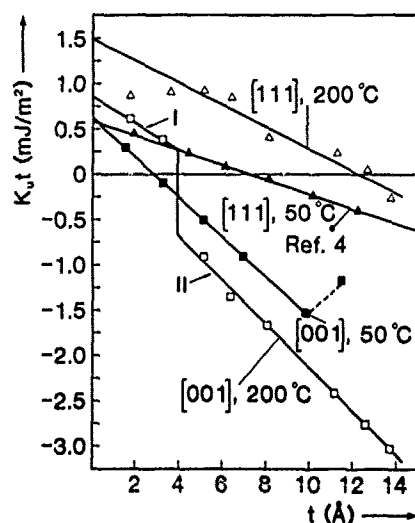


Fig.1. Plots of anisotropy energy  $K_u$  times cobalt thickness  $t$ , versus  $t$  for polycrystalline [111] and epitaxial [001] multilayers, both deposited at  $T_s = 50^\circ\text{C}$  and  $T_s = 200^\circ\text{C}$ . The data for the [001] orientation are the mean values of 3 independent measurements. The estimated error in these data is  $\pm 0.2 \text{ mJ/m}^2$ .

The anisotropy behaviour of both series of multilayers is seen to be quite different. For [111] films the crossover from in-plane towards perpendicular anisotropy occurs at  $t \approx 8 \text{ \AA}$  for  $T_s = 50^\circ\text{C}$ , and at  $t \approx 12 \text{ \AA}$  for  $T_s = 200^\circ\text{C}$ . The [001] films however, have a perpendicular anisotropy only for monolayers of Co when  $T_s = 50^\circ\text{C}$ , and also for bilayers at  $T_s = 200^\circ\text{C}$ . For the samples prepared at  $T_s = 200^\circ\text{C}$  there is an abrupt transition in the anisotropy between two and three monolayers of Co. The origin of this transition is not yet clear.

The behaviour of  $K_u \cdot t$  vs.  $t$  can phenomenologically be described as:

$$K_u \cdot t = K_v \cdot t + 2K_s \quad (1)$$

in which the *surface term*  $K_s$  is a contribution to the anisotropy originating from the interface per unit area, and the *volume term*  $K_v$  is the contribution per volume unit cobalt. The factor of 2 for the surface term refers to the two interfaces of each Co layer. In table I we list values for  $K_s$  and  $K_v$  obtained by fitting the data points of figure 1 to equation (1). For the [001] films prepared at  $T_s = 200^\circ\text{C}$ , we give two sets of coefficients corresponding to the branches I and II on either side of the abrupt transition near  $t \approx 4 \text{ \AA}$  (see above).

**Table I.** Values for the surface anisotropy term  $K_s$  and volume anisotropy term  $K_v$  of equation (1) obtained by fitting the data points of figure 1 (see text).

orientation	$T_s$ ( $^\circ\text{C}$ )	$K_s$ ( $\text{mJ}/\text{m}^2$ )	$K_v$ ( $\text{MJ}/\text{m}^3$ )
[111] (on glass)	50	+0.26	-0.72
	200	+0.75	-1.3
[001] (on NaCl)	50	+0.32	-2.19
	200 (I)	+0.45	-2.45
	(II)	+0.15	-1.5

### Interpretation

In table I we see a systematic increase of  $K_s$  with higher substrate temperature, which we attribute to increased surface diffusion during deposition, leading to smoothing of the layers [2].

The volume terms  $K_v$  for the [001] oriented films are much more negative than those for the [111] oriented films. In principle this contribution is made up of three terms:

$$K_v = -\frac{1}{2} \mu_0 M_s^2 + K - \frac{3}{2} \lambda \sigma \quad (2)$$

where the first term is the demagnetization energy,  $K$  is the magneto-crystalline anisotropy energy and the last term is the anisotropy due to stress ( $\sigma$ ) via magnetostriction ( $\lambda$ ).

Decreasing the Co thickness the saturation magnetizations of the [001] films per unit volume Co were found to be progressively larger compared to the value for bulk Co,  $\mu_0 M_s = 1.76$  T. As before [3], this is attributed to a polarization of Pd interfacial atoms. Assuming that the demagnetization energy is equal to that of an hcp Co film ( $-1.23$  MJ/m<sup>3</sup>), the larger negative  $K_v$  value for the [001] oriented films implies the presence of an additional *easy-plane* anisotropy  $\Delta K = -0.96$  MJ/m<sup>3</sup>. The origin of this in-plane anisotropy term may be magneto-crystalline anisotropy connected with the tetragonal Co structure, caused by the stretching of the (001) Co layers by the larger Pd atoms. On the other hand this anisotropy may also be described by  $\frac{3}{2} \lambda \sigma$ , in which  $\sigma$  is the coherency strain. This then corresponds to a positive magnetostriction constant  $\lambda_{100} \approx +45 \cdot 10^{-6}$ , which is in contrast to the negative  $\lambda$  of hcp Co [6]. In order to know the exact origin, independent measurements of magnetostriction are necessary. It is to be noted that  $K_u \cdot t$  for  $\gamma\text{Co}/10\text{Pd}$  ( $t \approx 12$  Å) of the [001] oriented film prepared at  $T_s = 50$  °C is significantly larger than corresponding to the linear dependence of formula (1). This could be explained by the structural transformation observed by TED (see above), which might relieve some coherency stress.

For the [111] films deposited at  $T_s = 200$  °C the magnitude of  $K_v$  is roughly equal to the demagnetization energy, which is expected for a  $[111]_{\text{fcc}}$  Co film with no substantial strain anisotropy. This may either indicate that the Co layers are not very much stretched by lattice coherence with Pd, or that the magnetostriction constant,  $\lambda_{111}$ , is small. The smaller negative  $K_v$  for the films deposited at  $T_s = 50$  °C points to an additional *perpendicular* anisotropy [4]. Since these films also differ from the [001] oriented films in microstructure (crystallinity), the effects of orientation are not completely clear. For this we also need a study of epitaxially grown [111] superlattices. This investigation is still in progress.

#### ACKNOWLEDGEMENT

The authors are indebted to A.Fonken and H.C.Donkersloot for preparing the samples.

## REFERENCES.

- [1] F.J.A. Den Broeder, D.Kuiper, H.C.Donkersloot and W.Hoving, submitted to Appl.Phys.A.
- [2] F.J.A. Den Broeder, D.Kuiper and H.C.Donkersloot, to be published in J.de Physique (1989).
- [3] F.J.A. Den Broeder, H.C.Donkersloot, H.J.G.Draaisma, W.J.M. De Jonge, J.Appl. Phys. 61 4317 (1987).
- [4] H.J.G.Draaisma, F.J.A. Den Broeder, and W.J.M. De Jonge, J.Magn. Magn. Mater. 66, 351 (1987).
- [5] F.J.A. Den Broeder, D.Kuiper, and H.J.G.Draaisma, IEEE Trans. on Magn., Vol.MAG-23 5, 3696 (1987).
- [6] R.M.Bozorth, Ferromagnetism (Van Nostrand, London, 1951), p.663.



## STRUCTURAL AND MAGNETIC PROPERTIES OF EPITAXIAL Co-Au SUPERLATTICES

C.H. LEE, HUI HE, F. LAMELAS, W. VAVRA, C. UHER and ROY CLARKE  
Department of Physics, The University of Michigan, Ann Arbor,  
MI 48109

### ABSTRACT

We describe measurements on the structural and magnetic properties of Co-Au superlattices grown on Ge-buffered (110) GaAs by molecular beam epitaxy. Samples have been prepared with Co layer thicknesses ranging from 5-40Å and Au spacer layers of constant thickness, ~16Å. X-ray scattering and high-resolution transmission electron microscopy show that the hcp Co layers grow epitaxially with the (0001) axis parallel to (111)Au and with the in-plane Co[11 $\bar{2}$ 0] axis parallel to GaAs[001]. SQUID magnetometer measurements reveal a crossover in the magnetic anisotropy of the as-grown samples such that the easy axis is perpendicular to the substrate plane when the Co layer thickness is less than ~19Å.

### INTRODUCTION

There is much current interest in thin film magnetic structures<sup>1</sup> having perpendicular anisotropy, not only for fundamental studies of magnetic interactions but also for their importance in high-density recording applications. The anisotropy can arise by several distinct mechanisms, including magnetostriiction, shape anisotropy, or from the reduced dimensionality of the structure at a surface or interface.<sup>2</sup> Shape anisotropy commonly leads to an in-plane alignment of the magnetic easy axis whereas magnetocrystalline anisotropy may favor an easy axis perpendicular to the film plane, as in the case of Co(80)-Cr(20) alloy films grown in the c-axis orientation.<sup>3</sup> Surface or interface anisotropy has been observed in ultrathin films and this type of anisotropy is thought to be responsible for the perpendicular spin alignment in single-layer films<sup>4,5</sup> and in superlattices.<sup>6-8</sup>

In this paper we report on measurements of the magnetic anisotropy of Co-Au superlattices which we have grown by molecular beam epitaxy (MBE), techniques. Clearly, the structural quality of the samples will have a strong influence on the magnetic properties, particularly at the heterostructure interfaces. Thus, we will also emphasize the results of some detailed structural characterization studies which have a direct bearing on the nature of the interface structure.

### EXPERIMENTAL DETAILS

The superlattices were grown<sup>9</sup> on (110) GaAs substrates held at 50°C in a Vacuum Generators V80 MBE system. The substrates were annealed at 600°C for 15 minutes before a 500Å buffer layer of epitaxial Ge(110) was grown on the substrates. Au layers were grown at a rate of 0.08Å/sec using a standard Knudsen cell operating at 1300°C. Co layers were deposited from an electron-beam-heated source at 0.3Å/sec. Background pressures prior to grow were ~10<sup>-10</sup> mbar, rising to ~10<sup>-9</sup> mbar during growth.

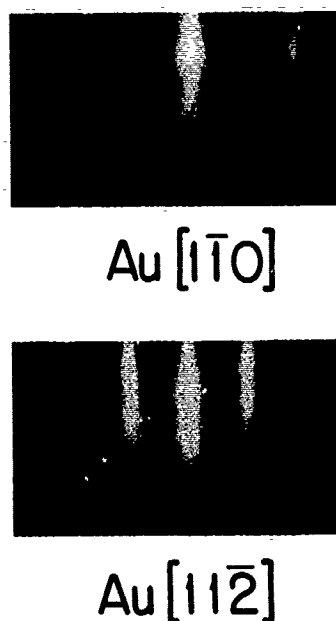
Magnetization measurements were performed using a Quantum Design MPMS SQUID magnetometer and x-ray scattering studies were made using a Rigaku 12kW generator

producing  $\text{MoK}\alpha$  ( $\lambda \approx 0.71 \text{ \AA}$ ) x-rays monochromatized by pyrolytic graphite. A four-circle computer controlled Huber goniometer was used to perform various x-ray scans in order to characterize the structural quality of the superlattices. Direct images of transverse sections through the structures were obtained on a JEOL 4000 EX transmission electron microscope (TEM), operating at 400kV. The structure was viewed along GaAs  $[1\bar{1}0]$  with the GaAs(110) surface parallel to the beam direction.

#### RESULTS AND DISCUSSION: STRUCTURE

Reflection high energy electron diffraction (RHEED) patterns recorded immediately after superlattice growth (Fig. 1) indicate that the films are highly oriented within the growth plane. Cross-sectional TEM images (Fig. 2) show that the Co and Au layer thicknesses are uniform and continuous across the entire film and that there is no evidence of interlayer mixing. A selected area electron diffraction pattern [Fig 2 inset (b)] shows that the Au layers grow in the (111) orientation with  $\text{Au}[1\bar{1}0]$  parallel to  $\text{GaAs}[001]$ . Similarly,  $\text{Co}[11\bar{2}0]$  is parallel to  $\text{Au}[1\bar{1}0]$  in the plane of the substrate.

Fig. 1 RHEED patterns on Au top layer of  $\text{Co}(20\text{\AA})\text{-Au}(16\text{\AA})$  superlattice with the electron beam along the indicated azimuthal Au crystal axes.



Our x-ray scattering measurements confirm these epitaxial relationships and can also provide additional information on the interfacial quality. For example, Fig. 3 shows a  $00\ell$  x-ray scan fit with a model having nominally 6 monolayers (ML) of Au and 11 of Co, repeated 20 times. The model includes interfacial penetration and random layer thickness fluctuations ( $\pm 1.5 \text{ ML}$ ). We deduce an interface width of 2 ML from these measurements. Given the immiscibility of Au and Co in the bulk we believe that the interface interpenetration is step-like (see Fig. 3) rather than due to uniform diffusion. A number of other x-ray scans have been performed on the samples, probing the in-plane structure, the effects of misfit (about 14% in this case) and the stacking coherence of the layers. More details can be found in Ref 9.

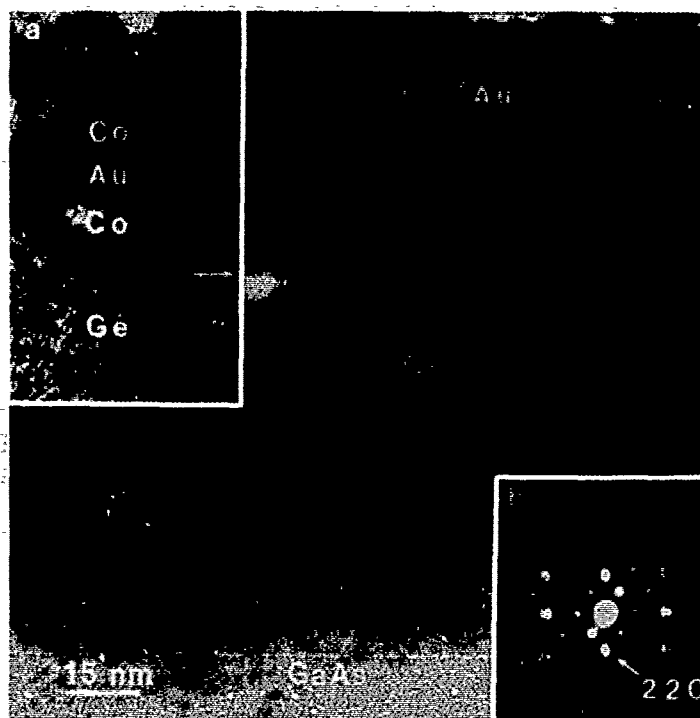


Fig. 2 CTEM image of Co(20Å)-Au(16Å) superlattice on GaAs(110) with a 500Å Ge buffer layer; electron beam along GaAs[1 $\bar{1}$ 0]. Inset (a): High resolution TEM image. Inset (b): Electron diffraction pattern.

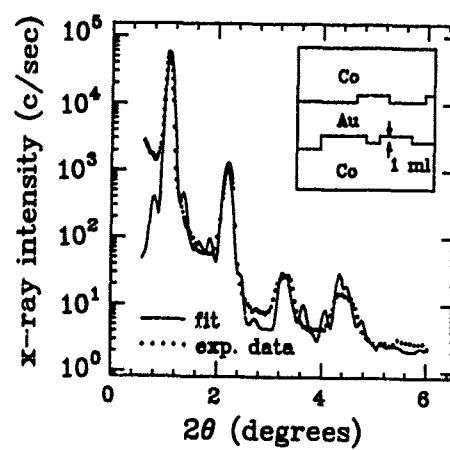
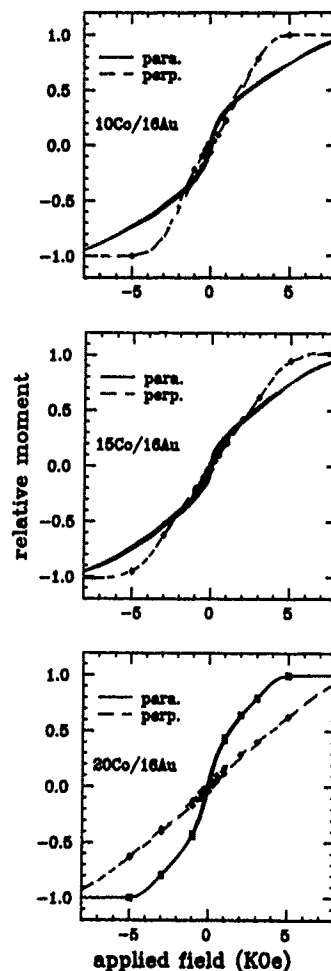


Fig. 3 Low angle x-ray data (points) of Co(20Å)-Au(16Å) superlattices and calculated intensity from the model described in the text. Inset: Schematic interface structure derived from the model.

## RESULTS AND DISCUSSION: MAGNETIC PROPERTIES

We performed magnetic measurements on five samples with Co layer thicknesses in the range 5-40Å and constant Au spacer layers of  $\sim 16$ Å. Fig. 4 shows a series of hysteresis loops measured at ambient temperature for various thicknesses of the Co layers. Data for the field both parallel and perpendicular to the film plane are shown. The measurements show a crossover in the direction of the easy axis from parallel to perpendicular as the Co layer thickness is decreased below  $\sim 19$ Å (Fig. 5). This is a somewhat greater thickness than that reported earlier by den Broeder et al.<sup>8</sup> on sputtered Co-Au films. The latter samples had to be annealed before the perpendicular anisotropy could be observed. A comparison of the MBE and sputtered samples shows very clearly the importance of interface quality in influencing the magnetic properties.

Fig. 4 Series of magnetization curves for Co-Au superlattices measured at  $T=300$ K. The labels 10 Co/16 Au etc., refer to thicknesses of respective layers in Å.



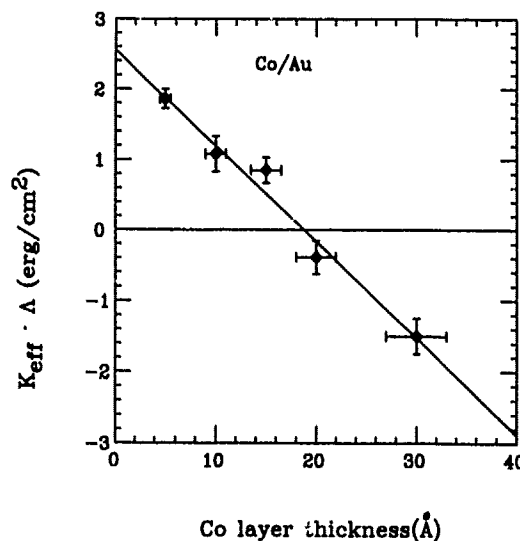
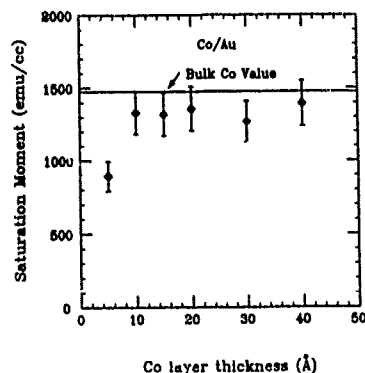


Fig. 5 Perpendicular anisotropy of Co-Au superlattices as a function of Co layer thickness at  $T=300K$ .  $K_{eff}$  is defined as  $\frac{1}{V} \int_0^{H^{sat}} (M_{\perp} - M_{\parallel}) dH$  where  $V$  is the sample volume.  $A$  is the superlattice periodicity.

A further probe of the interface quality of our samples, in addition to the x-ray, TEM and magnetic anisotropy results presented above, is the measurement of the specific magnetic moment of the Co layers at saturation. Fields up to 50kOe were used in order to ensure saturation. In Fig. 6 we see that the saturation moment is within 10% of the bulk Co value for Co layer thicknesses down to 10Å, below which the value drops considerably.

This data supports the conclusion drawn from our other measurements that intermixing of Co and Au is confined to the monolayer level at the interfaces. For the very thinnest layers ( $< 10\text{\AA}$ ) the sample is dominated by interface roughness ( $\pm 1ML$ ) and it is not surprising that the specific moment would be significantly reduced in this case.

Fig. 6 Specific magnetization of Co in Co-Au superlattices as a function of Co layer thicknesses. Measured at  $T=5K$ .



## CONCLUSIONS

We have demonstrated the growth of high-quality Co-Au superlattices. Measurements from various techniques show that the interfaces in our MBE-grown samples are surprisingly abrupt in view of the large lattice mismatch in this system. Misfit dislocations and interface steps appear to be confined to monolayers neighboring the interface and do not disrupt the epitaxial structure of the superlattice. Our results clearly establish an important link between the magnetic properties and interfacial structural quality, particularly the observation of perpendicular anisotropy in as-grown, unannealed samples.

## ACKNOWLEDGEMENTS

This work was supported in part by NSF Materials Research Group Grant No. DMR 8602675. One of us (F.L.) was supported by U.S. Army Research Office Grant No. DAAL-03-86-G-0053.

## REFERENCES

1. See, for example, U. Gradmann, in *Thin Film Growth Techniques for Low-Dimensional Structures*, ed. R.F.C. Farrow, S.S.P. Parkin, P.J. Dobson, J.H. Neave and A.S. Arrott (Plenum, New York, 1987).
2. R.M. Bozorth, *Ferromagnetism*, (Van Nostrand, Princeton) 1951.
3. S. Iwasaki and K. Ouchi, *IEEE Trans. Magns.* **14**, 849 (1978).
4. C. Chappert, K. LeDang, P. Beauvillain, H. Hurdequint and D. Renard, *Phys. Rev. B* **34**, 3192 (1986).
5. C. Liu, E.R. Moog and S.D. Bader, *Phys. Rev. Lett.* **60**, 2422 (1988).
6. H.J.G. Draaisma and W.J.M. DeJonge, *Jour. Magn. Magn. Mat.*, **66**, 351 (1987).
7. P.F. Carcia, A.D. Meinhaldt and A. Suna, *Appl. Phys. Lett.* **47**, 178 (1985).
8. F.J.A. den Broeder, D. Kuiper, A.P. van de Mosselaer and W. Hoving, *Phys. Rev. Lett.* **60**, 2769 (1988).
9. C.H. Lee, Hui He, F. Lamelas, W. Vavra, C. Uher and Roy Clarke, *Phys. Rev. Lett.* **62**, 653 (1989).

## MAGNETIZATION PROCESSES ANALYSIS IN Co-Cu SUPERLATTICES

J.P. REBOUILLAT(1), G. FILLION(1), B. DIENY(1), A. CEBOLLADA(2),  
J.M. GALLEG0(2), J.L. MARTINEZ(3)

(1) Laboratoire Louis Néel, CNRS, 166X, F-38042 Grenoble Cedex, France

(2) Dept. Fisica Materia Condensada (C-3), Universidad Autonoma de Madrid,  
E-28049 Madrid, Spain

(3) Institut Laue-Langevin, 156X, F-38042 Grenoble Cedex, France

## ABSTRACT

The analysis of the magnetization measurements performed on two Co-Cu multilayers confirm the antiferromagnetic coupling already observed with neutron experiments. Both exchange and anisotropy energies are taken into account and estimated. Their competitive role in the individual moment orientation leads to typical moment arrangements and hysteresis loops.

## INTRODUCTION

Recent polarized and unpolarized neutron diffraction experiments [1] on Co-Cu single crystal multilayers have revealed antiferromagnetic ordering between Co layers with magnetic moments in the film plane. Preliminary magnetic measurements have shown a complex hysteresis behaviour in the low field range. In the present study, we report detailed magnetization results for two previously studied samples. These are discussed in terms of a phenomenological model with assumed antiferromagnetic coupling between adjacent layers [2]. Anisotropy and exchange energies are estimated.

## EXPERIMENT

Details of epitaxial growth of f.c.c. Co or Cu (100) are given in ref. (3). The general formula of Co-Cu superlattices is written as  $[x\text{Co}/y\text{Cu}]_n$ , consisting of  $n$  repeating bilayers with  $x$  atomic planes of Co and  $y$  atomic planes of Cu. The two samples studied correspond to  $[6\text{Co}/8\text{Cu}]_{62}$  and  $[9\text{Co}/5\text{Cu}]_{103}$ .

The experimental set-up used is a 2-SQUID magnetometer which permits 2 types of measurements to be made, with the applied field in the plane of the film. Firstly, conventional magnetization measurement ( $M_{//}$ ) may be made by displacement of the sample along the field axis. Secondly, the variations of both  $M_{//}$  and  $M_{\perp}$  in-plane components of the magnetization may be measured by rotating the sample about the axis perpendicular to its plane (fig. 1). [4]

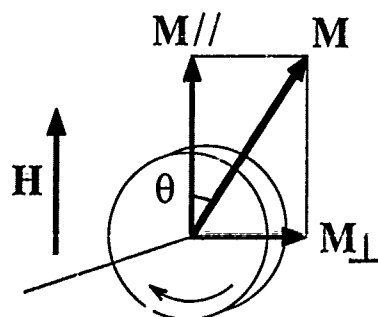


Fig. 1 : Disc shaped sample rotating about the axis perpendicular to its plane

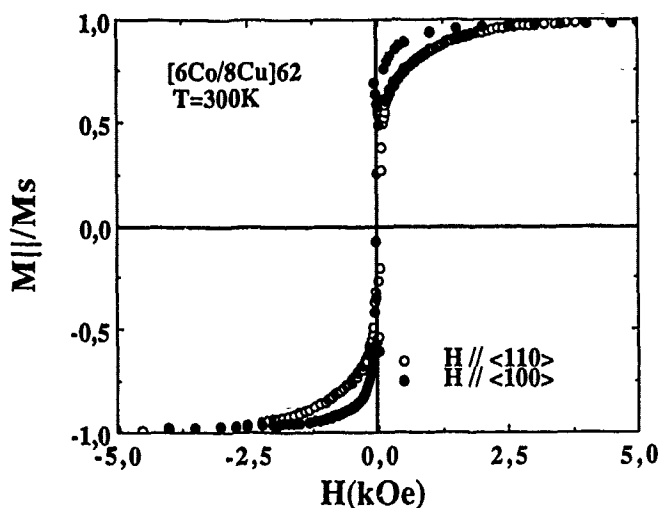


Fig. 2 : Example of magnetization curves measured along the two in-plane symmetry axes

## RESULTS

Representative magnetization curves are shown in fig. (2). Their shape is mainly ferromagnetic with a small amount of hysteresis and a clear anisotropy between the two in-plane symmetry axes. The saturation magnetizations for both samples (Table I) are in good agreement with that of bulk hcp Co, their temperature dependence shows a small decrease (7 to 8%) between 4.2 and 300 K revealing that the Curie temperature is much higher than room temperature.

Without the previous neutron results [1], these magnetization curves could hardly be thought to be those of an antiferromagnetic system. Before estimating the exchange coupling responsible for this A-F arrangement, we first present rotating sample results leading to a determination of the anisotropy constants.

### Rotating sample data analysis

In any magnetic system, at a high enough field value, the exchange energy may be neglected compared to the anisotropy energy  $E_a$  and the Zeeman energy. The total energy is written :

$$E_t = -MH \cos\theta + E_a \quad (1)$$

where  $\theta$  is the angle between the saturated magnetic moment and the applied field.

At equilibrium, the magnetization component perpendicular to the field,  $M \sin\theta$ , may be deduced :

$$M_{\perp} = -\frac{1}{H} \frac{\partial E_a}{\partial \theta}$$

in the present cubic symmetry system, with  $E_a = K \sin^2\theta \cos^2\theta$ , we get :

$$M_{\perp} = -\frac{K}{2H} \sin 4\theta = a_4 \sin 4\theta$$



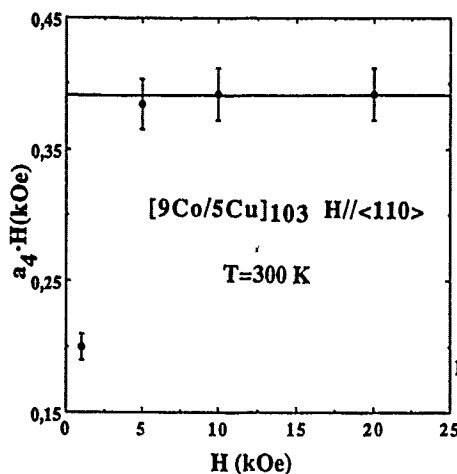


Fig. 3 : Determination of K-value in high field (experimental units)

The  $a_4$  coefficient is obtained by Fourier transform analysis of the recorded  $M_{\parallel}$  variation during continuous rotation of the sample. The  $2a_4H$  versus  $H$  plot (fig. 3) allows the extrapolation of the  $K$  value in high fields. Values for both samples are given in table I, first in  $\text{erg/cm}^2/\text{layer}$  as given by experiment, then in  $\text{erg/cm}^3$  to be compared with those of 3d metals : they are found much lower than the value for pure h.c.p. Co, but comparable to those for f.c.c. Fe and Ni.

#### Magnetization curve analysis from saturation to zero field

Let us now focus on the magnetization curves measured in decreasing field along the hard axis  $\langle 110 \rangle$  (fig. 4). With Eq. 1, the magnetic moments should lie along the  $\langle 100 \rangle$  axes in zero field, leading to a magnetization  $M/\sqrt{2}$ . The lower remanent magnetization measured (Table I) may be understood by the antiferromagnetic coupling already observed in neutron experiments. Then we have to take into account the exchange interaction energy.

Referring to [2], we suppose that each of the  $n$  Co layers behaves like a single domain whose resultant moment  $M_S$  moves in the film plane, making an angle  $\theta_i$  with the direction of the applied field. If  $J$  is the exchange interaction between two adjacent moments, the total energy is written as :

$$E_t = J \sum_{i=1}^{n-1} \cos(\theta_i - \theta_{i+1}) - M_S H \sum_{i=1}^n \cos \theta_i + K \sum_{i=1}^n \sin^2 \theta_i \cos^2 \theta_i \quad (2)$$

For the  $i$ th layer, the equilibrium condition is given by :

$$\sin \theta_i (M_S H - 4J \cos \theta_i - 2K(1 - 2\cos^2 \theta_i) \cos \theta_i) = 0 \quad (3)$$

This allows the magnetization  $M_{\parallel} = M_S \cos \theta_i$  to be calculated as a function of decreasing field  $H$  (fig. 4).

A remanent magnetization  $M_r$  is expected if  $|K/2J|$  is higher than 1.5

with  $M_r/M_S = 1/\sqrt{2} \sqrt{1 + 1/K}$  and  $k = K/2J$ .

The  $M_r/M_S$  experimental values give the anisotropy to exchange ratio for both samples (table I) and the fit of the magnetization curves in decreasing field allows the determination of both  $K$  and  $J$  constants (table I). These  $K$  values are in good agreement with those obtained from the rotating sample experiment.

The very high anisotropy to exchange ratio is characteristic of a very low interlayer coupling as expected in such multilayers, where interactions take place through the non-magnetic material.

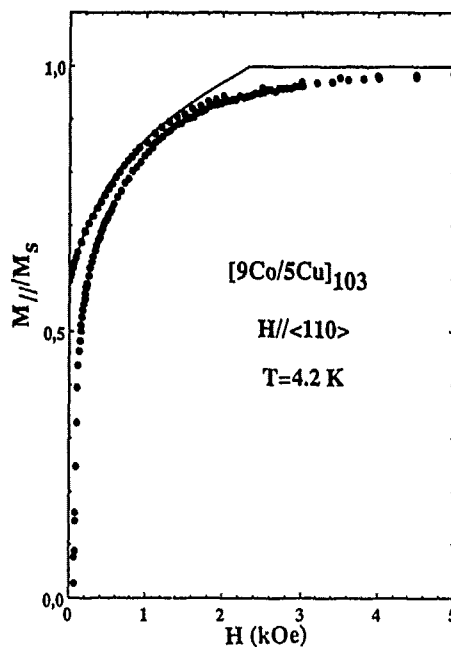


Fig. 4 : Example of magnetization curve measured along the hard axis with calculated curve fitted using eq.(3)

Formula	[9Co/5Cu] <sub>103</sub>		[6Co/8Cu] <sub>62</sub>		
Temperature	4.2 K	300 K	4.2 K	300 K	Units
$M_S$	1.65	1.52	1.73	1.65	$\mu_B$
$M_S$	2.34	2.15	1.63	1.55	$10^4 \text{ emu/cm}^2/\text{layer}$
$K^*$	-0.166	-0.138	-0.143	-0.088	$\text{erg/cm}^2/\text{layer}$
$K^*$	-1.03	-0.86	-1.34	-0.83	$10^6 \text{ erg/cm}^3$
$K$	-1.32	-0.95	-1.87	-1.09	$10^6 \text{ erg/cm}^3$
$J$	0.030	0.021	0.044	0.026	$\text{erg/cm}^2/\text{layer}$
$k=K/2J$	-3.57	-3.57	-2.28	-2.28	
$M_{\text{r}} < 100^\circ / M_S$	0.6	0.6	0.53	0.53	

\* Values deduced from rotating sample experiment

Table I

### Hysteresis loops analysis

Minimizing the total energy (Eq. 2) using a steepest descent method [2], allows the whole magnetization curve to be calculated. Various hysteresis loop shapes are obtained depending on the  $k$  value. The  $k = -2.28$  case is illustrated in fig. (5) for an  $n = 62$  multilayer when the field is applied along a hard axis. Several transitions are expected, the largest is arising in a very low field during the demagnetization process. The experiment shows a very good agreement with this calculation. Other magnetization jumps are better seen at room temperature than at low temperature due to the larger thermal activation. Their occurrence at lower fields than expected may be understood as follows. In calculation procedure, the system may be in a state

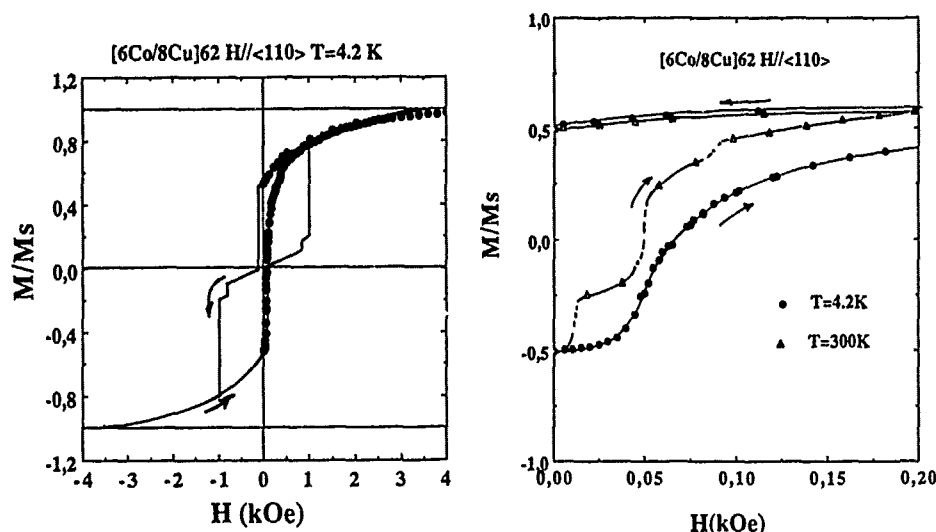


Fig. 5 : Hysteresis loop calculated with  $k = 2.28$  and experimental measurements

of energy which is not the absolute minimum of energy. In physical systems, transition to this state can be nucleated by crossing the separating barrier energy. The same remark may be made for easy axis hysteresis loops, calculated to be square with a remanent magnetization equal to the saturation value. Here, non-symmetrical magnetic states may be nucleated leading to a zero-field configuration as illustrated in fig. (6). As the field cannot be applied very precisely along the  $z$  easy direction, the two perpendicular  $x$  easy directions ( $x > 0$  and  $x < 0$ ) are non-symmetrical and there will be an imbalance of the states nucleated along that direction. The consequence expected is that the remanent magnetization may not lie along the direction of the field applied. Our observations using the rotating sample set-up confirm clearly this expectation with typical  $M_z$  magnetization of 20%  $M_{//}$ . As a consequence, the magnetic order in zero-field may be expected to be greater when the magnetic field has been applied along a hard axis than along an easy axis.

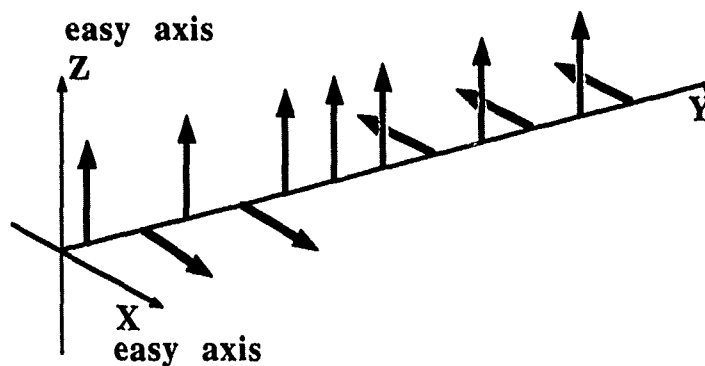


Fig. 6 : Non-symmetrical states nucleated in low field when decreasing the field applied along the easy z-axis

#### References

- [1] A. Cebollada, J.L. Martinez, J.M. Gallego, J.J. de Miguel, R. Miranda, S. Ferrer, F. Batallan, G. Fillion and J.P. Rebouillat, Phys. Rev. 39, 1 May 89
- [2] B. Dieny, J.P. Gavigan, J.P. Rebouillat, this Symposium Session G1.7 and B. Dieny, J.P. Gavigan, J.P. Rebouillat, submitted to J. of Phys. : Condensed Matter
- [3] J.J. de Miguel, A. Cebollada, J.M. Gallego, J. Ferron and S. Ferrer, J. Cryst. Growth 88 (88) 442
- [4] B. Dieny, B. Barbara, G. Fillion, M. Maeder and B. Michelutti, J. Physique 48 (1987) 1741

MAGNETIC AND STRUCTURAL STUDIES ON Au/3d-metal MULTILAYERED FILMS  
WITH ARTIFICIAL SUPERSTRUCTURES.

SATORU ARAKI\*, TSUTOMU TAKAHATA\*\*, HITOSHI DOHNOMAE\*\*\*, TETSUO OKUYAMA\*\*\*\*,  
and TERUYA SHINJO  
Institute for Chemical Research, Kyoto University, Uji, Kyoto 611, Japan

ABSTRACT

Au/3d-metal(Fe, Co, and Ni) artificial multilayered films were prepared by alternate deposition technique in ultrahigh vacuum. Well defined superstructures were confirmed by transmission electron microscopy and X-ray diffraction method. All 3d-metals were epitaxially grown on (111) oriented Au buffer layers. A large perpendicular magnetic anisotropy was observed in Au/Co multilayered films. When Co layer thickness was 4.7 Å, the effective perpendicular anisotropy energy  $K_u$  was  $9.6 \times 10^6$  erg/cm<sup>3</sup>. The surface (interface) anisotropy energy constants,  $K_s$ , of Au/Co and Au/Fe multilayered films were estimated to be 0.42 erg/cm<sup>2</sup> and 0.51 erg/cm<sup>2</sup>, respectively. The volume contribution,  $K_v$ , was interpreted from the observed value of saturation magnetization and the bulk values of magneto-crystalline anisotropy energy constants  $K_1$  and  $K_2$ .

INTRODUCTION

Many works have been devoted to investigate metallic multilayered films with interest in magnetic anisotropy effect at the interfaces. Combinations of a noble metal and a 3d-metal have been studied by several groups, and the existence of a large perpendicular magnetic anisotropy was reported [1]-[3]. Recently Velu et al. reported the results on Au-Co bilayer films and suggested that the perpendicular anisotropy is related closely with the flatness of interface and the highly-oriented structure of Au underlayer.

The present study is concerned with the structure and magnetic properties of Au/3d-metal multilayered films. Particularly the surface anisotropy contribution to the total anisotropy is discussed.

EXPERIMENTAL

Au/3d-metal multilayered films were prepared on glass and polyimide substrates, using alternate deposition technique in ultrahigh vacuum. Achieved initial pressure was  $3 \times 10^{-10}$  Torr. The background pressure during deposition was maintained in the range of  $10^{-9}$  Torr. The typical deposition rate was 0.3 Å/s for Au and 0.2 Å/s for 3d-metals. Before the preparation of artificial superstructure, a buffer layer of Au 250 Å was deposited on the substrate at the room temperature, and was annealed at 150°C for 1 hour. After cooled the substrate down to the room temperature, the deposition process to prepare artificial superstructure was carried out onto the Au buffer layer. On the surface of multilayered films, another

-----  
Permanent Address: \*R&D Center, TDK Corp., Higashi Owada 2-15-7, Ichikawa, Chiba 272, Japan

\*\*Advanced Materials Research Lab., TOSOH Corp., Hayakawa, 2743-1, Ayase, Kanagawa 252, Japan

\*\*\*Materials Research Lab.II, NIPPON STEEL Corp., Ida 1618, Nakahara, Kawasaki 211, Japan

\*\*\*\*TOYOBO Research Inst., TOYOBO Corp., Katata 2-1-1, Ohtsu Shiga 520-02, Japan

Au layer with the thickness of 250 Å was deposited in order to protect the sample from oxidation.

The artificial superstructure was analyzed by X-ray diffractometry (XRD) with the scattering vector perpendicular to the film plane. The cross-sectional observation by transmission electron microscope (TEM) was performed to observe the Au/3d-metal interfaces. Each layer thickness of both Au and 3d-metals was detected with a quartz microbalance. We calibrated the thicknesses from the analysis of XRD measurements and inductively coupled plasma spectrometry (ICP). The Au interlayer thickness was chosen as 28.0 Å, which seems to be sufficient thickness to separate 3d-metal layers and to maintain the periodic structure. The 3d-metal layer thickness was changed from 4 to 30 Å. The total number of Au/3d-metal bilayers was fixed to be 10.

The magnetizations of the prepared samples were measured with a vibrating sample magnetometer (VSM) in fields up to 15 kOe at 300 K, both in parallel and perpendicular to the film plane. Torque measurements were made with a self balancing torque magnetometer in several magnetic fields up to 20 kOe at 300 K. Since Au/Co system exhibits a large perpendicular anisotropy, saturated torque value was evaluated by an inverse plot of measured magnetic field. Thus effective perpendicular magnetic anisotropy energy  $K_u$  per unit 3d-metal volume was determined from the saturated torque value.

## RESULTS AND DISCUSSION

### (a) Structural Analysis

Figure 1 shows typical XRD patterns in high angle regions. All Au/3d-metal multilayered films show similar profiles. These profiles are interpreted as the superposition of the following two reflections: the reflection from (111) oriented Au buffer layer, and 0-th main peak accompanied with many satellite reflections. This 0-th main peak means the

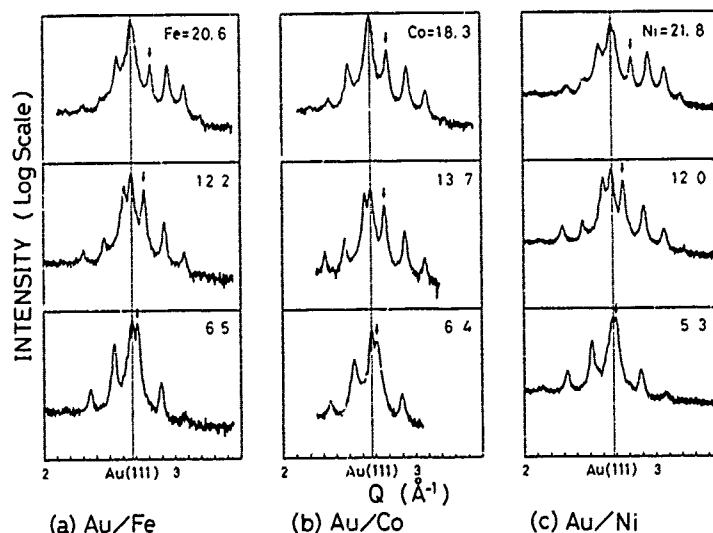


Fig.1: X-ray diffraction patterns of Au/3d-metal multilayered films. The thickness of Au layer is fixed to be 28.0 Å, and 3d-metal is varied from 5.3 Å to 21.8 Å. The number of bilayers in each sample is 10. The arrow shows the main peak of the superstructure.

reflection from the average plane spacing value of artificial superstructure. Around the Au(111) reflection, from 4 to 9 satellite lines were observed for every sample. In small-angle region, up to 5-th Bragg reflections caused by the artificial period were observed. These indicate that Au and 3d-metal superstructures grew epitaxially, having sharp interfaces.

Figure 2 shows TEM photograph of Au/Ni multilayered film. The Ni layer thickness is 31.0 Å, and Au layer thickness, 28.0 Å. Clear contrast of Au and Ni layers is observed. Lattice fringes appear in each layer continuously, indicating that Ni layers also grow epitaxially on the Au buffer

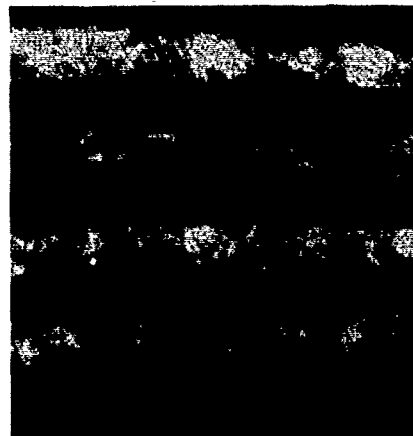


Fig.2: Cross-sectional TEM photograph of an Au/Ni multilayer composed of 31.0 Å Ni and 28.0 Å Au layers. The bright portion is Ni and the dark is Au layer.

film. From another TEM observation, an atomically flat interface is confirmed between the Au buffer layer and the first 3d-metal layer. By the annealing up to 150°C, Au grain size of buffer layer had grown larger, and crystal surface turned out to be flat. The grain size of Au buffer layer was estimated to be  $2 \times 10^5$  Å on an average, which is similar to the results of Chauvineau et al.[6] and Cherns[7]. The average grain sizes of Au deposited on a substrate at 150°C is not more than  $1 \times 10^5$  Å without annealing. Thus, in order to obtain large grain sizes and flat surfaces the annealing procedure is essential. For Au/Co and Au/Fe system, the cross-sectional photograph was very similar, showing lattice fringes as well as the Au/Ni system. Although each 3d-metal has a different crystal structure; Fe, Co, and Ni are bcc, hcp, and fcc, respectively, they all grow epitaxially on fcc (111) Au surfaces.

The microscopic crystal structure at the interfaces is difficult to make clear. The analysis of the XRD profiles for Au/Co indicate a texture in which (111) of fcc Au layer alternate with (002) of hcp Co layers, which is consistent to the result of Renard and Nihoul[8]. According to the observation by Reflection High Energy Electron Diffraction (RHEED), when Fe is deposited extremely thinly onto an Au (111) poly-crystalline buffer layer, the fcc structure due to epitaxy is maintained. Gradually Fe changed its structure from fcc(111) to bcc(110) when the Fe layer thickness becomes more than around 10 Å[9]. Thus, the precise characterization of the first few atom layers at the interface is very difficult.

The mean atomic plane spacing,  $d(\text{mean})$ , along the stacking direction is obtained from  $2\theta$  value of the main peak. Hereafter,  $t(M)$  means 3d-metal layer thickness. The  $d(\text{mean})$  value of all the multilayered films increases with decreasing  $t(M)$ . Moreover,  $d(\text{mean})$  value is always larger than that from a theoretical calculation assuming that both Au and 3d-metal layers keep their bulk values of plane spacing. It is to be considered that this increase of  $d(\text{mean})$  is due to lattice strain caused by in-plane lattice mismatch or intermixing of one or a few atomic layers at the interfaces.

#### (b) Magnetic Properties

The coercive force as a function of  $t(M)$  is shown in Fig.3. Since Au/Co system has a perpendicular easy direction, coercive force  $H_c(n)$  means

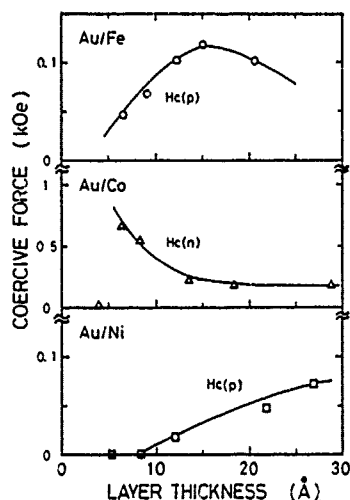


Fig.3: Coercive force against 3d-metal layer thickness  $d(M)$  measured at 300 K. Data were taken with the field parallel (for Au/Fe and Au/Ni), and perpendicular (for Au/Co) to the film plane.

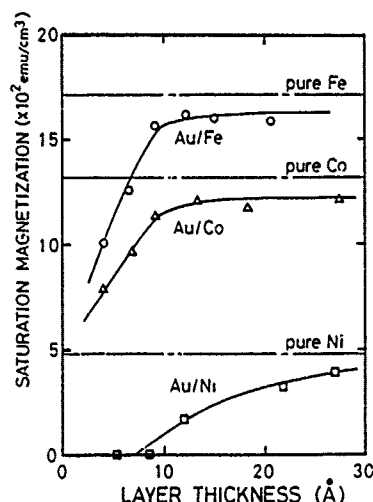


Fig.4: Saturation magnetization with various 3d-layer thickness  $d(M)$  measured at 300 K. The dashed line shows the bulk value of Fe, Ni, and Co.

the value in perpendicular to the film plane, and  $H_c(p)$  in Au/Fe or Ni means in-plane value. For Au/Fe system,  $H_c(n)$  takes the maximum at around  $t(Fe)$  of 15 Å, and decreases with decreasing  $t(Fe)$ . On the other hand  $H_c(n)$  in Au/Co increases with decreasing  $t(Co)$ . This behavior is interpreted that the perpendicular anisotropy increases (as shown later) with decreasing  $t(Co)$ , and consequently the normal element of coercive force increases. The multilayered films consist Co layers with the thickness of 3.7 Å or Fe layers with 4.0 Å show small coercive force. It is simply because the Curie temperatures of very thin Fe and Co layers are rather low, which are near the room temperature. The residual magnetization  $M_r$  also becomes to nearly zero at 300 K by the same reason. For Au/Ni system  $H_c(p)$  decreases monotonously with decreasing  $t(Ni)$ , and reaches zero at  $t(Ni)=8$  Å. Since bulk Ni has a lower Curie temperature ( $T_c=358^\circ C$ ) than Fe( $T_c=770^\circ C$ ) and Co( $T_c=1131^\circ C$ ), Curie temperature in Au/Ni multilayers decreases more rapidly than in Au/Fe or Au/Co system.

Figure 4 shows the saturation magnetization  $M_s$  per unit 3d-metal volume as a function of  $t(M)$ .  $M_s$  is almost constant for thicker  $t(Fe)$  and  $t(Co)$  than 9 Å, which is about 90 % of bulk Fe and Co. This reduction of magnetization is explained if the local magnetization at the interface atom layer is smaller than the inner part. From the  $M_s$  data at various  $t(Fe)$  and  $t(Co)$ , the reductions of magnetization of Fe and Co correspond to be equivalent to one-half of a monolayer per each interface. However, the drastic decrease of magnetization in Fe and Co layers thinner below 9 Å should be due to the decrease of Curie temperature. For Au/Ni system,  $M_s$ , as well as  $H_c(p)$ , becomes smaller if  $t(Ni)$  decreases to less than 18 Å and reaches zero below at  $t(Ni)$  of 9 Å. Chappert et al. reported that for Au/Ni/Ai sandwich films, Curie temperature decreases abruptly below  $t(Ni)$  of 12 Å, though that is near the bulk value above  $t(Ni)$  of 13 Å [10]. Although there are some differences between the behaviors of sandwich films and those of multilayered films, the results for  $M_s$  and  $H_c$  are in consistent with each other. For a more quantitative discussion, magnetization



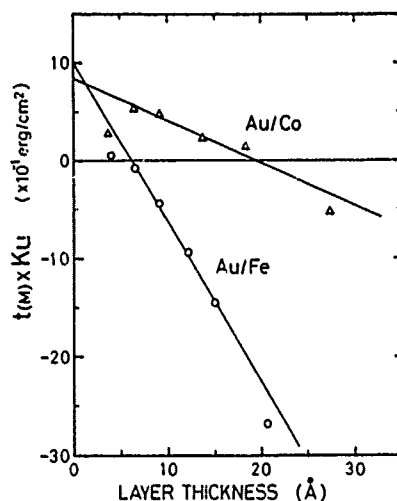


Fig.5: Effective Perpendicular anisotropy energy  $K_u$  times the magnetic layer thickness of  $t(M)$  ( $M=Fe$  or  $Co$ ) versus  $t(M)$ . The solid lines are the least square fits. The Value of intercepted vertical axis yield the interface anisotropy, and the slopes give the volume anisotropy.

buffer layer[11]. In the case of Au/Co multilayered film with  $t(Co)$  of 6.4 Å and  $t(Au)$  of 28.0 Å,  $K_u$  was  $8.6 \times 10^6$  erg/cm<sup>3</sup> when the Au buffer layer was formed at room temperature, and annealed at 150°C (the adopted condition). However, when a Au buffer layer was deposited at 150°C or at room temperature and without annealing, we have obtained much smaller  $K_u$  values. This results showed that both flatness and large grain sizes of Au buffer layer are essential for the large perpendicular anisotropy[12].

Figure 5 shows the plot of  $(K_u \times t(M))$  values versus  $t(Fe)$  and  $t(Co)$  with a fitted solid line. We note that  $K_u$  turns to positive in Au/Fe system at  $t(Fe)$  of 4.0 Å. According to den Broeder et al. [3] the effective magnetic anisotropy energy  $K_u$  is described as follows:

$$K_u = K_v + 2K_s / t(M) \quad (1)$$

$K_v$  is a volume contribution including shape magnetic anisotropy and magneto-crystalline anisotropy, since the measured magnetization value can not be separated.  $K_s$  is an interface anisotropy energy per unit area caused from the reduced symmetry at a surface[4]. In both systems  $K_u$  is well described by Eq.(1). From Fig.5  $K_s$  for Au/Co and Au/Fe interfaces are evaluated as 0.42 and 0.51 erg/cm<sup>2</sup>, respectively. Chappert and Bruno reported that Au/Co/Au sandwich films has  $K_s=0.53$  erg/cm<sup>2</sup> obtained from FMR measurement[13]. den Broeder et al. reported that for as-prepared Au/Co multilayered films has  $K_s=0.1$  erg/cm<sup>2</sup>, and  $K_s=0.45$  erg/cm<sup>2</sup> after annealing [3]. They also claimed that the sharpening of the interfaces by annealing enabled to increase the  $K_s$  value. Our results of  $K_s=0.42$  erg/cm<sup>2</sup> for Au/Co system is comparable to that of the annealed Au/Co multilayered films, but is smaller than that of Au/Co/Au sandwich films. Since, Au/Co/Au sandwich films have only two interfaces, they may thus keep the flatness and compositional steepness of the interfaces more easily than the case of

measurement at low temperatures is required to exclude the effects due to the decrease of Curie temperature.

In the present work the effective perpendicular magnetic anisotropy energy  $K_u$  includes the shape magnetic anisotropy energy  $K_d$  of the 3d-metal layers. Since  $K_d$  for multilayered films cannot be evaluated exactly, we will discuss  $K_u$ . For the Au/Fe and Au/Co systems  $K_u$  is increased with the decrease of  $t(Fe)$  and  $t(Co)$ , and changes the sign at  $t(Fe)$  of 6 Å and  $t(Co)$  of 18 Å to have an easy axis of magnetization normal to the film plane. These thickness values for  $K_u=0$  are roughly in agreement with the previously reported ones[3][10]. The  $K_u$  took maximum values of  $9.6 \times 10^6$  erg/cm<sup>3</sup> (Au/Co) at  $t(Co)=6.4$  Å, and  $1.3 \times 10^6$  erg/cm<sup>3</sup> (Au/Fe) at  $t(Fe)=4.0$  Å. It is to be noted that Au/Fe has a perpendicular magnetization below  $t(Fe)$  of 4.0 Å.

As we reported previously, the magnetic properties of Au/Co artificial superstructures depend strongly on the texture of Au

multilayers.

Although the magneto-crystalline anisotropy energy of pure Fe is fairly large, our Au/Fe system overcame the high shape anisotropy to possess a perpendicular anisotropy with  $t(\text{Fe})$  below 4 Å. However no studies have been reported about  $K_s$  in Au/Fe system, in case of Pd/Fe system their easy magnetized direction was always in plane for various Fe thicknesses[2]. This indicates that if the magneto-crystalline anisotropy energy is large, easy magnetization axis is in the film plane unless the  $K_s$  value is large enough to overcome the shape anisotropy.  $K_v$  for Au/Co and also Au/Fe are estimated from the slopes of lines in Fig.5. We obtain  $K_v = -4.34 \times 10^6$  erg/cm<sup>3</sup> for Au/Co, and  $K_v = -16.3 \times 10^6$  erg/cm<sup>3</sup> for Au/Fe system, respectively. The volume contribution  $K_v$  is described as follows:

$$K_v = -K_d + K_1 + K_2 \quad (2)$$

$K_1$  and  $K_2$  are magneto-crystalline anisotropy energies. Assuming that the shape magnetic anisotropy energy  $K_d$  is  $2\pi M_s^2$  and  $K_1$  and  $K_2$  take bulk values,  $K_v$  is calculated from Eq.(2). As for  $M_s$ , we adopt the average of measured values in the constant region. We thus obtain  $K_v = -16.1 \times 10^6$  erg/cm<sup>3</sup> for Au/Fe and  $K_v = -4.1 \times 10^6$  erg/cm<sup>3</sup> for Au/Co system, respectively. This calculation gives a good agreement with the estimated value of  $K_v$ . For our multilayered films the contribution of the volume anisotropy was small because of the loss magnetization about 10 % from the bulk value. Therefore, the interface anisotropy came to be effective, as the shape anisotropy reduced.

#### CONCLUSION

Au/Co and Au/Fe multilayers with perpendicular magnetizations were obtained if the Co and Fe layer thickness are less than 18 Å for Au/Co and 6 Å for Au/Fe, respectively. For Au/Fe and Au/Co system the contribution of the interface anisotropy is higher than that of the volume anisotropy. Both the flatness and large grain sizes of Au buffer layer by annealing at 150°C are essential to obtain the large perpendicular anisotropy.

#### REFERENCES

1. P.F.Carcia, A.D.Meinhaldt, and A.Suna, Appl.Phys.Lett. 47, 178 (1985)
2. H.J.G.Draaisma, W.J.M.de Jonge, and F.J.A.den Broeder, J.Mag.Mag. Mater. 66, 351 (1987); J.Appl.Phys. 63, 3479 (1988)
3. F.J.A.den Broeder, D.Kuiper, A.P.van de Mosselaer, and W.Hoving, Phys.Rev.Lett. 60, 2769 (1988)
4. U.Gradmann, Appl.Phys. 3, 161 (1974); J.Mag.Mag.Mater. 6, 173 (1977)
5. E.Velu, C.Dupas, D.Renard, J.P.Renard, and J.Seiden, Phys.Rev.B 37, 668 (1988)
6. J.P.Chauvineau, P.Croce, G.Devaut, and M.F.Verhaeghe, J.Vac.Sci.Tech. 6, 776 (1969)
7. D.Cherns, Phil.Mag. 30, 549 (1974)
8. D.Renard, and G.Nihoul, Phil.Magazine B 55, 75 (1987)
9. T.Takahata, T.Okuyama, S.Araki, and T.Shinjo, in preparation
10. C.Chappert, D.Renard, P.Beauvillain, J.P.Renard, J.Physique Lett. 46, 59 (1985); J.Mag.Mag.Mater. 54, 795 (1986)
11. S.Araki, T.Takahata, and T.Shinjo, J.Mag.Soc.Jpn. 13, 339, (1989)
12. T.Takahata, S.Araki, and T.Shinjo, send to J.Mag.Mag.Mater. (1989)
13. C.Chappert and P.Bruno, J.Appl.Phys. in press (1989)

## NOVEL MAGNETIC AND OPTO-ELECTRONIC PHENOMENA IN DILUTED MAGNETIC SEMICONDUCTOR MULTILAYERS

J. K. FURDYNA AND N. SAMARTH

Department of Physics, University of Notre Dame, Notre Dame, IN 46556.

### ABSTRACT

We begin by reviewing earlier work involving the epitaxial growth of diluted magnetic semiconductor (DMS) layers, heterostructures and superlattices. We also describe current efforts at introducing new materials -- such as  $\text{Cd}_{1-x}\text{Mn}_x\text{Se}$  -- to the family of MBE-grown DMS alloys. We then discuss some of the unique properties of DMS materials that make the study of thin film structures attractive, with particular emphasis on two general aspects. First, we look at the new opportunities in magnetism that are provided by epitaxially grown DMS films. Second, we examine some of the novel phenomena made possible by sp-d exchange effects in the context of DMS quantum well structures.

### INTRODUCTION

The growth of diluted magnetic semiconductor (DMS) epilayers, superlattices and heterostructures by molecular beam epitaxy (MBE) [1] and atomic layer epitaxy (ALE) [2] has received much attention in recent years. When the exceptional magnetic and electronic properties of DMS alloys [3] are examined within the context of quantum wells and reduced dimensionality, a number of novel phenomena can occur. For instance, the low temperature magnetic ordering in DMS layers shows a dramatic change as the layers approach two dimensionality [4-7]. Furthermore, other fascinating effects, associated with spin-spin exchange between localized magnetic moments and band electrons in DMS quantum well structures, such as selective spin tunneling, have been proposed by Kossut and Furdyna [8]. In this paper, we begin with a brief review of the various DMS materials grown so far by MBE, including recent attempts by our group at enlarging this category. We then look at the problem of magnetic ordering and magnetic phases in DMS alloys, and show how new insights might be gained by studying epitaxial layers. Finally, we examine some unusual electronic effects that might result from the large sp-d exchange in DMS superlattices.

### GROWTH OF DMS EPILAYERS, HETEROSTRUCTURES AND SUPERLATTICES

The established work on the growth of DMS systems by MBE has been extensively reviewed by Gunshor *et al* [1]. The earliest DMS materials grown by MBE were  $\text{Cd}_{1-x}\text{Mn}_x\text{Te}$  epilayers grown on CdTe and GaAs substrates. The first reports of successful preparation of quantum wells

and superlattices of  $\text{Cd}_{1-x}\text{Mn}_x\text{Te}/\text{Cd}_{1-y}\text{Mn}_y\text{Te}$  by MBE date back to 1984. This was followed by the growth of epilayers and modulated structures involving  $\text{Zn}_{1-x}\text{Mn}_x\text{Se}$  and  $\text{Hg}_{1-y}\text{Mn}_y\text{Te}$ . All these superlattices are of excellent structural quality, showing sharp layer boundaries as seen by transmission electron microscopy (TEM) (see, for instance, Fig. 1), narrow x-ray rocking curves, and clear evidence of zone folding of the acoustic phonon dispersion curves, as observed by Raman scattering. The high quality of the  $\text{Cd}_{1-x}\text{Mn}_x\text{Te}$  and  $\text{Zn}_{1-x}\text{Mn}_x\text{Se}$  superlattices is attested to by the manifestation of stimulated emission [9,10]. More recently, epitaxial layers of  $\text{Zn}_{1-x}\text{Fe}_x\text{Se}$  [11] and  $\text{Zn}_{1-x}\text{Co}_x\text{Se}$  [12] have also been grown by MBE. To the best of our knowledge, *superlattices* containing these materials have not been reported so far. In this review, we will restrict ourselves to epitaxial structures involving Mn-based wide gap DMS.

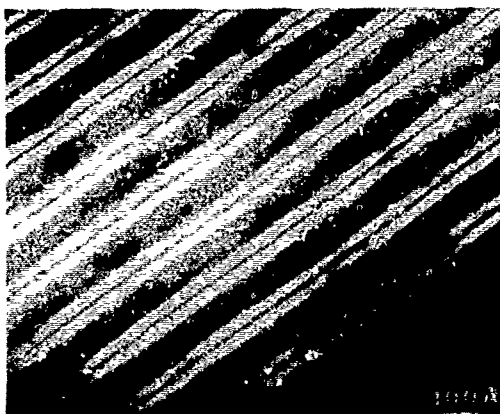


Fig.1. Dark-field image of the MnSe "spin sheet" superlattice reported in Ref. [6]. In the image, bright bands correspond to ZnSe layers, the wide dark bands are zinc-blende  $\text{Zn}_{0.55}\text{Mn}_{0.45}\text{Se}$ , and the thin dark bands are zinc-blende MnSe layers 6-8 Å thick.

A variant of the MBE technique known as *atomic layer epitaxy* (ALE) has also been used to grow epilayers of  $\text{Cd}_{1-x}\text{Mn}_x\text{Te}$ ,  $\text{Zn}_{1-x}\text{Mn}_x\text{Se}$  and  $\text{Zn}_{1-x}\text{Mn}_x\text{Te}$  [2]. Unlike MBE, in which different atomic species are deposited on a substrate *simultaneously* (for instance, ZnSe is grown by using Zn and Se fluxes at the same time), ALE proceeds by depositing one layer of a single atomic species at a time (for example, by exposing the substrate to alternate fluxes of Zn and Se). The growth of DMS superlattices using ALE still remains to be explored. However, successful ALE growth of DMS heterostructures such as  $\text{Zn}_{1-x}\text{Mn}_x\text{Se}/\text{Zn}_{1-y}\text{Mn}_y\text{Se}$  has been reported. We will show later how the layer-by-layer growth scheme of ALE might present unique opportunities for the growth of atomically ordered DMS structures such as a famatinite form of  $\text{Zn}_3\text{MnSe}_4$ .

Finally, we would like to mention some new developments relevant to the MBE growth of DMS materials. We have recently demonstrated the growth of epitaxial layers of CdSe on [100] GaAs substrates [13]. Although CdSe has the hexagonal (wurtzite) structure when grown in the bulk, the epitaxial layers adopt the cubic zinc blende structure of the GaAs substrate. This has further enabled us to demonstrate the growth of zinc-blende epilayers of  $\text{Cd}_{1-x}\text{Mn}_x\text{Se}$  ( $0 < x < 0.8$ ), thus adding a new DMS material to the list outlined earlier. Note also that bulk  $\text{Cd}_{1-x}\text{Mn}_x\text{Se}$

can only be grown reliably up to  $x = 0.5$ , so that MBE substantially extends the composition range of the alloy. We have also been able to demonstrate the growth of  $\text{Cd}_{1-x}\text{Zn}_x\text{Se}$  over the entire range of  $x$ . This material -- although not a member of the DMS family -- is especially interesting within the context of DMS epilayers because it can be lattice-matched with  $\text{Zn}_{1-x}\text{Mn}_x\text{Se}$  and  $\text{Cd}_{1-x}\text{Mn}_x\text{Se}$ . A schematic summary of the range of energy gaps and lattice constants accessible by using the alloys  $\text{Zn}_{1-x}\text{Mn}_x\text{Se}$ ,  $\text{Cd}_{1-x}\text{Mn}_x\text{Se}$  and  $\text{Cd}_{1-x}\text{Zn}_x\text{Se}$  is given in Fig. 2. Preliminary experiments also show promise of growing  $\text{ZnSe}/\text{Cd}_{1-x}\text{Mn}_x\text{Se}$  superlattices with deep magnetic wells, as well as  $\text{CdSe}/\text{Cd}_{1-x}\text{Mn}_x\text{Se}$  superlattices. We believe that superlattices consisting of  $\text{Cd}_{1-x}\text{Mn}_x\text{Se}/\text{Cd}_{1-y}\text{Zn}_y\text{Se}$  combinations should also be feasible. The opportunities provided by such structures will be discussed later in this paper. Finally, it should be noted that of all the wide-gap DMS alloys,  $\text{Cd}_{1-x}\text{Mn}_x\text{Se}$  is by far the easiest to dope (n-type) in the bulk, which augurs well for attempts at doping  $\text{Cd}_{1-x}\text{Mn}_x\text{Se}$  layers during MBE growth.

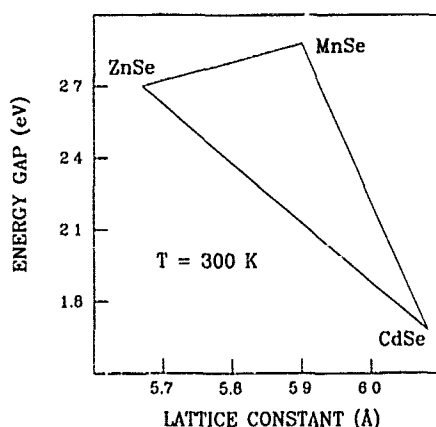


Fig.2. Schematic depiction of range of energy gaps and lattice constants made available by the zinc-blende alloys composed of ZnSe, CdSe and MnSe.

## MAGNETIC ORDERING

The magnetic properties of DMS materials arise from the Heisenberg-like d-d exchange between the Mn ions [14]. This exchange interaction is short-ranged (being primarily confined to nearest and next-nearest neighbors) and is known to be antiferromagnetic. The d-d exchange interaction in various DMS alloys has been well-characterized through a number of experimental investigations. Hence, DMS materials provide ideal systems in which to study the magnetism of a randomly diluted FCC (or HCP) antiferromagnet with short-range interactions. However, the problem of magnetic ordering and magnetic phases in DMS remains at the center of debate despite several studies involving neutron scattering, as well as dc magnetic susceptibility and ac magnetic susceptibility measurements.

The consensus at present is that DMS alloys show two magnetic phases, as shown in Fig. 3. The high temperature phase is paramagnetic, while the low temperature phase is commonly referred to as a "spin glass" because of a number of similarities to conventional spin glasses. For instance, the temperature variation of the low field magnetic susceptibility shows a cusp at a critical temperature  $T_g$ , but there is no evidence for a transition to an ordered magnetic phase. The phase boundary shown in Fig. 3 is determined solely by the occurrence of the cusp in the dc magnetic susceptibility. It is suspected that the spin glass phase arises from a combination of the random distribution of magnetic ions and the frustration inherent in the FCC (and HCP) lattices of DMS. We should stress that the exact nature of this low temperature phase is still the subject of much controversy. The only clear picture of the nature of magnetic ordering in DMS alloys is obtained from neutron scattering studies of DMS with  $0.3 < x < 0.75$  [15]. These measurements show that, as the temperature decreases, these materials form clusters exhibiting internal short-range antiferromagnetic order of the third kind (AFM-III). These clusters individually increase in size with decreasing temperature, but there is no indication of any transition to long-range order.

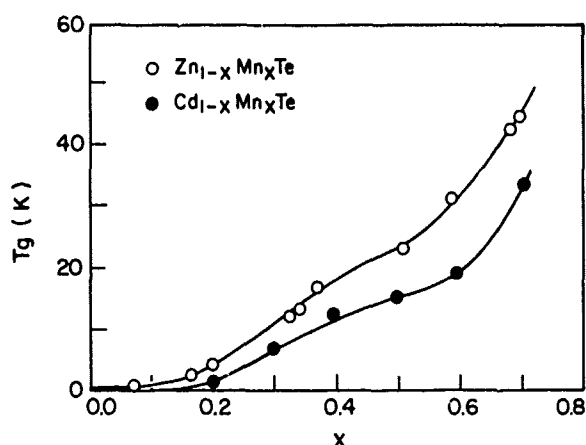


Fig.3. Magnetic phase diagram for  $\text{Zn}_{1-x}\text{Mn}_x\text{Te}$  and  $\text{Cd}_{1-x}\text{Mn}_x\text{Te}$  (after [14]).

So far, most studies of magnetism in DMS alloys have involved bulk-grown crystals. An important limitation of these crystals is that there is an upper limit on the Mn ion concentration, e.g., single phase  $\text{Zn}_{1-x}\text{Mn}_x\text{Se}$  cannot be grown above  $x > 0.57$  [3]. Further, in such crystals, the distribution of Mn ions is known to be random. The growth of DMS epilayers by MBE and ALE can relax these restrictions and hence broadens the scope of problems that can be addressed. There are three aspects that stand out:

- MBE growth provides access to a fundamentally new problem: the effect of reduced dimensionality on magnetism in DMS systems.
- Both  $\text{Zn}_{1-x}\text{Mn}_x\text{Se}$  and  $\text{Cd}_{1-x}\text{Mn}_x\text{Se}$  epilayers can be grown over almost the entire range of  $x$ , so that one may study magnetism at much higher Mn concentrations than in the bulk.

- (c) By growing short period superlattices such as ZnSe-MnSe-ZnSe-MnSe..., either by MBE or ALE, one may be able to create DMS structures with an *ordered* distribution of magnetic ions.

We now examine each of these three aspects.

### Magnetism of Two Dimensional DMS Layers

The effects of reduced dimensionality on the magnetism of DMS layers have been studied in two extreme limits: metastable MnSe layers [6,7] and  $\text{Cd}_{1-x}\text{Mn}_x\text{Te}$  layers in the vicinity of  $x = 0.2$  [5]. The observations indicate that the type of magnetism occurring in these quasi-two-dimensional systems differs in many ways from that observed in corresponding bulk materials. The study of this problem is important not only because of its fundamental nature, but also because the optical and electrical properties of 2D DMS systems are expected to depend in a very sensitive way on the magnetization of these materials via the sp-d exchange process.

The first indication of differences between the magnetic behavior in 2D and bulk DMS samples came from Raman scattering measurements on superlattices containing thin layers of  $\text{Cd}_{0.5}\text{Mn}_{0.5}\text{Te}$  [4]. In bulk  $\text{Cd}_{0.5}\text{Mn}_{0.5}\text{Te}$ , magnon lines are prominently present in Raman spectra, reflecting the formation of magnetic order, even if only short ranged in nature. In contrast, the spectrum from the superlattice showed only well-resolved paramagnetic resonance Raman lines, indicating that the layered samples showed paramagnetic rather than magnetically ordered behavior.

Systematic studies of the change in magnetic behavior with decreasing dimensionality were carried out on superlattices consisting of metastable (zinc-blende) MnSe epilayers (ranging from  $\sim 8 \text{ \AA}$  to around  $30 \text{ \AA}$ ) sandwiched between "thick" ( $45 \text{ \AA}$ ) layers of non-magnetic ZnSe [6,7]. We might expect three dimensional MnSe layers to show long-range AFM-III. Indeed, photoluminescence and magnetization studies suggested that the thicker layers did exhibit antiferromagnetic ordering. However, as the layers were made thinner, approximating two dimensionality, there were no signs of antiferromagnetic ordering and the layers remained paramagnetic even at the lowest temperatures studied.

Similar conclusions were obtained during low-temperature magnetic susceptibility studies in  $\text{Cd}_{1-x}\text{Mn}_x\text{Te}$  layers for various layer thicknesses and various values of  $x$ , using a SQUID magnetometer (Fig. 4) [5]. Briefly, thick  $\text{Cd}_{1-x}\text{Mn}_x\text{Te}$  layers ( $d = 85 \text{ \AA}$ ) exhibited a well-defined cusp at a temperature closely corresponding to the spin-glass transition in the bulk. However, as the layers became progressively thinner, the cusp in the susceptibility became distorted, and eventually disappeared, giving way to a monotonic paramagnetic behavior.

All these studies suggest that magnetic ordering in DMS alloys undergoes a drastic change in the limit of two dimensionality. It is unclear at present whether the inability of quasi-2D DMS layers to order antiferromagnetically is a fundamental consequence of reduced dimensionality or whether it might be a result of interface disorder. More work is needed to clarify the magnetism

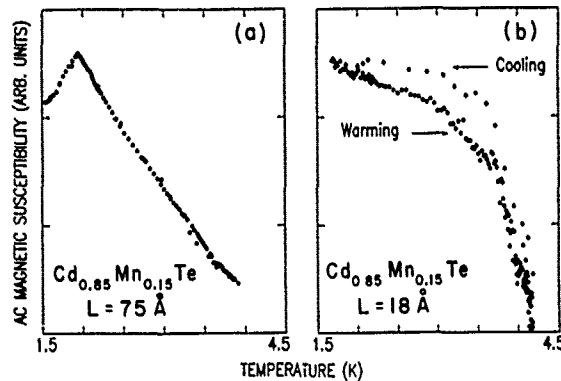


Fig.4. Magnetic susceptibility as a function of temperature observed in epitaxial layers of  $\text{Cd}_{0.85}\text{Mn}_{0.15}\text{Te}$  for two different thicknesses. The spin-glass-like transition cusp is well defined for the 75 Å layer, but disappears for the 18 Å layer [5].

of these 2D DMS layers. In this context, we believe that it is important to grow strain-free DMS layers, since the absence of strain-related distortions would simplify any attempted theoretical models. For example, instead of growing strained MnSe layers between ZnSe layers, one may try using  $\text{Cd}_{0.55}\text{Zn}_{0.45}\text{Se}$  as a lattice-matched non-magnetic buffer.

#### Neutron Scattering Studies of Magnetic Ordering in DMS Epilayers

The most direct information about magnetic ordering in DMS is obtained from neutron scattering studies of DMS with high Mn concentrations ( $x > 0.3$ ). Since epilayers of  $\text{Cd}_{1-x}\text{Mn}_x\text{Se}$  and  $\text{Zn}_{1-x}\text{Mn}_x\text{Se}$  can now be grown over a much wider range of  $x$  by MBE, it is possible to examine magnetic ordering over the entire range  $0.3 < x < 1$ . This allows us to address a fundamental question: what happens as an FCC Heisenberg antiferromagnet (such as zinc-blende MnSe) is randomly diluted with non-magnetic components (such as Cd)? Is there a gradual decrease of the magnetic correlation length, or might there be a sudden breakdown of long-range AFM-III order at some critical concentration? Until recently, such questions were of academic interest because neutron scattering studies of bulk crystals have necessarily been limited to Mn concentrations below the maximum allowable in bulk growth (for instance,  $x = 0.50$  in  $\text{Cd}_{1-x}\text{Mn}_x\text{Se}$ ). However, we have now been able to demonstrate the *first* neutron scattering measurements in a DMS alloy with Mn concentration beyond the limits imposed by bulk growth [16]. The experiments were carried out on  $\text{Cd}_{1-x}\text{Mn}_x\text{Se}$  epilayers with  $x = 0.75$  (Fig. 5). The spectra clearly show the presence of magnetic peaks which are consistent with AFM-III. Further, a comparison of the half-widths of the magnetic scattering peaks with those of the nuclear scattering peaks indicate *long-range* magnetic ordering within the plane of the epilayer. This is the very first observation of such long range order in any DMS. These results also establish the viability of neutron scattering as a tool for probing magnetic order in thin DMS films. A systematic program to investigate the magnetic order in  $\text{Cd}_{1-x}\text{Mn}_x\text{Se}$  ( $0.5 < x < 1$ ) is currently underway.



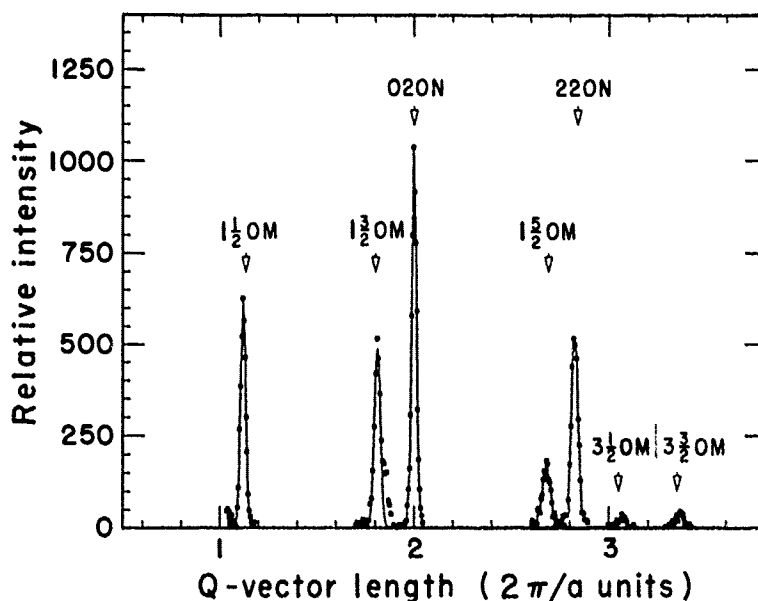


Fig.5. Neutron scattering data from a 2μm thick epilayer of  $Cd_{0.25}Mn_{0.75}Se$  grown on [100] GaAs. Note that the full width at half maximum of the magnetic scattering peaks is comparable to that of the nuclear scattering peaks, indicating long-range magnetic order [16].

#### Ordered DMS Structures

We now examine a more speculative aspect of DMS epitaxial structures -- the creation of *ordered* DMS alloys by the growth of short period superlattices i.e. superlattices in which the period is of the order of a few monolayers. The growth of such alloys by MBE has already been demonstrated in III-V materials [17]. The ALE technique might also naturally lend itself to such "atomic architecture" by allowing the deposition of atomic monolayers one at a time. For instance, one can imagine the growth of a superlattice consisting of alternate single layers of ZnSe and MnSe. This will then result effectively in a  $Zn_{0.5}Mn_{0.5}Se$  structure with an ordered distribution of Mn ions (i.e.,  $ZnMnSe_2$ ). Similarly, by using different sequences of ZnSe and MnSe layers, ordered versions of  $Zn_{1-x}Mn_xSe$  with various values of  $x$  can be made. A comparison between the magnetic properties of such "atomically ordered" DMS systems and those of DMS alloys with identical concentrations of *randomly* distributed Mn will help elucidate the role of randomness in determining the magnetism of DMS alloys.

Such short period superlattices can also permit us to tailor magnetic interactions by selecting different growth directions. The idea is to vary the number of nearest magnetic neighbors and the distance between nearest Mn ions by "stacking" appropriate  $\{hkl\}$  planes [18]. Consider, for instance, a superlattice grown in the  $[111]$  direction consisting of MnSe layers *isolated* from each other by a few layers of non-magnetic ZnSe (e.g., ZnSe-ZnSe-MnSe-ZnSe-ZnSe-, etc.). It is easy to see that the number of nearest neighbors of each Mn ion is reduced from  $z = 12$  in the bulk, to  $z = 6$ . Another interesting situation is provided by stacking  $\{110\}$  planes. Here, it can be shown that isolated  $\{110\}$  planes of MnSe will contain linear "chains" of strongly coupled Mn ions, with  $z = 2$ . An even more interesting case is that of growth in the  $[201]$  direction. Here, an appropriate sequence of atomic layers of Zn, Mn and Se can produce a famatinite version of  $\text{Zn}_{0.75}\text{Mn}_{0.25}\text{Se}$  (i.e.,  $\text{Zn}_3\text{MnSe}_4$ , see Fig. 6). Note that in this structure the closest Mn neighbors are at a distance corresponding to the *second nearest neighbor* distance in a random DMS alloy. All these artificially engineered structures have two elements in common: they enable us to reduce the antiferromagnetic Mn-Mn interactions by decreasing the number of interacting Mn ions and by increasing the nearest neighbor distance between Mn ions. In general, this will increase the magnetization, and hence have a profound effect on both the magnetic and electronic properties of these materials. The growth of such structures has not yet been demonstrated, but we strongly believe it to be worthy of exploration.

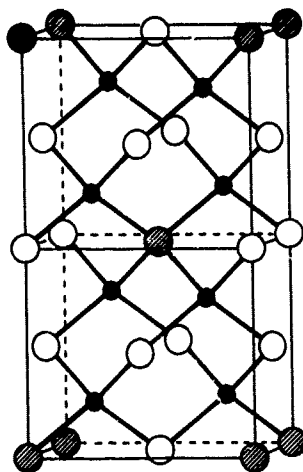


Fig.6. An ordered form of  $\text{Zn}_{0.75}\text{Mn}_{0.25}\text{Se}$  (i.e.,  $\text{Zn}_3\text{MnSe}_4$ ) known as famatinite. The Mn, Zn and Se ions are shown as hatched, blank and black circles, respectively.

#### EFFECTS OF SP-D EXCHANGE

A physical property that makes the DMS alloys extremely interesting is the sp-d exchange coupling between the localized Mn moments and the band electrons [3]. This coupling strongly affects the energies of the band and impurity states (particularly in the presence of an external

magnetic field), and leads to significant modifications of various electronic properties of DMS materials. In particular, the sp-d exchange interaction has a dramatic effect on the spin splitting of the electronic states. The spin splitting is best described by an effective g-factor which is directly related to the magnetization of the DMS lattice. Since the magnetization is a sensitive function of temperature and magnetic field, the effective g-factor -- and hence the spin splitting -- will also vary over a broad range.

This variation of the band structure with temperature and magnetic field can result in new phenomena in quantum wells and superlattices. Several such effects have been postulated in the literature. Here, we describe some of the unusual phenomena which may be expected to occur in the quantum well structures involving DMS alloys. The effects described here depend on two important features, namely: a) the spin splitting of the electronic states in DMS alloys is much larger than in non-magnetic semiconductors; and b) the spin splitting of the electronic states in the DMS material can be comparable to the ionization energy of shallow impurities even at moderate magnetic fields.

#### Quantum Well Structures Involving Doped DMS Layers

Selectively doped quantum well structures involving DMS alloys can be expected to show a variety of effects due to magnetic-field-induced changes in the relative position of the donor levels in the barriers with respect to the confined electronic states in the wells. For example, consider a non-magnetic (i.e., non-DMS) well between doped DMS barriers. Such a lattice-matched structure may be achieved by using a  $\text{Cd}_{1-y}\text{Zn}_y\text{Se}$  well between n-type  $\text{Cd}_{1-x}\text{Mn}_x\text{Se}$  barriers. By an appropriate choice of well and barrier parameters, the ground electronic state  $E_1$  in the well can be situated slightly below the donor level in the barrier (Fig. 7).

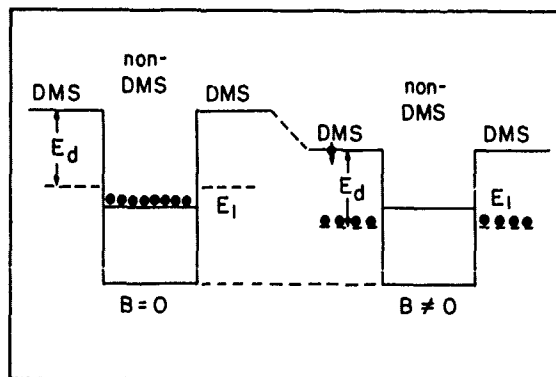


Fig.7. A non-DMS quantum well between DMS barriers, indicating the sp-d exchange-induced freeze-out. Only the ground state (spin-down) is shown for non-zero magnetic field.

At low temperatures, the donor electrons will in this situation transfer to the  $E_1$  states, yielding the sample conducting in two dimensions. However, when a magnetic field is applied, one of the spin components of the donor state will shift strongly down in energy, while the position of the  $E_1$  state in the non-magnetic material will remain relatively unaffected. The electrons can then "spill back" into the donor states, resulting in a sudden increase of the sample resistivity -- an effect that may be termed a magnetic "freeze-out" (Fig. 7).

A reverse effect (magnetic-field-induced "boil off") can be expected to occur in a structure consisting of DMS wells and selectively doped n-type non-magnetic barriers. A viable example of such a structure is a  $\text{Cd}_{1-x}\text{Mn}_x\text{Se}$  well between n-type doped ZnSe barriers.

A final example involving doped DMS layers is the possibility of sequential magnetic-field-tunable resonant tunneling. This may be achieved by employing a multiple quantum well structure with non-magnetic barriers (say, ZnSe) and DMS wells (say,  $\text{Cd}_{1-x}\text{Mn}_x\text{Se}$ ). One may envision a situation such as the one depicted in Fig. 8. Here, the application of a magnetic field leads to splitting of the spin-up and the spin-down states in the quantum wells. Then, an electric field is applied so as to make the quantum well states resonant with the donor levels in the manner shown in Fig. 8. This will lead to a spin-selective tunnelling through the barriers. Further, as the excited spin-up electron falls to the spin-down ground state in the well, a circularly polarized far-infrared photon is emitted. Thus the resonant tunneling device depicted in Fig. 8 may operate as a far-infrared source (and possibly a far-infrared laser), which can be tuned by simultaneously adjusting the applied electric and magnetic fields.

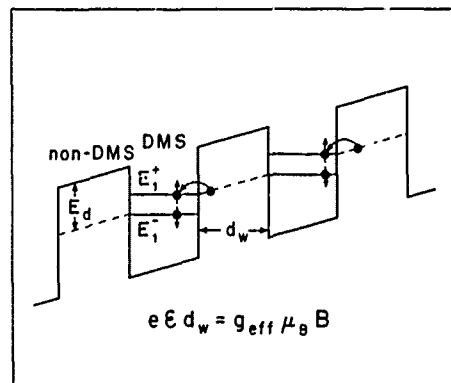


Fig. 8. DMS quantum wells between doped non-DMS barriers in the presence of an external magnetic and electric field, showing sequential resonant tunneling between spin-split states in the wells facilitated by the donor levels in the barrier.

#### Magnetic-field-induced Superlattices using Wide Gap DMS

Referring to Fig. 2, it is clear that it should be possible to create a  $\text{Cd}_{1-x}\text{Mn}_x\text{Se}/\text{Cd}_{1-y}\text{Zn}_y\text{Se}$  superlattice with appropriate  $x$  and  $y$  values such that the energy gaps of the two materials are approximately the same. In the absence of a magnetic field, the potential seen by electrons will

be relatively uniform, or --- depending upon the band offset -- might consist of very shallow wells in a type-II superlattice configuration. However, when a magnetic field is applied, the band-edge of the  $\text{Cd}_{1-x}\text{Mn}_x\text{Se}$  layer will undergo a much larger shift than that of the non-magnetic layer because of the spin splitting. The application of a magnetic field hence induces the formation of a superlattice, and should lead to dramatic changes in the photoluminescence spectra, particularly at low temperatures, where energy shifts of over 100 meV are expected.

Another possible scenario is that the  $\text{Cd}_{1-x}\text{Mn}_x\text{Se}/\text{Cd}_{1-y}\text{Zn}_y\text{Se}$  superlattice may be a type-I superlattice in zero field. However, upon application of a magnetic field, the valence band edge can shift downwards sufficiently to induce a change to a type-II superlattice. Once again, such an effect will be dramatically manifested by a change in the photoluminescence spectra.

The illustrative examples cited above are by no means exhaustive. The wide range of effects based on the sp-d exchange, together with the rich spectrum of phenomena made possible by the quantum well and superlattice physics, will without doubt make layered DMS structures extremely attractive to both experimentalists and theoreticians, in the fundamental as well as the applied context for some time to come.

#### ACKNOWLEDGEMENTS

The authors wish to acknowledge the support of NSF Grant No. DMR-8520866 and DARPA-ONR Grant No. N00014-86-K-0760.

#### REFERENCES

1. R. L. Gunshor, L. A. Kolodziejski, A. V. Nurmikko, and N. Otsuka, *Annual Rev. Mater. Sci.*, **18**, 325 (1988).
2. M Pessa, J. Lilja, O. Jylha, M. Ishiko and H. Asonen, in *Diluted Magnetic Semiconductors*, edited by R. L. Aggarwal, J. K. Furdyna and S. von Molnar (Materials Research Society, Pittsburgh, PA, 1987), Vol. 89, p. 303.
3. J. K. Furdyna, *J. Appl. Phys.* **64**, R29 (1988).
4. S. Venugopalan, L. A. Kolodziejski, R. L. Gunshor, and A. K. Ramdas, *Appl. Phys. Lett.* **45**, 974 (1984).
5. D. D. Awschalom, J. M. Hong, J. L. Chang and G. Grinstein, *Phys. Rev. Lett.* **59**, 1733 (1987).
6. L. A. Kolodziejski, R. L. Gunshor, N. Otsuka, B. P. Gu, Y. Hefetz, and A. V. Nurmikko, *Appl. Phys. Lett.* **48**, 1482 (1986).
7. D. Lee, S. K. Chang, H. Nakata, A. V. Nurmikko, L. A. Kolodziejski and R. L. Gunshor, *J. Phys., Colloq.*, **C5**, 311 (1987).
8. J. Kossut and J. K. Furdyna, in *Diluted Magnetic Semiconductors*, edited by R. L. Aggarwal, J. K. Furdyna, and S. von Molnar (Materials Research Society, Pittsburgh, PA, 1987), Vol. 89, p. 97.

9. R. B. Bylsma, W. M. Becker, T. C. Bonsett, L. A. Kolodziejski, R. L. Gunshor, M. Yamanishi, and S. Datta, *Appl. Phys. Lett.* **47**, 1039 (1985).
10. R. N. Bicknell, N. C. Giles-Taylor, J. F. Schetzina, N. G. Anderson, and W. D. Laidig, *Appl. Phys. Lett.* **46**, 238 (1985).
11. B. T. Jonker, J. J. Krebs, S. B. Qadri, and G. A. Prinz, *Appl. Phys. Lett.* **50**, 848 (1987).
12. B. T. Jonker, J. J. Krebs, and G. A. Prinz, *Appl. Phys. Lett.* **53**, 450 (1988).
13. N. Samarth, H. Luo, J. K. Furdyna, S. B. Qadri, Y. R. Lee, A. K. Ramdas and N. Otsuka, *Appl. Phys. Lett.* (to be published).
14. J. K. Furdyna and N. Samarth, *J. Appl. Phys.* **61**, 3526 (1987).
15. T. M. Giebultowicz and T. M. Holden, in *Semiconductors and Semimetals*, R. K. Willardson and A. C. Beer, Treatise Editors; J. K. Furdyna and J. Kossut, Volume Editors (Academic, Boston, 1988), Vol. 25, p. 125.
16. P. Klosowski, T. Giebultowicz, N. Samarth, H. Luo, and J. K. Furdyna (unpublished).
17. A. C. Gossard, *IEEE J. Quant. Electronics* **QE-22**, 1649 (1986).
18. D. Heiman, E. D. Isaacs, P. Becla, and S. Foner, in *Diluted Magnetic Semiconductors*, edited by R. L. Aggarwal, J. K. Furdyna, and S. von Molnar (Materials Research Society, Pittsburgh, PA, 1987), Vol. 89, p. 21.

METASTABLE ZINCBLLENDE MnTe AND MnSe:  
MBE GROWTH AND CHARACTERIZATION

R.L.GUNSHOR\*, L.A.KOŁODZIEJSKI\*\*, M.KOBAYASHI\*, A.V.NURMIKKO\*\*\*,  
and N.OTSUKA\*

\* Purdue University, West Lafayette IN 47907

\*\* Permanent Address: Massachusetts Institute of Technology,  
Cambridge, MA 02139

\*\*\* Brown University, Providence RI 02912

ABSTRACT

Epilayers of metastable zincblende MnSe and MnTe have been grown by molecular beam epitaxy. The MnSe structures have been used to study magnetic ordering in thin layers by means of optical and magnetic measurements. Preliminary optical reflectance measurements performed on samples of zincblende MnTe indicate a bandgap of approximately 3.15eV, while double barrier quantum structures demonstrate optical transitions corresponding to 2D electron and hole confinement. Optical measurements further provide insight into the band offsets existing between MnTe and CdTe, as well as between MnTe and ZnTe epilayers.

INTRODUCTION

Molecular beam epitaxy (MBE), is a nonequilibrium growth technique that has allowed the fabrication of compounds having differing crystal structures from those exhibited in equilibrium. One recent illustration of metastable growth using MBE was the formation of epilayers of the zincblende phase of the magnetic semiconductor MnSe [1]; MnSe exists in the NaCl crystal structure in equilibrium. The optical, magnetooptical and magnetic properties of structures, incorporating zincblende MnSe layered with ZnSe in a variety of superlattice structures, were described [2]. The magnetic properties of the ultrathin MnSe were determined by the degree of Zeeman splitting of optical transitions induced by application of a magnetic field. Complementary information was obtained by direct determination of the magnetization using a SQUID magnetometer. The first epitaxial layers of the zincblende phase of MnTe have also been grown. The growth studies were undertaken in response to considerable speculation in recent years concerning the physical properties of the hypothetical zincblende MnTe [3-7]. A series of double barrier heterostructures were fabricated with MnTe forming the barrier layers for quantum wells of either CdTe or ZnTe; thick epilayers of zincblende MnTe have been grown to thicknesses of 0.5 $\mu$ m. Optical transitions from the structures provide information with regard to the bandgap of the zincblende MnTe, as well as insight into the band offsets when layered with either CdTe or ZnTe. The microstructure of both MnSe and MnTe epilayers were characterized using transmission electron microscopy (TEM) and X-ray diffraction; optical properties were studied using reflectance, photoluminescence, Raman, and resonant Raman spectroscopies.

## ZINCBLLENDE MnSe

The existence of zincblende MnSe is a consequence of the kinetic (non-equilibrium) nature of the MBE growth method employed; bulk crystals of MnSe have the NaCl crystal structure. Extrapolations of data on lattice constant and bandgap, obtained for zincblende (Zn,Mn)Se epilayers with up to 66% Mn, predict a bandgap and lattice constant for zincblende MnSe of 3.4 eV (6.5 K) and 5.93 Å, respectively [8]. The implied lattice constant mismatch for a MnSe/ZnSe heterostructure is expected to be about 4.7%. A variety of superlattice structures composed of ZnSe layered with ultrathin MnSe (3 to 32 Å) have been grown using a Perkin-Elmer model 400 MBE system. Three separate effusion cells containing elemental, high purity, vacuum distilled Zn, Se, and Mn were used. All films were grown at a calibrated substrate temperature of 400°C on n<sup>+</sup> Si-doped GaAs (100) substrates with a growth rate of 0.5–1.5 Å/sec. Each superlattice was grown on a 2–2.5 μm ZnSe buffer layer.

The zincblende MnSe served as the barrier layer when combined with ZnSe in superlattice structures. By controlling the thickness of, and spacing between, layers of the magnetic semiconductor, an opportunity was provided to investigate the magnetic properties of ultrathin layers of a magnetic semiconductor. It was crucial in a study of this type however, for the MnSe layer thickness to be controlled to one monolayer. RHEED intensity oscillations were employed during the superlattice fabrication to provide the requisite one monolayer resolution.

A series of "comb-like" superlattices, consisting of 30 to 100 periods, were grown with MnSe layer thicknesses of one, three, and four monolayers [1]; the MnSe layers were separated by approximately 45 Å of ZnSe. For later comparison of physical properties, the superlattices with one and three monolayer MnSe thicknesses were grown with and without growth interruption [9] at each interface. A fourth related superlattice structure consisted of 30 periods containing ten monolayers (32 Å) of MnSe alternated with 24 Å of ZnSe.

Photoluminescence measurements, performed in the presence of an external magnetic field (up to 5 Tesla), were used initially to determine the magnetic behavior of the MnSe/ZnSe magnetic superlattices; complementary information was acquired through magnetization measurements using a SQUID magnetometer [2,10,11]. In photoluminescence, the observed magneto-optical shifts of the ground state excitonic transition originate from the exchange interaction between electron-hole states of the superlattice and the magnetic moments of the Mn ions in the thin MnSe layers. In the absence of a magnetic field, the observed optical transition energies are in agreement with predictions of a Krönig-Penney model for the ZnSe-based superlattices with ultrathin MnSe barriers. These estimates were performed using a bandgap energy for zincblende MnSe of 3.4 eV, which is the value predicted by extrapolation from optical data obtained on (Zn,Mn)Se epilayers. In the absence of band offset information in these highly strained structures, the valence band offset was taken to be zero.

Bulk MnSe with the rock-salt crystal structure is known to be an antiferromagnetic semiconductor. Susceptibility measurements [12], performed on Bridgman-grown bulk crystals of Zn<sub>1-x</sub>Mn<sub>x</sub>Se existing in the wurtzite phase (the maximum x value obtained was 0.57), indicated an increased tendency towards



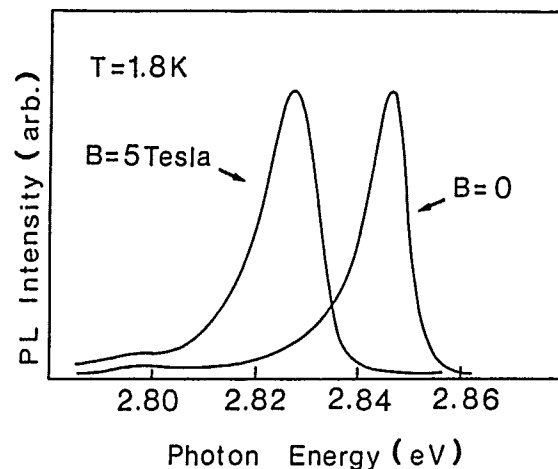


Figure 1 Exciton luminescence from a ZnSe/MnSe superlattice (3 monolayers of MnSe) showing a well defined superlattice bandgap which is strongly influenced in an external magnetic field.

antiferromagnetic ordering (at low temperature) as the Mn mole fraction was increased. Magneto-optical measurements on zincblende MBE-grown epilayers also showed a reduction of Zeeman shifts with increasing Mn mole fraction; the decreasing amount of red shift has been attributed to the increasing role of antiferromagnetic coupling of the Mn-ion spins. The similarity in magnetic behavior between zincblende and wurtzite (Zn,Mn)Se crystals was not surprising, as nearest neighbor distances are very nearly the same for the two crystal structures. For ultrathin layers of MnSe (within MnSe/ZnSe superlattices), some reduction in the antiferromagnetic interaction can be expected due to the decrease of nearest neighbor (Mn) spins. In the monolayer limit for (100)-oriented layers, the reduction is a factor of three. Nonetheless, a "perfect" MnSe monolayer is still expected to show definite antiferromagnetic ordering at low lattice temperatures ( $T < 50\text{K}$ ). However, quite to the contrary, large Zeeman shifts were observed in the superlattices, implying a significant degree of nearly paramagnetic behavior (Figure 1). The largest Zeeman shifts were measured for superlattices containing MnSe layer thicknesses approaching the monolayer ( $3\text{\AA}$ ) limit; in contrast, no Zeeman shift was observed for the superlattice containing ten monolayers ( $32\text{\AA}$ ) of MnSe in each period.

To confirm the magnetic behavior inferred from optical data, direct magnetization measurements [2,11] were made using a SQUID magnetometer. Subtracting the diamagnetic (negative) GaAs substrate contribution, the striking result exhibited by the superlattice samples was the large positive contribution at low temperature. In strong contrast, the  $400\text{\AA}$  MnSe epilayer behaved qualitatively as a normal bulk antiferromagnetic insulator at lower temperatures, although its high temperature susceptibility was clearly affected by the many misfit dislocations present due to the lattice constant mismatch.

Although further studies are necessary to rigorously identify the origin of the observed frustrated antiferromagnetism, the present interpretation is that the tendency for spins to align in an external magnetic field arises

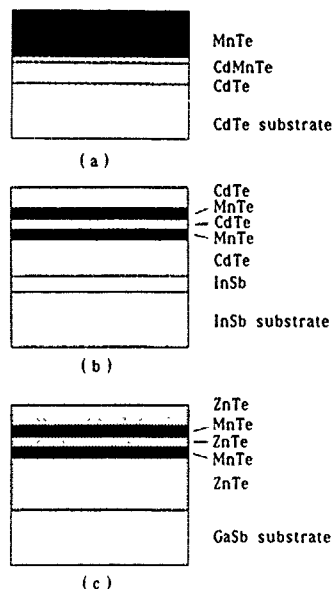


Figure 2 Schematic diagram of sample structures used in the study. (Detailed descriptions are provided in the text.)

from "loose" spins at the MnSe/ZnSe heterointerfaces. The thinner the MnSe layer, the greater is the influence of the heterointerface, whereas for thicker MnSe layers, the antiferromagnetic "inner core" begins to dominate the magnetic behavior [2]. The magnetic 'probes' examine microstructure on a scale of the order of chemical bond lengths due to the short range nature of the superexchange paths in insulators such as MnSe (nearest neighbor Mn-ions coupled through the intervening Se anion). The magnetic measurements thus have an enhanced sensitivity to deviations from 'perfect' atomic arrangements (vs. ideal bulk) within a monolayer or so at the interface region. Some qualitative arguments can be applied concerning the roles of intrinsic and extrinsic microstructure effects at the MnSe/ZnSe heterointerfaces which are thought to underlie the frustration of antiferromagnetic interactions seen in the experiments. Diffusion or chemical intermixing effects can provide regions of diluted Mn-ion concentration, but would also cause significant linewidth broadening of the luminescence beyond what is observed. On the other hand, while two-dimensional growth is characteristic of this superlattice system [1,9,13,14], the possibility of incomplete layer growth during the heteroepitaxy cannot be eliminated. Finite size islands at the interfaces, i.e., two-dimensional clusters, can be effective in frustrating antiferromagnetic ordering.

#### ZINCBLLENDE MnTe

As in the case of MnSe, the MBE growth technique has provided thin films of zincblende MnTe; bulk crystals of MnTe have the hexagonal NiAs crystal structure. The variation of lattice parameter and excitonic bandgap with Mn concentration for zincblende (Cd,Mn)Te epilayers suggests values of 6.328 Å and 3.18 eV (10K) [15], respectively for zincblende MnTe. The

difference in bandgap energy between the two crystal structures is especially dramatic as the NiAs phase has a bandgap of 1.3eV [16].

Figure 2 shows schematically three types of structures in which the MnTe has been incorporated: i) thick epitaxial layers (up to 0.5  $\mu\text{m}$ ), ii) double barrier quantum well structures where MnTe forms the barrier when layered with CdTe, and iii) MnTe is the barrier when layered with ZnTe. CdTe substrates were used (obtained from Galtech) for the structures involving relatively thick epilayers of MnTe (Fig. 2a). The configurations having CdTe quantum wells (Fig. 2b) are grown using InSb substrates with a buffer layer of InSb. The InSb is grown in a separate chamber of the Perkin Elmer modular 430 MBE system and transferred under ultrahigh vacuum to a second chamber for MnTe and CdTe growth. The MnTe/ZnTe double barrier structures (Fig. 2c) employ GaSb substrates with buffer layers of ZnTe.

The commercially supplied, chemi-mechanically prepared bulk substrates are degreased, etched, and then subjected to a thermal etch prior to nucleation in the ultrahigh vacuum growth chamber. The CdTe (100) substrates were chemically etched with a 1%  $\text{Br}_2$ :methanol solution and mounted with Ga onto a molybdenum sample holder. Thermal treatment of the CdTe substrates consisted of elevating the substrate temperature to between 325 and 370°C, followed by a reduction of the temperature to 260°C for nucleation of the CdTe buffer layer. The degreased InSb (100) substrates were chemically etched in a 10:1 lactic/nitric acid solution for 90 seconds. The oxide was then desorbed in vacuum in the presence of an Sb flux at a substrate temperature ranging from 540-575°C. An InSb buffer layer was grown on the bulk InSb substrate to provide an optimal surface prior to nucleation of the MnTe/CdTe-based structures. The degreased GaSb(100) substrates were etched in HCl and mounted onto Mo blocks with In. Sb-stabilized surfaces resulted when thermal treatment occurred under an Sb flux at approximately 520-580°C. ZnTe buffer layers were then grown on the GaSb bulk substrates.

The majority of the data reported in this paper has been obtained from the series of MnTe/CdTe double barrier structures. In these structures the CdTe layers are grown (1.2Å/sec.) using a compound source, while the MnTe is grown at 300°C at a growth rate of 1.1Å/sec using elemental sources. The Te flux (in atoms/cm<sup>2</sup>-sec.) used for the growth of MnTe matched the intensity of the Te flux used during the growth of CdTe. The Mn flux was adjusted to approximate a unity cation/anion flux ratio. The ZnTe epilayers were grown using elemental sources at a substrate temperature of 320°C with a growth rate of 1.5Å/sec.

Reflection high energy electron diffraction (RHEED) was used to monitor the crystal structure and provided evidence of the growth of metastable zincblende MnTe. During the sequential growth of barrier and well layers for the MnTe/CdTe structures, the RHEED patterns appeared to be virtually identical with both exhibiting a (2x1) reconstruction. The zincblende phase of MnTe was also confirmed in x-ray diffraction ( $\theta$ -2 $\theta$  scans). The diffraction peaks obtained by x-ray diffraction measurements, performed on samples containing relatively thick epilayers of MnTe, could be identified as corresponding only to the zincblende phases of CdTe and MnTe (Figure 3).

The microstructure of MnTe epilayers and MnTe double barrier structures have been examined by cross-sectional transmission electron microscopy. The MnTe layers have the cubic

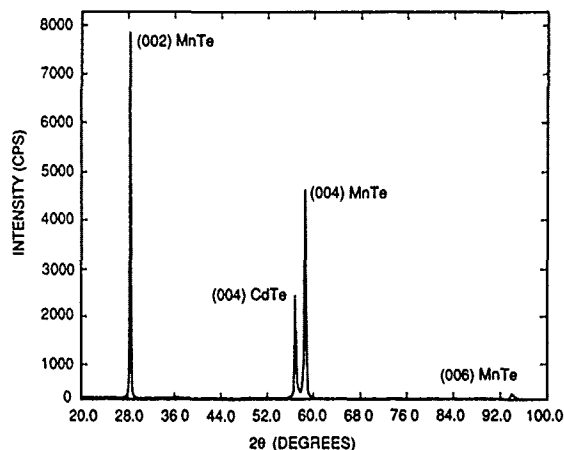


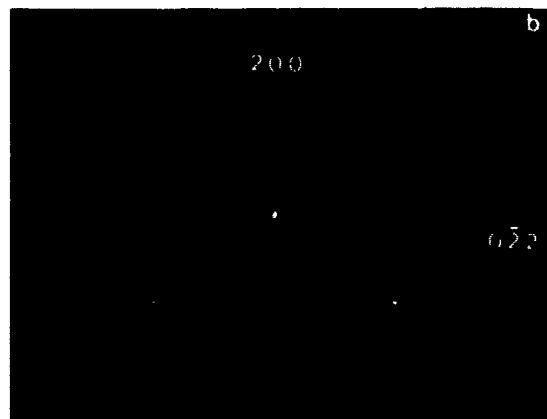
Figure 3 ( $\theta$ - $2\theta$ ) x-ray diffraction scan of a 0.5  $\mu$ m MnTe epilayer grown on a CdTe buffer layer.

zincblende structure and have formed epitaxially on CdTe or ZnTe epilayers. A high resolution image of the interface region between a 0.5  $\mu$ m MnTe epilayer and a CdTe buffer layer is shown in Fig. 4(a). The interface between the MnTe epilayer and the CdTe crystal is indicated by arrows. Fig. 4(b) is the [011] electron diffraction pattern obtained from the same area of the sample. It is seen from both the high resolution image and the diffraction pattern that the MnTe epilayer has a perfect epitaxial relation with the CdTe crystal. In the diffraction pattern, each diffraction spot of the MnTe crystal forms a pair with a spot of the CdTe crystal as expected from the cubic zincblende structure of the MnTe crystal. Nearly complete relaxation of the lattice mismatch at the interface due to formation of misfit dislocations is suggested by the degree of separation of  $0\bar{2}2$  type diffraction spots. A large number of stacking faults are seen along the interface in the high resolution image, but bright field and dark field images of the MnTe epilayer show that the density of these defects decrease considerably in the areas of the epilayer far from the interface. TEM examination of double barrier structures shows that the MnTe layers (having thicknesses of 30 to 40 Å) maintain coherent interfaces with CdTe layers to form strained-layer structures. The interfacial regions of the MnTe barrier layers appear to be free from dislocations or stacking faults.

In the four MnTe/CdTe/MnTe double barrier structures, spanning CdTe well thicknesses from approximately 56 Å to 28 Å, strong photoluminescence (PL), originating from the well, was detected in all samples, even under excitation at energies below the MnTe barrier layer absorption edge. Strong evidence for confinement effects is obtained from the systematic shifts to higher photon energies of the PL emission with decreasing CdTe quantum well thickness. For the narrowest well sample (28 Å), an overall average blueshift of nearly 400 meV was realized. (Note that separate optical measurements on (bulk) thin MnTe films have yielded a measurement for the s-p bandgap of 3.2 eV.) The PL emission is usually composed of two emission lines which are 40-



Figure 4(a) High resolution (HREM) image of the MnTe epilayer/CdTe epilayer interface. (b) [011] electron diffraction pattern taken from this area.



60 meV apart. These lines, individually 20meV in width, may be associated with transitions between  $n=1$  heavy- and light-hole like confined valence band states and the  $n=1$  conduction band state. Further study of the lineshape details is needed and is in progress. Important ingredients acting to shape the photoluminescence features include the role of the large lattice mismatch, the degree and nature of exciton binding, the exchange of electron-hole states with the Mn-ion d-electron moments, and possible deviations from the ideal square well problem due to interfacial steps.

Initial Raman scattering measurements (measured under near resonance conditions vs. the  $n=1$  quantum well transition) show a well resolved CdTe longitudinal optical phonon mode (LO), as well as a broader MnTe mode. In order to further examine issues of confinement, the magnetic field dependence of the PL emission has been examined up to 40kG (4 Tesla). In diluted magnetic semiconductors (e.g., (Cd,Mn)Te), giant Zeeman effects are seen at low lattice temperatures due to the exchange coupling of the

exciton states to the Mn-ion d-electron states. In the fully antiferromagnetic state of bulk-like MnTe, such Zeeman effects should be much reduced in weak magnetic fields. The situation in the quantum well samples considered here involves, however, relatively thin layers of MnTe (35Å) under large biaxial lattice mismatch strain. Experimentally, the PL shows measurable Zeeman shifts from a few meV up to 10 meV depending on the sample, as well as some lineshape distortion. The Zeeman shifts are small, however, on the scale of such shifts which would be expected under conditions of significant Cd/Mn interdiffusion in the quantum wells. Ongoing magneto-optical spectroscopy is focussing on the question of the implications of the observed Zeeman effects in terms of the magnetic properties of the MnTe layers, with emphasis on the nature and degree of antiferromagnetic ordering.

#### SUMMARY

The MBE growth technique has presented an opportunity for the growth of novel structures incorporating previously hypothetical magnetic semiconductors, specifically the zincblende phases of MnSe and MnTe. The MnSe structures described in this paper were used to study magnetic ordering in thin layers by means of optical and magnetic measurements. Double barrier quantum structures exhibit 2D electron and hole confinement and serve to confirm the zincblende MnTe bandgap at 3.2eV.

#### ACKNOWLEDGEMENT

The authors gratefully acknowledge the assistance of A.K. Ramdas, Y.R.Lee, D.L. Mathine, S.M. Durbin, S. Datta, D.R. Menke, J. Han, Sungki O, D. Lee, S.K. Chang, Q. Fu, N. Pelekanos, and D. Lubelski. Research support was provided by the Office of Naval Research under N00012-82-K0563, and N00014-82-K0563, Air Force Office of Scientific Research grant AFOSR83-0237, Defense Advanced Research Projects Agency/Office of Naval Research URI contract N00014-86-K0760, and National Science Foundation equipment grant ECS-8606241.

#### REFERENCES

1. L.A.Kolodziejski, R.L.Gunshor, N.Otsuka, B.P.Gu, Y.Hefetz, and A.V.Nurmikko, Appl. Phys. Lett. **48**, 1482 (1986).
2. S.-K.Chang, D.Lee, H.Nakata, A.V.Nurmikko, L.A.Kolodziejski, and R.L.Gunshor, J.Appl.Phys. **62**, 4835 (1987).
3. S.H.Wei and A.Zunger, Phys. Rev. Lett. **56**, 2391, (1986).
4. H.Ehrenreich, Science **235**, 1029 (1987).
5. J.Tersoff, Phys. Rev. Lett. **56**, 2755 (1986).
6. J.K.Furdyna, and J.Kossut, Superlattice and Microstructure **2**, 89 (1986).
7. J.O.McCaldin, and T.C.McGill, J Vac. Sci. Technol. **B6**, 1360 (1988).
8. L.A.Kolodziejski, R.L.Gunshor, N.Otsuka, S.Datta, W.M.Becker, and A.V.Nurmikko, IEEE J.Quantum Electron. **QE-22**, 1666 (1986).
9. L.A.Kolodziejski, R.L.Gunshor, A.V.Nurmikko, and N.Otsuka, in *Thin Film Growth Techniques for Low Dimensional Structures*, R.F.C.Farrow, S.S.P.Parkin, P.J.Dobson, J.H.Neave, and A.S.Arrott, Eds., New York: Plenum Press, (1987), 247.

10. D.Lee, S.-K.Chang, H.Nakata, A.V.Nurmikko, L.A.Kolodziejski, and R.L.Gunshor, : Mat. Res. Soc. Proc., 77, 253 (1987).
11. D.Lee, S.-K.Chang, H.Nakata, A.V.Nurmikko, L.A.Kolodziejski, and R.L.Gunshor, J.del Physique C5, 311 (1987).
12. J.K.Furdyna, R.B.Frankel, and U.Debska, unpublished.
13. R.L.Gunshor, L.A.Kolodziejski, N.Otsuka, B.P.Gu, Y.Hefetz, and A.V.Nurmikko, Superlattice and Microstructures 3, 5 (1987).
14. L.A.Kolodziejski, R.L.Gunshor, N.Otsuka, B.P.Gu, Hefetz, A.V.Nurmikko, J.Crystal Growth 81, 491 (1987).
15. Y.Lee and A.K.Ramdas, Phys. Rev. B38, 10600 (1988).
16. J.W.Allen, G.Lucovsky, and J.C.Mikkelsen, Solid State Commun. 24, 367 (1977).

# MBE Growth and Characterization of Fe- and Co-Based Diluted Magnetic Semiconductors

B.T. Jonker, J.J. Krebs and G.A. Prinz  
Naval Research Laboratory, Washington, D.C. 20375-5000

X. Liu and A. Petrou  
Dept. of Physics & Astronomy, SUNY Buffalo, NY 14260

L. Salamanca-Young  
Dept. of Chemical & Nuclear Engineering  
University of Maryland, College Park, MD 20742

## ABSTRACT

We have grown single crystal zincblende epilayers of the diluted magnetic semiconductors  $\text{Zn}_{1-x}\text{Fe}_x\text{Se}$  and  $\text{Zn}_{1-x}\text{Co}_x\text{Se}$  on GaAs(001) by molecular beam epitaxy. We summarize the growth and the structural, magnetic and optical properties of these materials, and contrast their properties with those of the more well-studied Mn-based family of diluted magnetic semiconductor (DMS) compounds. Both materials exhibit larger values for the band electron-magnetic ion and ion-ion exchange parameters than found in  $(\text{Zn},\text{Mn})\text{Se}$ . These values are most strongly enhanced in  $(\text{Zn},\text{Co})\text{Se}$ , which represents the first member of a new Co-based family of DMS compounds. Thus the incorporation of  $(\text{Zn},\text{Fe})\text{Se}$  and  $(\text{Zn},\text{Co})\text{Se}$  layers in quantum well and superlattice structures holds very exciting prospects for future work.

## INTRODUCTION

Diluted magnetic (or semimagnetic) semiconductors form an important subset of semiconducting compounds [1]. These materials are most commonly based on II-VI or IV-VI semiconductors, and are formed by the random substitutional incorporation of a magnetic ion for the cation in the host lattice. The resultant ternary or quaternary compounds exhibit a compositionally dependent band gap, lattice constant and effective mass typical of ternary alloy systems, and therefore share the advantages offered by lattice-matching and band gap tunability, which find such wide-spread application in modern device structures. In addition, the incorporation of the magnetic ions leads to a number of very interesting magneto-optic and magneto-transport properties which offer great potential for device applications.

The great majority of the work to date has focussed on Mn-based diluted magnetic semiconductor (DMS) materials, and several excellent review articles summarize their growth and properties [2-4]. These Mn-based compounds have been grown in both bulk and thin film form, the latter as single crystal epilayers using atomic layer epitaxy (ALE) [5] and molecular beam epitaxy (MBE) [6,7] techniques.

In the last decade [8,9], a small number of Fe-based DMS materials have been grown from the bulk, and have been shown to exhibit very different properties from their Mn-based counterparts. The difference in properties is due in part to the very different and rather unusual magnetic ground state of the  $\text{Fe}^{2+}$  ion in a tetrahedrally coordinated lattice, and to the energy levels the iron introduces relative to the band structure of the host semiconductor.  $\text{Hg}_{1-x}\text{Fe}_x\text{Se}$  ( $x \leq 0.12$ ) is one of the more well-studied of these materials, and has been found to exhibit significant improvements in material bonding and uniformity in composition relative to  $(\text{Hg},\text{Mn})\text{Se}$  [10,11]. In addition, the position of the  $\text{Fe}^{2+}$  level 230 meV above the conduction band minimum allows the  $\text{Fe}^{2+}$  to act as a resonant donor in this material, thereby establishing the Fermi level and producing improved stability in carrier concentration [11-13].

Even more recently, a number of Co-based DMS compounds have emerged [14-18], and show significant enhancements in the strength of the band electron-magnetic ion and ion-ion exchange interactions relative to either their Mn- or Fe-based counterparts. These interactions are the source of the pronounced magneto-optic and magneto-transport properties which make diluted magnetic semiconductors such an exciting class of materials. Thus the incorporation of Co is expected to be an especially fruitful area of study.



Although the growth and study of bulk materials is certainly an important aspect of this area of materials research, the growth of such relatively new DMS compounds as *epitaxial single crystal films* greatly enhances their potential for both basic study as well as for applied research and eventual incorporation in device structures. Therefore our own work has focussed on the growth of Fe- and Co-based DMS compounds as epilayers on bulk semiconductor substrates. The advantages of epilayers are numerous, not the least of which is an inherent compatibility with the methods of fabrication and planar configuration of today's monolithic microelectronic circuitry. Epilayers provide the basis for modern device structures ranging from simple heterostructures to quantum wells and superlattices, which in turn have come to form an important and growing subfield of study in semiconductor physics. These structures enable one to address the physics of carrier confinement and the behavior of two-dimensional electronic and magnetic systems. Another advantage of thin film growth is that one can often achieve higher magnetic ion concentrations with a non-equilibrium growth process such as MBE than in bulk samples, allowing the study of metastable phases and their accompanying magnetic behavior.

In this paper, we describe the growth and characterization of single crystal epilayers of two wide-gap DMS compounds:  $\text{Zn}_{1-x}\text{Fe}_x\text{Se}$  ( $0 < x \leq 1$ ), which has previously been grown and studied in bulk form for  $x \leq 0.22$  [19,20], and a new Co-based DMS,  $\text{Zn}_{1-x}\text{Co}_x\text{Se}$  ( $0 < x \leq 0.1$ ). We summarize their structural, magnetic and optical properties as determined to date from a variety of x-ray diffraction, transmission electron microscopy (TEM), SQUID magnetometry, magneto-reflectivity and photoluminescence data.

## EXPERIMENTAL

The (Zn,Fe)Se and (Zn,Co)Se samples were grown in a PHI Model 400 MBE system equipped with Auger electron spectroscopy (AES) and reflection high energy electron diffraction (RHEED) [14,21]. The substrates were GaAs(001) device grade wafers prepared in a conventional fashion using a 0.2% Br-methanol polish and a 5:1:1 etch of  $\text{H}_2\text{SO}_4:\text{H}_2\text{O}_2:\text{H}_2\text{O}$  followed by a deionized water rinse, and mounted with indium on a molybdenum sample holder. The substrate was briefly annealed in ultra-high vacuum just before growth to desorb the final oxide layer as monitored by AES, and then transferred to the growth chamber which contained elemental Knudsen cell sources of Zn, Se, Fe, Co and Mn. The epilayers were grown at a substrate temperature of 320-330°C at rates which ranged from 0.3-1.0  $\mu\text{m/hr}$  to a typical thickness of 1-1.5  $\mu\text{m}$ . Composition and thickness were determined by x-ray fluorescence measurements calibrated against known standards.

The films exhibit a single crystal zincblende structure for a wide range of magnetic ion concentrations and thicknesses, as summarized in Table I. This table simply summarizes the samples grown to date, and is not intended to place limits on the parameters listed. However, it becomes increasingly difficult to stabilize single crystal growth for thicker films as the magnetic ion concentration increases for both materials. In the case of  $\text{Zn}_{1-x}\text{Fe}_x\text{Se}$ , epilayers can readily be grown up to a thickness in excess of 2  $\mu\text{m}$  for Fe concentrations  $x \leq 0.22$ , but only up to some "critical" thickness which decreases as  $x$  increases to 1.0. This "critical" thickness varies somewhat and appears to depend on the growth parameters and substrate preparation. The growth of  $\text{Zn}_{1-x}\text{Co}_x\text{Se}$  exhibits similar behavior, although

Table I. Summary of magnetic ion concentrations and epilayer thicknesses grown by MBE.

DMS	Composition	Thickness
$\text{Zn}_{1-x}\text{Fe}_x\text{Se}$	$x \leq 0.22$	$t \geq 2 \mu\text{m}$
	$0.22 < x \leq 1.0$	$t < 2 \mu\text{m}$
$\text{Zn}_{1-x}\text{Co}_x\text{Se}$	$x \leq 0.074$	$t \geq 1 \mu\text{m}$
	$0.074 < x \leq 0.10$	$t < 1 \mu\text{m}$

maximum Co concentrations of only 10% have been achieved to date in single crystal thin films. Higher Co concentrations lead to polycrystalline growth for the MBE growth parameters investigated thus far.

### $\text{Zn}_{1-x}\text{Fe}_x\text{Se}$

#### Structural Characterization

As noted in Table I, (Zn,Fe)Se can be grown for the full range of concentrations up to the binary endpoint of pure FeSe, as has been reported for (Zn,Mn)Se [22]. Figure 1 shows a sequence of RHEED patterns obtained at various stages of growth for an FeSe epilayer grown with isotopically enriched  $\text{Fe}^{57}$  source material for later characterization with Mossbauer spectroscopy [23]. The diffraction patterns rapidly evolve from a rather spotty pattern produced by the GaAs(001) substrate (a,b) to one which exhibits well-defined streaks (c-e) at 10 to 100 Å of growth, characteristic of a predominantly two-dimensional mode of growth for a surface with a non-zero step density. Similar behavior is observed for all Fe concentrations. This is in contrast to our RHEED observations of (Zn,Mn)Se grown under identical conditions - in this case the initial mode of film growth appears to be predominantly three-dimensional as evidenced by the appearance and persistence of a spotty RHEED pattern, which later assumes a streaked character with continued deposition. In addition, for a given set of incident fluxes the (Zn,Fe)Se exhibits a higher growth rate than (Zn,Mn)Se under identical growth conditions, indicating a larger sticking coefficient, i.e., probability for bonding. We have also observed large changes (25%) in surface stoichiometry for (Zn,Mn)Se epilayers during electron beam exposures typical of AES measurements, resulting in a Zn-depleted and Mn-enriched surface, while no such variations have been found for the (Zn,Fe)Se surfaces. These observations indicate that the Fe not only promotes growth of the epilayer, but produces a more stable bonding configuration and superior material stability compared to the Mn-based compound, as well. Similar conclusions were drawn by Reifenberger and co-workers [10] in their study of (Hg,Fe)Se and (Hg,Mn)Se.

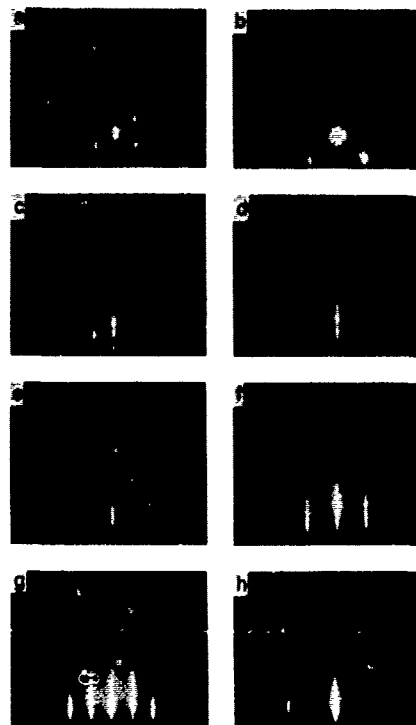


Figure 1. RHEED patterns obtained at various stages of growth of an FeSe epilayer on GaAs(001). The top frames show the pattern produced by the GaAs substrate with the electron beam incident along the (a)  $\langle 110 \rangle$  and (b)  $\langle 100 \rangle$  directions. (c) 10 Å FeSe,  $\langle 110 \rangle$ ; (d) 100 Å,  $\langle 100 \rangle$ ; (e) 100 Å,  $\langle 110 \rangle$ ; (f)-(h) 1,100 Å FeSe for the  $\langle 100 \rangle$ ,  $\langle 110 \rangle$  and  $\langle 130 \rangle$  azimuths, respectively.

A variety of x-ray diffraction techniques have been used to evaluate the lattice structure and crystalline quality of the epilayers.  $\theta$ - $2\theta$  scans of a number of Bragg reflections were obtained to determine the change in lattice parameter as a function of Fe concentration. The epilayer reflections exhibit well-resolved  $K\alpha_1$  and  $K\alpha_2$  components except where overlap with the substrate peaks occurs. The out-of-plane or perpendicular lattice parameter was measured directly from the  $(00\ell)$   $\ell = 2,4,6$  reflections and the Bragg equation using the Nelson-Riley extrapolation method. The in-plane or parallel lattice parameter was obtained from the  $(220)$ ,  $(440)$  and  $(444)$  reflections. All of these measurements were referenced to the corresponding reflection of the GaAs substrate. The arithmetic average  $\bar{a} = (a_{\perp} + a_{\parallel})/2$  is plotted in Figure 2 for film thicknesses of at least 1  $\mu\text{m}$  (to minimize corrections due to tetragonal distortion especially evident in thinner films) along with the misfit to the GaAs substrate ( $a_0 = 5.6533 \text{ \AA}$ ). A least-squares linear fit to the data is given by

$$\bar{a}(x) = (5.6684 \pm 0.0005) + (0.058 \pm 0.004) x. \quad (1)$$

With these data, one may proceed in the spirit of the virtual crystal approximation [24], which has been shown to work so well for the Mn-based DMS family, to extrapolate the change in lattice parameter for other Fe-based DMS compounds which share the common FeSe endpoint, such as  $(\text{Hg,Fe})\text{Se}$  and  $(\text{Cd,Fe})\text{Se}$ , as shown in Figure 3. These latter materials have only been grown in bulk form for Fe concentrations up to  $\sim 12\%$ . The vertical axis in Figure 3 is not the actual lattice parameter, but rather the distance  $d$  between nearest like atoms (cations or anions), since this parameter is independent of structure (e.g. zincblende or wurtzite). The true lattice constant  $a$  is very simply derived from these data by  $a = d\sqrt{2}$  for the zincblende structure. Further discussion of this approach may be found in references 1 and 2.

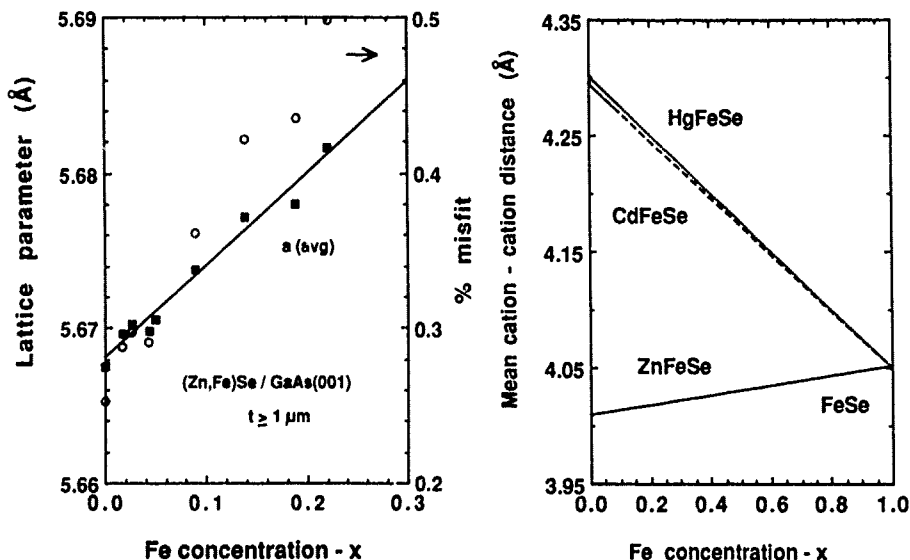


Figure 2. Variation of the average lattice parameter (squares) and percent misfit to the GaAs substrate (circles) for  $(\text{Zn,Fe})\text{Se}$  epilayers on  $\text{GaAs}(001)$ . The line is a least squares fit to the lattice parameter data as given by Equation (1). The percent misfit is calculated as  $100 \times 2(a_f - a_s)/(a_f + a_s)$  with  $a_s = a_{\text{GaAs}} = 5.6533 \text{ \AA}$ .

Figure 3. Mean cation-cation distance plotted as a function of Fe concentration for three DMS compounds which share the FeSe endpoint.  $(\text{Hg,Fe})\text{Se}$  and  $(\text{Cd,Fe})\text{Se}$  have only been grown in bulk form for Fe concentrations  $x \leq 0.12$ .

Very recently, the variation of lattice constant with Fe concentration for bulk-grown  $\text{Zn}_{1-x}\text{Fe}_x\text{Se}$  has been published by Swagten et al. [25] for  $x \leq 0.22$ . They obtain a least-fit as given by

$$a(x) = (5.666 \pm 0.001) \pm (0.051 + 0.01)x, \quad (2)$$

and compare their data with that of Jonker et al. [21] which was obtained for the perpendicular lattice parameter of  $(\text{Zn,Fe})\text{Se}$  epilayers. Due to the small tetragonal distortion exhibited by these epilayers, a more appropriate comparison may be made to the average lattice parameter as given by Equation (1) above [26,27]. Excellent agreement is then obtained between the two sets of data, aside from a difference in the intercept, which may be attributed to some error in absolute calibration.

The crystalline quality of the  $(\text{Zn,Fe})\text{Se}$  epilayers was further evaluated by double crystal x-ray rocking curve and topography measurements [26,27]. The rocking curve linewidth (FWHM) for the (004) reflection of films at least  $1 \mu\text{m}$  thick increases from 175 arc sec for  $x = 0$  to approximately 475 arc sec for  $x = 0.22$ , and shows no dependence on x-ray wavelength (Cu, Co, Fe and Cr  $K\alpha_1$ ). The predominant contribution to the linewidth is therefore due to dislocations [28], and the dislocation density  $\rho$  may be estimated from the rocking curve FWHM  $W$  from the simple relation [29]

$$\rho = W^2 / 4.35 b^2 \quad (3)$$

where  $b$  is the Burgers vector, which is expected to be  $a_0/\sqrt{2}$ . Values for the dislocation density range from 1 to  $7.5 \times 10^8/\text{cm}^2$ , and appear to reflect the increase in misfit to the substrate, as shown in Figure 4. This is an important observation, since it indicates that the crystalline quality of the epilayer is limited by the dislocations arising from simple misfit to the substrate rather than by disruption of the lattice by the substitutional iron impurities. One would therefore expect substantial improvement in crystal quality through growth on an appropriate lattice-matched substrate such as  $(\text{Ga,In})\text{As}$ .

Transmission electron microscopy (TEM) samples were prepared by mechanical thinning and subsequent ion milling at liquid nitrogen temperature and relatively low ion energy (3 keV  $\text{Ar}^+$ , 1 mA) to minimize ion-induced damage. High resolution (110) lattice images of the film/substrate interface are shown in Figures 5a and b for an  $x = 0.22$  and pure  $\text{FeSe}$  epilayer, respectively. In either case the films are seen to be of high quality with coherent and atomically abrupt interfaces. The images exhibit well-defined {111} lattice fringes which are completely continuous across the interface, as well, demonstrating well-ordered single crystal growth.

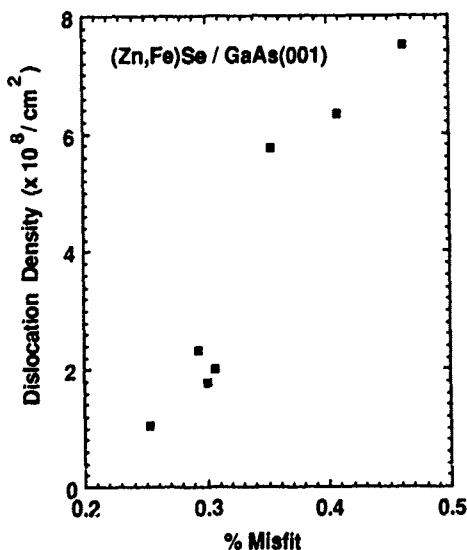


Figure 4. Values for the dislocation density in the  $(\text{Zn,Fe})\text{Se}$  epilayer obtained from the rocking curve linewidth (Eqn. 3) as a function of misfit to the  $\text{GaAs}$  substrate. The quality of the epilayer is limited by the consequent misfit dislocations.

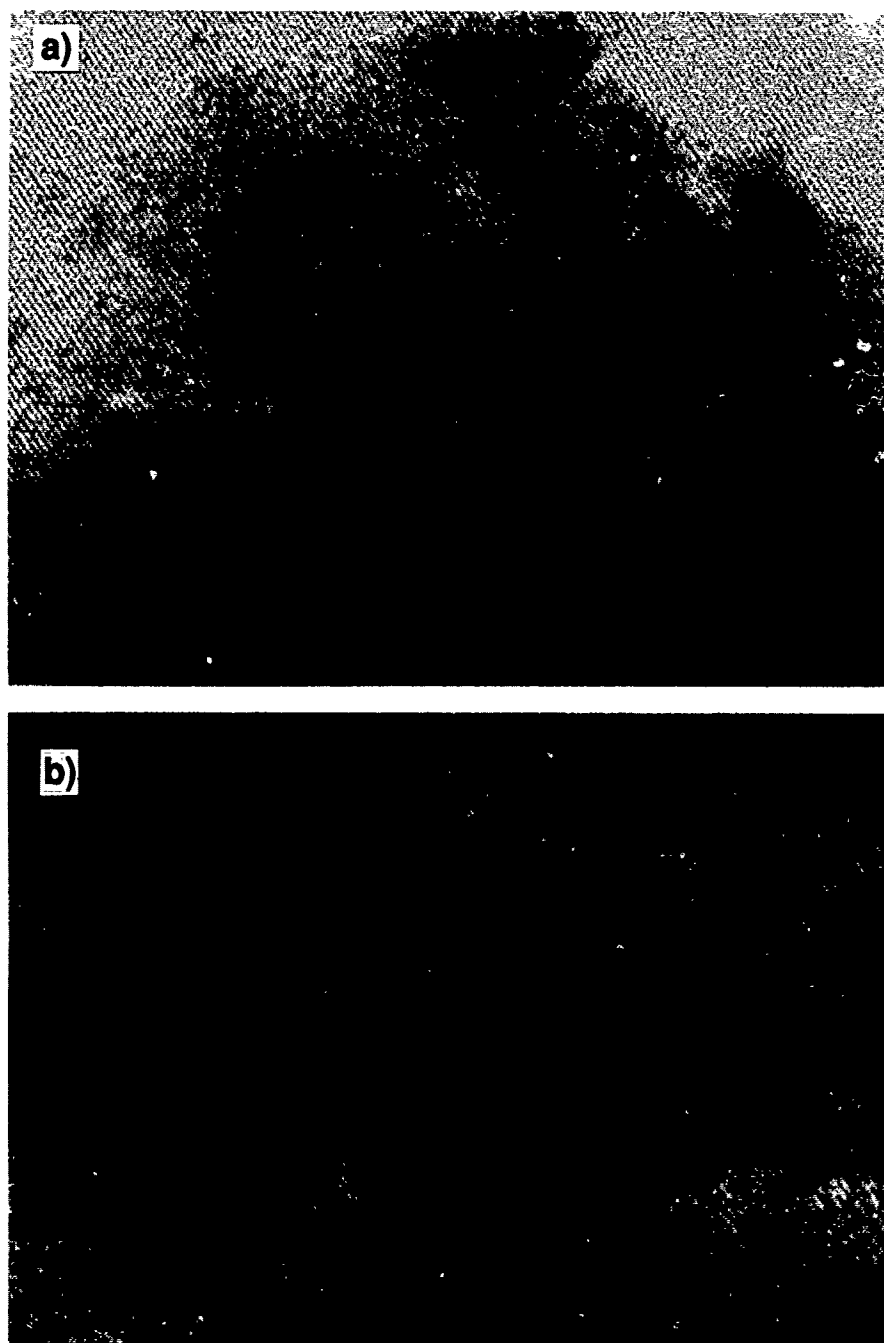


Figure 5. High resolution (110) cross-sectional images of the film/substrate interface for a) an  $x = 0.22$  (Zn,Fe)Se epilayer and b) a pure FeSe film on GaAs(001). Note that the lattice fringes are well-resolved and completely continuous across the interface, indicating high crystalline quality and coherent interfaces. The horizontal arrows indicate the interface.

### Magnetic Properties

The magnetic and magneto-optic behavior of (Zn,Fe)Se and other Fe-based DMS materials which distinguishes them from their Mn-based counterparts derives from the unique ground state of the  $\text{Fe}^{2+}$  ion in a tetrahedrally coordinated lattice [30,31]. The free ion  $^5\text{D}_4$  ground state is split by the crystal field into an upper  $^5\text{T}$  orbital triplet and a lower  $^5\text{E}$  doublet, which is further split by the spin-orbit interaction in second order into five closely spaced ( $\sim 2.2$  meV) levels. The lowest level is a completely non-degenerate  $\text{A}_1$  orbital singlet which has no permanent magnetic moment, and it is this feature which leads to Van Vleck paramagnetic behavior: at modest temperatures ( $T \geq 8\text{K}$ ) or through the application of a magnetic field, other states are occupied or mixed into the  $\text{A}_1$  state, producing a paramagnetic moment that is a function of both field and temperature independently. One characteristic feature is that the magnetization becomes independent of temperature, but not field, at temperatures sufficiently low to avoid population of the first excited state ( $kT \ll$  level spacing  $\sim 2.2$  meV). This behavior has been clearly shown for both bulk [19,20] and epitaxial thin film [23,32,33] (Zn,Fe)Se samples.

The rather complicated level splitting and unusual ground state described above make a quantitative treatment of the magnetic properties for Fe-based DMS compounds very involved and beyond the scope of this text. The interested reader is therefore referred to recent publications by Swagten et al [25] and Twardowski et al [34] for a detailed modeling of the magnetization, magnetic specific heat and susceptibility.

### Magneto-optic properties

As noted in the introduction, DMS materials are noteworthy for their dramatic magneto-optic properties, such as giant Faraday rotations and large Zeeman splittings. These effects result from the strong exchange coupling of the valence ( $p$ ) and conduction ( $s$ ) band electrons to the localized  $d$  states of the magnetic ions in the lattice, referred to as the  $sp-d$  exchange interaction. The magnetic field splitting of the valence and conduction bands therefore reflects the magnetization of those ions, which in turn is a function of the applied magnetic field. The magnetic ions therefore modify the internal field seen by the band electrons, serving to amplify the external applied field. Magneto-optic studies are thus sensitive probes of the magnetization of the transition-metal ions, and of the strength of the exchange interaction between those ions and the band electrons.

Using the notation of Gaj et al. [35], in a simplified mean field approximation the  $sp-d$  exchange contribution to the Hamiltonian may be written

$$H_{ex} = -J x N_0 \langle S_z \rangle S_{e,h} \quad (4)$$

where  $x$  is the magnetic ion concentration,  $\langle S_z \rangle$  is the thermally averaged projection of their spin along the applied field ( $z$ ) direction,  $N_0$  is the number of unit cells per unit volume, and  $S_{e,h}$  denotes the  $z$  component of the band electron (hole) spin.  $J$  is the exchange operator which, when applied to the band wavefunctions  $\langle Y | J | Y \rangle$ , results in the conduction band-magnetic ion and valence band-magnetic ion exchange integrals  $\alpha$  and  $\beta$ , respectively. These parameters are thus a measure of the strength of the interaction between the band electrons and magnetic ions, and may be obtained directly from magneto-optic data.

The Zeeman splitting of the conduction and valence bands and the possible interband transitions are shown in Figure 6. The band edges split according to the equations

$$E_{CB}(M_s) = E_g + x N_0 \alpha \langle S_z \rangle M_s \quad M_s = \pm 1/2 \quad (5)$$

$$E_{VB}(M_s) = (1/3) x N_0 \beta \langle S_z \rangle M_s \quad M_s = \pm 3/2, \pm 1/2 \quad (6)$$

where  $E_g$  is the band gap at zero field. The interband excitonic transitions may be observed in both magnetorefectivity and photoluminescence measurements, although band-edge luminescence may be observed only for the lower Fe concentrations (1-2%) in (Zn,Fe)Se due to recombination involving Fe levels within the gap.

Figure 7 shows the field dependence of the interband transitions as obtained from magnetorefectivity data from an  $x = 0.043$   $\text{Zn}_{1-x}\text{Fe}_x\text{Se}$  epilayer on GaAs(001) [32]. All of the allowed transitions are observed. The completeness of the data and the polarization

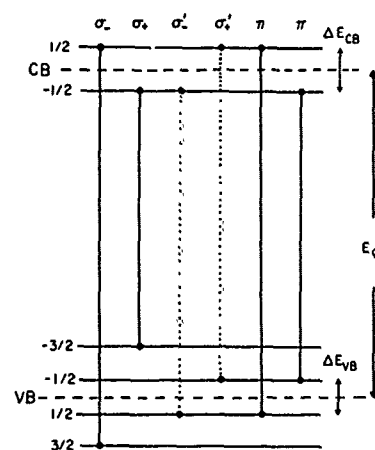


Figure 6. Magnetic field splitting of the conduction band (CB) and valence band (VB). The six allowed interband transitions are shown, with the sign of the splitting reflecting the sign of the exchange constants.

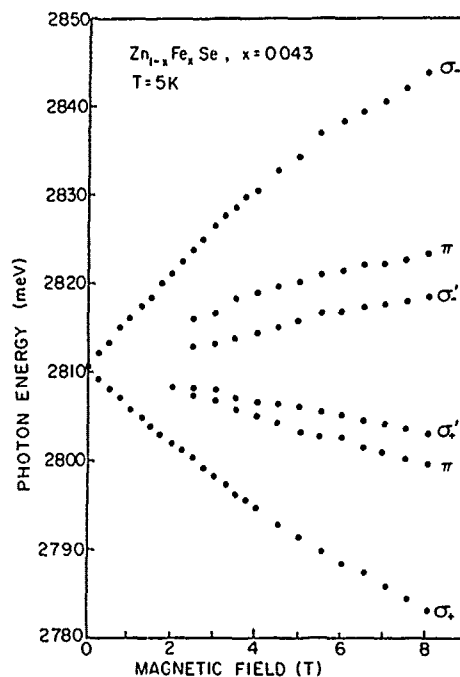


Figure 7. Field dependence of the transition energies as labeled in Figure 6 as obtained in the Faraday ( $\sigma$ ) and Voigt ( $\pi$ ) geometries, for a (Zn,Fe)Se epilayer ( $x = 0.043$ ,  $t = 1 \mu\text{m}$ ) at  $T = 5 \text{ K}$ .

dependence of the spectra permit identification of the transitions as labeled in Figure 6.

Similar data may be obtained from photoluminescence measurements for Fe concentrations  $x < 0.02$  [33]. From such data one can determine values for the exchange integrals  $\alpha$  and  $\beta$ , as follows: from Eqns. (5) and (6), the energy difference

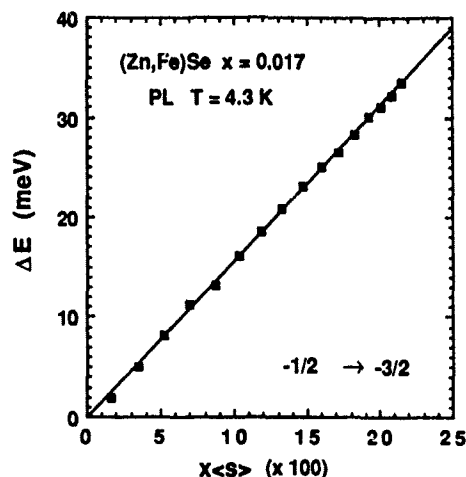
$$\begin{aligned} \Delta E &= 2 [E_g - E(-1/2 \rightarrow -3/2)] \\ &= x \langle S_z \rangle N_0 (\alpha - \beta). \end{aligned} \quad (7)$$

Thus a plot of  $\Delta E$  for a single transition as a function of its field dependence as given by  $x \langle S_z \rangle$  (obtained independently from magnetometry data) provides a value for the quantity  $N_0(\alpha - \beta)$  from the slope. The field dependence of a second transition allows a determination of both  $\alpha$  and  $\beta$  independently. Figure 8 summarizes such data obtained from photoluminescence measurements of the  $(-1/2 \rightarrow -3/2)$  transition from an  $x = 0.017$   $\text{Zn}_{1-x}\text{Fe}_x\text{Se}$  epilayer at 4.3 K. The data exhibit very linear behavior and yield a slope  $N_0(\alpha - \beta) = 1560 \text{ meV}$ , about 15% larger than in (Zn,Mn)Se [2]. Combining these data with that obtained from the  $(1/2 \rightarrow -1/2)$  transition, the experimental values for the exchange integrals are

$$N_0 \alpha = (226 \pm 10) \text{ meV}, \quad N_0 \beta = (-1334 \pm 14) \text{ meV}. \quad (8)$$

These values compare well with those obtained from bulk (Zn,Fe)Se samples [20], and are determined to greater precision.

Figure 8. Magnetic field dependence of the energy of the  $(-1/2 \rightarrow -3/2)$  transition relative to its zero field value  $E_0$  for an  $x = 0.017$  (Zn,Fe)Se epilayer. The data points were obtained from photoluminescence measurements at 4.3 K, and the values  $x\langle S_z \rangle$  were obtained from corresponding SQUID magnetometry data. The line is a least squares fit with a slope  $N_0(\propto -\beta)$  as given by Eqn. (7).



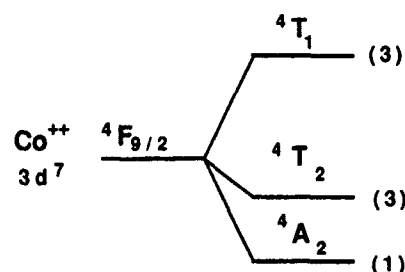
$\text{Zn}_{1-x}\text{Co}_x\text{Se}$

Why Co?

The unusual magnetic field-dependent properties of the DMS materials derive from both the interaction of the magnetic ions with the band electrons through the exchange integrals  $\alpha$  and  $\beta$  just described, as well as through the exchange interaction between the magnetic ions themselves [36]. These interactions are strongly influenced by the ground state of the particular substitutional magnetic ion used.

In such materials one generally desires that the magnetic ion possess an orbital singlet ground state, since orbital degeneracy is likely to lead to fast relaxation processes or produce complicating Jahn-Teller effects. Of the magnetically active 3d transition metals in the  $2^+$  charge state and a tetrahedral site, three fill this criterion:  $\text{Mn}^{2+}$ ,  $\text{Fe}^{2+}$  and  $\text{Co}^{2+}$ . The  $\text{Mn}^{2+}$  ( $3d^5$ ) ion is by far the simplest of the three, since it is not subject to crystal field or spin-orbit splitting and has a very simple  ${}^6\text{A}_1$  orbital singlet ground state, making it very amenable to calculation and quantitative modeling.  $\text{Fe}^{2+}$  ( $3d^6$ ) is certainly the most complicated, exhibiting a magnetically inactive  $\text{A}_1$  ground state in a manifold of closely spaced levels, resulting in Van Vleck paramagnetic behavior as described in the preceding sections. The level splitting for the  $\text{Co}^{2+}$  ( $3d^7$ ) ion is intermediate in complexity, as shown in Figure 9: the  ${}^4\text{F}_{9/2}$  free-ion level is split by the tetrahedral crystal field into an upper  ${}^4\text{T}_1$  orbital triplet, a  ${}^4\text{T}_2$  triplet, and a lower  ${}^4\text{A}_2$  orbital singlet ground state [37,38]. Thus Co-based DMS compounds are expected to exhibit Brillouin paramagnetic behavior, like those based on Mn.

Figure 9. Level splitting for a  $\text{Co}^{2+}$  ion in a tetrahedral crystal field (not to scale). The ground state is an orbital singlet.



Unlike  $\text{Mn}^{2+}$ , the  $\text{Co}^{2+}$  ground state has a significant orbital angular momentum component due to spin-orbit mixing with the low-lying  ${}^4\text{T}_2$  triplet, producing a larger effective Lande  $g$  factor of 2.27 (vs 2.0 for  $\text{Mn}^{2+}$ ) [37,39]. This is manifested in an enhanced Zeeman splitting ( $\Delta E_z = g\mu_B H$ ) distinct from the band electron-magnetic ion exchange contribution discussed earlier, as well as an enhanced ion-ion exchange splitting [40]. In addition, the Co-Co exchange interaction is generally larger than that of Mn [41], so that Co-based DMS compounds may be expected to exhibit magnetic ordering phenomena at correspondingly higher temperatures. Thus the incorporation of Co into a DMS structure offers exciting possibilities.



The first reported growth of a Co-based diluted magnetic semiconductor was the growth of single crystal (001) zincblende epilayers of  $\text{Zn}_{1-x}\text{Co}_x\text{Se}$  ( $0 < x \leq 0.1$ ) on GaAs(001) by molecular beam epitaxy [14]. In the following sections, we briefly summarize the growth, structure, and magnetic and magneto-optic properties of these samples, and contrast the properties with those of (Zn,Fe)Se and (Zn,Mn)Se.

#### Growth and Structural Characterization

The (Zn,Co)Se epilayers were grown under the same conditions used for the growth of (Zn,Fe)Se. In contrast with (Zn,Fe)Se, initial growth appears to be dominated by three-dimensional nucleation as evidenced by a rather spotty RHEED pattern, which evolves into a more two-dimensional mode by approximately 75–100 Å. Single crystal samples have been grown to a thickness of 1 μm for  $x \leq 0.075$ , but only to some critical thickness which decreases with increasing  $x$  for  $0.075 < x \leq 0.10$ . Growth beyond 0.3 μm for  $x = 0.095$ , for example, results in the appearance of multicrystalline features in the RHEED pattern. Magnetometry data confirm that the Co is being incorporated in a random, substitutional manner for this entire range of concentrations [15].

A variety of x-ray diffraction techniques were again used to evaluate the structure and quality of the epilayers [16]. Oscillation photographs confirm that the films exhibit a single crystal zincblende structure, and  $\theta$ - $2\theta$  measurements indicate that the average lattice parameter increases linearly with Co concentration for  $0 < x \leq 0.04$  with a slope nearly identical to that determined for (Zn,Fe)Se [26,27]. The (Zn,Co)Se samples typically exhibit some degree of tetragonal distortion even for thicknesses of 1–2 μm, which becomes more pronounced for  $x > 0.04$ , making quantitative evaluation of the lattice parameter more difficult.

X-ray double crystal rocking curves were obtained from each sample for the (004) reflection with  $\text{Cu K}\alpha_1$  radiation. Examples of these data are shown in Figure 10 for two samples of similar composition but different thickness. Note that the rocking curve linewidth (FWHM) for the thinner 0.3 μm film is only 71 arc sec, comparable to that of the GaAs substrate (30 arc sec), while that of the 1 μm sample is 312 arc sec. The thinner film accommodates the misfit to the substrate via elastic strain, while in the case of the thicker film it has become energetically favorable to accommodate the mismatch through the formation of misfit dislocations, which more dramatically broaden the rocking curve. These observations are further supported by accompanying  $\theta$ - $2\theta$  and double crystal topography measurements. These results are significant in that they demonstrate that the crystalline quality of the epilayer is not limited here by the incorporation of Co into the host ZnSe lattice, but rather by the misfit to the substrate. Therefore crystalline quality should improve significantly by growth on an appropriately lattice matched substrate layer such as (Ga,In)As, as noted above for (Zn,Fe)Se.

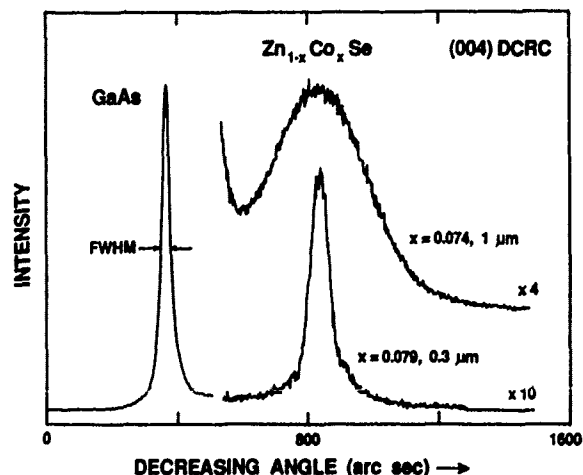


Figure 10. X-ray double crystal rocking curves ( $\text{Cu K}\alpha_1$ , (004) reflection) for (Zn,Co)Se epilayers of similar composition but different thicknesses, as noted in the figure. The rocking curve linewidth (FWHM) for the 0.3 μm film is only 71 arc sec, indicating a high crystal quality approaching that of the GaAs substrate (FWHM = 30 arc sec). The linewidth for the thicker film is broadened by misfit dislocations.

TEM data further demonstrate the high crystalline quality of the (Zn,Co)Se epilayers. High resolution (110) lattice images are shown in Figure 11 for a) a 0.8  $\mu\text{m}$  thick,  $x = 0.01$  sample, and b) a 0.12  $\mu\text{m}$  thick,  $x = 0.095$  sample. In both cases, the interface is clearly coherent with complete continuity of the lattice planes crossing it, and atomically abrupt. These images also show that the films are homogeneous and well-ordered, and exhibit no evidence for twin crystal formation.

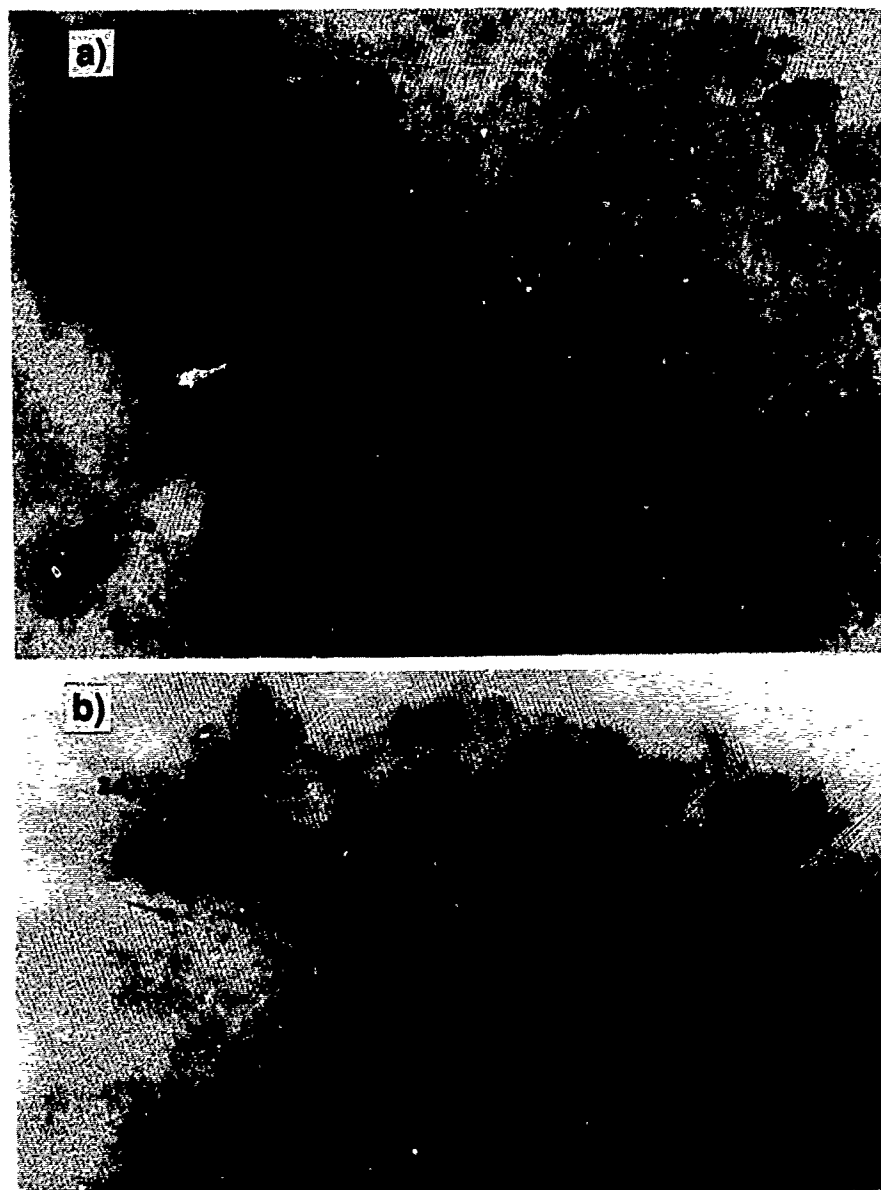


Figure 11. High resolution TEM lattice images ( (110) cross-sections) for  $\text{Zn}_{1-x}\text{Co}_x\text{Se}$  epilayers on GaAs: a)  $x = 0.01$ , and b)  $x = 0.095$  samples. The films are well-ordered and exhibit coherent interfaces with the GaAs substrate.

### Magnetic characterization

Electron paramagnetic resonance (EPR) and SQUID magnetometry were used to confirm the substitutional nature of the  $\text{Co}^{++}$  and to determine the magnetic properties of the samples for the full range of concentrations grown. These data have recently been described in detail elsewhere [14,15], and will be only briefly summarized here.

The EPR spectra (9.3 GHz, 5-6 K) generally exhibit a single dominant isotropic line at  $g = 2.27$  which broadens with Co concentration due to the statistical presence of exchange coupled nearest neighbor and next nearest neighbor pairs. Spectra for samples with  $x < 0.01$  exhibit in addition a number of weak satellite lines which are strongly angularly dependent. These features are attributed to  $\text{Co}^{++}$  ions in low symmetry sites, probably in the vicinity of dislocations -- the large orbital contribution ( $g = 2.27$ ) implies that the ground state of the ion is very sensitive to local low symmetry crystal fields. For the low Co concentration samples, the number of ions in such sites represents a larger fraction of the total number of  $\text{Co}^{++}$  ions in the sample than for the higher concentration films.

SQUID magnetometry data (6-100 K,  $H \leq 5$  T) show that the magnetization is a joint function of  $H/T$ , indicating Brillouin paramagnetic behavior as expected, similar to that of (Zn,Mn)Se and in marked contrast to the behavior of (Zn,Fe)Se. The magnetization can be calculated as [19,42]

$$M = AN_0 x g \mu_B \langle S_z \rangle \quad (9)$$

where  $g = 2.27$ ,  $\mu_B$  is the Bohr magneton, and the reduction factor  $A$  ( $0 < A \leq 1$ ) allows for the presence of  $\text{Co}^{++}$  ions with magnetically inactive ground states due to the occupation of low symmetry sites or the occurrence of antiferromagnetically coupled pairs, which removes their contribution to the moment. It is well known [42] that  $\langle S_z \rangle = SB_S(y)$ , where  $B_S(y)$  is the Brillouin function for  $S = 3/2$  and  $y = g\mu_B SH/kT$ . The data for all concentrations studied  $0 < x \leq 0.094$  and  $T \leq 100$  K are well fit by a simple Brillouin function as given by Eqn. (9) with  $A$  as the only adjustable parameter. A comparison of the values of  $A$  thus obtained from fits to the data with a simple model which assumes a random, statistical distribution of ions indicates that both nearest and next nearest neighbor  $\text{Co}^{++}$  pairs are antiferromagnetically coupled [15].

### Optical Properties

The variation of band gap with Co concentration was obtained from optical absorption measurements by measuring the incident wavelength at which the interference fringes produced by reflection at the (Zn,Co)Se/GaAs interface and film surface were extinguished. These data are plotted in Figure 12 for  $T = 5$  K and show that the band gap increases linearly with Co concentration as given by the least squares fit  $E_g = 2.797 + 0.743x$  eV for the samples studied to date. Interference fringes were not well resolved for the thinner, higher concentration samples in the normal incidence geometry used.

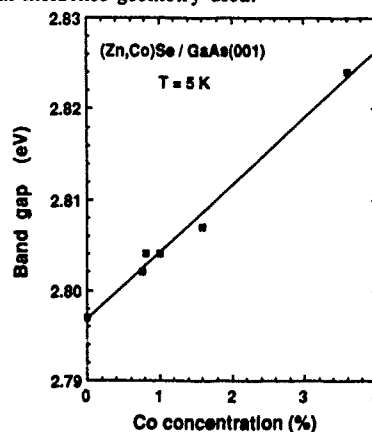
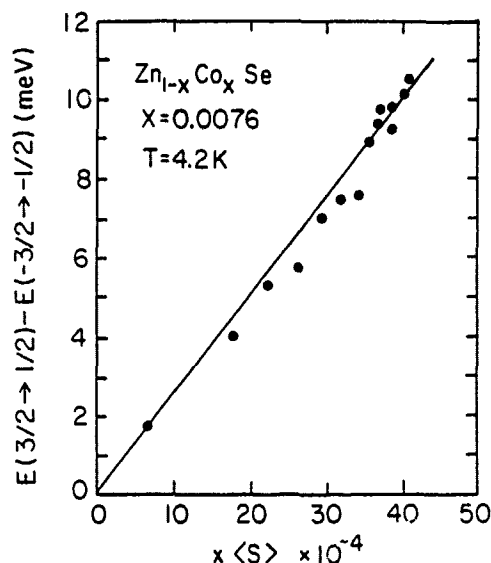


Figure 12. Variation of the optical band gap at  $T = 5$  K with Co concentration for (Zn,Co)Se (001) epilayers.

Magnetorefectivity studies show that the strength of the interaction between the band electrons and the  $\text{Co}^{++}$  ions as given by the difference in exchange parameters  $N_0(\alpha - \beta)$  is significantly larger than that found in either Fe- or Mn-based DMS materials [17]. Reflectivity spectra were obtained in the Faraday geometry in magnetic fields up to 8 T and for the temperature range 4.2-70 K. The interband excitonic transitions ( $-3/2 \rightarrow -1/2$ ) and ( $3/2 \rightarrow 1/2$ ) were observed (see Figure 6), and show that the band splitting saturates for fields  $> 5$  T, further confirming Brillouin paramagnetic behavior. The two weaker transitions allowed in the Faraday geometry, ( $-1/2 \rightarrow 1/2$ ) and ( $1/2 \rightarrow -1/2$ ), were not resolved.

The energy difference between these observed transitions at 4.2 K for the  $x = 0.0076$  sample is plotted in Figure 13 as a function of  $x\langle S \rangle$  as determined from corresponding magnetization measurements [15]. From Eqns. (5) and (6), the least squares linear fit to the data has a slope  $N_0(\alpha - \beta) = (2530 \pm 90)$  meV. Similar data for an  $x = 0.01$  sample yield a value of 2290 meV. These values are approximately twice as large as those obtained for Mn-based DMS materials [1,2].

Figure 13. The energy difference of the excitonic transitions ( $3/2 \rightarrow 1/2$ ) and ( $-3/2 \rightarrow -1/2$ ) versus the quantity  $x\langle S \rangle$  as obtained from SQUID magnetometry measurements. From Eqns. (5) and (6), a least squares fit (solid line) to the data has a slope  $N_0(\alpha - \beta) = 2530$  meV, nearly a factor of two larger than for (Zn,Mn)Se.



## SUMMARY

The growth of these new Co-based DMS materials is especially significant due to the much stronger exchange interactions which are obtained relative to the Fe- and Mn-based compounds. Table II summarizes two important parameters which may be taken as a measure of the strength of the exchange coupling between the band electrons (holes) and the magnetic ions, and between the magnetic ions themselves. The quantity  $N_0(\alpha - \beta)$  as defined earlier is a measure of the exchange interaction between the carriers and the magnetic ions, and indicates the effectiveness of the ions in amplifying an external magnetic field to an effective internal field seen by the carriers. This value increases by about 15% from  $\text{Mn}^{++}$  to  $\text{Fe}^{++}$ , but nearly doubles for (Zn,Co)Se, indicating that the new Co-based DMS compounds should exhibit much more dramatic magneto-optic properties.

The magnitude of the exchange interaction between the magnetic ions themselves is given by the nearest-neighbor ion-ion exchange parameter  $J$  as it appears in the contribution to the Hamiltonian

$$H_J = -2J \vec{S}_1 \cdot \vec{S}_2, \quad (10)$$

where  $\vec{S}_i$  denotes the magnetic ion's net spin. In the MnSe-based DMS compounds,  $J$  ranges from  $-8$  to  $-13$  K [2]; for (Zn,Mn)Se, values of  $-12.3$  K [43] and  $-13$  K [44] have been reported. Since the ground state of  $\text{Fe}^{++}$  is magnetically inactive,  $J$  is not well defined,

although recent calculations by Twardowski et al [34] yield a somewhat model-dependent value of  $-22$  K, which should be interpreted within the framework of their detailed treatment. Since  $\text{Co}^{++}$  and  $\text{Mn}^{++}$  share similar ground states, the corresponding values for  $J$  may be directly compared. Giebultowicz et al. have very recently reported extraordinarily large values of  $J \approx -50$  K for  $\text{Co}^{++}$  in bulk-grown  $(\text{Zn},\text{Co})\text{Se}$  and  $(\text{Zn},\text{Co})\text{S}$  [18] from neutron diffraction data, which represents a four-fold enhancement relative to  $\text{Mn}^{++}$  in  $(\text{Zn},\text{Mn})\text{Se}$  as measured by the same technique [43]. Thus the interaction between the  $\text{Co}^{++}$  ions is significantly larger than between the  $\text{Mn}^{++}$  ions in similar compounds, as suggested by a comparison of the ordering temperatures in Mn- and Co-bearing non-DMS materials [41] as discussed earlier.

In conclusion, the growth of  $\text{Zn}_{1-x}\text{Fe}_x\text{Se}$  and  $\text{Zn}_{1-x}\text{Co}_x\text{Se}$  extends the family of transition metal alloyed wide-gap diluted magnetic semiconductors that can be grown as epitaxial single crystal films.  $\text{Co}^{++}$  has a ground state which differs significantly from that of  $\text{Mn}^{++}$  and  $\text{Fe}^{++}$ , so that a variety of magnetic behavior is available from these three systems.  $(\text{Zn},\text{Fe})\text{Se}$  is a Van Vleck paramagnet, while  $(\text{Zn},\text{Mn})\text{Se}$  and  $(\text{Zn},\text{Co})\text{Se}$  are both Brillouin paramagnets, the former without significant orbital momentum and the latter with considerable admixture in the ground state. The x-ray diffraction data demonstrate that the substitutional incorporation of Fe or Co into the host ZnSe lattice does not inherently limit the crystalline quality of these DMS epilayers on GaAs. Therefore growth on an appropriate lattice-match<sup>ed</sup> layer may be expected to result in DMS films with a crystalline quality which rivals that of the bulk substrate. This feature together with the dramatic enhancement in the exchange parameters relative to the Mn-based DMS compounds shows that the incorporation of  $(\text{Zn},\text{Fe})\text{Se}$  and  $(\text{Zn},\text{Co})\text{Se}$  in quantum wells and superlattices holds very exciting prospects for future study.

Table II. Summary of DMS exchange parameters.

	<u>ZnMnSe</u> <sup>a</sup>	<u>ZnFeSe</u>	<u>ZnCoSe</u>
$N_0 (\alpha - \beta)$ (meV)	1360	1560	2410
$J$ (K)	-13	$(-22)^b$	$-50^c$

<sup>a</sup> Parameters obtained from Reference 2.

<sup>b</sup> Model dependent -- see Reference 34.

<sup>c</sup> Reference 18.

#### ACKNOWLEDGMENTS

This work was supported by the Office of Naval Research. One of us (LSY) acknowledges support by the National Science Foundation. The work at SUNY was supported by ONR/SDIO under the MMFEL program. The authors gratefully acknowledge the technical assistance of F. Kovanic and D. King at the Naval Research Laboratory.

#### REFERENCES

1. See *Semiconductors and Semimetals*, vol. 25: *Diluted Magnetic Semiconductors*; R.K. Willardson and A.C. Beer, Treatise Editors; J.K. Furdyna and J. Kossut, Volume Editors (Academic Press, San Diego, 1988).
2. J.K. Furdyna, *J. Appl. Phys.* 64, R29 (1988).
3. J. Mycielski, *Prog. Cryst. Growth Char.* 10, 101 (1985).
4. N.B. Brandt and V.V. Moshchalkov, *Adv. Phys.* 33, 193 (1984).
5. M.A. Herman, O. Jylha and M. Pessa, *J. Cryst. Growth* 66, 480 (1984).

6. R.N. Bicknell, R.W. Yanka, N.C. Giles-Taylor, D.K. Blanks, E.L. Buckland and J.F. Schetzina, *Appl. Phys. Lett.* 45, 92 (1984).
7. L.A. Kolodziejski, T. Sakamoto, R.L. Gunshor and S. Datta, *Appl. Phys. Lett.* 44, 799 (1984).
8. A.V. Komarov, S.M. Ryabchenko and O.V. Terletskii, *Phys. Status Solid B* 102, 603 (1980).
9. Y. Guldner, C. Rigaux, M. Menant, D.P. Mullin and J.K. Furdyna, *Solid State Commun.* 33, 133 (1980).
10. M. Vaziri, U. Debska and R. Reifenberger, *Appl. Phys. Lett.* 47, 407 (1985); A. Wall, C. Caprile, A. Franciosi, M. Vaziri, R. Reifenberger and J.K. Furdyna, *J. Vac. Sci. Technol.* A4, 2010 (1986); F.S. Pool, J. Kossut, U. Debska and R. Reifenberger, *Phys. Rev. B* 35, 3900 (1987).
11. R. Reifenberger and J. Kossut, *J. Vac. Sci. Technol.* A5, 2995 (1987).
12. A. Mycielski, in *Diluted Magnetic (Semimagnetic) Semiconductors*, edited by R.L. Aggarwal, J.K. Furdyna and S. von Molnar (*Mater. Res. Soc. Proc.* 89, Pittsburgh, PA 1987) p. 159.
13. A. Mycielski, *J. Appl. Phys.* 63, 3279 (1988).
14. B.T. Jonker, J.J. Krebs and G.A. Prinz, *Appl. Phys. Lett.* 53, 450 (1988).
15. J.J. Krebs, B.T. Jonker and G.A. Prinz, *IEEE Trans. Magnetics* 24, 2548 (1988).
16. B.T. Jonker, S.B. Qadri, J.J. Krebs, G.A. Prinz and L. Salamanca-Young, *J. Vac. Sci. Technol.* A7, 1360 (1989).
17. X. Liu, A. Petrou, B.T. Jonker, G.A. Prinz, J.J. Krebs and J. Warnock, submitted for publication.
18. T.M. Giebultowicz, private communication and presented at the 1989 March Meeting of the American Physical Society; T.M. Giebultowicz, P. Klosowski, J.J. Rhyne, T.J. Udovic, U. Debska, J.K. Furdyna and W. Giriat, *Bull. Amer. Phys. Soc.* 34, F15.2, p. 592 (1989).
19. A. Twardowski, M. von Ortenberg and M. Demianiuk, *J. Crystal Growth* 72, 401 (1985).
20. A. Twardowski, P. Glod, W.J.M. de Jonge and M. Demianiuk, *Sol. St. Commun.* 64, 63 (1987).
21. B.T. Jonker, J.J. Krebs, S.B. Qadri and G.A. Prinz, *Appl. Phys. Lett.* 50, 848 (1987).
22. L.A. Kolodziejski, R.L. Gunshow, N. Otsuka, B.P. Gu, Y. Hefetz and A.V. Nurmikko, *Appl. Phys. Lett.* 48, 1482 (1986).
23. B.T. Jonker, J.J. Krebs, S.B. Qadri, G.A. Prinz, F. Volkening and N.C. Koon, *J. Appl. Phys.* 63, 3303 (1988).
24. D.R. Yoder-Short, U. Debska and J.K. Furdyna, *J. Appl. Phys.* 58, 4056 (1985).
25. H.J.M. Swagten, A. Twardowski, W.J.M. de Jonge and M. Demianiuk, *Phys. Rev.* B39, 2568 (1989).
26. B.T. Jonker, S.B. Qadri, J.J. Krebs and G.A. Prinz, *J. Vac. Sci. Technol.* A6, 1946 (1988).
27. S.B. Qadri, B.T. Jonker, J.J. Krebs and G.A. Prinz, *Thin Solid Films* 164, 111 (1988).
28. S.B. Qadri, B.T. Jonker, G.A. Prinz and J.J. Krebs, *J. Vac. Sci. Technol.* A6, 1526 (1988).
29. P. Gay, P.B. Hirsch and A. Kelly, *Acta Metall.* 1, 315 (1953).
30. W. Low and M. Weger, *Phys. Rev.* 118, 1119 (1960).
31. G.A. Slack, S. Roberts and J.T. Wallin, *Phys. Rev.* 187, 511 (1969).
32. X. Liu, A. Petrou, B.T. Jonker, G.A. Prinz, J.J. Krebs and J. Warnock, *J. Vac. Sci. Technol.* A6, 1508 (1988).
33. X. Liu, A. Petrou, B.T. Jonker, G.A. Prinz, J.J. Krebs and J. Warnock, *Appl. Phys. Lett.* 53, 476 (1988).
34. A. Twardowski, A. Lewicki, M. Arciszewska, W.J.M. de Jonge, H.J.M. Swagten and M. Demianiuk, *Phys. Rev.* B38, 10749 (1988).
35. J.A. Gaj, J. Ginter and R.R. Galazka, *Phys. Status Solidi B* 89, 655 (1978).
36. J.K. Furdyna and N. Samarth, *J. Appl. Phys.* 61, 3526 (1987), and references therein.
37. F.S. Ham, G.W. Ludwig, G.D. Watkins and H.H. Woodbury, *Phys. Rev. Lett.* 5, 468 (1960).
38. A. Abragam and B. Bleaney, *Electron Paramagnetic Resonance of Transition Ions* (Oxford, London, 1970) p. 470.
39. U. Kaufman and J. Schneider, *Solid State Commun.* 25, 1113 (1978) and references therein.
40. G.H. Dieke, *Spectra and Energy Levels of Rare Earth Ions in Crystals* (Interscience - Wiley, New York, 1968) chap. 11.
41. J.B. Goodenough, *Magnetism and the Chemical Bond* (Wiley, New York, 1963).
42. C. Kittel, *Introduction to Solid State Physics* (Wiley, New York, 1956) chap. 9.
43. T.M. Giebultowicz, J.J. Rhyne and J.K. Furdyna, *J. Appl. Phys.* 61, 3537 (1987).
44. Y. Shapira, S. Foner, D.H. Ridgley, K. Dwight and A. Wold, *Phys. Rev. B* 30, 4021 (1984).

## ELECTRON-SPIN POLARIZATION IN TUNNEL JUNCTIONS WITH FERROMAGNETIC EuS BARRIERS

Xin Hao\*, J. S. Moodera, and R. Meservey

Francis Bitter National Magnetic Laboratory (\* and the Department of Materials Science and Engineering), Massachusetts Institute of Technology, 150 Albany Street, Cambridge, MA 02139

### ABSTRACT

Spin-resolved tunneling in the structure metal-EuS-metal has been obtained. The metal electrodes used in our experiments being non-magnetic, polarization of the tunnel current is attributed to the conduction band splitting in EuS below its ferromagnetic Curie temperature. Enhanced Zeeman splitting in the superconducting aluminum film is also observed.

### INTRODUCTION

We report here spin-polarized tunneling experiments using non-ferromagnetic electrodes and ferromagnetic EuS barriers. Because of the conduction band in EuS splits into spin-up and spin-down subbands when the temperature is below 16.7 K [1], the Curie temperature of EuS, the tunnel barrier for electrons with different spin directions is different, therefore giving rise to tunnel current polarization. The spin-filter effect, as it may be called, was observed earlier, directly or indirectly, by several groups: Esaki *et al.* [2] made a tunneling study on junctions having EuS and EuSe barriers; Thompson *et al.* [3] studied Schottky barrier tunneling between In and doped EuS; Müller *et al.* [4] and Kisker *et al.* [5] performed electron field emission experiments on EuS-coated tungsten tips. The field emission experiments gave a maximum polarization of  $(89 \pm 7)\%$  for the emitted electrons. Although the previous tunneling studies did not directly show electron polarization, their results were explained by the same spin-filter effect. This work uses the spin-polarized tunneling technique [6] to show directly that tunnel current is indeed polarized and polarization can be as high as 85%.

### EXPERIMENTS AND RESULTS

Tunnel junctions of Al/EuS/Al, Au/EuS/Al, Ag/EuS/Al, and Al/EuS/Au were prepared by vacuum deposition on glass substrates, where the materials are listed in the order of their deposition. We report here mainly the results on two sets of junctions: Au/EuS/Al (sample no. 3-6470) and Ag/EuS/Al (sample no. 3-6491). Both set of junctions have a EuS thickness of 33 Å and Al thickness of 42 Å; the Au and Ag films are 110 Å and 200 Å thick, respectively.

Tunneling conductance was measured at 0.45 K with and without applied magnetic field. There two major results: (1) the Zeeman splitting of the quasiparticle density of states in superconducting Al is greatly enhanced, and (2) there is a high polarization in the tunnel current.

Figure 1 shows the tunnel conductance curves of an Au/EuS/Al junction (3-6470) in various applied magnetic fields with field direction parallel to the film surface. Polarization of the tunnel current gives rise to the asymmetry of the curves. The total Zeeman splitting and the value of polarization were obtained by fitting the curves using

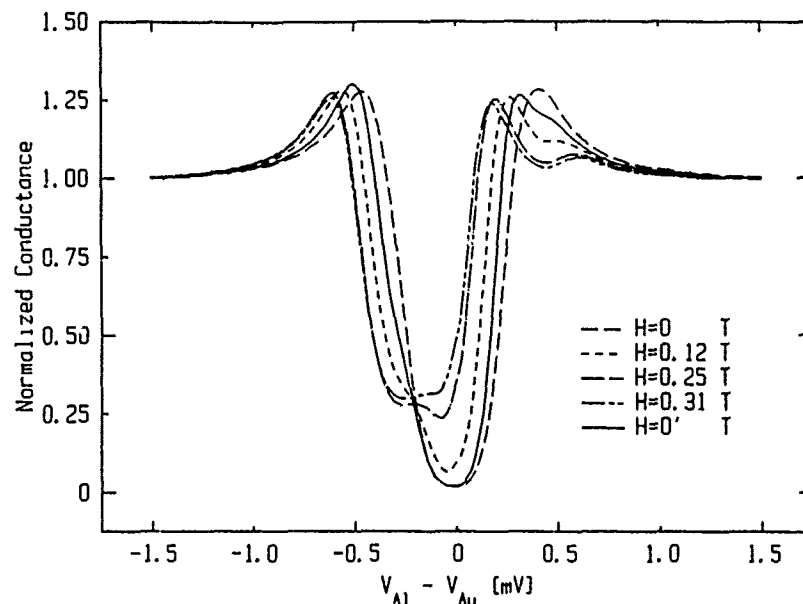


Figure 1. Tunneling conductance curves in various applied field. The one labeled  $H=0'$  was taken after the applied field had been reduced to zero, and there is remanent Zeeman splitting.  $B^*$  at  $H=0.31$  T is about 4 T. Polarization is about 80%.

the theory of thin film superconductors in high magnetic fields that takes into account also the spin-orbit scattering and the Fermi liquid effect [7]. Polarization was found to be about 80% for this junction. Similar results were obtained on the Ag/EuS/Al junctions which gave a slightly higher polarization of about 85%. The degree of polarization did not seem to change with the applied field.

On the other hand, the effective total field ( $B$ ) as determined from the size of the Zeeman splitting increased with the applied magnetic field ( $H$ ); the apparent Zeeman splitting was much bigger than that should result from the external field. This enhanced Zeeman splitting was also found by Tedrow *et al.* [8] in their study of proximity effects of Al thin films in contact with various rare-earth compounds. Their explanation for the extra magnetic field ( $B^*$ ) is that it is caused by the exchange interaction between the quasiparticles in Al and the magnetic ions, and they found that  $B^* = 1.7$  T when Al was backed by oxidized europium. The enhancement was more pronounced in our case:  $B^*$  reached 4 T in an applied field of only 0.31 T.

In certain junctions there was a Zeeman splitting even before any external magnetic field (except the ambient field of about 1 Oe) had been applied. This initial Zeeman splitting in zero applied field is sample dependent, the maximum  $B^*$  being observed was 3.5 T in one junction from the set 3-6491. The existence (or lack) of the initial zero field Zeeman splitting also depends on the temperature of the substrate during deposition of the bottom electrode and the EuS barrier. Junctions deposited on liquid-nitrogen-cooled substrates showed little initial zero field Zeeman splitting, while the ones with the bottom electrode and EuS deposited at room temperature showed zero field splitting most of the time. However, in all the junctions a remanent Zeeman splitting



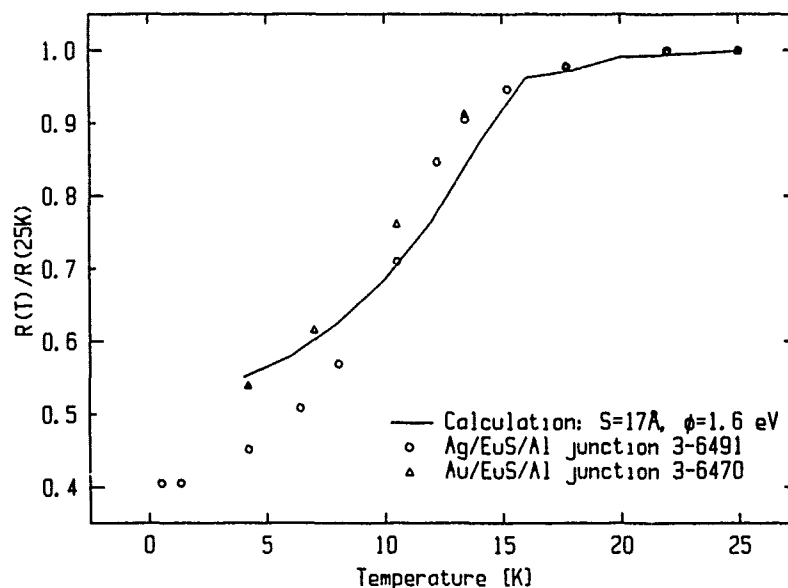


**Figure 2.** Junction resistance as a function of temperature for two samples. The solid line is a calculation based on the temperature variation of the red shift of the absorption edge measured in single crystal EuS.

was observed after the applied field had been reduced to zero.

The junction resistance,  $R_j$ , as a function of temperature was also measured for the range of 1 K to 25 K. A significant change of  $R_j$  started to occur around 17 K.  $R_j$  dropped by 54% from 25 K to 4.2 K in junction 3-6470, and by 60% from 25 K to 1.3 K in junction 3-6491.  $R_j$  versus  $T$  for these two junctions are shown in figure 2. The decrease of junction resistance is a direct consequence of barrier lowering and is closely related to the observed polarization, though its observation does not invoke the superconducting property of the Al electrode while Zeeman splitting of the quasiparticle density of states in superconducting Al is necessary to detect polarization.

## DISCUSSIONS

We have estimated the degree of polarization and the junction resistance decrease using Simmons's [9] formula of tunnel current for trapezoidal barriers. The barrier height and barrier thickness were estimated from the I-V measurements at temperatures above the Curie temperature of EuS. Polarization is defined by  $P = \frac{J_{\downarrow} - J_{\uparrow}}{J_{\downarrow} + J_{\uparrow}}$  with  $J_{\downarrow}$  and  $J_{\uparrow}$  being the tunneling current densities for the down, up spin directions respectively, and

$$J_{\uparrow,\downarrow} = J_0 \left( \phi_{\uparrow,\downarrow} - \frac{eV}{2} \right) \exp \left[ -A \left( \phi_{\uparrow,\downarrow} - \frac{eV}{2} \right)^{\frac{1}{2}} \right] \\ - J_0 \left( \phi_{\uparrow,\downarrow} + \frac{eV}{2} \right) \exp \left[ -A \left( \phi_{\uparrow,\downarrow} + \frac{eV}{2} \right)^{\frac{1}{2}} \right],$$

where  $\phi_{1,2} = \phi_0 \pm (\gamma/2)\Delta E_{ex}$  with  $\Delta E_{ex}$  being the splitting of the EuS conduction band; the constants  $J_0$ ,  $A$ , and  $\phi_0$  are defined in Ref. [9]. For the polarization calculation, a value of  $\Delta E_{ex} = 0.36$  eV [10] was used.  $\Delta E_{ex}$  as a function of temperature has been investigated by measuring the red shift of the optical absorption edge of single crystal EuS [10], and we used these bulk values to estimate the resistance decrease. The decrease in junction resistance and the degree of polarization are related so that a larger decrease in  $R_j$  corresponds with a higher polarization. For a barrier thickness  $S=17$  Å, a barrier height of 1.6 eV, and a junction area of  $4 \times 10^{-4} \text{ cm}^2$ , we have a calculated junction resistance of about 2 kΩ and a polarization of 82%, which is close to the measured  $R_j$  and polarization of our junctions.  $R_j$  versus  $T$  for these parameters is also depicted in figure 2. We find that in order to have a reasonable junction resistance, we need to use a smaller value for the barrier thickness than the nominal value. This may be explained by the non-uniformity of the barrier, since the most important contribution to the tunnel current comes from the thinnest part of the barrier.

In summary, spin-polarized tunneling has been observed in junctions with ferromagnetic EuS barriers. Polarization is attributed to the conduction band splitting in EuS below its Curie temperature. Calculations of the value of polarization and the decrease of junction resistance with the lowering of temperature using a simple tunneling theory and parameters obtained in measurements on bulk EuS agree well with the experiments. From the reasonable agreement we see that our thin EuS films have close to bulk properties: its Curie temperature is around 17 K, and the temperature dependence of the conduction band splitting of the film is very similar to that of the single crystal.

#### ACKNOWLEDGMENT

We thank Richard MacNabb for fabricating the junctions. This research was supported by the National Science Foundation Grant No. DMR-8619087.

#### REFERENCES

1. Watcher in Handbook on the Physics and Chemistry of Rare Earths, edited by K. A. Gschneider Jr. and L. Eyring, (North Holland, Amsterdam, 1979).
2. L. Esaki, P. J. Stiles, and S. von Molnar, Phys. Rev. Lett. **19**, 852 (1967).
3. W. A. Thompson, F. Holtzberg, T. R. McGuire, and G. Petrich, AIP Conf. Proc. No. 5, 827 (1971).
4. N. Müller, W. Eckstein, W. Hailand, and W. Zinn, Phys. Rev. Lett. **29**, 1651 (1972).
5. E. Kisker, G. Baum, A. H. Mahan, W. Raith, and B. Reihl, Phys. Rev. **B18**, 2256 (1978).
6. R. Meservey, P. M. Tedrow, and J. S. Moodera, J. Mag. and Mag. Mat. **35**, 1 (1983).
7. J. A. X. Alexander, T. P. Orlando, D. Rainer, and P. M. Tedrow, Phys. Rev. **B31**, 5811 (1986).
8. P. M. Tedrow, J. E. Tkaczyk, and A. Kumar, Phys. Rev. Lett. **56**, 1746 (1986).
9. J. G. Simmons, J. Appl. Phys. **34**, 2581 (1963).
10. P. Watcher, CRC Crit. Rev. Solid State Sci. **3**, 189 (1972).

# CARRIER-CONCENTRATION-DEPENDENT MAGNETIC PROPERTIES OF THE DILUTED MAGNETIC SEMICONDUCTOR $\text{SnMnTe}$

H.J.M. SWAGTEN, S.J.E.A. ELTINK AND W.J.M. DE JONGE  
Eindhoven University of Technology, Department of Physics,  
P.O. Box 513, 5600 MB Eindhoven, The Netherlands.

## ABSTRACT

*In this paper experimental evidence is presented for the carrier concentration dependence of the magnetic properties of  $\text{Sn}_{0.97}\text{Mn}_{0.03}\text{Te}$ , yielding a critical concentration above which ferromagnetic interactions are dominant. The observed behavior can be fairly well explained within a modified RKKY-model. Preliminary experiments on the low temperature magnetic phases indicate re-entrant spinglass behavior, which is qualitatively described with the spinglass model of Sherrington and Kirkpatrick.*

## INTRODUCTION

A strong and intriguing coupling between the magnetic and electronic structure has been discovered in the Diluted Magnetic Semiconductors (DMS: [1])  $\text{PbSn}(\text{Mn})\text{Te}$ . More specifically, Story *et al.* [2] established that a critical carrier density (roughly  $3 \times 10^{20} \text{ cm}^{-3}$ ) exists in  $\text{Pb}_{0.25}\text{Sn}_{0.72}(\text{Mn}_{0.03})\text{Te}$ , above which ferromagnetic interactions were observed, while below the critical density a spinglass-like cusp in the AC susceptibility was reported [3], accompanied by small antiferromagnetic (AF) interactions. The same effect has been observed for other compounds such as  $\text{Pb}_{0.52}\text{Sn}_{0.45}(\text{Mn}_{0.03})\text{Te}$  with a critical carrier density only slightly different from the value for  $\text{Pb}_{0.25}\text{Sn}_{0.72}(\text{Mn}_{0.03})\text{Te}$  [3]. This critical density of free carriers divides the magnetic phase diagram into a ferromagnetic and a spinglass region with strong ferromagnetic and small antiferromagnetic interactions respectively.

A modified RKKY-model [4] enables us to describe the existence of the critical density as well as the magnitude of the ferromagnetic Curie-Weiss temperatures above  $p_{\text{crit}}$ . The model is based on the conventional RKKY-interaction applied to carriers located at different regions of the Brillouin zone. The interesting increase of the interactions at  $p_{\text{crit}}$  is then attributed to the entrance of the Fermi-level into a second set of heavy hole valence bands, located along the  $\Sigma$ -axis.

On the basis of this model one could speculate about the contrasting difference between the magnetic behavior of  $\text{Pb}(\text{Mn})\text{Te}$  and  $\text{Sn}(\text{Mn})\text{Te}$ . Both IV-VI group DMS materials have a similar bandstructure and were subject to many studies [5], but somewhat puzzling, there seems to be no logical correlation between their low temperature magnetic properties. We feel encouraged by the basic results of our modified RKKY-model that this might be caused by their considerable difference in carrier density. The  $\text{Sn}(\text{Mn})\text{Te}$  semimetallic compound is an extreme case since it possesses such high densities that the second set of valence bands is commonly populated. Indeed, in all present studies on this material the system exhibits strong ferromagnetic interactions. By reducing the carrier density of  $\text{Sn}(\text{Mn})\text{Te}$  below  $p_{\text{crit}}$ , which causes a redistribution of the carriers in favor of the first set of valence bands, one could therefore expect that the system transforms into a paramagnet. Fortunately, it seems possible in  $\text{SnTe}$  to decrease  $p$  in such a way that it reaches  $p_{\text{crit}}$ , see for instance Allgaier *et al.* [6] and Inoue *et al.* [7].  $\text{Pb}(\text{Mn})\text{Te}$  is an extreme case too since it possesses such small densities that only the primary valence bands are populated. However, for  $\text{Pb}(\text{Mn})\text{Te}$  it is not possible to raise the carrier density into the critical region ( $\approx 10^{20} \text{ cm}^{-3}$ ), due to technological problems.

Therefore we thought it worthwhile to investigate the influence of a reduction of

the carrier density on the low temperature magnetic properties of  $\text{Sn}_{0.97}(\text{Mn}_{0.03})\text{Te}$ , in order to corroborate our conjecture and observe the expected breakdown of the strong RKKY-interactions. In the second part of this paper we will focus on the so-called ferromagnetic regime (i.e.  $p > p_{\text{crit}}$ ), in order to characterize the low temperature magnetic phases in a more detailed way. Earlier reports [5,8-10] denote these phases as ferromagnetic, spinglass as well as a re-entrant spinglass. We therefore measured the ZFC-FC magnetization and the AC susceptibility in the presence of additional DC fields. These experiments are commonly regarded as crucial to distinguish between spinglass-like and other magnetic phases.

## EXPERIMENTAL RESULTS AND DISCUSSION

The  $\text{Sn}_{0.97}(\text{Mn}_{0.03})\text{Te}$  samples were grown by a Bridgman method. Stoichiometric amounts of non-metal and metal elements were sealed in carbon coated quartz ampoules and heated up to approximately  $560^\circ\text{C}$  above the melting point of SnTe. The ampoule was then pulled down slowly, at a rate of 3 mm/day, through a temperature gradient. The samples were all single-phased and consist of single crystals with dimensions up to 10 mm. The Mn concentration was checked by micro-probe analysis and varies slightly over the ingot. The apparent carrier concentration at liquid nitrogen temperature varies roughly between 2 and 10 times  $10^{20} \text{ cm}^{-3}$ . Carrier concentrations below  $4 \times 10^{20} \text{ cm}^{-3}$  have been obtained by isothermal annealing in a Zn-vapor, analogous to Ref. [7].

### Variation of the carrier concentration

In Fig. 1 the results are shown of the AC susceptibility, specific heat and magnetization for a sample in the ferromagnetic interaction regime ( $p > p_{\text{crit}}$ ), where the RKKY interaction is assumed to be strong enough to induce a magnetic ordering at helium temperatures. It is precisely this regime where earlier investigations were confined to. We will now focus on the variation of the carrier concentration and its influence on the AC susceptibility.

A sharp transition to a magnetically ordered state is observed in the samples with  $p > 5 \times 10^{20} \text{ cm}^{-3}$ , what is illustrated in Fig. 2 (see also Fig. 1). For smaller  $p$ , we observe a considerable shift of the transition temperature to lower temperatures. The transition becomes less sharp and at the lowest density,  $p \approx 3 \times 10^{20} \text{ cm}^{-3}$ , where the interaction energies become very small, even a second transition seems to appear at  $T = 100 \text{ mK}$ . The carrier concentration dependence of the magnetic properties is additionally manifested by the Curie-Weiss

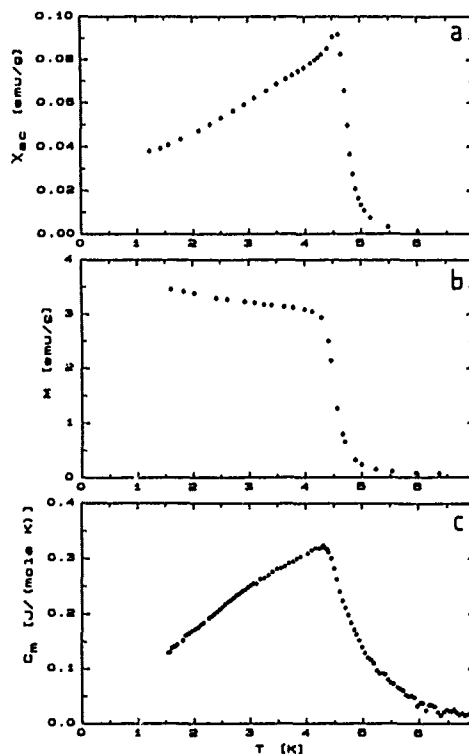


Fig. 1. AC susceptibility (a), magnetization for  $H_{\text{DC}} = 5 \text{ G}$  (b), and magnetic specific heat (c) of  $\text{Sn}_{0.97}\text{Mn}_{0.03}\text{Te}$ ,  $p = 7-10 \times 10^{20} \text{ cm}^{-3}$ .

temperature ( $\Theta$ ), illustrated in Fig. 3. The Curie-Weiss temperatures have been extracted from the high temperature susceptibility data, in the temperature range between 5 and 40 K. Although the number of data at the present stage is rather poor, it is clear that the ternary compound  $\text{Sn}_{0.97}\text{Mn}_{0.03}\text{Te}$  reveals induced ferromagnetism analogous to  $\text{Pb}_{0.25}\text{Sn}_{0.72}(\text{Mn}_{0.03})\text{Te}$  and  $\text{Pb}_{0.52}\text{Sn}_{0.45}(\text{Mn}_{0.03})\text{Te}$ .

Two remarks should be made while examining this figure. First of all, it seems that the increase of the ferromagnetic interactions at  $p_{\text{crit}}$  is more critical (step-like) for  $\text{Sn}(\text{Mn})\text{Te}$  than for the systems with additional Pb (see the inserted lines in Fig. 3). Further, the critical carrier densities deduced from our magnetic phase diagram seem to be only slightly affected by variation of the Pb to Sn ratio. This is in agreement with reports on the pure non-magnetic system  $\text{PbSnTe}$ . From the temperature dependence of the Hall-coefficient in these systems, critical carrier densities roughly between 1 and  $3 \times 10^{20} \text{ cm}^{-3}$  could be inferred.

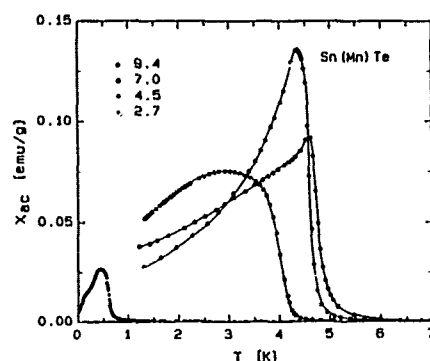
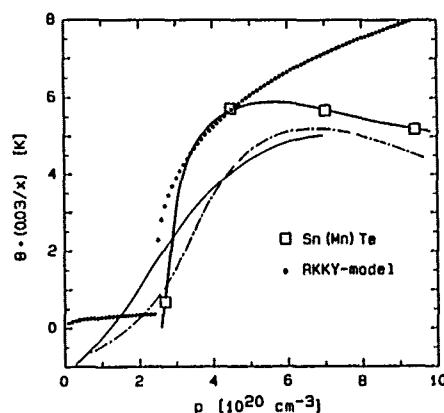


Fig. 2.

AC susceptibility of  $\text{Sn}_{0.97}(\text{Mn}_{0.03})\text{Te}$  for several carrier concentrations (in units  $10^{20} \text{ cm}^{-3}$ ); driving AC field: 0.016 G, 920 Hz

Fig. 3.

Curie-Weiss temperature (scaled on  $x = 0.03$ ) as a function of the carrier concentration; the open squares are the data for  $\text{Sn}_{0.97}(\text{Mn}_{0.03})\text{Te}$ , whereas the boldfaced solid line only represents a guide to the eye. The solid and dashed-dotted line represent the experimental behavior for  $\text{Pb}_{0.52}\text{Sn}_{0.45}(\text{Mn}_{0.03})\text{Te}$  and  $\text{Pb}_{0.25}\text{Sn}_{0.72}(\text{Mn}_{0.03})\text{Te}$ , respectively. Calculations within the modified RKKY-model are given by the closed circles.



Secondly, we have performed numerical calculations within our modified RKKY-model, showing that a similar variation of the magnetic interaction is indicated by the calculations. A comment should be made though on the absolute value of  $\Theta$  in the ferromagnetic regime, which is roughly proportional to the effective mass ( $m^*$ ) of the second valence band. Values for  $m^*$  between 0.4 and 3.0 have been reported [11], depending on the specific experiment and interpretation. We have chosen, rather arbitrary,  $m^* = 1.0$  and therefore quantitative agreement with the data is somewhat coincidental. Despite this, at higher carrier concentrations model calculations and

experimental data diverge. This could be due to the decrease of the mean free path of the carriers at higher  $p$ , although simple inclusion of an exponential damping factor in the RKKY-formula [4] does not affect the Curie-Weiss temperature in that amount.

Summarizing, the results for the Diluted Magnetic Semiconductor Sn(Mn)Te seem to confirm our conjecture that the carrier concentration induced ferromagnetism is rather universal in the IV-VI DMS materials. Some compounds are however somewhat restricted to either the (small) antiferromagnetic interaction regime (PbMnTe) or the ferromagnetic regime (SnMnTe), by a restriction in the variation of their carrier density.

### The ferromagnetic regime

Several reports exist on the magnetic properties of  $\text{Sn}_{1-x}\text{Mn}_x\text{Te}$  with  $x$  (Mn concentration) up to 0.5 [5,8-10], in the ferromagnetic regime. The low temperature magnetic behavior indicates a sharp transition at  $T_C$  which only slightly deviates from  $\Theta$ . The character of the magnetic phase was generally assumed to be ferromagnetic. However, Escorne *et al.* reported in their latest report on Sn(Mn)Te a spinglass phase for  $x$  below 0.03, while for higher concentrations a re-entrant spinglass phase appeared, gradually transformed to a normal ferromagnetic phase above  $x = 0.06$ . In conventional re-entrant systems like PdMn and PdFe [12,13], convenient experiments to explore this magnetic phase were the ZFC (zero field cooled) versus FC (field cooled) magnetization and the AC susceptibility in the presence of external DC fields. Moreover a surprisingly fair agreement with the Sherrington Kirkpatrick (SK) re-entrant spinglass model [14] was obtained by that means.

Some preliminary experiments on the ZFC-FC magnetization in  $\text{Pb}_{0.20}\text{Sn}_{0.72}\text{Mn}_{0.08}\text{Te}$  have been published very recently [15], showing similar effects as for our systems. The results for the DMS  $\text{Sn}_{0.97}\text{Mn}_{0.03}\text{Te}$  are shown in Fig. 4. The observed difference between the ZFC and FC magnetization is strongly dependent on temperature as well as the (driving) DC field. This increase of irreversibility is also reflected by an increasing coercitive force. The AC susceptibility shows a remarkable splitting into two contributions, both shifting in opposite direction with increasing DC field; see Fig. 5a. These phenomena might be attributed to a mixed ferro- and spinglass phase, where the spinglass part is hindered by the application of an external field, while it is favorable for the ferromagnetism [12]. A satisfactory qualitative description of the AC susceptibility can be achieved with the SK model, if the interaction regime is chosen in the vicinity of the phase line between spinglass and re-entrant behavior. The qualitative agreement with the data is illustrated in Fig. 5b.

As a conclusion, the results seem to indicate the existence of a mixed ferro-spinglass or re-entrant spinglass phase in Sn(Mn)Te. In spite of the fact that

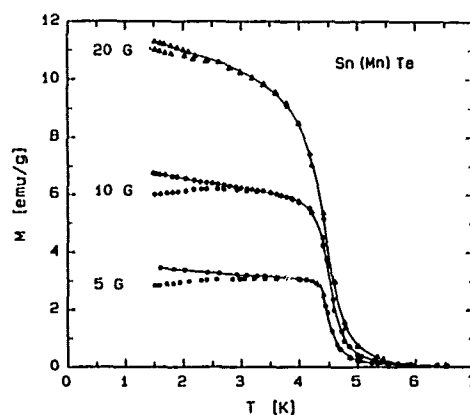


Fig. 4. ZFC-FC magnetization of  $\text{Sn}_{0.97}(\text{Mn}_{0.03})\text{Te}$ ,  $p = 9.4 \times 10^{20} \text{ cm}^{-3}$ , for three DC fields; ZFC: open symbols, FC: closed symbols.

experimental evidence for this behavior has been gathered in numerous magnetic systems, the physical mechanism behind the re-entrant behavior in general is still somewhat obscure, although additional random anisotropies are probably an important factor as they are for conventional spinglass systems [16,17]. The comparison with the SK-model seems to be promising for further exploration of the effect of both

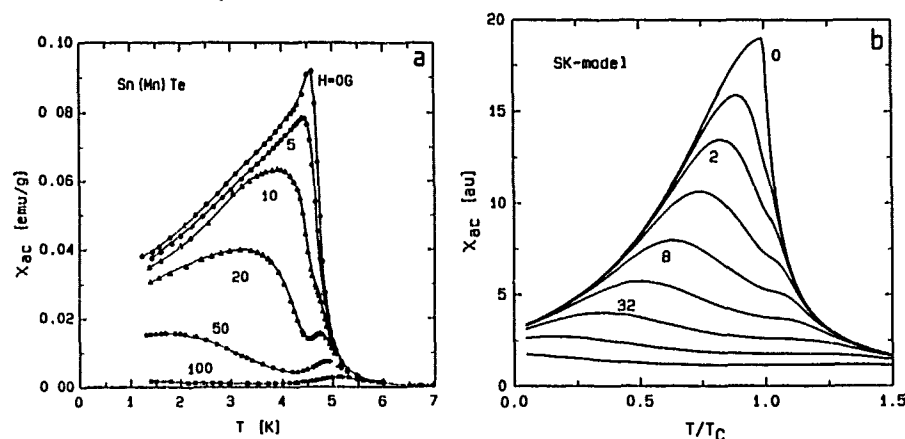


Fig. 5. AC susceptibility in the presence of external DC fields; (a)  $\text{Sn}_{0.91}\text{(Mn}_{0.09}\text{)Te}$ ,  $p = 9.4 \times 10^{20} \text{ cm}^{-3}$ , (b) model calculations with the SK model, using  $\eta = 0.95$ ; DC fields are in units  $0.001 \times H_{DC}/T_C$ .

Mn-concentration and carrier concentration on the magnetic phase diagram of  $\text{Sn(Mn)Te}$ . This should eventually result in the determination of a three dimensional  $(T, x, p)$  magnetic phase diagram of  $\text{Sn(Mn)Te}$ , in which antiferromagnetic and ferromagnetic interactions, as well as spinglass, re-entrant spinglass and ferromagnetic phases appear in one compound.

#### ACKNOWLEDGMENTS

The authors wish to acknowledge for the indispensable experimental assistance of H.J.M. Heyligers, H. van der Hoek, C. van der Steen, N.M.J. Stoffels and J. Zeegers. This work has been financially supported by the Foundation for Fundamental Research on Matter (FOM), which forms part of the Dutch Organization for the Advancement of Research (NWO).

#### REFERENCES

- [1] for a recent review see: J.K. Furdyna, J. of Appl. Phys. **64** (4), R29 (1988).
- [2] T. Story, R.R. Galazka, R.B. Frankel and P.A. Wolff, Phys. Rev. Lett. **56** (7), 777 (1986).

- [3] H.J.M. Swagten, H. v.d. Hoek, W.J.M. de Jonge, R.R. Gałazka, P. Warmenbol and J.T. Devreese in Proceedings of the 19th International Conference on the Physics of Semiconductors, Warsaw (Poland), 1988.
- [4] H.J.M. Swagten, W.J.M. de Jonge, R.R. Gałazka, P. Warmenbol and J.T. Devreese, Phys. Rev. B **37**, 9907 (1988); W.J.M. de Jonge, H.J.M. Swagten, R.R. Gałazka, P. Warmenbol and J.T. Devreese, IEEE trans. on magn. **24** (6), 2542 (1988).
- [5] for some recent reports see: A. Mauger, M. Escorne, Phys. Rev. B **35**, 1902 (1987); M. Escorne, A. Mauger, J.L. Tholence and R. Triboulet, ibid. **29**, 6306 (1984).
- [6] R.S. Allgaier and B. Houston, Phys. Rev. B, 2186 (1972).
- [7] M. Inoue, M. Tanabe, H. Yagi and T. Tatsukawa, J. of the Phys. Soc. of Japan **47** (6), 1879 (1979).
- [8] M.P. Mathur, D.W. Deis, C.K. Jones, A. Patterson, W.J. Carr and R.C. Miller, J. of Appl. Phys. **41** (3), 1005 (1970).
- [9] U. Sondermann, J. of Magn. and Magn. Mat. **2**, 216 (1976).
- [10] M. Escorne, M. Godinho, J.L. Tholence and A. Mauger, J. of Appl. Phys. **57** (1), 3424 (1985).
- [11] G. Nimtz and B. Schlicht in Narrow-Gap Semiconductors, edited by G. Hohler (Springer-Verlag Berlin Heidelberg New York Tokyo 1983), p. 1-117.
- [12] B.H. Verbeek, G.J. Nieuwenhuys, H. Stocker and J.A. Mydosh, Phys. Rev. Lett. **40** (9), 586 (1978).
- [13] G.J. Nieuwenhuys, H. Stocker, B.H. Verbeek and J.A. Mydosh, Solid State Comm. **27**, 197 (1978).
- [14] D. Sherrington and S. Kirkpatrick, Phys. Rev. Lett. **35** (26), 1792 (1975).
- [15] G. Karczewski, A. Wisniewski, T. Story, M. Baran and R.R. Gałazka, Proceedings of the 19th International Conference on the Physics of Semiconductors, Warsaw (Poland), 1988.
- [16] B.R. Coles, Phil. Mag. B **49** (1), L21 (1984).
- [17] A. Chakrabarti and C. Dasgupta, Phys. Rev. Lett. **56** (13), 1404 (1986).



# *IN-SITU* TECHNIQUES FOR STUDYING EPITAXIALLY GROWN LAYERS AND DETERMINING THEIR MAGNETIC PROPERTIES

**B. HEINRICH, A.S. ARROTT, J.F. COCHRAN, K.B. URQUHART, K. MYRTLE,  
Z. CELINSKI, AND Q.M. ZHONG,** Surface Physics Laboratory, Physics Department, Simon  
Fraser University, Burnaby BC, CANADA V5A-1S6

## ABSTRACT

Ultrathin films of bcc Fe (001) on Ag (001) and Fe/Ni (001) bilayers on Ag were grown by molecular beam epitaxy. A wide range of surface science tools (RHEED, REELFS, AES, and XPS) were employed to establish the quality of epitaxial growth. Ferromagnetic resonance and Brillouin light scattering were used to extract the magnetic properties. Emphasis was placed on the study of magnetic anisotropies. Large uniaxial anisotropies with the easy axis perpendicular to the film surface were observed in all ultrathin structures studied. In sufficiently thin samples the saturation magnetization was oriented perpendicular to the film surface in the absence of an applied field. It has been demonstrated that in bcc Fe films the uniaxial perpendicular anisotropy originates at the film interfaces. Fe/Ni bilayers were also investigated. Ni grows in the pure bcc structure for the first 3-6ML and then transforms to a new structure which exhibits unique magnetic properties. Transformed ultrathin bilayers possesses large in-plane 4th order anisotropies far surpassing those observed in bulk Fe and Ni. The large 4th order anisotropies originate in crystallographic defects formed during the Ni lattice transformation.

## INTRODUCTION

The structure and magnetic properties of ultrathin films and superlattices have been vigorously studied recently. Interest in ultrathin structures was triggered both by first principle calculations of enhanced magnetic moments and surface anisotropies<sup>1-3</sup> and by the availability of Molecular Beam Epitaxy (MBE) systems. MBE techniques allow one to prepare well defined, clean structures which can be directly compared with theoretical calculations. The properties of ultrathin films differ, sometimes strongly, from bulk properties due to the broken symmetry at their surfaces. The interfaces create valence electron surface states which often possess unique magnetic properties. The growth of ultrathin films is also often strongly affected by the substrate template resulting, in some cases, in metastable structures which otherwise do not occur naturally.

Ultrathin films (layers, overlayers, bilayers) are epitaxial structures thinner than the exchange length:  $[A/(2\pi M_s^2)]^{1/2}$  ( $\approx 33\text{\AA}$  for Fe). Magnetic moments separated by a distance smaller than the exchange length are locked together by the exchange interaction. A system having a spatial scale smaller than the exchange length responds as a single unit to the total torque acting on the system. In particular, ultrathin films and bilayer structures behave like single systems with magnetic properties of their own.

This paper reports on extensions of our detailed studies of bcc Fe ultrathin films and Fe/Ni ultrathin bilayers in which we use extensively our abilities to characterize the growth and measure the magnetic properties in-situ. Our previous work has provided insight into the magnetism of ultrathin films, but has also raised important questions, some of which we answer here. In

particular, we have added to our result that the magnetization of ultrathin layers of bcc Fe points perpendicular to the surface by showing that the dominant uniaxial surface anisotropy ( $\cos 2\theta$ ) is virtually unopposed by the perpendicular four-fold surface anisotropy ( $\cos 4\theta$ ). We have refined the ferromagnetic resonance (FMR) technique to extract the spontaneous magnetization from the integrated intensity of the resonance. By using FMR we have established that the very large in-plane anisotropies of our Ni/Fe bilayers are independent of applied magnetic field. The effects of magnetic domain wall motions and the resulting magnetic hysteresis were observed with FMR and the Magneto-Optic Kerr Effect. These results are put in the context of our previous work which rests upon the foundation of detailed growth studies used to characterize the layer formation and sharpness of interfaces in ultrathin structures.

Epitaxial growth of bcc Fe films and Fe/Ni bilayers deposited on Ag(001) substrates has been studied by Reflection High Energy Electron Diffraction (RHEED), by Reflection High Energy Electron Loss Fine Structure (REELFS) and by monitoring the Auger (AES) and X-ray photoelectron (XPS) substrate peak intensities as a function of overlayer thickness. The oscillations in the intensity of the RHEED specular spot monitored during the growth provided an accurate method of determining at each instant of time the number of monolayers (ML) already deposited. RHEED oscillations in conjunction with realistic growth models can be used to characterize the quality of growth as well. Magnetic properties of ultrathin structures were investigated primarily by Ferromagnetic Resonance (FMR) and Brillouin Light Scattering (BLS). FMR measurements at 10, 24, 36 and 73 GHz (room and cryogenic temperatures) and BLS studies in fields 2–10 kOe were carried out ex-situ on samples protected by epitaxial Au(001) coverlayers. FMR studies at 17 GHz were performed in-situ in the MBE chamber.

FMR and BLS techniques are well suited to study both the static and the dynamic magnetic properties of a specimen. The static properties include the saturation magnetization  $M_s$ , all anisotropies, the effective demagnetizing field  $(4\pi D_{\perp} M_s)_{\text{eff}}$  and magnetic hysteresis loops. The dynamic properties include the spectroscopic  $g$ -factor and damping parameters.

## GROWTH STUDIES

Epitaxial growth of Fe ultrathin films and Fe/Ni bilayers was carried out in a Physical Electronics molecular beam epitaxy (PHI-MBE 400) system. This MBE system was equipped with RHEED and a double pass cylindrical analyzer for AES and XPS electron spectroscopies. The RHEED screen was equipped with a magnifying lens which focussed a small area of the RHEED screen onto a photomultiplier tube in order to measure either the intensity of the RHEED specular spot as a function of film thickness or to scan a diffracted beam to obtain a measure of the atom-atom correlation function of the surface. The Ag(001) substrates were 15 mm in diameter and 3.5 mm thick. They were prepared using standard metallographic techniques.<sup>4,5</sup> We used vicinal ( $1.5^\circ$ ) and singular ( $\leq 0.25^\circ$ ) Ag(001) substrates. These substrates were sputter etched with a 2keV  $\text{Ar}^+$  ion beam at 450 °C and then annealed at 350 °C. During deposition the vacuum in the growth chamber remained in the low  $10^{-10}$  torr range. Depositions were carried out with the sample substrates held at room temperature. The overall homogeneity of deposited films was determined by monitoring the thickness dependence of the dominant XPS and AES peaks of the substrate material. In addition, the AES and XPS spectra showed that the bulk Ag(001) substrates and the Fe and Ni films were free of surface contaminants. Good epitaxial growth is expected when the overlayer and substrate lattice meshes are well matched. bcc

Fe(001) matches well the Ag(001) surface template when their square cells are mutually rotated by  $45^\circ$ . However an appreciable vertical mismatch remains due to the difference in the (001) layer spacings of fcc Ag and bcc Fe. The presence of atomic steps affects the initial stages of growth and, consequently, the magnetic properties of the first few Fe layers. The Fe films epitaxially grown on vicinal Ag substrates showed regular RHEED oscillations only after 3-4 ML had been deposited.<sup>4</sup> At least a complete bcc unit cell had to be grown in order to obtain a well defined layer by layer growth. This is a healing distance for covering atomic steps. The growth on singular substrates showed RHEED oscillations during the entire growth, see Fig.1. However even in this case the first 1 1/2 layers were formed in a complex manner as was clear from the initial stages of the RHEED oscillations, see Fig.1.

Ni overlayers grow very well on an Fe(001) template.<sup>6-9</sup> The first 3-6 ML grow in a perfect bcc structure.<sup>9</sup> After reaching a critical thickness (3-5ML) the Ni overlayer transforms gradually to a more complicated structure. We do not yet know the detailed atomic structure but we refer to it as "bcc Ni" as distinct from bcc Ni which is the structure of the thinner layers. It is this thicker transformed Ni that shows interesting magnetic properties.<sup>8,10</sup> The main structural features of the transformed "bcc Ni" can be summarized as follows: (1) bcc RHEED features remain along the {100} and {110} principal azimuths, see Fig.2. RHEED patterns along {110} azimuths differ from the pure bcc pattern by the addition of weak diffraction streaks positioned 2/5 of the way between the bcc streaks, see Fig.2. 3-dimensional diffraction features, elongated normal to the surface, developed for thicker samples with sufficient clarity so that the periodicity perpendicular to the film surface could be identified. These  $\lambda$ -like diffraction features correspond to the bcc Fe lattice spacing along the [001] crystallographic direction. (2) The additional superlattice streaks are visible for azimuths away from the {100} and {110} directions. Their complicated angular dependence indicates that the Ni transformation is a rather severe distortion of the basic bcc lattice. (3) The Fourier transform of in situ REELFS spectra, obtained from transformed "bcc Ni" overlayers, was mainly useful for determining the nearest neighbor distance (n.n.d.). The n.n.d. was found to be identical with that of fcc Ni (2.49Å) and nearly the

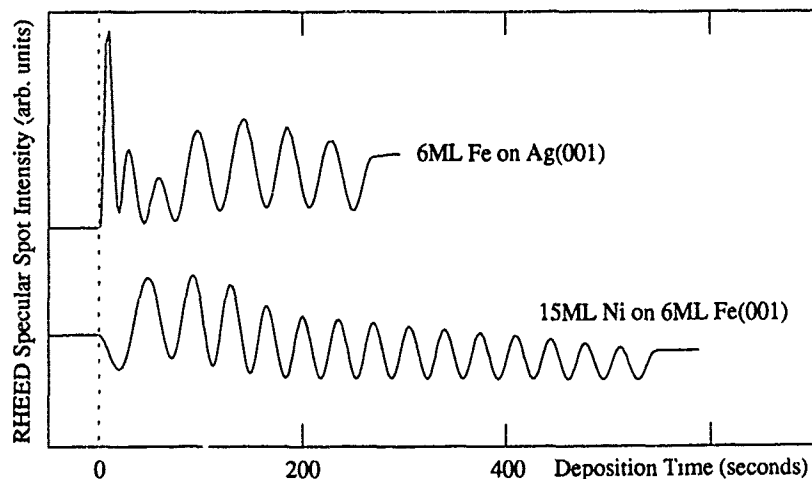


Fig. 1. RHEED pattern oscillations. The intensity of the specular spot is plotted against growth time. (a) 6ML Fe grown on Ag(001). (b) 15ML of Ni on the 6ML Fe film.

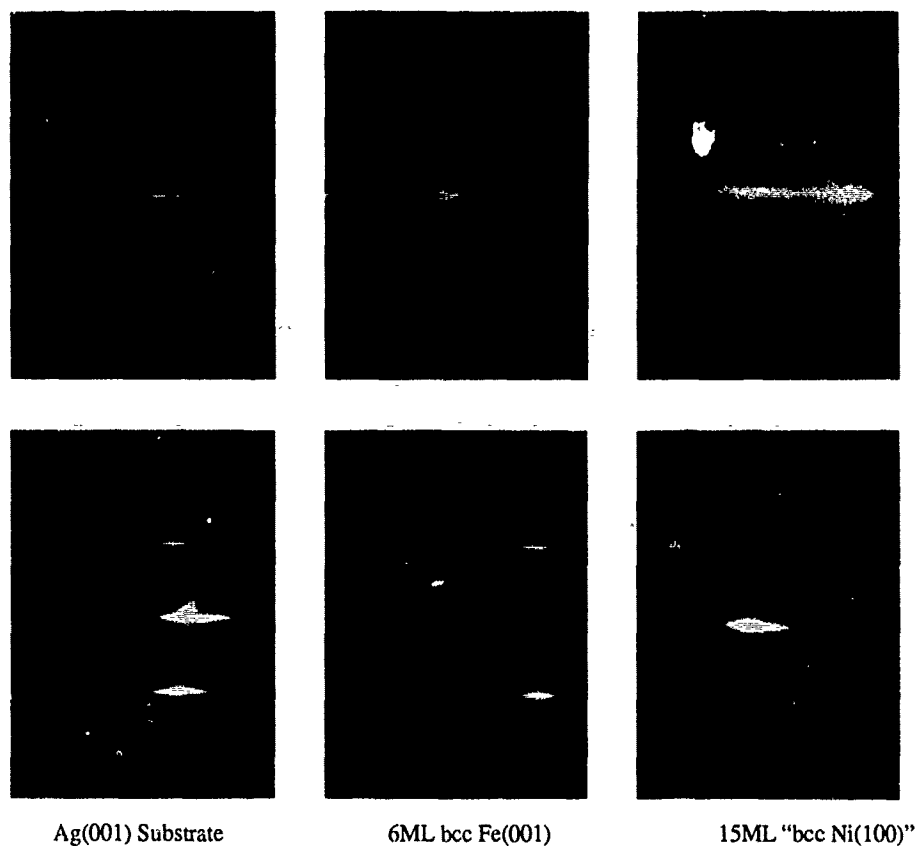


Fig. 2. RHEED patterns of 15ML "bcc Ni(001)" grown on 6ML Fe(001) deposited on a singular Ag(001) substrate. The upper three and lower three photographs correspond to a 10keV electron beam oriented along the [110] and the [100] azimuths respectively.

same as the n.n.d. in bcc Fe ( $2.48\text{\AA}$ ). However REELFS spectra of the transformed Ni overlayer more closely resemble fcc Ni than bcc Fe.<sup>7</sup> Indeed, the glancing incidence EXAFS measurements, carried out on a [Au(10ML)/Ni(9ML)/Fe(9ML)/Ag(001)] sample, indicated that the second n.n. atoms of "bcc Ni" equally appear in both fcc and bcc unit cells.<sup>11</sup> (4) Ni overlayers, even after lattice transformation, grew very uniformly. The Fe KLL AES and Fe  $2p_{3/2}$  XPS peak intensities decreased exponentially with increasing amount of Ni deposited, and their respective electron mean free paths were in good agreement with the inelastic electron mean free path values (IMFP) as determined from Seah's formula.<sup>12</sup> Furthermore the amplitude of the RHEED oscillations remained strong and decreased slowly during further growth, see Fig. 1.

The maintenance of RHEED oscillations after transformation to "bcc Ni" and the film homogeneity indicates clearly that the growth proceeded layer by layer. It might be that the transformed "bcc Ni" is formed by fcc blocks. One can consider rectangular (011) fcc blocks because the average lattice spacing in the (011) plane is close to that of the Fe(001) square mesh. The

RHEED 4-fold symmetry would then be satisfied by distributing (011) blocks symmetrically along two mutually perpendicular directions, that is along either {110} and  $\{1\bar{1}0\}$  or {100} and {010} Fe substrate crystallographic axes. The width of the specular spot indicates that the block size is 20-40Å on a side. The decreased period of the RHEED oscillations after Ni transformation suggests that the average atomic coverage per atomic plane is decreased by 7-20 %. The atomic coverage of an fcc Ni (011) plane is 7% lower than that in (001) bcc Fe and would be further decreased due to the high density of misfit dislocations along the block boundaries.

Much as we might like to know whether the local order is bcc or fcc, it is more important to realize that "bcc Ni" overlayers in Fe/Ni bilayers form a unique structure accompanied by magnetic properties which are truly different from those observed for ordinary Ni and Fe. Even though we do not know the atomic structure of "bcc Ni", we can use in-situ RHEED to identify this structure from its characteristic diffraction features. Additional surface science tools are needed to develop a clear picture of the "bcc Ni" overlayer.

### RESONANCE STUDIES IN ULTRATHIN STRUCTURES

FMR and BLS are powerful tools in the study of magnetic materials and have become particularly useful for the characterization of ultrathin magnetic films. The power of resonance techniques lies in the dependence of the rf susceptibility ( $\chi = \chi' - i\chi''$ ) on all participating torques. This is summarized by the Landau-Lifshitz (L-L) equation of motion for the magnetization  $\mathbf{M}$ :  $(-1/\gamma)\partial\mathbf{M}/\partial t = \mathbf{M} \times \mathbf{H}_{\text{eff}}$  where  $\mathbf{M}$  and  $\mathbf{H}_{\text{eff}}$  contain contributions from both static and rf components, that is  $\mathbf{M} = \mathbf{M}_s + \mathbf{m}$  and  $\mathbf{H}_{\text{eff}} = \mathbf{H}_0 + \mathbf{h} + \mathbf{h}_d + \mathbf{H}_K + \mathbf{h}_K + \mathbf{h}_G + \mathbf{h}_{\text{ex}}$ .  $\mathbf{M}_s$  is the saturation magnetization and  $\mathbf{m}$  is the rf component of  $\mathbf{M}$ .  $\mathbf{H}_0$  is the static internal field which is parallel with the plane of the ultrathin film sample (parallel configuration) and  $\mathbf{h}$  is the parallel component of the internal rf field.  $\mathbf{h}_d = -4\pi D_{\perp} \mathbf{m}_{\perp}$  is the demagnetizing field perpendicular to the film surface. The demagnetizing factor  $D_{\perp}$  in ultrathin films is dependent on the number of atomic planes,<sup>5,10</sup> see Table I. The anisotropy fields  $\mathbf{H}_K$  and  $\mathbf{h}_K$  depend on the direction of the magnetization  $\mathbf{M}$  with respect to the crystallographic axes. They are derived from the magnetic anisotropy energies which satisfy the ultrathin film lattice symmetry requirements. The intrinsic damping is described by the Gilbert effective damping field  $\mathbf{h}_G = -i(\omega/\gamma)(G/\gamma)\mathbf{m}/M_s^2$ . The exchange field due to spatial variations of  $\mathbf{m}$  is given by  $\mathbf{h}_{\text{ex}} = 2A(\nabla^2\mathbf{m})/M_s^2$ , where  $A$  is the exchange coupling coefficient. The internal field in FMR is given by the rf field at the sample surface. In BLS measurements the resonance mode is excited by thermal fluctuations and the corresponding internal  $\mathbf{h}$  field can be derived from equipartition of energy.<sup>13</sup>

#### Magnetic anisotropies

Ultrathin films of cubic materials grown along the [001] crystallographic direction exhibit tetragonal symmetry. The magnetocrystalline anisotropy energy can therefore be written as:

$$E_K = -\frac{1}{2}K_{11}[\alpha_x^4 + \alpha_y^4] - \frac{1}{2}[K_{11}\alpha_z^4] - K_u\alpha_z^2 \quad (1)$$

where  $\alpha_x, \alpha_y, \alpha_z$  are directional cosines with respect to [100], [010] and [001] crystallographic axes. When the saturation magnetization,  $\mathbf{M}_s$ , is oriented in the plane of the film (parallel configuration) the 4th order uniaxial anisotropy perpendicular to the sample surface plays a negligible role in resonance measurements since the corresponding effective field is proportional to the

3rd power of the rf perpendicular magnetization component. On the other hand when the saturation magnetization is oriented along the sample normal (perpendicular configuration) the in-plane 4th order anisotropy plays no role and the 4th order perpendicular anisotropy acts as an effective d.c. field  $2K_{1\perp}/M_s$  oriented along the sample normal. Note that in the parallel configuration the first part of equation (1) is equivalent to a full cubic anisotropy,  $K_1(\alpha_x^2\alpha_y^2 + \alpha_y^2\alpha_z^2 + \alpha_z^2\alpha_x^2)$ , in as much as  $\alpha_x^4 + \alpha_y^4 + \alpha_z^4 = 1 - 2(\alpha_x^2\alpha_y^2 + \alpha_y^2\alpha_z^2 + \alpha_z^2\alpha_x^2)$ . In ultrathin films the surface anisotropies play a significant role. The anisotropy energy at the surface can be written:

$$E_K = -\frac{1}{2}K_{1\parallel}^S[\alpha_x^4 + \alpha_y^4] - \frac{1}{2}[K_{1\perp}^S\alpha_z^4] - K_u^S\alpha_z^2 \quad (2)$$

In ultrathin films the magnetic moments across the sample are nearly parallel. The system responds as a rigid unit. The total torque is shared equally by all magnetic moments. Consequently the surface anisotropies divided by the film thickness,  $d$ , appear as effective bulk-like anisotropies:

$$K_{1\parallel}^{\text{eff}} = K_{1\parallel} + \frac{K_{1\parallel}^S}{d}; \quad K_u^{\text{eff}} = K_u + \frac{K_u^S}{d} \quad (3)$$

where  $K_{1\parallel}^S$  and  $K_u^S$  include contributions from all interfaces of the ultrathin film structure. In our analyses we will assume  $K_u = 0$ . The linearized L-L equations of motion for the parallel configuration become (for the time dependence of  $\exp(i\omega t)$ ):

$$-i\frac{\omega}{\gamma}\mathcal{M}_x + \left[ H_0 + 4\pi D_{\perp}M_s - \frac{2K_u^{\text{eff}}}{M_s} + \frac{K_{1\parallel}^{\text{eff}}}{2M_s}(3 + \cos[4\phi]) + \frac{K_u^v}{M_s}(1 + \cos[2(\phi - \phi_u^v)]) + i\frac{\omega}{\gamma}\frac{G}{\gamma M_s} \right] \mathcal{M}_z = 0 \quad (4a)$$

$$\left[ H_0 + \frac{2K_{1\parallel}^{\text{eff}}}{M_s}\cos[4\phi] + \frac{2K_u^v}{M_s}\cos[2(\phi - \phi_u^v)] + i\left(\frac{\omega}{\gamma}\right)\frac{G}{\gamma M_s} \right] \mathcal{M}_x + i\frac{\omega}{\gamma}\mathcal{M}_z = M_s d h \quad (4b)$$

where  $\mathcal{M}_x$  and  $\mathcal{M}_z$  are the integrated rf magnetization components across the specimen thickness and  $\phi$  is the angle between the saturation magnetization,  $M_s$ , and the in-plane [100] axis. Vicinal surfaces exhibit in-plane uniaxial anisotropies and  $\phi_u^v$  is the angle between the preferred axis and the [100] direction and  $K_u^v$  is the anisotropy constant due to the effect of the vicinal cut. Note that  $(4\pi D_{\perp}M_s - 2K_u^{\text{eff}}/M_s)$  appears as a unit and can be defined as the effective demagnetizing field  $(4\pi D_{\perp}M_s)_{\text{eff}}$ . Equations (4a) and (4b) summarize algebraically the power of FMR and BLS measurements. The in-plane angular dependence of the resonance fields (FMR) or frequencies (BLS) determine  $K_{1\parallel}^{\text{eff}}$  and  $K_u^v$ . The variation of the resonant fields with applied microwave frequencies determines the effective demagnetizing field,  $(4\pi D_{\perp}M_s)_{\text{eff}}$  and the spectroscopic splitting factor,  $g$ . The BLS measurements have a relatively poor frequency resolution ( $\sim 1$  GHz) but they cover a broad frequency range (1–100 GHz) so that  $(4\pi D_{\perp}M_s)_{\text{eff}}$  and the  $g$ -factor can be accurately measured. BLS measurements can be confined to a very small spot ( $\sim 10\mu\text{m}$ ); they are

therefore particularly convenient for studying Fe whiskers which possess almost ideal surfaces useful in the examination of the role of atomic steps.

Note, that the saturation magnetization,  $M_s$ , cannot be determined from the FMR field,  $H_{FMR}$ , alone; that is, the zero crossing of the field derivative of the absorbed microwave power ( $d\chi''/dH_0$ ). However, the total intensity of the FMR signal (doubly integrated field derivative of the absorption or  $\chi''$ ) is directly proportional to the total magnetization of the specimen:

$$I \propto M_s d \frac{[H_{FMR} + (4\pi D_{\perp} M_s)_{eff}]}{[2H_{FMR} + (4\pi D_{\perp} M_s)_{eff}]} \quad (5)$$

The dynamic properties are contained in the FMR linewidth  $\Delta H$  (the field interval between extrema of the absorption derivative  $d\chi''/dH_0$ ). The frequency dependence of the FMR linewidth in ultrathin films can be described by:  $\Delta H = \Delta H(0) + 1.16(\omega/\gamma)G/(\gamma M_s)$  where the frequency dependent part is related to the intrinsic Gilbert damping arising from the spin-orbit contribution to the electron valence band energies<sup>14</sup> and the frequency independent part,  $\Delta H(0)$ , is caused by magnetic inhomogeneities.<sup>15</sup>  $\Delta H(0)$  is a measure of the quality of the overlayer growth.

#### Resonance Measurements in Magnetic Bilayers

The theory of exchange-coupled magnetic bilayers has been described elsewhere.<sup>10</sup> Here we restrict the discussion to tightly exchange coupled bilayers where the magnetic moments in the constituent ultrathin films A and B are nearly parallel. It can be shown, after appreciable algebraic steps, that the bilayer magnetic response can be described by L-L equations of motion for an ultrathin film where the effective fields are replaced by a linear combination of the effective fields of the individual layers A and B. In terms of the parameter  $\alpha$  defined by:

$$\alpha \equiv \frac{\mu^A N^A}{\mu^A N^A + \mu^B N^B} \quad (6)$$

where  $\mu_{A,B}$  and  $N_{A,B}$  are the magnetic moments per atom and the number of atomic planes in layers A and B respectively, the effective field in the bilayer is:

$$H_{eff}^{bilayer} = \alpha H_{eff}^A + (1 - \alpha) H_{eff}^B \quad (7)$$

The total magnetic moment in a bilayer A/B, evaluated from FMR intensity measurements, is given by the sum of the total magnetic moments in layers A and B: that is,  $M_s^{bilayer} = d^A M_s^A + d^B M_s^B$  where  $d^A$  and  $d^B$  are the individual film thicknesses.

#### THE MAGNETIC PROPERTIES OF bcc Fe(001)

The calculations of Gay and Richter<sup>3</sup> have shown that in an Fe(001) monolayer the contribution of the spin-orbit interaction to the valence electron energy bands can result in a large uniaxial anisotropy with easy axis oriented perpendicular to the surface. This theoretical prediction was indirectly supported by Jonker et al.<sup>16</sup> in spin-polarized experiments carried out on ultrathin bcc Fe(001) films grown on Ag(001). The lack of a spin-polarized signal parallel to the

specimen surface for layers thinner than 2.5 ML pointed to the possibility that the saturation magnetization in these samples could be oriented perpendicular to the specimen surface. However, the origin and existence of these anisotropies were unambiguously established by FMR measurements carried out by Heinrich et al.<sup>5</sup> Subsequently, Stampanoni et al.,<sup>17</sup> using modified spin-polarized photoemission experiments, reported a remanent state magnetized perpendicularly to the sample surface. They found that uncovered iron films 3ML thick at temperatures less than 30K showed this behavior. Volkening et al.,<sup>18</sup> employing Conversion Electron Mössbauer Spectroscopy and Krebs et al.,<sup>19</sup> using SQUID Magnetometry, studied the orientation of the saturation magnetization in [Ag/Fe(0.9–5.5ML)/Ag] superlattices. Their samples showed also that a remanent state having the saturation magnetization perpendicular to the sample surface is observable only at low temperatures,  $T < 30\text{K}$ .

The main results of our investigations are summarized in Table I. Further details can be found in the original papers.<sup>4,5,20</sup> FMR and BLS studies were performed outside of the UHV system on samples protected by epitaxial Au(001) or Ag(001) overlayers – the latter being further protected by a Au(001) coverlayer. FMR measurements on bare and subsequently covered Fe films were carried out in UHV at 16.85 GHz thereby allowing us to determine the role of the Fe/vacuum, Fe/Ag and Fe/Au interfaces. None of our samples grown on vicinal surfaces and covered by Au showed a negative value of  $(4\pi D_{\perp} M_s)_{\text{eff}}$ . For vicinal surfaces only samples covered by Ag and cooled to  $\text{LN}_2$  temperature exhibited negative  $(4\pi D_{\perp} M_s)_{\text{eff}}$  see Table I. These specimens were likely magnetized perpendicular to the plane in zero applied field.

The importance of vertical mismatch between Ag and Fe layers was demonstrated on a 3ML thick Fe film grown on Ag(001) deposited on an Fe whisker (001) facet, see Table I. Though this sample was covered by a Au overlayer, it exhibited a negative value  $(4\pi D_{\perp} M_s)_{\text{eff}} = -2.4 \text{ kG}$  even at room temperature. Clearly, a decreased density of atomic steps resulted in an increased value of the perpendicular anisotropy which was large enough to overcome the dipolar demagnetizing field.

The thickness dependence of  $(4\pi D_{\perp} M_s)_{\text{eff}}$  in Fe films ( $d > 4\text{ML}$ ) covered by Au shows clearly that the perpendicular uniaxial anisotropy is inversely proportional to the film thickness,  $d$ , and is therefore likely caused by surface anisotropy (see Tables I and II).<sup>21</sup>

In situ measurements on ultrathin films grown on singular Ag(001) substrates<sup>20</sup> were used to investigate the properties of the individual interfaces. An uncovered 7.6ML Fe film, which had a smooth and uncontaminated surface, exhibited a strong uniaxial anisotropy corresponding to a total surface anisotropy  $K_u^S = 1.58 \text{ ergs/cm}^2$ . This anisotropy decreased to  $1.26 \text{ ergs/cm}^2$  when this sample was covered by Ag, and decreased in value to  $1.0 \text{ ergs/cm}^2$  when Au was used as a coverlayer. On the assumption that surface anisotropies are additive for two interfaces these results imply that the Fe/vacuum, Fe/Ag and Fe/Au interfaces were characterized by  $K_u^S = 0.95$ ,  $0.63$  and  $0.37 \text{ ergs/cm}^2$  respectively. The strongest surface anisotropy was observed for Fe/vacuum interfaces. Extrapolation of the 7.6ML result predicts that well prepared samples thinner than 7ML and having a vacuum interface would be magnetized perpendicular to the surface; in this case no ferromagnetic resonance could be observed at room temperature over the 0–5.8 kOe field range of the *in-situ* FMR probe because the resonance field,  $H_{\text{FMR}}$ , would exceed 5.8 kOe. This is in accord with our unsuccessful attempts to find a resonance for a 5ML sample having one vacuum interface.<sup>20</sup> The sensitivity of the *in-situ* FMR was sufficient to observe FMR signals in 2ML samples. We concluded that a 5ML Fe(001) film having a vacuum interface must be magnetized perpendicular to the surface in its remanent state even at room temperature.



The negative value of  $(4\pi D_{\perp} M_s)_{\text{eff}}$  is a necessary, but not a sufficient, condition to have a remanent state with the saturation magnetization perpendicular to the sample surface. The presence of higher order perpendicular anisotropy terms,  $K_{11}(\alpha_z^n)$  ( $n \geq 4$ ), can affect the remanent state of the saturation magnetization. A negative value of  $K_{11}$  having the effective field  $|2K_{11}/M_s| > |(4\pi D_{\perp} M_s)_{\text{eff}}|$  would in fact rotate the saturation magnetization,  $M_s$ , away from the specimen normal. However, one should realize that this rotation is only partial. Torques originating in higher order anisotropies become negligible as the saturation magnetization approaches the specimen surface and therefore  $M_s$  can reach the specimen surface only asymptotically. The values of the fourth order perpendicular anisotropy fields can be obtained from FMR measurements carried out in the perpendicular configuration. Results of our analysis are shown in Table II. The fourth order perpendicular anisotropy fields are small in ultrathin iron films and therefore all of our specimens with  $(4\pi D_{\perp} M_s)_{\text{eff}} < 0$  were oriented perpendicularly to the speci-

TABLE I: Measured magnetic properties of ultrathin bcc Fe(001) films grown on Ag(100).

d (ML)	T (K)	Cover Metal	$(4\pi D_{\perp} M_s)_{\text{eff}}$ (kOe)	g	$4\pi M_s$ (kOe) <sup>a</sup>	$D_{\perp}$	$H_u^S$ (kOe) <sup>b</sup>	$K_u^S$ (ergs/cm <sup>2</sup> )	$K_{11}^{\text{eff}}$ (ergs/cm <sup>2</sup> )	$H_{11}^S$ (kOe) <sup>c</sup>
28.0	300	Au	18.084	2.09	21.55	0.985	3.1	0.94	$4.8 \times 10^5$	2.7
17.3	300	Au	16.578	2.08	21.55	0.975	4.4	0.86	$4.2 \times 10^5$	2.7
5.3	300	Au	6.811	2.09	20.7	0.920	12.2	0.76	$1.1 \times 10^5$	2.7
5.3	77	Au	7.791	2.09	21.3	0.920	11.8	0.76	$2.7 \times 10^5$	
5.1 <sup>d</sup>	300	Au	6.77	2.08	20.7	0.915	12.9	0.79	$1.0 \times 10^5$	2.7
3.0 <sup>e</sup>	300	Au	-2.4	2.09	15.0	0.848	15.1	0.38	0.0	
2.8	300	Au	0.562	2.09	15.2	0.848	12.3	0.30	0.0	
2.8	77	Au	0.876	2.09	22.5 <sup>f</sup>	0.848	18.2	0.65	0.0	
3.0	300	Ag	0.320	2.00	14.3	0.856	11.9	0.29	0.0	
3.0	77	Ag	-0.727	1.98	21.0 <sup>f</sup>	0.856	18.7	0.67	0.0	
7.6 <sup>d</sup>	300	bare	2.81	2.14	21.55	0.944	17.5	1.58	$1.5 \times 10^5$	
7.6 <sup>d</sup>	300	Ag	6.38	2.14	21.55	0.944	14.0	1.26	$1.5 \times 10^5$	

a)  $4\pi M_s$  was determined from FMR absolute intensity measurements using a 15ML Fe(001) reference sample which was assumed to have the bulk iron value of  $4\pi M_s = 21.55$  kOe.

b) The perpendicular uniaxial anisotropy field,  $H_u^S$ , was obtained assuming  $K_u = 0$ . The perpendicular uniaxial surface anisotropy constant was calculated from  $2K_u^S/(M_s d) \equiv H_u^S$ .

c)  $H_{11}^S \equiv 2K_{11}^S/(M_s a/2)$  describes the 4th order surface anisotropy field corresponding to a 1ML Fe film.  $K_{11}^S$  was calculated by fitting the data for 300K and  $d \geq 5$ ML to  $K_{11}^{\text{eff}} = K_{11} - K_{11}^S/d$ . The fit gave  $K_{11} = 5.5 \times 10^5$  ergs/cm<sup>3</sup> which is 15% larger than the cubic anisotropy constant of bulk Fe ( $4.8 \times 10^5$  ergs/cm<sup>3</sup>).

d) These films were grown on a singular Ag(001) single crystal oriented within  $\pm 0.25^\circ$  of (001).

e) Fe film grown on a 10 ML Ag(001) substrate deposited on Fe(001) whisker.

f)  $4\pi M_s$  at LN<sub>2</sub> temperature was increased from its room temperature value by a factor of 1.5 as measured in the spin polarized experiments by Stampanoni, et al.<sup>17</sup>

men surface. The additional perpendicular anisotropy does not necessarily have to be of the fourth order. However, an excellent fit between experimental FMR data and the theory, see Fig. 3, using only the second and fourth order perpendicular anisotropies strongly indicates that the perpendicular anisotropy is indeed described by the sum of second and fourth order terms.

All Fe films studied showed a decrease in the in-plane 4th order anisotropy with decreasing film thickness. It is interesting to note that the difference between the bulk anisotropy coefficient,  $K_{111} = 5.5 \times 10^5$  (ergs/cm<sup>3</sup>), and the measured effective anisotropy coefficient,  $K_{111}^{\text{eff}}$ , scales inversely with the sample thickness, see Table I. The observed decrease in the in-plane 4th order anisotropy can therefore be ascribed to the presence of an in-plane 4th order surface anisotropy in which the easy axis is oriented along the {110} axes contrary to bulk Fe in which the easy axis is oriented along the {100} axes. A slightly increased value of  $K_{111}$  from the value in bulk Fe (~15%) is not surprising since it is not uncommon that ultrathin films exhibit significantly increased in-plane 4th order anisotropies<sup>22</sup> (see the next section on Ni/Fe bilayers).

It is possible that the large surface pinning observed in ultrathin films is not an intrinsic result of the abrupt interfaces, but is created by a lattice mismatch induced strain,<sup>23</sup> e.g., due to surface steps. An obvious question to ask is whether a large pinning exists at the surface of bulk Fe. We have measured the surface anisotropies for {bulk Fe(001)/noble metal} interfaces. Values of the surface anisotropies deduced from FMR and BLS measurements<sup>24,25</sup> were in good agreement,  $K_u^S = 0.79, 0.54$  ergs/cm<sup>2</sup> for Fe/Ag and Fe/Au interfaces and were found to be consistent with those deduced from the ultrathin iron film studies. This confirms that the surface anisotropies observed in thin films originate in the broken symmetry of their surfaces. It is also remarkable that the original predictions by Gay and Richter agree well with our observations. Recent theoretical calculations<sup>26</sup> indicate that the theory of magnetic anisotropies in ultrathin films is far from being well understood.

The agreement between our data and the calculations of Gay and Richter could be merely coincidental, however their basic conclusion must be correct. The perpendicular anisotropy in ultrathin Fe(001) films is an intrinsic effect, and in this respect the measured surface anisotropies provide data against which proposed theoretical models can be compared quantitatively.

TABLE II: Measured magnetic properties of Au covered bcc Fe(001) films grown on Ag(100).

d (ML)	$(4\pi D_{\perp} M_s)_{\text{eff}}$ (kOe)	g	$4\pi M_s$ (kOe) <sup>a</sup>	$D_{\perp}$	$K_u^S$ (ergs/cm <sup>2</sup> )	$H_{111}$ (kOe) <sup>b</sup>	$H_p$ (kOe) <sup>c</sup>	$K_p$ (ergs/cm <sup>3</sup> )
9	11.20	2.09	21.55	0.953	1.03	0.310	0.019	$0.2 \times 10^5$
7	9.50	2.09	21.55	0.939	0.93	0.240	-0.223	$-1.9 \times 10^5$
5	6.54	2.09	21.55	0.915	0.81	0.094	-0.223	$-1.9 \times 10^5$
3	1.82	2.09	15.0	0.848	0.28	~0	-0.839	$-5.1 \times 10^5$
10/8 <sup>d</sup>	10.25	2.1	—	—	—	0.903	-1.691	—

a)  $4\pi M_s$  was determined from FMR absolute intensity measurements using a 15ML Fe(001) reference sample which was assumed to have the bulk iron value of  $4\pi M_s = 21.55$  kOe.

b)  $H_{111} \equiv 2K_{111}/M_s$  is the in-plane four-fold anisotropy field.

c)  $H_p \equiv 2K_p/M_s$  is the perpendicular four-fold anisotropy field.

d) This specimen was a Ni(10ML)/Fe(8ML) bilayer film grown on bulk Ag(001).

# THE MAGNETIC PROPERTIES OF Ni/Fe BILAYERS

In Table III one can see that the Fe/Ni bilayer with an untransformed homomorphic bcc Ni overlayer ( $d_{\text{Ni}} = 3.5\text{ML}$ ) showed almost the same in-plane anisotropies and g-factors as the individual Fe layer ( $d_{\text{Fe}} = 5.6\text{ML}$ ). However there was a noticeable increase in  $(4\pi D_{\perp} M_s)_{\text{eff}}$ . This behavior persisted even at  $\text{LN}_2$  temperatures ( $T = 77\text{K}$ ). The observed increase in  $(4\pi D_{\perp} M_s)_{\text{eff}}$  is very likely caused by a change in the surface anisotropy due to the Fe/Ni interface. We have measured the contributions of the bcc Ni overlayer to the total bilayer magnetic moment. FMR absolute intensity measurements carried out at room temperature indicated that the 3ML bcc Ni is nonmagnetic at room temperature. All bilayers composed of the thicker transformed "bcc Ni" exhibited very large in-plane 4th order anisotropies having the easy axis parallel with the {100} Fe crystallographic axis.  $2K_1/M_s$  is strongly temperature dependent: it increases  $\sim 2.5$  times upon cooling from room temperature to liquid nitrogen temperature, see Table III.

The fourth-order anisotropy fields,  $2K_1/M_s$ , in bilayers with 10ML Ni overlayers were well described by the bilayer scaling laws using  $(2K_1/M_s) \approx 2\text{kOe}$  for the fourth-order anisotropy field in Ni.<sup>10</sup> Other parameters such as  $(4\pi D_{\perp} M_s)_{\text{eff}}$ ,  $2K_u/M_s$ , and g-factors scaled poorly. The scaling laws are expected to be valid when the Fe and Ni layers interact only through the interfacial exchange coupling. In real bilayers, the intrinsic magnetic properties of one layer can be influenced by the proximity of the other. The "bcc Ni" overlayers are magnetic at room temperatures. FMR absolute intensity measurements showed that the 15ML Ni overlayer in a [20ML Au/15ML Ni/9ML Fe/Ag(001)] sample (which we shall denote as Ni(15)/Fe(9)) was magnetic with the saturation magnetization,  $4\pi M_s = 6.4\text{ kG}$ , very close to the bulk fcc Ni value.

A strong 4th order in-plane anisotropy was observed also in the FMR linewidth.<sup>10</sup> The narrowest and the widest FMR lines were observed along the easy {100} and hard {110} axes respectively. The angular dependencies of the FMR linewidth and the FMR field in reconstructed bilayers showed a very similar behavior.<sup>10</sup> Obviously both anisotropies have a common origin. The microwave frequency dependence of  $\Delta H$  showed a linear dependence with a zero-frequency offset  $\Delta H(0)$ . The linear slope corresponded to the intrinsic Gilbert damping and is isotropic; the

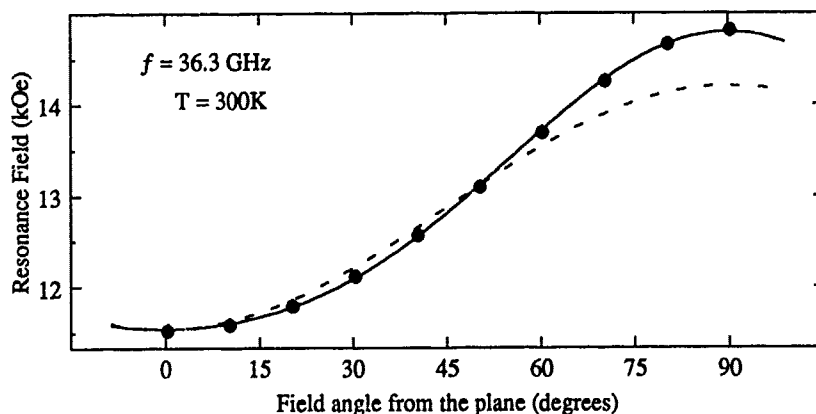


Fig. 3. The FMR field for a Au covered 3ML bcc Fe(001) film as a function of the angle between the specimen surface and the applied d.c. magnetic field. The solid line is the theoretical fit using the parameters listed in Table II. The dashed line omits the fourth order perpendicular anisotropy constant  $K_{\perp}$ . The dots are experimental data.

offset  $\Delta H(0)$  exhibited a large angular dependence. Since  $\Delta H(0)$  is caused by sample magnetic inhomogeneities the origin of the 4th order in plane anisotropy must lie in the growth defects generated during the Ni overlayer transformation.

Magnetostatic and magnetoclastic energies stored in growth defects contribute to the total magnetic energies and result in effective fields which affect magnetic resonance conditions. The observed 4th order in-plane magnetic anisotropies require that the crystallographic defects satisfy a fourfold in-plane symmetry. If we were to assume that "bcc Ni" consists of fcc Ni (011) blocks then these rectangular blocks would have to be symmetrically distributed along mutually perpendicular principal axes, and crystallographic defects around the (011) block boundaries would be responsible for the observed 4th order anisotropies. Dislocation arrays might contribute to large anisotropic effects either through the Dzialoshinski-Moriya mechanism of enhancing anisotropy through the off-diagonal components of the exchange interaction, which appear with broken symmetry, or because of magnetoelastic strains.

Since the large fourth-order in-plane anisotropies observed in Ni/Fe bilayers are due to a network of misfit dislocations, it was important to determine whether the deposition of Au coverlayers affected the strength of these anisotropies. In-situ FMR measurements were carried out on the Ni(15)/Fe(9) specimen. The single 9ML Fe(001) film showed a small value of  $2K_{111}/M_s = 0.31$  kOe. After depositing 15ML of Ni, the fourth order anisotropy increased significantly to 0.92 kOe. However, this anisotropy was further increased to  $2K_{111}/M_s = 1.45$  kOe after growth of a 20ML Au(001) coverlayer. The Au atoms were very likely slightly (Au grows layer by layer) diffused into the block boundaries and this resulted in a further increase of the fourth-order in-plane anisotropy.

Table III: Properties of Au covered Ni/Fe bilayers at 300 K and 77 K.

Sample	T (K)	$(4\pi D_{\perp} M_s)_{\text{eff}}$ (kOe)	g	$H_{111}$ (kOe) <sup>a</sup>	$H_u^V$ (kOe) <sup>b</sup>	$\phi_u^V$ (degrees) <sup>c</sup>
3.5 ML Ni / 5.6 ML Fe (vicinal Ag substrate)	300	8.9	2.09	0.14	-0.044	0
	77	9.29	2.09	0.28	-0.050	0
9.4 ML Ni / 5.7 ML Fe (singular Ag substrate)	300	9.82	2.11	0.74	0.025	45
10 ML Ni / 6 ML Fe (vicinal Ag substrate)	300	9.75	2.1	0.77	0.15	45
	77	9.35	2.10	2.09	0.25	41
10.5 ML Ni / 3.5 ML Fe (singular Ag substrate)	300	5.38	2.15	0.99	0.12	35
	77	4.83	2.15	2.57	0.16	38
15 ML Ni / 9 ML Fe (singular Ag substrate)	300	11.07	2.1 <sup>d</sup>	1.45	0.0	
	77	10.08	2.1 <sup>d</sup>	2.57	0.0	

a)  $H_{111} = 2K_{111}/M_s$  is the effective 4-fold in-plane anisotropy field.

b)  $H_u^V = 2K_u^V/M_s$  is the effective 2-fold in-plane anisotropy field due to a vicinal surface.

c) Angle of the uniaxial anisotropy axis with respect to the in-plane Fe [100] direction.

d) Assumed value of the g-factor.

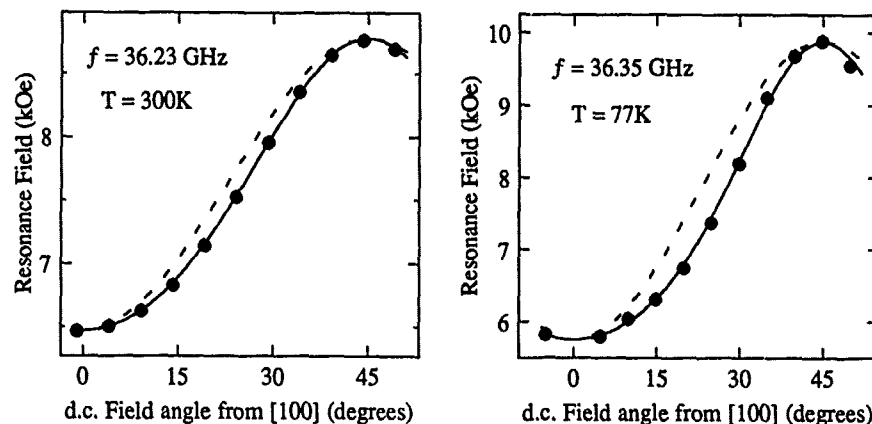


Fig. 4. In-plane angular dependence of FMR fields for [20ML Au/15ML Ni/9ML Fe/Ag(001)] singular specimen. The dashed and solid lines are the calculated angular variation; the dots are experimental values. The solid lines correspond to the case where the magnetization is allowed to drag behind the applied d.c. field. The dashed lines correspond to the case where the magnetization is assumed to be parallel to the applied field. The theoretical fits were carried out using  $(4\pi D_{\perp} M_s)_{\text{eff}} = 11.07$  kOe and  $2K_{111}/M_s = 1.45$  kOe at  $T = 300$  K and  $(4\pi D_{\perp} M_s)_{\text{eff}} = 10.08$  kOe and  $2K_{111}/M_s = 2.57$  kOe at  $T = 77$  K.

A strong angular dependence of the FMR linewidth could indicate that measured fourth-order anisotropies were of dynamic origin. However, the angular dependence of the FMR field was not adequately described by a simple  $\cos(4\phi)$  terms but exhibited clear features of a lag of the direction of the saturation magnetization behind the in-plane applied d.c. magnetic field when the magnetization was oriented away from the magnetically easy [100] and hard [110] axes (see Fig. 4). A lag of the saturation magnetization is a clear indication that the measured in-plane anisotropies are a direct consequence of a static fourth-order anisotropy energy term (see eq. 2). However, these anisotropies were caused by a network of misfit dislocations and could in principle exhibit a strong dependence on applied external field. Microwave measurements carried out between 16–73 GHz (corresponding to applied fields ranging from 2–18 kOe) exhibited magnetic properties which were independent of the applied d.c. field. The behavior of the in-plane anisotropies in small applied fields can be investigated at microwave frequencies for specimens exhibiting a large value of  $2K_{111}/M_s$ . The specimen Ni(15)/Fe(9) exhibited a large value of  $2K_{111}/M_s$  which, at 9.5 GHz, shifted the easy axis FMR field to a negative value and the hard axis to a positive value of 2.2 kOe. A second resonant branch should be observed at 9 GHz when the applied d.c. field is along the in-plane [110] hard axis. The second resonance corresponds to a multi-domain resonance in which the saturation magnetization is rotated from the d.c. field direction towards the hard axis.<sup>27</sup> The Ni(15)/Fe(9) bilayer exhibited these characteristic features (see Fig. 5). The FMR fields of both resonant branches were correctly predicted using the fourth order anisotropy parameter determined at higher magnetic fields. Clearly, Ni/Fe bilayers behave like specimens with field-independent cubic anisotropy.

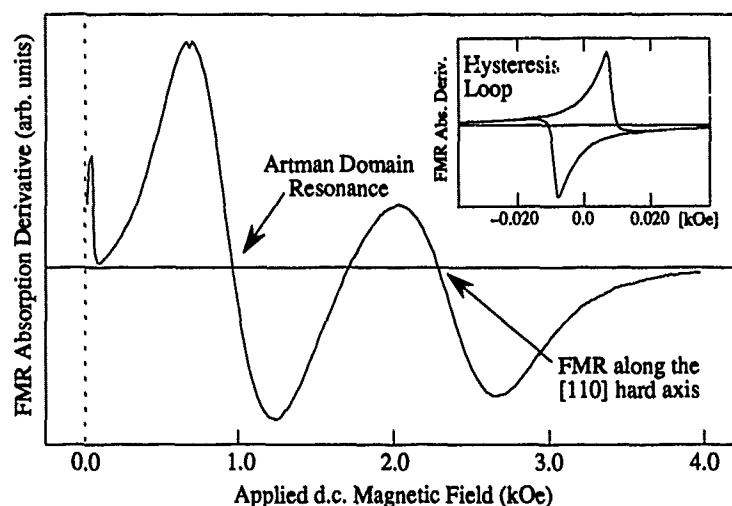


Fig. 5. Field dependence of the FMR absorption derivative on the applied d.c. magnetic field measured for a [20ML Au/15ML Ni/9ML Fe/Ag(001)] specimen at  $f = 9.51$  GHz. The insert shows the hysteresis loop obtained from the absorption derivative at low magnetic fields.

The inset in Fig. 5 also shows that, at low microwave frequencies, hysteresis loops can be easily measured by monitoring the absorbed microwave power near zero applied field. This microwave absorption is caused by the high field tail of the unobservable FMR peak corresponding to the saturation magnetization,  $M_s$ , along the [100] easy crystallographic axis. An abrupt change in the absorbed microwave power at the field corresponding to removal of the domain walls (the departure field) is caused by a change of the internal d.c. field from a negative to a positive value which occurs when the saturation magnetization reverses its orientation. The departure field along the hard axis was approximately 0.8 times smaller than that observed for fields directed along the easy axis. This result was consistent with a  $90^\circ$  domain wall closure pattern in the remanent state.

Magneto-optic Kerr effect measurements have shown that the magnetic moment, measured at the departure field, along the hard axis was  $1.38 (\approx \sqrt{2})$  smaller than the corresponding magnetic moment along the easy axis. This indicates that the specimen was fully saturated when it was magnetized along the easy axis and probably formed  $90^\circ$  stripe domains when the applied field was directed along the hard axis.

#### ACKNOWLEDGEMENTS

The authors would like to thank Dr. Stephen Purcell and Mr. Jeff Rudd for their valuable contributions to this work and the National Science and Engineering Research Council of Canada for financial support without which this work would not be possible.

## REFERENCES

1. C.L. Fu, A.J. Freeman and T. Oguchi, Phys. Rev. Lett. **54**, 2700 (1985).
2. V.L. Moruzzi and P.M. Marcus, Phys. Rev. **B38**, 1613 (1988).
3. J.G. Gay and Roy Richter, Phys. Rev. Lett. **56**, 2728 (1986).
4. B. Heinrich, K.B. Urquhart, J.R. Dutcher, S.T. Purcell, J.F. Cochran, A.S. Arrott, D.A. Steigerwald, and W.F. Egelhoff, Jr., J. Appl. Phys. **63**, 3863 (1988).
5. B. Heinrich, K.B. Urquhart, A.S. Arrott, J.F. Cochran, K. Myrtle and S.T. Purcell, Phys. Rev. Lett. **59**, 1756 (1987).
6. B. Heinrich, A.S. Arrott, J.F. Cochran, C. Liu and K. Myrtle, J. Vac. Sci. Technol. **A4** 1376 (1986).
7. B. Heinrich, A.S. Arrott, J.F. Cochran, S.T. Purcell, K.B. Urquhart, N. Alberding, and C. Liu, Thin Film Techniques for Low Dimensional Structures, edited by R.F.C. Farrow et al. (Plenum Press, New York, 1987), p. 521.
8. B. Heinrich, A.S. Arrott, J.F. Cochran, S.T. Purcell, K.B. Urquhart and K. Myrtle, J. Cryst. Growth **81**, 562 (1987).
9. Z.Q. Wang, Y.S. Li, F. Jona and P.M. Marcus, Sol. St. Com. **61**, 623 (1987).
10. B. Heinrich, S.T. Purcell, J.R. Dutcher, K.B. Urquhart, J.F. Cochran and A.S. Arrott, Phys. Rev. **B38**, 12879 (1988).
11. D. Jiang, E.D. Crozier, N. Alberding and B. Heinrich (to be published).
12. M.P. Seah and W.A. Dench, Surface and Interface Analysis **1**, 2 (1979).
13. J.F. Cochran and J.R. Dutcher, J. Magn. Magn. Matr. **73**, 299 (1988).
14. V. Kambersky, Czech. J. Phys. **B26**, 1366 (1976).
15. B. Heinrich, J.F. Cochran and R. Hasegawa, J. Appl. Phys. **57**, 3690 (1985).
16. B.T. Jonker, K.H. Walker, E. Kisker, G.A. Prinz and C. Carbone, Phys. Rev. Lett. **57**, 142 (1986).
17. M. Stampanoni, A. Vaterlaus, M. Aeschlimann and F. Meier, Phys. Rev. Lett. **59**, 2483 (1987).
18. F.A. Volkening, B.T. Jonker, J.J. Krebs, N.C. Koon, and G.A. Prinz, J. Appl. Phys. **63**, 3869 (1988).
19. J.J. Krebs, B.T. Jonker, and G.A. Prinz, J. Appl. Phys. **63**, 3467 (1988).
20. K.B. Urquhart, B. Heinrich, J.F. Cochran, A.S. Arrott, and K. Myrtle, J. Appl. Phys. **64**, 5334 (1988).
21. Our previously reported values of  $K_s$  in ultrathin Fe films covered by  $\text{Au}^{4,5}$  were multiplied by mistake by a factor  $D_L$  which resulted in an apparent stronger dependence of  $K_s$  on the sample thickness.
22. B.T. Jonker, J.J. Krebs and G.A. Prinz, J. Appl. Phys. **64**, 5340 (1988).
23. C. Chappert and P. Bruno, J. Appl. Phys. **64**, 5736 (1988).
24. S.T. Purcell, B. Heinrich and A.S. Arrott, J. Appl. Phys. **64**, 5337 (1988).
25. J.R. Dutcher, J.F. Cochran, B. Heinrich and A.S. Arrott, J. Appl. Phys. **64**, 6095 (1988).
26. W. Karas, J. Noffke and L. Fritsche, 12th International Colloquium on Magnetic Films and Surfaces, Le Creusot, France (1988).
27. J.O. Artman, Phys. Rev. **105**, 62 (1957).

## CHARACTERIZATION OF EPITAXIAL Fe ON GaAs(110) BY SCANNING TUNNELING MICROSCOPY

R. A. DRAGOSET, P. N. FIRST, JOSEPH A. STROSCIO,  
D. T. PIERCE AND R. J. CELOTTA  
National Institute of Standards and Technology, Gaithersburg, MD 20899

### ABSTRACT

Iron on GaAs(110) comprises an interesting system not only due to small lattice mismatch, 1.4%, but also because of the magnetic properties of the overlayer. In the present work, scanning tunneling microscopy (STM) was used to investigate bcc Fe films in the 0.1 Å to 20 Å thickness range, grown at 300 K and 450 K substrate temperatures. STM images show Volmer-Weber growth with the formation of 3-D Fe islands 20–30 Å in diameter for 0.1–1 Å deposition at 300 K, increasing to 40–50 Å for thicker films. Iron island sizes at low coverage and thin film roughness at higher coverages both show significant dependence upon growth temperature.

### INTRODUCTION

There is considerable interest in understanding the growth and properties of small metal structures on semiconductor surfaces. In particular, a system such as Fe on GaAs, which exhibits a small lattice mismatch, is interesting because of the possibility of growing Fe films or structures with novel properties.<sup>1,2</sup> The (110) face of fcc GaAs has a basis vector of 5.654 Å in the [001] direction, which is nearly twice the unit cell spacing of bulk bcc Fe ( $a_0 = 2.856$  Å). The lattice mismatch between Fe and GaAs in the [001] direction is 1.4% with an equivalent mismatch in the  $[1\bar{1}0]$  direction. Single-crystal bcc Fe films have been successfully grown on GaAs(110) using molecular beam epitaxy with a substrate growth temperature of 450–500 K.<sup>1–3</sup> In this paper, we report the observation by scanning tunneling microscopy (STM) of the growth of Fe on GaAs(110) substrates. The initial growth is found to be in the form of 3-D Fe clusters characteristic of the Volmer-Weber growth mode.<sup>4</sup> The degree of 3-D growth is found to be dependent on the substrate temperature, and the GaAs substrate exhibits no apparent disorder in the vicinity of the Fe clusters. It was also found that the surface roughness of thin Fe films is dependent on substrate temperature during growth.

### EXPERIMENTAL

The experiments were performed in an ultra-high vacuum chamber with a base pressure  $< 4 \times 10^{-11}$  torr. The scanning tunneling microscope, similar to the IBM/Zurich design,<sup>5</sup> consists of a glass frame support with a double spring suspension for vibration isolation, a piezoelectric/electrostatic clamping device for coarse sample motion and a piezoelectric tripod for tip motion along the sample surface. All STM images were recorded at room temperature. Fe clusters and films were grown by molecular beam



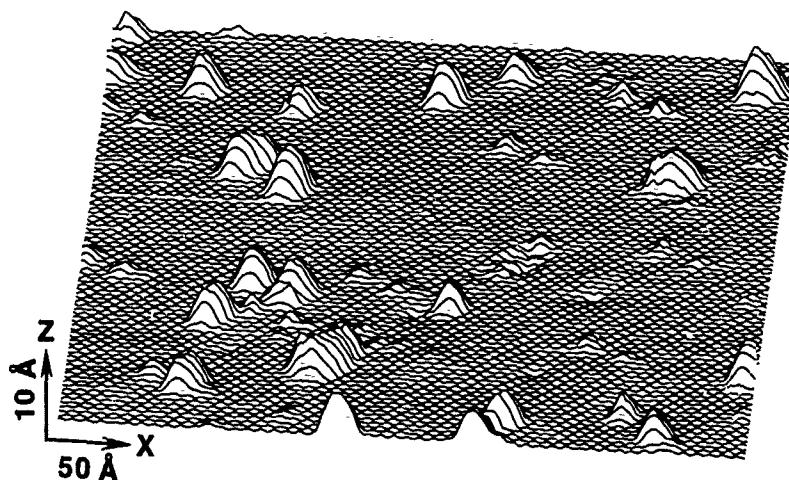


Figure 1: STM image,  $400 \times 384 \text{ \AA}$ , of  $0.1 \text{ \AA}$  Fe/GaAs(110) epitaxially grown at 300 K substrate temperature. The sample bias was  $-2.5 \text{ V}$ . The image is displayed by line scans with hidden line removal showing a 3-D perspective of the surface. Fe clusters, substrate As rows, and surface defects are observed in the STM image. (Note the Z scale magnification.)

epitaxy with GaAs substrate temperatures of 300 K and 450 K. Fe evaporation was monitored using a quartz microbalance, but for small depositions, coverages were estimated by measuring cluster volumes. Coverages are specified as the equivalent thickness of a uniform Fe layer (1 monolayer =  $2 \text{ \AA}$ ). Surface order and cleanliness were monitored with low energy electron diffraction (LEED) and Auger spectroscopy before and after growth. The substrates consisted of *p*-type GaAs, Zn doped at a concentration of  $2 \times 10^{19} \text{ cm}^{-3}$ .

## RESULTS

Figure 1 shows an STM line scan of the GaAs(110) surface with  $0.1 \text{ \AA}$  coverage of Fe grown at 300 K. The GaAs substrate appears as rows of atoms along the  $[\bar{1}\bar{1}0]$  direction, which is at  $45^\circ$  with respect to the  $+x$  direction. Only the substrate As atom locations are observed in the bare surface regions, since the image was obtained at negative sample bias.<sup>6</sup> A variety of different size Fe clusters are observed in the image. Many of the cluster heights are greater than the  $2 \text{ \AA}$  interplanar spacing of Fe, indicating 3-D cluster growth. LEED observations of coalesced clusters (see Fig. 2) showed the bcc Fe diffraction pattern, consistent with previous work which determined the growth to be epitaxial.<sup>3</sup> Volume estimates of the clusters were achieved by integrating the STM height contours of the clusters. This is a good estimate since the charge density contours

of metals closely follow the positions of the metal atoms. For very small clusters, this method overestimates the volume due to the finite resolution of the tunneling probe. The volumes of the clusters shown in Fig. 1 range from 100–1500 Å<sup>3</sup>, corresponding to 9–127 atoms per cluster.

Figure 2 shows an STM image in 3-D perspective view of a 10 Å Fe film grown on a GaAs(110) surface at 300 K. The Fe clusters range in diameter from 40–50 Å and fill the entire surface. Since the GaAs substrate cannot be imaged with this coverage of Fe, volume calculations could not be made for these crystallites. Even though the Fe

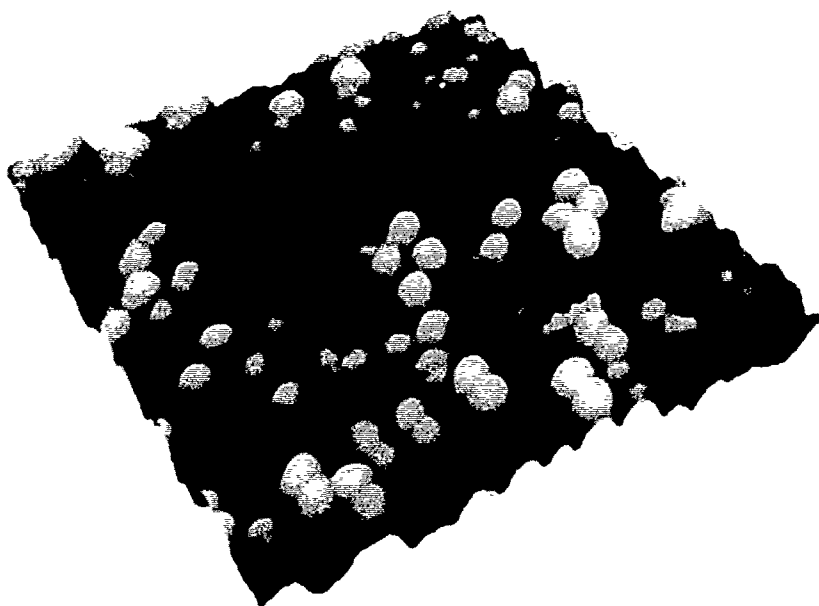


Figure 2: STM image (3-D perspective view with gray scale height shading, 740 × 750 Å) of 10 Å Fe/GaAs(110) shows Fe crystallites 40–50 Å in diameter. The sample bias was +1.5 V, and the substrate temperature during film growth was 300 K.

clusters are in contact with neighboring clusters, the Fe does not coalesce into a smooth film with the substrate temperature at 300 K during evaporation; the small crystallites appear to be distinct. The surface roughness of the image in Fig. 2 was calculated to be  $\sim 3$  Å rms. In Figure 3, two contours are shown for Fe films grown on GaAs(110) at substrate temperatures of 300 K and 450 K. The contour from the 17 Å film grown at 450 K is clearly smoother than that of the film grown at 300 K. The surface roughness of the Fe film grown at 450 K was calculated to be  $\sim 1$  Å rms. Thus, it appears that at an elevated substrate temperature, the Fe clusters tend to coalesce into a more uniform epitaxial film. Further work is in progress to determine the effect of film thickness on the surface quality.

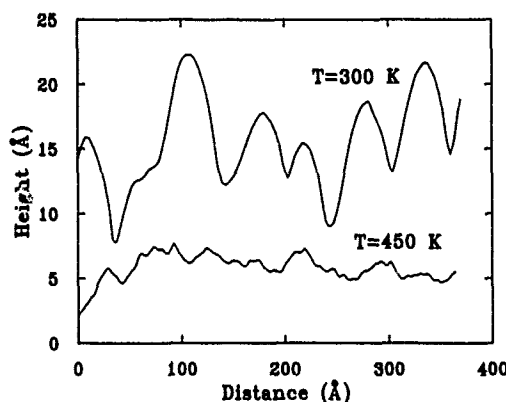


Figure 3: Height versus distance profiles taken from STM images of Fe films epitaxially grown on a GaAs(110) surface. The top curve is a profile from a 10 Å Fe film grown at 300 K with a surface roughness of  $\sim 3$  Å rms. The bottom curve is a profile from a 17 Å Fe film grown at 450 K with a surface roughness of  $\sim 1$  Å rms.

## DISCUSSION

For low coverages of Fe on GaAs(110), the growth of single clusters on the bare semiconductor surface can be observed with the STM. Even for coverages as low as 0.1 Å of Fe, 3-D Volmer-Weber growth<sup>4</sup> is observed. Using high-energy-resolution x-ray photoelectron spectroscopy, Ruckman *et al.* and Chambers *et al.* have reported that Fe grown on the (110) and (001) faces of GaAs at room temperature contain Ga and As impurities in the interstitial face-center sites of the bcc Fe.<sup>7,8</sup> However, Carbone *et al.* have reported that a photoemission study with synchrotron radiation revealed no intermixing of Fe (deposited at 450 K) with the GaAs(110) substrate for Fe coverages of less than one monolayer.<sup>9</sup> The STM measurements (Fig. 1 and higher resolution images) reveal no disruption of the GaAs substrate immediately surrounding the Fe clusters. (Due to the finite size of the STM tunneling tip, a small portion of the substrate near a cluster can not be imaged.) Thus, if there is intermixing at the Fe/GaAs interface, the disorder is primarily localized at the Fe/GaAs interface, or extends into the GaAs crystal, producing no long range surface disorder.

In order to better characterize the cluster growth, the areas and volumes of clusters were determined from the STM data for isolated Fe clusters grown on GaAs(110) at 300 K and at 450 K (Fig. 4). For comparison, the data have been fit with a two parameter power law,  $V = cA^n$ , where  $V$  is the cluster volume and  $A$  is the cluster area. For 2-D growth the parameter  $n$  is 1.0, whereas for 3-D growth,  $n = 1.5$ . The dashed line in Figure 4 shows the relationship for theoretical hemispherical growth with  $V = (2/3\sqrt{\pi})A^{1.5}$ . As shown in Fig. 4, clusters grown at a substrate temperature of 300 K best fit the volume-area equation with  $n = 1.2$ , while clusters grown at the elevated temperature yield  $n = 1.4$ . Thus, even though the 300 K clusters exhibit 3-D structure, the nature of the growth is more two-dimensional; whereas, the growth pattern of the 450 K clusters is more representative of 3-D growth.

As the isolated clusters merge with increasing Fe deposition, the character of the resultant thin film is also dependent on the substrate temperature. The results presented in this paper agree with earlier work<sup>3</sup> in concluding that evaporation onto a 450 K substrate produces smoother films than a substrate temperature of 300 K. The crystalline structure of the Fe films could not be resolved with the STM, but the surface roughness

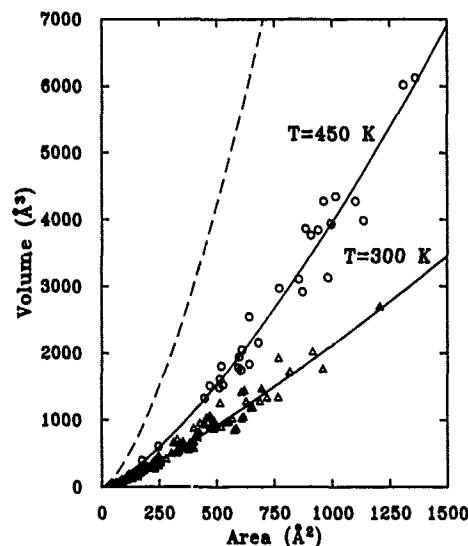


Figure 4: Cluster volume ( $V$ ) versus cluster area ( $A$ ) calculated from STM images of Fe on GaAs(110). Different growth modes are observed (with the data being fit to a power law) for substrate temperatures of 300 K ( $\Delta$ ;  $V \propto A^{1.2}$ ) and 450 K ( $\circ$ ;  $V \propto A^{1.4}$ ) during epitaxial growth. The dashed line represents hemispherical growth with  $V = (2/3\sqrt{\pi})A^{1.5}$ .

decreases by a factor of three and the clusters appear to coalesce into a uniform layer for the case of Fe deposition at the elevated temperature. LEED measurements established the crystalline nature of the Fe films. The diffuse LEED spots of the 10 Å, 300 K Fe film are indicative of small ( $< 100$  Å) crystalline clusters in registry; whereas the 17 Å, 450 K Fe film exhibited sharper LEED spots, characteristic of a uniform crystalline film.

The temperature dependence of the growth patterns of the Fe clusters at low coverages (Fig. 4) and the character of the thin Fe films at higher coverages (Fig. 3) is consistent with the temperature dependence of the Fe atom mobility on the substrate. At an elevated temperature, the Fe atoms will have an increased surface diffusion rate, thereby driving the system closer to a minimum in the surface free energy of the Fe clusters or films. For low coverages, the surface free energy is minimized by the formation of clusters on the surface. As the coverage is increased the clusters contact one another, and the configuration of minimum surface free energy becomes a uniform, flat film. The data reported here are consistent with this simple model in that the clusters deposited at 450 K exhibit a greater mean height (volume/area) than those grown at 300 K, and the film grown at 450 K is smoother ( $\sim 1$  Å surface roughness) than that film deposited at 300 K ( $\sim 3$  Å surface roughness).

We would like to thank S. Mielczarek and R. Cutkosky for expert technical assistance. We gratefully acknowledge the partial support of this work by the Office of Naval Research. P. N. First is a National Research Council Postdoctoral Research Associate.

## REFERENCES

1. K. B. Hathaway and G. A. Prinz, Phys. Rev. Lett. **47**, 1761 (1981).
2. G. A. Prinz, G. T. Rado, and J. J. Krebs, J. Appl. Phys. **53**, 2087 (1982).

3. G. A. Prinz and J. J. Krebs, Appl. Phys. Lett. **39**, 397 (1981).
4. Andrew Zangwill, Physics at Surfaces, (Cambridge University Press, Cambridge, U. K., 1988), p. 428.
5. G. Binnig and H. Rohrer, Sci Am, **253** (2), 50 (1985).
6. R. M. Feenstra, J. A. Stroscio, J. Tersoff, and A. P. Fein, Phys. Rev. Lett. **58**, 1192 (1987).
7. M. W. Ruckman, J. J. Joyce, and J. H. Weaver, Phys. Rev. B **33**, 7029 (1985).
8. S. A. Chambers, F. Xu, H. W. Chen, I. M. Vitomirov, S. B. Anderson, and J. H. Weaver, Phys. Rev. B **34**, 6605 (1986).
9. C. Carbone, B. T. Yonker, K. -H. Walker, G. A. Prinz, and E. Kisker, Solid State Commun. **61**, 297 (1987).

# IN-SITU INVESTIGATION OF STRUCTURE AND MAGNETIC PROPERTIES OF THE EPITAXIAL SYSTEM Pd(111)/Fe(110) ON W(110) BY MEANS OF BRILLOUIN SPECTROSCOPY

P. BAUMGART, B. HILLEBRANDS, J.V. HARZER AND G. GÜNTHERODT  
2. Physikalisches Institut, RWTH Aachen, D-5100 Aachen, FRG

The *in-situ* observation of magnetostatic spin waves by Brillouin spectroscopy offers a versatile dynamical probe for the investigation of magnetic properties of thin films. The measured spin wave spectra of thin films contain a variety of information about their magnetic as well as structural properties. The frequency of a spin wave allows to determine, e.g., the *g*-factor, the magnetic anisotropy constants and also the saturation magnetization. The spectral line shape allows conclusions about the film quality, i.e., steps or islands. Furthermore, the unidirectional propagation of the surface spin wave with respect to the magnetization allows to measure the coercivity field of a film. The latter can be used as an additional characterization parameter of a magnetic film.

Here we report on Brillouin spectroscopy investigations, which have been performed on the epitaxial system Pd(111)/Fe(110) on W(110). Additional detailed investigations of the epitaxy of this system, i.e., of the growth mode, structure and thermal stability have been carried out using LEED and Auger spectroscopy.

The epitaxial growth and the magnetostatic spin waves of an uncovered Fe(110) film on W(110) were studied earlier [1]. These investigations have shown that the interface anisotropies affect dominantly the spin wave frequencies of ultrathin (less than 40 Å) Fe(110) films on W(110). The question addressed here is the influence of thin overlayers (from a fraction of a monolayer to a few atomic layers (AL)) of Pd on Fe(110) on the magnetic properties of the Fe film. Since Pd is known to be an incipient ferromagnet, i.e. that it can easily be polarized by ferromagnetic impurities, a strong influence of Pd overlayers on Fe was expected.

The films have been prepared in UHV on clean W(110) single crystal substrates using e-beam evaporators. The optimized procedure for preparing high quality epitaxial Fe(110) films on W(110) was described elsewhere [1]. The Pd overlayers were prepared at low evaporation rates ( $\approx 0.5$  AL/min.) at relatively low substrate temperatures of  $\approx 50^\circ\text{C}$  in order to avoid possible intermixing of Pd and Fe at the interface. As checked by LEED, Pd grows in well ordered (111)-planes on Fe(110) in the so-called "Kurdjumov-Sachs" growth mode, i.e., with the Pd[101]-direction along the Fe[111]-direction or with Pd[011] along Fe[111]. In addition, Pd builds a coincidence lattice on Fe(110) in such a way that 10 interatomic Pd distances coincide with 11 interatomic Fe distances in the directions of mutual lattice alignment as specified above. This leads to a (11 x 11)-superstructure in the LEED patterns for coverages from 1 to approximately 5 AL of Pd. The epitaxy of this system is very good, i.e., high quality LEED patterns with low background and sharp spots can be observed for coverages at least up to 50 AL Pd. Initial layer-by-layer growth, for the first two atomic layers of Pd(111) on Fe(110), is revealed by the kinks of the straight lines of the Auger intensities of Fe and Pd as a function of Pd coverage. This system shows good thermal stability up to  $\approx 200^\circ\text{C}$ . Heating the sample above this temperature changes the relative Auger peak intensities, i.e., leads to an increase of the Auger signal of Fe accompanied by a simultaneous decrease of the respective Pd signal, indicating the onset of alloying.

The Brillouin spectra of magnetostatic spin waves (or "Damon-Eshbach modes") were measured *in-situ* first for the uncovered Fe film and subsequently for the same film covered by Pd. The different coverages of Pd were always put onto freshly prepared Fe films. Since the sampling time needed to record a Brillouin spectrum did not exceed a few minutes at a UHV base pressure in the  $10^{-11}$  mbar range, there was no significant contamination. During the measurement a magnetic field *H* of up to 2 kGauss could be applied in the film plane and perpendicular to the light scattering

plane. The surface-parallel component of the wavevector of the spin wave,  $\vec{q}_{||}$ , defined by the scattering geometry, lies in the scattering plane and perpendicular to  $\vec{H}$ . The angle of incidence of the laser beam was  $45^\circ$  with respect to the film normal. The experiments have been performed in backscattering geometry using the 5145 Å line of an Ar-laser.

#### Evaluation of out-of-plane anisotropy constants

An influence of the Pd overlayer on the frequency  $\nu$  of the spin wave measurable by Brillouin spectroscopy sets in at coverages of less than approximately half an AL. With increasing Pd overlayer thickness ( $d_{Pd}$ ) the spin wave frequency  $\nu$  decreases and shows a pronounced minimum at  $d_{Pd} \approx 1$  AL. For  $d_{Pd}$  larger than 1 AL  $\nu$  increases and saturates for  $d_{Pd} \gtrsim 3$  AL at a value which is an average between the frequency of the uncovered film and its minimum value at  $d_{Pd} \approx 1$  AL. The maximum frequency decrease for 1 AL Pd is proportional to  $1/d_{Fe}$ , with  $d_{Fe}$  the Fe film thickness, revealing the interface character of the effect. An explanation of this behavior can be given by assuming a strong reduction of the out-of-plane surface anisotropy constant  $k_s$  of the uncovered Fe film induced by the Pd overlayer and a simultaneous magnetic polarization of Pd at the interface. Magnetically polarized Pd introduces an additional magnetic interface to the vacuum which gradually disappears with an increasing Pd thickness, since only the Pd layers in intimate contact to Fe layers can be magnetically polarized.

To evaluate the respective out-of-plane interface anisotropy constants for each of the two interfaces of the Fe film separately, it is necessary to know the data of  $k_s$  for an Fe/Pd interface, e.g., from a symmetric sandwich Pd/Fe/Pd or from a Fe/Pd multilayer. Estimates for these two cases have been determined from experimental data and show good agreement [2,3]. Using this value of  $k_s \approx -0.3$  erg/cm<sup>2</sup> as input, the results of the evaluation of  $k_s$  of the remaining types of interfaces in the Pd(111)/Fe(110)/W(110) system are: 4.9 erg/cm<sup>2</sup> for the Fe(110)/W(110) interface, 0.7 erg/cm<sup>2</sup> for the free Fe(110) surface and -1.2 erg/cm<sup>2</sup> for the free surface of magnetically polarized Pd. The mean error for all these values can be estimated to  $\pm 0.3$  erg/cm<sup>2</sup>. A negative value of  $k_s$  means that the magnetization tends to align perpendicular to the film surface. However, the interface anisotropies of negative sign are too small to overcome the shape anisotropy forcing the magnetization to lie in the film plane. Remarkable in this context is the strong asymmetry of  $k_s$  at the two interfaces of an Fe(110) film on W(110). This is for the first time that the anisotropy constants of the two different interfaces could be determined explicitly instead of dividing their sum by two as done in previous investigations [4].

#### In-plane surface and interface anisotropies of Fe(110)

The twofold symmetry of an Fe(110) surface gives rise to an additional anisotropy, the in-plane surface anisotropy, described by the corresponding anisotropy constant  $k_{s,p}$ . Since in the case of Fe(110) this anisotropy acts perpendicular to the bulk anisotropy (the easy axis of bulk Fe is [100]) there exists a critical thickness  $d_c$  below which in zero applied field the Fe(110) film becomes spontaneously magnetized in the [011] direction. Introducing the term corresponding to  $k_{s,p}$  in the free energy density as  $-(k_{s,p}/d) \cdot \sin^2 \phi$ , with  $\phi$  denoting the angle between the magnetization vector  $\vec{M}$  and the [100] direction in the surface,  $k_{s,p}$  is given by

$$k_{s,p} = \frac{d_c \cdot K_1}{8} \quad (1)$$

where  $K_1 = 4.5 \cdot 10^5$  erg/cm<sup>3</sup> is the bulk anisotropy constant of Fe at room temperature [5]. The switching of the direction of  $\vec{M}$  from [100] to [011] occurs in zero applied field for  $d_{Fe} < d_c$  or for  $d_{Fe} > d_c$  if the magnetic field applied parallel to [011] exceeds a critical value  $H_c$ . The critical thickness can be measured by means of Brillouin

spectroscopy. In the Brillouin spectrum this switching manifests itself as a discontinuity of the measured spin wave frequency. For  $\vec{M}$  turning towards the direction of  $\vec{q}_{||}$  the spin wave frequency drops down by approximately 30-50% depending on the film thickness. This transition has a width of less than 2 G and a hysteresis of less than 5 G. Measuring the critical field  $H_c$  for a series of Fe films with  $d_{Fe} > d_c$  allows to determine  $d_c$  in zero applied field very precisely by extrapolation. The result is:  $d_c = 84 \pm 1$  Å for an uncovered Fe(110) film on W(110) and  $58 \pm 2$  Å for the same film covered by 1 AL of Pd. Again a kind of "relaxation" is observed for thicker Pd coverages, although not as pronounced as in the case of Pd induced modification of  $k_z$ .  $d_c$  amounts to  $62 \pm 2$  Å for an overlayer of 2 AL Pd on the Fe film and to  $65 \pm 2$  Å for coverages of 5 AL Pd and thicker. It should be noted that  $H_c$  is strongly temperature dependent which reflects the fact that  $H_c$  is a value that has its origin in a competition of two anisotropy contributions which themselves are quite strongly temperature dependent varying with at least the 10th power of the saturation magnetization [6,7]. This implies that it is necessary to keep the samples at exactly the same temperature measuring  $H_c$  for different  $d_{Fe}$ . To the first order the temperature dependences of  $K_1$  and  $k_z$ , are found to be the same since curves through the values of  $H_c$  as a function of  $d_{Fe}$  measured at different temperatures (50-300° C) extrapolated to  $H_c = 0$  merge approximately at the same value of  $d_c$ .

#### The coercitivity of Fe(110)/W(110) and of Pd(111)/Fe(110)/W(110)

The unidirectional propagation of magnetostatic spin waves about the direction of magnetization due to the violation of the time reversal symmetry of a magnetic system manifests itself in the Brillouin spectrum in a pronounced Stokes/anti-Stokes asymmetry of the corresponding peak intensities. In a given scattering geometry a unidirectionally propagating wave can either be absorbed or be created in the scattering process depending on the relative direction of  $\vec{M}$  which causes the observed asymmetry in the Brillouin spectrum. Reversing the direction of  $\vec{M}$  reverses this asymmetry. This effect can be used to measure the coercitivity field  $H_k$  of a film provided the applied field lies parallel to an easy axis of the film. For  $d < d_c$  this is the case if  $\vec{H} \parallel [011]$ .  $H_k$  starts at 0 G for  $d = d_c$  and increases monotonously for  $d \rightarrow 10$  Å (in a similar way as the frequency of the corresponding spin wave does [1]) to a value of  $\approx 515 \pm 5$  G for the uncovered Fe(110) film and to  $\approx 350 \pm 5$  G if the film is covered by 1 AL of Pd. This means that an ultrathin Fe(110) film becomes magnetically harder compared to thicker films. A Pd overlayer reduces this hardening considerably. The range of magnetic field  $\Delta H_k$  in which the reversal of the magnetization vector takes place is extremely narrow ( $\Delta H_k < 2$  G  $\approx$  experimental resolution) which means that the hysteresis loops of these films have a rectangular shape. A Fe(110) film with  $d_{Fe} = 30$  Å consisting of islands (due to a too high substrate temperature ( $T_s$ ) during preparation) shows a much larger coercitivity, e.g.,  $H_k \approx 200$  G or more, depending on  $T_s$ , instead of  $78 \pm 2$  G for an optimally prepared film of same thickness. Such an island film shows in addition a relatively large  $\Delta H_k$  of approximately  $30 \pm 5$  G. The spin wave of such a film shows a reduced frequency and has a very broad asymmetric line shape which is smeared out towards lower frequencies as compared to the spectrum of an optimally prepared film. The situation is reversed for a film with a high density of steps parallel to [100] (caused by a too low  $T_s$ ). Such films are magnetically very soft,  $H_k = 24$  G, and show a small transition width  $\Delta H_k < 2$  G.

#### References

1. B. Hillebrands, P. Baumgart, G. Güntherodt, Phys. Rev. B, Rapid Commun. **36**, 2450 (1987)
2. B. Hillebrands, A. Boufelfel, C.M. Falco, P. Baumgart, G. Güntherodt, E. Zirngiebl and J.D. Thomson, J. Appl. Phys. **63**, 3880 (1988)
3. P. Baumgart, B. Hillebrands, J.V. Harzer, G. Güntherodt, to be published
4. H.J. Elmers, U. Gradmann, J. Appl. Phys. **64**, 5328 (1988)



5. Landolt-Börnstein, Numerical Data and Functional Relationships in Science and Technology, New Series, Ed. by K.-H. Hellwege and O. Madelung, Volume III/19a
6. M.J. Peachan, J. Appl. Phys. **64**, 5754 (1988)
7. P. Baumgart, B. Hillebrands, G. Güntherodt, to be published

STRUCTURAL AND MAGNETIC CHARACTERIZATION OF RARE EARTH AND TRANSITION METAL FILMS GROWN ON EPITAXIAL BUFFER FILMS ON SEMICONDUCTOR SUBSTRATES.+ R.F.C. Farrow\*, S.S.P. Parkin\*, V.S. Speriosu\*, A. Bezinge \*, A.P. Segmuller\*\*

\* IBM Research Division , Almaden Research Center, 650 Harry Road, San Jose , Ca 95120-6099. \*\* IBM Research Division , T.J. Watson Research Center , Yorktown Heights , NY 10598.

+ This work was supported in part by ONR Contract N00014- 87-C-0339.

# ABSTRACT

Structural and magnetic data are presented and discussed for epitaxial films of rare earth metals ( Dy, Ho, Er) on  $\text{LaF}_3$  films on the GaAs(TTT) surface and Fe on Ag films on the GaAs(001) surface. Both systems exhibit unusual structural characteristics which influence the magnetic properties of the metal films. In the case of rare earth epitaxy on  $\text{LaF}_3$  we present evidence for epitaxy across an incommensurate or discommensurate interface. Coherency strain is not transmitted into the metal which behaves much like bulk crystals of the rare earths. In the case of Fe films , tilted epitaxy and long-range coherency strain are confirmed by X-ray diffractometry. Methods of controlling some of these structural effects by modifying the epitaxial structures are presented.

# 1.INTRODUCTION

In a recent paper [1] we described several new approaches to epitaxy of rare earth and transition metals. One aim of these approaches is to explore the effects of strain , imposed through coherency across epitaxial interfaces , on the magnetic properties of the films. In the case of the rare earth metals, basal plane epitaxy of Dy onto epitaxial films of  $\text{LaF}_3$  grown onto the 3-fold symmetry GaAs(TTT) surface were described [1] In the present paper we describe the extension of this epitaxial system to Ho and Er films and report the characterization of the structures using double-crystal (DCD) and grazing incidence X-ray diffractometry (GID) in addition to XPS depth profiling and Rutherford Back Scattering Spectrometry (RBS). A major finding of these studies is that the rare earth lattice is rotated by  $30^\circ$  about the c-axis from the setting expected from in plane translational registry of the rare earth and  $\text{LaF}_3$  lattices. Thus the interface is either incommensurate or discommensurate. Here we use the definition of interface type given by Gibson and Phillips [2]. In the former case there is no tendency for in-plane lattice matching of the overlayer to the substrate. In this case there are no interfacial misfit dislocations. On the other hand , the discommensurate interface is one in which the overlayer initially adjusts its in-plane lattice constant to match the substrate but subsequently relaxes to its normal lattice constant by formation of misfit dislocations. This is also known as a semi-coherent interface. At present we have insufficient experimental evidence to distinguish between the two cases. However , we do find that coherency strain is not transmitted across the interface and , as a result , epitaxial films of Dy, Ho and Er are strain-free over the thickness range ( 25-8000 Å). Although RBS shows no evidence for F contamination of the films, XPS depth profiling suggests that F is transported across the interface by as much as 500Å in some cases. Thus it is possible that

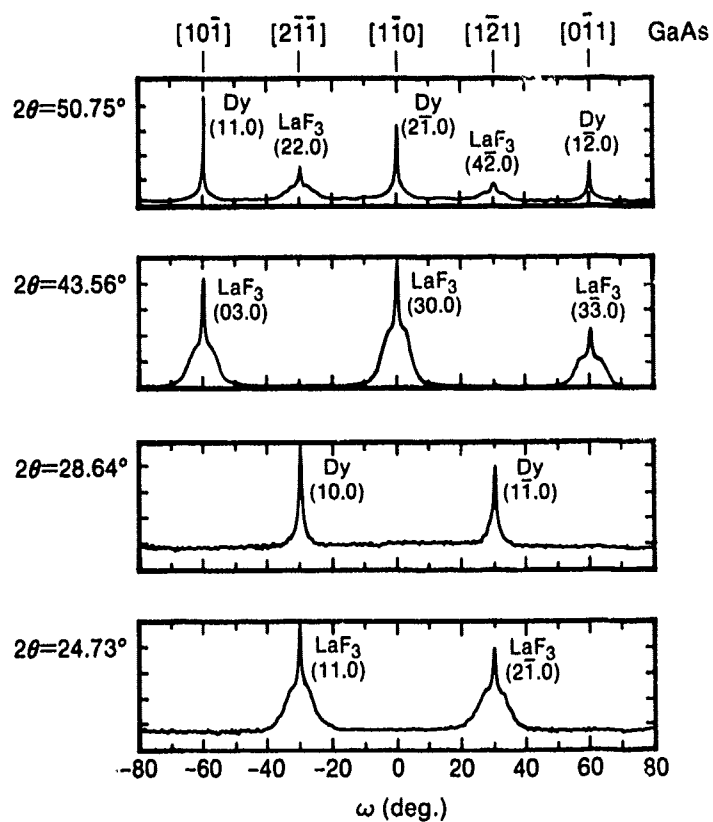


Figure 1 - GID  $\omega$  scan for structure comprising 400Å  $\text{LaF}_3$  / 2000Å  $\text{Dy}$  / 2500Å  $\text{LaF}_3$  / GaAs(TTT). Note the parallelism of Dy(10.0) and  $\text{LaF}_3$ (11.0) planes indicating an orientational misfit between the two lattices of 30°.

the magnetic properties of films thinner than this may be influenced by impurity F. These two findings prevented our original intention of exploring the magnetic implications of strain and dimensionality in rare earth films by adjusting coherency strain through lattice misfit across the rare earth - fluoride interface. However, by using a modified epitaxial structure we are still able to achieve this aim and at the same time eliminate the complicating effect of impurity outdiffusion of F.

In the case of epitaxy of Fe films on Ag films on GaAs (001) substrates we showed [1,8] previously that long range coherency strain and tilted epitaxy were present in Fe films grown on GaAs substrates cut  $2^\circ$  off the (001) plane. We find that tilted epitaxy is not present if growth occurs on exactly (within  $0.12^\circ$ ) oriented substrates.

**2. EXPERIMENTAL TECHNIQUES.** The sample preparation techniques were identical to those described previously [1]. Double-crystal diffractometry was carried out using an automated diffractometer (manufactured by Blake Instruments) operating in the parallel setting with a Si (004) Bragg diffraction from the (001) face of a Si crystal. Slits were used to cut out the  $\text{CuK}\alpha_2$  diffracted beam from the Si crystal. Grazing incidence diffractometry was carried out using the system described by Segmüller[3]. RBS studies of the films were carried out at the University of Arizona and at Almaden Research Center. SQUID magnetometry, and in some cases vibrating sample magnetometry was used to study the magnetic properties of the films.

### 3. EPITAXIAL $\text{LaF}_3$ /Rare Earth Metal/ $\text{LaF}_3$ SANDWICH STRUCTURES.

As described previously for Dy [1,5] the rare earth metals Ho and Er were also found to grow epitaxially on  $\text{LaF}_3$  films on GaAs(TTT) surfaces at  $300^\circ\text{C}$ . In all cases the  $\text{LaF}_3$  growth was carried out at a substrate temperature of  $500^\circ\text{C}$ . This initial film was 1000-2000 Å thick. After growth of the rare earth film, a protective film of  $\text{LaF}_3$  was grown at  $300^\circ\text{C}$  to protect the rare earth film from atmospheric oxidation. The sandwich structures were removed from the MBE system and characterized structurally and magnetically.

Figure 1 shows the GID data for a structure comprising 2500Å  $\text{LaF}_3$  / 2000Å Dy/ 400Å  $\text{LaF}_3$ . The 4 scans are each for a particular  $2\theta$  value and the crystal is rotated about the GaAs(111) axis. The peaks correspond to Bragg diffraction from planes of Dy and  $\text{LaF}_3$  which are parallel to the c-axis of these materials. The parallelism of Dy(10.0) and (11.0)  $\text{LaF}_3$  planes is evident from the fact that the Bragg diffractions occur at the same crystal ( $\omega$ ) setting. The composite shape of the Bragg peaks for  $\text{LaF}_3$  is due to superposition of peaks from the  $\text{LaF}_3$  under and overlayer. The latter was grown at  $300^\circ\text{C}$  and is of lower structural perfection than the underlayer. Figure 2 shows schematically the relative orientation of basal planes of  $\text{LaF}_3$  and Dy for (a) the setting in which Dy(11.0) is parallel to  $\text{LaF}_3$ (11.0) and (b) the observed setting. We had expected that the epitaxial relation would be as in (a) in view of the close (within 0.1%) match between the doubled (2a) lattice constant of Dy and the value of a for  $\text{LaF}_3$  (7.1871Å in the space group  $\text{P6}_3\text{cm}$ . See reference 4). However, the observed relation has no translational registry between the lattices. The interface is therefore either incommensurate or discommensurate and in either case the lack of translational registry implies relaxation of the metal overlayer to its bulk lattice constant. Similar scans for sandwich structures of Ho and Er confirmed that these metals had identical epitaxial relations. Furthermore, in plane lattice constants

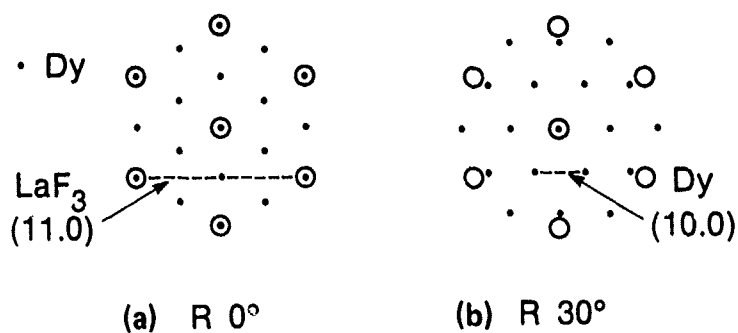


Figure 2 - Schematic diagram showing (a) the expected commensurate interface between  $\text{LaF}_3$  (open circles) and rare earth lattices in the basal plane and (b) the observed 30° rotation of Dy about the c-axis leading to an absence of translational registry between the lattices.

TABLE 1

In-Plane Lattice Constants and Coherency Lengths for Epitaxial Rare Earth Films, Determined by Grazing Incidence X-Ray Diffraction

	Thickness (Å)	a (Å)	l (Å)	$\Delta a$ (%)	$a_{\text{meas.}} - a_{\text{Bulk}}$ (%)
Dy	2000	$3.5945 \pm 0.001$	180	0.03	+0.12
Er	4000	$3.5586 \pm 0.0012$	250	0.03	0.00
Er	100	$3.5547 \pm 0.001$	97	0.03	-0.11
Er	50	$3.5610 \pm 0.0014$	80	0.04	+0.06
Ho	500	$3.5773 \pm 0.0012$	145	0.03	0.00
Ho	25	$3.5780 \pm 0.001$	65	0.03	+0.02

derived from  $\omega$  and  $\theta$ - $2\theta$  scans showed that the metal lattice constant was indeed relaxed to the bulk value, even for films as thin as 25Å. Table 1 summarizes this data and the coherency length ( $l$ ) for the films. The latter values were derived from the peak widths in the  $\omega$  scans [3]. The column headed ' $\Delta a$ ' gives the standard deviation of the measured lattice constants. Clearly there is no significant coherency strain in any of the films. There is, however, a systematic trend towards smaller coherency lengths with decreasing film thickness, indicating a greater degree of in-plane disorder in the thinner films. XPS depth profiling suggested F transport across the interface by as much as 100Å for one structure containing a 500Å film of Dy grown from an effusion cell. The RBS studies showed no evidence for contamination of the films with F. However, the depth resolution and sensitivity of this technique is not as great as for XPS depth profiling. It seems likely therefore that the thinnest (<200Å) rare earth films may contain impurity F which introduces structural disorder leading to broadening of the magnetic transitions.

SQUID magnetometry data for two representative films of Ho are shown in Figure 3. The magnetic behaviour of the 2000Å film is identical with bulk Ho (see for example Coqblin[6]). In particular, the temperature of the transition to the helical state occurs at 132K but the ferromagnetic ordering is strongly field dependent. The field dependence of ferromagnetic ordering is similar to bulk. Note that the field is applied at 30° to the a-axis (the 'easy' direction). At the lowest temperatures the magnetisation approaches the bulk value of 10.4 Bohr magnetons per Ho atom. On the other hand, the data for the thin Ho film shows less abrupt transitions and the helical ordering transition is barely evident.

#### 4. MODIFIED $\text{LaF}_3$ SANDWICH STRUCTURES: $\text{LaF}_3/\text{Er}/\text{Dy}/\text{Er}/\text{LaF}_3$ .

In order to impose a uniform coherency strain on Dy it is necessary to establish a coherent interface on both sides of the Dy. We have arranged this by sandwiching the Dy between films of Er grown on the  $\text{LaF}_3$ . The Er film, as we have shown, has no strain imposed by the substrate. The Dy film, however, grows coherently on the Er and is subjected to coherency strain. The magnitude of the elastic strain in the Dy depends on the thickness of the Dy film and on the thickness of the Er under and overlayers. One would expect coherency strain to relax with Dy film thickness and that the maximum strain would occur for a thin Dy film sandwiched between much thicker Er films. In our test structure we sandwiched a 500Å film of Dy between a 2000Å underlayer and a 1000Å overlayer. The Dy and Er films were grown at 300°C. An added benefit of this structure was that F outdiffusion from the  $\text{LaF}_3$  into the Er was limited to the near interface region. XPS depth profiling confirmed that the Dy film was free of impurity F.

Double crystal diffractometry studies [7] showed that the Dy film was indeed strained in the sense expected from the lattice misfit between Dy and Er. The perpendicular elastic strain was found to be  $+0.27 \pm 0.02\%$  in the c-axis (ie. an expansion along the c-axis). On the other hand the Er film was close to the fully relaxed state with a perpendicular elastic strain of  $-0.014 \pm 0.01\%$ . Clearly, misfit dislocations have reduced but have not fully relaxed the coherency strain (maximum perpendicular value of 0.58%) in Dy.

Interestingly, SQUID measurements for this structure showed that the ferromagnetic ordering temperature for the Dy was higher than for bulk Dy. This is illustrated in Figure 4

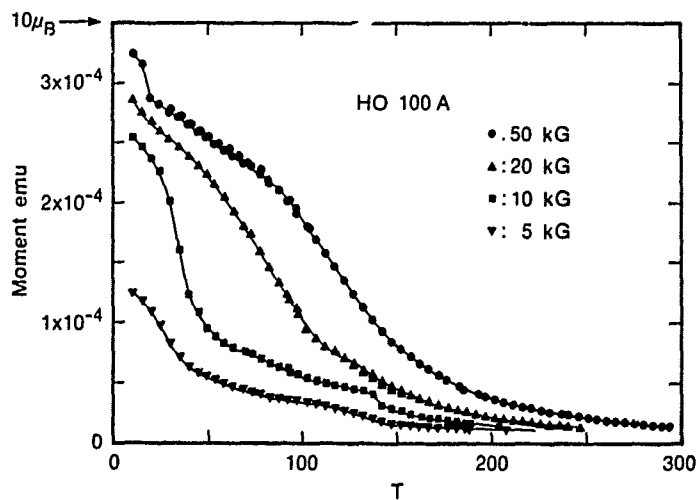
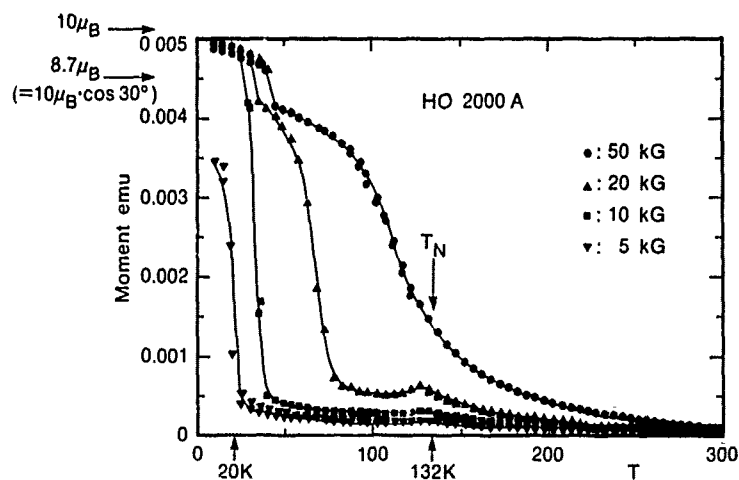


Figure 3 - SQUID magnetometer data for films of Ho in  $\text{LaF}_3$  / Ho /  $\text{LaF}_3$  sandwich structures. The magnetization is measured as a function of temperature for several values of applied field along the b direction in the basal plane.

(a) 2000Å Ho. (b) 100Å Ho.

Note that the saturation magnetization at low temperature and highest fields approaches the bulk value of 10 Bohr magnetons/ Ho atom.

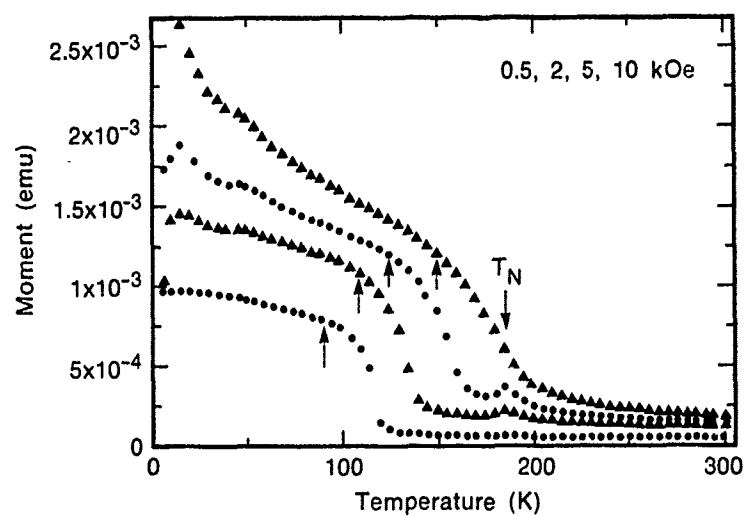


Figure 4- SQUID magnetometer data for a sandwich structure comprising  $1000\text{\AA}$   $\text{LaF}_3$ /  $1000\text{\AA}$  Er /  $500\text{\AA}$  Dy /  $2000\text{\AA}$  Er /  $50\text{\AA}$   $\text{LaF}_3$  / GaAs(TTT).  
 Note the paramagnetic to helical transition at 178K and the helical-ferromagnetic transition at lower temperatures. The arrows indicate the onset of ferromagnetic ordering in bulk crystals. In each case the films order at higher temperature than bulk.



which shows data for 4 different values of applied field along the a-axis (easy axis of bulk crystal i.e. [11.0]). The arrows indicate the onset of ferromagnetic ordering in bulk Dy. The ferromagnetic ordering in the film is in all cases completed at higher temperatures than the onset temperature for ordering in the bulk crystal. We attribute this to the imposed elastic strain in the film since, in bulk crystals, ferromagnetic ordering is accompanied by a discontinuous c-axis expansion and in-plane contraction. By mechanically imposing the structure of the ferromagnetic phase at a temperature above the bulk  $T_c$  we have made it energetically favourable for ferromagnetic ordering to occur at higher temperatures. The possibility of interference from ferromagnetic ordering of the Er is not possible since ordering of the Er film occurs at much lower temperatures ( $<50\text{K}$  for fields below  $10\text{kOe}$ ) than Dy. In addition, differential thermal expansion between Er and Dy as the film is cooled from room temperature to  $100\text{K}$  is less than  $0.1\%$  and would not significantly modify the much larger misfit-imposed strain in the Dy.

If a coherency strain of opposite sign were imposed on the Dy, by for example, growing it on a Y substrate then we would expect the ferromagnetic ordering to be suppressed. Data from Kwo et al.[10] does indeed show such an effect but no strain measurements were reported for those films.

#### 5. EPITAXIAL Fe FILMS GROWN ON Ag FILMS ON GaAs(001).

In two recent papers [1,8] we reported long-range coherency strain and tilted epitaxy in Fe films grown on Ag films on GaAs(001) substrates. In that case the substrates were cut  $2^\circ$  off the (001) plane. We have recently found that tilted epitaxy does not occur when the GaAs(001) substrates are cut to within  $0.12^\circ$  of the (001) plane. Preliminary studies indicate that coherency strain is still present in Fe films grown on these substrates. It therefore seems likely that tilted epitaxy is not a strain relief mechanism as suggested by others[9], but is a result of the symmetry-breaking cut of the substrate. This view is supported by the in-plane isotropy [8] of elastic strain in the Fe films grown on the vicinal substrates. Clearly, tilt and coherency strain have different origins and are uncoupled.

#### 6. DISCUSSION AND CONCLUSIONS.

The origin of the  $30^\circ$  rotation of the rare earth lattice on  $\text{LaF}_3$  is presently unclear. However, one possibility is that the rare earth atoms in the overlayer bond preferentially to specific F atoms, in the  $\text{LaF}_3$  surface, which occupy lattice sites rotated by  $30^\circ$  from the unit cell setting in Figure 2a. Alternatively, the observation of F in the near-interface region of the rare earth films may indicate a reactive interface, possibly with a second phase present. The GID data show no clear evidence for such a phase but simply indicate a greater degree of structural disorder in the thinnest ( $25\text{\AA}$ ) films. The lattice constant data also show no evidence of interstitial F in the rare earth films. High resolution TEM and in-situ photoelectron diffraction studies are planned to probe the interface.

The ability of the fluoride films to decouple the rare earth films from substrate-imposed strains is significant and distinguishes our structures from rare earth films grown by others; in particular from the data of Kwo et al [10] for Dy and of Flynn et al [11] for Er films on sapphire or Y substrates. In these latter cases, depression and suppression of ferromagnetic ordering is very clear and is attributed to 'lattice clamping' of the films to the substrate. Flynn et al. find that the magnetic properties of Er films remain strongly modified to film thicknesses as great as  $8000\text{\AA}$ . We on the other hand find that Er films grown on  $\text{LaF}_3$  films on GaAs substrates are strain-free and behave similarly to bulk crystals at thicknesses greater than  $500\text{\AA}$ .

The prototype Er/Dy/Er sandwich structures define a promising approach to investigating the effects of strain on magnetic ordering in rare earths without the complicating artefact of F as an impurity. The preliminary result of an enhancement in  $T_c$  is interesting but needs to be confirmed by further samples with varying coherency strain in the Dy and by parallel studies of Dy/Y structures which should invert the strain in the Dy.

In the case of Ag/Fe/Ag/GaAs structures it remains to be seen to what extent the coherency strain and tilted epitaxy influence the perpendicular and in-plane anisotropy of the Fe films. Studies of these anisotropies in structures grown on exact orientation substrates are in progress. It is possible that the 2-fold in-plane anisotropy seen [12] in earlier structures grown on vicinal substrates may arise from the symmetry breaking effect of the substrate cut.

#### REFERENCES.

1. R.F.C. Farrow , S.S.P. Parkin, V.S. Speriosu, J.Appl. Phys. **64**, 5315 (1988).
2. J.M. Gibson and J.M. Phillips, Appl.Phys. Lett. **43**, 828 (1983).
3. A. Segmuller, I. Noyan, V.S. Speriosu, Progress In Crystal Growth, (1988).
4. D. Gregson, C.R.A. Catlow, A.V Chadwick, G.H. Lander, A.N. Cormack, B.E. Fender, Acta. Cryst. **B 39**, 687 (1983).
5. R.F.C. Farrow , S.S.P. Parkin, M. Lang, K.P. Roche, Mat. Res.Soc. Symp. Proc. **103**, 205, (1988).
6. B. Coqblin, THE ELECTRONIC STRUCTURE OF RARE-EARTH METALS AND ALLOYS: THE MAGNETIC HEAVY RARE EARTHS, Academic Press, 1977.
7. W. Bennett, R.F.C. Farrow, S.S.P. Parkin, V.S. Speriosu, A. Segmuller, Paper presented at MRS Spring Meeting , 1989. Symposium G. Mat.Res.Soc.Symp. Proc.**151** (1989).
8. R.F.C. Farrow, V.S.S. Speriosu, S.S.P. Parkin, J. Chien, J.C. Bravman, R.F. Marks, P.D. Kirchner, Mat. Res. Soc. Symp. Proc. **130**, (1989).
9. L.J. Schowalter, E.L. Hall, N. Lewis, S. Hashimoto, Mat. Res. Soc. Symp. Proc.**130**, (1989).
10. J. Kwo in THIN FILM GROWTH TECHNIQUES FOR LOW DIMENSIONAL STRUCTURES, NATO ASI Series B: Physics, Vol.163 . Edited by R.F.C. Farrow , S.S.P. Parkin , P.J. Dobson , J.H. Neave , A.S. Arrott. Plenum Press , New York (1987).
11. J. Borchers, M.B. Salamon, R. Du , C.P. Flynn, R.W. Erwin, J J. Rhyne, Superlattices and Microstructures, **4**, 439, (1988).
12. R.F.C. Farrow, S.S.P. Parkin, R.B. Beyers, M. Lang, V. Speriosu, P. Pitner, J.M. Woodall, S.L. Wright, P.D. Kirchner, G.D. Pettit., Mat. Res. Soc. Symp. Proc.**102**, 483 (1988).

## MAGNETIC DOMAINS IN EPITAXIAL (100) FE THIN FILMS

JEFFREY M. FLORCZAK<sup>\*</sup>, P.J. RYAN<sup>\*\*</sup>, J.N. KUZNIA<sup>+</sup>, A.M. WQWCHAK<sup>+</sup>, P.I. COHEN<sup>+</sup>, R.M. WHITE<sup>++</sup>, G.A. PRINZ<sup>++</sup>, AND E. DAN DAHLBERG<sup>+</sup>  
<sup>\*</sup>School of Physics and Astronomy, University of Minnesota, Minneapolis, MN 55455

<sup>\*\*</sup>Control Data Corp., 8100 34th. Ave. S., Mpls., MN 55440

<sup>+</sup>Department of Electrical Engineering, University of Minnesota, Minneapolis, MN 55455

<sup>++</sup>Naval Research Laboratory, Washington, D.C. 20375-5000

ABSTRACT

By use of Kerr microscopy, the domain patterns of thin Fe films (10 nm) grown on  $\text{In}_{1-x}\text{Ga}_x\text{As}$  ( $0.09 \leq x \leq 0.25$ )/GaAs substrates have been investigated. For this investigation, two types of InGaAs buffer layers were prepared. One consisted of a single, thick InGaAs layer and the second composed of an InGaAs strained layer superlattice. Both were grown on (100) GaAs substrates. The study showed that many of the domain walls were approximately parallel to the easy axis of Fe for those films grown on the low x alloy, e.g.  $x=0.1$ , InGaAs buffer layers. In the alloy films with larger values of x, e.g.  $x=0.2$ , the domain pattern of the Fe overlayer was strongly influenced by dislocations of the strain relieved InGaAs buffer layer. These dislocations manifested themselves as corrugations parallel to the  $\langle 110 \rangle$  directions in the InGaAs. Kerr microscopy of a  $x=0.2$  film indicated the presence of long, narrow domains with their long axes parallel to the striations. Although shape anisotropy arguments predicted that the magnetization should be parallel to the striations, magnetometer data indicated that a substantial component of magnetization was oriented perpendicular to the corrugations at low fields. The Fe film grown on the superlattice had magnetic domains very similar to a thick Fe film ( $0.5 \mu\text{m}$ ) grown on GaAs.

INTRODUCTION

Recently there has been a surge of activities in the area of thin-film magnetics focusing on interfacial effects. These activities are stimulated by new developments in growth and characterization of magnetic films as well as theoretical predictions concerning two-dimensional magnetism [1,2]. The systems investigated thus far range from the single interface of monolayer films to the complex multilayered films. Multilayer films magnify interfacial effects by increasing the number of interfaces of the entire film [3,4]. These studies addressed questions in physics as well as magnetic recording technology.

In this paper we examine how the domain patterns of thin Fe films (10 nm) are influenced by the substrate morphology of InGaAs/GaAs substrates.

Two distinct substrates used are (100) GaAs with a single  $\text{In}_{1-x}\text{Ga}_x\text{As}$  buffer layer and a strained layer superlattice consisting of alternating mole fractions of indium in InGaAs. The  $\text{In}_{1-x}\text{Ga}_x\text{As}$  buffer layers grown on GaAs have the property that the lattice constant<sup>x</sup> can be changed by altering the indium concentration provided that the thickness of the

buffer layer exceeds the critical thickness,  $h_c$ . In buffer layers of this type, the lattice constant is linearly related to the indium concentration and ranges from 5.6537 to 6.0538 angstroms at room temperature for  $x=0.0$  to  $x=1.0$  respectively.

An important feature of these InGaAs/GaAs substrates is the formation of defects in the strain relieved InGaAs layer. At thicknesses greater than  $h_c$ , the strained layers relax as misfit dislocations form. These dislocations manifest themselves as corrugations along the  $\langle 110 \rangle$  directions. Since the average dislocation density is linearly related to the indium concentration [5], the number of corrugations present in the substrate can be controlled to some extent. In general, it is desirable to create a thin film of strain free single crystal Fe. For this to occur, the InGaAs lattice constant must be twice that of Fe. This happens when  $x=0.2$ . However, at this mole fraction the defect density is quite large.

One technique used to limit the propagation of the defects is to grow a strained layer superlattice. This method was utilized to fabricate an approximately lattice matched substrate with superlattice layers having indium mole fractions of 0.1 and 0.3. The magnetic domains of a 10 nm Fe film grown on this superlattice closely resembled that of a 0.5  $\mu\text{m}$  Fe film deposited on smooth GaAs. This 0.5  $\mu\text{m}$  film was sufficiently thick so that the mismatch between the Fe and GaAs lattice constants had little effect on the domains.

In the next section, the procedures used to grow the films will be described. This will be followed by a discussion of the results of Kerr microscopy and magnetometry to determine the magnetic properties of the films. The last section discusses the conclusions drawn from this investigation.

## EXPERIMENTAL

Preparation of the standard (100) GaAs substrates were made by etching the surface in an aqueous solution of sulfuric acid and hydrogen peroxide. To remove the residual oxide and to anneal the surface, the standard substrates were inserted in a MBE system and heated at 640°C in the presence of arsenic. Initially, a 50 nm layer of GaAs was grown at a substrate temperature of 580°C to provide a smooth surface for later growth of the buffer layers. For the thick buffer, 0.25  $\mu\text{m}$  of InGaAs was deposited. But for the superlattice, a more involved process is required.

The first step in construction of the superlattice required 30 nm of InGaAs at  $x=0.2$  to surpass the critical thickness. This was followed by alternating layers of  $x=0.1$  and  $x=0.3$  with thicknesses of 20 and 10 nm respectively. These layers have fallen below the critical thickness to deter the formation of misfit dislocations. This alternating structure was reproduced ten times to yield an average mole fraction of 0.2. To complete the superlattice, 0.3  $\mu\text{m}$  of InGaAs at  $x=0.2$  was deposited.

For both buffers, four monolayers of GaAs were deposited pseudomorphically on the InGaAs to act as a diffusion barrier for indium. After the system was allowed to reach desired background pressures of no greater than  $4 \times 10^{-9}$  Torr, 10 nm of Fe was deposited on the buffers at a rate of 3 angstroms per minute. The substrate temperatures ranged between 100°C - 150°C during this deposition process. The growth rate of Fe was calibrated by RHEED oscillations of Fe grown on Fe whiskers. The Fe growth on the InGaAs (100) surface was also a (100) plane. This orientation provided two in-plane axes,  $\langle 100 \rangle$  and  $\langle 110 \rangle$ . When the samples were removed from the system and placed into the atmosphere, a self

passivating oxide layer formed. Typically, 15 angstroms of metallic iron was removed from the film during the oxidation process [6]. The samples were then investigated with a Kerr microscope and Kerr effect magnetometer [7].

## RESULTS AND DISCUSSION

Bright and dark field optical microscopy was used to examine the surfaces of the single layer InGaAs buffers and the strained layer superlattice. Observations showed that the InGaAs buffers at mole fractions of  $x=0.1$  and  $x=0.2$  were preferentially striated along one of the in-plane  $\langle 110 \rangle$  directions. Comparison of the two buffers indicated that a considerably higher density of striations existed when  $x=0.2$ . The thick Fe film on the GaAs substrate and the Fe film on the superlattice were both observed to be optically smooth.

The Fe film on the single layer buffer with  $x=0.2$  has a profoundly different domain structure from the Fe films on the superlattice and the GaAs substrate. The highly corrugated film, i.e.  $x=0.2$ , has narrow domains whose long axes are parallel to the striations of the film. Even though the domain's long axis is parallel to the striations, this does not necessarily imply that magnetization lies in the same direction.

In figures 1 and 2, all edges of the photos are parallel to the  $\langle 110 \rangle$  directions and the diagonals are parallel to the  $\langle 100 \rangle$  directions. To improve the contrast of the domains within one figure, the image has been computer enhanced to reduce the influence of the film's surface

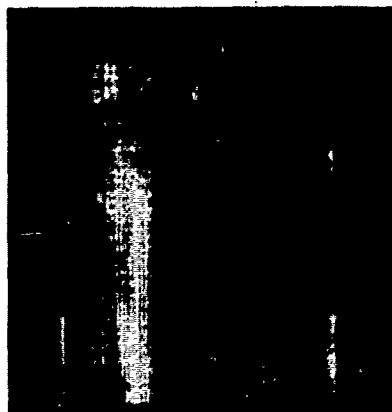


FIG. 1. This is a Kerr photo of a 10 nm Fe film grown on  $x=0.2$  InGaAs. The striations, which are thin dark lines, are parallel to the domain walls. Bright and dark regions represent different magnetization directions.

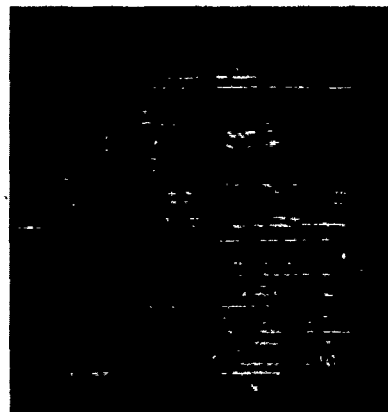


FIG. 2. This is the same sample as fig. 1 rotated  $90^\circ$ . Here, the striations are perpendicular to the domain walls.

features. This is accomplished by subtracting an image of the saturated state from the image of the demagnetized state. In this experimental setup, the Kerr microscope has a higher sensitivity to the magnetization in the vertical direction. Hence, it becomes more difficult to determine the absolute orientation of magnetization.

Figure 1 shows a demagnetized state obtained by reducing an oscillating magnetic field parallel to the striations. The photograph suggests that the magnetization is parallel to the long axes of the domains. However, Kerr magnetometer data indicate otherwise [7]. These films exhibit a complex domain structure because there is a compromise between the shape anisotropy energy due to the corrugations, the dipolar interactions between adjacent channels in the film, and the crystalline anisotropy energy. One possible orientation for magnetization amongst the domains is a canted structure. For example, if in one particular domain the magnetization lies along the [100], then the next adjacent domain has magnetization along the [010]. This configuration repeats itself resulting in a large net component of magnetization perpendicular to the striations.

In figure 2 the demagnetizing field is perpendicular to the striations. This results in domains with their long axes perpendicular to the visible corrugations. This result may be explained if there are striations in both of the in-plane  $\langle 110 \rangle$  directions [5]. Figure 2 shows only one striation pattern due to the optical microscope's insufficient resolution.

Finally it is observed that the residual magnetization parallel to the magnetizing field is approximately 0.7 of the saturation magnetization. For all directions of the applied field, the coercivity is on the order of 20 Oe. These two facts indicate that films of this nature provide large magnetic fields that can be controlled by rather small applied magnetic fields.

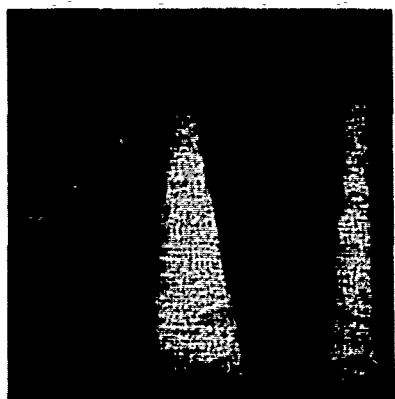


FIG. 3. This Kerr photo is of a demagnetized 10 nm Fe film on a lattice matched superlattice.



FIG. 4. This demagnetized 0.5  $\mu\text{m}$  Fe film on GaAs substrate was taken with a Kerr microscope.

The domain patterns in figures 3 and 4 should be contrasted with those in figures 1 and 2. The similarities of the films' domain patterns in figures 3 and 4 attest to the high quality of the 10 nm Fe film and the success of the superlattice approach in eliminating the striated surface.

### CONCLUSION

In these thin ferromagnetic films, the presence of interfacial structures change the magnetic properties in various ways. Striated surfaces tend to induce narrow domains parallel to the corrugations and smooth surfaces tend to have larger domains with walls parallel to the easy axis. The striations may be controlled by varying the indium concentration in the buffer layer or by fabricating a superlattice structure. In general, surface irregularities are considered harmful to the magnetics. There are some applications, such as magneto-optic devices, where it is desirable to have a large magnetic field controlled by a small applied magnetic field. In these situations the corrugated surface and the subsequent control of the magnetics may be applicable.

Work supported under AFOSR Grant AFOSR-89-0248

### References

- [1] C.L. Fu, A.J. Freeman, and T. Oguchi, Phys. Rev. Lett. 54 2700 (1985)
- [2] B.T. Jonker, K.H. Walker, E. Kisker, G.A. Prinz, and C. Carbone, Phys. Rev. Lett. 57 142 (1986)
- [3] M.N. Baibich, J.M. Broto, A. Fert, F. Nguyen Van Dau, F. Petroff, P. Eitenne, G. Creuzet, A. Friederich, and J. Chazelas, Phys. Rev. Lett. 61, 2472 (1988)
- [4] J. Araya-Pochet, C.A. Ballentine, and J. L. Erskine, Phys. Rev. B 38, 7846 (1988)
- [5] K.L. Kavanagh, M.A. Capone, L.W. Hobbs, L.C. Barbour, P.M.J. Maree, W. Schaff, J.W. Mayer, D. Pettit, J.M. Woodall, J.A. Stroscio, and R.M. Feenstra, J. Appl. Phys. 64, 4843 (1988)
- [6] J.J. Krebs, F.J. Rachford, P. Lubitz, and G.A. Prinz, J. Appl. Phys. 53, 8058 (1982)
- [7] J.M. Florczak and E. Dan Dahlberg, to be submitted for publication.

MAGNETIC ANISOTROPY CONSTANTS OF EPITAXIAL (110) Fe/GaAs FILMS  
FROM 77K TO 293K STUDIED BY MAGNETO-RESISTANCE.

DANIEL K. LOTTIS\*, G.A. PRINZ\*\*, and E. DAN DAHLBERG\*

\* School of Physics and Astronomy, University of Minnesota, Minneapolis,  
MN 55455

\*\* Naval Research Laboratory, Washington, D.C. 20375-5000.

ABSTRACT

A first-order phase transition in the magnetization of Fe films, driven by an applied magnetic field, was first reported by Hathaway and Prinz [1]. Further studies were performed on this phase transition using anisotropic magnetoresistance measurements by Riggs and Dahlberg [2]. Here we report the extension of these studies to include temperatures between 77K and 293K. Emphasis is on a determination of the fourth-order and uniaxial anisotropy constants ( $K_1$  and  $K_u$ ). It is shown that the temperature dependence of the anisotropy energies in these films varies with thickness, which may be useful in sorting out the origin and magnitude of different contributions to the total effective anisotropy. The present study suggests that similar studies of (110) iron on other substrates might contribute to achieving a better understanding of in-plane anisotropies in epitaxial films.

INTRODUCTION

An important challenge in the area of magnetism in thin films and multilayers is to improve our understanding of the anisotropy energy associated with the orientation of the magnetization. Attention has been given to first-principles calculations of the contribution to the magnetic anisotropy arising from the presence of free surfaces and interfaces with the substrate or with an overlayer [3,4], and to first-principle calculations of magnetic anisotropy in metals [5]. Experimental measurements of such energies in the ultrathin film and multilayer film cases have shown qualitative agreement with these calculations [6-8]. For many applications, however, the anisotropy energies in films with thicknesses in the range of 5 to 50 nm is of great interest. In particular, the possibility of controlling the in-plane anisotropy by appropriate choice and preparation of the substrate is especially promising. A careful characterization of the magnetic anisotropy in epitaxial films could allow tests of calculations in ways not possible in conventional single-crystal systems. This would require a sufficiently good characterization of the thin-film anisotropy to allow interface and surface effects to be subtracted off. Currently available epitaxial techniques allow growth of crystals with strains which would be difficult to achieve in bulk samples, and which would allow measurements of anisotropy constants for non-equilibrium values of the lattice constant.

Our choice of (110) iron films as the object of such studies has several advantages. Measurements on thin film iron can readily be



compared with well established results for the bulk case. The (110) plane contains three major symmetry directions for iron: the [100] or magnetically easy direction, the [111] or magnetically hard direction, and the [110] or magnetically "intermediate" direction. By using GaAs wafers doped as insulators, we are able to carry out magneto-transport measurements on these films. In particular, measurements of the anisotropic magneto-resistance allow us to detect changes in the orientation of the magnetization.

Another major advantage of using (110) iron films for studies of the magnetic anisotropy is that this system is known to exhibit a dramatic first-order reorientation of the magnetization for fields applied near the [110] direction. The sudden reorientation becomes possible when the Zeeman or M.H contribution to the free energy of the system makes the [110] direction more favorable than the [001] direction, which is the easy direction in the absence of an applied field (samples with thickness less than about 5 nm display an easy axis along the [110], as discussed below). Further increases in the applied field are found experimentally to result in the reorientation of the magnetization along the new energy minimum near the [110]. There is evidence that the reorientation occurs by means of the nucleation and subsequent propagation of domain walls [9]. This effect, known as the Magnetic Reorientation Phase Transition or MRPT was first measured in iron by Hathaway and Prinz [1]. The sharp nature of this transition and its strong dependence on the direction of the applied field makes it an ideal probe of the anisotropy energies in (110) Fe films. Previously we have used a simple model of the MRPT to extract the anisotropy energies from phase diagrams measured experimentally at room temperature [9]. In this paper we report the first results obtained by extending this study to temperatures ranging from room temperature down to liquid nitrogen temperature.

## EXPERIMENT

Our samples, which were prepared at the Naval Research Laboratory, have been described in detail in a number of other publications eg. ref. 11. The resistance measurements are carried out using a standard 4-probe, a.c. resistance bridge technique. A temperature controller is used with a GaAs diode temperature sensor to maintain temperature stabilities of 0.5K or better during the measurements. The measurements of the temperature are performed with two silicon diodes, which are on an entirely independent circuit. The diodes are several cm apart along the vertical direction, where the largest temperature gradients are expected, and allow us to monitor the uniformity of the temperature in the sample space. The apparatus is operated as a gas flow cryostat from 77K up to room temperatures, using  $N_2$  as the cryogen. Data can be taken simultaneously by x-y recorder and lab computer, for later analysis.

For the purposes of mapping out the MRPT diagram, the resistance is measured as the magnitude of the applied magnetic field is increased and then decreased. Prior to each trace, the sample is "poled" by applying a field along the easy axis. The value of this field is chosen to be larger than the anisotropy fields, i.e., larger than the field required to saturate the magnetization (and hence the resistance) in any in-plane direction. Each trace is measured up to fields sufficiently large to saturate the signal. Attention is generally restricted to fields applied near the [110] direction, for which the sudden reorientation is observed.

## ANALYSIS

Our data analysis is performed as described in [9]. Individual resistance traces are used to determine the magnitude of the applied field at which the MRPT occurs for both increasing and decreasing fields, and for each orientation of the applied field with respect to the [110] direction. The data from a series of traces is then condensed into a phase diagram, such as the one exhibited in figure 1. The phase boundaries corresponding to increasing and decreasing field magnitudes, obtained by fitting the transitions for individual traces to a low-order polynomial, converge at a critical point, described by its polar coordinates  $H_c$  and  $\theta_c$  (angles measured from the [110] direction).

The overall shape of the phase diagram can be summarized by giving the position of the critical point and the intercepts of the increasing-field and decreasing-field phase boundaries with the [110] direction (that is, the values of the transition field along the [110] axis). The phase diagram for a given sample is found to depend significantly on temperature.

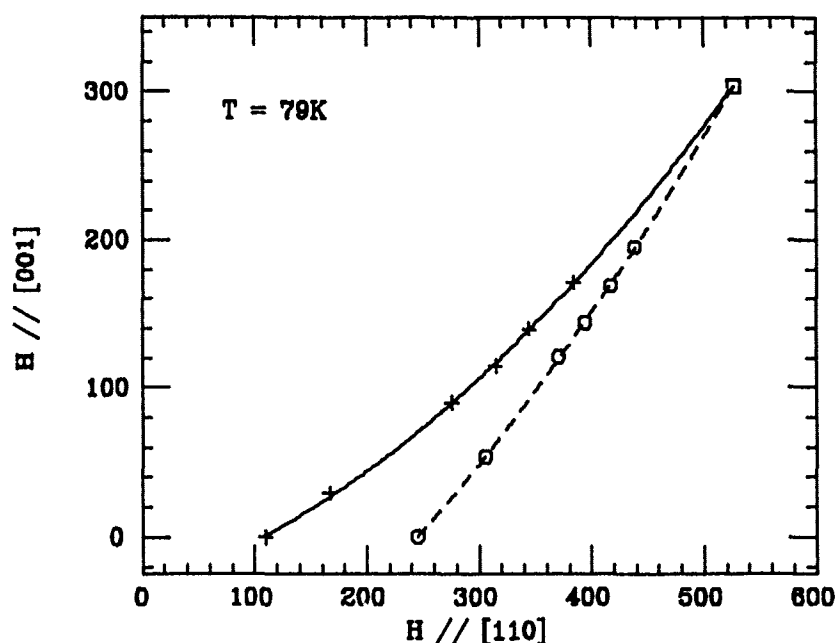


**FIGURE 1** Phase diagram of the MRPT in a 10nm sample, at  $T=79K$ . Circles represent reorientation transitions observed while increasing magnitude of applied field, plus signs for decreasing fields. Curves are 2nd order polynomial fits. Box is intersection of phase boundaries: the critical point.

The anisotropy fields  $K_1/M$  and  $K_u/M$  are obtained from each phase diagram by using the method described in [9]. Before quoting the results, we shall review some of the features of this method and the model which is used for the MRPT.

#### MODEL FOR THE MRPT

The magnetic reorientation phase transition (MRPT) has been discussed in great detail in a number of publications [10]. This section is intended only to list results which are needed for our analysis.

To fourth order in the direction cosines of the magnetization, the orientational free energy of our samples is taken as

$$E_a = -M \cdot H + K_1 (\alpha_1 \alpha_2 + \alpha_2 \alpha_3 + \alpha_3 \alpha_1) + 2\pi (M_n/M)^2 + K_s (M_n/M)^2 + K_u \sin^2(\theta) \quad (1)$$

$M_n$  is the normal component of  $M$ , and the  $\alpha$ 's are the direction cosines of  $M$ . The first two terms correspond to the bulk iron limit, the third term represents the shape anisotropy, the fourth term is the surface anisotropy term arising from breakdown in four-fold symmetry at the interfaces, and the fifth term is an in-plane uniaxial term associated with effects arising from the epitaxial nature of these films. This last term is necessary to fit the data, and to explain the fact that in films thinner than about 50 angstroms, the [110] direction becomes the magnetic easy axis. It is generally regarded as arising from strains produced by lattice-mismatch and from the different thermal expansion coefficients in iron and GaAs. It has recently been pointed out, however, that there are other effects that could contribute to such a term, such as steps in the substrate due to slight misorientation, or preferential directions for the formation of dislocations.

Considerations of the relative magnitudes of these terms for our experimental conditions (all fields applied in plane of the film, etc.) lead to the following dimensionless equation

$$\epsilon_a = -h \cos(\theta - \theta_H) - 1/2 [\sin^4 \theta + 1/2 \cos^4 \theta] - \kappa \sin^2 \theta \quad (2)$$

where the  $\epsilon_a = E_a/K_1$ ,  $h = K_1/M$ , and  $\kappa$  is the ratio  $K_1/K_u$ .

The equilibrium orientation for the magnetization can then be calculated for any value (orientation and magnitude) of the applied field. If we then treat the component of the magnetization in the [110] direction as a phase parameter, we find that there is a first order phase boundary, across which our phase parameter changes in a discontinuous manner. The shape of this phase boundary is a function of  $\kappa$ , and this functional relationship allows us to extract  $\kappa$  and  $K_1$  from our data by fitting it to the theoretical curve.

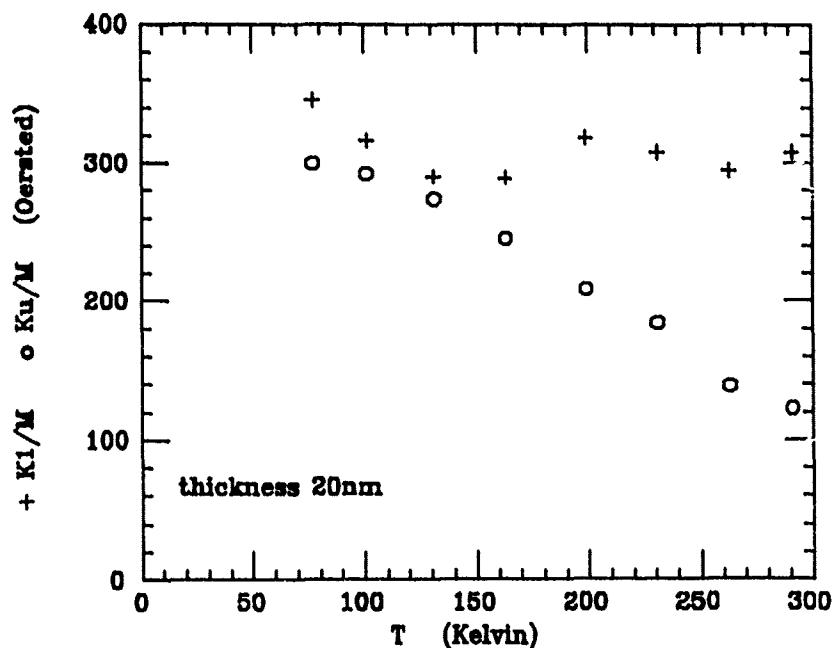


FIGURE 2 Anisotropy fields  $K_1/M$  (plus signs) and  $K_u/M$  (circles), obtained by fitting MRPT phase diagrams to model, vs. temperature. Errors are about  $\pm 30$  Oe. Note that straight line through circles intersects T axis near growth temperature of 450K.

## RESULTS AND DISCUSSION

The results of fitting our temperature-dependent data to the above model are displayed in figure 2, which shows the temperature dependence of the anisotropy energies  $K_1$  and  $K_u$  thus obtained for 20 nm thick sample.

The cubic term  $K_1/M$  is not observed to vary from its bulk iron value and temperature dependence, within the error bars of our data. The uniaxial term  $K_u/M$  is seen to be comparable in magnitude to the cubic term throughout the temperature range. This is consistent with the FMR data taken at 293K and 77K [11]. Here, however, we can see that the dependence on T is nearly linear in this range, again within the resolution of the data. An extrapolation to higher temperatures gives  $K_u=0$  at a point very near the 450K growth temperature. This is consistent with the argument of Krebs et al [11] to the effect that  $K_u$  arises from an interplay between two competing mechanisms that introduce strain into the system: the lattice mismatch of bcc iron to the GaAs substrate, and the difference in thermal contraction of the two materials. The lattice-mismatch induced

compression is largely relaxed in films grown to larger thicknesses, and upon cooling from the growth temperature of 450K the iron film is stretched. This, through the magneto-elastic coupling constants for iron, can be shown [11] to lead to a uniaxial, in-plane correction to the free energy similar to the uniaxial term in equation 1 above. Thinner films show little relaxation of the lattice-mismatch induced compression, which then tends to relax as the film is cooled below the growth temperature. For the 10nm film, the magnitude of  $K_u/M$  from our measurements is smaller, and it becomes more difficult to make significant extrapolations. In the future we expect to report on a complete study of temperature dependences for the thickness range spanned by our samples, extending the present data down to liquid He temperatures as well.

#### REFERENCES

- [1] K. Hathaway and G.A. Prinz, Phys. Rev. Letter 47, 1761 (1981)
- [2] E.D. Dahlberg, K.T. Riggs, and G.A. Prinz, J. Appl. Phys. 63, 4270 (1988)
- [3] Roy Richter, J.G. Gay and J.R. Smith, PRL 54, 2704 (1985)
- [4] J.G. Gay and Roy Richter, PRL 56, 2728 (1986)
- [5] H.J.F. Jansen, J. Appl. Phys 64, 5604 (1988)
- [6] B.T. Jonker, K.H. Walker, E. Kisker, G.A. Prinz, and C. Carbonne, PRL 57, 142 (1986)
- [7] N.C. Koon, B.T. Jonker, F.A. Volkening, J.J. Krebs, and G.A. Prinz, PRL 59, 2463 (1987)
- [8] D. Pescia, M. Starnpanoni, G.L. Bona, A. Vaterlaus, R.F. Willis, and F. Meier, PRL 58, 2126 (1987)
- [9] K.T. Riggs, G.A. Prinz, and E.D. Dahlberg, to be submitted for publication.
- [10] References [1] and [10] and works cited therein.
- [11] J.J. Krebs, F.J. Rachford, P. Lubitz, and G.A. Prinz, J. Appl. Phys. 53, 8058 (1982)

# CRITICAL BEHAVIOR OF EPITAXIAL ANTIFERROMAGNETIC INSULATOR FILMS: INTERDIGITAL CAPACITANCE MEASUREMENT OF MAGNETIC SPECIFIC HEAT

M. IUI\*, A. R. KING\*, V. JACCARINO\* and G. L. SNIDER\*\*

\*Department of Physics, University of California, Santa Barbara, CA 93106

\*\*Department of Electrical and Computer Engineering, University of California, Santa Barbara, CA 93106

## ABSTRACT

An interdigital capacitance technique (ICT) for the measurement of magnetic specific heat ( $C_m$ ) critical behavior of micron-thick epitaxial films of antiferromagnetic insulators (AF) has been developed. It was first applied to a study of high quality  $3\mu\text{m}$  epitaxial films of  $\text{FeF}_2$  on lattice matching (001) oriented  $\text{ZnF}_2$  substrates. Under ideal preparatory conditions, the ( $C_m$ ) results exhibit the divergent critical behavior of a 3-D Ising system. The ICT appears to be a useful method for characterizing the quality of AF films in regard to rms variations in the exchange interactions.

## INTRODUCTION

In an earlier study, we reported the results of antiferromagnetic resonance (AFMR) measurements of micron-thick epitaxial films of  $\text{MnF}_2$  grown on  $\text{ZnF}_2$  substrates.<sup>1</sup> Since then a considerable effort has been made to improve the quality of the epitaxy process and to investigate other systems (e.g.  $\text{FeF}_2$  and  $\text{CoF}_2$  grown on  $\text{ZnF}_2$ ).

One of the most fundamental properties of magnetic systems is their critical behavior in the vicinity of the phase transition. The study of the critical behavior of epitaxial films and superlattices could thus be a powerful technique for studying the properties of these structures. If one hopes to, say, measure the magnetic specific heat  $C_m$  of a magnetic superlattice then certain formidable obstacles have to be overcome. The total volume of material contained in superlattices is conveniently no more than  $10^{-4} \text{ cm}^3$  and is epitaxially grown on a substrate conveniently no less than  $10^{-1} \text{ cm}^3$  in volume. Conventional specific heat techniques would entail trying to separate the purely magnetic contribution of the layered structure from the combined phonon contributions of the superlattice plus substrate.

There is another technique, however, which indirectly measures only the magnetic part of the specific heat. It has been demonstrated in our laboratory<sup>2</sup> that the temperature derivative of the capacitance, through the dielectric constant, is proportional to  $C_m$  and this method has been applied to critical phenomena studies in both pure<sup>2</sup> and random<sup>3,4,5</sup> magnetic systems. However, for a thin film on a relatively thick substrate, the fractional change in the total capacitance arising from the changes in  $C_m$  of the film would be very small, if the usual disk geometry were used.<sup>2</sup> In the present work we have circumvented this difficulty by using an interdigital capacitance technique in which, primarily, the dielectric properties of the film, and not the substrate, are being measured.

## INTERDIGITAL CAPACITANCE TECHNIQUE (ICT)

The ICT involves evaporating a pattern of interdigitated metal fingers directly on to the surface of the material to be measured. The capacitance is then measured between the interdigitated fingers, rather than between metal films on either face of the disk, as is conventionally done. If the spacing between the interdigitated fingers is on the order of the film thickness, the measured capacitance is mostly that of the film, not that of the vacuum immediately above it or that of the substrate.

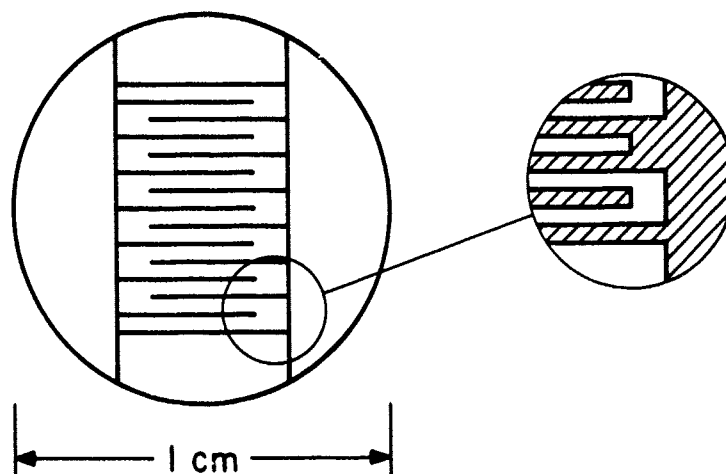


Fig. 1. Interdigital device pattern consisting of an array of  $5\text{ }\mu\text{m}$ -wide lines of metal separated by  $5\text{ }\mu\text{m}$  spaces.

The mask design used for the interdigital device pattern is shown in Fig. 1. The pattern consists of an array of  $5\text{ }\mu\text{m}$  lines of metal separated by  $5\text{ }\mu\text{m}$  spaces. The choice of  $5\text{ }\mu\text{m}$  spacings was dictated by this being the smallest structure that could be easily fabricated without the use of a low particle-count clean room. Since the pattern covers an area of  $4\text{ mm}$  by  $5\text{ mm}$ , and a foreign particle of a few microns anywhere in that area can cause failure, it was deemed important to choose a line width and spacing large enough to insure good yield. With  $5\text{ }\mu\text{m}$  spacings, filling factors are expected to be adequate for film thickness of  $3\text{ }\mu\text{m}$  or more.

The interdigital pattern is formed photo-lithographically using the lift-off technique. The  $\text{FeF}_2$  substrates and  $\text{FeF}_2$  epitaxial films on  $\text{ZnF}_2$  substrates are spin coated with Shipley 1400-25 positive photoresist, and exposed using the interdigital mask. Before developing, the samples were soaked in chlorobenzene, which hardens the surface of the photoresist. When developed, the exposed areas of photoresist are removed, and the hardened upper layer is undercut along the edges of the pattern, forming an overhang. A  $1000\text{ \AA}$  layer of titanium is deposited to insure good metalization adhesion, followed by a  $2000\text{ \AA}$  layer of gold, to obtain a low resistance. The metals were deposited by e-beam evaporation. Because of the overhang in the photoresist, there is a clean break between metal in the patterned areas and metal atop the photoresist. When the sample is placed in acetone, the photoresist dissolves and the metal on the photoresist is removed, leaving only the metal interdigital pattern. The most vexing problem encountered in the lithograph process is that occasional shorts would occur between the "digits", thereby making capacitance measurements impossible. However, with all parameters in the processing optimized, we have obtained a success rate of about 70%. Subsequently, electrical contact to the interdigital device is made mechanically and good thermal contact to the substrate is insured by the use of thermal compound.

The bulk  $\text{FeF}_2$  surfaces and the  $\text{ZnF}_2$  substrates used for epitaxial growth were prepared in the following fashion: The polishing method involved an initial grinding of the substrates with alumina powder on glass. This was followed by a successively smaller series of diamond grits down to  $1/4 \mu\text{m}$ , in which, at each stage, all visible damage produced by each previous step was removed. This was checked by examination with a Normarski microscope. The amount of time spent on each step was then increased by a factor of three to insure that any unseen sub-surface damage introduced by the previous step was completely removed. Each step was then checked by a chemical etch in a dilute solution of  $\text{HCl}$  which selectively etches damaged areas and thus exposes any residual sub-surface damage. Finally, the substrates were etch polished with a dilute solution of  $\text{HCl}$ , rinsed in deionized water, and blow-dried with nitrogen gas. The fact that such elaborate polishing procedures were necessary became evident in early ICT measurements made on a  $\text{FeF}_2$  substrate, prepared by polishing at each step until only the visible damage from the previous step is removed. These results showed a marked rounding of the phase transition as discussed below.

The epitaxial films were grown in a modified Varian UHV vacuum system using Molecular Beam Epitaxy techniques. The  $\text{ZnF}_2$  substrates are heat cleaned at  $450^\circ \text{C}$  for 10 minutes. The temperature is then lowered to a growth temperature of  $300^\circ \text{C}$ . The  $\text{FeF}_2$  is evaporated from an open pyrolyzed graphite crucible at a rate of approximately  $1 \mu\text{m}/\text{hour}$ .

The epitaxial film used in this study was characterized by the use of high resolution double crystal diffraction (X-ray rocking curves) which provides a rapid and nondestructive means of characterization. The details and results of this technique on epitaxial  $\text{FeF}_2$  and  $\text{CoF}_2$  films will be discussed more thoroughly elsewhere.<sup>6</sup> The theoretical intrinsic rocking curve linewidth has been calculated using x-ray dynamical diffraction theory as given by A. T. Macrander et al.<sup>7</sup> As one would expect, the calculated value of the intrinsic linewidth increases with decreasing epitaxial layer thickness.

A rocking curve linewidth (FWHM) of better than 60 arc sec. was measured on the  $3 \mu\text{m}$  sample. This is very respectable, keeping in mind that the theoretical value for a  $\text{FeF}_2$  film of this thickness is 10 arc sec. However, this is not the best epitaxial film of  $\text{FeF}_2$  grown to date. A rocking curve linewidth of 30 arc sec. was obtained on a  $0.8 \mu\text{m}$  film of  $\text{FeF}_2$  with an expected diffraction-limited linewidth of 22 arc sec. This is an extremely high perfection epitaxial film. The slight discrepancy in linewidth from the ideal value strains caused by probably due to the small ( $< 0.2\%$ ) lattice mismatch between the  $\text{FeF}_2$  film and  $\text{ZnF}_2$  substrate.

A three-terminal capacitance technique was used<sup>8</sup> at a frequency of 1 kHz. The capacitance of the interdigital on  $\text{FeF}_2$  was typically about 40 pF at room temperature. A 39 pF NPO capacitor was used for the reference. It was mounted in the cryostat close to the interdigital and maintained at the same temperature. The reference arm of the bridge utilized a 7-digit ratio transformer. One "step" of the ratio transformer corresponds to a change in capacitance of  $\Delta C/C = 2 \times 10^{-7}$ . The ICT had about a quarter of the sensitivity in  $1/C \, dC/dT$  as compared to the conventional disk capacitance technique.<sup>2</sup> This is probably explained by the fact that, in  $\text{FeF}_2$ ,  $C^{-1} \, dC/dT$  is anisotropic; with the value measured with the E-field parallel to the c-axis being one-third of the magnitude, and of opposite sign, as is obtained for  $E \perp c$ . In addition, there was an increase in noise by about a factor of five over conventional measurements. However, the critical behavior data was still of high enough quality to determine reasonably accurate values for the critical exponents.

The ICT was first tested on bulk  $\text{FeF}_2$  since its critical properties are well known. It was polished using the initial procedures described above. The results are shown in Fig. 2a. Instead of the expected sharp transition, a very noticeably rounded transition was apparent at reduced temperatures beginning at  $|t| \approx 10^{-2}$ , where  $t = (T - T_n)/T_n$ . This can be seen by plotting  $dC/dT$  vs  $\log |t|$  as shown in Fig. 3a. This seemed odd in light of the extremely sharp transition found in conventional capacitance measurements<sup>2</sup> of thick ( $\sim 1\text{mm}$ ) slabs of  $\text{FeF}_2$ . It was this result which made us suspect our initial surface preparation methods and resulted in the new procedures, discussed above, to be adopted.



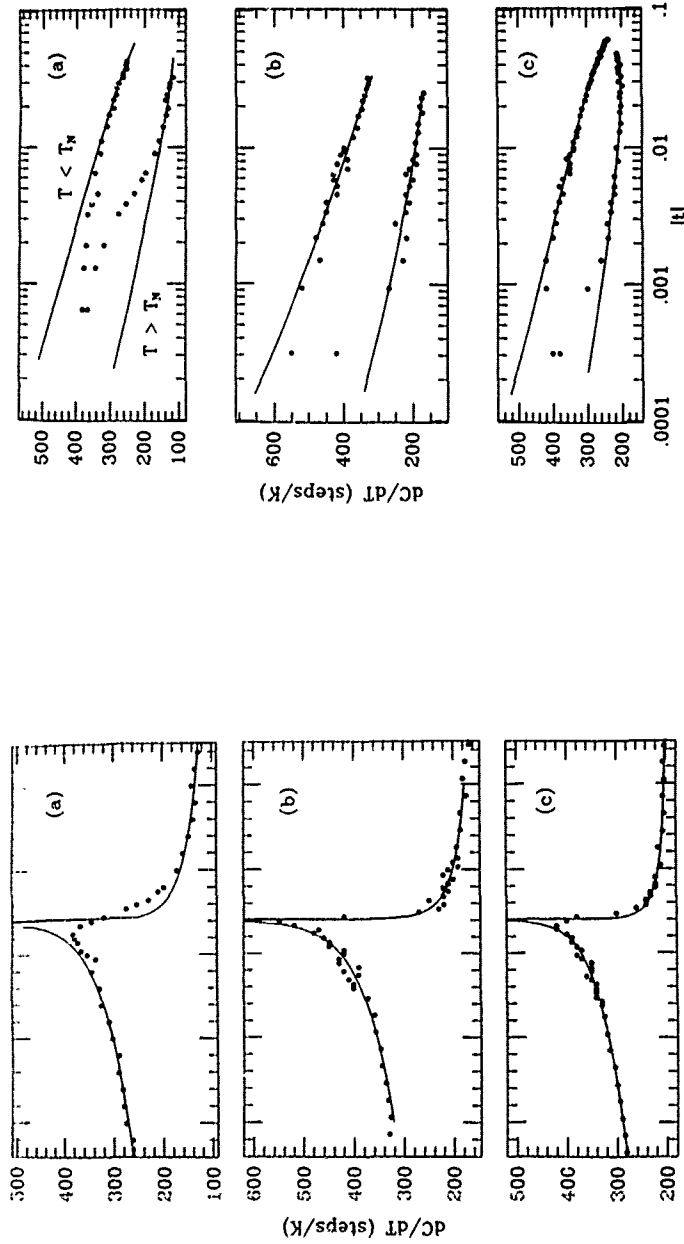


Fig. 2. a)  $dC/dT$  vs  $T$  for the  $\text{FeF}_2$  substrate polished using the initial procedure. b)  $dC/dT$  vs  $T$  for  $\text{FeF}_2$  substrate polished using the elaborate surface preparation procedure. c)  $dC/dT$  vs  $T$  for the  $3\mu\text{m}$   $\text{FeF}_2$  epitaxial film. The solid lines in a) - c) represent the best fit to the theory.

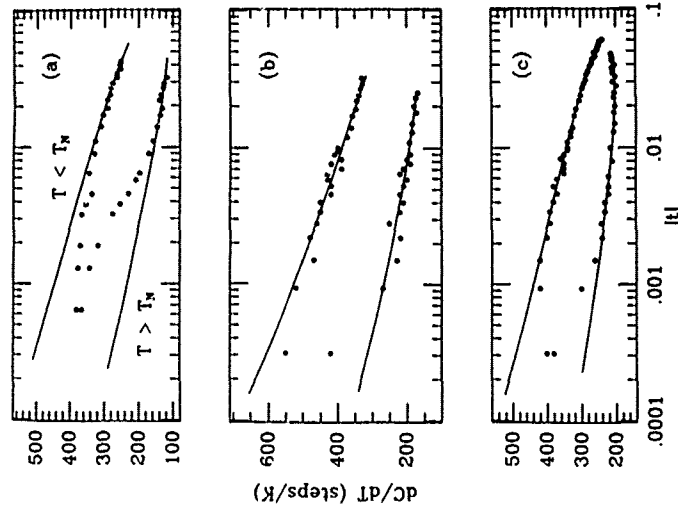


Fig. 3. a)  $dC/dT$  vs  $\log |t|$  for the  $\text{FeF}_2$  substrate polished using the initial procedure. Departure from theory (solid line) first occurs for  $|t| \sim 10^3$ . b)  $dC/dT$  vs  $\log |t|$  for the  $\text{FeF}_2$  substrate polished using the elaborate surface preparation procedure. Rounding occurs for  $|t| \leq 10^{-3}$ . c)  $dC/dT$  vs  $\log |t|$  for the  $3\mu\text{m}$   $\text{FeF}_2$  epitaxial film. Rounding occurs for  $|t| \leq 2 \times 10^3$ .

The capacitance measurements using the ICT were then repeated on a "carefully" polished  $\text{FeF}_2$  substrate using the elaborate surface preparation procedure. The results are shown in Fig. 2b and in a  $\log |t|$  plot in Fig. 3b. Now the expected divergent critical behavior of a 3-D Ising system is found with no noticeable rounding to better than  $|t| = 10^{-3}$  in reduced temperature. The data was fitted to  $C_m^\pm = A^\pm |t|^{-\alpha}$ , where  $\alpha$  is the critical exponent and  $A^\pm$  is the amplitude ratio, using a nonlinear least squares fit including corrections to scaling and allowing all variables to float<sup>9</sup>. We find the exponent  $\alpha = 0.10 \pm 0.01$  and amplitude ratio  $A^+/A^- = 0.60 \pm 0.05$  which are identical, within experimental error, to those found in previous capacitance<sup>2</sup> ( $\alpha = 0.110$ ,  $A^+/A^- = 0.544 \pm 0.0011$ ), birefringence<sup>9</sup> ( $\alpha = 0.11 \pm 0.007$ ,  $A^+/A^- = 0.543 \pm 0.020$ ), measurements and theory for the  $d=3$  Ising model ( $\alpha = 0.110 \pm 0.005^{10}$ ,  $A^+/A^- = 0.5^{11}$ ).

Finally a  $3\mu\text{m}$  epitaxial film of  $\text{FeF}_2$  grown on a  $\text{ZnF}_2$  substrate was measured using the ICT. (This film was characterized by double crystal diffractions as discussed earlier). The results are shown in Fig. 2c and 3c. The epitaxial film showed the same 3-D Ising divergent critical behavior as seen on the  $\text{FeF}_2$  substrate. This film showed signs of rounding at reduced temperatures less than  $|t| = 2 \times 10^{-3}$ . We therefore judge the perfection of the film to be less than a well-polished  $\text{FeF}_2$  surface, but much better than a poorly polished one. When the data were fitted with the nonlinear least squares fit, the exponent  $\alpha = 0.1 \pm 0.01$  and amplitude ratio  $A^+/A^- = 0.60 \pm 0.05$  were in satisfactory agreement with the bulk sample and theoretical results. To our knowledge, this is the first detailed study of critical behavior of an epitaxial film.

## CONCLUSION

The greatest difficulty encountered in the ICT has been the processing procedure used in depositing the interdigital pattern on the material. The use of a class 100 clean room could eliminate some of the shorting problems. The other drawback in this method is once the interdigital is placed on the material, it cannot be removed without destroying the film.

Our earlier low temperature (4K) AFMR study of  $\text{MnF}_2$  epitaxial films exhibited larger than expected resonance linewidths. The broadening of the AFMR was interpreted as resulting from strain induced variations in the exchange and/or anisotropy interaction in the film, to which the linewidth is extremely sensitive. But while the linewidth of the AFMR may directly correlate with the degree of perfection and the strain state of the film, it is only indirectly sensitive to the substrate surface and subsurface properties. The ICT, in contrast, provides a means whereby the quality of the substrate surface and subsurface may be judged for the sharpness of the magnetic phase transition. It may be shown that the rounding of the antiferromagnetic phase transition at  $T_N$  may be produced by any rms variation in the exchange interactions in the first few microns below the surface of the crystal.<sup>12</sup>

The ICT opens the possibility of studying a wide variety of novel systems studied through their critical behavior. In the 3-d transition metal difluorides, several antiferromagnets with different properties exist with good lattice matches to the non-magnetic  $\text{ZnF}_2$ . Superlattices of magnetic/magnetic and magnetic/non-magnetic layers are expected to exhibit a rich variety of unusual critical behavior. For example, one would be able to examine dimensional crossover from  $d=3$  to  $d=2$  critical behavior which would occur at a value of  $|t|$  such that the correlation length  $\xi$  in the bulk would have become approximately equal to the thickness of the magnetic layer.

We would like to thank N. Nighman for growing the substrate crystals and for providing the source material. We would also like to express our gratitude to R.F.C. Farrow for allowing us use of the double crystal diffractometer at IBM Almaden Research Center, San Jose. This work has been supported in part by NSF Grant number DMR85-16787.

## REFERENCES

1. M. Lui, J. Drucker, A. R. King, J. P. Kotthaus, P. K. Hansma, and V. Jaccarino, Phys. Rev. B 33, 7720 (1986).
2. A. R. King, D. P. Belanger, P. Nordblad and V. Jaccarino, J. Appl. Phys. 55 (6), 2410 (1984).
3. S. M. Rezende, A. R. King, and V. Jaccarino, J. Appl. Phys. 55(6) 2413 (1984).
4. A. R. King, V. Jaccarino, D. P. Belanger and S. M. Rezende, Phys. Rev. B 32, 503 (1985).
5. A. R. King and D. P. Belanger, J. Magn. Magn. Mater. 54-57, 19 (1986).
6. M. Lui, A. R. King, V. Jaccarino, R. F. C. Farrow and S. S. P. Parkins (to be published).
7. A. T. Macrander and K. E. Strege, J. Appl. Phys. 59 (2), 442 (1986).
8. A. M. Thompson, IRE Trans. Instrum. 1-7, 245 (1958).
9. D. P. Belanger, P. Nordblad, A. R. King, V. Jaccarino, L. Lundgen and O. Beckman, J. Magn. Magn. Mater. 31-34, 1095 (1983).
10. J. C. LeGuillou and J. Zinn-Justin, Phys. Rev. B 21, 3976 (1980).
11. M. Barmatz, P. C. Hohenberg and A. Kornblit, Phys. Rev. B 12 1947 (1975).
12. M. Lui, A.R. King, V. Jaccarino, and G.L. Snider (submitted to Phys. Rev. B).

## X-RAY SCATTERING STUDIES OF THIN FILMS AND MULTILAYERS

G. S. CARGILL III

IBM Research Division, T. J. Watson Research Center, Yorktown Hts., NY 10598

### ABSTRACT

X-ray scattering experiments provide important information about the atomic scale structure and the microstructure of thin films and multilayers. The high intensity, brightness, and broad energy spectrum of synchrotron radiation greatly extend capabilities of scattering experiments, particularly for scattering from ultrathin films and for anomalous dispersion scattering from alloys. Examples of scattering studies of both crystalline and amorphous materials are given in this overview.

### INTRODUCTION

X-ray scattering has been used for atomic scale characterization of solids for more than seventy-five years. However, considerable progress has been made in the last ten years in applying x-ray scattering to ultrathin films and multilayers. In part this has resulted from increased scientific and technological interest in these types of materials, and the need for detailed structural characterizations. Also, progress has been aided by development of synchrotron and storage ring x-ray sources.

This paper gives overviews of several different x-ray scattering methods for characterizing thin films and multilayers. By necessity, the coverage is selective rather than comprehensive. Although all of the methods described are applicable to magnetic films and multilayers, the examples used to illustrate the methods involve materials which are not of particular magnetic interest.

In the next section, the basic features of x-ray scattering relevant to studies of thin films and multilayers are reviewed briefly [1]. In the following sections, x-ray scattering methods are described for characterizing the smoothness, thickness, and dimensional perfection of substrates, of single films on substrates, and of multilayers, using low angle, grazing incidence reflectivity measurements which are applicable to both amorphous and crystalline materials. Next, grazing incidence methods are described for characterizing epitaxy and in-plane structure and perfection of crystalline thin films. Large angle methods for characterizing out-of-plane structure and perfection for crystalline multilayers and thin films are then discussed. Anomalous dispersion techniques for characterizing short range order in amorphous alloys are described.

### FUNDAMENTALS OF X-RAY SCATTERING

X-rays used for structural studies have wavelengths  $\lambda$  of 0.5Å to 2Å, which correspond to photon energies of 25keV to 6keV. The absorption lengths  $\mu$  range from about 1 $\mu$ m to 1000 $\mu$ m, depending on the photon energy and on the density of the material being considered.

The fundamental features of x-ray scattering are illustrated in Fig. 1, where the direction of the incident plane wave x-ray beam is indicated by the vector  $\mathbf{k}_i$  and the direction in which the scattered intensity is being measured is given by the vector  $\mathbf{k}_f$ . Both  $\mathbf{k}_i$  and  $\mathbf{k}_f$  have magnitude  $2\pi/\lambda$ . X-rays are scattered by the electron density distribution within the material being studied,  $\rho_e(\mathbf{r})$ , and the scattered amplitude  $A(\mathbf{K})$  depends upon the scattering vector  $\mathbf{K} = \mathbf{k}_f - \mathbf{k}_i$  and the electron density distribution  $\rho_e(\mathbf{r})$ ,

$$A(\mathbf{K}) = \int \rho_e(\mathbf{r}) e^{i\mathbf{K} \cdot \mathbf{r}} d\mathbf{r} = \sum_j^N f_j(K) e^{i\mathbf{K} \cdot \mathbf{r}_j} \quad (1)$$

By expressing the electron density distribution in terms of atomic scattering factors  $f_j(K)$  for atoms located at positions  $\mathbf{r}_j$ , the scattered amplitude can be written as a sum over the  $N$  atoms of the scatterer, as in Eq. (1). The scattered intensity is given by the square of the magnitude of the scattered amplitude.

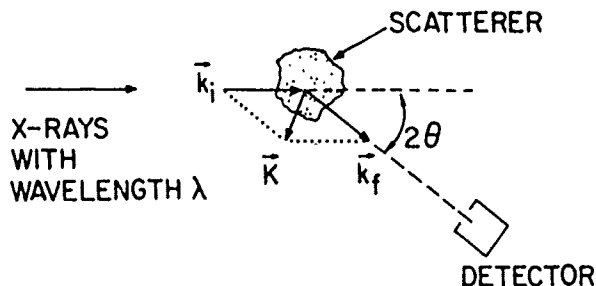


Fig. 1. Idealized scattering geometry.

If the scatterer has a periodic structure then the scattered intensity has Bragg maxima at positions  $\mathbf{K} = \mathbf{G}_{hkl}$ , where  $\mathbf{G}_{hkl}$  are reciprocal lattice vectors for the periodic structure. This corresponds to Bragg's law,

$$K = \frac{2\pi}{d_{hkl}} \quad \text{or} \quad \lambda = 2d_{hkl} \sin \Theta \quad (2)$$

For a d-spacing of  $1\text{\AA}$  and a wavelength of  $1\text{\AA}$ ,  $2\Theta = 60^\circ$ . For  $d = 100\text{\AA}$ ,  $2\Theta = 0.6^\circ$ .

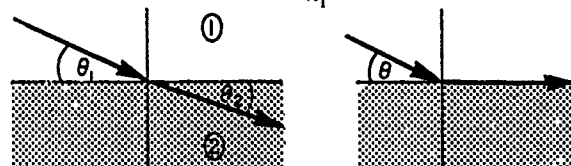
Atomic scattering factors for x-rays depend only on the magnitude of the scattering vector  $K$  except for photon energies near characteristic absorption energies for each element, where dispersion terms  $f'(K, E)$  and  $f''(K, E)$  become important. For example, the dispersion corrections for Ge near the Ge K absorption edge can change  $f(K, E)$  by as much as 10% from its value far from the absorption edge. This is the basis for the anomalous dispersion scattering technique for amorphous alloys, to be discussed later.

X-ray scattering also depends very weakly on local magnetic moments, spin and orbital. This is the basis for recent activities in magnetic x-ray scattering [2]. Since the magnetic scattering is typically  $10^6$  weaker than the charge scattering, these measurements are practical only in special cases.

The refractive index for x-rays incident on solids and liquids is less than one and depends mainly on the average electron density  $\rho_e$  of the solid or liquid,

$$n \approx 1 - \delta < 1 \text{ and } \delta \approx 2.7 \times 10^{-6} \rho_e \lambda^2 \approx 10^{-5} \dots 10^{-6}. \quad (3)$$

As illustrated in Fig. 2, total external reflection occurs for incident angles  $\Theta_1$  less than  $\Theta_c$ , the critical angle, given by

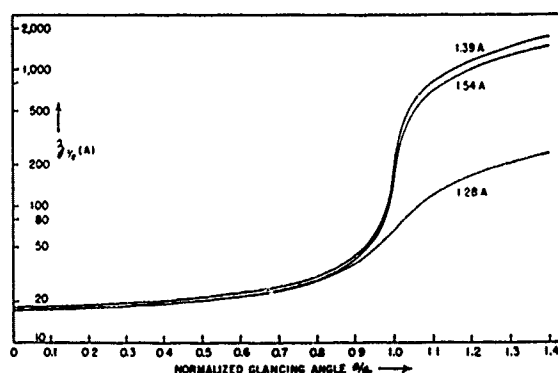
$$\cos \Theta_c = \frac{n_2}{n_1}. \quad (4)$$


$$n_2 \cos \Theta_2 = n_1 \cos \Theta_1 \quad \Theta_1 < \Theta_c \text{ (critical angle)}$$

Fig. 2. Refraction and total external reflection for x-rays.

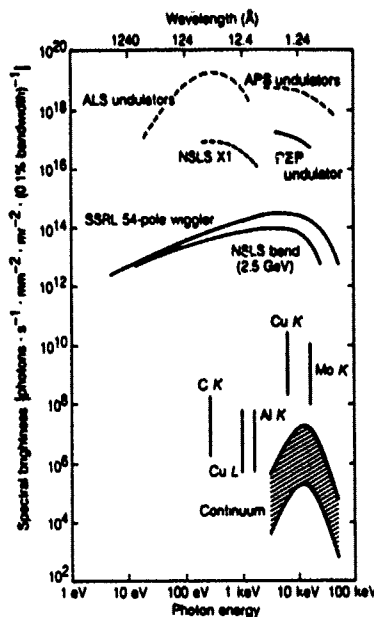
For  $\lambda = 1.54 \text{ \AA}$  ( $\text{CuK}\alpha$ ), critical angles for various solids and liquids range from  $0.2^\circ$  to  $0.6^\circ$ . Because of the total external reflection of x-rays incident at angles  $\Theta \leq \Theta_c$ , grazing incidence x-ray scattering is extremely sensitive to the very near surface region [3]. For example, penetration depths  $\zeta$  for x-rays incident on an ideal Cu surface with  $\Theta < \Theta_c$  are less than  $100 \text{ \AA}$ , as shown in Fig. 3.

Fig. 3. Penetration depths for a perfect copper surface for three different x-ray wavelengths (from Parratt, 1954).



Synchrotron radiation x-ray sources provide much greater brightness than conventional sealed tube or rotating anode x-ray sources [4]. This high brightness, which combines high intensity with tight collimation, is particularly important for grazing incidence studies which must extend to regions of very weak scattering. The broad energy spectrum available from synchrotron radiation sources is essential for anomalous dispersion scattering techniques. The orders of magnitude improvements in brightness for two existing synchrotron x-ray sources (SSRL and NSLS) over that for conventional x-ray sources can be seen from Fig. 4. Also shown are even higher brightnesses expected from the next generation of synchrotron sources.

Fig. 4. Spectral brightness for two existing synchrotron x-ray sources, solid lines; for several planned synchrotron x-ray sources, dashed lines; and for various conventional x-ray generators, vertical lines and cross-hatched region (from Kim, 1989).



#### SMOOTHNESS OF SUBSTRATES FROM SPECULAR REFLECTIVITY

Because of the short wavelength of x-rays, their reflectivity from a solid or liquid surface depends sensitively on the smoothness of that surface at the Angstrom level. For an ideally smooth surface, the specular reflectivity is given by the Fresnel equation [3]. Neglecting absorption, this ideal reflectivity

$$R_F(\Theta) = \frac{I_R\left(\frac{\Theta}{\Theta_c}, \delta\right)}{I_0} \quad (5)$$

depends on the index of refraction and on the incident angle normalized by the critical angle, Fig. 5. Note that the reflectivity measured for a polished glass surface falls below the ideal Fresnel reflectivity, since interface roughness reduces specular reflectivity. This can be expressed in terms of a roughness factor  $\Phi(\Theta)$ ,

$$R(\Theta) = R_F(\Theta) \Phi(\Theta) \quad (6)$$

and for  $R \ll 1$   $\Phi(\Theta)$  can be expressed in terms of the average electron density at different depths  $z$ ,

$$\Phi(\Theta) \sim \int \frac{d\rho(z)}{dz} e^{ik_z z} dz \quad (7)$$

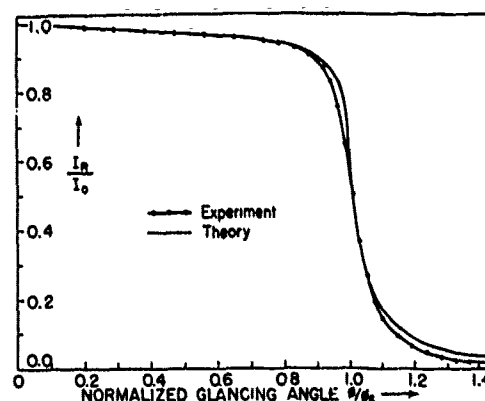
This can be simplified by assuming a Gaussian form for the surface roughness,

$$w(z) = \frac{d\rho(z)}{dz} = e^{-\frac{1}{2}\left(\frac{z}{\sigma}\right)^2} \quad (8)$$

as

$$\Phi(\Theta) = e^{-\frac{1}{2}\sigma^2 K^2} \quad (9)$$

Fig. 5. Reflectivity calculated from the Fresnel equation for an ideal glass surface and measured for a polished glass surface (from Parratt, 1954).



#### UNIFORMITY AND THICKNESS OF THIN FILMS FROM SPECULAR REFLECTIVITY

Grazing incidence reflectivity is also a sensitive probe of the uniformity and thickness of thin films on smooth substrates. Analysis of these measurements requires that reflections from both film-vacuum and film-substrate interfaces be included. Modelling of these reflectivity measurements are usually based on the Fresnel equation. Toney and Thompson [5] have made this type of measurements for amorphous carbon films on silicon substrates, as shown in Fig. 6(a). The normalized reflectivity is shown in Fig. 6(b), and the density versus thickness relation shown in Fig. 7 was obtained by fitting calculated and observed reflectivities shown in Fig. 6(b).

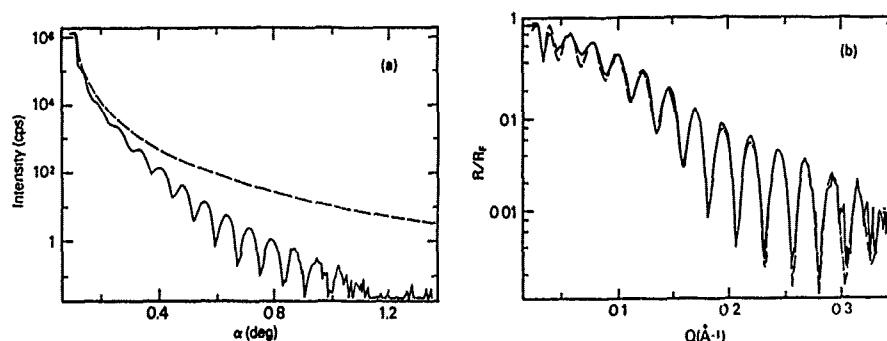
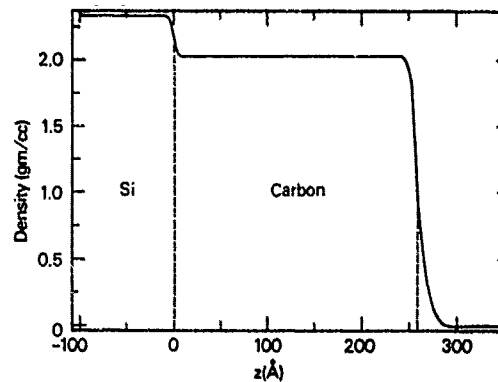


Fig. 6. (a) Reflectivity and (b) normalized reflectivity for an amorphous carbon film on a silicon substrate. The dashed line in (a) is the Fresnel reflectivity for an ideal Si surface. The dashed line in (b) is the normalized reflectivity calculated for the density distribution shown in Fig. 7. (From Toney and Thompson, 1989.)



Fig. 7. Density distribution deduced by fitting observed and calculated reflectivities shown in Fig. 6(b).



#### UNIFORMITY OF PERIODICITY AND SHARPNESS OF INTERFACES FOR MULTILAYERS FROM GRAZING INCIDENCE REFLECTIVITY

Grazing incidence reflectivity provides a sensitive measurement of periodicity and sharpness of interfaces for multilayers, whether the layers comprising the multilayer are amorphous or crystalline.

One type of information obtained from reflectivity measurements for periodic multilayers is the standard deviation SD of the actual thicknesses from the ideal thicknesses [6]. These thickness errors reduce reflectivities, especially for higher order superlattice Bragg peaks, and increase reflected intensity between these peaks. Another characteristic obtained from reflectivity measurements is the average boundary roughness, represented a roughness factor  $\exp(-\sigma^2 K^2/2)$  in the Gaussian approximation, with rms roughness  $\sigma$ . Examples of observed and calculated reflectivities for a ReW-C multilayer are shown in Fig. 8(a) and 8(b). The values determined for average layer thicknesses  $d$ , thickness variation SD, and roughnesses  $\sigma$  are listed in Fig. 8(b).

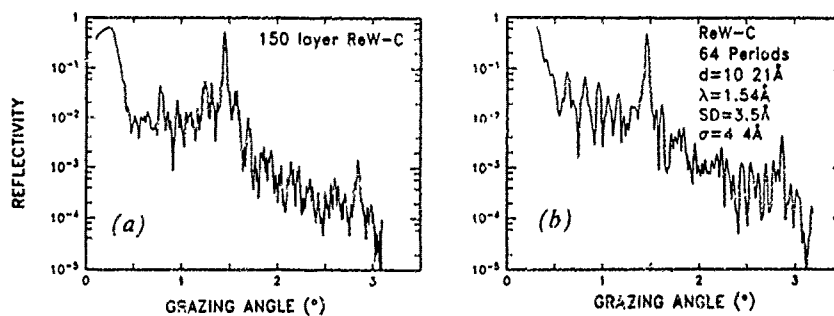


Fig. 8. Observed (a) and calculated (b) reflectivities for ReW-C multilayers. The fitting of observed and calculated reflectivities was used to determine the thickness error SD and roughness  $\sigma$  for the multilayer (from Spiller and Rosenbluth, 1986).

For reflectivities  $R \ll 1$ , kinematic theory can be used to analyze the reflectivity measurements from multilayers [1]. Expanding the periodic electron density as in

$$\rho_e(z) = \sum_{m=1}^{\infty} A_m \sin\left(\frac{2\pi m z}{p} + \phi_m\right) \quad (10)$$

it is clear that the reflectivity has intensity maxima at  $K_m = 2\pi m/p$  with  $I(K_m) \propto A_m^2$ .

### EPITAXIAL RELATIONSHIPS FROM GRAZING INCIDENCE LARGE ANGLE DIFFRACTION

Grazing incidence can also be used to maximize near-surface sensitivity in large angle scattering measurements, as illustrated in Fig. 9. A good demonstration of this surface sensitivity is provided measurements [7] shown in Fig. 10 for a film of tungsten, approximately  $18\text{\AA}$  thick, deposited on an  $\text{Al}_2\text{O}_3$  (1102) substrate. The  $W[001]$  direction makes an angle of approximately  $5^\circ$  with the  $\text{Al}_2\text{O}_3$  [1102] direction. Results of a  $\Theta - 2\Theta$  grazing incidence scan are shown. The  $W(110)$  peak position is shifted only very slightly from the  $2\Theta$  position expected for bulk  $W$ ; the resulting in-plane strain for the islands of this discontinuous  $W$  film is  $\epsilon_{\text{parallel}} = 0.6\%$ . Observation of the  $\text{Al}_2\text{O}_3$  (110) reflection with the same  $\omega$  orientation as the  $W(110)$  reflection confirms the alignment of  $W[110]$  parallel to  $\text{Al}_2\text{O}_3$  [1120]. Confirmation of the in-plane perfection is provided by  $\omega$ -scan results, which show a full width  $\Delta\omega = 1.2^\circ$  for  $W(110)$ .

Fig. 9. Orientations of incident and diffracted x-ray beams for grazing incidence large angle diffraction.

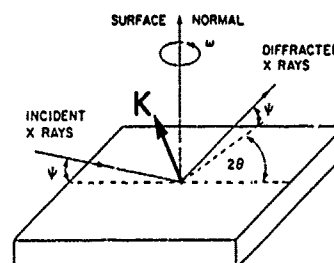
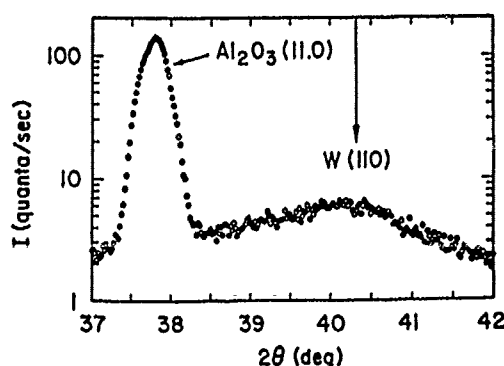


Fig. 10. A  $\Theta - 2\Theta$  grazing incidence scan for  $W$  on  $\text{Al}_2\text{O}_3$  (from Segmüller, 1987).



# OUT-OF-PLANE STRAIN AND PERFECTION FOR EPITAXIAL FILMS FROM LARGE ANGLE DIFFRACTION

Large angle diffraction, as illustrated in Fig. 11, can be used to characterize the out-of-plane strain and perfection for epitaxial films. As an example, consider the Si:As on Si (100) sample prepared by ion implantation and laser annealing [8] and described in the inset of Fig. 12.

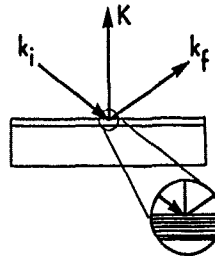


Fig. 11. Experimental arrangement for large angle diffraction to probe out-of-plane strain and perfection for epitaxial films.

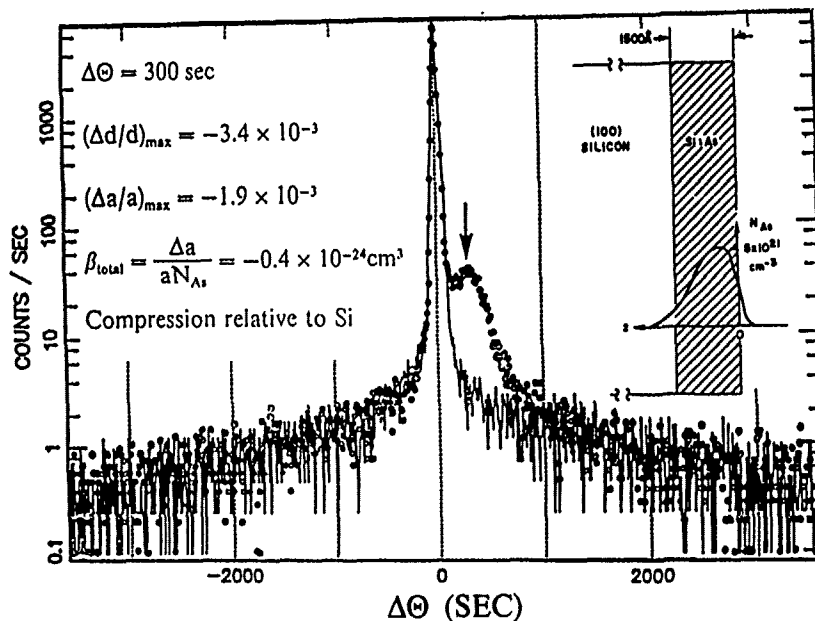


Fig. 12. X-ray rocking curve for as-laser-annealed Si:As sample. Inset: cross-section view of Si:As sample (from Cargill et al., 1988).

High resolution large angle diffraction was used to determine the lattice strain caused by incorporation of the As in the 1500 Å near surface region. The (400) rocking curve for this sample is shown in Fig. 12 (points), superimposed on the rocking curve for an undoped sample. The central maximum is the (400) reflection from the pure Si, and the smaller peak at  $\Delta\Theta \approx 300\text{sec}$  is the (400) reflection from the As-containing region. Because of the non-uniform As-concentration and the very strong substrate scattering, modelling with dynamical scattering calculations was used to determine the strain corresponding to the maximum As concentration,  $(\Delta d/d)_{\text{max}} = -3.4 \times 10^{-3}$ , which corresponds to the overlayer being slightly compressed relative to pure Si.

# INFORMATION ABOUT EPITAXIAL MULTILAYERS AND SUPERLATTICES FROM LARGE ANGLE DIFFRACTION MEASUREMENTS

Crystalline multilayers are characterized by periodic variation in both interplanar spacing  $\epsilon(z)$  and scattering power  $\Delta F(z)$  [9]. Consider the scattering arrangement shown in Fig. 13. The multilayer periodicity is  $p$ , the interplanar spacing in layers of type  $a$  is  $d_a$ , and the interplanar spacing in layers of type  $b$  is  $d_b$ . The combined periodicities cause intensity maxima as satellites at

$$\mathbf{K} = \mathbf{G}_{hkl} \pm \frac{2\pi m}{p} \hat{z} \quad (11)$$

in addition to the primary intensity maxima at the reciprocal lattice points for the average superlattice periodicity,  $\mathbf{K} = \mathbf{G}_{hkl}$ . For  $\mathbf{G}_{hkl} \neq 0$ , satellite intensities depend on both  $\epsilon_m$  and  $\Delta F_m$ .

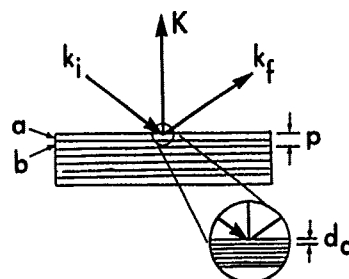
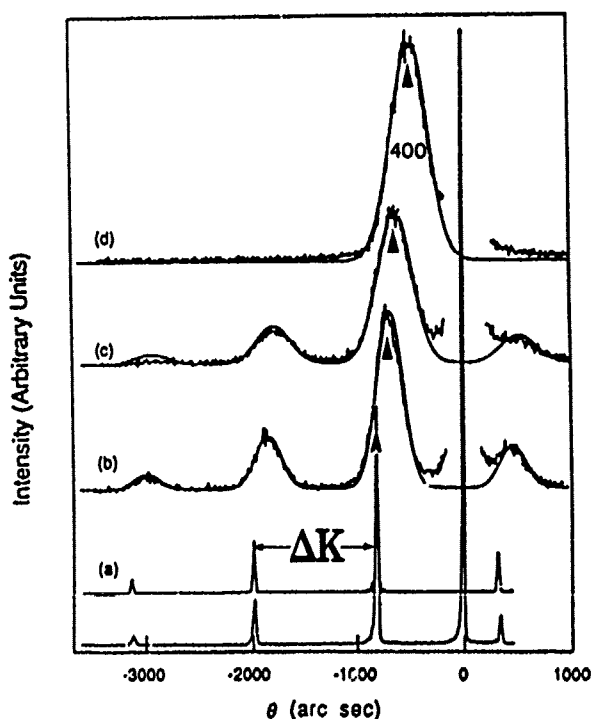


Fig. 13. Scattering arrangement for large angle diffraction measurements on epitaxial multilayers and superlattices.

Fig. 14. X-ray rocking curves for a  $\text{Si}/\text{Si}_{81}\text{Ge}_{19}$  superlattice as grown (a), and annealed at  $600^\circ\text{C}$  (b),  $800^\circ\text{C}$  (c), and  $900^\circ\text{C}$  (d) (from Houghton et al., 1989).



An example of large angle diffraction from an epitaxial superlattice is shown in Fig. 14, for a  $\text{Si}/\text{Si}_{11}\text{Ge}_{19}$  superlattice on Si (100), in both as-grown and annealed conditions [10]. The superlattice (400) reflection is displaced from the Si (400) reflection because of the larger average (400) interplanar spacing for the superlattice. Annealing caused broadening of the superlattice maxima because of strains and loss of coherency resulting from misfit dislocations. This also caused shift of the (400) superlattice reflection, but the satellite spacing  $\Delta K = 2\pi/p$  remained unchanged. The decrease in satellite intensities for higher annealing temperatures is caused by decrease of  $\Delta F(z)$  resulting from interdiffusion.

### SHORT RANGE ORDER IN AMORPHOUS ALLOYS FROM X-RAY SCATTERING

Radial distribution functions  $4\pi r^2\rho(r)$  are used to describe correlations between atomic positions in liquids and in amorphous solids [1]. For amorphous alloys with more than one kind of atom, partial distribution functions  $\rho_{ij}(r)$  describe correlations between atomic positions for atoms of type  $i$  with respect to atoms of type  $j$ . However, only composite distribution functions

$$\rho(r) = \sum_{i,j} W_{ij} \rho_{ij}(r) / c_j \quad (12)$$

can be obtained from conventional x-ray scattering measurements for amorphous alloys. The weighting factors  $W_{ij}$  depend on the alloy composition  $c_i$  and on the scattering factors  $f_i(K)$ . An example is shown in Fig. 15 for liquid  $\text{GeBr}_4$  [11], for which

$$RDF(r) = 4\pi r^2\rho(r) = 4\pi r^2[0.147\rho_{\text{Ge-Ge}}(r) + 0.355\rho_{\text{Ge-Br}}(r) + 0.858\rho_{\text{Br-Br}}(r)]. \quad (13)$$

Without further information, it is not possible to determine whether the two prominent maxima in Fig. 15 correspond to Ge-Ge, Ge-Br, or Br-Br correlations, or to a mixture of these. However, by using synchrotron radiation to make scattering measurements with three different photon energies -- near the Ge K absorption edge, near the Br K absorption edge, and well away from both of these edges -- and by exploiting dispersion corrections to  $f_i(k, E)$  it is possible to calculate *differential distribution functions* which describe the correlations which involve only Ge-Ge and Ge-Br correlations,

$$4\pi r^2\rho_{\text{Ge}}(r) = 4\pi r^2[0.808\rho_{\text{Ge-Ge}}(r) + 1.05\rho_{\text{Ge-Br}}(r)] \quad (14)$$

and which involve only Br-Br and Br-Ge correlations,

$$4\pi r^2\rho_{\text{Br}}(r) = 4\pi r^2[0.984\rho_{\text{Br-Br}}(r) + 1.06\rho_{\text{Br-Ge}}(r)]. \quad (15)$$

These are shown in Fig. 16, from which it is seen that the first maximum involves both Ge and Br, but that the second maximum involves only correlations between Br atoms.

With the high brightness and energy selectivity of synchrotron x-ray sources, measurements of differential distribution functions are now possible for amorphous thin films [12]. In principle, scattering measurements of this type can also be used to determine the individual partial distribution functions  $\rho_{ij}(r)$ , but in this case the results are extremely sensitive to accumulated measurement errors.

## CONCLUSIONS

X-ray scattering can provide important structural information about thin films and multilayers, as illustrated by the methods described in this overview. However, these techniques do not provide real space images like those which can be obtained from transmission electron microscopy or scanning tunneling microscopy. Complete characterization of thin films and multilayers usually requires combinations of x-ray scattering and microscopy, together with other complementary techniques, such as Rutherford backscattering spectroscopy and channeling, EXAFS, and in-situ techniques such as LEED and RHEED.

Fig. 15. Total radial distribution function  $RDF(r) = 4\pi r^2 \rho(r)$  for liquid  $\text{GeBr}_4$  (from Ludwig et al., 1987).

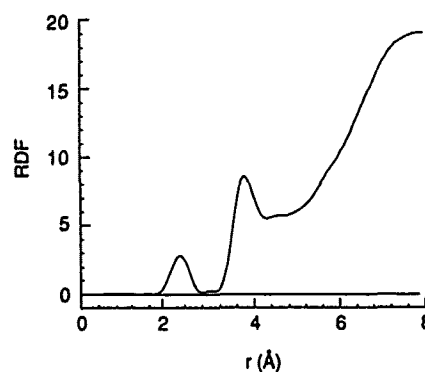
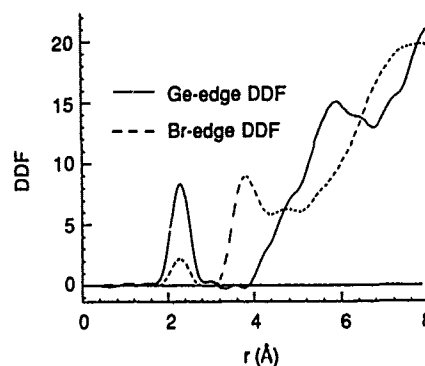


Fig. 16. Differential distribution functions  $\rho_{\text{Ge}}(r)$  and  $\rho_{\text{Br}}(r)$  for liquid  $\text{GeBr}_4$  (from Ludwig et al., 1987).



## ACKNOWLEDGEMENTS

I am grateful for assistance from Karen Kavanagh, Armin Segmüller, and Carol Thompson with different parts of this review. Also, I thank them and others for permission to reproduce figures and other results in this review.

## REFERENCES

1. A. Guinier, *X-Ray Diffraction*, W. H. Freeman and Co., San Francisco, 1963.
2. D. Gibbs, D. R. Harshman, E. D. Isaacs, D. B. McWhan, D. Mills, and C. Vetter, *Phys. Rev. Letters* **61**, 1241 (1988).
3. L. G. Parratt, *Phys. Rev.* **95**, 359 (1954).
4. K.-J. Kim, in *Physics of Particle Accelerators*, AIP Conf. Proc. **184**, M. Month and M. Dienes, eds., American Institute of Physics, New York, 1989, p. 565.
5. M. F. Toney and C. Thompson, "X-ray Reflectivity of Perfluoropolyether Polymer Molecules on Amorphous Carbon," to be published. See also, A. Segmüller, *Thin Solid Films* **18**, 287 (1973).
6. E. Spiller and A. E. Rosenbluth, *Opt. Eng.* **25**, 954 (1986). See also, A. M. Kadin and J. E. Keem, *Scripta Met.* **20**, 445 (1986).
7. A. Segmüller, *MRS Symp. Proc.* **77**, 151 (1987). See also, W. C. Marra, P. Eisenberger, and A. Y. Cho, *J. Appl. Phys.* **50**, 6927 (1979).
8. G. S. Cargill III, J. Angilello, and K. L. Kavanagh, *Phys. Rev. Letters* **61**, 1748 (1988).
9. R. M. Fleming, D. B. McWhan, A. C. Gossard, W. Wiegmann, and R. A. Logan, *J. Appl. Phys.* **51**, 357 (1980); D. B. McWhan, in *Synthetic Modulated Structures*, L. L. Chang and B. C. Giessen, eds., Academic Press, Orlando, 1985, p. 43.
10. D. C. Houghton, J.-M. Baribeau, K. Song, and D. D. Perovic, *MRS Symp. Proc.* **130**, 159 (1989).
11. K. F. Ludwig Jr., W. K. Warburton, L. Wilson, and A. I. Bienenstock, *J. Chem. Phys.* **87**, 604 (1987).
12. J. B. Kortright and A. Bienenstock, *Phys. Rev. B* **31**, 2979 (1988); P. H. Fuoss, P. Eisenberger, W. K. Warburton, and A. Bienenstock, *Phys. Rev. Letters* **46**, 1537 (1981).

## FERROMAGNETIC AND NUCLEAR MAGNETIC RESONANCE STUDY OF Co/Pd MULTILAYERS.

H. A. M. DE GRONCKEL, C. H. W. SWUSTE, K. KÖPINGA, W. J. M. DE JONGE,  
Department of Physics, Eindhoven University of Technology, PO Box 513,  
5600 MB Eindhoven, The Netherlands.

### ABSTRACT

The microscopic properties of Co/Pd multilayers were studied by ferromagnetic and nuclear magnetic resonance. In addition to previous results the magnetic anisotropy is found to be also a function of the Pd layer thickness, increasing below 20 Å for decreasing thickness. This is ascribed to a decrease in the Pd/Co interface contribution to the anisotropy.

Hyperfine field spectra show a shift to lower hyperfine fields upon decreasing Co sublayer thickness. This is attributed to an expansion of the Co 'lattice'. Comparison of the results on the [111] multilayers with those on almost single phased [100] multilayers suggests that this expansion is nearly isotropic.

### Introduction.

The development and research on magnetic multilayers received considerable attention in recent years since they exhibit properties which are of interest both from a theoretical and a technological point of view [1-3]. In this aspect we specifically mention the influence of the interface between the magnetic and non-magnetic metal, leading to changes in magnetic moment and crystal anisotropy [3-8].

One of the systems exhibiting such new effects is the Co/Pd multilayer [6,7]. Magnetization and torque measurements showed that the preferential direction of the magnetization changes from in-plane to perpendicular to the plane below a Co sublayer thickness of about 8 Å [6,7,11]. Since, however, these macroscopic techniques probe the overall contribution to the magnetization whereas the change in anisotropy has been attributed to the reduced symmetry at the interface, which is on a microscopic scale, we thought it worthwhile to perform a series of ferromagnetic resonance (FMR) and nuclear magnetic resonance (NMR) experiments probing, respectively, the local behavior of the magnetic moments and their local environment.

### Experimental techniques.

The samples were prepared at the Philips Research Laboratories in UHV by e-beam evaporation of Co and Pd after subsequent deposition of a 100 Å Ti and 100 Å Pd base layer on a rotating glass substrate (12×4×0.3 mm<sup>3</sup>) at room temperature. The thickness of the samples was about 3000 Å. After preparation the layers were characterized by X-ray and TEM. This showed them to be polycrystalline FCC with [111] texture [3].

In the NMR experiments also samples have been used which were initially grown on a NaCl substrate in the same way as described above. Their thickness amounted to about 1200 Å. X-ray characterization revealed that these samples were almost perfectly single phased [100] FCC [9]. For practical reasons these multilayers were glued onto Si substrates and the NaCl was dissolved before experimenting.

The FMR experiments were performed at room temperature in fields up to 1 T at frequencies of 9.5 GHz and 20 GHz. When necessary with regard to sensitivity, some of the samples were mounted in a cavity.

The NMR spin echo experiments were performed with a home made incoherent NMR



spectrometer in the frequency range 170 MHz to 240 MHz and at temperatures of 4.2 K and 1.4 K. By using a superconducting split pair magnet, fields up to 6 T could be applied both parallel and perpendicular to the film plane. In order to avoid the effect of, for instance, domain wall enhancement on the shape of the spectra the NMR frequency was, if possible, chosen such that the spectra could be recorded at fields larger than 1.8 T (the saturation field).

### FMR, results and interpretation.

Interpretation of the data is based on conventional theory [10]. Since the data concerning the dependence of the anisotropy on the Co thickness have already been treated extensively [7,8,11], we will confine ourselves here to the question of magnetic coupling between the Co layers. Light-scattering experiments by Grünberg showed that for multilayers with a Pd layer thickness of 27 Å and less an isotropic exchange coupling between the Co layers exists [12]. In FMR experiments such a coupling may manifest itself in the occurrence of extra (spinwave) modes in addition to the uniform mode. It therefore seemed very interesting to search for these extra modes and to study their dependence on the Pd thickness. However, although such modes have been observed in the case of, e.g., Co/Ni multilayers [8], they were not observed in the present materials. What has been found is a dependence on the Pd layer thickness of the anisotropy field  $B_a$ , defined by  $B_a = -2K_{\text{eff}}/M_s$ , as

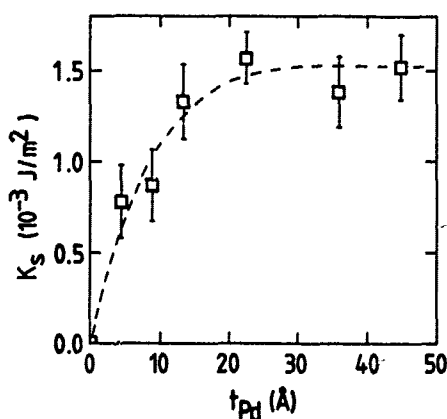


Fig. 2. Surface anisotropy  $K_s$  as function of the Pd thickness  $t_{\text{Pd}}$  for Co/Pd/Co sandwiches with 100 Å Co sublayer thickness.

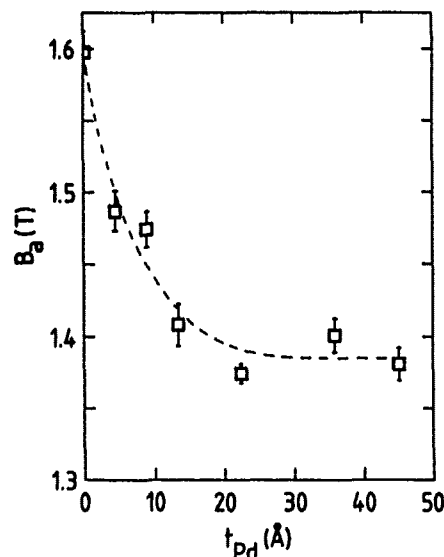


Fig. 1. Anisotropy field  $B_a$  (see text) as function of the Pd thickness  $t_{\text{Pd}}$  for Co/Pd/Co sandwiches with 100 Å Co sublayer thickness.

shown in figure 1. There is an evident increase in the anisotropy field  $B_a$  towards the value for bulk Co below a Pd layer thickness of approximately 20 Å. The deviation of  $B_a$  at  $t_{\text{Pd}} = 0$  from the bulk value ( $B_a = 1.75$  T) is due to the non negligible anisotropy contribution of the Co surfaces at the sample boundaries. For constant Pd thickness the anisotropy can be described in terms of volume- and surface contributions  $K_v$  and  $K_s$ , respectively, by the phenomenological relation [5,11]

$$t_{\text{Co}} K_{\text{eff}} = t_{\text{Co}} K_v + 2K_s \quad (1)$$

Since in the limit of zero Pd thickness no interface contribution to the anisotropy should be left, one is tempted to believe that the systematic increase of  $B_a$  with decreasing Pd thickness is due to a de-

crease of the anisotropy contribution of the Co/Pd interface. Calculating the interface contribution  $K_s$  from the difference in anisotropy field,  $B_a(0) - B_a(t_{Pd})$ , leads to the results shown in figure 2. This figure reveals that, as one would expect, the interface contribution steeply increases from zero at zero Pd thickness, reaching a constant value of approximately  $1.5 \times 10^{-3} \text{ J/m}^2$  above a Pd thickness of about 20 Å. The latter value is in reasonable agreement with the previously published results [7,8].

Since  $K_s$  is thought to arise from reduced symmetry at the interface, the decrease of  $K_s$  when the distance between the different Co layers is reduced to zero may be explained by the restoration of high local symmetry of the Co ions. A second possible cause is the existence of pinholes in the Pd layer, i.e., the Pd layer is not perfect but is penetrated by small Co 'bridges', thus leading to a lowering of the average surface anisotropy. Since the probability for the existence of pinholes increases for thinner Pd thicknesses, this leads to a decrease of the surface contribution to the total anisotropy. The latter assumption is supported by the somewhat irregular structure of the data in figures 1 and 2, as the formation of the pinholes is a random process and therefore differs from sample to sample.

#### NMR, results and interpretation.

Interpretation of the NMR spectra is based on the fact that for an in-plane applied magnetic field the hyperfine field  $B_{hf}$  can be inferred from the well known relation

$$f = \gamma |B_{hf} - B_{ex}|. \quad (2)$$

Here  $\gamma$  represents the gyromagnetic ratio of the nucleus under study ( $\gamma = 10.054 \text{ MHz/T}$  for Co),  $f$  is the resonance frequency and  $B_{ex}$  denotes the external magnetic field. A typical set of data collected with the magnetic field parallel to the film-plane is shown in figure 3. This figure reveals that for the thicker Co layers ( $t_{Co} \geq 20 \text{ Å}$ ) the spin echo intensity is concentrated in the hyperfine field region between about 21.3 T and 23 T and shows a rather pronounced structure, while for the multilayers with small Co sublayer thickness the spectra are concentrated below a hyperfine field  $B_{hf}$  of 22 T, they are broadened with respect to the spectra of the thicker layers and do not show any pronounced structure. For the latter multilayers the center of these spectra also show a tendency to shift to lower hyperfine fields with decreasing Co thickness.

Detailed analysis of the spectra of the thicker layers reveals that they consist of a pure FCC phase at  $B_{hf} = 21.7 \text{ T}$  as well as contributions due to HCP-like stacking faults in a FCC structure at  $B_{hf} = 22.4 \text{ T}$  and a polycrystalline phase at  $B_{hf} = 22.0 \text{ T}$  [13]. These contributions are denoted by the dotted curves in figure 3. For the multilayers with  $t_{Co} \leq 20 \text{ Å}$  the distinct phases seem to have disappeared completely. The spectra are not only broadened but the main contribution to the spectra is now situated at lower hyperfine fields (about 20 T to 21 T). These results can only be understood in terms of changes in the structure of the multilayers for decreasing Co sublayer thickness.

Addressing the origin of this change in structure we recall that for bulk FCC Co under pressure, i.e., for compression of the lattice, the hyperfine field shifts to higher values [15,16]. Since the lattice constant of FCC Pd is 9.1 % larger than that of FCC Co, we believe that in the case of these multilayers the observed shift to lower hyperfine fields is due to an expansion of the Co 'lattice' because the Co layers neighboring the Pd are forced to adapt to the less dense Pd structure. In the case of very thin Co layers this implies a deformation of the complete layer. If the thickness of the Co layer is increased the effect on the interior of the layers decreases and this is reflected in the development of signals at higher hyperfine fields and restoration of the bulk structure of the spectrum. The influence of the lattice mismatch on the structure even extends to sublayers with up to 20 atomic layers of Co as is revealed by the shift in hyperfine field of the 41 Å multilayer spectrum.

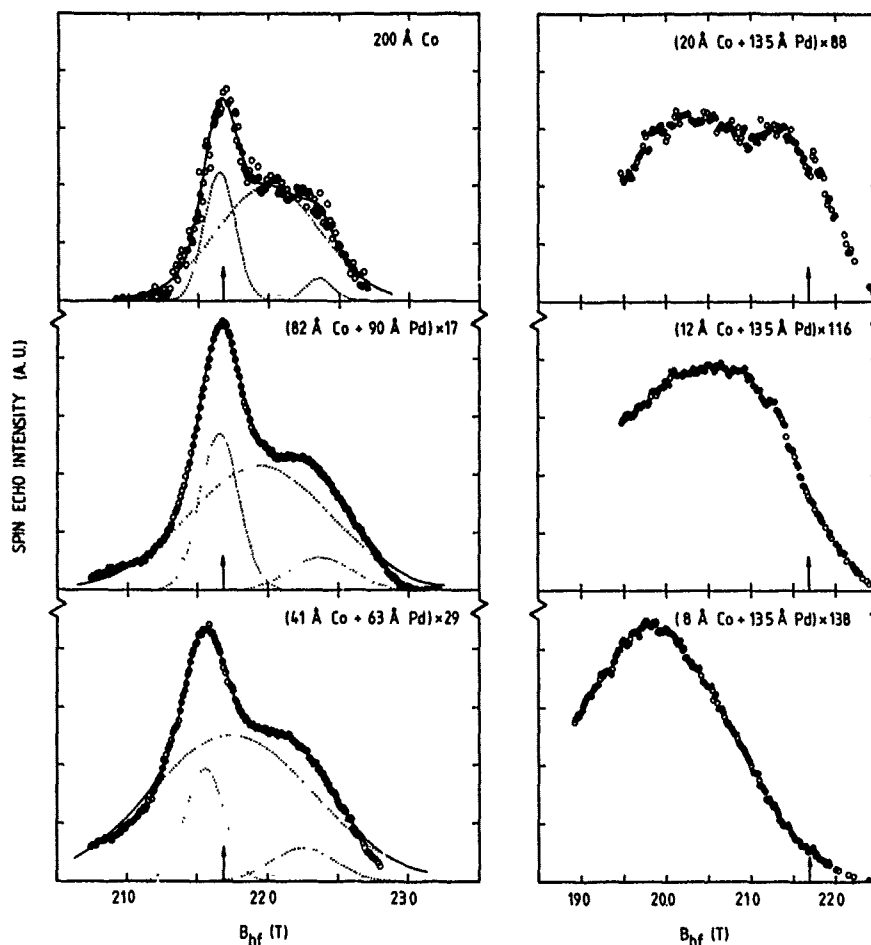


Fig. 3. Hyperfine field distribution of Co single layer and Co/Pd multilayers with [111] texture as recorded by means of magnetic field sweeps at fixed frequencies. The circles denote the data. The solid lines represent the results of fits using a superposition of simple Gaussian curves, the dotted curves show the composing Gaussian lines as found by these fits. The arrows denote the value of the hyperfine field in pure FCC Co. The three spectra on the left hand side are recorded at a frequency of 195 MHz, those on the right hand side at 180 MHz. The spectra of the multilayers with a characteristic Co thickness of 12 Å and 8 Å were recorded at a temperature of 1.4 K, the others at 4.2 K.

The mechanism through which the expansion influences the hyperfine field is not completely clear. However, the experiments of Riedi [14] on BCC Co show that on going from a closed packed structure as FCC Co to a less compact structure like BCC Co, both magnetic moment and hyperfine field decrease but the ratio between magnetic moment and hyperfine field remains about the same. This indicates that the decrease of the hyperfine field is due to a decrease of the magnetic moment.

In order to obtain more information we also performed experiments on FCC Co/Pd multilayers with the [100] direction normal to the film-plane. Some typical results are shown in figure 4.

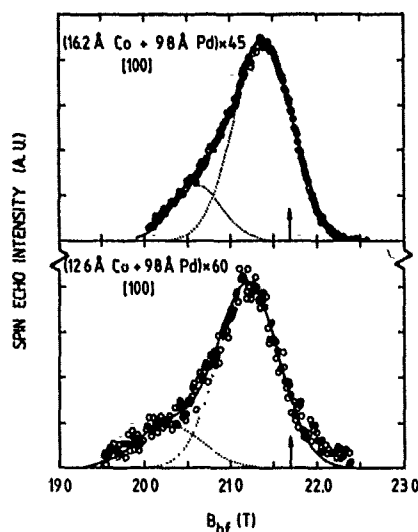


Fig. 4. Hyperfine field distribution of Co/Pd multilayers with [100] texture as recorded by means of magnetic field sweeps at fixed frequencies. The circles denote the data. The solid curves represent the results of fits using a superposition of simple Gaussian curves, the dotted curves show the composing Gaussian lines as found by these fits. The arrows denote the value of the hyperfine field in pure FCC Co. The spectra are recorded at a frequency of 185 MHz and at a temperature of 1.4 K.

The single phase character of these layers is reflected by the occurrence of one resonance line accounting for the major part of the intensity. Also in this case of well defined layers, a shift to lower hyperfine fields away from the bulk FCC value, is clearly visible. Table 1 summarizes the observed shifts of the FCC line. The behavior of the [111] layers and the [100] layers differs only slightly, indicating that the decrease in hyperfine field is due to a nearly isotropic expansion. From the data in this table one can also see that for thin Co sublayers field sweeps are less reliable than frequency scans. The reason for this is not yet clear.

Table 1. Shift  $\Delta B_{hf}$  of the FCC hyperfine field with respect to the bulk value. The shifts denoted by  $\Delta B_{hf}^*$  are obtained from frequency scans instead of field sweeps. The errors in the hyperfine field shift are obtained by comparison of the results at different frequencies or, in the case of frequency scans, at different fields.

[111] Co/Pd multilayers			[100] Co/Pd multilayers		
$t_{Co}(\text{\AA})$	$\Delta B_{hf}(\text{\AA})$	$\Delta B_{hf}^*(T)$	$t_{Co}(\text{\AA})$	$\Delta B_{hf}(T)$	$\Delta B_{hf}^*(T)$
8.2	$-2.1 \pm 0.5$	$-0.51 \pm 0.1$	9.0	$-1.2 \pm 0.7$	$-0.36 \pm 0.1$
12.3	$-1.1 \pm 0.5$		12.6	$-0.45 \pm 0.15$	
20.5	$-0.2 \pm 0.1$		16.2	$-0.26 \pm 0.04$	
41	$-0.1 \pm 0.05$				
82	$0.02 \pm 0.03$				
200	0	$0 \pm 0.05$			

### Conclusions.

In conclusion, the FMR study on Co/Pd multilayers showed the surface anisotropy to decrease with reduction of the Pd thickness below 20 Å. This is very likely due to irregularities at the interface, which become more dominant for small Pd thicknesses. In

contrast to the reported light scattering experiments no evidence of a magnetic coupling between the Co layers is observed.

The NMR experiments show that the [111] multilayers are composed of different phases, the dominant one being polycrystalline. The change in the hyperfine field spectrum on decreasing thickness of the Co sublayers is believed to result from a decrease of the magnetic moment, caused by expansion of the Co "lattice" due to the lattice mismatch with Pd. We would like to emphasize that this supports the view that for thin Co sublayers the increase of the average magnetic moment per Co atom observed in the magnetization experiments [3] is not due to an enhancement of the Co magnetic moment, but to a polarization of Pd atoms neighbouring Co. Of course, a determination of the Pd hyperfine field distribution would be valuable to complete this physical picture.

We also feel that the observed expansion of the Co sublayers may be important in explaining the behavior of the anisotropy in these multilayers.

The strong similarity between the results on [111] and [100] multilayers indicates that the expansion of the Co lattice is nearly isotropic. A detailed analysis of the angular variation of the hyperfine field is being performed at the moment to consolidate this picture.

#### Acknowledgements.

We gratefully acknowledge the cooperation with Philips Research Laboratories which, among others, provided the samples and F. J. A. den Broeder for his continuous interest and stimulating discussions on this subject.

#### References

1. A. S. Arrot, B. Heinrich, S. T. Purcell, J. F. Cochran, K. B. Urquhart, *J. Appl. Phys.* **61**, 3721 (1987).
2. L. L. Hinchey, D. L. Mills, *J. Appl. Phys.* **57**, 3687 (1985).
3. F. J. A. den Broeder, H. J. Donkersloot, H. J. G. Draaisma, W. J. M. de Jonge, *J. Appl. Phys.* **61**, 4317 (1987).
4. G. Bayreuther, *J. Magn. Magn. Mater.* **38**, 273 (1983).
5. U. Gradmann, *J. Magn. Magn. Mater.* **54-57**, 723 (1986).
6. P. F. Garcia, A. D. Meinhaldt, A. Suna, *Appl. Phys. Lett.* **47**, 178 (1985).
7. H. J. G. Draaisma, F. J. A. den Broeder, W. J. M. de Jonge, *J. Magn. Magn. Mater.* **66**, 351 (1987); H. J. G. Draaisma, W. J. M. de Jonge, *J. Appl. Phys.* **62**, 3318 (1987).
8. C. H. W. Swüste, H. J. G. Draaisma, W. J. M. de Jonge, *Proc. Int. Conf. on Magnetism*, Paris, 1988, to be published.
9. F. J. A. den Broeder, D. Kuiper, H. C. Donkersloot, W. Hoving, to be published in *J. Appl. Phys.*
10. J. Smit, H. G. Beljers, *Philips Res. Rep.* **10**, 113 (1955).
11. H. J. G. Draaisma, W. J. M. de Jonge, *J. Appl. Phys.*, **64**, 3610 (1988); H. J. G. Draaisma, W. J. M. de Jonge, F. J. A. den Broeder, to be published.
12. P. Grünberg, KFA Jülich, F. R. G., private communication.
13. H. A. M. de Gronckel, J. A. W. Derks, K. Kopinga, W. J. M. de Jonge, *Proc. of the Conf. on Nuclear Methods in Magnetism*, Munich, 1988 (to be published in *Hyp. Int.*).
14. P. C. Riedi, T. Dumelow, M. Rubinstein, G. A. Prinz, S. B. Qadri, *Phys. Rev.* **B36**, 4595 (1987).
15. R. V. Jones, I. P. Kaminov, *Bull. Am. Phys. Soc.* **5**, 175 (1960).
16. A. M. Bessmertnyi, E. S. Mushailov, *Sov. Phys. Solid State* **20**, 1651 (1978).

## EXAFS STUDY OF THE STABILITY OF AMORPHOUS TbFe THIN FILMS

Mahesh G. Samant, Ernesto E. Marinero, Clifford Robinson<sup>†</sup>, and G. S. Cargill III<sup>††</sup>  
IBM Research Division, Almaden Research Center, 650 Harry Road, San Jose, CA  
95120-6099.

<sup>†</sup> Raytheon Corporation, Research Division, 131 Spring St, Lexington, MA 02173.

<sup>††</sup> IBM Research Division, T. J. Watson Research Center, Yorktown Heights, NY 10598.

### Abstract

EXAFS is used to measure the local atomic structure of Fe in Au doped Tb-Fe thin film alloys. The as deposited sample shows structural features which are essentially identical to those of the undoped films. Au additions stabilizes the amorphous structure against recrystallization, however, the loss of magnetic anisotropy under thermal annealing is not reduced. This demonstrates that magnetic relaxation in these alloys does not involve crystallization of the amorphous structure.

### Introduction

Recently we used Extended X-ray Absorption Fine-structure Spectroscopy (EXAFS) to characterize the structure and to study annealing induced structural changes in  $Tb_{20}Fe_{80}$  amorphous films [1]. The key aim was to correlate these changes to magnetic relaxation and obtain a better understanding of the origins of the magnetic anisotropy in these films. Three samples were studied: as deposited (AD), 200°C annealed for 20h (LT), and 400°C annealed for 2h (HT). Analysis of the EXAFS data (Figure 1) for the AD sample revealed that the Tb local environment consists of Tb-Fe clusters with a wide distribution of interatomic distances. This is a consequence of an atomically strained environment around Tb and this contributes to the perpendicular anisotropy of the sample. Evidence for relaxation of this atomic order as a consequence of thermal annealing was also presented. Both the AD and LT samples exhibited perpendicular magnetic anisotropy and were amorphous. Yet, the LT anneal caused a reduction in coercivity by causing the structural anisotropy around the Tb atoms to randomize. The HT sample which possessed in-plane magnetization showed Fe microcrystallites and XPS analysis revealed Tb as  $Tb_xN_y$ . Thus the question remained whether the total loss in magnetic anisotropy was accompanied by a complete transformation of the amorphous structure to the microcrystalline structure? We wish to address this question here.

The approach chosen involved addition of a third row transition element such as Au to these amorphous alloys. The presence of Au whose size is intermediate between that of Fe and Tb is expected to hinder the recrystallization of TbFe alloys. Thus, it should in principle be possible to induce more extensive magnetic relaxation in TbFe by utilizing higher annealing temperatures and delay further the onset of recrystallization. In order to probe the local environment of Fe, EXAFS was employed since it provides element specific structural information on the local environment of the absorbing atom [2].

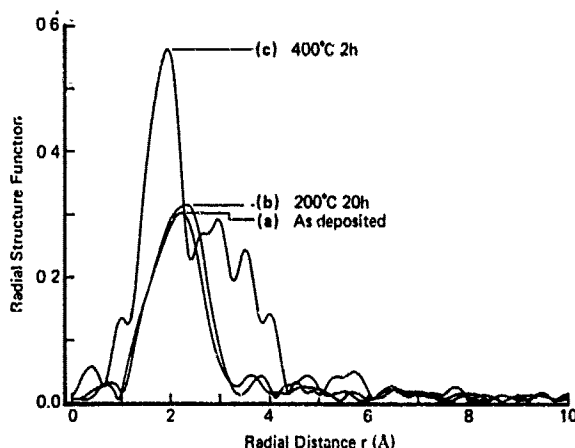


Figure 1. Radial structure functions obtained from Tb  $L_{III}$  edge data for TbFe samples (AD), as-deposited; (LT), 200°C 20h annealed; and (IT) 400°C 2h annealed.

### Experimental

The thin amorphous Au-TbFe alloy films ( $Au_{75}Tb_{18}Fe_{75}$ ) with a thickness of 1000 Å supported on a quartz substrate were prepared by co-sputtering. These alloy films were sandwiched between layers of 750 Å of  $Si_3N_4$  prior to exposure to air. The  $Si_3N_4$  layers functioned as protective barriers against oxidation by atmospheric oxygen during the subsequent annealing treatments. Three samples were prepared: as deposited (AD), annealed at 200°C for 20 h (LT), and annealed at 400°C for 20h (IT).

The EXAFS measurements were made at the Cornell High Energy Synchrotron Source (CHESS) on beamline C-1. A Ge (111) double crystal was used as a monochromator. The incident x-ray intensity was monitored by an ion chamber. The x-ray beam illuminated about 20 mm x 1 mm area of the sample with the beam incident along the sample normal. The EXAFS signal was detected by measuring the total electron yield from the sample as a function of the x-ray energy near the Fe K edge (7111 eV). At these x-ray energies the penetration depth of the electrons contributing to the total electron yield is more than 1000 Å [3]. Thus, results obtained are representative of the entire thickness of the sample. The close proximity of Fe and Tb edges limited the EXAFS range for the Fe K edge data to  $k < 10 \text{ Å}^{-1}$ . The phase shift and back scattering amplitude functions evaluated from Ni foil EXAFS data were used to obtain the structural parameters from the Fe K edge data.

### Results

Figure 2 shows the radial structure functions (RSFs) obtained by Fourier transforming the  $k^2$  weighted EXAFS function  $\chi(k)$ , at the Fe K edge for all the three samples. The RSFs for all samples appear to be identical and exhibit a single peak. In the case of the AD sample, this peak could be adequately fitted to a single Gaussian distribution of Fe neighbors centered at  $2.50 \pm 0.02 \text{ Å}$  (in bulk iron the near neighbor distance is  $2.46 \text{ Å}$ ) with a coordination number of  $8 \pm 0.8$  and a Debye-Waller type factor of  $0.01 \text{ Å}^2$ . No significant improvement in the fit to the experimental EXAFS could be obtained by inclusion of the back scattering contributions from Tb which is indicative of a broad distribution

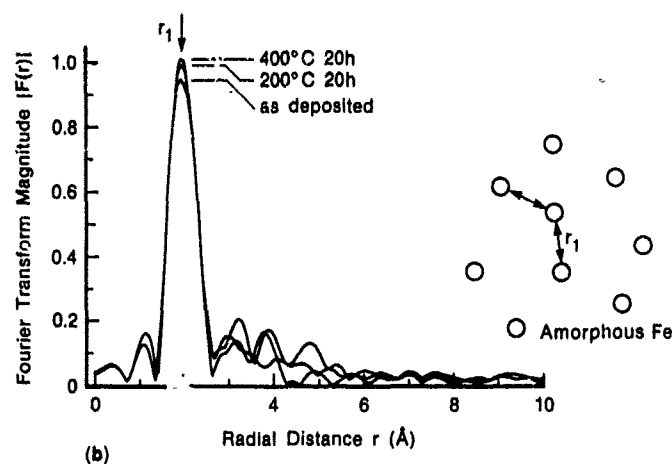


Figure 2. Radial structure functions obtained from Fe K edge data for Au-TbFe samples (AD), as-deposited; (LT), 200C 20h annealed; and (HT) 400C 20h annealed.

of Fe-Tb distances. The presence of Au in fairly low concentration meant a negligible back scattering contribution from Au to Fe EXAFS and this was confirmed by the EXAFS data analysis.

A slight sharpening of the near neighbor peak with annealing is observed in the RSFs shown in Fig. 1. This represents an increase in the coordination numbers for the annealed samples, however they lie well within the indicated error bars to those obtained for the AD sample.

### Discussion and Conclusions

These EXAFS results as well as those obtained earlier on  $Tb_{20}Fe_{80}$  alloy films show that in the as deposited case the radial distribution around Fe atoms can be fitted quite well by a single Gaussian. This rules out the existence of Fe in a bcc structure as no peak corresponding to the next neighbor distance of 2.84 Å is observed. Thus, the local structure around Fe atoms is best described as being close packed with a Fe-Fe nearest neighbor distance of approximately 2.50 Å. For a perfect closed packed structure a coordination number of 12 is expected. The observed coordination number of 8 suggests presence of domains of close packed Fe with a size of few nanometers. Doping with Au does not affect the amorphous structure of the as deposited samples. The most important effect of Au doping is the thermal stabilization of the amorphous structure even at high anneal temperature which was sufficient to crystallize the undoped sample. This stabilization which arises because of reduction in mobility of various atoms in the alloy is a consequence of achieving a more stable amorphous structure by addition of Au whose atomic size is intermediate between that of Fe and Tb. Yet, in spite of this stabilization the HT sample had its magnetization in plane of the film.

This study indicates that the loss of uniaxial magnetic anisotropy seen in the Au-TbFe alloys can not be associated simply to the crystallization of the amorphous structure. These results do indicate that it is possible to stabilize the amorphous structure of the  $Tb_{20}Fe_{80}$  alloy films by incorporation of small amounts of Au in the films.



**References**

1. M. G. Samant, C. J. Robinson, E. E. Marinero, and G. S. Cargill III, *J. Non-Crystal. Sol.* **106**, 178 (1988).
2. P. A. Lee, P. H. Citrin, P. Eisenberger, and B. M. Kincaid, *Rev. Mod. Phys.* **53**, 769 (1981).
3. A. Erbil, G. S. Cargill III, R. Frahm, and R. F. Boehme, *Phys. Rev. B* **37**, 2450 (1988).

## HREM STRUCTURAL STUDIES OF TbFeCo THIN FILMS

Z.G. LI, DAVID J. SMITH AND K. SICKAFUS\*\*

Center for Solid State Science, Arizona State University, Tempe,  
Arizona 85287

\*General Products Division, IBM Tucson, Arizona 85744

## ABSTRACT

The microstructure of TbFeCo thin films prepared under different deposition conditions has been observed in cross-section and top-view using high-resolution electron microscopy, as well as conventional bright-field and dark-field techniques. A comparison has been made with FeCo thin films prepared under identical experimental conditions. Very fine microcrystals (sizes 2-5nm) were observed in the basically amorphous TbFeCo thin films whereas much larger crystals (sizes 20-50nm) were visible in the primarily crystalline FeCo thin films. It was also found that the size of the nanocrystals in the TbFeCo films depended upon the argon partial pressure during deposition.

## INTRODUCTION

Rare-earth transition-metal (RE-TM) alloys have great potential for applications involving magneto-optic (MO) storage media because of their thermo-magnetic storage and Kerr contrast characteristics, as first demonstrated by Chaudhari [1]. Attempts to explain the pronounced magnetic anisotropy of thin films of these materials have been made, based upon traditional characterization techniques, such as electron, neutron and X-ray diffraction [2], but without much success, possibly because these methods can not provide sufficiently localized structural information. The required local information should, however, be available using electron microscopy techniques, and a number of recent studies have made useful contributions to our knowledge of RE-TM thin films. For example, phase separation on the 2.5 to 3.5nm scale as a function of the substrate bias voltage was found in GdCoAu thin films [3]. Changes of morphology were observed in thin films of TbFeCo due to different partial pressures of argon during the sputter deposition process [4]. Columnar structures, from 5 to 25nm in diameter, were visible perpendicular to the substrate plane in RE-TM thin films [5]. For a large range of deposition conditions, it was generally concluded that thin films of these materials appeared to have an amorphous structure, although the presence of very small crystals was recently proposed [4].

Based upon the apparently amorphous nature of the TbFeCo thin films, different structural models have been suggested to explain the magnetic anisotropy, such as "anisotropy phase-separation" [3], "columnar microstructure" [5], "atomic-scale structure anisotropies" [6] and "stress-induced anisotropy" [7]. Nevertheless, explanations for the anisotropy of the thin films remain inadequate. Our recent high-resolution electron microscopy studies at interpretable resolutions of better than 0.18nm have revealed that the thin films of amorphous TbFeCo, in fact, contain very fine microcrystals in the basically amorphous background [8]. In this paper we describe further structural studies of the TbFeCo thin films which have been prepared by sputtering, with deposition onto several kinds of substrate.

\*Present address: Los Alamos National Laboratory, Los Alamos,  
New Mexico 87545

# EXPERIMENTAL

The RE-TM films were mainly prepared by co-sputtering using either a DC magnetron or by RF sputtering methods, at typical pressures in the 5-25m Torr range. Thin films which had been deposited upon crystalline and oxidized silicon or amorphous quartz were prepared for observation in the electron microscope by the same basic method [9]. Thin slices were cut from the bulk sample, followed by mechanical polishing to thicknesses of about 20 microns, then dimpling and finally argon ion-milling to perforation. Samples were also deposited onto mica and onto a carbon-coated Cu grid. Since the samples in these latter two cases do not suffer from any ion-milling artefacts, useful comparisons could be made with those samples deposited onto the substrates mentioned above.

A JEM-200CX (operated at 200kV) and a JEM-4000EX (operated at 400kV) were used for high resolution electron microscope (HREM) observations. The structural resolution limit of about 0.17nm of the latter HREM was beyond the 0.20nm spacing commonly seen in many of the selected area electron diffraction (SAED) patterns. Standard electron microscope methods, such as bright-field imaging and SAED were also used in observations of the RE-TM thin films. High-resolution micrographs were usually recorded at several objective lens defoci with magnifications of 500kX or 600kX times. A standard optical bench was used to measure lattice spacings and the angles between lattice plane directions, with images of the Si substrate used to provide internal calibrations of spacings and angles. Alternataively, the images were digitized for analysis with the suite of image processing programs known as SEMPER [10].

# RESULTS

A systematic comparison between thin films of FeCo and TbFeCo prepared under the same deposition conditions. Figures 1(a) and (b), respectively, show regions of the FeCo and TbFeCo samples, viewed in cross-section, as deposited upon quartz sub-

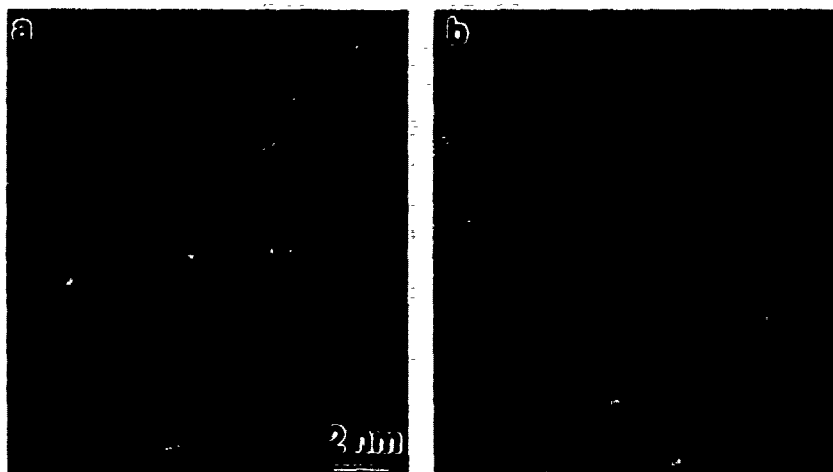


Fig. 1. High-resolution electron micrographs recorded at 400kV showing characteristic thin-film microstructure of (a) Fe-Co and (b) TbFeCo. Lattice fringe spacings correspond to  $\alpha$ -Fe and Co.

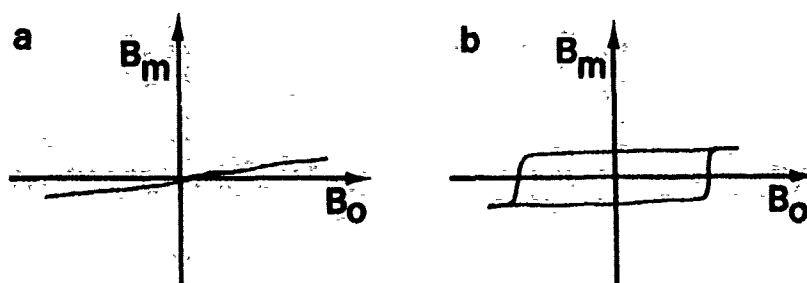


Fig. 2. Kerr loop magnetometer measurements of (a) FeCo and (b) TbFeCo thin films before observation by electron microscopy.

strates. Figure 1(a) shows that the FeCo samples consist of comparatively large crystals (30–50nm) with a basically columnar structure. Measurements from the images, as well as SAED patterns, confirm that these crystals have either the  $\alpha$ -Fe or Co structures. The TbFeCo thin films in Fig. 1(b) contains nanocrystals well dispersed throughout a basically amorphous film. The microstructure of the film is clearly very different from that of the FeCo film, but measurement of the lattice fringe spacings in the nanocrystals indicates that they still have either the  $\alpha$ -Fe or Co structure.

The corresponding Kerr loop magnetometer measurements from these two samples, as shown in Figs. 2(a) and (b), confirm the differences in the magnetic properties of the FeCo and TbFeCo thin films. The square hysteresis loop characteristic of marked perpendicular anisotropy which is exhibited by the TbFeCo sample represents the specific property desired for the use of RE-TM films in MO recording media.

The spacings of the one- and two-dimensional lattice fringes visible in the thin films could be measured to an accuracy of  $\pm 2\%$  using the image processing programs. Specific regions of particular micrographs were first digitized and then their power spectra were calculated using a special subroutine. Figure 3(a) shows a region from the TbFeCo thin film which had been deposited on the Si substrate; its power spectrum is shown in Fig. 3(b). By reference to the 0.314nm spacings of the Si{111} lattice planes, the diffraction spots originating from the nanocrystals were determined to have lattice spacings of 0.203nm, which suggests that they correspond to either  $\alpha$ -Fe or Co crystals. The diffuse ring centered at a radius corresponding to the Si {111} diffracted planes originates from the amorphous Si oxide located between the crystalline Si substrate and the RE-TM thin film.

Because of the possibility of crystallization artefacts being induced by ion-milling during sample preparation, thin films were deposited on mica under the same experimental conditions as the samples shown in Fig. 1. The SAED pattern has diffraction rings corresponding to the bcc  $\alpha$ -Fe structure, as shown in Fig. 4(a), with the first ring at about  $(0.2\text{nm})^{-1}$ . This appearance of the SAED pattern is very similar to that of the thin films which had already been shown to contain nanocrystals – see Fig. 4(b) – thus confirming that the existence of the crystals was independent of the techniques used for sample preparation.

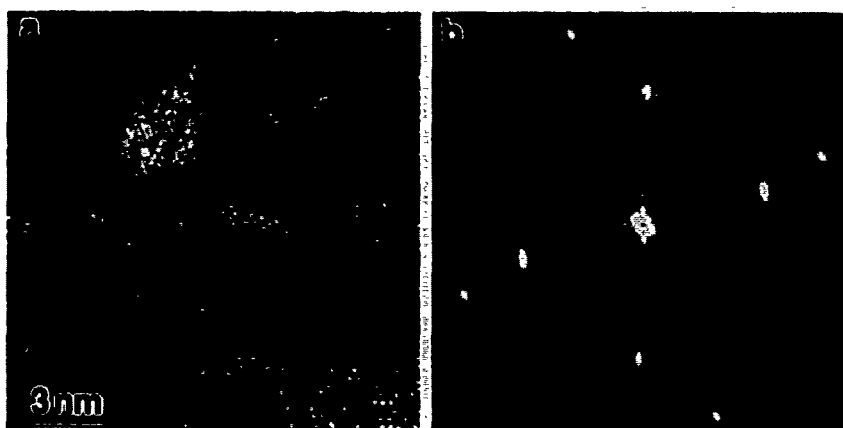


Fig. 3. (a) Region of TbFeCo thin film deposited on Si substrate. (b) Corresponding power spectrum showing diffraction spots due to nanocrystals and Si substrate.

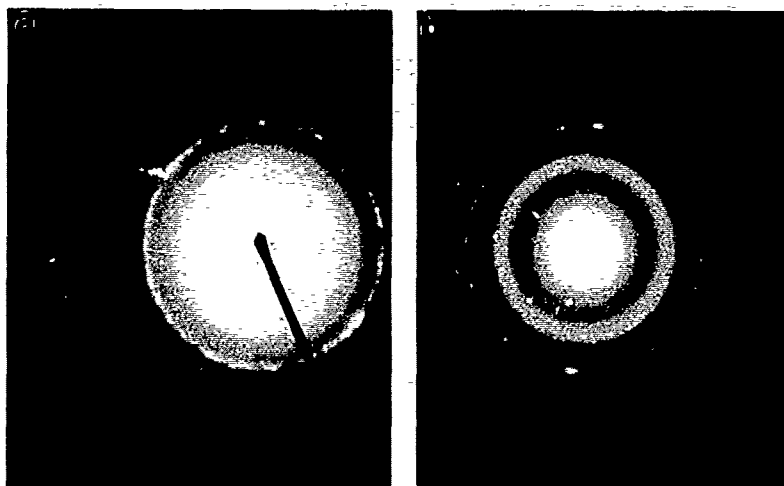


Fig. 4. Selected area electron diffraction patterns from plan-view samples of TbFeCo: (a) quartz substrate after ion-milling; (b) mica substrate but no ion-milling.

It has already been shown that the morphology of TbFeCo thin films depends markedly upon the partial pressure of argon during sputter deposition [4]. Samples prepared under low,  $p_{Ar}=5\text{mTorr}$ , and moderate,  $p_{Ar}=20\text{mTorr}$ , partial pressures are compared in the plan-view micrographs shown in Figs. 5(a) and (b) respectively. Nanocrystals in the former typically had sizes estimated to be around 4nm; bright- and dark-field observations of cross-section samples also gave nanocrystal sizes of the same order. The latter sample had larger crystal sizes, with maximum diameters as much as 7nm, and the films were clearly much more crystalline overall than those deposited at lower partial pressure.

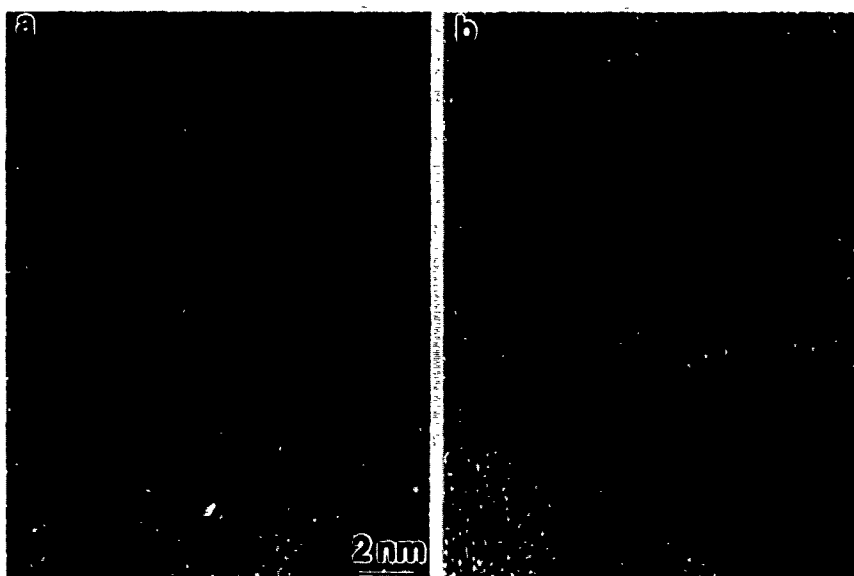


Fig. 5. High-resolution electron micrographs of TbFeCo thin films: (a)  $p_{Ar}=5\text{mTorr}$ ; (b)  $p_{Ar}=20\text{mTorr}$ .

#### DISCUSSION

The most important result from this high-resolution electron microscope study was that these RE-TM films have a basically amorphous structure, but they also contain nanocrystals of  $\alpha\text{-Fe}$  or  $\text{Co}$ . The microstructure of the films is independent of the substrate used for deposition but depends sensitively on the partial pressure of argon during sputter deposition. The absence of the rare earth element Tb leads, however, to a dramatic change in microstructure: crystal sizes increase by almost an order of magnitude and virtually no amorphous regions are visible. It is interesting to note that evidence for crystals of terbium and terbium oxide was not visible in high-resolution electron micrographs nor in the SAED patterns, suggesting that they must be present in the amorphous state.

#### ACKNOWLEDGEMENTS

This work has been supported by the IBM Shared University Research (SUR) Program and by IBM Tucson, and made use of facilities at the National Center for High Resolution Electron Microscopy, in the Center for Solid State Science at Arizona State University, supported by National Science Foundation Grant DMR-86-11609.

#### REFERENCES

1. P. Chaudhari, J.J. Cuomo and R.J. Gambino, *Appl. Phys. Letts.*, **22**, 337 (1973).
2. K.H.J. Buschow, *Handbook on the Physics and Chemistry of Rare Earths*, ed. by K.A. Gschneidner and L. Eyring (Elsevier, 1984).

3. S.R. Herd, J. Appl. Phys., 50, 1645 (1979).
4. J.-W. Lee, H.-P.O. Shieh, M.H. Kryder and D.E. Laughlin, J. Appl. Phys., 63, 3624 (1988).
5. A.G. Dirks and H.J. Leamy, Thin Solid Films, 4, 219 (1977).
6. R.J. Gambino, P. Cnaudhari and J.J. Cuomo, AIP Conf. Proc., 18, 578 (1973).
7. A.G. Dirks and H.J. Leamy, J. Appl. Phys., 49, 1735 (1978).
8. Z.G. Li, D.J. Smith and K. Sickafus, Appl. Phys. Letts., in press.
9. J. Bravman and R. Sinclair, J. Electron Micro. Tech., 1, 53 (1984).
10. W.O. Saxton, T.J. Pitt and M. Horner, Ultramicroscopy 4, 343 (1979).

\*Note added in proof: The possibility remains that the formation of the iron/cobalt microcrystals is somehow related to the oxidation of terbium which could take place either during deposition or sample preparation for microscopy. Further experiments are in progress with capped samples.

**LASER ABLATION DEPOSITION (LAD)  
OF METALLIC THIN FILMS**

**J.P. REBOUILLAT, B. MICHELUTTI, Y. SOUCHE, J.P. GAVIGAN\*, D. GIVORD, A. LIENARD**  
Laboratoire Louis Néel, C.N.R.S., 166 X, 38042 GRENOBLE cedex, France

\* Post doctoral research fellow of the Commission of the European Communities  
DG XII - EURAM

**ABSTRACT**

Several experiments have been carried out to characterize the laser ablation deposition of metallic thin films as a function of the various process parameters. Ablation thresholds have been investigated for Al, Cu and Au targets as a function of wavelength as well as the fluence dependence of ablation rate. The effect of electric fields on the particle component of the ablated material has been investigated. Measurements of the velocity distribution of these particles have also been carried out for Al, Cu and Au targets as a function of the laser parameters with a view to using a velocity filter to remove the particles from the ablated beam.

**INTRODUCTION**

Laser Ablation Deposition (LAD) equipment has recently been installed in our laboratory with a view to preparing and characterizing the properties of novel metallic magnetic thin films. The sample preparation set up includes a specially designed double chamber Riber UHV system ( $5 \times 10^{-11}$  Torr), a HV chamber ( $10^{-7}$  Torr) and a Quantel Nd : YAG nano/picosecond laser with three possible wavelengths (1064 nm, 532 nm, 335 nm). Determining factors in the choice of the LAD technique were its simplicity, versatility and the possibility of congruent evaporation of multicomponent targets for the deposition of thin film compounds. However, the "development" state-of-the-art of LAD and its limited use compared to other techniques (eg. MBE, sputtering) has meant that much preliminary work has been necessary to characterize the important aspect of LAD (ablation thresholds, beam composition, deposition rate, film quality...) as a function of the various process parameters (wavelength, laser fluence, target material...) and to surmount a number of technical difficulties. In this paper we report some results of this on-going work.



# ABLATION RATE AND ABLATION THRESHOLDS

One of the studies carried out consisted of an investigation of the ablation rate for three different metal targets (Al, Cu, Au) as a function of laser fluence,  $\Phi$ , and wavelength. The ablation rate was quantified by measuring the rate of deposition on a quartz microbalance placed 17 mm from the target in the path of the ablated beam. The laser was operated at 30 Hz giving single mode pulses of 20 ns. Fluence variation and control were achieved by means of a polarizer and focusing lens ( $f \approx 30$  cm), and by measuring both the laser power with a wattmeter and the impact crater size. The results of the measurements are plotted in figure 1.

The general shape of the curves reveals an initial steep rise in ablation rate above threshold followed by a progressively more gentle slope with increasing fluence, and apparently then saturating in the case of Cu. A rough estimate of the ablation threshold made using these curves gives a value of  $1 \text{ Jcm}^{-2}$  ( $50 \text{ MW cm}^{-2}$ ). This value was corroborated by measurements made with a VG quadrupole mass spectrometer, used to detect the ablation threshold for Cu and Au with  $\lambda = 532 \text{ nm}$  and  $355 \text{ nm}$ ; values of  $1 \text{ Jcm}^{-2}$  were also found. These results are in reasonable agreement with threshold fluence values for Cu reported by Husslaa and Viswanathan (1984) [1] and for several transition metals reported by Bykovskii et al (1987) [2].

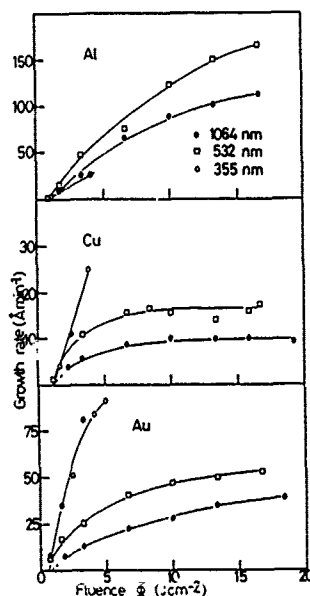


**Figure 1** : Measured deposition rate with a quartz microbalance as a function of wavelength and fluence  $\Phi$  for Al, Cu and Au targets using 20 ns laser pulses at 30 Hz.

TABLE I

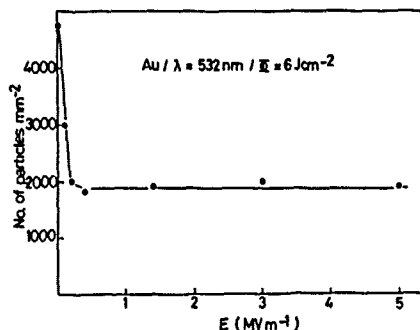
$\lambda$	Room temperature $\epsilon$ values			Room temperature thermal conductivity (W cm <sup>-1</sup> K <sup>-1</sup> ) [6]	Melting point °C [5]
	1064 nm	532 nm	355 nm		
Al	/	0.0837	0.0769	2.37	660.4
Cu	0.0277	0.4000	0.6075	4.01	1083.4
Au	0.0206	0.3040	0.6113	3.17	1064.4

Figure 1 also shows that for a given  $\Phi$  value, the ablation rate increases with decreasing wavelength except for Al with  $\lambda = 355$  nm. Given that thermal effects dominate the ablation process for the range of parameters considered, it is reasonable that the observed trend for each metal be consistent with the calculated values of the room temperature emissivities ( $\epsilon$ ) reported in Table I.  $\epsilon$  was calculated following Cheung and Sankur [3] using the equation  $\epsilon = 4n/((1+n)^2 + k^2)$  and using values of the optical constants  $n, k$  reported by Johnson and Christy (1972) [4] and in the American Institute of Physics Handbook [5]. Furthermore, the high ablation rate for Al compared to Cu and Au may be explained by the comparatively low value of the thermal conductivity (Table I); i.e. for Cu and Au, the more efficient conduction of heat away from the impact area of the laser pulses, results in less heat being available for ablation than for Al.

#### THE SPLASHING EFFECT AND PARTICLE ELIMINATION

The main drawback of the LAD technique is the production of micron and submicron size particles in the ablation process. Indeed, all metallic films prepared were invariably found to contain such particles upon examination by optical and electron microscopy. Therefore, a number of different experiments have been carried out to investigate ways of eliminating these particles from the ablated beam.

The first series of experiments investigated the effect of static electric fields on the particles with the expectation that some or all of them may be charged and hence deviated from their flight path. All these experiments were carried out with a gold target, laser fluence of approximately 6 Jcm<sup>-2</sup> and  $\lambda = 532$  nm. The effect of the electric field was estimated indirectly by depositing films for each field configuration followed by optical microscopy examination. Films were deposited with fields of up to 5 MVm<sup>-1</sup> applied trans-



**Figure 2** : Particle density in Au films deposited for different values of a transversely applied electric field to the ablated beam (see text).

versely to the flight path of the ablated material as well as with the substrate polarized with respect to the target. The most significant results were obtained in the former case where a reduction of about 50 % in the particle density was achieved for fields greater than  $0.2 \text{ MVm}^{-1}$  (figure 2). The effect of polarizing the substrate was not at all favourable. In fact, as in reference [7] it appeared that the deposited material was partially sputtered off the substrate by charged species being accelerated in the electric field, thereby resulting in very poor quality films.

These results show that a significant proportion of the particles are charged, but the large neutral component prevents one from envisaging the use of electrostatic deviation as a means of obtaining particle free thin films, barring some method of charging all the particles.

A second series of experiments was undertaken with a view to eliminating the particles by means of a mechanical velocity filter. For this purpose, a rotating substrate device was built in order to estimate the velocity distribution of the particles. The device consists of a rotating disc substrate ( $\phi = 30 \text{ mm}$ ) which sees the ablated beam through a stationary 2 mm wide slit along a radius (figure 3). Rotation is coupled via a ferrofluid feedthrough to the

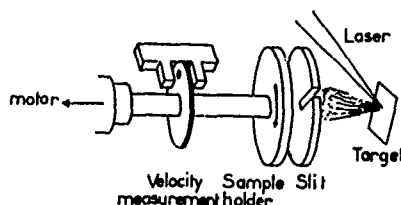


**Figure 3** : Diagram of the rotating substrate device used to obtain time/velocity resolved deposition of ablated material.

substrate from a motor of adjustable rotation frequency  $\omega/2\pi$  up to a maximum of 300 Hz. The laser is fired in synchronization with the rotation. In this way, the angular position ( $\theta = \omega t$ ) where a particle is deposited on the substrate depends on the time ( $t = v/d$ ) taken for the particle to traverse the distance  $d$  between target and substrate and thus on its velocity  $v$ . Therefore by keeping  $\omega$  constant, we obtain a time/velocity resolved deposition of the ablated material and subsequent microscopy studies permit an estimation of the particle velocity distribution.

12 samples of Al, Cu and Au have been prepared and studied as a function of wavelength and fluence. All samples were prepared for the same geometry ( $d = 43$  mm) and value of  $\omega/2\pi$  (150 Hz). Figure 4 shows as an example velocity distributions determined for four Al samples, where a greater droplet density was observed than for Cu or Au. This fact corroborates with the thermal data listed in Table I. From the observation of the particles in all the samples, the following points can be made. Firstly, the velocity of the particles is of the order of a few hundred meters per second and an order of magnitude smaller than the velocity of ionic and atomic species. The peak of the velocity distribution  $\bar{v}$  depends on the laser fluence with  $\bar{v} \approx 100 \text{ ms}^{-1}$  for  $\Phi \approx 4 \text{ Jcm}^{-2}$  and  $\bar{v} \approx 300 \text{ ms}^{-1}$  for  $\Phi \approx 15 \text{ Jcm}^{-2}$ , and the distribution itself is asymmetric extending from  $0.5 \bar{v}$  to  $2 \bar{v}$ . No wavelength dependence of the distribution is apparent. It was also clear from microscopic observations that the size of the particles decreased as a function of their velocity, as expected. Sizes ranged from a few hundred nanometers for the fastest up to 10 microns.

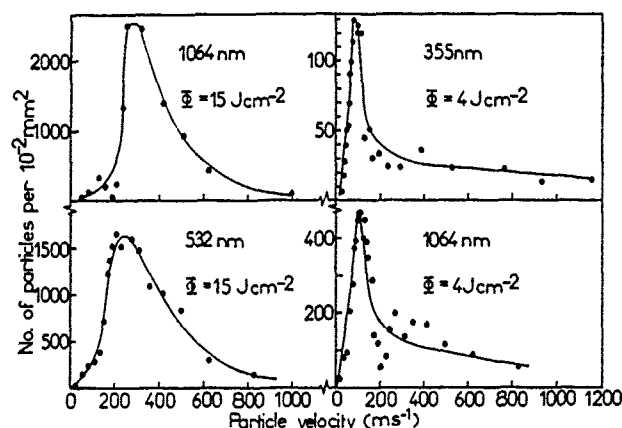


**Figure 4** : Velocity distributions of particles produced by ablating Al target for different conditions of fluence and wavelength.

In conclusion, this latter set of experiments shows that by using a velocity filter to eliminate species with velocities less than  $\approx 500 \text{ ms}^{-1}$ , one can obtain clean films due to the deposition of atomic and ionic ablated species which travel at velocities of a few thousand meters per second [2].

#### REFERENCES

- 1 - I. HUSSLA and R. VISWANATHAN, *Surface Science*, 145, 1448 (1984).
- 2 - A.Y. BYKOVSKII, S.M. SIL'NOV, E.A. SOTNICHENKO and B.A. SHESTAKOV  
*Sov. Phys. JETP*, 66 (2), 285 (1987).
- 3 - J.T. CHEUNG and H. SANKUR, *CRC Critical Reviews in Solid Stat. and  
Mat. Sciences*, 15 (1), 63 (1988).
- 4 - P.B. JOHNSON and R.W. CHRISTY, *Phys. Rev. B*, 6 (12), 4370 (1972).
- 5 - American Institute of Physics Handbook, 3rd edition (McGraw and Hill Inc  
USA, 1972).
- 6 - R.W. POWELL and Y.S. TOULOUKIAN, *Science*, 181, 999 (1973).
- 7 - D. LUBBEN, S.A. BARNETT, K. SUZUKI, S. GORBATKIN and J.E. GREENE  
*J. Vac. Sci. Technol. B*, 3 (4), 968 (1985).

TIME-DEPENDENT LANDAU-GINZBURG MODELLING OF MAGNETIC INHOMOGENEITIES  
AND SPIRAL DOMAIN STRUCTURES IN THIN FILMS

J.A. TUSZYŃSKI

Department of Physics, The University of Alberta,  
Edmonton, Alberta, Canada, T6G 2J1

ABSTRACT

A Landau-Ginzburg model for a uniaxial ferromagnetic thin film is presented which includes inhomogeneities due to nearest neighbor exchange interactions. The role of external magnetic fields is studied in the determination of exact symmetries of the equation of state. Spiral domain structures allowed by symmetry considerations as exact solutions at the critical and tricritical points have recently been found experimentally in epitaxially grown single-crystal garnet ferrite films. These experiments are discussed from the point of view of our model.

THE DYNAMICAL LANDAU-GINZBURG MODEL

The Landau-Ginzburg free energy functional

$$F = \int d^n x \left[ A_2 \eta^2 + A_4 \eta^4 + A_6 \eta^6 - h\eta + \frac{1}{2} D(\nabla\eta)^2 \right] \quad (1)$$

where  $n$  is spatial dimensionality,  $A_2 = \alpha(T-T_c)$ ,  $A_4$ ,  $A_6$  are constants,  $\eta$  is the order parameter and  $h$  is the conjugate field, has played a prominent role in the theory of critical phenomena [1] since it can be used to describe a number of phase transitions, both field- and temperature-induced ( $h \neq 0$  and  $h=0$ , respectively), first - as well as second-order ones (when  $A_4 < 0$  and  $A_4 > 0$ , respectively). The inclusion of the term  $(1/2)D(\nabla\eta)^2$  is crucial in going beyond the mean field approximation.

The relaxation kinetics for nonconservative order parameters is described by the time-dependent Landau-Ginzburg equation:

$$\nabla^2 \eta + \frac{\partial \eta}{\partial t} = a + b\eta + c\eta^3 + d\eta^5 \quad (2)$$

where  $a = -h/D$ ;  $b = 2A_2/D$ ;  $c = 4A_4/D$  and  $d = 6A_6/D$ . Recently, extensive analyses of this equation have been performed using the symmetry reduction method for partial differential equations, both in the dynamic ( $\partial\eta/\partial t \neq 0$ ) [2] and the static ( $\partial\eta/\partial t = 0$ ) [3] regimes. The results of these studies can be very briefly summarized as follows. For  $h=0$  and at either the critical ( $A_2=A_6=0$ ) or the tricritical points ( $A_2=A_4=0$ ), the exact symmetries of the equation of state involve translations, rotations and scaling transformations. This results in a very large number of solutions which involve: translationally-invariant elliptic waves, cylindrical or spherical standing waves, accelerating plane waves, multivalued (layered) solutions, damped cylindrical and spherical waves and, finally, spiral solutions. It is worth noting that the cylindrical and spherical waves have asymptotic behavior identical to that of plane waves. Low frequency (and low energy) elliptic patterns of the latter type can, in the infinite limit, become solitary waves ( $\tanh$  for  $D>0$  and  $\text{sech}$  for  $D<0$ ). However, when  $h \neq 0$  or, in general, when the system is not at the critical or tricritical point, the exact symmetries are not as rich. They only involve translations and rotations and the exact solutions of eq. (2) can only be: homogeneous in space or time, translationally-invariant, or standing cylindrical or spherical waves. The energies of translationally-invariant solutions can also be calculated exactly [3] through the integral

$$\frac{F}{V} = N \int_0^{\Lambda} (\nabla\eta)^2 dx \quad (3)$$

where  $V$  is the volume of the sample,  $N$  is the number of full periods ( $\Lambda$ ) of the solution in the sample's length. Analytical expressions for the energy of each solution exist [3] and involve elliptic integrals of the first, second or third type. For  $D > 0$  the energies increase in the following order: from the mean field phases to domain walls (tanh-kinks) to low frequency snoidal elliptic waves and finally to high frequency elliptic waves. For  $D < 0$  the lowest energy solutions are high frequency cnoidal waves, then low frequency ones, then nucleation centers (sech-bumps), then mean fields, then dnoidal waves. In the latter case the role of inhomogeneities is clearly manifest.

Inhomogeneous equilibrium fluctuations can be modelled as structures with constant energy density, i.e. they satisfy:

$$A_2 n^2 + A_4 n^4 + A_6 n^6 - h n + \frac{1}{2} D (\nabla n)^2 = C. \quad (4)$$

This ensures detailed equilibrium conditions of maximum entropy by equalizing local temperature variable throughout the sample. Interestingly, the exact symmetries admitted by this equation coincide with those of the stationary limit of eq. (2). Moreover, all the solutions of eq. (4) can be found from the analysis of eq. (2) by changing the sign of  $D$  in the first integral of the latter equation. Thus, minimum free energy structures for  $D > 0$  become equilibrium fluctuations for  $D < 0$ , and vice versa. This then allows to construct a complete energy spectrum for the free energy functional.

#### APPLICATION TO UNIAXIAL FERROMAGNETS

The Heisenberg exchange Hamiltonian:

$$H_0 = - \sum_{\langle i,j \rangle} J_{ij} \hat{S}_i \cdot \hat{S}_j$$

leads in the continuum limit to terms proportional to  $(\nabla M)^2$  where  $M$  is the sample's mean magnetization. Terms proportional to even powers of  $M$  can be arrived at from higher coordination spheres and they form the well-known "molecular field". Thus, uniaxial ferromagnets can be well described using a Landau-Ginzburg free energy. For spin-ordering processes (close to  $T_c$ ), we simply set  $n=M_z$ ,  $h=H_z$  and  $D > 0$  refers to ferromagnetic while  $D < 0$  to anti-ferromagnetic nearest neighbor interactions. We can then use all the results of the previous section directly with their appropriate interpretation.

On the other hand, for reorientational processes magnetocrystalline anisotropy is more important and one should use as a starting point the free energy:

$$F = \int d^3x = \left[ \frac{D}{2} \sum_{i=1}^3 (\nabla \alpha_i)^2 + K_1 \alpha_s^2 + K_2 \alpha_s^4 - \hat{H} \cdot \hat{M}_s \right] \quad (5)$$

where  $\hat{M}_s = M_s \hat{e}(\vec{x})$  and  $\hat{e} = (\alpha_1, \alpha_2, \alpha_3)$ ;  $K_1, K_2$  are magnetocrystalline anisotropy constants and  $\alpha_s$  refers to the direction cosine of spontaneous magnetization  $\hat{M}_s$ . In planar situations, such as exist for example in thin films, we choose  $\hat{M}_s = M (\sin \theta, \cos \theta, 0)$  whereupon the first integral of the Euler-

Lagrange equation becomes either

$$-\frac{D}{2} (\nabla \alpha)^2 + (1 - \alpha^2) [K_1 \alpha^2 + K_2 \alpha^4 - H_1 M_s \alpha] = 0 \quad (6)$$

for  $\alpha = \cos \theta$  and  $\hat{H} = (0, H_1)$  or

$$-\frac{D}{2} (\nabla \alpha)^2 + (1 - \alpha^2) [K_1 (1 - \alpha^2) + K_2 (1 - \alpha^2)^2 - H_1 M_s \alpha] = 0 \quad (7)$$

for  $\alpha = \sin\theta$  and  $\vec{H} = (H_1, 0)$ . In both cases, however, the equations are of the same type as those analysed in [2] and [3], namely they are first integrals of the cubic ( $K_2=0$ ) or quintic ( $K_2 \neq 0$ ) nonlinear Klein-Gordon equation. A particular solution for  $H_1=H_2=0$  and  $K_2=0$  in the form of a domain wall  $\cos\theta = -\tanh \sqrt{K_1/D} x$  has been known for many years. The results presented in [2] and [3], however, allow a systematic analysis of excitations in uniaxial magnets. Many of the geometries discussed in previous section have been commonly observed in magnets, e.g. spherical  $\alpha\text{-Fe}_2\text{O}_3$  microparticles [4], cylindrical iron whiskers [5], multilayered structures [6], and very recently spirals [7]. The formation of solitons in magnetic systems has also been given extensive exposure [8]. In our model both sech and tanh solitary waves are obtained as limiting cases of elliptic functions becoming of very long wavelengths, i.e. their elliptic modulus tends to one. Moreover, exact energies of all these solutions can be directly calculated.

#### SPIRAL DOMAINS IN UNIAXIAL THIN FILMS

A particularly interesting application of our method can be made to model spiral domains of uniaxial ferromagnetic thin films. It has been recently reported [7] that epitaxially grown single-crystal garnet ferrite films  $(\text{Y}_1\text{Sm})_3(\text{FeGa})_5\text{O}_{12}$  exhibit the formation of spiral domains when subjected to an alternating square magnetic field along the easy magnetization axis along the normal to the sample for  $80 \text{ Oe} < |H| < 87 \text{ Oe}$  and at a frequency of  $\omega = 300 \text{ Hz}$ . The spiral domains of large area ( $\sim 1 \text{ mm}$ ) were formed following a destabilization of the typical labyrinthine domain structure leading to complete randomization in the magnetic structure of the sample. The lifetimes of the created spirals were large, on the order of 10s and they persisted for as long as the external field was applied. This tends to indicate a very peculiar nonequilibrium metastable phase. These structures also exhibited soliton-like qualities of stability with respect to collisions when pairs were created.

We believe that these observations can be explained using the Landau-Ginzburg model presented in this paper. First of all, it is not uncommon to use Landau-Ginzburg modelling for thin films [9]. Symmetry reduction analysis for two-dimensional systems is summarized in Table 1 following [2]. Secondly, at both the critical ( $N=3$ ) and tricritical ( $N=5$ ) points exact minimum free energy solutions in two-dimensional space have been demonstrated to contain spiral patterns [2,3] in addition to the less exotic plane and spherical waves. Their form is given by:

$$M_z(\underline{x}, t) = \rho(\underline{x}) f(\xi) \quad (8)$$

where  $M_z$  denotes the magnetization component along the easy magnetization axis perpendicular to the sample and

$$\rho = [4B^2/|c|(B^2+1)(x^2+y^2)]^{1/2}$$

which is a damping factor;

$$\xi = \frac{-2B}{B^2+1} \left[ \arctan\left(\frac{y}{x}\right) + \frac{1}{2} B \log(x^2+y^2) \right]$$

which is the so-called symmetry variable in the case of the critical point, and

$$\rho = [4B^2/|d|(B^2+1)(x^2+y^2)]^{1/4}$$

with the same  $\xi$  for the tricritical point. The function  $f(\xi)$  satisfies the equation:

$$f'' + f' + \frac{B^2+1}{4B^2} f + \epsilon f^N = 0 \quad (9)$$



Table 1. The Results of Symmetry Reduction for eq. (2) in two-dimensional space following [2].

No.	Symmetry variable $\xi$	Damping $\rho$	Reduced ODE
I. Reductions for arbitrary values of a, b, c and d			
1	t	1	$\frac{df}{d\xi} = a + bf + cf^3 + df^5$
2	x	1	$\frac{d^2f}{d\xi^2} = a + bf + cf^3 + df^5$
3	$v(x+vt)$	1	$\frac{d^2f}{d\xi^2} \frac{df}{d\xi} = \frac{1}{v^2}(a+bf+cf^3+df^5)$
4	$\sqrt{x^2+y^2}$	1	$\frac{d^2f}{d\xi^2} + \frac{1}{\xi} \frac{df}{d\xi} = a+bf+cf^3+df^5$

II. Additional reductions at the critical ( $a=b=d=0$ ;  $\epsilon=-\text{sgn}(c)$ ,  $N=3$ ,  $\Delta=|c|$ ) or the tricritical point ( $a=b=c=0$ ;  $\epsilon=-\text{sgn}(d)$ ,  $N=5$ ,  $\Delta=|d|$ ).

1	$(\frac{2}{N-1})\arctan(\frac{y}{x})$	$[\Delta(x^2+y^2)]^{-1/(N-1)}$	$\frac{d^2f}{d\xi^2} + f + \epsilon f^N = 0$
2	$\frac{-2B}{B^2+1} \{ \arctan \frac{y}{x} + \frac{B}{2} \log(x^2+y^2) \}$	$[\frac{4B^2}{\Delta(B^2+1)(x^2+y^2)}]^{1/(N-1)}$	$\frac{d^2f}{d\xi^2} + \frac{df}{d\xi} + \frac{B^2+1}{4B^2} f + \epsilon f^N = 0$
3	$\frac{t}{2(x^2+y^2)}$	$[\Delta(x^2+y^2)]^{-1/(N-1)}$	$\xi^2 \frac{d^2f}{d\xi^2} + (\frac{1}{2} + \alpha\xi) \frac{df}{d\xi} + \beta f + \epsilon f^N = 0$ $\alpha=4, \quad \beta=1 \quad \text{for } N=3$ $\alpha=3, \quad \beta=1/4 \quad \text{for } N=5$
4	$\frac{t}{2x^2}$	$(\Delta x)^{-1/(N-1)}$	$\xi^2 \frac{d^2f}{d\xi^2} + (\frac{1}{2} + \alpha\xi) \frac{df}{d\xi} + \beta f + \epsilon f^N = 0$ $\alpha=5, \quad \beta=2 \quad \text{for } N=3$ $\alpha=4, \quad \beta=3/4 \quad \text{for } N=5$

where  $f' = df/d\xi$ ,  $f'' = d^2f/d\xi^2$ ,  $N = 3, 5$ , respectively and  $\epsilon = -\text{sgn}(c)$  or  $-\text{sgn}(d)$  in the two cases. A constant solution of eq. (9) could define a spiral mean field which is radially damped and can be written as:

$$M(\xi) = [-\epsilon |M_0| (x^2 + y^2)]^{-1/(N-1)} \quad (10)$$

where  $M_0 = c$  or  $d$  and  $\epsilon = +1$  or  $-1$ . Expanding a  $\xi$ -dependent solution of eq. (9) about its mean field approximation

$$f = (-\epsilon \frac{B^2+1}{4B^2})^{1/(N-1)}$$

would lead to its damping along the direction normal to the spiral which is defined as  $r \equiv (x^2+y^2)^{1/2} = \exp(-2B\phi)$  with  $\phi = \arctan(y/x)$ , and thus would

lead to a finite width  $w$ . It is easy to demonstrate that the energy  $\Delta E$  required to form a spiral is in the vicinity of the critical point

$$\Delta E = w(A_4 m^2 + \frac{D}{2}) m^2 \frac{\sqrt{1+v^2}}{2v} (1 - e^{-4\pi v N_0}) \quad (11)$$

where  $m = [-\epsilon |M_0|]^{-1/2}$ ,  $N_0$  is the number of turns, and  $v = -2B > 0$  for the spiral to unwind. In the vicinity of the tricritical point, however

$$\Delta E = w(A_6 m^4 + \frac{D}{8}) m^2 \frac{\sqrt{1+v^2}}{v} (1 - e^{-2\pi v N_0}) \quad (12)$$

where  $m = [-\epsilon |M_0|]^{-1/4}$  in this case. Thus, the energy increases rather slowly with the size of the spiral. This could explain why it was so easy to form very large spiral structures. In [7] the pitch of the spirals was typically 20-30  $\mu\text{m}$  which would correspond to our  $4\pi B$  provided  $B$  is small enough to linearize the exponential. The lifetime of a spiral  $\Delta\tau \sim \exp(-\beta\Delta E)$  should depend rather sensitively on temperature.

We believe that the alternating magnetic field is necessary first to gradually disallow more and more low energy periodic magnetic structures (starting from domain walls) and distort the form of the high energy ones, as can be seen analyzing the solutions of eq. (2). Even infinitesimally small fields lead to the abolition of tanh-kinks which are replaced by bumps. In fact, at the saturation field

$$H_s = \frac{1}{\sqrt{A_4}} \left(-\frac{2A_2}{3}\right)^{3/2} \quad (13)$$

(here  $H_s \approx 91.5$  Oe) no propagating solutions would be stable except for singular ones. It has been shown that spirals can be exact solutions only at the critical or tricritical points [2,3]. However, with an alternating field present, the effective free energy for solutions with relaxation times  $\Delta\tau$  greater than the period of magnetic field oscillation  $\omega^{-1}$  would be:

$$F = \int d^2x [A_2(M_z)^2 + A_4(M_z)^4 + |H_z| |M_z| + \frac{D}{2} (\nabla M_z)^2] \quad (14)$$

Effectively then, when  $|H_z| \approx -A_2 |M_z|$ , (note that  $A_2 < 0$  below  $T_c$ ) the experimental conditions would be almost identical to those at the critical point at least in the vicinity of  $M_z = 0$ . The difference between this and the actual critical or tricritical point is that this present situation is strictly non-equilibrium while the latter two represent thermodynamic equilibrium. We have analyzed this requirement on  $H_z$  and found it to correspond to the vanishing (as a result of applying  $H_z$ ) of the mean field part of the free energy for  $M_z$  equal to between 57% and 62% of the equilibrium magnetization. In fact, one could afford a prediction based on the approximate relationship written below eq. (14). Namely, lowering the temperature in this type of experiment would require a larger magnitude of the field in order to produce spirals and  $|H_z|$  should be roughly proportional to  $|T - T_c|^{3/2}$  since  $A_2 \sim (T - T_c)$  and  $M_z \sim (T - T_c)^{1/2}$ . The reason why increasing the field further destroys the spirals is that this would cause a departure from the nonequilibrium situation equivalent to the critical point and a decrease of  $\Delta\tau$ . Finally, it is easy to see that spiral solutions are metastable by substituting their form to eq. (2) and linearizing the full equation about them with the presence of an external field so that  $\eta \approx M(\xi) + \psi(x, y)$ . In the vicinity of the critical point one obtains

$$\nabla^2 \psi = (a + bM) + (b + 3cM^2)\psi \quad (15)$$

while in the vicinity of the tricritical point:

$$\nabla^2 \psi = (a + cM^3) + (b + 3cM^2 + 5dM^4)\psi \quad (16)$$

Thus, with the increase of the external magnetic field, the term  $a$  increases and leads to the growth of fluctuations which may destroy the spiral patterns completely.

#### CONCLUSIONS

In this paper we have presented a Landau-Ginzburg model for a uniaxial ferromagnetic thin film including magnetic inhomogeneities which result from nearest neighbor exchange interactions. The method of calculations, called the symmetry reduction method for partial differential equations, has been extensively used in recently published work. In this paper we focussed on two-dimensional applications, and specifically on the role of external magnetic fields.

As a particularly interesting class of solutions we have studied spiral domain structures which satisfy the equation of state exactly only at the critical or tricritical points. However, they may be obtained as approximate solutions elsewhere on the phase diagram. Recent experiments confirm this hypothesis with unambiguous observations of such structures in single-crystal garnet ferrite films. We have provided a theoretical discussion and interpretation of these results.

#### ACKNOWLEDGEMENTS

This research has been supported by a grant from the Natural Sciences and Engineering Research Council of Canada.

#### References

- [1] J.C. Toledano and P. Toledano, The Landau Theory of Phase Transitions, (World Scientific, Singapore, 1987).
- [2] M. Skierski, A.M. Grundland and J.A. Tuszyński, *Phys. Lett. A* **133**, 213 (1988).
- [3] P. Winternitz, A.M. Grundland and J.A. Tuszyński, *J. Math. Phys.* **28**, 2194 (1987); *J. Phys. C* **21**, 4931 (1988).
- [4] N. Amin and S. Ajaaj, *Phys. Rev. B* **35**, 4810 (1987).
- [5] T.L. Templeton and A.S. Arrott, *J. Appl. Phys.* **55**, 2189 (1984).
- [6] D. Schwenk, F. Fishman and F. Schwable, *Phys. Rev. B* **38**, 11618 (1988).
- [7] G.S. Kandaurova and A.E. Sviderskii, *J.E.T.P. Lett.* **47**, 490 (1988).
- [8] A.M. Kosevich, B.A. Ivanov and A.S. Kovalev, *Sov. Sci. Rev. A Phys.* **6**, 161 (1985).
- [9] S.P. Chizhik, L.K. Grigor'eva, R.N. Kuklin and V.N. Kuz'min, *Sov. Phys. Solid State* **30**, 655 (1988).

# EXCHANGE ANISOTROPY IN AMORPHOUS/MICROCRYSTALLINE CO-GD FILMS

A.M. Toxen\*, A. Hopkins\*, S.B. Hagstrom\*, and R.M. White\*\*

\*Stanford Univ., Stanford, CA 94305-4045

\*\*Control Data Corp., Minneapolis, MN 55440

## ABSTRACT

Magnetization, TEM, and x-ray diffraction studies have been carried out on  $\text{GdCo}_x$  films sputtered onto Si or sapphire substrates at  $\sim 90^\circ\text{C}$ , ambient temperature. The composition range studied was  $x=2-8.5$ . Over the composition range defined approximately by  $5 > x > 3$ , the films, which are 1-3 microns thick, exhibit a unidirectionally displaced B-H loop, characteristic of an exchange-biased phase. TEM studies indicated that the samples with the shifted loops indeed consist of a mixture of amorphous and microcrystalline phases. The characteristic size of the microstructure is 10-20 Å. Electron diffraction shows a very broad ring characteristic of amorphous phase together with six or seven sharper rings characteristic of crystalline material which index best to the hexagonal  $\text{GdCo}_5$  structure or to a high temperature hexagonal  $\text{Gd}_2\text{Co}_{17}$  phase. The diffraction pattern remains virtually unchanged over the composition range  $x=2-8$ . This leads us to conclude that the microcrystalline material consists of one, or perhaps more than one, metastable phase over the indicated composition range. X-ray diffraction shows only one broad maximum.

## INTRODUCTION

We previously reported<sup>1</sup> that macroscopically uniform thin films of  $\text{GdCo}_x$  exhibited unidirectionally displaced B-H hysteresis loops in the composition range approximately defined by  $3 < x < 5$ . The films were 1-3 microns thick and were co-sputtered from Co and Gd sources onto Si or Sapphire substrates at ambient temperature, about  $90^\circ\text{C}$ . The samples were coated in situ with 100-200 Å of Nb to prevent oxidation and were stored in a desiccator. At room temperature the loop displacements or "exchange fields" were  $\sim 5$  Oe and the coercivities were  $\sim 10-20$  Oe. Transmission electron microscopy measurements indicate that the samples which exhibit the unidirectionally shifted B-H loops are, on a microscopic scale, nonuniform, with structure about 10-20 Å in size. Electron diffraction measurements show the samples to be a mixture of amorphous and microcrystalline material. We identify the amorphous material with the "soft" magnetic phase and the crystalline material with the "hard" magnetic phase. Magnetic measurements indicate that the hard phase constitutes about 10-20% of the sample. Preliminary analysis of the electron diffraction data leads us to conclude that the crystalline material is a metastable high temperature phase or mixture of phases. These results also have relevance to previously reported results<sup>2</sup> on multilayer samples of Co/GdCo<sub>2</sub> which when appropriately annealed exhibited unidirectionally displaced hysteresis loops i.e. exchange biasing. The present results suggest that the microcrystalline phase reported here is similar to or identical to the "hard" magnetic phase formed in the above

multilayer samples upon annealing.

## RESULTS

Additional experiments have verified that the  $\text{GdCo}_x$  samples with unidirectionally shifted B-H loops are obtained over the composition range  $\text{GdCo}_3$  to  $\text{GdCo}_5$ . Actually the existence range extends beyond the above limits. However, samples of composition  $\text{GdCo}_2$  or  $\text{Gd}_2\text{Co}_{17}$ , the line compounds to either side of the above range do not show the shifted loops. Magnetic measurements made on the samples exhibiting shifted loops clearly show two magnetic phases. When one saturates a sample with a field greater than 200 Oe and applies a reverse field, one observes a sharp transition which accounts for 80-90% of the magnetization and a long "tail". The coercivity of the sharp transition is  $\sim 10$ -20 Oe, with the tail extending 30-100 Oe. The material corresponding to the sharp transition is exchange coupled to the "tail" material. Hence by varying the field sweep range i.e. how far out on each tail one goes, one can displace the +H transition, the -H transition, or both. Hence one can displace the loop in the +H direction, the -H direction, or obtain a higher coercivity loop centered about 0. In Fig. 1 is shown a B-H loop shifted to +H, obtained by saturating the sample in the +H direction by raising the field to +200 Oe, but going only to -30 Oe, just beyond the

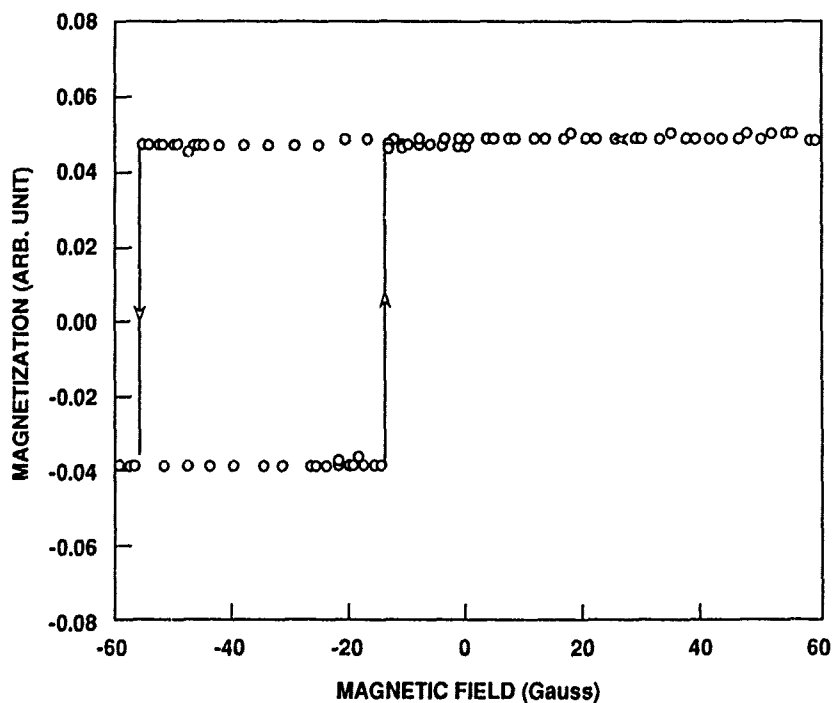


Fig. 1. Magnetization of a Gd-Co Film containing 17.7 at. % Gd. The sample was saturated in the +H direction.

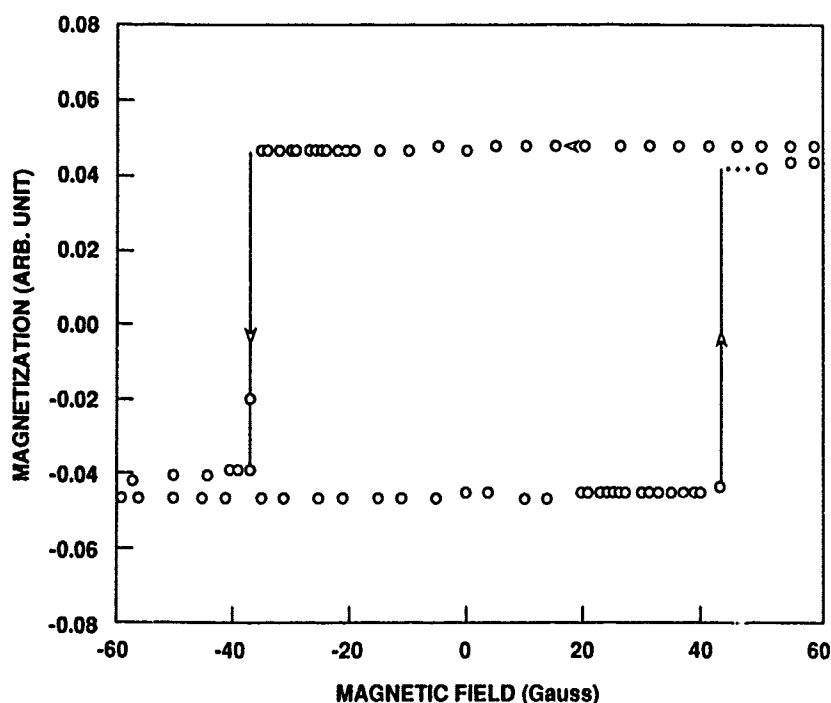


Fig. 2. Magnetization of a Gd-Co Film containing 17.7 at. % Gd. The Sample was saturated in both the +H and -H directions.

sharp portion of the transition. In Fig. 2 is shown a B-H loop for the same sample obtained by saturating in both the +H and -H directions. The composition of the sample is 17.7 at. % Gd. From the direction of the loop displacement one can infer that the "soft" phase is ferromagnetically coupled to the "hard" phase. Low temperature magnetization measurements on samples for which  $x \sim 5$  show that the coercivity of the "soft" phase monotonically increases for decreasing temperature with no increase in the exchange field until at  $T < 100\text{K}$  the material shows neither a sharp magnetic transition nor a displaced loop. Transmission electron microscopy studies have been carried out on samples whose composition varied from  $\text{GdCo}_2$  to  $\text{Gd}_2\text{Co}_{17}$ . The TEM results indicate the samples to be a mixture of amorphous and microcrystalline material over the composition range exhibiting the displaced loops. These samples appear to be two phase with structure 10-20 Å in diameter. Electron diffraction shows a broad ring characteristic of amorphous material plus sharper rings indicative of crystalline material. In Fig. 3 is shown a TEM micrograph of a sample from the same deposition run as that of the sample of Figs. 1 and 2 at a magnification of 340000 X. In Fig. 4 is the electron diffraction pattern obtained from this sample. Note the "arcs" indicative of a preferred orientation of the crystallites. A surprising result is that the crystalline diffraction pattern appears to be similar over the indicated composition range, even though the phase diagram shows several line compounds differing in crystal structure. There are, however, small differences in



Fig. 3 Transmission Electron Micrograph of Gd-Co film containing 17.7 at. % Gd.



Fig. 4 Electron Diffraction Pattern from Gd-Co film containing 17.7 at. % Gd.

the electron diffraction pattern for different samples. For example, the relative intensity of the rings vary and one ring is absent for some samples. Also the d-spacings vary somewhat with composition. The observed d-spacings index best to either the hexagonal  $\text{GdCo}_5$  (1/5) structure or a high temperature hexagonal  $\text{Gd}_2\text{Co}_{17}$  (2/17) structure for which the d-spacings have many similarities. At compositions corresponding to the compounds  $\text{GdCo}_3$  or  $\text{Gd}_2\text{Co}_7$  one does not see the strong lines peculiar to these compounds. There is in fact other evidence for a metastable high temperature phase spanning a wide composition range. Buschow and Van Der Goot<sup>3</sup> reported that in bulk samples of  $\text{GdCo}_5$  there exists above 900 C a relatively large homogeneity region extending primarily toward higher Co concentrations. Likewise, above 1200 C the 2/17 compound has an existence region extending toward lower Co concentrations. One can visualize these wide existence regions by observing that the 2/17 structure can be derived from the 1/5 structure by the ordered substitution of two Co atoms at one third of the Gd sites. Thus the ordered substitution of Co pairs for Gd atoms gives the 2/17 homogeneity range; the disordered substitution gives the 1/5 homogeneity range. Since films are quenched from high temperature it seems possible that the entire composition range from 1/5 to 2/17 could be spanned by the 1/5 metastable phase described above. Also the 1/2, 1/3, and 2/7 compounds can be obtained from the 1/5 structure by the ordered substitution of Gd for Co. If the substitution were disordered as would be possible in a high temperature phase, then one could conceive of a single metastable phase or, more accurately, a continuum of related metastable phases over this entire composition range. Of course, the symmetry and lattice parameter would vary so that the diffraction lines would shift somewhat and vary in intensity, as is observed. One point in the above discussion deserves further clarification. We stated that samples of composition near  $\text{GdCo}_2$  and  $\text{Gd}_2\text{Co}_{17}$  do not exhibit shifted B-H loops. We may have implied that they were completely amorphous with no microcrystalline phase. While the  $\text{GdCo}_2$  samples do appear to be amorphous, at least some regions of the  $\text{Gd}_2\text{Co}_{17}$  samples appear to contain microcrystalline phase. Hence there may be a more subtle explanation for the absence of displaced loops in these samples. If one examines the observed magnetic coercivities of the compounds over the composition range of interest, one finds a very suggestive result. The 1/3, 2/7, and 1/5 compounds have extremely large coercivities<sup>2</sup>: 20,000-40,000 Oe. The 2/17 compound has a relatively low coercivity<sup>2</sup> of 200 Oe. From the work of Burzo<sup>4</sup> we estimate the coercivity of the 1/2 compound to be 2500 Oe at 4.2 K. At room temperature it is likely to be smaller. Hence the absence of displaced loops in the 1/2 and 2/17 samples may be due to the absence of a microcrystalline phase or may result from a microcrystalline phase of low coercivity at these compositions. This issue will be resolved by additional annealing experiments. X-ray diffraction measurements show a single broad amorphous-like peak at about the same d-spacing as that of the electron diffraction. We have not yet been able to resolve any crystalline peaks by x-ray diffraction using a Bragg-Brentano machine. This is not too surprising when we realize that the x-rays are scattered more weakly by the small crystals than are the electrons and have a much longer wavelength. The first effect decreases the integrated intensity of the x-ray peaks relative to the electron diffraction peaks. The second effect broadens the x-ray peaks.



Both increase the difficulty of resolving the x-ray peaks. Annealing studies have been carried out on macroscopically uniform samples such as those discussed above as well as on GdCo<sub>2</sub>/Co multilayers. The annealing studies have been carried out at low temperature under isothermal conditions for longer times to emphasize low activation energy processes as well as at temperatures in the range 300-550 C for short times to emphasize high activation energy processes, using rapid thermal anneal techniques. Samples containing 17.7 at.% Gd with unidirectionally displaced B-H loops show no discernable change in magnetic properties when annealed up to four hours @100 C or up to 15 sec. at 450 C. Multilayers of Co/GdCo<sub>2</sub> have been annealed for 15 second periods at temperatures up to 550 C. Up to 300 C, no change in magnetic properties is observable. In the range 300-450 C there are small increases in coercivity. Above 450 C there are major changes including an increase in coercivity and decrease in magnetization. None of these multilayer samples have exhibited the shifted B-H loops, however.

We can summarize our results as follows: We have observed exchange-biased samples ie. unidirectionally displaced B-H loops in two different types of samples: macroscopically uniform GdCo<sub>x</sub> samples in the composition range approximately defined by 3<x<5, and multilayered samples of GdCo<sub>2</sub>/Co which have been annealed. For the former, we have a model which on a microscopic scale is two phase and consists of a magnetically "soft" amorphous phase exchange coupled to a magnetically "hard" microcrystalline phase. We believe that this "hard" microcrystalline phase is similar or identical to the "hard" phase of the annealed multilayer samples. Electron diffraction studies on the microcrystalline material seem to indicate that it consists of the same phase or very similar phases over the above composition range. The best fit to the diffraction data is to the hexagonal GdCo<sub>5</sub> structure or to a high temperature hexagonal Gd<sub>2</sub>Co<sub>17</sub> structure.

#### REFERENCES

1. A.M. Toxen, T.H. Geballe and R.M. White, J. Appl. Phys. 64, 5431 (1988).
2. D.J. Webb, A.F. Marshall, A.M. Toxen, T.H. Geballe, and R.M. White, IEEE Trans. Magn. 24, 2013 (1988).
3. K.H.J. Buschow and A.S. Van Der Goot, J. Less-Common Metals, 17,249 (1969).
4. E. Burzo, Int. J. Magn. 3, 161 (1972).

## X-RAY DIFFRACTION STUDY OF RARE EARTH EPITAXIAL STRUCTURES GROWN BY MBE ONTO $(\bar{1}\bar{1}\bar{1})$ GaAs

W.R. Bennett, R.F.C. Farrow, S.S.P. Parkin, E.E. Marinero. IBM Almaden Research Center, San Jose CA. A.P. Segmüller, IBM Thomas J. Watson Research Center, Yorktown Heights, NY.

### ABSTRACT

We report on the new epitaxial system  $\text{LaF}_3/\text{Er}/\text{Dy}/\text{Er}/\text{LaF}_3/\text{GaAs}(\bar{1}\bar{1}\bar{1})$  grown by molecular beam epitaxy. X-ray diffraction studies have been used to determine the epitaxial relationships between the rare earths, the  $\text{LaF}_3$  and the substrate. Further studies of symmetric and asymmetric reflections yielded the in-plane and perpendicular strain components of the rare earth layers. Such systems may be used to probe the effects of magnetoelastic interactions and dimensionality on magnetic ordering in rare earth metal films and multilayers.

### INTRODUCTION

In this paper we report on a new epitaxial system prepared by molecular beam epitaxy: basal plane epitaxy of Dy onto Er and visa versa. The 0.88% lattice misfit between these rare earths generates a strain distribution that depends on the relative thicknesses of the Er and Dy layers. Strain in magnetic thin films may, in general, influence anisotropy [1], magnetic moment [2], and the ordering temperature [3] of the spin system. The ability to adjust the strain in a Dy layer by altering the Er thickness in an Er/Dy/Er symmetric structure will permit the effects of strain and dimensionality on magnetic properties to be separated.

The rare earth structures are protected against oxidation and interfacial reactions with the GaAs substrate by predeposition and postdeposition of  $\text{LaF}_3$ . Epitaxy of the rare earths onto  $\text{LaF}_3$  is possible because  $\text{LaF}_3$  has hexagonal (tysonite) structure with basal plane lattice constant approximately twice as large as the basal plane lattice constants of Dy and Er. Also, the free energy of formation of  $\text{LaF}_3$  (388.0 kcal mol<sup>-1</sup> at 300 K) is greater than those for  $\text{DyF}_3$  (385.8 kcal mol<sup>-1</sup>) and  $\text{ErF}_3$  (386.2 kcal mol<sup>-1</sup>) [4] yielding negative thermodynamic driving forces for interfacial reactions such as  $\text{Dy} + \text{LaF}_3 \rightarrow \text{DyF}_3 + \text{La}$ . Despite this we find some evidence of slight interfacial fluorine exchange which will be presented in another paper in these proceedings. This fluorine exchange is possibly due to irradiation of  $\text{LaF}_3$  with 10 keV electrons and x-rays during rare earth growth.

To simplify determination of the epitaxial relationships between the GaAs,  $\text{LaF}_3$  and rare earths we first grew the single rare earth structures,  $\text{LaF}_3/\text{Dy}/\text{LaF}_3$  and  $\text{LaF}_3/\text{Er}/\text{LaF}_3$ . We present results of a variety of x-ray diffraction techniques applied to determine these epitaxial relationships. We also discuss our determination of the in-plane and perpendicular strain components in the Er/Dy/Er structure.

### SAMPLE PREPARATION

The epitaxial magnetic structures described in this paper were prepared in a molecular beam epitaxy machine (V.G. instruments V80M). The background pressures during growth were in the range  $2 \cdot 10^{-11}$  to  $5 \cdot 10^{-10}$  Torr. GaAs  $(\bar{1}\bar{1}\bar{1})$  As-faced substrates were etched in a 1:1:200 solution of  $\text{H}_2\text{O}_2:\text{NH}_4\text{OH}:\text{H}_2\text{O}$  and heat cleaned in

situ to a temperature of 550-600°C. This treatment generated a (2x2) or (1x1) Ga-stabilized surface reconstruction with surface impurities below 1% of a monolayer.

The basal plane (00.1) of  $\text{LaF}_3$  was generated by epitaxy of  $\text{LaF}_3$  on the  $(\bar{1}\bar{1}\bar{1})$  As face of GaAs. The  $\text{LaF}_3$  was deposited from an effusion source onto the substrate at 500°C, at a growth rate of 70 Å/min. The Dy and Er were deposited from electron gun evaporation sources at rates  $\approx 40$  Å/min and at a substrate temperature of 300°C. The final  $\text{LaF}_3$  was grown onto the rare earth surface at 300°C. The results described below are obtained from studies of the following three structures: 1) 400 Å  $\text{LaF}_3$ /2000 Å Dy/2500 Å  $\text{LaF}_3$ ; 2) 400 Å  $\text{LaF}_3$ /4000 Å Er/2500 Å  $\text{LaF}_3$ ; 3) 1000 Å  $\text{LaF}_3$ /1000 Å Er/500 Å Dy/2000 Å Er/500 Å  $\text{LaF}_3$ .

## RESULTS

Using a glancing incidence x-ray diffractometer (GID) [5], a  $\theta/2\theta$  in-plane scan of the  $\text{LaF}_3/\text{Dy}/\text{LaF}_3$  structure was recorded, as shown in figure 1. The angle of incidence,  $\theta$ , was measured from the  $\text{LaF}_3$   $\bar{a}_2$  axis shown in figure 2a. Using the bulk value for the planar lattice constant of  $\text{LaF}_3$  ( $a=7.1871$  Å) we expect to see the  $\text{LaF}_3$  (30.0) peak at  $2\theta = 50.77^\circ$ . The small shift in this peak position recorded in figure 1 indicates that the  $\text{LaF}_3$  is essentially unstrained ( $\approx 0.01\%$ ). The observation of a Dy peak in figure 1, at  $50.75^\circ$   $2\theta$  demonstrates that a scattering vector belonging to the (112 0) family of planes is parallel to the scattering vector for the  $\text{LaF}_3$  (30.0) plane. For simplicity we associate this Dy peak with the  $(2\bar{1}.0)$  plane. In this case, the Dy lattice and lattice vectors are rotated by  $30^\circ$  counter clockwise with respect to the  $\text{LaF}_3$  lattice, as shown in figure 2b. This relative orientation of the  $\text{LaF}_3$  and Dy basal planes gives rise to a large,  $\approx 15\%$ , misfit which explains why there is a negligible strain transfer across the interface. The Dy  $(2\bar{1}.0)$  peak is only slightly shifted from its bulk value of  $50.82^\circ$  indicating a small in-plane tensile strain in Dy  $\approx 0.1\%$ . From the linewidths, an average in-plane crystallite size of approximately 180 Å is derived for the  $\text{LaF}_3$  and Dy layers. Finally we note, from figure 1, that the GaAs (220) plane is parallel to the  $\text{LaF}_3$  (30.0) and Dy  $(2\bar{1}.0)$  planes.

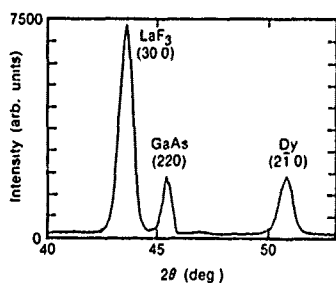


Figure 1. In-plane  $\theta/2\theta$  diffraction spectrum of  $\text{LaF}_3/\text{Dy}/\text{LaF}_3$ .

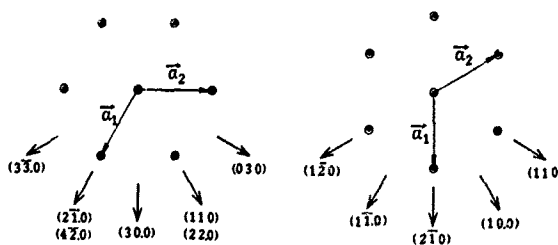


Figure 2a and 2b. Relative orientation of basal planes and crystal axes of  $\text{LaF}_3$  (left) and Dy (right) in  $\text{LaF}_3/\text{Dy}/\text{LaF}_3$ . The scattering vectors are labeled by their associated planes.

Epitaxial relationships of the  $\text{LaF}_3/\text{Dy}/\text{LaF}_3$  system are further explored by the series of in-plane diffraction studies illustrated in figure 3. In each case the diffracting angle  $2\theta$  is fixed and the sample is rotated allowing us to determine the angle between diffracting planes of the Dy and  $\text{LaF}_3$  lattice. For convenience the sample orientation is defined by  $\omega$  in such a way that, at  $\omega = 0$ , the scattering vector is parallel to the Dy lattice vector  $\vec{a}_1$ . To simplify the following analysis we illustrate, in figure 2, the relative orientation of scattering vectors in the  $\text{LaF}_3$  and Dy lattices. If we assume a fixed orientation between these lattices and the GaAs substrate we can easily predict what to expect for the in-plane diffraction studies shown in figure 3. First, setting  $2\theta = 50.75^\circ$ , as in figure 3a, isolates two families of planes: the Dy (11 0) planes, for which  $2\theta_{\text{bulk}} = 50.82^\circ$ , and the  $\text{LaF}_3$  (224 0) planes, for which  $2\theta_{\text{bulk}} = 50.77^\circ$ . From figure 2 we expect to observe Dy (21 0) at  $\omega = 0^\circ$ , Dy (11 0) at  $\omega = -60^\circ$ , Dy (12 0) at  $\omega = 60^\circ$ ,  $\text{LaF}_3$  (22 0) at  $\omega = -30^\circ$ , and  $\text{LaF}_3$  (42 0) at  $\omega = 30^\circ$ . Setting  $2\theta = 43.56^\circ$ , as in figure 3b, isolates the  $\text{LaF}_3$  (303 0) family of planes. From figure 2 we expect to observe  $\text{LaF}_3$  (30 0) at  $\omega = 0^\circ$ ,  $\text{LaF}_3$  (03 0) at  $\omega = -60^\circ$  and  $\text{LaF}_3$  (33 0) at  $\omega = 60^\circ$ . The presence of broad and narrow peaks ... figure 3b is a consequence of diffraction from the less ordered  $\text{LaF}_3$  layer (spread in orientation of  $\text{LaF}_3$  basal axes) deposited at  $300^\circ\text{C}$  superimposed on diffraction from the more highly ordered  $\text{LaF}_3$  layer adjacent to the GaAs and deposited at  $500^\circ\text{C}$ . In a similar fashion, setting  $2\theta = 28.64^\circ$  isolates the Dy (101 0) family of planes and we expect to observe Dy (10 0) at  $\omega = -30^\circ$  and Dy (11 0) at  $\omega = 30^\circ$ . Finally, setting  $2\theta = 24.73^\circ$  isolates the  $\text{LaF}_3$  (112 0) family of planes and we expect to observe  $\text{LaF}_3$  (11 0) at  $\omega = -30^\circ$  and  $\text{LaF}_3$  (21 0) at  $\omega = 30^\circ$ .

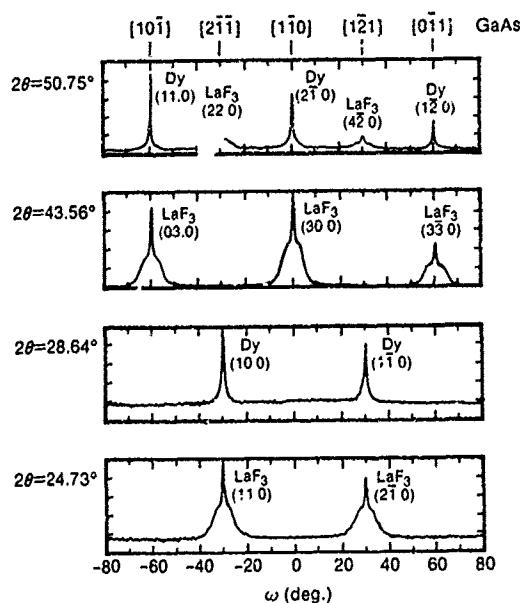


Figure 3. Several in-plane spectra of  $\text{LaF}_3/\text{Dy}/\text{LaF}_3$ . In each case  $2\theta$  is fixed and the sample azimuth varied. The crystal-line directions for GaAs are illustrated above figure 3a.

The excellent agreement between these simple predictions and the x-ray spectra demonstrate fixed orientation of the Dy and  $\text{LaF}_3$  basal planes to each other and to the GaAs surface. Data obtained from a similar scan of the  $\text{LaF}_3/\text{Er}/\text{LaF}_3$  structure are illustrated in figure 4. Comparison between figure 4 and figure 3a demonstrates the Er has the same epitaxial relationship with  $\text{LaF}_3$  and GaAs as does Dy. This is illustrated in figure 4, where  $\omega$  was defined with respect to an arbitrary axis. The large misfit,  $\approx 15\%$ , between the Er and  $\text{LaF}_3$  lattices prevent the transfer of strain across the interface, leaving the Er essentially unstrained (0.03%).

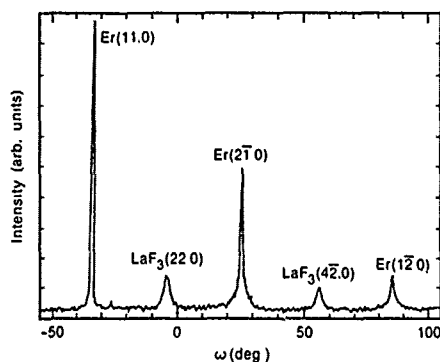


Figure 4. In-plane spectrum of  $\text{LaF}_3/\text{Er}/\text{LaF}_3$ . In this case  $\omega$  is defined with respect to an arbitrary in-plane axis.

We now consider the strain developed between the Dy and Er lattices in the  $\text{LaF}_3/\text{Er}/\text{LaF}_3$  structure. To determine the strain we must measure the angle for Bragg diffraction,  $\theta_B$ , and use  $\lambda = 2d \sin \theta_B$  to calculate the strain-modified interplanar spacing,  $d$ .

Referring to figure 5, a coordinate system is set up with  $\hat{z}$  along the axis for azimuthal rotation of the sample. The x-ray beam is directed toward the sample in the  $yz$  plane. The condition on the angle of incidence,  $\theta$ , for diffracting from the crystal plane having normal  $\hat{c}$  pointing in a direction defined by  $(\alpha, \phi)$  is:

$$\theta = \theta_1 = \theta_B - \tan^{-1}(\tan \alpha \sin \phi) \quad (1)$$

Rotating the sample about  $\hat{z}$  by  $180^\circ$  changes  $\phi$  to  $\phi + 180^\circ$  giving the new diffraction condition:

$$\theta = \theta_2 = \theta_B + \tan^{-1}(\tan \alpha \sin \phi) \quad (2)$$

By recording the diffracting angles  $\theta_1$  and  $\theta_2$ , the Bragg angle can be calculated, as can be seen from equations (1) and (2), by using  $\theta_B = (\theta_1 + \theta_2)/2$ . In the case of symmetric reflections this technique eliminates errors in determination of the Bragg angle caused by tilting of the crystal axis away from the scattering vector.

We examined the  $\text{LaF}_3/\text{Er}/\text{Dy}/\text{Er}/\text{LaF}_3$  structure with a double crystal diffractometer using  $\text{CuK}_\alpha$  radiation and a silicon monochromator operating in the (004) Bragg condition from the (001) surface. To minimize angular dispersion, the  $\text{CuK}_\alpha$  diffraction from the monochromator was blocked. We collected data from symmetric and asymmetric reflections allowing determination of the perpendicular and parallel strain components,  $\epsilon^\perp$  and  $\epsilon^\parallel$  respectively.

We first consider symmetric reflections from the Dy and Er (00.6) planes. It was necessary to use these high order planes in order to clearly separate the Dy and Er peaks. From figure 6 the angles  $\theta_1$  and  $\theta_2$  for the Dy and Er peaks can be measured (In each case the angular position of the origin of the angular shift axis is referenced to the GaAs  $(\bar{3}\bar{3}\bar{3})$  peak). Using these values in the above equations we determine  $\epsilon_{\text{Dy}}^\perp = 0.27 \pm 0.02\%$  and  $\epsilon_{\text{Er}}^\perp = -0.014 \pm 0.010\%$ . Since Dy has a larger lattice constant than Er we expect Dy to be under an in-plane compressive strain which will give a positive perpendicular strain, as observed. The Er also has the expected behavior; since it is under tensile in-plane strain the perpendicular strain is negative.

Figure 5. Coordinate system used to define the diffraction geometry. The x-ray beam incident on the origin is in the yz plane. The normal to the diffracting plane points in a direction defined by  $(\alpha, \phi)$ .

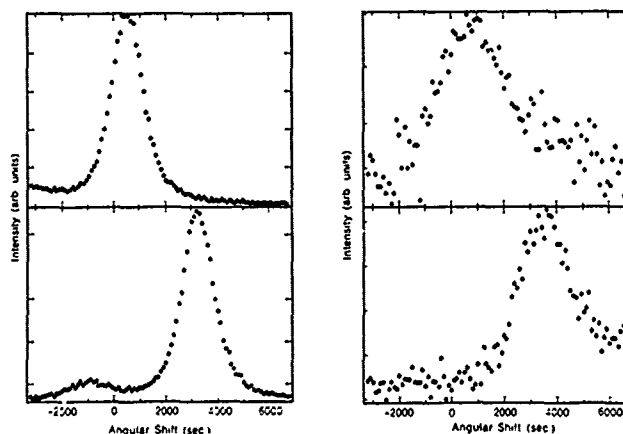
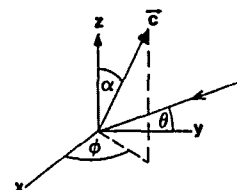


Figure 6. X-ray spectra of  $\text{LaF}_3/\text{Er}/\text{Dy}/\text{Er}/\text{LaF}_3$  taken with the scattering vector perpendicular to the sample surface. The Dy (00.6) reflection (right) and the Er (00.6) reflection (left) are taken at azimuth angles of  $\phi$  (top) and  $\phi + 180$  (bottom).

Using the same method described above we collected data for the asymmetric reflections from the Dy and Er (11.4) planes. From this data we determine the Er strain in the  $[11\bar{4}]$  direction to be  $0.05 \pm 0.02\%$ . From the Er strain in the  $[11\bar{4}]$  and the  $[00\bar{6}]$  directions we calculate the parallel component to be  $\epsilon_{\text{Er}}^\parallel = 0.16 \pm 0.06\%$ . The absence of a Dy (11.4) peak in both spectra prevents us from directly determining the Dy in-plane strain. However, from the room temperature value of Poissons ratio for  $\alpha\text{-Dy}$ ,  $\sigma = 0.247$ , we calculate using  $\epsilon^\parallel = (1-\sigma)\epsilon^\perp/(2\sigma)$  (i.e. assuming isotropic basal plane stress) that  $\epsilon_{\text{Dy}}^\parallel = -0.41\%$ . Putting these results together we see that the basal plane lattice misfit between Dy and Er has been reduced from the bulk value of 0.88% to 0.31%.

## DISCUSSION

We demonstrate basal plane epitaxy of Dy and Er onto  $\text{LaF}_3$ . Despite the small lattice misfit between the  $\text{LaF}_3$  and the rare earths we determine the rare earth lattices are rotated by  $30^\circ$  about their common c axis with respect to the  $\text{LaF}_3$ . This generates  $\approx 15\%$  lattice misfit and is, we believe, responsible for the approximately strain-free growth of the rare earths onto  $\text{LaF}_3$ .

Strain measurements demonstrate that the Er applies a compressive in-plane strain to the Dy which therefore expands along the c axis. Kwo [6] reports that films of Dy grown epitaxially between Y films exhibited a ferromagnetic transition which shifted progressively lower with film thickness. In the Y/Dy/Y case the lattice misfit is 1.6% with Dy having the smaller lattice. Coherency strain would then induce an in-plane tension of Dy and a perpendicular compressive strain. Hence, in Y/Dy/Y there exists a built in coherency strain which opposes the c-axis expansion required for ferromagnetic ordering. This can be expected to depress the magnetic transition, as Kwo [7] finds. In our case the Dy c-axis strain aids the expansion required for ferromagnetic ordering. An increase in the ordering temperature of Dy in Er/Dy/Er over its bulk value is reported elsewhere in these proceedings [8]. This increase in ordering temperature of Dy under tensile c-axis strain is consistent with the observed trend in Y/Dy/Y. Further experiments are planned to uniquely define the role magnetoelastic interactions play in the magnetic properties of Dy.

## REFERENCES

1. G.F. Dionne, *Mater. Res. Bull.* 6, 805 (1971).
2. O.K. Andersen, J. Madsen, U.K. Poulsen, O. Jepsen, and J. Kollar, *Physica B + C* 86-88, 249 (1977).
3. B. Coqblin, *The Electronic Structure of Rare-Earth Metals and Alloys: The Magnetic Heavy Rare Earths* (Academic, New York, 1977).
4. L.B. Pankratz, *Thermodynamic Properties of Halides*, Bulletin 674, United States Department of the Interior, Bureau of Mines.
5. A. Segmüller, I. Noyan, V.S. Speriosu, *Progress in Crystal Growth*, (1988).
6. R. Ludeke in "Thin Film Growth Techniques for Low-Dimensional Structures," ed. by R.F.C. Farrow, S.S.P. Parkin, P.J. Dobson, J.H. Neave, A.S. Arrot, *Nato ASI Series B* 163, 319 (1987).
7. J. Kwo in "Thin Film Growth Techniques for Low-Dimensional Structures," ed. by R.F.C. Farrow, S.S.P. Parkin, P.J. Dobson, J.H. Neave, A.S. Arrot, *Nato ASI Series B* 163, 337 (1987).
8. R.F.C. Farrow, S.S.P. Parkin, V.S. Speriosu, A.P. Segmüller, Paper presented at MRS Spring Meeting, 1989. Symposium G. *Mat. Res. Soc. Symp.* 151 (1989).

## HCP-FCC TRANSITION IN EPITAXIAL Co-Cu SUPERLATTICES

F. J. LAMELAS, C. H. LEE, HUI HE, W. VAVRA, and ROY CLARKE  
 Department of Physics, The University of Michigan, Ann Arbor,  
 MI 48109

## ABSTRACT

A series of epitaxial Co-Cu superlattices has been grown on GaAs (110) substrates by molecular beam epitaxy. Detailed analysis of x-ray diffuse scattering scans along Co (10 $\bar{1}l$ ) reveals a crossover from the bulk hcp phase of Co to metastable fcc stacking. Our measurements indicate a strong correlation between structural symmetry and the magnetic anisotropy in Co - noble metal superlattices. In particular, the perpendicular easy axis of magnetization onsets at Co layer thickness  $\lesssim 19$  Å in Co<sup>hcp</sup>-Au compared to only  $\sim 11$  Å in Co<sup>fcc</sup>-Cu.

## INTRODUCTION

One of the most recent and exciting applications of molecular beam epitaxy (MBE) is to grow structures which are stabilized in phases that have no counterpart in the bulk under ambient thermodynamic conditions. The growth and properties of such metastable structures are particularly interesting in the context of novel magnetic materials [1].

In this paper we report on our observation of a crossover from the bulk hcp structure of cobalt to fcc stacking in a Co-Cu superlattice with ultrathin Co layers. We show that stacking coherence of the superlattices improves markedly in the ultrathin regime and conclude that the observed change in crystalline symmetry is the likely cause of dramatic differences in the magnetic anisotropy between fcc and hcp ultrathin Co layers.

## EXPERIMENTAL DETAILS

Samples of Co-Cu superlattices were prepared in a Vacuum Generators VG-80 MBE system on annealed GaAs (110) substrates held at 50 °C. A growth orientation along close-packed planes was established by the deposition of a buffer layer consisting of 20 Å Co followed by 200 Å Cu. The Co layer, which probably grows as (110) bcc Co [2], is essential as a bridge between mismatched (110) GaAs and (111) Cu.

After growing the buffer layer, sequential layers of Co and Cu were deposited. The rate of deposition was  $0.5 \pm 0.05$  Å/sec for Cu (from a Knudsen cell at 1260 °C) and  $0.3 \pm 0.1$  Å/sec for Co (from an electron beam hearth). Six samples were prepared with Co layer thicknesses of 5, 10, 15, 20, 30, and 40 Å, accurate to  $\pm 10\%$ . In each sample the Co layers were alternated with Cu layers of nominally constant thickness  $25 \pm 3$  Å. The total superlattice thickness was approximately 1500 Å in all cases. Finally, a protective 20 Å Au cap was grown on the top Cu layer of the superlattices. X-ray measurements were performed on a Huber 4-circle diffractometer using a 12 kW Rigaku x-ray source (MoK $\alpha$ ,  $\lambda \sim 0.71$  Å).



## RESULTS AND DISCUSSION

Reflection high energy electron diffraction (RHEED) patterns observed after the growth of the final Cu layer indicated that the films consist of well oriented close-packed planes. We note that one cannot distinguish (111) fcc growth from (0001) hcp growth with the RHEED technique. Information complementary to that contained in the RHEED patterns is provided by the map of the in-plane x-ray scattering intensity shown in Fig. 1. As described previously [3] this type of x-ray scan is performed in transmission and in this case the absorption of GaAs necessitates thinning the substrates to approximately  $100\mu\text{m}$  in order to allow penetration of  $\text{MoK}\alpha$  x-rays. The x-ray intensity contours of Fig. 1 confirm the orientation and epitaxially ordered nature of the superlattices indicated by the RHEED patterns. The map also determines the epitaxial relationship of the superlattice with respect to the GaAs substrate (inset). Both (111) fcc growth and (0001) hcp growth consist of the stacking of close-packed planes which exhibit six-fold rotational symmetry. Thus there are close similarities in the diffraction patterns of lattice-matched fcc and hcp crystals growing in a close-packed orientation. Specifically, the fcc  $(2\bar{2}0)$  and hcp  $(11\bar{2}0)$  reciprocal lattice points will coincide. Thus the peak labeled h  $(11\bar{2}0)$  and c  $(2\bar{2}0)$  in Fig. 1 arises from a combination of fcc and hcp scattering. We note that in contrast to the Co-Au system [4] this peak is not split.

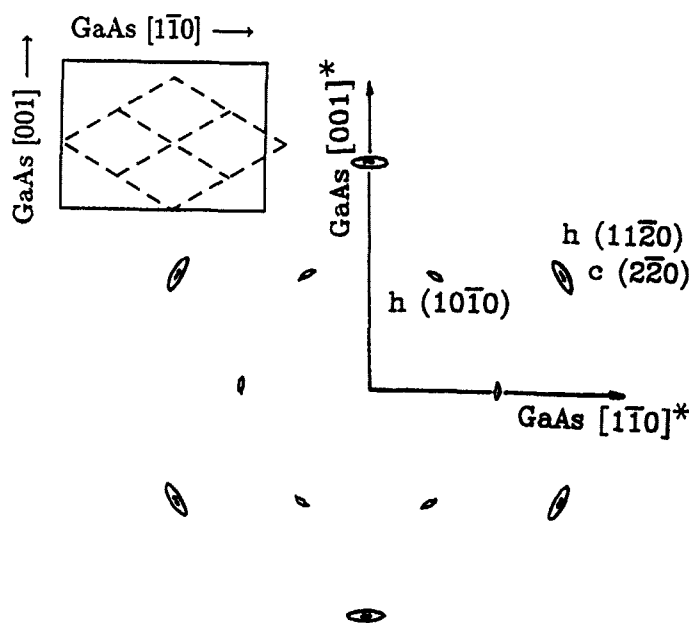


Fig. 1. In-plane scattering intensity of a  $40\text{ \AA}$  Co -  $25\text{ \AA}$  Cu superlattice. The two intensity contours are drawn at 130 and 65 c/sec. The background is approximately 60 c/sec for these scans. GaAs peaks are not included in the figure; the GaAs axes indicate the orientation of the superlattice with respect to the substrate. Inset: epitaxial relationship (in direct space) between the unit cells of the metal superlattice (dashed lines) and the GaAs substrate (solid lines).

This indicates that the Co and Cu layers are strained into coherence within the plane of the substrate. The peak labeled h ( $10\bar{1}0$ ) is due to the presence of hcp stacking. There is no fcc reflection at this reciprocal lattice point. Whereas we expect a significant contribution to the structure factor from hcp Co, the h ( $10\bar{1}0$ ) reflection is actually much weaker than one would estimate from a model containing purely hcp Co and fcc Cu layers. We therefore decided to analyze the stacking structure in detail as a function of Co layer thickness.

Whether a close-packed structure stacks according to the fcc (ABC...) sequence or the hcp (AB...) sequence is revealed by x-ray scans along ( $10\bar{1}\ell$ ), or by similar scans parallel to  $c^*$  subject to the condition that  $h - k \neq 3m$ , where  $m$  is an integer. Diffraction intensities where  $h - k = 3m$  are unaffected by the hcp-fcc transition [5]. Fcc periodicity is revealed by peaks which occur at  $k_{c^*} = \pm 2\pi/3d_{111} \text{ \AA}^{-1}$  along ( $10\bar{1}\ell$ ), while hcp periodicity is revealed by peaks at  $\pm 2\pi/2d_{0001} \text{ \AA}^{-1}$  as well as at ( $10\bar{1}0$ ).

In order to interpret the x-ray data quantitatively it is necessary to employ a model which gives x-ray intensities for varying distributions of stacking sequences of close-packed planes. Models treating *random* distributions of stacking faults in hcp lattices predict a broadening of hcp peaks without the appearance of fcc peaks. We analyze our data using the model of Sebastian and Krishna (SK) [6] who treat the insertion of *correlated* fcc regions into an hcp matrix. In their model they consider the hcp to fcc transition to occur by a random insertion (nucleation) of faults in an hcp crystal, followed by growth at these sites into fcc domains by the occurrence of stacking faults at every alternate set of planes. This arrangement of stacking faults transforms hcp to fcc stacking symmetry. The SK model includes three parameters: the level of random growth faults in the parent hcp crystal, the probability of fcc crystal nucleation, and the probability of continued growth at a nucleation site. In Fig. 2 we plot the x-ray intensity measured along ( $10\bar{1}\ell$ ) together with the profile predicted by the SK model.

In addition to revealing the stacking form of the Co layers, the ( $10\bar{1}\ell$ ) scans provide a measure of the stacking coherence length within the superlattice. In Fig. 3 we plot  $2\pi/\Delta_q$  vs. Co layer thickness, where  $\Delta_q$  is the measured FWHM of the fcc peak in the ( $10\bar{1}\ell$ ) scan; here  $2\pi/\Delta_q$  provides an estimate of the distance over which atomic planes are coherently stacked according to the fcc sequence. An interesting finding here is that the fcc stacking coherence increases dramatically for Co layer thickness  $\lesssim 20 \text{ \AA}$ . Note that for the  $10 \text{ \AA}$  Co superlattice the stacking order is maintained across neighboring Co layers. That is, in addition to the excellent coherence of Co and Cu lattices within the growth plane indicated by Fig. 1, a high degree of stacking order extends in the growth direction as well, as shown by the narrow fcc peak widths in Fig. 2. In Fig. 3 we also include a plot of the ratio of hcp to fcc peak intensities as a function of Co layer thickness [7].

We turn now to discuss the origin of the hcp-fcc crossover in these superlattices. The stabilization of fcc phases of Co and Fe by epitaxial growth on substrates such as (001) Cu is well known [8] and can be understood in terms of the cubic symmetry of the substrate plane. It is less clear why fcc Co would be favored by a stacking arrangement of close-packed layers in a superlattice. One possible explanation [9] relates to the existence of oscillatory potentials at the interfaces of bi-metallic superlattices. As the modulation period in a superlattice is reduced (to  $\lesssim 10$  monolayers) the overlap of Friedel-like potentials of stacking faults close to the interfaces can lead to a situation

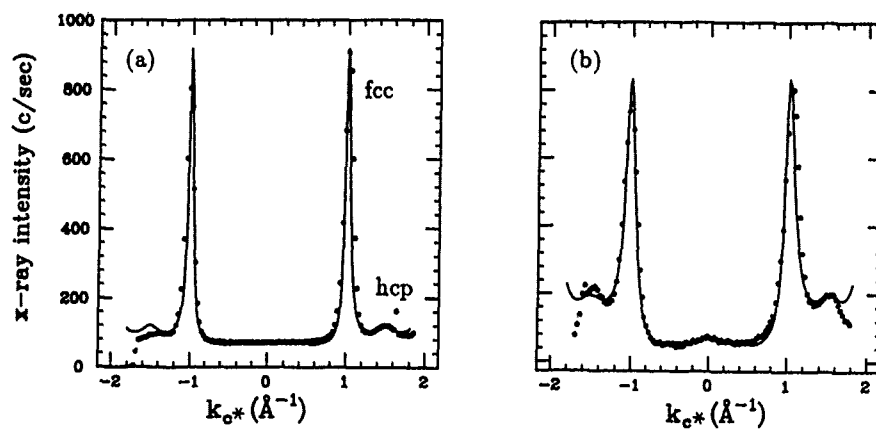


Fig. 2. X-ray scattering intensities along  $(10\bar{1}\ell)$ . Fcc reciprocal lattice points are located at  $\sim \pm 1 \text{\AA}^{-1}$  and hcp points occur at zero and  $\sim \pm 1.5 \text{\AA}^{-1}$ . The data are given by points and the solid line is the fit obtained with the model of Sebastian and Krishna [6]. (a) Sample with 10 Å Co layers. (b) Sample with 40 Å Co layers.

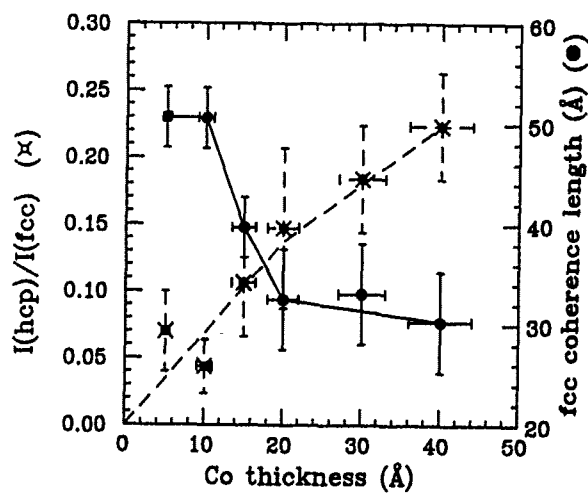


Fig. 3. Intensity ratios of the fcc and hcp peaks in the  $(10\bar{1}\ell)$  scan and coherence lengths estimated from the widths of the fcc peaks, both plotted as a function of Co layer thickness.

whereby a fault occurs on every alternate atomic plane converting hcp to fcc or *vice versa*. Our findings are consistent with such a model: the crossover to fcc stacking is gradual and, moreover, the coherence length of the fcc regions increases dramatically as the Cu-Co-Cu interface separation is reduced below  $\sim 20$  Å.

Finally we discuss some consequences of the hcp - fcc crossover for the magnetic behavior of Co - noble metal superlattices. Fig. 4 shows a significant difference in magnetic anisotropy between the (hcp Co)-Au and the predominantly fcc Co-Cu superlattices reported here. It is clear that the Co-Cu superlattices undergo the crossover to a perpendicular easy axis (indicated by  $\lambda K_{eff} > 0$ ) at a significantly lower Co thickness than the Co-Au superlattices. While this difference may be influenced by other factors, including the roughness of the Co-noble metal interface, we believe that the most plausible explanation is the difference in magnetocrystalline anisotropy present in the two systems. We have fitted out-of-plane (00 $\ell$ ) x-ray scans with a model which mimics interfacial penetration [10] and we obtain similar estimated interface thicknesses for Co-Cu and Co-Au superlattices (approximately 2 monolayers). Moreover, the equilibrium phase diagrams of Co-Cu and Co-Au are quite similar; in both cases mutual insolubility of Co and the noble metal favors the formation of sharp interfaces, as observed.

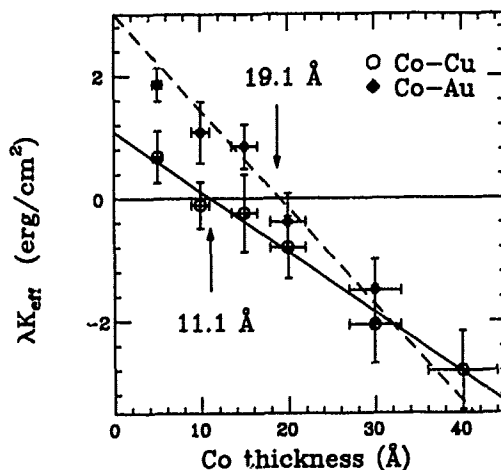


Fig. 4. Perpendicular magnetic anisotropy *vs.* Co thickness, showing crossover thickness of 11.1 Å Co and 19.1 Å Co for Co-Cu and Co-Au superlattices respectively. A perpendicular easy axis of magnetization is indicated by  $\lambda K_{eff} > 0$ , while a parallel easy axis is indicated by  $\lambda K_{eff} < 0$ . Data derived from magnetization measurements performed at 300 K.

## CONCLUSIONS

In summary, we have demonstrated the growth of epitaxial Co-Cu superlattices in which the Co atoms are predominantly arranged with cubic, rather than hcp symmetry. This transition in Co stacking occurs through the influence of the Cu layers which form a single coherent structure with the Co layers. Finally, we show that the contrasting stacking symmetry of Co planes in Co-Cu and Co-Au superlattices is the most likely cause of the different perpendicular magnetic anisotropies which are encountered in these two systems.

## ACKNOWLEDGEMENTS

We would like to thank C. Orme, B. Rodricks, and S. Swaminathan for their help during the course of this work.

The research was supported in part by NSF MRG Grant DMR-8602675 and NSF Low Temperature Physics Grant DMR-8805156. One of us (F.L.) was supported by an ARO fellowship under grant DAAL-03-86-G-0053.

## REFERENCES

1. For a review, see *Thin Film Growth Techniques for Low-Dimensional Structures*, edited by R. F. C. Farrow, S. S. P. Parkin, P. J. Dobson, J. H. Neave, and A. S. Arrott, (Plenum, New York, 1987).
2. G. A. Prinz, *Phys. Rev. Lett.* **54**, 1051 (1985).
3. F. Lamelas, Hui He, and Roy Clarke, *Phys. Rev. B* **38**, 6334 (1988).
4. C. H. Lee, Hui He, F. Lamelas, W. Vavra, C. Uher, and Roy Clarke, *Phys. Rev. Lett.* **62**, 653 (1989).
5. R. Gevers, *Acta Cryst.* **7**, 337 (1954).
6. M. T. Sebastian and P. Krishna, *Phys. Stat. Sol. (a)* **101**, 329 (1987).
7. The increase of this ratio with Co thickness would occur even in the case of purely hcp Co layers, however we note that the slope of the curve would be nearly an order of magnitude higher.
8. W. A. Jesser and J. W. Matthews, *Phil. Mag.* **17**, 461 (1968).
9. Andrew C. Redfield and Andrew M. Zangwill, *Phys. Rev. B* **34**, 1378 (1986).
10. Hui He, F. J. Lamelas, C. H. Lee, W. Vavra, and Roy Clarke, (to be published).

THIN-FILM  $\text{Gd}_4\text{Bi}_3$  GROWN ON A GLASS SUBSTRATE

KYUYA BABA, H. ISHII, I. YAMAGUCHI, O. NAKAMURA, and T. TAKEDA  
 Hachioji Research Center, Casio Computer Co. Ltd.,  
 2951-5 Ishikawa-cho, Hachioji, Tokyo 192, Japan

## ABSTRACT

Sputtered thin-films of Gd-Bi (4:3 in atomic ratio) were annealed in vacuum under various annealing conditions. The samples annealed at a temperature near  $530^\circ\text{C}$  and 4 hours contained 40% of poly-crystalline  $\text{Gd}_4\text{Bi}_3$  phase, which is of the anti- $\text{Th}_3\text{P}_4$  structure. The main peak in the x-ray diffraction spectrum due to  $\text{Gd}_4\text{Bi}_3$  is of (310). The phase of  $\text{Gd}_4\text{Bi}_3$  was not found for a lower annealing temperature; for a higher annealing temperature (above  $550^\circ\text{C}$ ), this phase could not be observed, because other phases or structures were beginning to grow, e. g.  $\text{Gd}_5\text{Bi}_3$  and/or  $\text{GdBi}$  phases.

The Curie temperature of the  $\text{Gd}_4\text{Bi}_3$  thin-films was estimated to be about 330 K; this value is nearly the same as that of bulk  $\text{Gd}_4\text{Bi}_3$ . The residual resistance of the  $\text{Gd}_4\text{Bi}_3$  thin-films was several times as large as that of bulk  $\text{Gd}_4\text{Bi}_3$  poly-crystal.

## INTRODUCTION

Thin-films of rare-earth compounds are very attractive from the point of view not only of fundamental physics but also of applied physics. Within these rare-earth compounds,  $\text{Gd}_4\text{Bi}_3$  and  $\text{Gd}_4\text{Sb}_3$  are ferromagnetic semimetals with Curie temperature in room temperature region, about 340K and 260K, respectively, and the crystallographical structure of these compounds is anti- $\text{Th}_3\text{P}_4$  structure [1][2][3]. The subject of this investigation is to seek the most adequate annealing condition for obtaining a  $\text{Gd}_4\text{Bi}_3$  thin film on a glass substrate.

We report the magnetism and the transport property of thin-film of  $\text{Gd}_4\text{Bi}_3$  grown on a fused quartz substrate with methods of both sputtering and low temperature annealing.

## SAMPLE PREPARATION

A thin-film (TF) of Gd-Bi is deposited on a glass substrate with an rf sputtering apparatus (for details, see Ref.[4]). A sample holder is rotated with the rotational speed of about 10 rpm. The targets are of fused Gd of 99.9 wt.% in purity (oxygen content is 0.1 wt.%) and of fused Bi of 99.9 wt.% in purity. The sputtering is carried out at room temperature in argon-gas atmosphere at pressures below  $1.1 \times 10^{-3}$  Torr (base pressure  $4.0 \times 10^{-7}$  Torr), and the plasma powers are set so as to get 4:3 in atomic ratio of Gd and Bi.

Without being exposed to air after deposition, the samples are annealed at different temperatures ( $T_a$ ) and times ( $t_a$ ) in the sputtering chamber. As is well known, Gd-bismuthides are much more sensitive to air compared with other Gd-pnictides, and thus the  $\text{Gd}_4\text{Bi}_3$  thin-films are oxidized in air in several seconds. We passivated Gd-Bi TF with Gd over-coat after annealing treatment.

## EXPERIMENT AND DISCUSSION

X-ray diffraction measurement

The x-ray diffraction spectra obtained for samples 1, 2, and 3 are shown in Figure

1, as an example. The annealing conditions of samples 1, 2, and 3 are  $t_a=2, 8,$  and  $16$  hours, respectively, and  $T_a=525^\circ\text{C}$ .

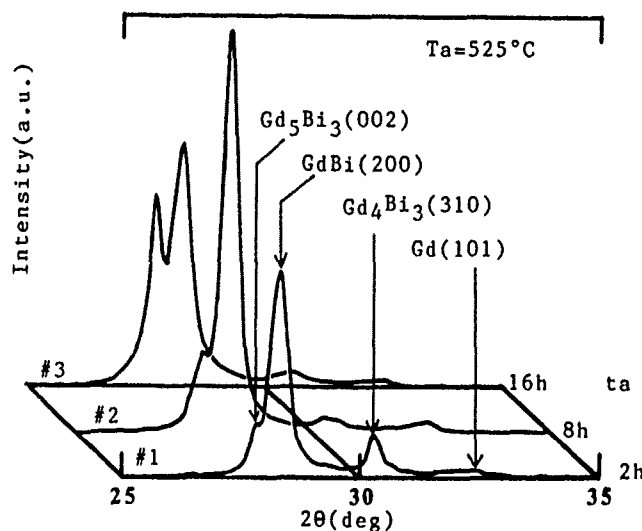


Fig. 1. X-ray diffraction spectra. The annealing conditions of samples 1, 2, and 3 are  $t_a=2, 8,$  and  $16$  hours, respectively, and  $T_a=525^\circ\text{C}$ .

These samples are not of single phase of  $\text{Gd}_4\text{Bi}_3$  but mixtures of  $\text{Gd}_4\text{Bi}_3$ ,  $\text{Gd}_5\text{Bi}_3$  and  $\text{GdBi}$  phases. Observed Miller indices of each structure are (310) for  $\text{Gd}_4\text{Bi}_3$ , (002) for  $\text{Gd}_5\text{Bi}_3$  and (200) for  $\text{GdBi}$ . Because of preferred orientation, these peaks and those higher order peaks are only observed. The coexistence of these three phases are not expected from the equilibrium phase diagram, but are typically observed in sputtered Gd-Bi TF. For longer annealing time, (310)-peak for  $\text{Gd}_4\text{Bi}_3$  is decreasing and (002)-peak for  $\text{Gd}_5\text{Bi}_3$  and (200)-peak for  $\text{GdBi}$  are increasing. Reproducibility of detailed change in x-ray diffraction spectrum is not so good, but this change is qualitatively the same for all samples. This may be the limitation of sputtering method. Most adequate condition found for obtaining  $\text{Gd}_4\text{Bi}_3$  phase is found that annealing temperature is about  $530 \pm 10^\circ\text{C}$  and annealing times are 2-5 hours. Note that this temperature is very low compared with the incongruent melting point of  $\text{Gd}_4\text{Bi}_3$ , just below which the samples of bulk are usually prepared.

#### Magnetic and transport properties

The magnetization of Gd-Bi TF is measured with a vibrating-sample magnetometer (VSM) (for details, see Ref.[4]). Measurement is done on the magnetization parallel to the sample surface.

In observed  $M$ - $H$  curves, small remanent magnetizations ( $M_r$ ) are found in the tem-

perature region of ferromagnetic ordering. The value of  $T_C$  was determined as a temperature, at which this  $M_r$  vanished by extrapolation below  $T_C$ . Figure 2 shows  $M_r$  versus temperature (measurement is done for  $H_{max}=1\text{kOe}$ ), and  $T_C$  is determined to be about 329K, which is almost the same as the value for bulk  $\text{Gd}_4\text{Bi}_3$  (332 to 340 K [5]). Note that  $M_r$  is linearly decreasing below  $T_C$  and decreases like square root near  $T_C$ .

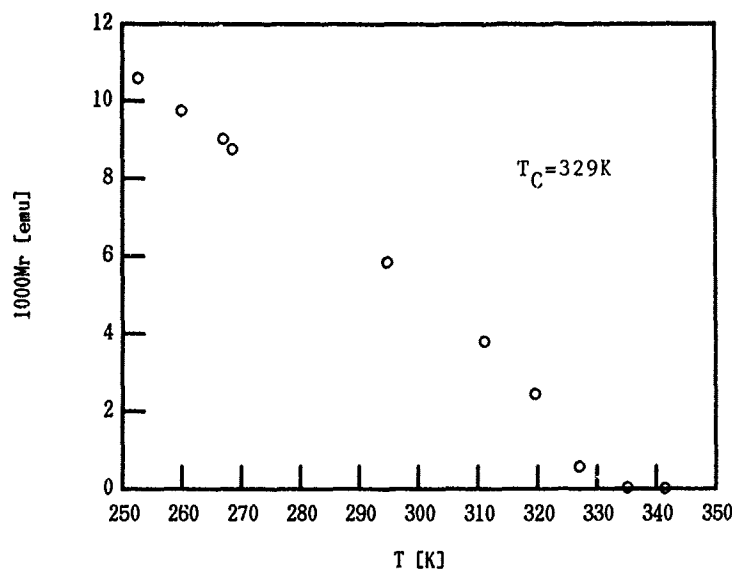


Fig. 2. Remanent magnetization versus temperature.

From the x-ray diffraction measurement Gd-Bi TF is not a single phase of  $\text{Gd}_4\text{Bi}_3$ , so we have estimated the extent of  $\text{Gd}_4\text{Bi}_3$  phase in the present Gd-Bi TF with the aid of a molecular field approximation. The result obtained in this scheme is coincident with that from x-ray diffraction analysis, qualitatively, that is, variation of integral intensity of (310)-peak for  $\text{Gd}_4\text{Bi}_3$  by the annealing corresponds to the change in the magnetically determined composition of  $\text{Gd}_4\text{Bi}_3$ .

Figure 3 shows representative shape of the temperature dependence of electrical resistance of Gd-Bi TF together with that of bulk  $\text{Gd}_4\text{Bi}_3$  [5], the values are subtracted by residual resistance, and normalized at  $T=300\text{K}$  (the residual resistance of the TF is several times as large as bulk value). Qualitative behavior of electrical resistance of the TF is the same as that of bulk  $\text{Gd}_4\text{Bi}_3$ , i.e. there is extreme point below  $T_C$  and point of inflection at  $T_C$ . However, the extreme point move into lower temperature than that of bulk  $\text{Gd}_4\text{Bi}_3$ , i.e., about 250K for Gd-Bi TF and about 280K for bulk  $\text{Gd}_4\text{Bi}_3$ . It is obvious that the dominant part of resistive behavior of Gd-Bi TF is due to  $\text{Gd}_4\text{Bi}_3$ . It is not still understood details of temperature dependence of resistance even for bulk  $\text{Gd}_4\text{Bi}_3$ , so further experimental and theoretical investigations are needed.



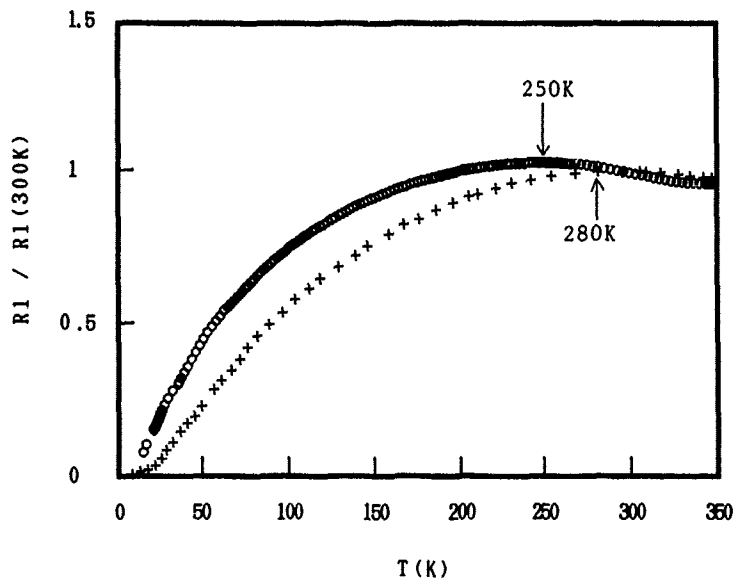


Fig. 3. Resistance as functions of temperature. The values are subtracted by residual resistance and normalized at  $T=300$  K. The open circle shows the data of Gd-Bi TF and the cross shows the values of bulk  $Gd_4Bi_3$  [5].

## CONCLUSION

It was clarified that, although single phase of  $Gd_4Bi_3$  had not been obtained yet in the most adequate condition and the sample contained  $Gd_3Bi_3$  and  $GdBi$  phases, more than 40% of  $Gd_4Bi_3$  phase is obtainable. This result suggests that we can supply  $Gd_4Bi_3$  TF in a very simple way, which is of  $T_C$  near room temperature.

The structural change in sputtered thin-films occurred in the annealing process is not easily expected from the binary phase diagrams for Gd-Bi reported by several authors. The mechanism of the formation of the  $Gd_4Bi_3$  phase in the thin-film samples in the annealing process is required to be clarified.

Detailed behavior of resistance is still not understood even for bulk  $Gd_4Bi_3$ , so further experimental and theoretical investigations are in necessity.

## ACKNOWLEDGMENTS

The authors would like to thank Prof. T. Suzuki, Tohoku University, Sendai, Japan, for valuable discussions and preparation of bulk samples of Gd-bismuthide and Dr. K. Takegahara, Tohoku University, Sendai, Japan, for the calculation of band structures for rare-earth pnictides, especially for  $Gd_4Bi_3$ .

## REFERENCES

1. D. Hohnke and E. Parthe, *Acta Cryst.* 21, 435 (1966).
2. R. J. Gambino, *J. Less-Common Metals*, 12, 344 (1967).
3. K. Yoshihara, J. B. Taylor, L. D. Calvert, and J. G. Despault, *J. Less-Common Metals*, 41, 329 (1975).
4. O. Nakamura, K. Baba, H. Ishii, and T. Takeda, *J. Appl. Phys.* 64, 3614 (1988).
5. F. Holtzberg, T. R. McGuire, S. Methfessel, and J. C. Suits, *J. Appl. Phys.* 35, 1033 (1964).

## Author Index

- Abraham, D.L., 59  
 Araki, Satoru, 123  
 Arrott, A.S., 177  
 Avci, Recep, 65  
  
 Baba, Kyuya, 289  
 Baibich, M.N., 43  
 Barthelemy, A., 43  
 Baumgart, P., 199  
 Bennett, W.R., 277  
 Bezing, A., 203  
 Broto, J.M., 43  
  
 Cabanel, R., 43  
 Cai, Qing, 65  
 Cargill III, G.S., 231, 249  
 Cebollada, A., 117  
 Celinski, Z., 177  
 Celotta, R.J., 49, 193  
 Clarke, Roy, 111, 283  
 Cochran, J.F., 177  
 Cohen, P.I., 213  
 Creuzet, G., 43  
  
 Dahlberg, E. Dan, 213, 219  
 de Gronckel, H.A.M., 243  
 deJonge, W.J.M., 171, 243  
 den Broeder, Frits J.A., 105  
 Dieny, B., 35, 117  
 Dohnomae, Hitoshi, 123  
 Dowben, P.A., 71  
 Dragoset, R.A., 193  
  
 Eltink, S.J.E.A., 171  
 Etienne, P., 43  
  
 Farrow, R.F.C., 203, 277  
 Fert, A., 43  
 Fillion, G., 117  
 First, P.N., 193  
 Florczak, Jeffrey M., 213  
 Friederich, A., 43  
 Furdyna, J.K., 129  
  
 Gallego, J.M., 117  
 Gavigan, J.P., 35, 259  
 Gay, Jack G., 3  
 Givord, D., 259  
 Gunshor, R.L., 141  
 Güntherodt, G., 199  
 Gutierrez, C.J., 11, 17  
  
 Hagstrom, S.B., 271  
 Hao, Xin, 167  
 Harzer, J.V., 199  
  
 He, Hui, 111, 283  
 Heinrich, B., 177  
 Hillebrands, B., 199  
 Hopkins, A., 271  
 Hopster, H., 59  
 Hosoi, Nobuyoshi, 87  
 Hoving, Willem, 105  
  
 Ishii, H., 289  
  
 Jaccarino, V., 225  
 Jonker, B.T., 23, 151  
  
 Kay, Eric, 77  
 King, A.R., 225  
 Kobayashi, M., 141  
 Kolodziejewski, L.A., 141  
 Kopinga, K., 243  
 Krebs, J.J., 23, 151  
 Kuiper, Dick, 105  
 Kuznia, J.N., 213  
  
 LaGraffe, D., 71  
 Lamelas, F., 111, 283  
 Lapeyre, Gerald J., 65  
 Lee, C.H., 111, 283  
 Lequien, S., 43  
 Li, Z.G., 253  
 Lienard, A., 259  
 Liu, X., 151  
 Lottis, Daniel K., 219  
 Lui, M., 225  
  
 Marinero, Ernesto E., 249, 277  
 Martinez, J.L., 117  
 Maurer, M., 99  
 Mayer, S.H., 11, 17  
 Meservey, R., 167  
 Mibu, Ko, 87  
 Michelutti, B., 259  
 Moodera, J.S., 167  
 Myrtle, K., 177  
  
 Nagakubo, M., 29  
 Nakamura, O., 289  
 Naoe, M., 29  
 Nuzmikko, A.V., 141  
  
 Ogawa, Shinichi, 87  
 Okuyama, Tetsuo, 123  
 Onellion, M., 71  
 Otsuka, N., 141  
 Ounadjela, K., 43  
 Ousset, J.C., 99

Pappas, D.P., 59  
Parkin, S.S.P., 203, 277  
Petrou, A., 151  
Piecuch, M., 99  
Pierce, D.T., 49, 193  
Prinz, G.A., 23, 151, 213, 219

Qiu, Z.Q., 17

Ravet, M.F., 99  
Rebouillat, J.P., 35, 117, 259  
Richter, Roy, 3  
Robinson, Clifford, 249  
Ryan, P.J., 213

Salamanca-Young, L., 151  
Samant, Mahesh G., 249  
Samarth, N., 129  
Sanchez, J.P., 99  
Scheinfein, M.R., 49  
Segmüller, A.P., 203, 277  
Shinjo, Teruya, 87, 123  
Sickafus, K., 253  
Smith, David J., 253  
Snider, G.L., 225  
Souche, Y., 259  
Speriosu, V.S., 203  
Stroschio, Joseph A., 193  
Swagten, H.J.M., 171  
Swuste, C.H.W., 243

Takahata, Tsutomu, 123  
Takeda, T., 289  
Tang, H., 17  
Toxen, A.M., 271  
Tuszyński, J.A., 265

Uher, C., 111  
Unguris, J., 49  
Urquhart, K.B., 177

Van Dau, F. Nguyen, 43  
Vavra, W., 111, 283

Walker, J.C., 11, 17  
White, R.M., 213, 271  
Wowchak, A.M., 213

Yamaguchi, I., 289  
Yamamoto, T., 29

Zhong, Q.M., 177

## Subject Index

- ablation
  - rate, 260
  - threshold, 259
- Al, target, 259
- amorphous
  - alloys, 93
  - films, 271
- anisotropy, 243-44, 271
  - energy, 117
  - interface, 105
  - large 4th order, 177
  - magnetic, 105, 111, 177, 199, 219-20, 243, 283
  - magnetocrystalline, 287
  - perpendicular, 87, 111, 123, 177
  - shape, 93
  - spin, 3
  - surface and interface, 105, 123, 177
  - temperature effects, 3
  - uniaxial, 35, 177
  - volume, 128
- annealing, 289
- anomalous dispersion, 231
- antiferromagnetism, 35, 45
  - coupling, 117
  - insulator films, 225
  - superstructure, 48
- artificial superstructures, 87
- atomic
  - layer epitaxy (ALE), 130
  - scale characterization, 231
- Au, 123
  - Au/3d-metal, 123
  - Au/Co, 125
  - Au/Fe, 125
  - Au/Ni, 125
  - target, 259
  - texture, 127
- Auger spectroscopy (AES), 178
- Bragg reflection, 125
- Bragg's law, 232
- Brillouin
  - Light Scattering (BLS), 178
  - paramagnetic behavior, 154
  - spectroscopy, 199
- buffer layer, 127
- capacitance, interdigitated, 225
- Co
  - bcc (110), 283
  - Co/Au, 111
  - Co/Cu, 283
  - Co/Gd, 271
  - Co/Pd, 105, 243, 247
  - films, 65
- coercive force, 249
- compensation temperature, 88
- critical
  - angles, 233
  - behavior, 225
  - points, 265
- crystal
  - cubic, 35
  - defects, 177
  - interactions, 29
  - interface, 125
- crystallite orientation, 29
- Cu, target, 259
- Curie temperature, 289
- deposition rate, 260
- dilute magnetic semiconductor (DMS), 129, 151, 171
- dislocation
  - density, 156
  - misfit, 116
- dispersion, anomalous, 231
- domain, 49
  - spiral structures, 265
  - walls, 49
- Dy, 204, 277
- dynamical scattering, 238
- electron microscopy, high
  - resolution, 253
- energy loss, 59
- epitaxy, 105, 213, 277
  - Fe/GaAs (110), 193
  - film, 203, 225
  - growth, 129, 177
  - molecular beam, 11, 17, 99, 111, 129, 151, 177, 277, 283
  - relationships, 237
  - tilted, 203
- equations of state, 265
- Er, 205, 277
- EuS, 167
- EXAFS, 249
- exchange, 271
  - coupling, 157
  - d-d, 131
  - electron interactions, 71
  - energy, 117
  - exchange-biased phase, 271

- ion-ion exchange parameters, 151
- nearest neighbor, 265
- scattering, 59
- splitting, 71
- sp-d exchange, 129
- weakening of coupling, 77
- e-beam evaporator, 199
- Fe, 3
  - bcc Fe(001)/Ag(001), 177
  - bcc Fe/GaAs(110), 193
  - clusters, 194-95
  - Fe/Ag(001), 23
  - Fe/Ag/GaAs(001), 203
  - Fe/Al, 29
  - Fe/Cu, 3
  - Fe/Dy, 88
  - Fe/GaAs, 193
  - Fe/GaAs(110), 193-94, 197
  - Fe/Mg, 89
  - Fe/Nd, 88
  - Fe/Ni(001) bilayers on Ag, 177
  - Fe/Ru, 99
  - FeSe, 153
  - Fe/Y, 88
  - films, 65, 195, 197
    - (110), 219-20
  - hcp Fe/Ru, 99, 103
  - layers, 23
  - Mössbauer transmission
    - spectroscopy, 89
    - pure amorphous, 89
  - ferromagnetic resonance (FMR), 178
  - ferromagnetism
    - alloys, 48
    - HCP Fe, 99, 103
    - interactions, 171-73, 175
    - thin films, 265
  - final state symmetry, 71
  - fluence, threshold, 260
  - Fresnel equation, 234
  - g-factor, 199
  - GaAs
    - (001), 151
    - (110), 193-94
    - Ge-buffered (110) GaAs, 111
    - substrates (110), 283
    - ( $\bar{1}\bar{1}\bar{1}$ ) surfaces, 203
  - garnet ferrite films, 265
  - Gd
    - 5d bands, 71
    - Gd<sub>4</sub>Bi<sub>3</sub>, 289
  - giant ferrimagnet, 96
  - grazing incidence, 235, 237
  - HCP-FCC transition, 283
  - heterostructures, 17, 129
  - hexagonal close packed (HCP), 99
  - Ho, 205
  - hyperfine fields, 17-18, 243-47
    - distribution, 89
  - hysteresis, 103
    - loops, 114
  - in-situ techniques, 177
  - interaction
    - band electron-magnetic ion, 151
    - crystallographic, interface, 29
  - interface
    - anisotropy, 105, 271
      - energy, 127
    - atomically flat, 125
    - roughness, 115, 234
  - intermixing, 91
  - inverse photoemission spin
    - polarized, 65
  - kinematic theory, 237
  - LaF<sub>3</sub>
    - films, 203
    - LaF<sub>3</sub>/Er/Dy/Er/LaF<sub>3</sub>/GaAs, 277
  - Landau-Ginzburg model, 265
  - Landau-Lifshitz equation of motion, 181
  - laser ablation deposition, 259
  - magnetic
    - domains, 213
    - easy direction, 87-98
    - inhomogeneity, 265
    - microstructure, 49
    - ordering, 141
    - properties, 46, 102, 199
    - relaxation, 23
    - reorientation phase
      - transition (MRPT), 222-23
    - resonance, 23
    - specific heat, 225
    - x-ray scattering, 232
  - magnetic anisotropy, 105, 111, 177, 199, 219-20, 243, 283
  - magnetism, 129
  - magnetization, 117, 271
    - direction, 95
    - imaging, high resolution, 49
    - saturation, 126, 199
    - soft, 29
  - magnetocrystalline anisotropy, 287
  - magneto-optics, 141, 151
    - Kerr effect, 178
  - magnetorefectivity, 152

- properties, 151
- recording media, 88
- magnetoresistance, 43, 45-46, 48
- magnetostatic spin waves, 199
- mechanical velocity filter, 262
- metals, 3d bands, 93, 99, 123
- metastable, 141
  - phases, 99, 152, 271
  - structures, 283
- microcrystalline films, 271
- microstructure, 105, 231
- MnSe, 141
- MnTe, 141
- molecular beam epitaxy (MBE), 11, 17, 100, 111, 141, 151, 177, 277, 283
- Mössbauer spectroscopy, 11, 17-18, 89, 100, 103
- multilayers and multilayered films, 46, 87, 117, 123, 236
- periodic multilayers, 236
- multi-domain resonance, 189
- nanocrystals, 253
- negative diffusion, 92
- neutron
  - diffraction, 88
  - scattering, 131
- Ni
  - lattice transformation, 177
  - (110) surface, 59
- nuclear magnetic resonance (NMR), 245
- orientation, 105
- oscillatory potentials, 285
- particle elimination, 261
- Pd, Pd/Fe, 199
- penetration depths, 233
- perpendicular
  - anisotropy, 87, 111, 123, 177
  - easy axis, 287
- photoluminescence, 152
- polycrystal, 105
- quantum structures and wells, 141
- rare earth, 93, 277
  - alloys, 253
  - metals, 205
- reflection
  - high energy electron diffraction (RHEED), 12, 17, 100, 112, 178, 284
  - loss fine structure (REELFS), 178
  - total external, 233
- residual resistance, 289
- resonant photoemission, 71
- RKKY, 171-174
- roughness factor, 234
- Ru, 99
- scanning
  - electron microscopy (SEM), 49
  - polarization analysis, 49
  - tunneling microscopy (STM), 49, 193-194, 197
- semiconductors, 151
- short range order, 231
- smoothing of layers, 105
- spectral brightness, 234
- specular reflectivity, 234
- spin
  - anisotropy, 3
  - filter effect, 167
  - glass, 132, 171-72, 174-75
  - magnetostatic spin waves, 199
  - polarized
    - cascade electron spectroscopy, 77
    - electrons, 49
    - inverse photoemission, 65
    - resolved tunneling, 167
  - waves, 199
- spiral domain structures, 265
- splashing effect, 261
- sp-d exchange, see exchange, 129
- SQUID magnetometer, 88, 111
- stability, 249
- stacking sequence, 285
- strain, 277
  - coherency, long-range, 203
  - out-of-plane, 238
- structural deformation, Co
  - layers from cubic to tetragonal, 105
- superlattices, 11, 43-44, 123, 129
- surface
  - anisotropy, 123, 177
  - large pinning, 186
  - sensitivity, 237
- synchrotron radiation, 231
- TbFe films, 249
- TbFeCo films, 253
- temperature, influence on
  - magnetic anisotropy, 3
- theory
  - anisotropy, 3
  - exchange-coupled magnetic bilayers, 183
  - magnetic inhomogeneities, 265
  - spiral domain structures, 265

- transition
  - amorphous to crystalline, 89
  - hcp-fcc, 283
  - magnetic reorientation, 222-23
  - metals, 48
- transmission electron microscopy (TEM), 124, 152, 271
  - high resolution, 111
- tricritical points, 265
- tunnel junctions, EuS barriers, 167
- tunneling, spin resolved, 167
- ultrathin films, 23, 77, 177
  - Co layers, 283
  - surface magnetism, 77
- ultra-high vacuum (UHV), 123
  - deposition, 87
- uniaxial
  - anisotropy, 35, 177
  - ferromagnetic thin film, 265
- Van Vleck paramagnet, 157
- vapour deposition in UHV, 105
- velocity
  - distribution, 259
  - filter, 259
- vibrating sample magnetometer (VSM), 124
- virtual crystal approximation, 154
- volume
  - anisotropy, 128
  - contribution, 105
- w-scan, 237
- x-ray
  - diffraction (XRD), 88, 101, 105, 124, 271, 277, 289
  - diffuse scattering, 283
  - photoelectron (XPS), 178
  - rocking curve, 156, 238
  - scattering, 111, 231
- Zeeman splitting, 157
  - enhanced, 167
  - (Zn,Co)Se, 151
  - $\text{Zn}_{1-x}\text{Co}_x\text{Se}$ , 151
  - (Zn,Fe)Se, 151
  - $\text{Zn}_{1-x}\text{Fe}_x\text{Se}$ , 151